

# The Interplay of Surfactant-Free Mesoscopic Structuring and (Bio-)Catalysis in Water

## Dissertation

zur Erlangung des Grades  
Doktor der Naturwissenschaften (Dr. rer. nat.)  
der Naturwissenschaftlichen Fakultät  
Chemie und Pharmazie  
Universität Regensburg



vorgelegt von

**Evamaria Hofmann**

aus Teisendorf

Mai 2023





The experimental work for this thesis was performed from November 2019 until April 2023 in the working group of Prof. Dr. Werner Kunz at the Institute of Physical Chemistry II (Department of Chemistry, University of Regensburg UR). Besides, experiments were conducted at the Institute of Organic Chemistry (Prof. Dr. Burkhard König, UR), at the Institute of Physical Chemistry I (Prof. Dr. Patrick Nürnberger, UR), and at the Institute of Pharmaceutical Biology (Prof. Dr. Jörg Heilmann, UR).

Official Registration: 24.05.2023

Defense: 31.07.2023

Ph.D. Supervisor: Prof. Dr. Werner Kunz

1<sup>st</sup> Examiner: Prof. Dr. Werner Kunz

2<sup>nd</sup> Examiner: Prof. Dr. Jean-Marie Aubry (emeritus)

Further examiner: Prof. Dr. Frank-Michael Matysik

Chair: Prof. Dr. Oliver Tepner



## Acknowledgment

First and foremost, I would like to express my sincere gratitude to my supervisor Prof. Dr. Werner Kunz for providing me the opportunity to do my doctoral thesis on a very fascinating and multifarious topic. His mentoring offered advice whenever required and, concurrently, the freedom to find my own path into research. Without his continuous incentive, the Ph.D. period would not have brought me the same professional and personal development.

Special thanks go to the *Fonds der Chemischen Industrie* for the well-paid Kekulé scholarship for two years and the University of Regensburg for the subsequent scholarship as part of the Bavarian program to realize equal opportunities for women in research and teaching.

I thank Prof. Dr. Jean-Marie Aubry, Prof. Dr. Frank-Michael Matysik, and Prof. Dr. Oliver Tepner for completing the board of examiners.

I deeply thank Dr. Didier Touraud, who has always been a second mentor, for countless discussions, advice, and ideas and for my daily French training. Many thanks belong to Dr. Fabrice Gallou and Prof. Dr. Burkhard König for the fruitful collaborations and their support. In this context, I thank Dr. Ya-Ming Tian for the joint projects and Regina Hoheisel for the experimental support. I also thank the group of Prof. Dr. Jörg Heilmann for the instruction and measuring time in their laboratories. Moreover, I thank Prof. Dr. Richard Buchner for patiently introducing me to the world of DRS.

Cordial thanks belong to my office colleagues Dr. Johannes Mehringer, Dominik Zahnweh, Lea Rohr, and Lena Schmauser for the always joyful and supportive atmosphere. Some very special thanks go to Johannes for turning even the pandemic years into a great time at the lab and to Lena for her support as part of her master's thesis and beyond.

Furthermore, I thank all the students who contributed to this work, namely Aysa Yelboga, Benedict Hofmann, David Rippert, Emily Gross, Karina Heilmeier, Lisa Tetek, Melissa Janesch, and Michael Schmidt. I thank Julia Neugebauer and Anna Mändl, who conducted a variety of experiments during their work at our institute.

Of course, I want to thank all my colleagues and friends for the wonderful atmosphere in our group: Adrien Fusina, Bastian Rödig, Dr. Eva Müller, Florian Kerkel, Manuel Rothe, Marcel Flemming, Maximilian Nützl, Moritz Köglmaier, Nadja Ulmann, Dr. Pierre E. L. Degot, Apl. Prof. Dr. Rainer Müller, Selina Reigl, Dr. Sergej Friesen, Dr. Simon Stemplinger, Dr. Sophia Sokolov, Dr. Theresa Höß, Vanessa Rudolph, Dr. Verena Huber, and Patrick Denk. I deeply thank Dr. Philipp Schmid and Jonas Blahnik, who accompanied my entire journey at the University and who supported and enriched me professionally and personally.

I thank Bianca Frömel, Rosemarie Röhrl, Franziska Wolf, Hellmuth Schönsteiner, Theresa Ferstl, and Dr. Peter Karageorgiev, who always managed all necessities.

Obviously, I thank my furry colleague Ylvi for the sportive compensation of my work-work balance and her emotional support during the last months.

Lastly, I would like to express my deep gratitude toward my family and close friends. In particular, I thank my parents, Gabriele and Heinrich Hofmann, for their tireless support and understanding, which made all this possible.

**THANK YOU! MERCI!**

## Abstract

In this dissertation, the effect of mesoscopic structuring in surfactant-free microemulsions (SFMEs) on organic reactions has been investigated. The work includes the characterization of different solvent systems as well as the performance and analysis of different reaction types with relevance for industrial applications. Micellar and unstructured solutions are considered to interpret the influence of the presence of an interface on the reactions. Besides the impact of solvent structuring, the focus is on the selection of sustainable systems.

In the first chapter, the photochemical synthesis of flavors from plant material is investigated in food-grade solvent systems. It is found that the presence of an interface does not give a competitive edge but that the great extraction and solubilization power of an SFME can be advantageous. In order to gain more information on the relevance of an interface, reactions reported in aqueous micellar solutions are investigated. Hence, the second chapter considers a cascade reaction combining chemo- and biocatalysis. The successful transfer to both SFMEs and unstructured solvents demonstrates once more that the mesoscopic interface is not the crucial parameter. Rather the solubilization and stabilization of the reactant components are the key points. The same is observed in the third chapter, which deals with the replacement of a micellar solvent in a 1,4-addition reaction by binary and ternary mixtures with different extent of solvent structuring. In the fourth chapter, cross-coupling reactions are performed in water using the green additive meglumine as a solubilizer and activator. Moreover, a promising organic photocatalyst is dissolved in water by means of the additive. The fifth chapter presents the idea and initial promising experiments on the optimization of the properties of a photocatalyst by mesoscopic interfaces.

The last two chapters do not directly deal with reactions but with topics that are generally relevant for their optimization. The sixth chapter describes the detailed investigation of binary solvent mixtures, which exhibit significant solubilization power. For this purpose, COSMO-RS-based predictions are combined with scattering and dielectric relaxation spectroscopy experiments. In the seventh chapter, ternary phase diagrams are predicted by means of COSMO-RS calculations. In addition to the predictions of critical points and tie lines, a method is suggested for predicting the compositions of mesoscopic structuring.

## Zusammenfassung

Im Rahmen dieser Dissertation, wird der Einfluss mesoskopischer Strukturierung in Tensidfreien Mikroemulsionen (TFME) auf organische Reaktionen untersucht. Die Arbeit beinhaltet die Charakterisierung verschiedener Lösungsmittelsysteme sowie die Durchführung und Analyse verschiedener Reaktionstypen mit Relevanz für industrielle Anwendungen. Zur Interpretation des Einflusses von Grenzflächen werden auch mizellare und unstrukturierte Lösungen herangezogen. Neben dem Einfluss der Strukturierung von Lösungsmitteln liegt der Fokus auf der Wahl nachhaltiger Systeme.

Im ersten Kapitel wird die photochemische Synthese von Aromen aus Pflanzenmaterial untersucht. Es stellt sich heraus, dass eine Grenzfläche keinen entscheidenden Vorteil bringt. Dahingegen können sich die besonderen Extraktions- und Solubilisierungs-Eigenschaften von TFMEs als vorteilhaft erweisen. Um genauere Informationen über die Relevanz von Grenzflächen zu erhalten, werden Reaktionen untersucht, die bereits in mizellaren Lösungen durchgeführt wurden. Im zweiten Kapitel werden daher die Kopplung von Übergangsmetall- und Biokatalyse betrachtet. Die erfolgreiche Überführung in sowohl TFME als auch unstrukturierte Lösungen zeigt erneut, dass mesoskopische Grenzflächen nicht den entscheidenden Parameter darstellen. Vielmehr ist es eine Frage von Lösen und Stabilisieren der Reaktionskomponenten. Gleiches ist im dritten Kapitel zu beobachten, das sich mit dem Ersetzen von mizellaren Lösungen in 1,4-Additionsreaktionen durch binäre und ternäre Mischungen unterschiedlich starker Strukturierung beschäftigt. Im vierten Kapitel werden Kreuzkopplungen in Wasser durchgeführt, unter Verwendung des grünen Additivs Meglumin. Meglumin dient dabei sowohl als Lösungsvermittler als auch als Aktivator. Zudem wird ein vielversprechender organischer Photokatalysator durch das Additiv in Wasser gelöst. Das fünfte Kapitel zeigt die Idee auf, die Eigenschaften eines Photokatalysators durch mesoskopische Grenzflächen zu optimieren. Erste vielversprechende experimentelle Ergebnisse werden diskutiert. Die letzten beiden Kapitel behandeln keine Reaktionen, aber Themen, die ganz allgemein für deren Optimierung relevant sind. Das sechste Kapitel beschreibt detaillierte Untersuchungen binärer Lösungsmittelmischungen, die eine ausgeprägte Solubilisierungskraft aufweisen. Zu diesem Zweck werden Vorhersagen basierend auf dem COSMO-RS-Modell mit Lichtstreuung und dielektrischer Relaxationsspektroskopie kombiniert. Im siebten Kapitel werden ternäre Phasendiagramme mithilfe von COSMO-RS vorhergesagt. Neben der Vorhersage von kritischen Punkten und Konoden wird eine Methode zur Vorhersage der Lage von mesoskopischen Strukturen im Phasendiagramm vorgestellt.

## List of abbreviations

<b>1BuOH</b>	1-butanol	<b>DMSO-d<sub>6</sub></b>	deuterated dimethyl sulfoxide
<b>2M2P</b>	2-methyl-2-pentanol	<b>DPnP</b>	di(propylene glycol) n-propyl ether
<b>μE</b>	microemulsion	<b>DRS</b>	dielectric relaxation spectroscopy
<b>AcN</b>	acetonitrile	<b>EDA</b>	electron donor-acceptor
<b>ADH</b>	alcohol dehydrogenase	<b>EHA</b>	2-ethylhexyl acrylate
<b>ANS</b>	8-anilino-1-naphthalene- sulfonic acid	<b>EI</b>	electron ionization
<b>APCI</b>	atmospheric pressure chemical ionization	<b>equiv.</b>	equivalent
<b>aq.</b>	aqueous	<b>ESI</b>	electrospray ionization
<b>BA</b>	benzyl alcohol	<b>ET</b>	electron transfer
<b>BIC</b>	bicontinuous structuring	<b>EtOAc</b>	ethyl acetate
<b>BINAP</b>	2,2'-bis(diphenylphosphino)- 1,1'-binaphthyl	<b>EtOH</b>	ethanol
<b>BM</b>	binary mixture	<b>FA</b>	ferulic acid
<b>C I</b>	curcumin I	<b>GC</b>	gas chromatography
<b>C II</b>	curcumin II	<b>HM</b>	hydrotrope mixture
<b>C III</b>	curcumin III	<b>HPLC</b>	high-performance liquid chromatography
<b>c. c.</b>	correlation coefficient	<b>HSQC</b>	heteronuclear single quantum coherence spectroscopy
<b>CC</b>	Cole-Cole	<b>iAAIc</b>	isoamyl alcohol
<b>cmc</b>	critical micelle concentration	<b>IPA</b>	isopropanol
<b>cat</b>	catalyst	<b>ISC</b>	intersystem crossing
<b>ChoAc</b>	choline acetate	<b>LCST</b>	lower critical solution temperature
<b>conPET</b>	consecutive photoinduced electron transfer	<b>LLE</b>	liquid-liquid equilibria
<b>COSMO-RS</b>	conductor-like screening model for real solvents	<b>MA</b>	methyl acrylate
<b>CP</b>	critical point	<b>MBA</b>	4-methoxybenzyl alcohol
<b>CPU</b>	central processing unit	<b>MBAId</b>	4-methoxybenzyl aldehyde
<b>CV</b>	cyclic voltammetry	<b>MMA</b>	methyl methacrylate
<b>D</b>	Debye	<b>MS</b>	mass spectrometry
<b>DCM</b>	dichloromethane	<b>NADPH</b>	β-nicotinamide adenine dinucleo- tide phosphate sodium salt hydrate
<b>dept</b>	distortionless enhancement by polarization transfer	<b>NDI</b>	1,8:4,5-naphthalenetetracar- boxdiimide
<b>DLS</b>	dynamic light scattering	<b>NMR</b>	nuclear magnetic resonance
<b>DMF</b>	N,N-dimethylformamide	<b>NPA</b>	n-propanol
<b>DMSO</b>	dimethyl sulfoxide	<b>o/w</b>	oil-in-water
		<b>PBS</b>	phosphate-buffered saline

<b>PC</b>	photocatalyst
<b>p-HBA</b>	p-hydroxybenzaldehyde
<b>PQS</b>	polyethylene glycol ubiquinol sebacate
<b>PQY</b>	product quantum yield
<b>PT</b>	proton transfer
<b>PTFE</b>	polytetrafluoroethylene
<b>RF</b>	riboflavin
<b>RMSD</b>	root-mean-square deviation
<b>s.o.s.</b>	self-organizing-system
<b>SBME</b>	surfactant-based microemulsion
<b>SCE</b>	saturated calomel electrode
<b>SEC</b>	spectroelectrochemistry
<b>SFME</b>	surfactant-free microemulsion
<b>SPentS</b>	sodium 1-pentanesulfonate
<b>SWAXS</b>	small-and-wide-angle X-ray scattering
<b>SXS</b>	sodium xylenesulfonate
<b>TARF</b>	tetraacetyl riboflavin
<b>tBuOH</b>	t-butanol
<b>TCSPC</b>	time-correlated single photon counting
<b>TEA</b>	triethylamine
<b>THC</b>	tetrahydrocurcumin
<b>THF</b>	tetrahydrofuran
<b>THL</b>	tetrahydro linalool
<b>TLC</b>	thin layer chromatography
<b>TM</b>	ternary mixture
<b>TPA</b>	tetrapropylammonium bromide
<b>TPGS-750-M</b>	DL- $\alpha$ -tocopherol methoxypolyeth- ylene glycol succinate
<b>TriA</b>	triacetin
<b>UV</b>	ultraviolet
<b>VIS</b>	visible light
<b>W</b>	water
<b>w/o</b>	water-in-oil

## Contents

Acknowledgment .....	IV
Abstract .....	VI
Zusammenfassung .....	VII
List of abbreviations.....	VIII
Chapter 0 Prologue.....	1
0.1 Introduction.....	1
0.2 (Bio-)Catalysis in aqueous, structured solutions – State of the art.....	3
0.3 Goals of this research.....	5
0.4 Fundamentals and methodology .....	6
0.5 References .....	10
Chapter 1 Novel green production of natural-like vanilla extract from curcuminoids....	21
1.0 Abstract .....	21
1.1 Introduction.....	22
1.2 Material and methods .....	25
1.3 Results and discussion .....	27
1.4 Conclusion and outlook .....	34
1.5 Supporting information.....	36
1.6 References .....	54
Chapter 2 Sustainable cascade reaction combining transition metal-biocatalysis and hydrophobic substrates in surfactant-free aqueous solutions .....	59
2.0 Abstract .....	59
2.1 Introduction.....	60
2.2 Material and methods .....	63
2.3 Results and discussion .....	66
2.4 Conclusion and outlook .....	75
2.5 Supporting information.....	77
2.6 References .....	109

Chapter 3	1,4-Addition of 3-bromophenylboronic acid to $\alpha,\beta$ -unsaturated cyclohexenone in surfactant-free aqueous solutions.....	115
3.0	Abstract.....	115
3.1	Introduction.....	116
3.2	Material and methods.....	118
3.3	Results and discussion.....	121
3.4	Conclusion and outlook.....	130
3.5	Supporting information .....	132
3.6	References.....	154
Chapter 4	The role of meglumine in aqueous cross-coupling reactions: Anti-stacking agent and solubilizer for substrates and the photocatalyst 1,8:4,5-naphthalenetetracarboxdiimide.....	159
4.0	Abstract.....	159
4.1	Introduction.....	161
4.2	Material and methods.....	163
4.3	Results and discussion.....	166
4.4	Conclusion and outlook.....	184
4.5	Supporting information .....	186
4.6	References.....	206
Chapter 5	Overcoming the unproductive singlet-born radical reaction in the flavin-catalyzed photooxidation of 4-methoxybenzyl alcohol by solvent structuring.....	211
5.0	Abstract.....	211
5.1	Introduction.....	212
5.2	Material and methods.....	215
5.3	Results and discussion.....	218
5.4	Conclusion and outlook.....	227
5.5	Supporting information .....	229
5.6	References.....	233

Chapter 6	In-depth study of binary ethanol-triacetin mixtures in relation with their excellent solubilization power.....	237
6.0	Abstract .....	237
6.1	Introduction.....	238
6.2	Material and methods .....	240
6.3	Results and discussion .....	243
6.4	Conclusion and outlook .....	250
6.5	Supporting information.....	252
6.6	References .....	259
Chapter 7	The application of the theoretical COSMO-RS model for predicting ternary phase diagrams.....	265
7.0	Abstract .....	265
7.1	Introduction.....	266
7.2	Material and methods .....	269
7.3	Results and discussion .....	272
7.4	Conclusion and outlook .....	282
7.5	Supporting information.....	284
7.6	References .....	290
Chapter 8	Epilogue .....	295
	Conclusion and outlook.....	295
	List of publications .....	302
	Declaration in lieu of oath.....	303
	Eidesstattliche Erklärung.....	304

## Chapter 0 Prologue

### 0.1 Introduction

Synthetic chemistry allows the creation of value-added products, which significantly contributes to the overall quality of life. For economic, energy-saving, and environmentally benign productions, catalysis plays a crucial role. Hence, catalytic processes are applied for 80 % of the chemicals produced worldwide.<sup>1,2</sup> As a cheap and sustainable solvent, water is attracting more and more attention as a potential reaction solvent. In this context, structured aqueous solutions are often considered due to their interesting features.<sup>3</sup> In the following, a brief description of the structured systems discussed in this work is provided.

A well-studied structured system applied for reactions is given by micellar solutions. Long-chain amphiphilic molecules, so-called surfactants, can shape spherical aggregates (direct micelles) in water, which results in the formation of a hydrophobic core (see Figure 0 - 1). Unlike in the absence of an amphiphile, the addition of oil does not necessarily result in macroscopic phase separation. Rather, the oil is solubilized in the micellar hydrophobic core, forming a transparent, thermodynamically stable oil-in-water microemulsion (o/w  $\mu$ E).<sup>3-5</sup>

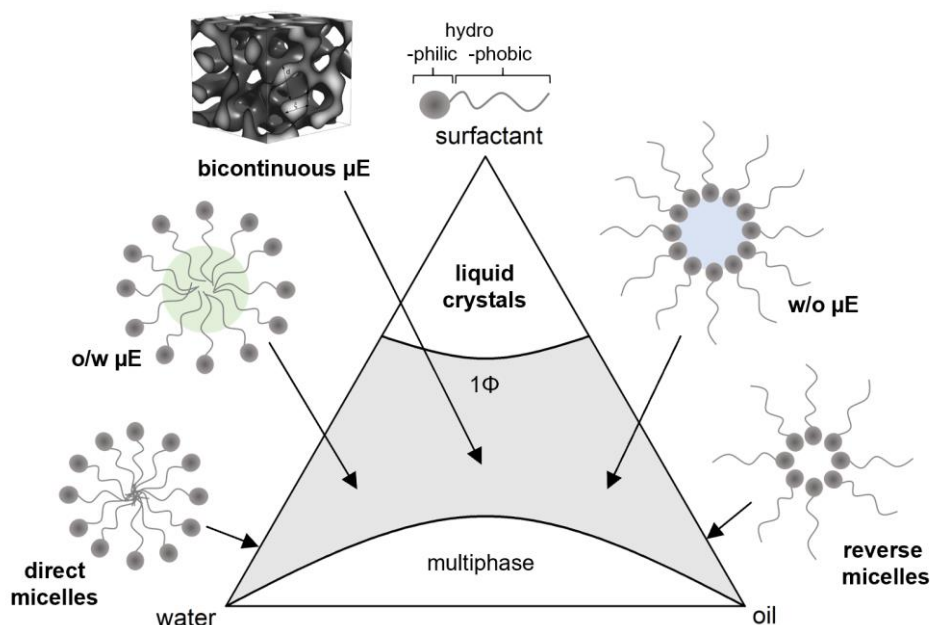


Figure 0 - 1: Schematic illustration of a ternary phase diagram of water, surfactant, and oil with the corresponding mesoscopic structuring: direct micelles, oil-in-water microemulsion (o/w  $\mu$ E), bicontinuous microemulsion (bicontinuous  $\mu$ E), water-in-oil microemulsion (w/o  $\mu$ E), and reverse micelles. The figure is inspired by the work of Krickl.<sup>6</sup> In addition, the 3D representation of the bicontinuous  $\mu$ E is taken from Mihalescu et al. and reprinted with the permission of AIP Publishing.<sup>7</sup>

The same is observed for water-in-oil microemulsions (w/o  $\mu$ E) containing reversed micelles. In the transition from o/w to w/o  $\mu$ E, three-dimensional sponge-like structures (bicontinuous  $\mu$ E) are present. Thus, depending on the composition of the components, different mesoscopic structures ( $\sim$  5-100 nm) are formed in ternary systems of water, surfactant, and oil. Although surfactants strongly tend to go to the oil-water interface, the structures experience a dynamic exchange of surfactant molecules between the interface and the outer pseudo-phase. The swollen micelles can even dissolve and reform again. Typically, the processes occur within  $\mu$ s to ms.<sup>5,6,8–10</sup>

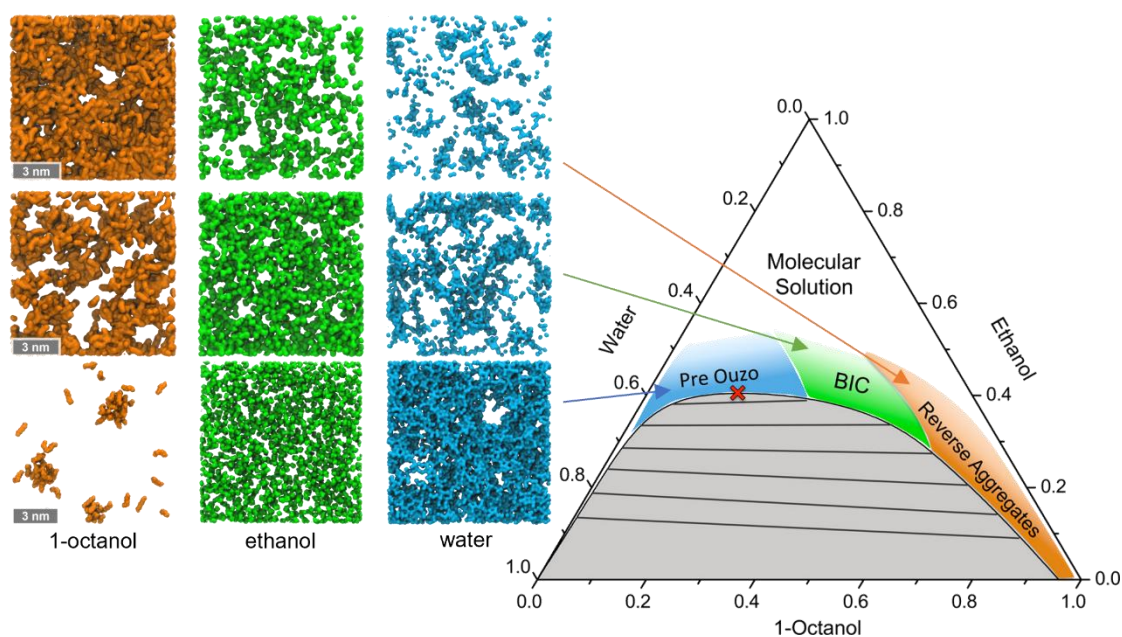


Figure 0 - 2: Ternary phase diagram of water, ethanol, and 1-octanol with snapshots of the molecular distribution in the three mesoscopic structured regions (pre ouzo (oil-in-water), bicontinuous (BIC) and reverse aggregates (water-in-oil)). The figure is taken from Lopian et al., modified in its representation, and reprinted with permission of ACS.<sup>11</sup>

In industry, micellar solutions and microemulsions find several applications, including enhanced oil recovery, cleaning, cosmetics, and syntheses - to mention just a few.<sup>12</sup> However, the surfactants' strong tendency to adsorb at interfaces can raise problems, such as foaming, complicated recycling, poor biodegradability, and (eco)toxicity.<sup>6</sup> For this reason, surfactant-free microemulsions (SFMEs) have received increasing attention in recent decades.<sup>13–15</sup> In SFMEs, the amphiphilic molecule is represented by a hydrotrope. Contrary to long-chain surfactants, short-chain hydrotropes are only weakly amphiphilic, commonly better biodegradable, and less foaming. Some hydrotropes, such as t-butanol, pre-aggregate in three water, however, the aggregates are rather loose accumulations than micellar-like defined structures. The addition of an oil enforces or induces mesoscopic structuring (see Figure 0 - 2).<sup>6,16,17</sup> As it is the case for surfactant-based microemulsions (SBMEs), o/w  $\mu$ E (pre ouzo region), bicontinuous structuring (BIC), and w/o  $\mu$ E (reverse aggregates) can be distinguished. The aggregates are expected to be at least  $10^3$  times more dynamic than

micellar aggregates and are a few nanometers up to ~ 100 nm in size.<sup>6,11,18,19</sup> As it is shown by the snapshots in Figure 0 - 2, the hydrotrope is less pronounced to accumulate at the interface and, therefore, also distributed over the pseudo-phases.<sup>6,11,18</sup> Overall, larger amounts of the amphiphile are required to close the miscibility gap compared to surfactant-based systems. Nevertheless, recovery of the individual components is facilitated, in particular for volatile hydrotropes like short-chain alcohols. Moreover, phase separation can be induced easily by the addition of water and oil, respectively, or the cleavage of components by changes in temperature and/or pH.<sup>6,20</sup> Consequently, SFMEs exhibit potential for usage in extractions, reactions, and in general for the solubilization of poorly water-soluble substances like drugs.<sup>6,13,21–23</sup>

## 0.2 (Bio-)Catalysis in aqueous, structured solutions – State of the art

A well-known application of mesoscopic structured solutions is their usage as reaction solvents in biocatalysis.<sup>24–31</sup> Martinek *et al.* pioneered the field with their research in solutions of hydrated reverse micelles in the year 1977.<sup>26,27,30,32</sup> In SBME, a hydrophilic enzyme is entrapped in an aqueous pseudo-phase within reverse micelles, which are dispersed in a continuous oil medium. The so built nanoreactors protect the enzyme against denaturation by the non-aqueous solvent, while improving the solubility of hydrophobic substrates. Surface-active enzymes can be localized at the micellar interface. The surface-active lipases are most commonly studied in microemulsions due to their great stability and activity in these systems.<sup>24,27,29–31,33</sup> In the structured solvents, enzyme activities greater than in pure aqueous buffer solutions are reported. This so-called superactivity is explained by conformational changes of the entrapped enzyme, the state of the micellar water, and/or an ionic effect of the surfactant head groups.<sup>25,31,34,35</sup> In 1987, Khmel'nitsky presented the SFME system of water, isopropanol, and hexane as a suitable reaction solvent for biocatalytic reactions.<sup>36</sup> In the following years, several publications documented the successful performance of enzymatic reactions in SFMEs.<sup>21,37–47</sup> Accordingly, the less defined and more dynamic aggregations are sufficient to maintain the stability and catalytic activity of an enzyme. However, to our knowledge, no superactivity has been reported in SFMEs so far. Most of the systems published are composed of water, a short-chain alcohol such as 1-propanol, isopropanol, and t-butanol, and an oil. Product isolation is thus facilitated compared to the surfactant-based systems.<sup>6,31,36,41</sup>

Another interesting application of structured solvents is given by the template syntheses of polymers and nanoparticles.<sup>48,49</sup> Hydrophobic monomers can be dissolved in the core of

micelle-like aggregates, forming an o/w  $\mu$ E. The compartmentation thus allows size control during a polymerization process, which results in a narrow size distribution.<sup>49,50</sup> Furthermore, the size and shape of nanoparticles are controllable during syntheses in the droplets of a microemulsion.<sup>48</sup> Due to the described drawbacks of surfactants, surfactant-free systems are attracting more and more attention in this field as well. However, there are currently only a few publications on the synthesis of both polymers and nanoparticles in SFMEs, although initial publications have already provided the proof of concept.<sup>51–54</sup>

Furthermore, structured solutions are more and more applied as reaction solvent for organic cross-coupling reactions.<sup>55–57</sup> In general, cross-coupling reactions are widespread in industry, including pharmaceutical, agrochemical, and fine chemical industry. The synthesis of many chemicals and products thus involves coupling reaction steps, which explains its prominent role in both industry and research.<sup>58–60</sup> Commonly, these reactions are carried out in organic solvents. In order to transfer the reactions to water despite poor water solubility of several substrates and catalysts, micellar solutions are often the method of choice.<sup>55–57,61</sup> Besides the enhancement of solubilities, the reaction rate and reactivity can be improved as a result of the compartmentation of the reactants. The reduction of dimensionality can also positively affect the reaction selectivity.<sup>57,62</sup> Lipshutz and co-workers have contributed significantly to this field of research in recent years. They develop designer surfactants suitable for micellar catalysis in water.<sup>61,63–66</sup> In particular the surfactant DL- $\alpha$ -tocopherol methoxypolyethylene glycol succinate (TPGS-750-M, discussed in Chapters 2, 3) has proven its applicability regarding aqueous cross-coupling reactions in several publications.<sup>63,67–71</sup> The surfactant is declared to be environmental benign. In addition, to overcome technical issues arising from the general foaming properties of surfactants, the low-foaming designer surfactant Coolade has been developed.<sup>63,64</sup> Lipshutz *et al.* demonstrated that the synthesis of designer surfactants can eliminate common issues connected to the usage of surfactants, such as poor biodegradability and foaming.<sup>63,64</sup> Nevertheless, the synthesis of the complex surfactants appear to be laborious and includes the usage of harmful chemicals.<sup>63,64,66</sup> Moreover, the great affinity for interfaces and surfaces may cause problems during the processing, even when foaming is reduced. The substitution with surfactant-free solutions, hence, seems to be beneficial. However, to the best of our knowledge, no successful organic cross-coupling reactions have been reported in SFMEs yet. The same is observed for photocatalytic conversions. Krickl *et al.* compared the photocatalytic oxidation of benzyl alcohol in surfactant-free solutions with different extends of structuring. The studies revealed a negative impact of the compartmentation in the SFME, which seems to separate the catalyst from the substrate.<sup>72</sup> In micellar solutions, successful photocatalytic transformations are reported.<sup>62,73,74</sup>

The research in surfactant-based systems goes even further, combining chemo- and biocatalysis in one pot. Several of these cascade reactions are reported in aqueous micellar solutions. Especially the already mentioned designer surfactant TPGS-750-M is frequently applied for this purpose. So far, mainly transition metal-catalyzed reactions are coupled with enzyme-catalyzed reactions.<sup>65,75–81</sup> Here, metal catalysts can denature enzymes. Accordingly, in addition to the aforementioned advantages, the structuring allows protection of the enzyme from denaturation by the components of the chemocatalytic step.<sup>76,82</sup> The literature on photocatalysis coupled with biocatalysis in aqueous solution is currently rather limited but existent.<sup>83–88</sup> To our knowledge, there are no photoenzymatic cascade reactions reported in micellar solutions. This is attributed to the novelty of this field. Furthermore, no literature is found on cascade reactions in aqueous SFMEs, which is reasonable due to the lack of work on organic reactions in these systems. The reported photocatalytic reactions performed in water in the absence of an amphiphile contain organic solvents such as dimethyl sulfoxide and acetonitrile.<sup>83–85</sup> Moreover, some reaction protocols included the usage of whole cells to achieve a compartmentalization required for enzyme protection from chemical reagents.<sup>86–88</sup>

### 0.3 Goals of this research

Based on the state of knowledge presented above, the following questions have arisen. Answering these questions is thus the aim of this work.

- ❖ Can micellar solutions, which are applied as an aqueous reaction solvent, be replaced by simple and green SFMEs? In this context, the leap from model-type reactions to challenging (organic) reactions relevant to the industry is made. Furthermore, the focus is on substituting expensive and complex designer surfactants.
- ❖ Which reaction types require which type of interface, and for what reason? Or beyond solvent structuring, what is decisive for the successful performance of organic reactions in water?
- ❖ Do SFMEs possess some unique advantages over micellar solvents with regard to organic reactions in water? The positive impact on the solvent recycling process appears rather evident, as is the usage of cheap and green compounds. But can the more dynamic interfaces also positively influence the reaction mechanism?
- ❖ Which promising industrial applications for SFMEs result from this in the synthetic chemistry?

In order to elucidate these questions, various topics are discussed, including different scopes as well as different measuring techniques. For this reason, each chapter is written independently from the others with individual Abstract, Introduction, Methods, Results and Discussion, Conclusion and Outlook, Supporting Information, and References.

## 0.4 Fundamentals and methodology

Explaining all of the methods applied in the different topics and collaborations would go too far. Dynamic light scattering (DLS) experiments represent the most commonly used method in this work to detect inhomogeneities in the solvents. In order to monitor the reaction outcome, nuclear magnetic resonance (NMR) spectroscopy is most frequently applied. Especially the heteronuclear single quantum coherence (HSQC) experiment is a valuable tool for quick product verification. For this reason, the methods are described in the following. Dielectric relaxation spectroscopy (DRS) and theoretical calculations based on the COSMO-RS model (COnductor-like Screening MOdel for Real Solvents) are not considered standard methods and are therefore discussed in the respective chapters. The same applies to the compounds, reactions, and associated issues presented in the chapters.

### 0.4.1 Dynamic light scattering

Dynamic light scattering (DLS) experiments enable the monitoring of particles and mesoscale inhomogeneities in solution.<sup>89–92</sup> As the name suggests, the method is based on light scattering, *i.e.*, the change of the direction of the photon through interaction with matter. Hence, the method is nondestructive and relatively rapid. Figure 0 - 3(a) illustrates a simplified experimental setup. The dispersed phase is presented by spherical particles.<sup>91,93</sup> A laser beam is focused with an approximated diameter of 0.1 mm on the sample, and the scattered photons are detected with time. The random motion of the particles induced by Brownian motion results in a time-dependent intensity of the scattered light (see Figure 0 - 3(b)). Besides the viscosity of the surrounding liquid, the diffusion of the particles is determined by their size and shape. For spherical, dilute particles, the relationship is given by the Stokes-Einstein equation (see Figure 0 - 3(c)).<sup>91,94,94</sup> As a consequence, DLS measurements enable the determination of the hydrodynamic radius of the dispersed particles, assuming a spherical shape. For this purpose, the autocorrelation function of the scattered intensity  $g^{(2)}(\tau)$  has to be determined, which is connected to the diffusion coefficient  $D$  (see Equation 0 – 1). The calculations consider the scattered intensity at an arbitrary time  $t$  ( $I(t)$ ) and the intensity after the lag time  $\tau$  ( $I(t + \tau)$ ).<sup>91,95</sup>

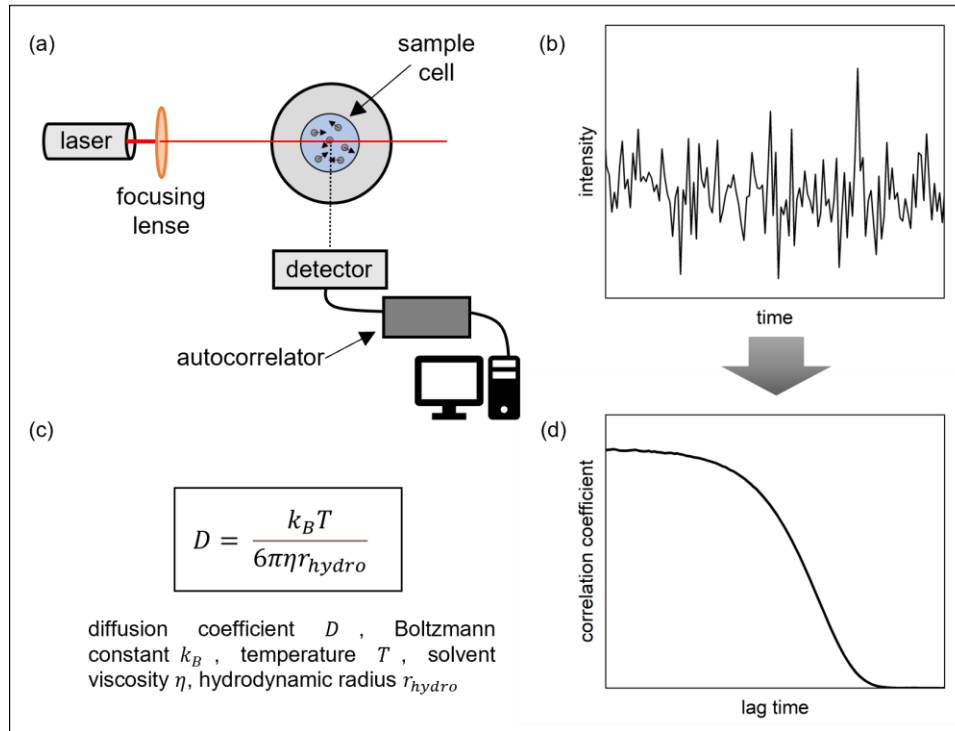


Figure 0 - 3: (a) Simplified representation of the experimental setup of DLS experiments, inspired by the cited literature.<sup>91</sup> (b) Detected intensity fluctuations with respect to the time of measurement. (c) The Stokes-Einstein equation.<sup>91</sup> (d) The determined correlation function.

$A$  describes the amplitude of the correlation function,  $B$  the baseline, and  $q$  the magnitude of the scattering vector with  $q = (4\pi n/\lambda) \sin(\theta/2)$ . The scattering vector thus depends on the refractive index of the medium  $n$ , the incident wavelength  $\lambda$ , and the scattering angle  $\theta$ . To ensure an observable light scattering, sufficient contrast has to be given, which is introduced by the difference between the refractive indices of the dispersed phase and the continuous medium. The intensity of the scattered light is directly proportional to this difference.<sup>6,95</sup>

$$g^{(2)}(\tau) = \frac{\langle I(t)I(t+\tau) \rangle}{\langle I(t) \rangle^2} = [A \exp(-Dq^2\tau) + B]^2 + 1 \quad \text{Eq. 0 - 1}$$

Buchecker<sup>16</sup> and Krickl<sup>41</sup> interpreted their DLS experiments in a more qualitative way. They assumed that a more pronounced mesoscopic structuring is indicated by a higher intercept of the correlation function for small lag times as well as by larger lag times of the correlation function.<sup>16,41</sup> In this work, the DLS measurements are also evaluated qualitatively.

## 0.4.2 Nuclear magnetic resonance spectroscopy

Nuclear magnetic resonance (NMR) spectroscopy is a valuable tool applied in several disciplines, such as chemistry, physics, and biology.<sup>96</sup> The method convinces by a nondestructive and selective detection without extensive sample preparation.<sup>97,98</sup> The prerequisite for nuclei to be NMR active is an odd mass number or an odd atomic number, which is the case for both  $^1\text{H}$  and  $^{13}\text{C}$  nuclei. Applying an external magnetic field results in the alignment of the spin of such nuclei due to their inherent magnetic field. The spin can align either parallel ( $\alpha$ -spin, lower energy state) or antiparallel ( $\beta$ -spin, higher energy state) to the applied magnetic field. In the absence of the magnetic field, both states are equivalent, and therefore no excitation is possible. But the presence of the magnetic field allows absorbance of an appropriate radiofrequency radiation, turning an  $\alpha$ -spin into the  $\beta$ -spin. The resonance frequency, *i.e.*, the transition energy, of a nucleus detected in NMR experiments depends on its electronic environment. The resonance frequency shift (chemical shift), therefore, provides information on the present functional groups. Moreover, magnetic nuclei can interact with each other, inducing a specific splitting of the signal (J-coupling). Consequently, information on the molecular structure of a compound can be gathered from NMR experiments by considering the chemical shift in combination with the J-coupling.<sup>97,99,100</sup> Besides the qualitative information, quantitative information is accessible since NMR signals are proportional to the number of the corresponding nuclei. The wealth of information explains an enormous number of applications and thus publications.<sup>97,101–104</sup>

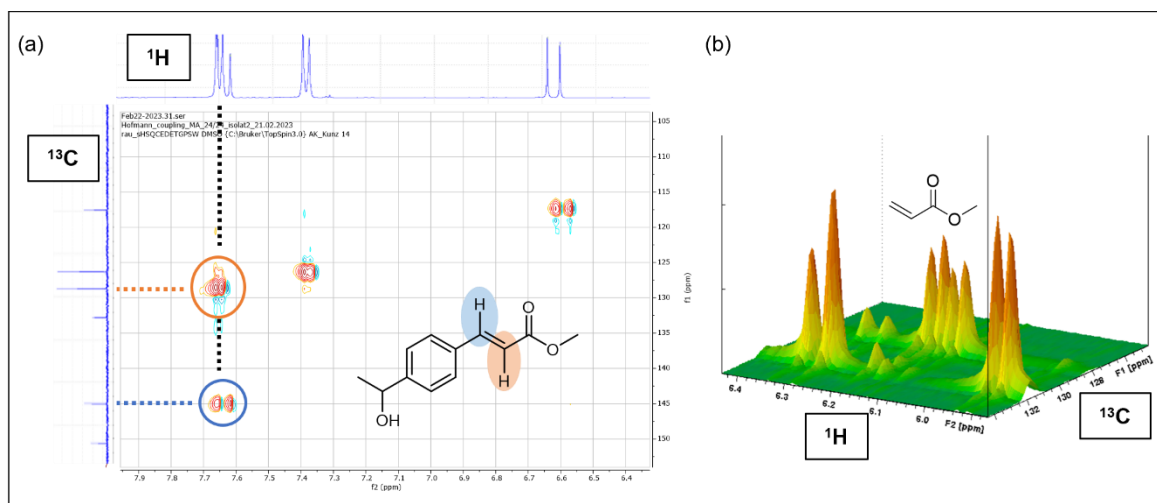


Figure 0 - 4: Exemplary illustration of HSQC-NMR spectra as contour plot (a) or 3D representation (b).

A problem arising particularly for larger molecules and mixtures is an increasing overlap of the signals in  $^1\text{H}$ -NMR spectra. In this case, 2-dimensional NMR experiments can provide the solution. The 2D NMR technique applied in this work is the heteronuclear single quantum coherence (HSQC) NMR. The method detects one-bond  $^{13}\text{C}$ - $^1\text{H}$  connectivity (see

Figure 0 - 4). Accordingly, only carbons directly bound to a proton are monitored, and vice versa. The second dimension allows for improved peak assignment and differentiation of peaks that overlap in the corresponding 1D  $^1\text{H}$ -NMR spectra. Complex organic molecules can be analyzed in this way. In the experiment, advantage is taken from the higher sensitivity of  $^1\text{H}$  compared to  $^{13}\text{C}$ . For this purpose,  $^1\text{H}$  is excited first, and the spin polarization is transferred to  $^{13}\text{C}$ . The  $^1\text{H}$  has a significantly higher natural abundance (99.985 %) than the  $^{13}\text{C}$  (1.108 %) and a greater magnetogyric ratio  $\gamma$ , which correlates with a higher energy difference between the spin levels and, thus, a greater difference in their population. Transferring the magnetization of the  $^1\text{H}$  to  $^{13}\text{C}$ , therefore, increases the sensitivity of the experiment. As shown in Equation 0 – 2, the sensitivity  $S$  depends on both the magnetogyric ratio of the excited nucleus  $\gamma_{ex}$  and of the detected nucleus  $\gamma_{det}$ .<sup>96,99,104</sup>

$$S \propto \gamma_{ex}\gamma_{det}^{3/2} \qquad \text{Eq. 0 - 2}$$

Accordingly, the spin polarization of the sensitive  $^1\text{H}$  is transferred to the insensitive  $^{13}\text{C}$ , and after performing the desired spin manipulations, a back-transfer follows to the  $^1\text{H}$  nuclei, which are detected (inverse technique). A more detailed description of the transfer and the pulse sequences is beyond the scope of this thesis, but further information can be found in the cited literature.<sup>96,99,104–106</sup>

## 0.5 References

- (1) Wohlgemuth, R. Biocatalysis — Key to Sustainable Industrial Chemistry. *Curr. Opin. Biotechnol.* **2010**, *21* (6), 713–724. <https://doi.org/10.1016/j.copbio.2010.09.016>.
- (2) Noyori, R. The Future of Chemistry. *Nat. Chem.* **2009**, *1*, 5–6. <https://doi.org/10.1038/nchem.139>.
- (3) Shen, T.; Zhou, S.; Ruan, J.; Chen, X.; Liu, X.; Ge, X.; Qian, C. Recent Advances on Micellar Catalysis in Water. *Adv. Colloid Interface Sci.* **2021**, *287*, 102299. <https://doi.org/10.1016/j.cis.2020.102299>.
- (4) Tartaro, G.; Mateos, H.; Schirone, D.; Angelico, R.; Palazzo, G. Microemulsion Microstructure(s): A Tutorial Review. *Nanomaterials* **2020**, *10* (9), 1657. <https://doi.org/10.3390/nano10091657>.
- (5) Evans, D. F.; Wennerström, H. *The Colloidal Domain: Where Physics, Chemistry, Biology, and Technology Meet*, Second.; Wiley-VCH Verlag: New York, 1999.
- (6) Krickl, S. Investigation of Potential Applications of Surfactant-Free Microemulsions - Solubilisation, Separation and Extraction Processes and Reaction Media, University of Regensburg, 2018. <https://doi.org/10.5283/epub.38134>.
- (7) Mihailescu, M.; Monkenbusch, M.; Endo, H.; Allgaier, J.; Gompper, G.; Stellbrink, J.; Richter, D.; Jakobs, B.; Sottmann, T.; Farago, B. Dynamics of Bicontinuous Microemulsion Phases with and without Amphiphilic Block-Copolymers. *J. Chem. Phys.* **2001**, *115* (20), 9563–9577. <https://doi.org/10.1063/1.1413509>.
- (8) Dekker, M. L.; Clause, M.; Rosano, H. L.; Zradba, A. S. *Microemulsion Systems*, 24th Ed.; Surfactant Science Ser., New York, PA, 1987.
- (9) Dörfler, H.-D. *Grenzflächen Und Kolloid-Disperse Systeme*; Springer: Berlin, Heidelberg, 2002.
- (10) Lawrence, M. J.; Rees, G. D. Microemulsion-Based Media as Novel Drug Delivery Systems. *Adv. Drug Deliv. Rev.* **2000**, *45*, 89–121. <https://doi.org/10.1016/j.addr.2012.09.018>.
- (11) Lopian, T.; Schöttl, S.; Prévost, S.; Pellet-Rostaing, S.; Horinek, D.; Kunz, W.; Zemb, T. Morphologies Observed in Ultraflexible Microemulsions with and without the Presence of a Strong Acid. *ACS Cent. Sci.* **2016**, *2* (7), 467–475.

- <https://doi.org/10.1021/acscentsci.6b00116>.
- (12) Chen, S.-H.; Rajagopalan, R. *Micellar Solutions and Microemulsions*; Chen, S.-H., Rajagopalan, R., Eds.; Springer-Verlag: New York, 1990.  
<https://doi.org/10.1007/978-1-4613-8938-5>.
- (13) Hou, W.; Xu, J. Surfactant-Free Microemulsions. *Curr. Opin. Colloid Interface Sci.* **2016**, *25*, 67–74. <https://doi.org/10.1016/j.cocis.2016.06.013>.
- (14) Liu, D.; Lu, H.; Zhang, Y.; Zhu, P.; Huang, Z. Conversion of a Surfactant-Based Microemulsion to a Surfactant-Free Microemulsion by CO<sub>2</sub>. *Soft Matter* **2019**, *15* (3), 462–469. <https://doi.org/10.1039/C8SM02444H>.
- (15) Abrar, I.; Bhaskarwar, A. N. Performance and Emission Characteristics of Constant Speed Diesel Engine Fueled by Surfactant-Free Microemulsions. *Sustain. Energy Technol. Assessments* **2021**, *47*, 101414.  
<https://doi.org/10.1016/j.seta.2021.101414>.
- (16) Buchecker, T.; Krickl, S.; Winkler, R.; Grillo, I.; Bauduin, P.; Touraud, D.; Pfitzner, A.; Kunz, W. The Impact of the Structuring of Hydrotropes in Water on the Mesoscale Solubilisation of a Third Hydrophobic Component. *Phys. Chem. Chem. Phys.* **2017**, *19* (3), 1806–1816. <https://doi.org/10.1039/c6cp06696h>.
- (17) Kunz, W.; Holmberg, K.; Zemb, T. Hydrotropes. *Curr. Opin. Colloid Interface Sci.* **2016**, *22*, 99–107. <https://doi.org/10.1016/j.cocis.2016.03.005>.
- (18) Zemb, T. N.; Klossek, M.; Lopian, T.; Marcus, J.; Schöttl, S.; Horinek, D.; Prevost, S. F.; Touraud, D.; Diat, O.; Marčelja, S.; Kunz, W. How to Explain Microemulsions Formed by Solvent Mixtures without Conventional Surfactants. *Proc. Natl. Acad. Sci.* **2016**, *113* (16), 4260–4265. <https://doi.org/10.1073/pnas.1515708113>.
- (19) Schöttl, S. Atomistic Studies of Structure and Dynamics of Aggregation in Solution: From Traditional Surfactant Micelles to Surfactant-Free Microemulsions, University of Regensburg, 2018. <https://doi.org/10.5283/epub.37989>.
- (20) Krickl, S.; Jurko, L.; Wolos, K.; Touraud, D.; Kunz, W. Surfactant-Free Microemulsions with Cleavable Constituents. *J. Mol. Liq.* **2018**, *271*, 112–117.  
<https://doi.org/10.1016/j.molliq.2018.08.120>.
- (21) Xenakis, A.; Zoumpantioti, M.; Stamatis, H. Enzymatic Reactions in Structured Surfactant-Free Microemulsions. *Curr. Opin. Colloid Interface Sci.* **2016**, *22*, 41–45.  
<https://doi.org/10.1016/j.cocis.2016.02.009>.
- (22) Degot, P.; Huber, V.; Hofmann, E.; Hahn, M.; Touraud, D.; Kunz, W. Solubilization

- and Extraction of Curcumin from *Curcuma Longa* Using Green, Sustainable, and Food-Approved Surfactant-Free Microemulsions. *Food Chem.* **2021**, 336, 127660. <https://doi.org/10.1016/j.foodchem.2020.127660>.
- (23) Han, Y.; Liu, S.; Du, Y.; Li, D.; Pan, N.; Chai, J.; Li, D. A New Application of Surfactant-Free Microemulsion: Solubilization and Transport of Drugs and Its Transdermal Release Properties. *J. Taiwan Inst. Chem. Eng.* **2022**, 138, 104473. <https://doi.org/10.1016/j.jtice.2022.104473>.
- (24) Shield, J. W.; Ferguson, H. D.; Bommarius, A. S.; Hatton, T. A. Enzymes in Reversed Micelles as Catalysts for Organic-Phase Synthesis Reactions. *Ind. Eng. Chem. Fundam.* **1986**, 25 (4), 603–612. <https://doi.org/10.1021/i100024a022>.
- (25) Luisi, P. L. Enzymes Hosted in Reverse Micelles in Hydrocarbon Solution. *Angew. Chemie Int. Ed.* **1985**, 24 (6), 439–450. <https://doi.org/10.1002/anie.198504393>.
- (26) Martinek, K.; Levashov, A. V.; Klyachko, N.; Khmel'nitski, Y. L.; Berezin, I. V. Micellar Enzymology. *Eur. J. Biochem.* **1986**, 155 (3), 453–468. <https://doi.org/10.1111/j.1432-1033.1986.tb09512.x>.
- (27) Biasutti, M. A.; Abuin, E. B.; Silber, J. J.; Correa, N. M.; Lissi, E. A. Kinetics of Reactions Catalyzed by Enzymes in Solutions of Surfactants. *Adv. Colloid Interface Sci.* **2008**, 136 (1–2), 1–24. <https://doi.org/10.1016/j.cis.2007.07.001>.
- (28) Carvalho, C. M. L.; Cabral, J. M. S. Reverse Micelles as Reaction Media for Lipases. *Biochimie* **2000**, 82 (11), 1063–1085. [https://doi.org/10.1016/S0300-9084\(00\)01187-1](https://doi.org/10.1016/S0300-9084(00)01187-1).
- (29) Orlich, B.; Schomäcker, R. Enzyme Catalysis in Reverse Micelles. *Adv. Biochem. Eng. Biotechnol.* **2002**, 75, 185–208. [https://doi.org/10.1007/3-540-44604-4\\_6](https://doi.org/10.1007/3-540-44604-4_6).
- (30) Liang, Y.; Yuan, X.; Zeng, G.; Zhong, H.; Li, H.; Wang, W. Effects of Surfactants on Enzyme-Containing Reversed Micellar System. *Sci. China Chem.* **2011**, 54 (5), 715–723. <https://doi.org/10.1007/s11426-011-4266-2>.
- (31) Mitsou, E.; Xenakis, A.; Zoumpantioti, M. Oxidation Catalysis by Enzymes in Microemulsions. *Catalysts* **2017**, 7 (2), 52. <https://doi.org/10.3390/catal7020052>.
- (32) Martinek, K.; Levashov, A. V.; Klyachko, N. I.; Berezin, I. V. Catalysis by Water-Soluble Enzyme in Organic Solvents. Stabilization of Enzyme against Denaturation (Inactivation) through Their Inclusion in Reversed Micelles of Surfactants. *Dokl. Akad. Nauk SSSR* **1977**, 236, 920-923 (in Russian), 951-953 (in English, 1978).
- (33) Martinek, K.; Levashov, A. V.; Klyachko, N. L.; Pantin, V. I.; Berezin, I. V. The

- Principles of Enzymes Stabilization. *Biochim. Biophys. Acta - Enzymol.* **1981**, 657 (1), 277–294. [https://doi.org/10.1016/0005-2744\(81\)90151-0](https://doi.org/10.1016/0005-2744(81)90151-0).
- (34) Viparelli, P.; Alfani, F.; Cantarella, M. Models for Enzyme Superactivity in Aqueous Solutions of Surfactants. *Biochem. J.* **1999**, 344 (3), 765. <https://doi.org/10.1042/0264-6021:3440765>.
- (35) Biswas, R.; Das, A. R.; Pradhan, T.; Touraud, D.; Kunz, W.; Mahiuddin, S. Spectroscopic Studies of Catanionic Reverse Microemulsion: Correlation with the Superactivity of Horseradish Peroxidase Enzyme in a Restricted Environment. *J. Phys. Chem. B* **2008**, 112 (21), 6620–6628. <https://doi.org/10.1021/jp711368p>.
- (36) Khmelnitsky, Y. L.; Zharinova, I. N.; Berezin, I. V.; Levashov, A. V.; Martinek, K. Detergentless Microemulsions A New Microheterogeneous Medium for Enzymatic Reaction. *Ann. N. Y. Acad. Sci.* **1987**, 501, 161–164. <https://doi.org/10.1111/j.1749-6632.1987.tb45701.x>.
- (37) Khmelnitsky, Y. L.; Hilhorst, R.; Veeger, C. Detergentless Microemulsions as Media for Enzymatic Reactions: Cholesterol Oxidation Catalyzed by Cholesterol Oxidase. *Eur. J. Biochem.* **1988**, 176 (2), 265–271. <https://doi.org/10.1111/j.1432-1033.1988.tb14277.x>.
- (38) Tziaila, A. A.; Kalogeris, E.; Gournis, D.; Sanakis, Y.; Stamatis, H. Enhanced Catalytic Performance and Stability of Chloroperoxidase from *Caldariomyces Fumago* in Surfactant Free Ternary Water–Organic Solvent Systems. *J. Mol. Catal. B Enzym.* **2008**, 51 (1–2), 24–35. <https://doi.org/10.1016/j.molcatb.2007.10.006>.
- (39) Topakas, E.; Stamatis, H.; Biely, P.; Kekos, D.; Macris, B. .; Christakopoulos, P. Purification and Characterization of a Feruloyl Esterase from *Fusarium Oxysporum* Catalyzing Esterification of Phenolic Acids in Ternary Water–Organic Solvent Mixtures. *J. Biotechnol.* **2003**, 102 (1), 33–44. [https://doi.org/10.1016/S0168-1656\(02\)00363-2](https://doi.org/10.1016/S0168-1656(02)00363-2).
- (40) Khmelnitsky, Y. L.; Gladilin, A. K.; Neverova, I. N.; Levashov, A. V.; Martinek, K. Detergentless Microemulsions as Media for Enzymatic Reactions: Catalytic Properties of Laccase in the Ternary System Hexane-2-Propanol-Water. *Collect. Czech. Chem. Commun.* **1990**, 55, 555–563.
- (41) Krickl, S.; Touraud, D.; Bauduin, P.; Zinn, T.; Kunz, W. Enzyme Activity of Horseradish Peroxidase in Surfactant-Free Microemulsions. *J. Colloid Interface Sci.* **2018**, 516, 466–475. <https://doi.org/10.1016/j.jcis.2018.01.077>.

- (42) Vulfson, E. N.; Ahmed, G.; Gill, I.; Kozlov, I. A.; Goodenough, P. W.; Law, B. A. Alterations to the Catalytic Properties of Polyphenoloxidase in Detergentless Microemulsions and Ternary Water-Organic Solvent Mixtures. *Biotechnol. Lett.* **1991**, *13* (2), 91–96. <https://doi.org/10.1007/BF01030457>.
- (43) O'Connor, J.; Aggett, A.; Williams, D.; Stanley, R. Candida Cylindracea Lipase-Catalyzed Hydrolysis of Methyl Palmitate in Detergentless Microemulsion and Paraffin/Water Biphasic Media. *Aust. J. Chem.* **1991**, *44* (1), 53. <https://doi.org/10.1071/CH9910053>.
- (44) O'Connor, J.; Cleverly, D. R. Bile Salt Stimulated Human Milk Lipase Catalyzed Ester Hydrolysis in Detergentless Microemulsion Media. *Biocatal. Biotransformation* **1995**, *12* (3), 193–204. <https://doi.org/10.3109/10242429508998162>.
- (45) Vafiadi, C.; Topakas, E.; Christakopoulos, P.; Faulds, C. B. The Feruloyl Esterase System of *Talaromyces Stipitatus*: Determining the Hydrolytic and Synthetic Specificity of TsFaeC. *J. Biotechnol.* **2006**, *125* (2), 210–221. <https://doi.org/10.1016/j.jbiotec.2006.02.009>.
- (46) Vafiadi, C.; Topakas, E.; Bakx, E.; Schols, H.; Christakopoulos, P. Structural Characterisation by ESI-MS of Feruloylated Arabino-Oligosaccharides Synthesised by Chemoenzymatic Esterification. *Molecules* **2007**, *12* (7), 1367–1375. <https://doi.org/10.3390/12071367>.
- (47) Vafiadi, C.; Topakas, E.; Christakopoulos, P. Regioselective Esterase-Catalyzed Feruloylation of l-Arabinobiose. *Carbohydr. Res.* **2006**, *341* (12), 1992–1997. <https://doi.org/10.1016/j.carres.2006.05.022>.
- (48) Liu, Y.; Goebel, J.; Yin, Y. Templated Synthesis of Nanostructured Materials. *Chem. Soc. Rev.* **2013**, *42* (7), 2610–2653. <https://doi.org/10.1039/C2CS35369E>.
- (49) Candau, F.; Selb, J. Hydrophobically-Modified Polyacrylamides Prepared by Micellar Polymerization. *Adv. Colloid Interface Sci.* **1999**, *79* (2–3), 149–172. [https://doi.org/10.1016/S0001-8686\(98\)00077-3](https://doi.org/10.1016/S0001-8686(98)00077-3).
- (50) Blackley, D. C. *Polymer Latices - Science and Technology, Volume 2: Types of Latices*, Second.; Blackley, D. C., Ed.; Springer Science+Business Media Dordrecht, 1997. <https://doi.org/10.1007/978-94-011-5848-0>.
- (51) Sun, B.; Chai, J.; Chai, Z.; Zhang, X.; Cui, X.; Lu, J. A Surfactant-Free Microemulsion Consisting of Water, Ethanol, and Dichloromethane and Its Template Effect for Silica Synthesis. *J. Colloid Interface Sci.* **2018**, *526*, 9–17.

- <https://doi.org/10.1016/j.jcis.2018.04.072>.
- (52) Raj, W. R. P.; Sasthav, M.; Cheung, H. M. Formation of Porous Polymeric Structures by the Polymerization of Single-Phase Microemulsions Formulated with Methyl Methacrylate and Acrylic Acid. *Langmuir* **1991**, *7* (11), 2586–2591. <https://doi.org/10.1021/la00059a032>.
- (53) Mirhoseini, S. B.; Salabat, A. A Novel Surfactant-Free Microemulsion System for the Synthesis of Poly(Methyl Methacrylate)/Ag Nanocomposite. *J. Mol. Liq.* **2021**, *342*, 117555. <https://doi.org/10.1016/j.molliq.2021.117555>.
- (54) Blahnik, J.; Krickl, S.; Schmid, K.; Müller, E.; Lupton, J.; Kunz, W. Microemulsion and Microsuspension Polymerization of Methyl Methacrylate in Surfactant-Free Microemulsions (SFME). *J. Colloid Interface Sci.* **2023**, *submitted*.
- (55) Lipshutz, B. H.; Ghorai, S.; Cortes-Clerget, M. The Hydrophobic Effect Applied to Organic Synthesis: Recent Synthetic Chemistry “in Water.” *Chem. - A Eur. J.* **2018**, *24* (26), 6672–6695. <https://doi.org/10.1002/chem.201705499>.
- (56) Ge, X.; Zhang, S.; Chen, X.; Liu, X.; Qian, C. A Designed Bi-Functional Sugar-Based Surfactant: Micellar Catalysis for C-X Coupling Reaction in Water. *Green Chem.* **2019**, *21* (10), 2771–2776. <https://doi.org/10.1039/c9gc00964g>.
- (57) La Sorella, G.; Strukul, G.; Scarso, A. Recent Advances in Catalysis in Micellar Media. *Green Chem.* **2015**, *17* (2), 644–683. <https://doi.org/10.1039/c4gc01368a>.
- (58) Colacot, T. J.; Negishi, E. -i.; Trost, B. M.; Fu, G. C. *New Trends in Cross-Coupling*, RSC Cataly.; Royal Society of Chemistry: Cambridge, UK, 2015.
- (59) Colacot, T. J. The 2010 Nobel Prize in Chemistry: Palladium-Catalysed Cross-Coupling. *Platin. Met. Rev.* **2011**, *55* (2), 84–90. <https://doi.org/10.1595/147106711X558301>.
- (60) Prajapati, D.; Gohain, M. Recent Advances in the Application of Supercritical Fluids for Carbon—Carbon Bond Formation in Organic Synthesis. *Tetrahedron* **2004**, *60* (666), 815–833. <https://doi.org/10.1002/chin.200421232>.
- (61) Lipshutz, B. H.; Taft, B. R.; Abela, A. R.; Ghorai, S.; Krasovskiy, A.; Duplais, C. Catalysis in the Service of Green Chemistry: Nobel Prize-Winning Palladium-Catalysed Cross-Couplings, Run in Water at Room Temperature. *Platin. Met. Rev.* **2012**, *56* (2), 62–74. <https://doi.org/10.1595/147106712X629761>.
- (62) Brüß, L.; Jeyaseelan, R.; Kürschner, J. C. G.; Utikal, M.; Næsborg, L. Micellar Effects and Their Relevance in Photochemistry and Photocatalysis. *ChemCatChem*

- 2023**, 15 (1). <https://doi.org/10.1002/cctc.202201146>.
- (63) Lipshutz, B. H.; Ghorai, S.; Abela, A. R.; Moser, R.; Nishikata, T.; Duplais, C.; Krasovskiy, A.; Gaston, R. D.; Gadwood, R. C. TPGS-750-M: A Second-Generation Amphiphile for Metal-Catalyzed Cross-Couplings in Water at Room Temperature. *J. Org. Chem.* **2011**, 76 (11), 4379–4391. <https://doi.org/10.1021/jo101974u>.
- (64) Lee, N. R.; Cortes-Clerget, M.; Wood, A. B.; Lippincott, D. J.; Pang, H.; Moghadam, F. A.; Gallou, F.; Lipshutz, B. H. Coolade. A Low-Foaming Surfactant for Organic Synthesis in Water. *ChemSusChem* **2019**, 12 (13), 3159–3165. <https://doi.org/10.1002/cssc.201900369>.
- (65) Kincaid, J. R. A.; Wong, M. J.; Akporji, N.; Gallou, F.; Fialho, D. M.; Lipshutz, B. H. Introducing Savie: A Biodegradable Surfactant Enabling Chemo- and Biocatalysis and Related Reactions in Recyclable Water. *J. Am. Chem. Soc.* **2023**, 145 (7), 4266–4278. <https://doi.org/10.1021/jacs.2c13444>.
- (66) Moser, R.; Ghorai, S.; Lipshutz, B. H. Modified Routes to the “Designer” Surfactant PQS. *J. Org. Chem.* **2012**, 77 (7), 3143–3148. <https://doi.org/10.1021/jo202564b>.
- (67) Braga, F. C.; Rafique, J.; Gomes, R. da S.; de Lima, D. P.; Beatriz, A. In Water Morita-Baylis-Hillman Reactions of Acrylates Enabled by Aqueous Micellar Catalysis Using TPGS-750 M. *Sustain. Chem. Pharm.* **2023**, 31, 100925. <https://doi.org/10.1016/j.scp.2022.100925>.
- (68) Parmentier, M.; Wagner, M.; Wickendick, R.; Baenziger, M.; Langlois, A.; Gallou, F. A General Kilogram Scale Protocol for Suzuki–Miyaura Cross-Coupling in Water with TPGS-750-M Surfactant. *Org. Process Res. Dev.* **2020**, 24 (8), 1536–1542. <https://doi.org/10.1021/acs.oprd.0c00281>.
- (69) Isley, N. A.; Gallou, F.; Lipshutz, B. H. Transforming Suzuki–Miyaura Cross-Couplings of MIDA Boronates into a Green Technology: No Organic Solvents. *J. Am. Chem. Soc.* **2013**, 135 (47), 17707–17710. <https://doi.org/10.1021/ja409663q>.
- (70) Takale, B. S.; Thakore, R. R.; Handa, S.; Gallou, F.; Reilly, J.; Lipshutz, B. H. A New, Substituted Palladacycle for Ppm Level Pd-Catalyzed Suzuki–Miyaura Cross Couplings in Water. *Chem. Sci.* **2019**, 10 (38), 8825–8831. <https://doi.org/10.1039/C9SC02528F>.
- (71) Lipshutz, B. H.; Isley, N. A.; Moser, R.; Ghorai, S.; Leuser, H.; Taft, B. R. Rhodium-Catalyzed Asymmetric 1,4-Additions, in Water at Room Temperature, with In-Flask Catalyst Recycling. *Adv. Synth. Catal.* **2012**, 354 (17), 3175–3179.

- <https://doi.org/10.1002/adsc.201200160>.
- (72) Krickl, S.; Buchecker, T.; Meyer, A. U.; Grillo, I.; Touraud, D.; Bauduin, P.; König, B.; Pfitzner, A.; Kunz, W. A Systematic Study of the Influence of Mesoscale Structuring on the Kinetics of a Chemical Reaction. *Phys. Chem. Chem. Phys.* **2017**, *19* (35), 23773–23780. <https://doi.org/10.1039/c7cp02134h>.
- (73) Giedyk, M.; Narobe, R.; Weiß, S.; Touraud, D.; Kunz, W.; König, B. Photocatalytic Activation of Alkyl Chlorides by Assembly-Promoted Single Electron Transfer in Microheterogeneous Solutions. *Nat. Catal.* **2019**, *3* (1), 40–47. <https://doi.org/10.1038/s41929-019-0369-5>.
- (74) Santos, M. S.; Cybularczyk-Cecotka, M.; König, B.; Giedyk, M. Minisci C–H Alkylation of Heteroarenes Enabled by Dual Photoredox/Bromide Catalysis in Micellar Solutions. *Chem. – A Eur. J.* **2020**, *26* (66), 15323–15329. <https://doi.org/10.1002/chem.202002320>.
- (75) Liu, Y.; Liu, P.; Gao, S.; Wang, Z.; Luan, P.; González-Sabín, J.; Jiang, Y. Construction of Chemoenzymatic Cascade Reactions for Bridging Chemocatalysis and Biocatalysis: Principles, Strategies and Prospective. *Chem. Eng. J.* **2021**, *420* (2), 127659. <https://doi.org/10.1016/j.cej.2020.127659>.
- (76) Hastings, C. J.; Adams, N. P.; Bushi, J.; Kolb, S. J. One-Pot Chemoenzymatic Reactions in Water Enabled by Micellar Encapsulation. *Green Chem.* **2020**, *22* (18), 6187–6193. <https://doi.org/10.1039/d0gc01989e>.
- (77) Cortes-Clerget, M.; Akporji, N.; Zhou, J.; Gao, F.; Guo, P.; Parmentier, M.; Gallou, F.; Berthon, J.; Lipshutz, B. H. Bridging the Gap between Transition Metal- and Bio-Catalysis via Aqueous Micellar Catalysis. *Nat. Commun.* **2019**, *10* (2169), 1–10. <https://doi.org/10.1038/s41467-019-09751-4>.
- (78) Cosgrove, S. C.; Thompson, M. P.; Ahmed, S. T.; Parmeggiani, F.; Turner, N. J. One-Pot Synthesis of Chiral N-Arylamines by Combining Biocatalytic Aminations with Buchwald–Hartwig N-Arylation. *Angew. Chemie - Int. Ed.* **2020**, *59* (41), 18156–18160. <https://doi.org/10.1002/anie.202006246>.
- (79) Akporji, N.; Singhanian, V.; Dussart-Gautheret, J.; Gallou, F.; Lipshutz, B. H. Nanomicelle-Enhanced, Asymmetric ERED-Catalyzed Reductions of Activated Olefins. Applications to 1-Pot Chemo- and Bio-Catalysis Sequences in Water. *Chem. Commun.* **2021**, *57* (89), 11847–11850. <https://doi.org/10.1039/D1CC04774D>.
- (80) Singhanian, V.; Cortes-Clerget, M.; Dussart-Gautheret, J.; Akkachairin, B.; Yu, J.;

- Akporji, N.; Gallou, F.; Lipshutz, B. H. Lipase-Catalyzed Esterification in Water Enabled by Nanomicelles. Applications to 1-Pot Multi-Step Sequences. *Chem. Sci.* **2022**, *13* (5), 1440–1445. <https://doi.org/10.1039/D1SC05660C>.
- (81) Tang, C.; McInnes, B. T. Cascade Processes with Micellar Reaction Media: Recent Advances and Future Directions. *Molecules* **2022**, *27* (17), 5611. <https://doi.org/10.3390/molecules27175611>.
- (82) Gröger, H.; Gallou, F.; Lipshutz, B. H. Where Chemocatalysis Meets Biocatalysis: In Water. *Chem. Rev.* **2022**. <https://doi.org/10.1021/acs.chemrev.2c00416>.
- (83) Betori, R. C.; May, C. M.; Scheidt, K. A. Combined Photoredox/Enzymatic C–H Benzylic Hydroxylations. *Angew. Chemie Int. Ed.* **2019**, *58* (46), 16490–16494. <https://doi.org/10.1002/anie.201909426>.
- (84) Litman, Z. C.; Wang, Y.; Zhao, H.; Hartwig, J. F. Cooperative Asymmetric Reactions Combining Photocatalysis and Enzymatic Catalysis. *Nature* **2018**, *560* (7718), 355–359. <https://doi.org/10.1038/s41586-018-0413-7>.
- (85) Zhang, W.; Fueyo, E. F.; Hollmann, F.; Martin, L. L.; Pesic, M.; Wardenga, R.; Höhne, M.; Schmidt, S. Combining Photo-Organic Redox- and Enzyme Catalysis Facilitates Asymmetric C–H Bond Functionalization. *European J. Org. Chem.* **2019**, No. 1, 80–84. <https://doi.org/10.1002/ejoc.201801692>.
- (86) Guo, X.; Okamoto, Y.; Schreier, M. R.; Ward, T. R.; Wenger, O. S. Enantioselective Synthesis of Amines by Combining Photoredox and Enzymatic Catalysis in a Cyclic Reaction Network. *Chem. Sci.* **2018**, *9* (22), 5052–5056. <https://doi.org/10.1039/C8SC01561A>.
- (87) Xu, J.; Arkin, M.; Peng, Y.; Xu, W.; Yu, H.; Lin, X.; Wu, Q. Enantiocomplementary Decarboxylative Hydroxylation Combining Photocatalysis and Whole-Cell Biocatalysis in a One-Pot Cascade Process. *Green Chem.* **2019**, *21* (8), 1907–1911. <https://doi.org/10.1039/C9GC00098D>.
- (88) Peng, Y.; Li, D.; Fan, J.; Xu, W.; Xu, J.; Yu, H.; Lin, X.; Wu, Q. Enantiocomplementary C–H Bond Hydroxylation Combining Photo-Catalysis and Whole-Cell Biocatalysis in a One-Pot Cascade Process. *European J. Org. Chem.* **2020**, No. 7, 821–825. <https://doi.org/10.1002/ejoc.201901682>.
- (89) Subramanian, D.; Boughter, C. T.; Klauda, J. B.; Hammouda, B.; Anisimov, M. A. Mesoscale Inhomogeneities in Aqueous Solutions of Small Amphiphilic Molecules. *Faraday Discuss.* **2013**, *167*, 217–238. <https://doi.org/10.1039/c3fd00070b>.

- 
- (90) Hahn, M.; Krickl, S.; Buchecker, T.; Jošt, G.; Touraud, D.; Bauduin, P.; Pfitzner, A.; Klamt, A.; Kunz, W. Ab Initio Prediction of Structuring/Mesoscale Inhomogeneities in Surfactant-Free Microemulsions and Hydrogen-Bonding-Free Microemulsions. *Phys. Chem. Chem. Phys.* **2019**, *21* (15), 8054–8066. <https://doi.org/10.1039/c8cp07544a>.
- (91) Ogendal, L. H. *Light Scattering Demystified Theory and Practice*; University of Copenhagen, 2017.
- (92) Pecora, R. Dynamic Light Scattering Measurement of Nanometer Particles in Liquids. *J. Nanoparticle Res.* **2000**, *2*, 123–131. <https://doi.org/10.1023/A:1010067107182>.
- (93) Michael Schurr, J.; Bloomfield, V. Dynamic Light Scattering Of Biopolymers And Biocolloid. *CRC Crit. Rev. Biochem.* **1977**, *4* (4), 371–431. <https://doi.org/10.3109/10409237709105461>.
- (94) Einstein, A. Über Die von Der Molekularkinetischen Theorie Der Wärme Geforderte Bewegung von in Ruhenden Flüssigkeiten Suspendierten Teilchen. *Ann. Phys.* **1905**, *17*, 549–560. <https://doi.org/10.1002/andp.19053220806>.
- (95) Hassan, P. A.; Rana, S.; Verma, G. Making Sense of Brownian Motion: Colloid Characterization by Dynamic Light Scattering. *Langmuir* **2015**, *31* (1), 3–12. <https://doi.org/10.1021/la501789z>.
- (96) Breitmaier, E. *Structure Elucidation by NMR in Organic Chemistry: A Practical Guide*, Third.; Wiley-VCH Verlag: Chichester, UK, 2002.
- (97) Dayrit, F. M.; Dios, A. C. de. <sup>1</sup>H and <sup>13</sup>C NMR for the Profiling of Natural Product Extracts: Theory and Applications. In *Spectroscopic Analyses - Developments and Applications*; InTech, 2017. <https://doi.org/10.5772/intechopen.71040>.
- (98) Ogrinc, N.; Košir, I. J.; Spangenberg, J. E.; Kidrič, J. The Application of NMR and MS Methods for Detection of Adulteration of Wine, Fruit Juices, and Olive Oil. A Review. *Anal. Bioanal. Chem.* **2003**, *376* (4), 424–430. <https://doi.org/10.1007/s00216-003-1804-6>.
- (99) Cavanagh, J.; Fairbrother, W. J.; Palmer III, A. G.; Rance, M.; Skelton, N. J. *Protein NMR Spectroscopy*, Second.; Elsevier: Burlington, USA, 2007.
- (100) Jameson, C. J. Understanding NMR Chemical Shifts. *Annu. Rev. Phys. Chem.* **1996**, *47* (1), 135–169. <https://doi.org/10.1146/annurev.physchem.47.1.135>.
- (101) Evilia, R. F. Quantitative NMR Spectroscopy. *Anal. Lett.* **2001**, *34* (13), 2227–2236.

<https://doi.org/10.1081/AL-100107290>.

- (102) Steinhof, O.; Kibrik, É. J.; Scherr, G.; Hasse, H. Quantitative and Qualitative  $^1\text{H}$ ,  $^{13}\text{C}$ , and  $^{15}\text{N}$  NMR Spectroscopic Investigation of the Urea-Formaldehyde Resin Synthesis. *Magn. Reson. Chem.* **2014**, *52* (4), 138–162. <https://doi.org/10.1002/mrc.4044>.
- (103) Diehl, B. Principles in NMR Spectroscopy. In *NMR Spectroscopy in Pharmaceutical Analysis*; Elsevier, 2008; pp 3–41. <https://doi.org/10.1016/B978-0-444-53173-5.00001-9>.
- (104) Rankin, D. W. H.; Mitzel, N. W.; Morrison, C. A. *Structural Methods in Molecular Inorganic Chemistry*; Wiley: Chichester, UK, 2013.
- (105) Parella, T.; Sánchez-Ferrando, F.; Virgili, A. Improved Sensitivity in Gradient-Based 1D and 2D Multiplicity-Edited HSQC Experiments. *J. Magn. Reson.* **1997**, *126* (2), 274–277. <https://doi.org/10.1006/jmre.1997.1164>.
- (106) Willker, W.; Leibfritz, D.; Kerssebaum, R.; Bermel, W. Gradient Selection in Inverse Heteronuclear Correlation Spectroscopy. *Magn. Reson. Chem.* **1993**, *31* (3), 287–292. <https://doi.org/10.1002/mrc.1260310315>.

# Chapter 1 Novel green production of natural-like vanilla extract from curcuminoids

## 1.0 Abstract

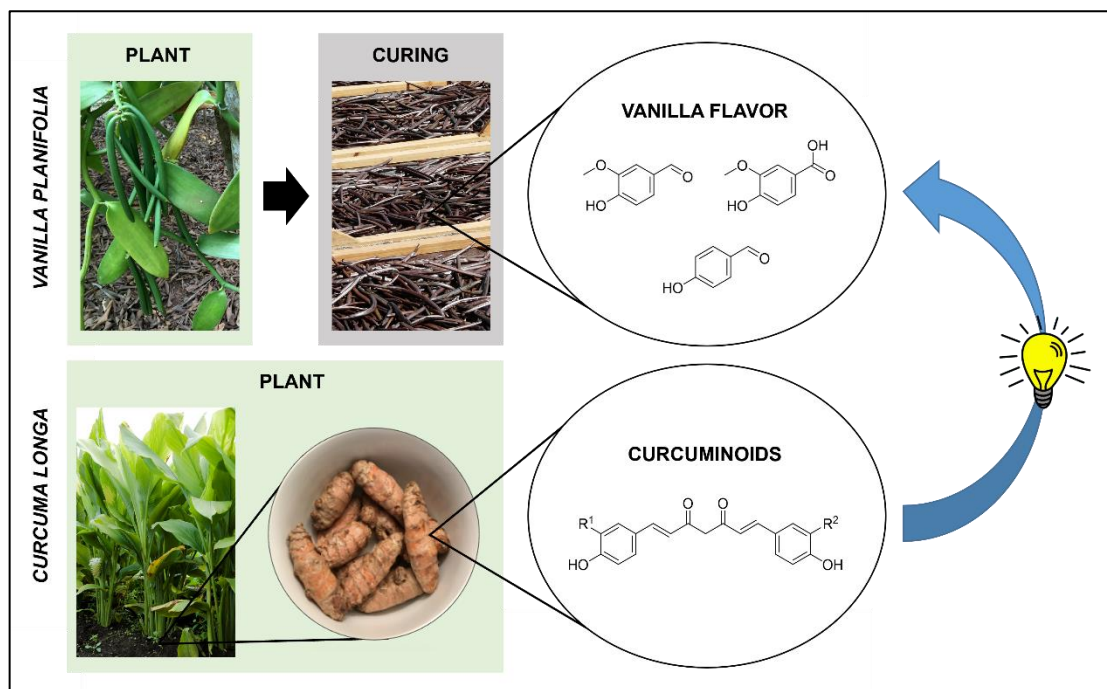


Figure 1 - 1: Graphical abstract illustrating the production of natural-like vanilla extract from the plant *Curcuma longa* instead of *Vanilla planifolia*.

The demand for natural vanilla extract, and vanillin in particular, by far exceeds the current production, as both the cultivation of vanilla beans and the extraction of vanillin are laborious. For this purpose, most vanillin used today is produced synthetically, contrary to the general trend toward bio-based products. The present study deals with the synthesis of nature-based vanillin, starting with the more accessible rhizomes of the plant *Curcuma longa*. Besides vanillin, vanillic acid and p-hydroxybenzaldehyde are synthesized that way, which are also found in the natural vanilla bean. The extraction of the curcuminoids and, finally, their conversion to the flavors are performed using visible light and food-grade chemicals only. A binary mixture of ethanol and triacetin, as well as a surfactant-free microemulsion consisting of water, ethanol, and triacetin, are investigated in this context. The results exceed the literature values for Soxhlet extraction of vanilla beans by a factor > 7. Besides, the impact of different parameters on the reaction, including solvent structuring, is studied in detail.

This chapter is published in *Food Chemistry* (Hofmann, E.; Degot, P.; Touraud, D.; König, B.; Kunz, W. Novel green production of natural-like vanilla extract from curcuminoids. *Food Chem.* **2023**).<sup>1</sup> Dr. Pierre Degot contributed to the extraction of the curcuminoids and developed the method for HPLC analysis (University of Regensburg, Germany). The photocatalyst tetraacetyl riboflavin was gratefully received from Dr. Andreas Graml (University of Regensburg, Germany).

### 1.1 Introduction

The application of vanilla, being the second most expensive flavoring in the world after saffron, spans various industries such as food, pharmaceuticals, and cosmetics.<sup>2,3</sup> The cultivation of the plant *Vanilla planifolia* (a member of the orchid family) and its processing make vanilla one of the most labor-intensive agricultural products. The plant has its origin in Mexico, but most of the vanilla is cultivated in Madagascar. Due to a lack of natural pollinators there, the flowers, which bloom and die within a few hours, have to be pollinated by hand. The harvest 9 months later follows an again labor-intensive curing process that takes several months. The aroma develops only during this process. The green beans themselves have almost no odor.<sup>4,5</sup> Although vanillin is the main component of the vanilla aroma, the natural flavor is the sum of more than 170 volatile aromatic compounds. Vanillic acid and p-hydroxybenzaldehyde represent two other major volatile constituents (see Figure 1 - 2). Their ratio varies depending on the geographic origin of the vanilla bean.<sup>6</sup> In the end, vanillin accounts for 1 - 2 % (w/w) of the cured beans.<sup>7,8</sup> Thus, natural vanillin from *Vanilla planifolia* only covers 1 % of the global vanillin market, which is still expected to grow further.<sup>5,9</sup> In addition, conventional extraction techniques often turned out to be time- and material-consuming.<sup>10,11</sup> All this makes vanilla such an expensive source of vanillin. In 2018, the price of natural vanillin reached that of silver.<sup>12,13</sup> While the cured beans are sold for 50 – 80 \$/kg, natural vanillin from vanilla beans nowadays achieves prices higher than 25'000 \$/kg.<sup>8,13</sup>

Accordingly, most of the vanillin consumed is produced synthetically.<sup>14</sup> However, this is contrary to the global megatrend toward natural products replacing synthetic ones.<sup>10,13,15</sup> In recent years, various methods have been developed, not all of them being suitable due to harmful effects on the environment or human health.<sup>12</sup> Vanillin synthesis from petroleum-derived phenol and glyoxylic acid supplies more than 85 % of the global demand. The two-step process requires high temperature (80 – 130 °C) and the use of a copper(II) catalyst.<sup>13</sup> Such synthetic vanillin is sold for only 16 – 20 \$/kg.<sup>16</sup>

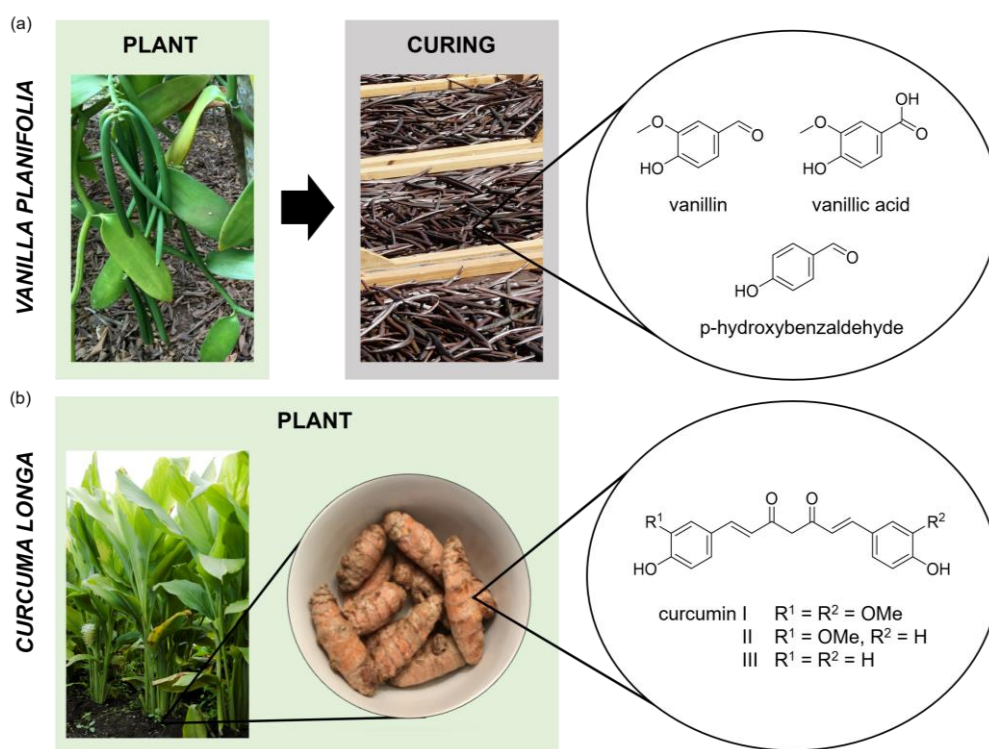


Figure 1 - 2: (a) The plant *Vanilla planifolia*, its beans during the curing process, and the molecular structure of vanillin, vanillic acid, and p-hydroxybenzaldehyde. (b) The plant *Curcuma longa*, its rhizomes, and the molecular structure of the three curcuminoids curcumin I, II, and III.

As a consequence, a lot of research focuses on biosynthesis, which allows labeling the produced vanillin as *natural*. A limited substrate solubility in water and a high price of the biocatalyst usually comes with this technique.<sup>2,13,17</sup> Ciriminna *et al.* reported a few photocatalytic syntheses toward vanillin starting from ferulic acid (see Figure 1 - 3(d)). All of them require the application of metal-based catalysts.<sup>13</sup> The green synthesis of vanillin is hence still a hot topic in research.<sup>18–21</sup>

Another plant compound that is also widely represented in research is curcumin.<sup>22–29</sup> Curcumin is widely used as a spice and natural food colorant.<sup>30</sup> Due to its anti-inflammatory, anti-diabetic, anti-oxidant, and even anti-cancer properties, it also finds applications in traditional medicine and cosmetics.<sup>31</sup> Curcumin (curcumin I), demethoxycurcumin (curcumin II) and bisdemethoxycurcumin (curcumin III) are the three main curcuminoids in the rhizomes of the plant *Curcuma longa* (see Figure 1 - 2) and responsible for their yellow color. The plant, also known as turmeric, is assigned to the ginger family and has its origin in Southwest India.<sup>30</sup> It is a perennial herb extensively cultivated in India, China, Africa, Australia, and Asia.<sup>30,32,33</sup> In Africa, the inhabitants even cultivate the turmeric in their home gardens.<sup>30</sup> Curcumin is the main curcuminoid at 77 % and makes up 1 – 6 % of turmeric powder, depending on the batch.<sup>31,34</sup> The availability at low prices makes curcumin a biomass of high interest in research.<sup>22–24</sup> The bulk price for turmeric is currently around 3 \$/kg, at least 17 times cheaper than cured vanilla beans.<sup>8,25</sup> There are several methods to extract

the curcuminoids from the rhizomes.<sup>24,26,35-37</sup> Degot *et al.* describe a simple extraction with a solvent consisting of the food-grade components water, ethanol, and triacetin.<sup>24</sup> Heffernan *et al.* also reported a technique to separate the three curcuminoids to finally produce pure fractions of either curcumin I, II, or III.<sup>37</sup> Some research also deals with the conversion of curcumin to vanillin. In this context, biotransformation is often the method of choice. However, only ppm amounts of the poorly water-soluble substrate can be used, or complex three-enzyme systems have to be applied.<sup>18,23,38</sup>

In this chapter, the photochemical conversion of natural curcuminoids to vanillin but also to vanillic acid and p-hydroxybenzaldehyde is described. Curcuminoids are extracted from the rhizomes of *Curcuma longa*, as reported by Degot *et al.*<sup>24</sup>, and converted in the same food-grade system using visible light in the absence of any additional photocatalyst.

## 1.2 Material and methods

### 1.2.1 Chemicals

Curcumin (C I, purity > 97 %) and bisdemethoxycurcumin (C III, > 98 %) were purchased from TCI (Eschborn, Germany). Triacetin (TriA, 99 %, FCC, FG), demethoxycurcumin (C II,  $\geq$  98 %), vanillin ( $\geq$  97 %, FCC; FG, kosher), vanillic acid ( $\geq$  98 %), p-hydroxybenzaldehyde (98 %), and acetic acid ( $\geq$  99.8 %) were bought from Sigma Aldrich (Darmstadt, Germany). Ethanol (EtOH, > 99 %), acetonitrile (HPLC grade), and methanol (HPLC grade) were received from Merck (Darmstadt, Germany). Kwizda Kräuterhandel delivered the dried rhizome powder from the *Curcuma longa* plant. Ferulic acid (FA, 99 %, FG) was from Alexmo Cosmetics. Tetraacetyl riboflavin (TARF) was synthesized as described by Larson *et al.*<sup>39</sup> All chemicals were used without further purification. Millipore water (W) was used with a resistivity of 18 M $\Omega$  cm.

### 1.2.2 Methods

#### 1.2.2.1 Standard reaction procedure

If not stated otherwise, 10 mL crimp cap vials equipped with a magnetic stirring bar were loaded with 2 mM curcumin (I, II, III) and 4 mM of ferulic acid, respectively, and 4 mL solvent. The solvent consisted of either the binary mixture (BM) EtOH/TriA 40/60 (w/w) or the SFME W/EtOH/TriA 40/24/36 (w/w/w). When used, the catalyst concentration was 1/10 of the substrate. Up to 10 reaction vials were placed in an air-cooled TAK 120 AC photoreactor that was connected to a control-unit TAK 120. The photochemical reactions were performed for 2 h using blue LEDs with a wavelength of 455 nm, and a power of 7 W. Samples were stirred at 500 rpm. Solvent volumes are determined by weight and calculated using their density given in Table S.1 - 1 (Supporting Information). All reactions were carried out in duplicate.

#### 1.2.2.2 HPLC measurements

The amount of flavor and curcuminoids was determined by means of a Waters HPLC system comprising 2 Waters 515 HPLC pumps, a Waters 717 autosampler, a Waters 2487 UV/Vis detector, and an ACE Equivalent 3 C18-Column (300 Å, 150 x 2.1 mm). 5  $\mu$ L of the filtered sample (PTFE-filter, 0.2  $\mu$ m pore size) were injected and eluted with a flow rate of

0.2 mL/min at 40 °C. Table S.1 - 2 (Supporting Information) shows the gradient applied to the mobile phase, which consisted of 0.3 % (v/v) acetic acid in water (solvent A) and acetonitrile (solvent B). All samples were analyzed twice. The calibration was performed in acetonitrile. Each compound was evaluated at a specific wavelength (see Figure S.1 - 2 in the Supporting Information). The amount of curcuminoids is determined using the calibration reported by Degot *et al.*<sup>24</sup> Solvent volumes are again determined by weight and calculated using their density given in Table S.1 - 1 (Supporting Information).

### **1.2.2.3 Extraction and photochemical conversion of natural Curcuma**

Curcumin was extracted from the rhizomes of *Curcuma longa* as described by Degot *et al.*<sup>24</sup> 3 g ground rhizomes were added to 12 g of solvent and stirred at 1300 rpm at room temperature for 1 h. Then, the mixture was centrifuged at 4'700 rpm (2'297 g) and filtered with a PTFE filter (0.45 µm pore size). 800 µL of the filtered solution was taken to determine the curcuminoid concentration by means of HPLC. The remaining solution was split into 1 mL aliquots and placed in the photoreactor. The samples were illuminated, as described in Chapter 1.2.2.1. The duration of exposure, however, was extended to 12 h for the extracts.

### **1.2.2.4 Oxygen solubility**

The amount of dissolved oxygen was measured in the solvents EtOH/TriA 40/60 (w/w) and W/EtOH/TriA 40/24/36 (w/w/w) at room temperature using a TPS Aqua-D oxygen-meter connected to a TPS ED1 electrode. The oxygen saturation was determined relative to the calibration media air (100 %) and an aqueous solution containing 0.02 g/mL sodium sulfite (0 %). The electrode was equilibrated for 5 min in 10 g of each solution.

### **1.2.2.5 Dynamic light scattering**

Dynamic light scattering (DLS) experiments were carried out with a CGS-3 goniometer system from ALV connected to an ALV-7004/FAST Multiple Tau digital correlator. A vertical-polarized 22-mW HeNe laser with a wavelength of 632.8 nm served as the light source. Samples were filtered into cylindrical light scattering cells (10 mm outer diameter), that were freed from dust, using a PTFE filter (0.2 µm pore size). The sealed cell was placed into a toluene bath which temperature was kept at  $25 \pm 0.1$  °C. Scattered light was detected at an angle of 90 ° for 300 s.

## 1.3 Results and discussion

### 1.3.1 Curcumin and ferulic acid as a precursor for vanillin synthesis in different solvents

Regarding their molecular structure (see Figure 1 - 3(d)), both curcumin and ferulic acid appear to be appropriate substrates for the photochemical synthesis of nature-based vanillin. They can be dissolved easily in the selected solvents consisting of the binary mixture ethanol and triacetin (EtOH/TriA) in a ratio 40/60 (w/w) or the ternary mixture, water, ethanol, and triacetin (W/EtOH/TriA) in a ratio 40/24/36 (w/w/w). The choice of the two solvents bases upon the work of Degot *et al.*, who extracted significant amounts of curcuminoids from the plant *Curcuma longa* by simply stirring the ground rhizomes in these same solvents. The best result was achieved with the ternary mixture, as water swells the rhizomes and thus opens the plant matrix.<sup>24</sup> The dynamic light scattering (DLS) study of the ternary mixture (see Figure 1 - 3(c)) depicts a distinct autocorrelation function with a correlation intercept of 0.5, indicating the presence of water- and oil-rich aggregates.<sup>40</sup> Hence, the solvent W/EtOH/TriA can be assigned as a surfactant-free microemulsion (SFME) that is composed of a pseudo-oil phase dispersed in a pseudo-water phase contrary to unstructured liquids in which molecules are distributed isotropically. The autocorrelation function of the binary mixture (BM) is of negligible intensity with a correlation intercept of only 0.15. It can be assumed that only loose pre-aggregation or even no aggregation at all is present. In order to study the influence of a photocatalyst on the reaction, the organic catalyst tetraacetyl riboflavin (TARF) is applied, which is a vitamin B<sub>2</sub> derivative.<sup>24,41</sup>

The formation of vanillin after illuminating the dissolved substrates curcumin and ferulic acid with blue light (455 nm) is successful as proven with 2D HPLC and mass spectrometry measurements (MS) (see Chapter 1.5.2 – 1.5.3 in the Supporting Information). The reaction conditions are optimized by means of an experimental design (see Chapter 1.5.4 in the Supporting Information). Figure 1 - 3 shows the impact of substrate, solvent, and catalyst on the reaction outcome. In the case of ferulic acid (see Figure 1 - 3(a), FA), the yield is only 1 % when the photocatalyst TARF (cat) is present. In the absence of TARF, no formation of vanillin is detected. Accordingly, the transfer of an electron from the substrate to the excited photocatalyst initiates the reaction and is thus inevitable for the reaction of ferulic acid to vanillin. The nature of the solvent (SFME, BM) has no significant impact.

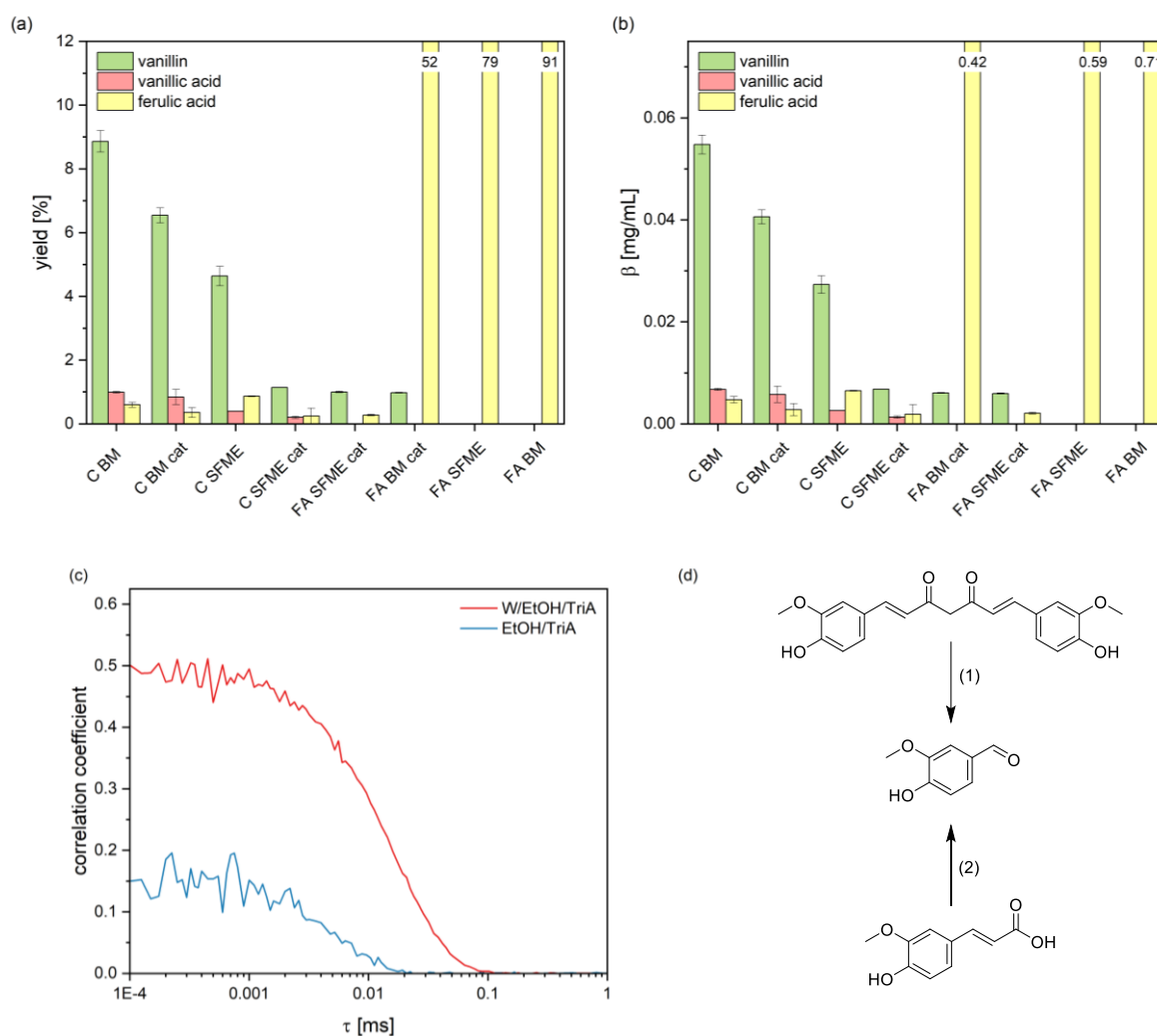


Figure 1 - 3: Detected yield (a) and mass concentration  $\beta$  (b) of vanillin, vanillic acid, and ferulic acid after photochemical conversion. The substrate is either curcumin (C) or ferulic acid (FA) dissolved in the binary mixture (BM) EtOH/TriA or the surfactant-free microemulsion (SFME) W/EtOH/TriA under standard conditions. The presence of the catalyst tetraacetyl riboflavin in the solution is indicated by "cat". (c) Normalized autocorrelation function of the pure solvents W/EtOH/TriA and EtOH/TriA obtained by DLS measurements at 25 °C. The results obtained with dissolved C are shown in Figure S.1 – 1 (Supporting Information). C leads to a slight decrease in the correlation functions, but there is still a distinct signal for the SFME. (d) Photochemical oxidation of either curcumin (1) or ferulic acid (2) toward vanillin.

Significantly higher vanillin yields of up to 9 % are achieved with the substrate curcumin (see Figure 1 - 3(a), C). Contrary to ferulic acid, the presence of the photocatalyst worsens the outcome. Curcumin absorbs the illuminated blue light. By reaching the excited state, the molecule becomes more oxidizing, which seems to be sufficient to start self-oxidation. Since both TARF and curcumin absorb at 455 nm, competition may arise for the incident light, which could explain the interfering effect of the catalyst on the reaction. In the BM, the catalyst reduces the yield of vanillin by 26 % and in the SFME by even 75 %. So, the choice of solvent also has a greater impact here. In the absence of TARF, the yield decreases by 48 % (from about 9 % to 5 %) when replacing the BM by the SFME. Since curcumin is oxidized in the presence of only light and air, oxygen solubility is considered to play an important role. In the BM EtOH/TriA, an oxygen saturation of 85.2 % is measured. In the

more hydrophilic SFME of W/EtOH/TriA, the oxygen saturation is reduced to 54.1 %. The fact that the amount of oxygen is reduced by 37 % seems to be the main reason for the 48 % reduced yield. Additional experiments revealed that there must be an optimum oxygen concentration. Further increasing the oxygen concentration in the BM, decreases the yield of synthesized vanillin while the yield of the further oxidized vanillic acid increases (see Figure S.1 - 8 in the Supporting Information). A detailed unravelling of the reaction mechanism would go beyond the scope. But considering the literature on the degradation of curcumin, it can be assumed that the mechanism consists of several steps, including the formation of radical and charged intermediates.<sup>42,43</sup> This would lead to the assumption that the intermediates are significantly more hydrophilic and, therefore, more likely dissolved in the aqueous pseudo-phase. At the same time, the uncharged, hydrophobic curcumin remains in the pseudo-oil phase of the SFME. The separation of the radical from the remaining starting material by solvent structuring could hinder a propagation of the reaction and thus further explain the reduced yield in the SFME compared to the unstructured binary mixture.

Despite optimization of several parameters, such as wavelength and power of the light, temperature, and oxygen concentration in solution (see Chapter 1.5.5 in the Supporting Information), the vanillin yield is limited to 9 % (see Figure 1 - 3(a)). However, the conversion of the curcumin substrate is 100 % leading to the conclusion that competitive reactions limit the yield of vanillin. Besides vanillin, ferulic acid is formed when degrading curcumin photochemically either through a parallel reaction or as an intermediate of vanillin. It has to be noted that the “yield” of ferulic acid corresponds to the unreacted residue when the acid itself is applied as a substrate. Even in the absence of the catalyst, part of the ferulic acid is depleted. The lack or the low yield of vanillin can, therefore, not only be attributed to insufficient substrate activation. Further studies on ferulic acid can be found in Chapter 1.5.6 in the Supporting Information. In addition to vanillin and ferulic acid, vanillic acid can be detected. Among these three, vanillin is the main product.

### **1.3.2 Conversion of curcuminoids to different flavoring components**

The natural Curcuma extract not only contains curcumin (I), but also demethoxycurcumin (II) and bisdemethoxycurcumin (III) (see Figure 1 - 2). Therefore, the photochemical conversion of all three curcuminoids dissolved in EtOH/TriA is investigated (see Figure 1 - 4). With regard to the molecular structure of curcumin I, the formation of two molecules of vanillin per molecule of curcumin are conceivable, provided that both benzyl moieties are reactive. Since there is one methoxy group less in the molecular structure of curcumin II compared to curcumin I, the substrate can only yield one molecule of vanillin in any case. Indeed, the amount of synthesized vanillin is reduced by 65 %, vanillic acid by 56 %, when

replacing curcumin I by II. This supports the assumption that both benzyl moieties of curcumin I are reactive. Moreover, curcumin II provides the opportunity of forming p-hydroxybenzaldehyde, which is equivalent to vanillin without the methoxy group. Curcumin III does not possess any methoxy group at the benzyl rings and hence can only yield p-hydroxybenzaldehyde. The amount of detected p-hydroxybenzaldehyde is not only twice, but almost 4 times the amount produced with curcumin II. The reason for this can be different reactivities of the two benzyl moieties, but also of the curcuminoids to each other. Altogether, the photochemical conversion of the three curcuminoids together allows the formation of vanillin, vanillic acid, and p-hydroxybenzaldehyde, that are among the most important aromatic compounds in vanilla beans. The ferulic acid vanishes using the demethoxylated curcuminoids.

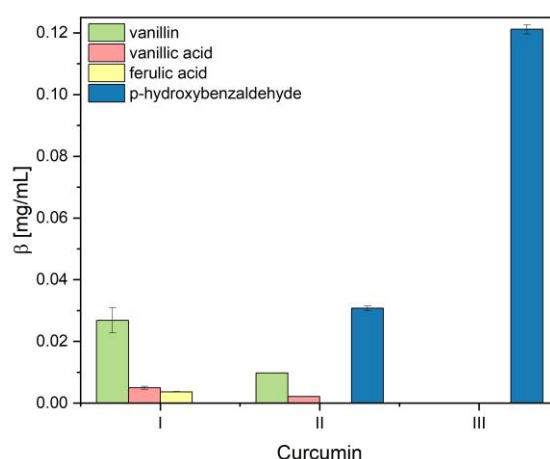


Figure 1 - 4: Detected mass concentration  $\beta$  of vanillin, vanillic acid, ferulic acid, and p-hydroxybenzaldehyde after photochemical conversion of 1 mM curcumin I, II, or III in the binary mixture EtOH/TriA under standard conditions.

### 1.3.3 Photochemical conversion of natural Curcuma extract

The previously discussed results are based on the usage of synthetic curcuminoids. Figure 1 - 5 depicts the results obtained by photochemical conversion of natural Curcuma extracts in either EtOH/TriA or W/EtOH/TriA. The amount of flavor is given relative to the amount of plant used for extraction and subsequent reaction. In the binary mixture EtOH/TriA as well as in the SFME W/EtOH/TriA, a total of  $1.3 \text{ mg}_{\text{flavor}}/\text{g}_{\text{rhizome}}$  can be generated, including the flavor components vanillin, vanillic acid, and p-hydroxybenzaldehyde. This value is more than 7 times higher compared to the literature value for Soxhlet extraction of cured vanilla beans in ethanol by Jadhav *et al.*<sup>11</sup> The vanillin content after photoconversion is  $0.6 \text{ mg}_{\text{flavor}}/\text{g}_{\text{rhizome}}$  in EtOH/TriA and in W/EtOH/TriA, which is more than 4 times the

literature Soxhlet value. The new method hence allows one to increase the output of flavor compounds while reducing the cost of the plant that serves as the source.

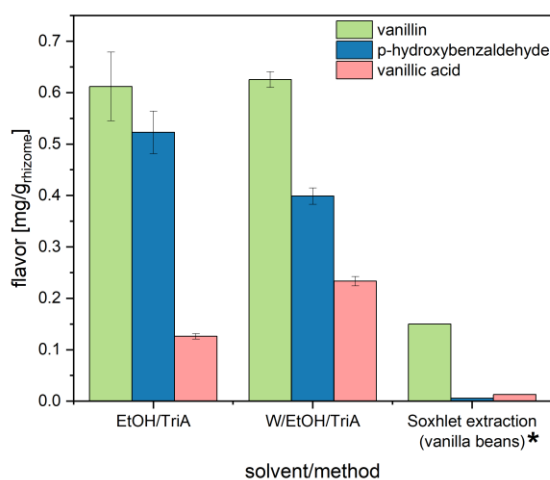


Figure 1 - 5: Amount of flavoring component vanillin, vanillic acid, and p-hydroxybenzaldehyde obtained by photochemical conversion of a *Curcuma* extract. The extraction and the subsequent reaction are performed with a solvent consisting of either the binary mixture EtOH/TriA or the SFME W/EtOH/TriA. The amount of flavor represents the detected amount relative to the plant mass used. \*The amount of flavoring components extracted from cured vanilla beans in ethanol using Soxhlet is shown for comparison and is taken from the literature.<sup>11</sup>

Since a significant amount of curcuminoids is extracted with the selected solvents, which is also visible through an intensive color of the solution (see Figure S.1 - 14 in the Supporting Information), the limitation of the volume per aliquot in the photoreactor is of great importance. Increasing the curcumin concentration at a constant sample volume results in a decrease in vanillin yield, while the absolute amount of synthesized vanillin still increases (see Figure S.1 - 9 in the Supporting Information). Since curcumin oxidizes itself when reaching the excited state, the absorbance of the molecule is a key parameter. The samples in the photoreactor are illuminated from below. When the curcumin concentration is too high, most of the light is absorbed by the molecules that are close to the bottom of the reaction vial and, thus, closer to the light source. Part of the curcumin behind remains in the dark. Reducing the sample volume, and thus the pathway of light, by the factor of the increase in the curcumin concentration leads to a constant absorbance according to Lambert-Beer's law.<sup>44</sup> Experiments revealed that the yield decreases less and at higher curcumin concentrations when adapting the sample volume (see Figure S.1 - 9 in the Supporting Information). Thereby, the absolute mass concentration shows a stronger increase. For this purpose, the extract is split into 1 mL aliquot for photoconversion, still enabling sufficient stirring at the same time. In addition, the extraction step is followed by centrifugation and filtration in order to remove the remaining *Curcuma* powder, which would reflect the incident light and, thus, reduce the absorption in the sample.

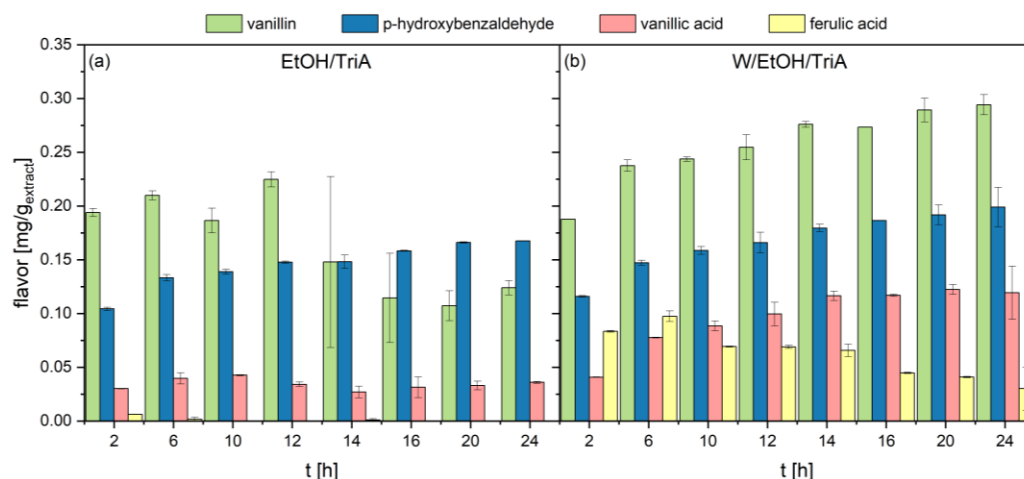


Figure 1 - 6: Detected amount of vanillin, p-hydroxybenzaldehyde, vanillic acid, and ferulic acid after photochemical conversion of a Curcuma extract as a function of reaction time ( $t$ ). The extraction and the subsequent reaction are performed with a solvent consisting of either the binary mixture EtOH/TriA (a) or the SFME W/EtOH/TriA (b).

Although the sum of flavor compounds is almost identical for the BM and the SFME, the ratio of the three flavors varies. Figure 1 - 6 depicts the reaction outcome in both solvents with respect to reaction time. Not only the solvent but also the duration of irradiation affects the ratios (see also Table 1 - 1). As Ranadive *et al.* reported, the ratio of flavoring components in cured vanilla beans varies depending on the geographic origin of the plant.<sup>6</sup> The presented method permits manipulating the ratio of flavors by choice of solvent and reaction time. It is beyond the scope of this publication, but different compositions of water, ethanol, and triacetin may allow additional ratios. Further, curcuminoids can be isolated after extraction.<sup>37</sup> By optimizing the starting concentrations of each curcuminoid, imitation of different flavor ratios in vanilla beans from different origins should be possible.

Regarding the amount of vanillin in Figure 1 - 6, a decrease is detected after 14 h of irradiation in the binary solvent EtOH/TriA. The vanillin starts to be destroyed by consecutive reactions. In the water-based SFME, the amount of vanillin continues to increase with longer reaction times. This may be due to the higher curcuminoid concentration after extraction providing more substrate. Under identical conditions, the concentration in the binary mixture is 4.8 mM curcumin I, 1.1 mM curcumin II, and 0.8 mM curcumin III and the SFME contains 7.7 mM curcumin I, 2.3 mM curcumin II, and 2.5 mM curcumin III. It becomes evident that not only reactivity but also solubility of the substrate is of great importance. Besides, additional (preparative) HPLC analysis with MS measurements in the Supporting Information (see Chapter 1.5.2 – 1.5.3) demonstrates the possibility of separating the flavors from the reaction solution.

Table 1 - 1: Ratios of vanillin to *p*-hydroxybenzaldehyde (*p*-HBA) and vanillic acid for some reaction times (*t*) shown in Figure 1 - 6 in both solvents.

<i>t</i> / <i>h</i>	ratio vanillin to		ratio vanillin to	
	<i>p</i> -HBA	vanillic acid	<i>p</i> -HBA	vanillic acid
2	1.86	6.43	1.62	4.61
10	1.34	4.38	1.54	2.75
24	0.74	3.44	1.48	2.47
	EtOH/TriA		W/EtOH/TriA	

A microemulsion-mediated extraction process may also allow the separation of the flavors from the reaction solution. Phase separation could be initiated by the addition of water or changes in temperature and pH. The extraction is, however, not part of this work. Further information and literature on this can be found in the Supporting Information (see Chapter 1.5.3.4).

## 1.4 Conclusion and outlook

In the present chapter, a green method for the synthesis of nature-based vanillin is reported. Starting from rhizomes of the plant *Curcuma longa*, the three curcuminoids curcumin, demethoxycurcumin, and bisdemethoxycurcumin are extracted according to the method described by Degot *et al.*<sup>24</sup> The solvents studied, which are composed of only food-grade components, are a binary mixture of ethanol and triacetin and a surfactant-free microemulsion (SFME) consisting of water, ethanol, and triacetin. The extracts can then be directly irradiated with blue light at 455 nm in a photoreactor. Since the curcuminoids undergo self-oxidation, no additional photocatalyst is required. In this way, the flavor vanillin, but also vanillic acid, and p-hydroxybenzaldehyde are formed which are important flavor components in the cured, natural vanilla bean.<sup>6</sup> For a given amount of plant, the photoreaction in both solvents results in 7 times more flavor components than in a Soxhlet extraction of vanilla bean. The content of vanillin is more than 4 times higher, while the cost of the plant source is reduced by at least a factor of 17.<sup>8,11,25</sup>

In comparison with other syntheses, our solvents allow solubilization of higher substrate concentrations of curcumin and our method dispenses with the usage of any components that are not considered to be green. Moreover, we are able to synthesize not only the main flavor vanillin but also two other important flavor components in one reaction step, which to the best of our knowledge has not been done before. We also showed that the ratio of these flavors can be varied by changing the solvent and/or reaction time. In a next step, additional compositions of the solvent mixture and their impact on the ratio of extracted curcuminoids should be considered. The curcuminoid ratio will directly influence the flavor ratio. The overall goal should be the imitation of the flavor ratio in the natural, cured vanilla bean. Moreover, the ratio of the curcuminoids could be adjusted by separation. As mentioned in the introductory chapter, Heffernan *et al.* presented a method to separate the curcuminoids after extraction.<sup>37</sup> This would allow a precise adjustment of the curcuminoid ratio in the extract before irradiating. Since the separation of the curcuminoids is expected to be a laborious step, it should be only included if a remarkable improvement of the flavor ratio is achieved. For this purpose, preliminary investigations with synthetic curcuminoids are recommended. Varying solvent composition and reaction time for changing the curcuminoid ratio will for sure be the simpler approach. In this context, additional binary and ternary systems can be taken into account.

The developed method bases upon detailed optimization studies. The impact of the different substrates curcumin and ferulic acid, of the catalyst tetraacetyl riboflavin, and several other parameters are demonstrated. Best results are achieved using curcumin in absence of the photocatalyst with a small sample volume to ensure sufficient light penetration in the sample. Based on these results, the application of a continuous flow reactor for the photochemistry step should be considered to ensure an optimum absorbance at high curcuminoid concentrations. This would certainly also be an interesting technique for an upscaling of our method. Of course, the purification of the flavor after photochemical conversion cannot be neglected in the next steps. Depending on the final application, the isolation of the single flavors, the flavor mixture, or the flavor mixture with selected essential oils, which are also present in the *Curcuma* extract<sup>45</sup>, can be of interest.

Overall, the optimization studies reveal a negative impact of the SFME on the reaction, which is attributed to the lower amount of dissolved oxygen and possibly an unfavorable separation of the reacting intermediates from the starting material by the pseudo-phases. Accordingly, the solvent structuring may impede the successful propagation of the reaction. This coincides with the observation by Krickl *et al.*, where solvent structuring limited the photocatalytic reaction by separating the photocatalyst from the substrate.<sup>46</sup> In the present work, however, significantly larger amounts of curcuminoids are extracted with the SFME. The extract in the ternary solvent mixture may allow even larger amounts of flavors if the reaction time is further extended. Thus, the structured system appears to be the more promising solvent, although the photochemical reaction itself is worse than in the binary solution.

## 1.5 Supporting information

### 1.5.1 Solvent characterization

Density measurements were performed using the vibrating-tube densimeter DMS 5000 A from Anton Paar. The temperature was controlled to  $25 \pm 0.01$  °C.

Table S.1 - 1: Density of W/EtOH/TriA 40/24/36 (w/w/w) and EtOH/TriA 40/60 (w/w) determined at 25 °C.

solvent	density [g/mL]
W/EtOH/TriA	1.004
EtOH/TriA	0.973

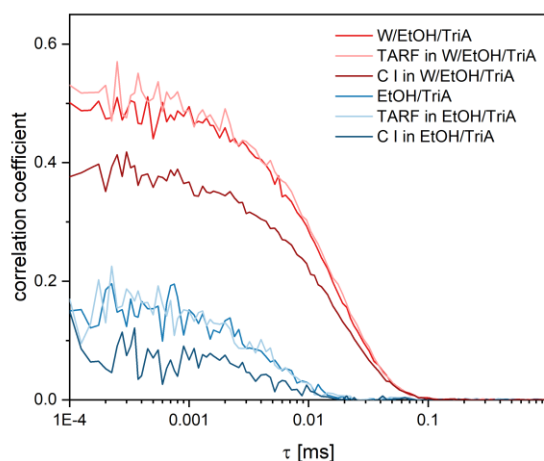


Figure S.1 - 1: Normalized autocorrelation function of W/EtOH/TriA (red) and EtOH/TriA (blue) obtained by DLS measurements at 25 °C. The spectra depict either the pure solvents or the solvents in the presence of 0.2 mM tetraacetyl riboflavin (TARF) and 2 mM curcumin (C I). While the catalyst has no remarkable impact on the correlation function, the curcumin leads to a decrease in the correlation intercept. However, there is still a distinct signal, especially for the ternary mixture indicating aggregation of water and oil pseudo-phases.

## 1.5.2 HPLC measurements

### 1.5.2.1 HPLC gradient

Table S.1 - 2: Gradient applied to the mobile phase during HPLC measurements. Solvent A consisted of 0.3 % (v/v) acetic acid in water and solvent B of acetonitrile.

time [min]	solvent A [% (v/v)]	solvent B [% (v/v)]
0	95	5
20	80	20
25	60	40
45	40	60
46	95	5
60	95	5

### 1.5.2.2 Calibration curves

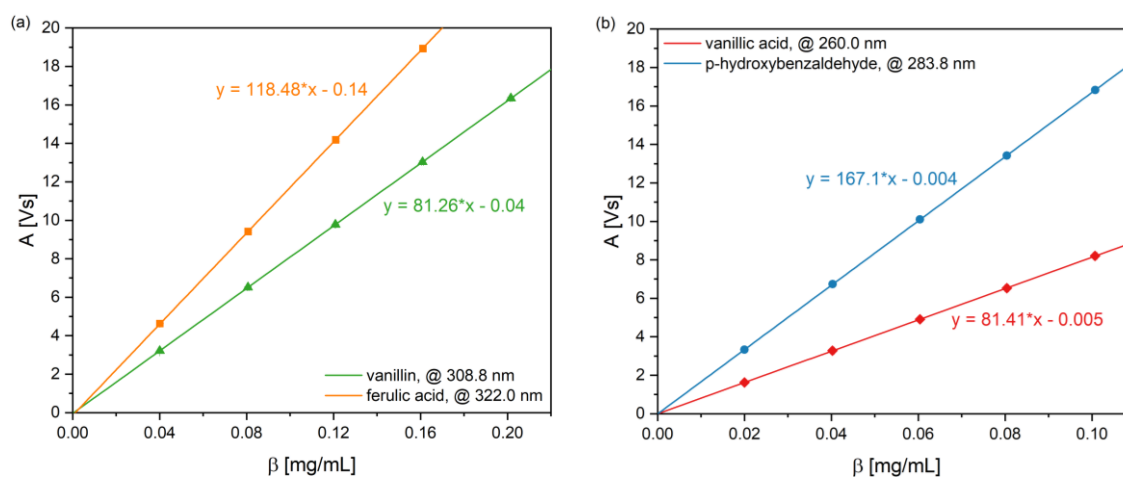


Figure S.1 - 2: HPLC calibration curves of vanillin and ferulic acid (a) and vanillic acid and p-hydroxybenzaldehyde (b) determined in acetonitrile. The peak area A at a specific wavelength given in the legend is plotted against the mass concentration  $\beta$ . The curves shown are means of a triple determination.

### 1.5.2.3 Detection measurements

HPLC measurements were performed as described in Chapter 1.2.2.2. The compounds were identified by their retention time and their characteristic absorption spectrum. The results of the pure compounds dissolved in acetonitrile are shown exemplarily in the following.

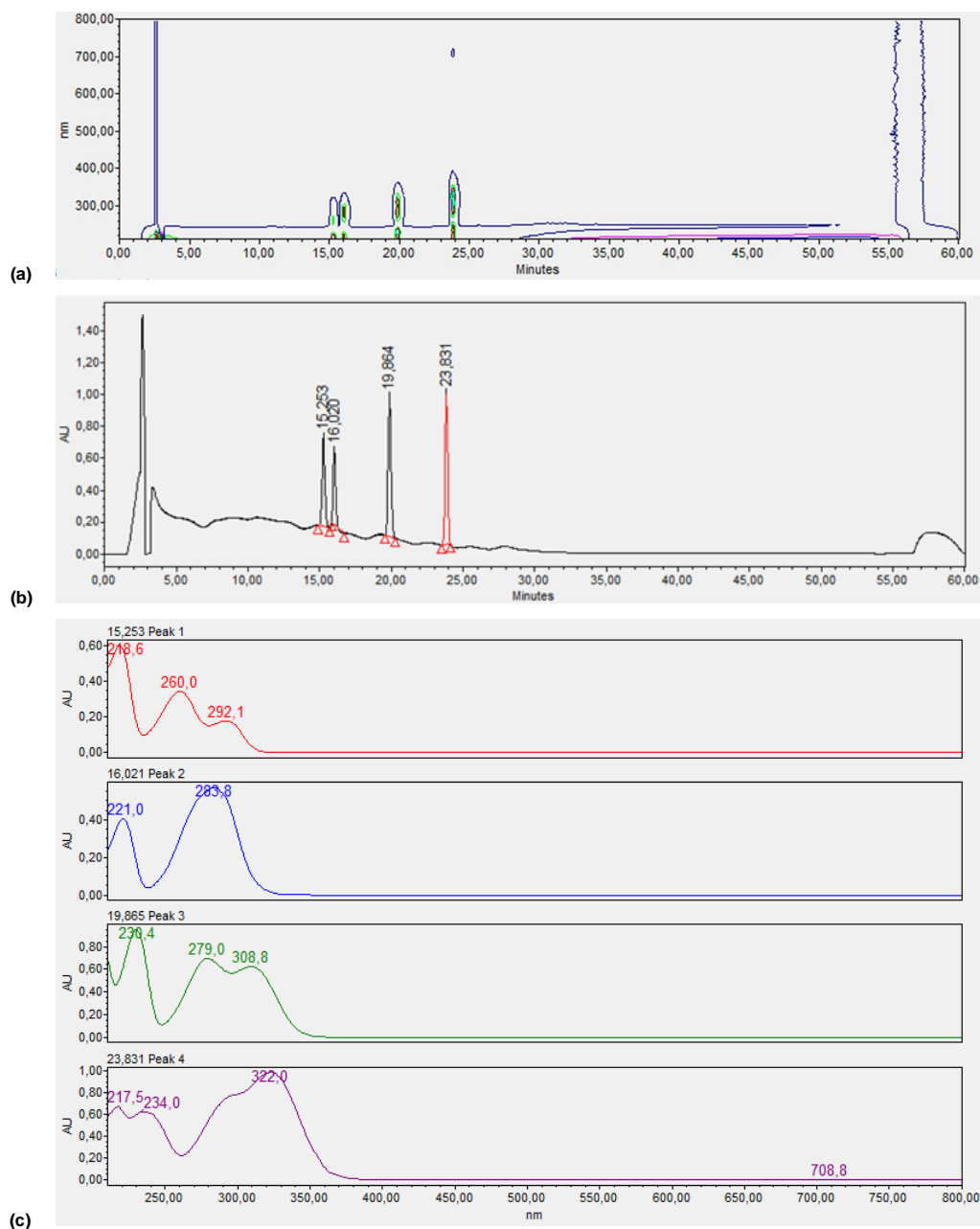


Figure S.1 - 3: (a) 2D contour plot of vanillic acid (15.2 min), p-hydroxybenzaldehyde (16.0 min), vanillin (19.9 min), and ferulic acid (23.8 min) dissolved in acetonitrile obtained by HPLC measurements. (b) The corresponding mono-dimensional chromatogram. (c) The detected absorbance spectra of the selected peaks.

#### 1.5.2.4 Preparative HPLC measurements

Preparative HPLC measurements were carried out using the binary Agilent Infinity 1260 HPLC connected to a 1260 Agilent diode array detector, a 1260 Agilent fraction collector, a 1260 Agilent manual injector and a Nucleodur C18 Isis 5  $\mu\text{m}$  21.2 x 250 mm column (Macherey-Nagel) equipped with a guard column. 0.6 mL aliquots of the converted extract in EtOH/TriA were injected manually. A flow of 21 mL/min and the gradient shown in Table S.1 - 3 were applied. Vanillin and p-hydroxybenzaldehyde were collected with retention times ranging from about 9.7 - 10.6 min. Vanillic acid could not be isolated because of the small amount. Prior concentration is necessary to make the corresponding peak visible.

*Table S.1 - 3: Gradient applied to the mobile phase during preparative HPLC measurements. Solvent A consisted of acetonitrile and solvent B of water.*

time [min]	solvent A [% (v/v)]	solvent B [% (v/v)]
0	90	10
15	35	65
16	100	0
19	100	0

#### 1.5.3 Mass spectrometry

Liquid chromatography coupled to a mass spectrometer was performed on a Q-TOF 6540 UHD (Agilent), applying electrospray ionization (ESI).

## 1.5.3.1 Photochemical conversion of synthetic curcumin I in EtOH/TriA

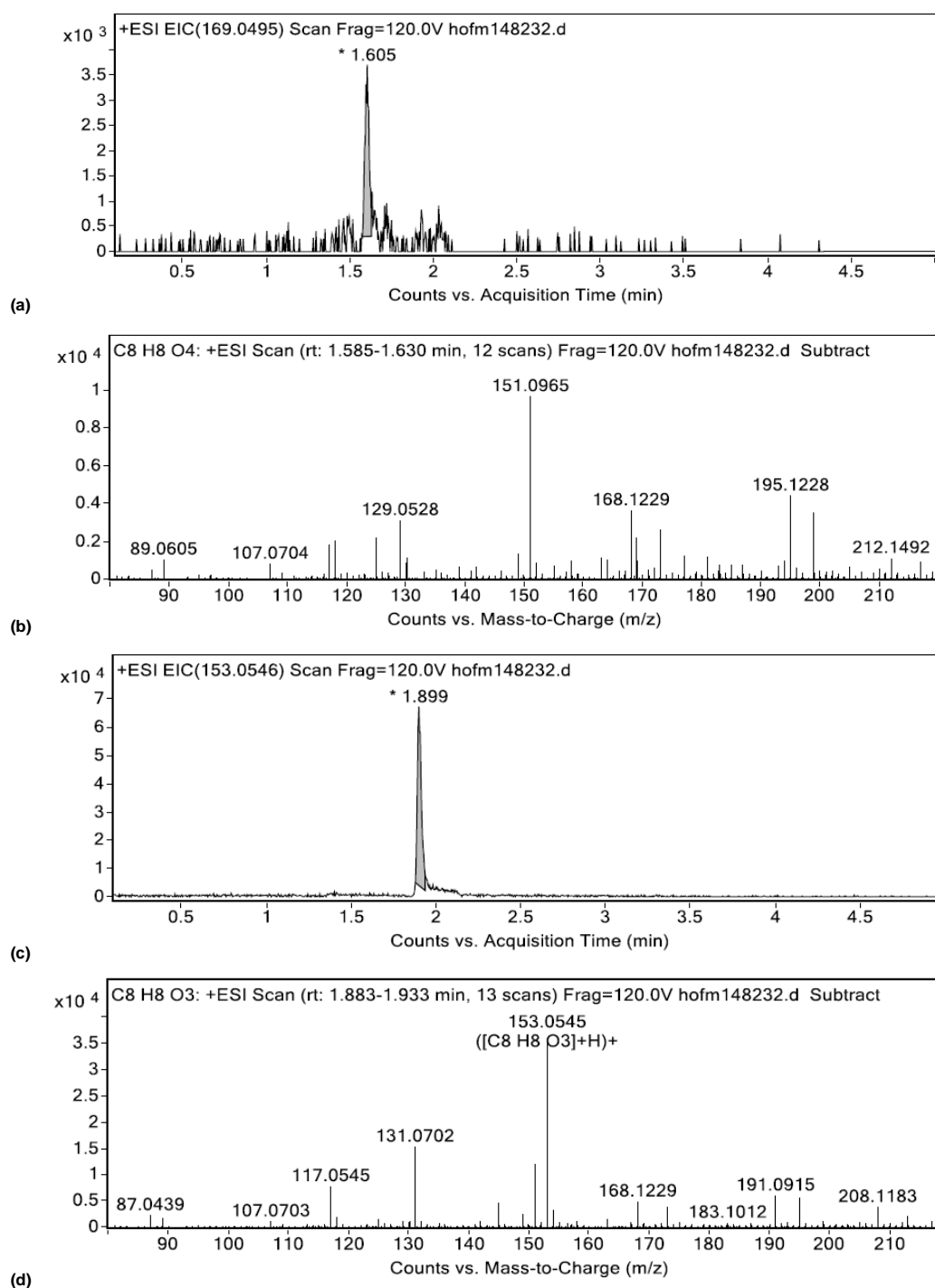
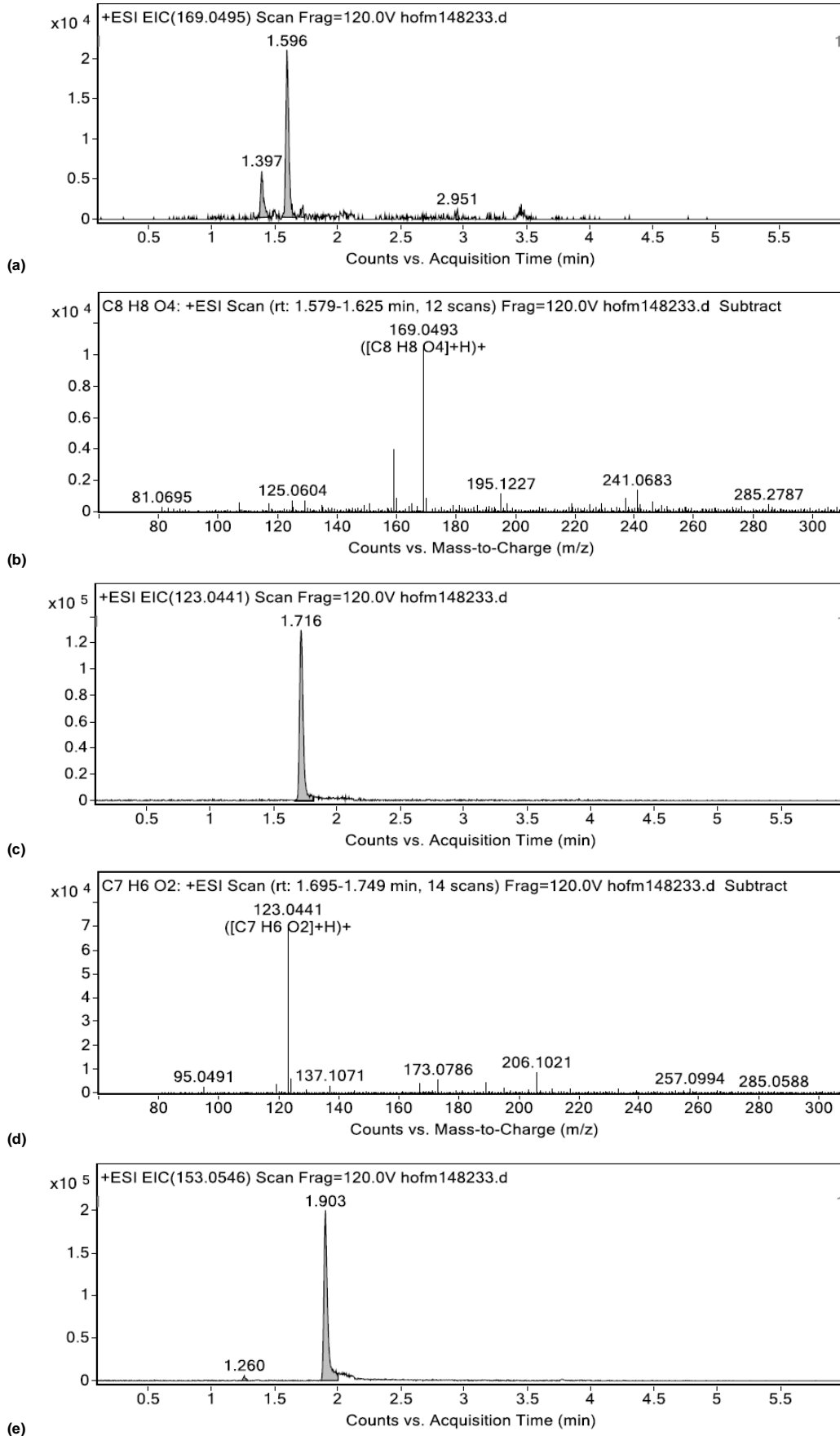


Figure S.1 - 4: MS results obtained after 1 h photochemical conversion of 2 mM curcumin I in the binary mixture EtOH/TriA. (a,b) Extracted ion chromatogram (EIC) at a mass-to-charge ( $m/z$ ) of 169.0495 with the corresponding mass spectrum at 1.6 min. (c,d) EIC at an  $m/z$  of 153.0546 with the corresponding mass spectrum at 1.9 min. The measurements prove the presence of vanillic acid with a molar mass of 168.2 g/mol (a,b) and vanillin with 152.1 g/mol (c,d).

1.5.3.2 Photochemical conversion of Curcuma extract in EtOH/TriA



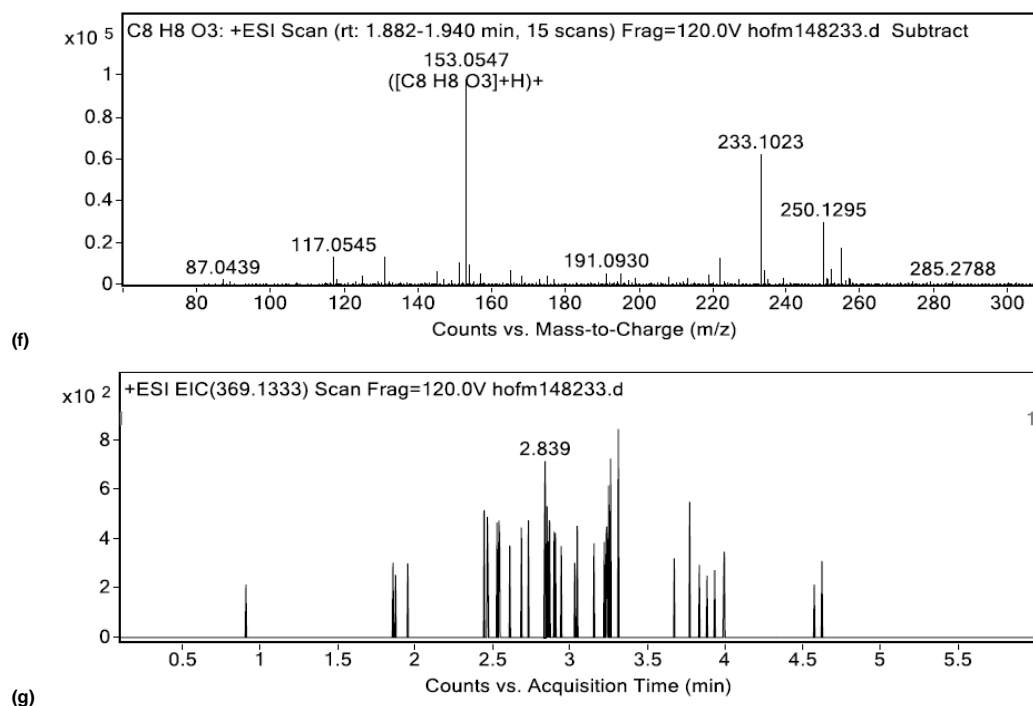
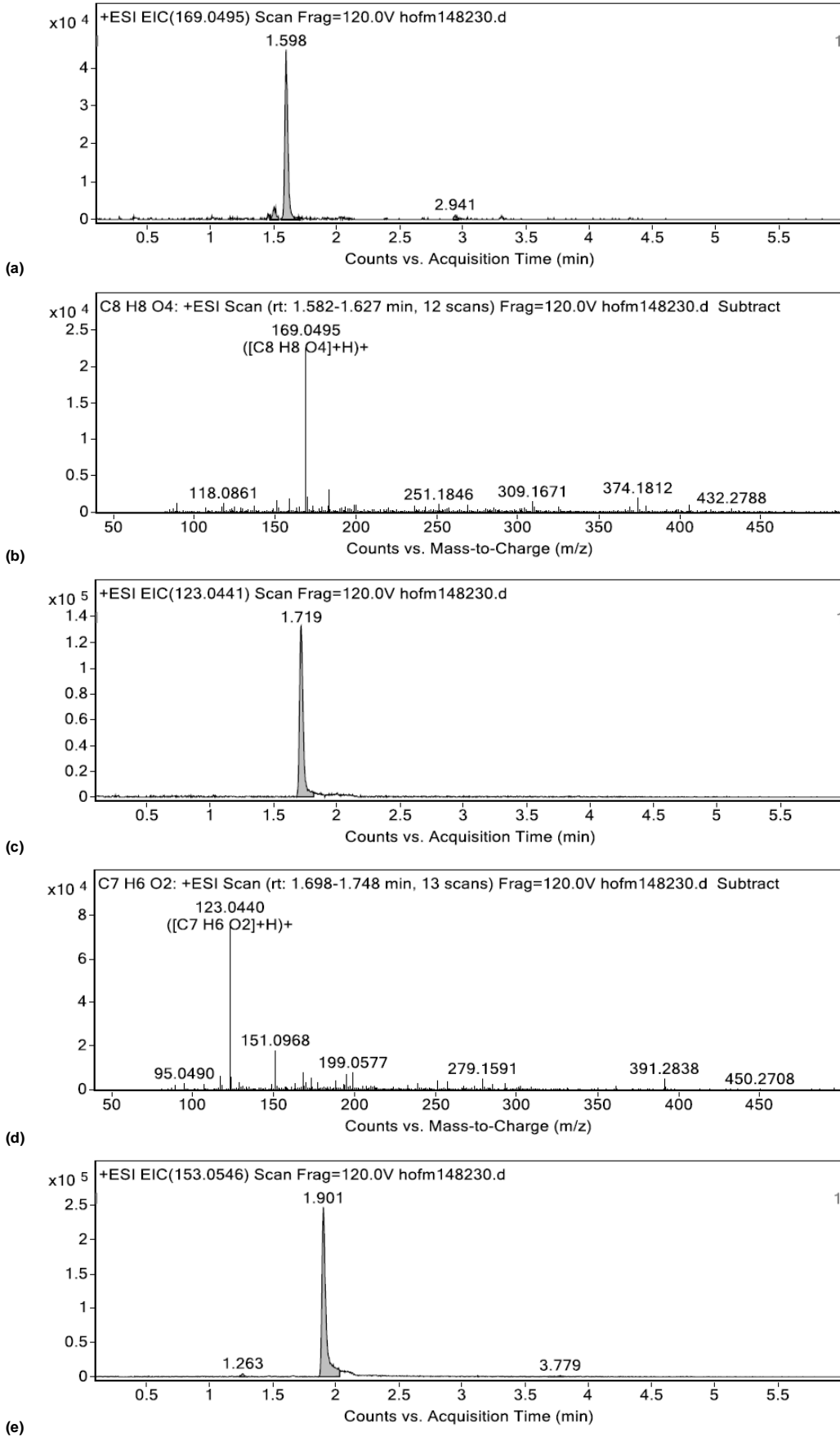


Figure S.1 - 5: MS results obtained after 12 h photochemical conversion of a *Curcuma* extract in the binary mixture EtOH/TriA. (a,b) Extracted ion chromatogram (EIC) at a mass-to-charge ( $m/z$ ) of 169.0495 with the corresponding mass spectrum at 1.6 min. (c,d) EIC at an  $m/z$  of 123.0441 with the corresponding mass spectrum at 1.7 min. (e,f) EIC at an  $m/z$  of 153.0546 with the corresponding mass spectrum at 1.9 min. (g) EIC at an  $m/z$  of 369.1333. The measurements prove the presence of vanillic acid with a molar mass of 168.2 g/mol (a,b), *p*-hydroxybenzaldehyde with 122.1 g/mol (c,d), and vanillin with 152.1 g/mol (e,f). Only traces of curcumin I (368.39 g/mol) are detectable, leading to the conclusion that almost all of the curcumin has reacted.

1.5.3.3 Photochemical conversion of Curcuma extract in W/EtOH/TriA



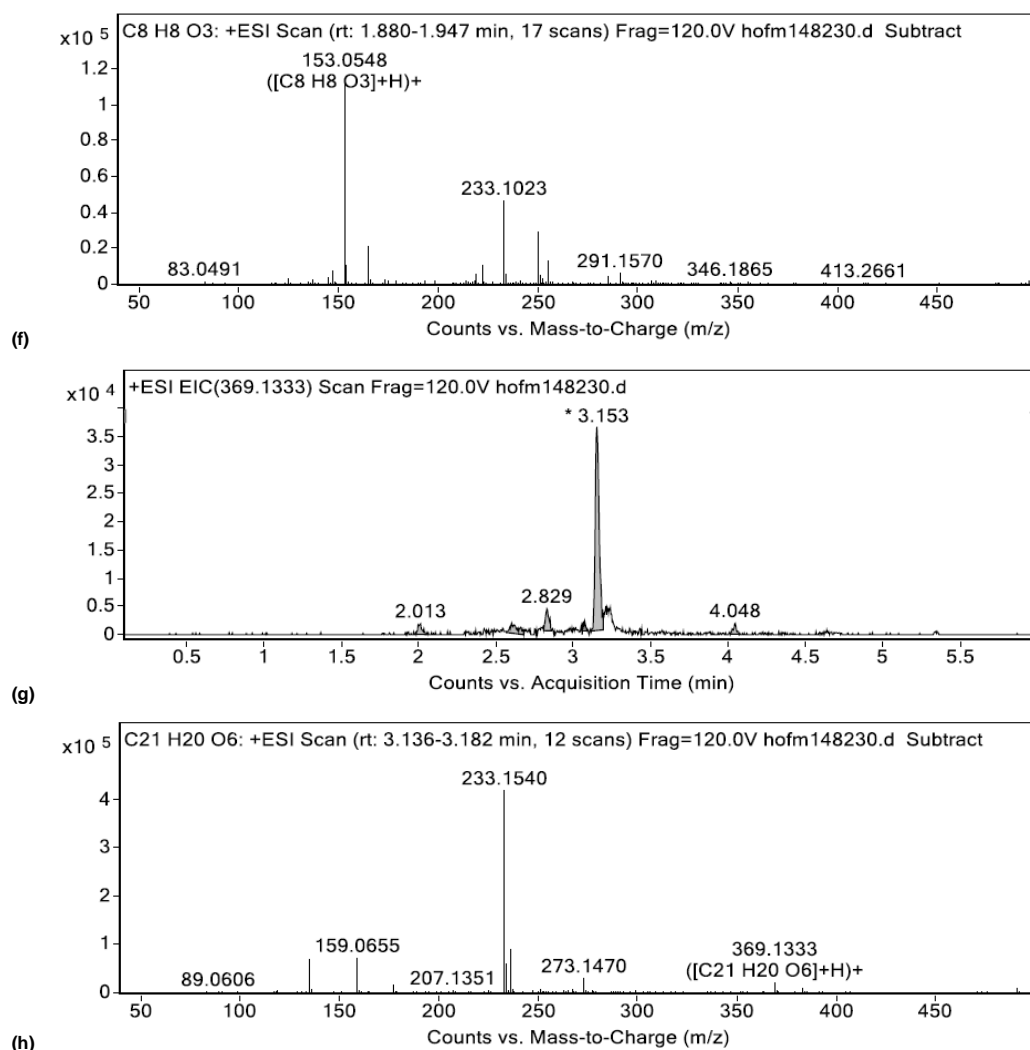


Figure S.1 - 6: MS results obtained after 12 h photochemical conversion of a Curcuma extract in the SFME W/EtOH/TriA. (a,b) Extracted ion chromatogram (EIC) at a mass-to-charge (m/z) of 169.0495 with the corresponding mass spectrum at 1.6 min. (c,d) EIC at an m/z of 123.0441 with the corresponding mass spectrum at 1.7 min. (e,f) EIC at an m/z of 153.0546 with the corresponding mass spectrum at 1.9 min. (g,h) EIC at an m/z of 369.1333 with the corresponding mass spectrum at 3.2 min. The measurements prove the presence of vanillic acid with a molar mass of 168.2 g/mol (a,b), p-hydroxybenzaldehyde with 122.1 g/mol (c,d), and vanillin with 152.1 g/mol (e,f). The signal of curcumin I (368.39 g/mol) is more pronounced than in the binary mixture. Thus, not all curcumin has reacted (g,h).

### 1.5.3.4 Isolated products after photochemical conversion of a Curcuma extract in EtOH/TriA

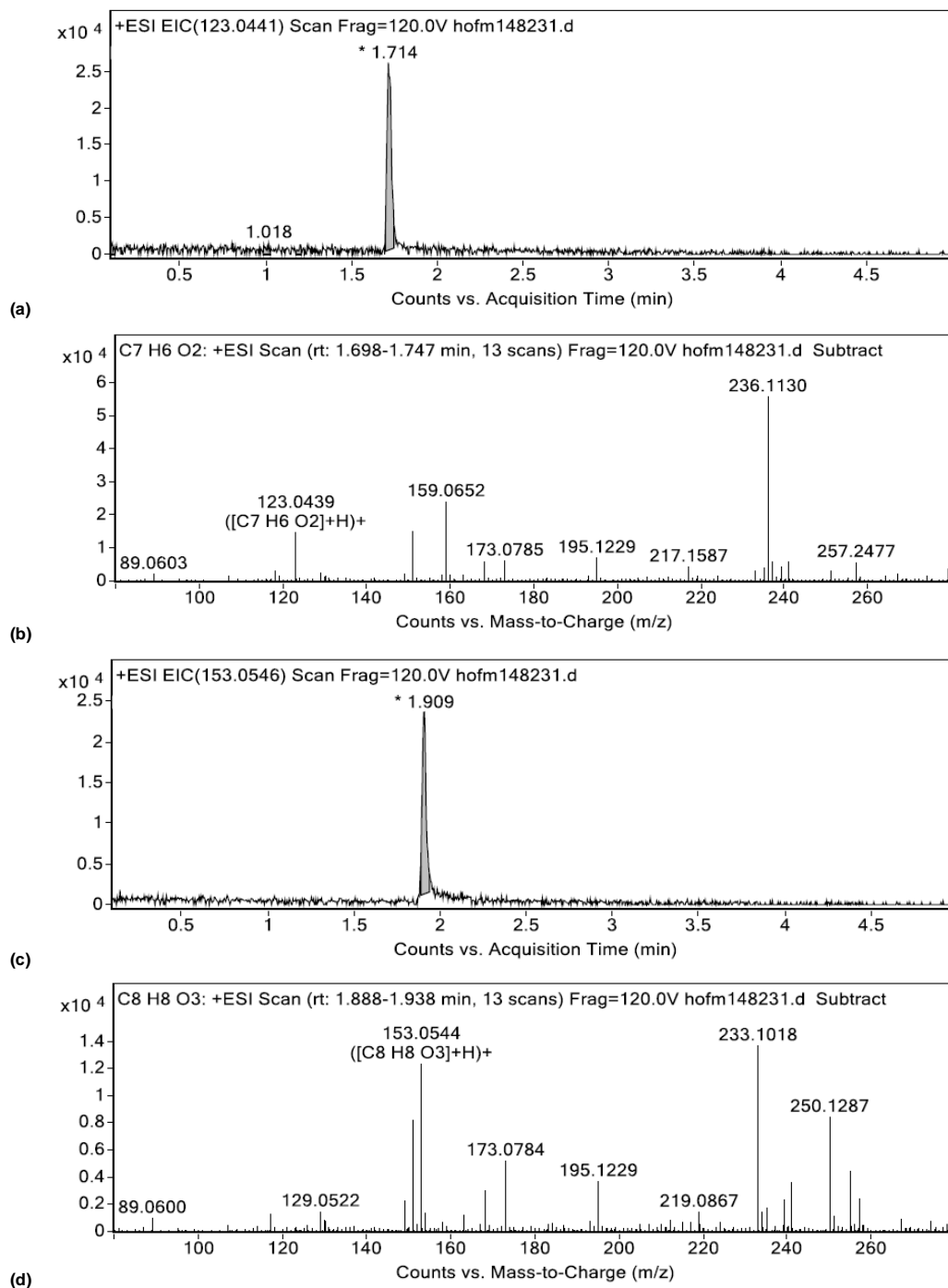


Figure S.1 - 7: MS results of the isolated products obtained by preparative HPLC (see Chapter 1.5.2.4). (a,b) Extracted ion chromatogram (EIC) at a mass-to-charge ( $m/z$ ) of 123.0441 with the corresponding mass spectrum at 1.7 min. (c,d) EIC at an  $m/z$  of 153.0546 with the corresponding mass spectrum at 1.9 min. The measurements prove the presence of *p*-hydroxybenzaldehyde with 122.1 g/mol (a,b) and vanillin with 152.1 g/mol (c,d).

As mentioned in Chapter 1.3.3, microemulsion-mediated extraction may also represent a suitable method for product separation. In this context, Krickl *et al.* studied SFMEs, which consist of cleavable components. The cleavage of the hydrotrope or the hydrophobic component could be initiated by changes in temperature and/or pH, which resulted in liquid-liquid phase separation. As a proof of concept, vanillic acid was dissolved in a ternary mixture and quantitatively separated by phase separation.<sup>47</sup> Triacetin can be cleaved by changing the pH, resulting in hydrolysis. Besides, phase separation can be initiated in the W/EtOH/TriA SFME by the addition of water and temperature changes.<sup>24,47,48</sup>

### 1.5.4 Experimental design

To evaluate quickly the best reaction setup, the experimental design shown in Table S.1 - 4 was performed. The factors studied are the substrate (ferulic acid/curcumin), its concentration, the usage of a catalyst, the stirring, the reaction time, the solvent (BM/SFME), and the power of incident light (see Table S.1 - 5).

*Table S.1 - 4: Matrix applied for the experimental design. Each row corresponds to one experiment (exp.) built up by 7 factors (Xi) that vary between the level "1" and "-1". The definition of factors and their levels are given in Table S.1 - 5. The mass concentration of vanillin detected by HPLC measurements is chosen as the response (Y).*

exp.	X1	X2	X3	X4	X5	X6	X7	Y [mg/L]
1	1	1	1	-1	1	-1	-1	37.2
2	-1	1	1	1	-1	1	-1	3.7
3	-1	-1	1	1	1	-1	1	0
4	1	-1	-1	1	1	1	-1	13.7
5	-1	1	-1	-1	1	1	1	0.6
6	1	-1	1	-1	-1	1	1	3.1
7	1	1	-1	1	-1	-1	1	54.2
8	-1	-1	-1	-1	-1	-1	-1	0

By conducting the 8 different experiments given in Table S.1 - 4, the best combination out of the 7 factors with 2 possibilities each can be found. The detected amount of vanillin is used as response Y. This allows calculating the coefficients  $b$  according to Equation 1 – 1, taking into account all experiments  $i$ . Whenever the coefficient is larger than 0, level 1 has a positive effect on the amount of synthesized vanillin. Whenever the coefficient is smaller than 0, level -1 improves the result. The  $b_0$  value is determined to be 14.1 mg/L.

$$b_1 = \frac{\sum X_{1i} Y_{1i}}{8} \quad \text{Eq. 1 - 1}$$

Accordingly, the perfect experimental setup includes 2 mM curcumin without the catalyst dissolved in the binary mixture EtOH/TriA. The reaction should be stirred at 500 rpm and irradiated with blue light (455 nm) with 7 W for 2 h. This corresponds to experiment 7. Especially the substrate, its concentration, and the choice of the solvent have a great impact resulting in a great coefficient value.

Table S.1 - 5: Factors and their levels that are used for the experimental design, shown in Table S.1 - 4, with their calculated coefficient (b).

factor		level		b [mg/L]
X1	substrate	ferulic acid	-1	13.0
		curcumin	1	
X2	substrate concentration	1 mM	-1	9.9
		2 mM	1	
X3	catalyst	none	-1	-3.1
		TARF	1	
X4	stirring	250 rpm	-1	3.8
		500 rpm	1	
X5	reaction time	2 h	-1	-1.2
		4 h	1	
X6	solvent	EtOH/TriA	-1	-8.8
		W/EtOH/TriA	1	
X7	power of incident light	3 W	-1	0.4
		7 W	1	

## 1.5.5 Parameter optimization

### 1.5.5.1 Impact of oxygen concentration and wavelength of the light

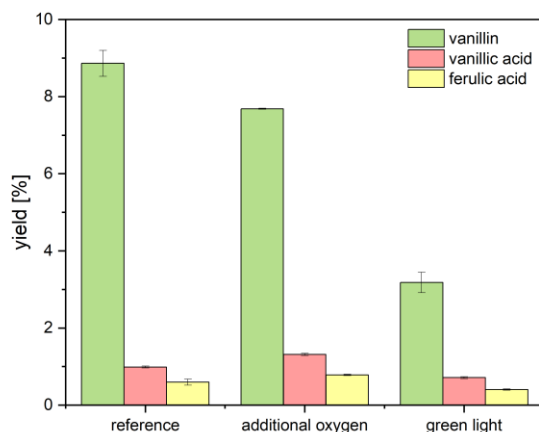


Figure S.1 - 8: Detected yield of vanillin, vanillic acid, and ferulic acid after photochemical conversion of curcumin I in the binary mixture. The reference sample is run under standard conditions (2 mM substrate, 2 h irradiation with blue light at 455 nm, 500 rpm stirring). In the sample with additional oxygen, the solution and the gas phase in the vial were each saturated with oxygen (instead of atmospheric air) for 1 min. The additional oxygen reduces the amount of synthesized vanillin. So, there is also an upper limit for the optimal oxygen concentration. The high amount of oxygen oxidizes the desired products further, which is confirmed by a higher amount of detected vanillic acid. In addition, it may favor the other side reactions. The third sample is irradiated with a green light with a wavelength of 528 nm. The small absorption of curcumin is still enough to stay reactive. However, the reaction outcome is reduced significantly.

### 1.5.5.2 Impact of substrate concentration and light path

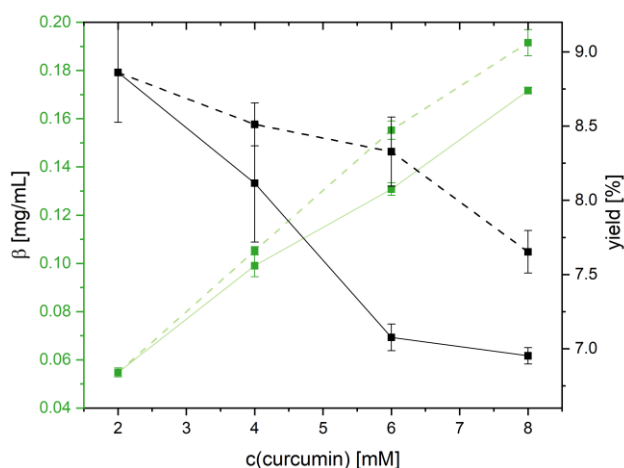


Figure S.1 - 9: Detected mass concentration  $\beta$  and yield of vanillin after photochemical conversion in the binary mixture as a function of the substrate concentration. The straight line depicts the result when using a constant sample volume of 4 mL. The dashed lines represent the outcome when adapting the length of the light pathway on the substrate concentration. For this purpose, the solvent volume is reduced by the factor of the increase in the curcumin concentration. In all samples, the substrate conversion achieved 100 %.

### 1.5.5.3 Impact of temperature

The experiments measured at 30 – 40 °C were run in the air-cooled TAK 120 AC photoreactor as described in Chapter 1.2.2.1. The temperature was measured in a vial filled with water. The reactions are performed without additional heating. The heating is only a consequence of the LEDs. In order to achieve 0 °C, the vials were placed in a TAK 120 LC (liquid-cooled) photoreactor connected to a control-unit TAK 120 LC. The vials were surrounded by a water-glycol-based bath fluid (Thermal G from Julabo), and the whole system was temperature-controlled using a WK 400 thermostat from Colora. In this case, the temperature was measured in the water-glycol bath fluid. The wavelength of the LEDs was 451 nm. The reactions run at 70 °C were performed in a temperature-controlled heating block. The wavelength of the LEDs was 455 nm. In every setup, the samples were placed on top of the light source and thus illuminated from below. All vials contained 2 mM curcumin I in 4 mL of the binary solution EtOH/TriA. The samples were stirred at 500 rpm and irradiated for 2 h.

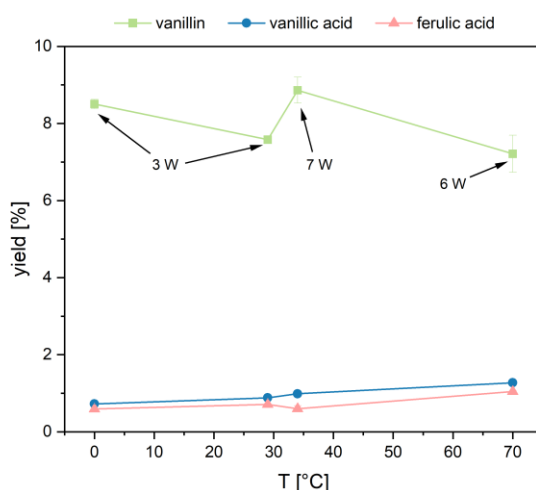


Figure S.1 - 10: Impact of temperature on the photochemical conversion of curcumin in EtOH/TriA. The power of light varies due to different setups that were applied to achieve the different temperatures. Increasing temperatures lead to a decrease in the yield of vanillin, while higher power of light improves the reaction outcome. In the case of vanillic acid and ferulic acid, higher temperatures result in an increase in yield. The impact of the power of light appears to be negligible. In all reactions, a conversion of 100 % of curcumin is achieved.

### 1.5.5.4 Impact of duration of exposure

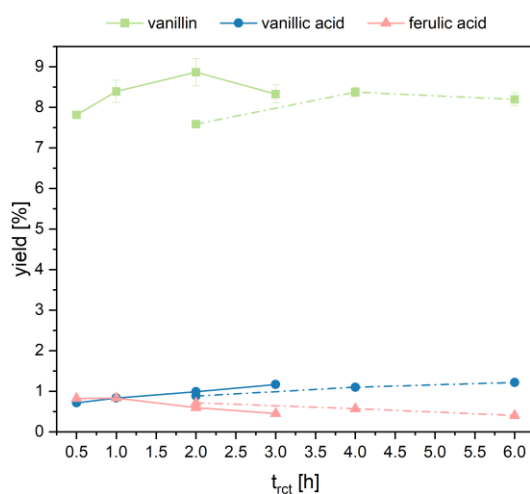


Figure S.1 - 11: Detected yield of vanillin, vanillic acid, and ferulic acid after conversion of curcumin I in EtOH/TriA as a function of reaction time ( $t_{\text{react}}$ ). The reaction was performed under standard conditions with 7 W irradiation (straight line) or with 3 W (dotted line). Irradiation with 7 W reveals an optimum in vanillin production after 2 h. The amount of ferulic acid starts to decrease after 1 h, while the amount of vanillic acid continues to increase due to further oxidation of vanillin. Since the amount of detected vanillin is reduced when applying 3 W, longer durations of exposure are considered. However, the limit is reached after 4 h, which is still below the maximum obtained with 7 W.

### 1.5.6 Photochemical conversion of ferulic acid

The role of ferulic acid as a possible substrate is studied further in the following. The experimental results revealed that the presence of a photocatalyst is essential to initiate the reaction. Gómez-López *et al.* reported a conversion of ferulic acid into vanillin that is initiated by thermal decarboxylation followed by a second step catalyzed by a Cu-based catalyst.<sup>49</sup> For this purpose, the effect of heating during irradiation with 455 nm is investigated. In order to obtain 70 °C, the setup described in Chapter 1.5.5.3 was applied. However, heating to 70 °C is not sufficient to activate ferulic acid, and no vanillin is detectable (see Figure S.1 - 12(a)). Furthermore, curcumin is applied in catalytic amounts to study its properties as a photocatalyst. As shown in Figure S.1 - 12, curcumin can initiate the conversion of ferulic acid into vanillin. The detected amount of vanillin is higher than obtained by conversion of the same amount of curcumin without ferulic acid. It can be seen that the amount of vanillin synthesized exceeds the result with TARF as the photocatalyst, although substrate conversion is higher in the latter case (see Figure S.1 - 12(b)). Hence, TARF seems to catalyze preferentially other parallel reactions.

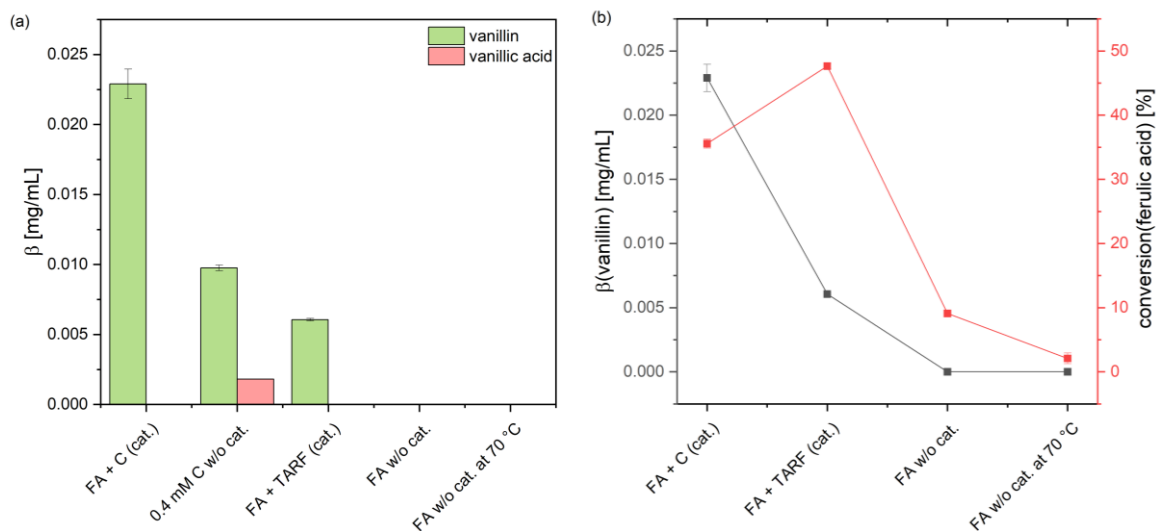


Figure S.1 - 12: Detected mass concentration  $\beta$  of vanillin and vanillic acid after photocatalytic conversion of ferulic acid (FA) or curcumin (C) dissolved in the binary mixture (BM) EtOH/TriA. The mixture contains curcumin (C) or tetraacetyl riboflavin (TARF) as catalyst (cat.) or is performed in absence of any catalyst (w/o cat.). (b) Detected mass concentration of vanillin and the conversion of ferulic acid in the corresponding samples.

### 1.5.7 Reference sample without exposure to light

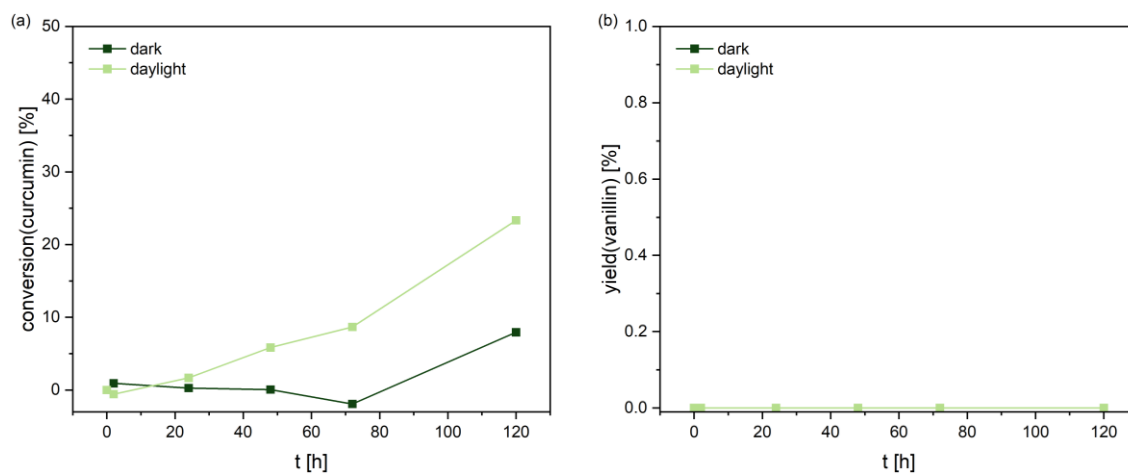


Figure S.1 - 13: Conversion of curcumin in EtOH/TriA without any exposure to light (dark) or with exposure to daylight only (daylight) (a) with the corresponding yield of vanillin (b). Although curcumin starts to degrade, there is no vanillin detectable after 5 d.

### 1.5.8 Curcuma extract

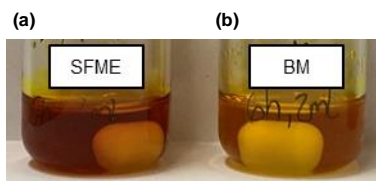


Figure S.1 - 14: Photograph of the Curcuma extract in the SFME W/EtOH/TriA (a) and BM EtOH/TriA (b).

## 1.6 References

- (1) Hofmann, E.; Degot, P.; Touraud, D.; König, B.; Kunz, W. Novel Green Production of Natural-like Vanilla Extract from Curcuminoids. *Food Chem.* **2023**, *417*, 135944. <https://doi.org/10.1016/j.foodchem.2023.135944>.
- (2) García-Bofill, M.; Sutton, P. W.; Straatman, H.; Brummund, J.; Schürmann, M.; Guillén, M.; Álvaro, G. Biocatalytic Synthesis of Vanillin by an Immobilised Eugenol Oxidase: High Biocatalyst Yield by Enzyme Recycling. *Appl. Catal. A Gen.* **2021**, *610* (117934). <https://doi.org/10.1016/j.apcata.2020.117934>.
- (3) Banerjee, G.; Chattopadhyay, P. Vanillin Biotechnology: The Perspectives and Future. *J. Sci. Food Agric.* **2019**, *99* (2), 499–506. <https://doi.org/10.1002/jsfa.9303>.
- (4) Anuradha, K.; Shyamala, B. N.; Naidu, M. M. Vanilla - Its Science of Cultivation, Curing, Chemistry, and Nutraceutical Properties. *Crit. Rev. Food Sci. Nutr.* **2013**, *53* (12), 1250–1276. <https://doi.org/10.1080/10408398.2011.563879>.
- (5) Fouché, J. G.; Jouve, L. Vanilla *Planifolia*: History, Botany and Culture in Réunion Island. *Agronomie* **1999**, *19* (8), 689–703. <https://doi.org/10.1051/agro:19990804>.
- (6) Ranadive, A. S. Vanillin and Related Flavor Compounds in Vanilla Extracts Made from Beans of Various Global Origins. *J. Agric. Food Chem.* **1992**, *40* (10), 1922–1924. <https://doi.org/10.1021/jf00022a039>.
- (7) Sinha, A. K.; Sharma, U. K.; Sharma, N. A Comprehensive Review on Vanilla Flavor: Extraction, Isolation and Quantification of Vanillin and Others Constituents. *Int. J. Food Sci. Nutr.* **2008**, *59* (4), 299–326. <https://doi.org/10.1080/09687630701539350>.
- (8) Hernandez-Hernandez, J. Mexican Vanilla Production. In *Handbook of Vanilla Science and Technology*; Havkin-frenkel, D., Belanger, F. C., Eds.; 2018. <https://doi.org/10.1002/9781119377320.ch1>.
- (9) Chattopadhyay, P.; Banerjee, G.; Sen, S. K. Cleaner Production of Vanillin through Biotransformation of Ferulic Acid Esters from Agroresidue by *Streptomyces Sannanensis*. *J. Clean. Prod.* **2018**, *182*, 272–279. <https://doi.org/10.1016/j.jclepro.2018.02.043>.
- (10) Sharma, A.; Verma, S. C.; Saxena, N.; Chadda, N.; Singh, N. P.; Sinha, A. K. Microwave- and Ultrasound-Assisted Extraction of Vanillin and Its Quantification by

- High-Performance Liquid Chromatography in Vanilla Planifolia. *J. Sep. Sci.* **2006**, *29* (5), 613–619. <https://doi.org/10.1002/jssc.200500339>.
- (11) Jadhav, D.; B.N., R.; Gogate, P. R.; Rathod, V. K. Extraction of Vanillin from Vanilla Pods: A Comparison Study of Conventional Soxhlet and Ultrasound Assisted Extraction. *J. Food Eng.* **2009**, *93* (4), 421–426. <https://doi.org/10.1016/j.jfoodeng.2009.02.007>.
- (12) Martău, G. A.; Călinoiu, L.-F.; Vodnar, D. C. Bio-Vanillin: Towards a Sustainable Industrial Production. *Trends Food Sci. Technol.* **2021**, *109*, 579–592. <https://doi.org/10.1016/j.tifs.2021.01.059>.
- (13) Ciriminna, R.; Fidalgo, A.; Meneguzzo, F.; Parrino, F.; Ilharco, L. M.; Pagliaro, M. Vanillin: The Case for Greener Production Driven by Sustainability Megatrend. *ChemistryOpen* **2019**, *8* (6), 660–667. <https://doi.org/10.1002/open.201900083>.
- (14) De Guzman, C. C.; Zara, R. R. 29 - Vanilla. In *Handbook of Herbs and Spices*; 2012; Vol. 1. <https://doi.org/10.1533/9780857095671.547>.
- (15) Chemat, F.; Vian, M. A.; Cravotto, G. Green Extraction of Natural Products: Concept and Principles. *Int. J. Mol. Sci.* **2012**, *13* (7), 8615–8627. <https://doi.org/10.3390/ijms13078615>.
- (16) Havkin-Frenkel, D.; Belanger, F. C. *Biotechnology in Flavor Production*, Blackwell Publishing Ltd, 2009. <https://doi.org/10.1002/9781444302493>.
- (17) Fang, Z.; Yong, Y. C.; Zhang, J.; Du, G.; Chen, J. Keratinolytic Protease: A Green Biocatalyst for Leather Industry. *Appl. Microbiol. Biotechnol.* **2017**, *101* (21), 7771–7779. <https://doi.org/10.1007/s00253-017-8484-1>.
- (18) Esparan, V.; Krings, U.; Struch, M.; Berger, R. G. A Three-Enzyme-System to Degrade Curcumin to Natural Vanillin. *Molecules* **2015**, *20*, 6640–6653. <https://doi.org/10.3390/molecules20046640>.
- (19) Ma, Q.; Liu, L.; Zhao, S.; Huang, Z.; Li, C.; Jiang, S.; Li, Q.; Gu, P. Biosynthesis of Vanillin by Different Microorganisms: A Review. *World J. Microbiol. Biotechnol.* **2022**, *38* (3), 1727. <https://doi.org/10.1007/s11274-022-03228-1>.
- (20) Liu, H. M.; Zou, Y.; Yao, C. Y.; Yang, Z. Enzymatic Synthesis of Vanillin and Related Catalytic Mechanism. *Flavour Fragr. J.* **2019**, *35* (1), 51–58. <https://doi.org/10.1002/ffj.3528>.
- (21) Camera-Roda, G.; Augugliaro, V.; Cardillo, A.; Loddo, V.; Palmisano, G.; Palmisano, L. A Pervaporation Photocatalytic Reactor for the Green Synthesis of Vanillin. *Chem.*

- Eng. J.* **2013**, 224 (1), 136–143. <https://doi.org/10.1016/j.cej.2012.10.037>.
- (22) Suprianto, T.; Winarto; Wijayanti, W.; Wardana, I. N. G. Synergistic Effect of Curcumin and Activated Carbon Catalyst Enhancing Hydrogen Production from Biomass Pyrolysis. *Int. J. Hydrogen Energy* **2021**, 46 (10), 7147–7164. <https://doi.org/10.1016/j.ijhydene.2020.11.211>.
- (23) Vollono, L.; Falconi, M.; Gaziano, R.; Iacovelli, F.; Dika, E.; Terracciano, C.; Bianchi, L.; Campione, E. Potential of Curcumin in Skin Disorders. *Nutrients* **2019**, 11 (9), 2169. <https://doi.org/10.3390/nu11092169>.
- (24) Degot, P.; Huber, V.; Hofmann, E.; Hahn, M.; Touraud, D.; Kunz, W. Solubilization and Extraction of Curcumin from Curcuma Longa Using Green, Sustainable, and Food-Approved Surfactant-Free Microemulsions. *Food Chem.* **2021**, 336, 127660. <https://doi.org/10.1016/j.foodchem.2020.127660>.
- (25) Michels, L.; Richter, A.; Chellappan, R. K.; Rost, H. I.; Behsen, A.; Wells, K. H.; Leal, L.; Santana, V.; Blawid, R.; Silva, G. J.; Cooil, S. P.; Wells, J. W.; Blawid, S. Electronic and Structural Properties of the Natural Dyes Curcumin , Bixin and Indigo. *RCS Adv.* **2021**, 11 (23), 14169–14177. <https://doi.org/10.1039/D0RA08474C>.
- (26) Chassagnez-Méndez, A. L.; Corrêa, N. C. F.; França, L. F.; Machado, N. T.; Araújo, M. E. Mass Transfer Model Applied to the Supercritical Extraction with CO<sub>2</sub> of Curcumins from Turmeric Rhizomes (Curcuma Longa L). *Brazilian J. Chem. Eng.* **2000**, 17 (3), 315–322. <https://doi.org/10.1590/S0104-66322000000300007>.
- (27) Aggarwal, B. B. *The Molecular Targets and Therapeutic Uses of Curcumin in Health and Disease*, Aggarwal, B. B., Surh, Y.-J., Shishodia, S., Eds.; Springer New York, NY, 2007. <https://doi.org/10.1007/978-0-387-46401-5>.
- (28) Goel, A.; Kunnumakkara, A. B.; Aggarwal, B. B. Curcumin as “Curecumin”: From Kitchen to Clinic. *Biochem. Pharmacol.* **2008**, 75 (4), 787–809. <https://doi.org/10.1016/j.bcp.2007.08.016>.
- (29) Hatcher, H.; Planalp, R.; Cho, J.; Torti, F. M.; Torti, S. V. Curcumin: From Ancient Medicine to Current Clinical Trials. *Cell. Mol. Life Sci.* **2008**, 65 (11), 1631–1652. <https://doi.org/10.1007/s00018-008-7452-4>.
- (30) Omosa, L. K.; Midiwo, J. O.; Kuete, V. *Curcuma Longa*; Elsevier, 2017. <https://doi.org/10.1016/B978-0-12-809286-6.00019-4>.
- (31) Rafiee, Z.; Nejatian, M.; Daeihamed, M.; Jafari, S. M. Application of Curcumin-Loaded Nanocarriers for Food, Drug and Cosmetic Purposes. *Trends Food Sci.*

- Technol.* **2019**, *88*, 445–458. <https://doi.org/10.1016/j.tifs.2019.04.017>.
- (32) Ayer, D. K. Breeding for Quality Improvement in Turmeric (*Curcuma Longa* L.): A Review. *Adv. Plants Agric. Res.* **2017**, *6* (6), 201–204. <https://doi.org/10.15406/apar.2017.06.00238>.
- (33) Ashraf, K.; Mujeeb, M.; Ahmad, A.; Ahmad, N.; Amir, M. Determination of Curcuminoids in *Curcuma Longa* Linn. by UPLC/Q-TOF – MS: An Application in Turmeric Cultivation. *J. Chromatogr. Sci.* **2015**, *53* (8), 1346–1352. <https://doi.org/https://doi.org/10.1093/chromsci/bmv023>.
- (34) Tayyem, R. F.; Heath, D. D.; Al-Delaimy, W. K.; Rock, C. L. Curcumin Content of Turmeric and Curry Powders. *Nutr. Cancer* **2006**, *55* (2), 126–131. [https://doi.org/10.1207/s15327914nc5502\\_2](https://doi.org/10.1207/s15327914nc5502_2).
- (35) Mandal, V.; Mohan, Y.; Hemalatha, S. Microwave Assisted Extraction of Curcumin by Sample-Solvent Dual Heating Mechanism Using Taguchi L9 Orthogonal Design. *J. Pharm. Biomed. Anal.* **2008**, *46* (2), 322–327. <https://doi.org/10.1016/j.jpba.2007.10.020>.
- (36) Baumann, W.; Rodrigues, S. V.; Viana, L. M. Pigments and Their Solubility in and Extractability by Supercritical CO<sub>2</sub> - I: The Case of Curcumin. *Brazilian J. Chem. Eng.* **2000**, *17* (3), 323–328. <https://doi.org/10.1590/S0104-66322000000300008>.
- (37) Heffernan, C.; Ukrainczyk, M.; Gamidi, R. K.; Hodnett, B. K.; Rasmuson, Å. C. Extraction and Purification of Curcuminoids from Crude Curcumin by a Combination of Crystallization and Chromatography. *Org. Process Res. Dev.* **2017**, *21* (6), 821–826. <https://doi.org/10.1021/acs.oprd.6b00347>.
- (38) Bharti, C.; Nagoure, A.; Gupta, R. K. Biotransformation of Curcumin to Vanillin. *Indian J. Chem. - Sect. B Org. Med. Chem.* **2011**, *5* (8), 1119–1122.
- (39) Larson, R. A.; Stackhouse, P. L.; Crowley, T. O. Riboflavin Tetraacetate: A Potentially Useful Photosensitizing Agent for the Treatment of Contaminated Waters. *Environ. Sci. Technol.* **1992**, *26* (9), 1792–1798. <https://doi.org/10.1021/es00033a013>.
- (40) Buchecker, T.; Krickl, S.; Winkler, R.; Grillo, I.; Bauduin, P.; Touraud, D.; Pfitzner, A.; Kunz, W. The Impact of the Structuring of Hydrotropes in Water on the Mesoscale Solubilisation of a Third Hydrophobic Component. *Phys. Chem. Chem. Phys.* **2017**, *19* (3), 1806–1816. <https://doi.org/10.1039/c6cp06696h>.
- (41) Mühldorf, B.; Wolf, R. C-H Photooxygenation of Alkyl Benzenes Catalyzed by Riboflavin Tetraacetate and a Non-Heme Iron Catalyst. *Angew. Chemie - Int. Ed.*

- 2016**, 55 (1), 427–430. <https://doi.org/10.1002/anie.201507170>.
- (42) Schneider, C.; Gordon, O. N.; Edwards, R. L.; Luis, P. B. Degradation of Curcumin: From Mechanism to Biological Implications. *J. Agric. Food Chem.* **2015**, 63 (35), 7606–7614. <https://doi.org/10.1021/acs.jafc.5b00244>.
- (43) Tønnesen, H. H.; Karlsen, J.; van Henegouwen, G. B. Studies on Curcumin and Curcuminoids VIII. Photochemical Stability of Curcumin. *Z. Lebensm. Unters. Forsch.* **1986**, 183 (2), 116–122. <https://doi.org/10.1007/BF01041928>.
- (44) Swinehart, D. F. The Beer-Lambert Law. *J. Chem. Educ.* **1962**, 39 (7), 333–335. <https://doi.org/10.1021/ed039p333>.
- (45) Degot, P.; Huber, V.; Touraud, D.; Kunz, W. Curcumin Extracts from *Curcuma Longa* – Improvement of Concentration, Purity, and Stability in Food-Approved and Water-Soluble Surfactant-Free Microemulsions. *Food Chem.* **2021**, 339, 128140. <https://doi.org/10.1016/j.foodchem.2020.128140>.
- (46) Krickl, S.; Buchecker, T.; Meyer, A. U.; Grillo, I.; Touraud, D.; Bauduin, P.; König, B.; Pfitzner, A.; Kunz, W. A Systematic Study of the Influence of Mesoscale Structuring on the Kinetics of a Chemical Reaction. *Phys. Chem. Chem. Phys.* **2017**, 19 (35), 23773–23780. <https://doi.org/10.1039/c7cp02134h>.
- (47) Krickl, S.; Jurko, L.; Wolos, K.; Touraud, D.; Kunz, W. Surfactant-Free Microemulsions with Cleavable Constituents. *J. Mol. Liq.* **2018**, 271, 112–117. <https://doi.org/10.1016/j.molliq.2018.08.120>.
- (48) Yamasaki, E. THE SUCCESSIVE STAGES OF THE HYDROLYSIS OF TRIACETIN. *J. Am. Chem. Soc.* **1920**, 42 (7), 1455–1468. <https://doi.org/10.1021/ja01452a020>.
- (49) Gómez-López, P.; Lázaro, N.; Alvarado-Beltrán, C. G.; Pineda, A.; Balu, A. M.; Luque, R. One-Pot Cu/TiO<sub>2</sub> Nanoparticles Synthesis for Trans-Ferulic Acid Conversion into Vanillin. *Molecules* **2019**, 24 (21), 1–9. <https://doi.org/10.3390/molecules24213985>.

## Chapter 2 Sustainable cascade reaction combining transition metal-biocatalysis and hydrophobic substrates in surfactant-free aqueous solutions

### 2.0 Abstract

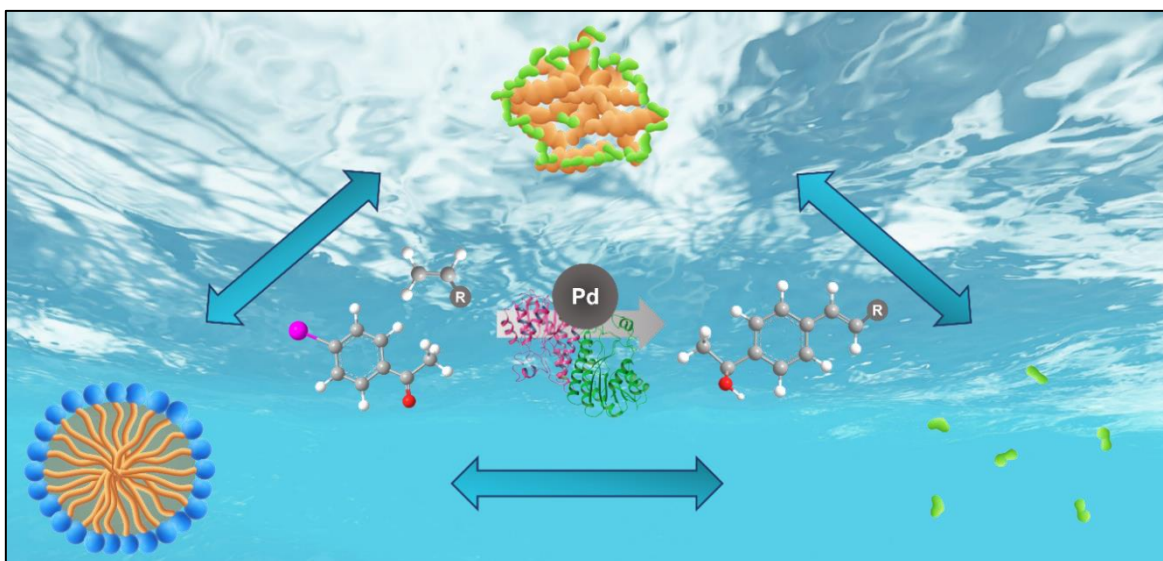


Figure 2 - 1: Schematic illustration of the transition metal-biocatalysis cascade reaction in reaction solvents exhibiting different types and extents of mesoscopic structuring.

A cascade reaction consisting of a Heck reaction followed by an enzyme-catalyzed reaction is carried out in different aqueous solutions. In particular, the impact of the structuring of the reaction solvent is investigated. For this purpose, several ternary mixtures of water, isopropanol, and benzyl alcohol, including surfactant-free microemulsions, as well as binary mixtures of water and isopropanol, are taken into account. A micellar solution of the surfactant TPGS-750-M serves as a reference system. The coupling of the two reactions can be successfully performed in all 3 types of solvents, whereby the best result is achieved in a surfactant-free microemulsion. In addition, our surfactant-free system allows for reducing the temperature during the Heck reaction. The studies further reveal that the structures built up by surfactants are not necessarily the main reason allowing organic reactions to be carried out in water. Rather, it is a question of solubility and stability of the reaction components. Better solubility does not always correlate with increased reactivity. We thus provide a deeper understanding of solvent-reactivity relationship and want to advert an approach beside micellar solvents for transferring organic reactions into environmentally friendly aqueous reaction solutions.

This chapter is submitted to *Chemical Engineering Journal* (Hofmann, E.; Schmauser, L.; Neugebauer, J.; Touraud, D.; Gallou, F.; Werner, K. Sustainable cascade reaction combining transition metal-biocatalysis and hydrophobic substrates in surfactant-free aqueous solutions. *Chem. Eng. J.* **2023**, in minor revision).<sup>1</sup> Lena Schmauser (University of Regensburg, Germany) contributed to the work as part of her master's thesis. Julia Neugebauer (University of Regensburg, Germany) provided support in carrying out the reactions.

### 2.1 Introduction

Organic solvents account for more than 80 % of the organic waste in the chemical industry. Being the largest fraction in liquid-phase organic reactions, solvents contribute significantly to the overall toxicity potential of the process.<sup>2,3</sup> Thus, there is a lot of research on applying water as a non-toxic, safe, sustainable, and cheap reaction solvent for organic reactions.<sup>2,4-10</sup> A common challenge poses the poor water solubility of substrates and catalysts. To make organic reactions *greener* yet, it seems likely to look to nature, an expert in Green Chemistry. Enzymes, *e.g.*, can allocate hydrophobic pockets that act like a vessel for lipophilic substances.<sup>2,11</sup> Inspired by nature, it is a common technique to use micelles (see Figure 2 - 2(a)) to provide hydrophobic pockets in water and, thus, to overcome the solubility issues for organic reactions. Besides enhancing solubility, the compartmentalization of organic reagents can positively impact the reaction rate.<sup>11-18</sup>

Another benefit of reactions in micellar solutions concerns enzyme-catalyzed reactions. It is well known that enzymes need to maintain their native conformation to stay active. Adequate hydration of an enzyme is also essential. Using organic solvents as the reaction medium facilitates the solubilization of lipophilic substrates but often results in a dramatic decrease or even loss of the catalytic activity of an enzyme.<sup>19-23</sup> Furthermore, metal catalysts can denature enzymes.<sup>24,25</sup> Chaotropes and surface-active molecules, such as hydrotropes and surfactants, can have the same effect. Their interactions with backbone and sidechains increase the enzyme solubility and, thus, facilitate its unfolding.<sup>21,26-28</sup> Nevertheless, micelles, which in turn are made up of surfactants, can act as a nanoreactor to protect enzymes. Accordingly, enzyme-catalyzed reactions can be performed in the presence of organic solvents and metal catalysts.<sup>19,24</sup>

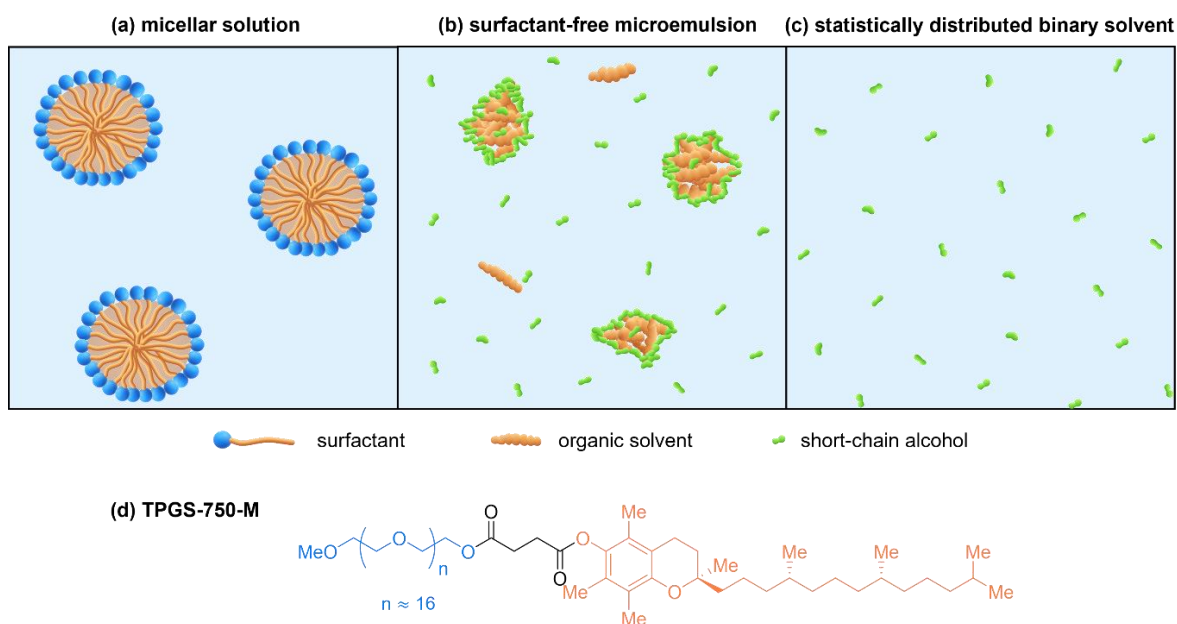


Figure 2 - 2: Schematic illustration of a micellar solution (a), a surfactant-free microemulsion (b), and a statistically distributed binary solvent (c). (d) Molecular structure of the designer surfactant TPGS-750-M.

This opens up the possibility of coupling enzyme- and transition metal-catalyzed reactions in one pot. Recently, a few cascade one-pot reactions have been reported in aqueous, micellar solution.<sup>24,29–36</sup> Particularly the non-ionic *designer* surfactant DL- $\alpha$ -tocopherol methoxypolyethylene glycol succinate (TPGS-750-M, see Figure 2 - 2(d)) is used in this context. The surfactant has been developed by Lipshutz and co-workers. Their designer surfactants find several applications as reaction media.<sup>12,24,29–31,37–40</sup> Cortes-Clerget *et al.* successfully carried out sequential Heck reactions coupled with an ADH(alcohol dehydrogenase)-catalyzed ketone reduction in a micellar solution of TPGS-750-M.<sup>29</sup>

Surfactants, however, possess some characteristics that make their usage challenging. Their strong tendency to adsorb at interfaces complicates recycling and can lead to foaming. In addition, the molecules can be poorly biodegradable and can exhibit a certain ecotoxicity.<sup>41–43</sup> For this reason, hydrotropes gain more and more attention when it comes to solubilizing hydrophobic substrates and creating solvent structuring. In general, hydrotropes often have better biodegradability, induce less foaming, and facilitate solvent recycling, especially for volatile hydrotropes like short-chain alcohols.<sup>42</sup> Unlike surfactants, hydrotropes do not necessarily structure in pure water, but the presence of an organic, water-immiscible solvent enforces structuring.<sup>44</sup> Microemulsions, consisting of such a ternary mixture of water, hydrotrope, and organic solvent, are called surfactant-free microemulsions (SFMEs) (see Figure 2 - 2(b)) and are successfully applied as reaction media for enzyme-catalyzed reactions.<sup>41,45–47</sup>

Here we investigate the impact of different aqueous solvents on a one-pot Heck reaction followed by an ADH-catalyzed ketone reduction. We compare a micellar solution, ternary mixtures including SFMEs, and simple, unstructured binary mixtures (see Figure 2 - 2(a-c)) with regard to their suitability as reaction media for the single reactions as well as the cascade reaction. The mixtures consisting of water, the hydrotrope isopropanol (IPA), and the oil benzyl alcohol (BA) are designated as sustainable. BA is an approved food additive (E 1519) and is present in several fruits and plants, including apricots and honey.<sup>48,49</sup> Moreover, sustainable production of IPA from biomass is reported in the literature.<sup>50</sup>

## 2.2 Material and methods

### 2.2.1 Chemicals

The enzyme ADH-101 (wild-type, expressed in *E. Coli*) was delivered by Johnson Matthey (Royston, UK). 2-Ethylhexyl acrylate (EHA, purity 98 %), 4'-iodoacetophenone ( $\geq 97$  %), deuterated dimethyl sulfoxide (DMSO- $d_6$ ,  $\geq 99.5$  atom % D), bis(tri-*tert*-butylphosphine) palladium(0) ( $\text{Pd}(\text{t-Bu}_3\text{P})_2$ ), phosphate buffered saline (PBS, tablets), DL- $\alpha$ -tocopherol methoxypolyethylene glycol succinate (TPGS-750-M, CAS 1309573-60-1), *trans*-4-phenyl-3-buten-2-one ( $\geq 99$  %), and triethylamine (TEA,  $\geq 99$  %) were obtained from Sigma Aldrich (Darmstadt, Germany). Methyl acrylate (MA, stabilized with 200 ppm MEHQ, 99 %) was from Acros Organics (Geel, Belgium).  $\beta$ -Nicotinamide adenine dinucleotide phosphate sodium salt hydrate (NADPH, reduced form, for biochemical research,  $> 90.0$  %) was purchased from TCI (Eschborn, Germany). Benzyl alcohol (BA,  $\geq 99$  %), and a 1 M hydrogen chloride solution (HCl, 1 N) were bought from Merck (Darmstadt, Germany). The 1 M sodium hydroxide solution (NaOH, 1 N) was from Carl Roth (Karlsruhe, Germany). Dichloromethane (DCM,  $\geq 99.8$  %) and isopropanol (IPA,  $\geq 99.8$  %) were delivered by Honeywell (Offenbach, Germany). Ethyl acetate (EtOAc,  $\geq 99.8$  %) was purchased from Fisher Scientific (Schwerte, Germany). All chemicals were used without further purification. Millipore water (W) was used with a resistivity of 18 M $\Omega$  cm.

### 2.2.2 Methods

#### 2.2.2.1 Ternary phase diagram

Ternary phase diagrams were determined according to Dekker *et al.*<sup>51</sup> For this purpose, 3 g of binary mixtures of water and hydrotrope or oil and hydrotrope, respectively, were prepared in screw tubes of borosilicate glass. The third compound (oil or water) was added gradually to the monophasic solutions until turbidity was perceived by the naked eye. The solutions were tempered to  $25 \pm 0.1$  °C with a heating thermostat A 111 equipped with an immersion thermostat A 100 from Lauda (Lauda-Königshofen, Germany). Precise weight measurements allowed for calculating the weight fractions of the mass of the individual compounds.

### 2.2.2.2 Dynamic light scattering

Dynamic light scattering (DLS) was performed as described in Chapter 1.2.2.5.

### 2.2.2.3 Polarimetry

The optical rotation value of the cascade reaction product was measured by means of an UniPol L1000 polarimeter from Schmidt + Haensch (Berlin, Germany) with a tube length of 50 mm and a wavelength of 589.44 nm. For this purpose, the reaction product was dissolved in DMSO with a concentration of 0.38 g/100 mL. The measurement was performed 10 times.

### 2.2.2.4 Enzyme-catalyzed reaction

A buffer solution (PBS) was prepared, containing 0.01 M phosphate buffer, 0.0027 M potassium chloride, and 0.137 M sodium chloride (pH 7.4, 25 °C). The pH was controlled by means of an Avantor pH glass electrode 211 from VMR (Darmstadt, Germany). For the reaction, 3.6 mL of a reaction medium was added to 2.4 mg NADPH and 27 µL of the reactant *trans*-4-phenyl-3-buten-2-one. The reaction media consisted of different mixtures of PBS solution, IPA, and BA, or 3.2 mL of 2 % (w/w) TPGS-750-M in PBS solution mixed with 0.4 mL IPA. The reaction was initiated by adding 20 mg of the enzyme ADH-101. The reaction solution was stirred for 2 h at 500 rpm at 37 °C. Afterward, the product was extracted 3 times with EtOAc. For this purpose, the reaction solution was transferred in centrifuge tubes and mixed with 3 mL EtOAc. After stirring the mixtures for 20 s with a Vortex, the solution was centrifuged at 4'000 rpm (1'790 g) for 60 s. The EtOAc phase was taken with a syringe, and the extraction process was repeated 2 times with the remaining aqueous phase. The collected EtOAc phases were treated with a rotary evaporator (Hei-VAP Advantage from Heidolph Instruments, Kelheim, Germany) to remove the remaining volatile solvent compounds. All reactions were performed in duplicates. The reaction yield was monitored by NMR measurements.

### 2.2.2.5 Heck reaction

For the Heck reaction, 0.4 mL of a reaction medium was added to 2 mg of the catalyst Pd(*t*-Bu<sub>3</sub>P)<sub>2</sub>, 49 mg of 4'-iodoacetophenone (1 equiv.), 2 equivalent of an alkene, and 84 µL of TEA. The reaction media consisted of different mixtures of water, IPA, and BA, or 2 % (w/w) TPGS-750-M in water. The alkene was either 36 µL of MA or 84 µL of EHA. The solution, as well as the gas phase in the vial, were each degassed for 45 s with N<sub>2</sub>. The reaction solution was stirred for 24 h at 500 rpm at 25 °C or 45 °C. The product was extracted as described in Chapter 2.2.2.4 using 1 mL of EtOAc for each extraction step. Afterward,

solvents were removed with the rotary evaporator. All reactions were again performed in duplicates, and the reaction yield was monitored by NMR measurements.

#### **2.2.2.6 Cascade reaction**

First, the Heck reaction was carried out as described in Chapter 2.2.2.5. The reaction media consisted of the binary mixture W/IPA 67/33 (w/w), the SFME W/IPA/BA 47/33/20 (w/w/w), or the surfactant solution with 2 % (w/w) TPGS-750-M in water. After 24 h, the basic reaction solution was neutralized to a pH of  $7.1 \pm 0.3$ . In the case of the surfactant solution, the reaction solution was neutralized with 1 M HCl. In the case of the binary mixture, a mixture of 1 M HCl and IPA (67/33 (w/w)) was used, and a mixture of 1 M HCl, IPA, and BA (47/33/20 (w/w/w)) was added to the SFME. When overshooting the desired pH, 1 M NaOH was added. The pH was controlled using the pH indicator strips MColorpHast (pH 6.5 – 10.0) from Merck (Darmstadt, Germany). After pH adjustment, 3.2 mL of the reaction medium was added. The reaction media consisted of PBS/IPA 67/33 (w/w), PBS/IPA/BA 47/33/20 (w/w/w), or 2.6 mL of 2 % (w/w) TPGS-750-M in PBS solution mixed with 0.6 mL IPA. For the cascade reaction, the concentrations of the PBS buffer were doubled. The pH was again controlled to be 7. 2.4 mg of NADPH and 20 mg of the enzyme ADH-101 were added to initiate the second reaction step. The reaction solution was stirred for 24 h at 500 rpm at 37 °C. The product was again extracted 3 times with 3 mL EtOAc and further purified with the rotary evaporator, as described in Chapter 2.2.2.4. The reactions were carried out in duplicates, and the reaction yield was again monitored by NMR measurements.

## 2.3 Results and discussion

### 2.3.1 Solvent characterization

First, a micellar solution containing 2 % (w/w) TPGS-750-M is studied as a reaction solvent for both Heck and enzyme-catalyzed reactions, as reported by Cortes-Clerget.<sup>52</sup> In the case of the enzyme-catalyzed ketone reduction, the solution is mixed with IPA, resulting in a ternary mixture of water(W)/IPA/TPGS-750-M 80/18/2 (w/w/w).<sup>52</sup> Information on the designer surfactant TPGS-750-M can be found in the literature.<sup>40</sup> In addition, investigations on the formation of micelles by means of DLS and fluorescence measurements can be found in the Supporting Information (see Chapter 2.5.2.1). The studies confirm that micelles with a size of 6 nm are present in the aqueous reaction solution of 2 % (w/w) TPGS-750-M.

The second aqueous solvent system consists of water, IPA, and BA. In the ternary system, only 28 % (w/w) of IPA is required to close the miscibility gap between water and BA (see Figure 2 - 3(a)). In order not to be too susceptible to phase separation, ternary mixtures containing 33 % (w/w) of IPA are considered as possible reaction media. Figure 2 - 3(b) depict the correlation functions obtained by dynamic light scattering (DLS) measurements for ternary mixtures with varying W/BA ratio. Starting in the binary mixture W/IPA 67/33 (w/w), no signal is detected, indicating the absence of structuring. With an increasing amount of BA, increasing correlation functions arise. It is assumed that a higher correlation intercept as well as larger lag times of the correlation functions correlates with a more pronounced structuring.<sup>53</sup> Accordingly, mixtures c and d exhibit the most pronounced structuring expecting aggregates of BA to be dispersed in water. Mixtures c – e are, thus, classified as SFMEs, with the correlation coefficient beginning to decrease with sample e. As the BA content continues to rise, the correlation function drops down to a negligible signal in the binary IPA/BA 33/67 (w/w) mixture.

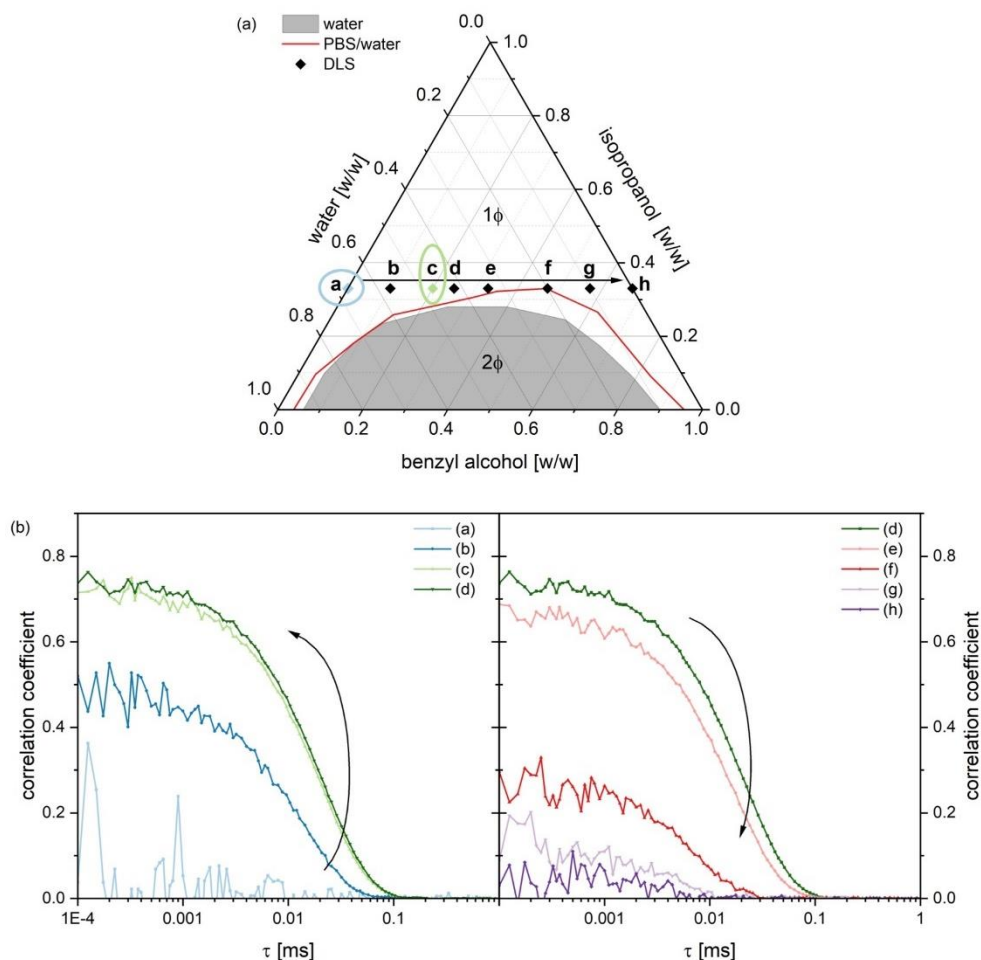


Figure 2 - 3: (a) Ternary phase diagram of water, IPA, and BA at 25 °C. The gray shaded area represents the miscibility gap ( $2\phi$ ), separated from the monophasic area ( $1\phi$ ). The red curve represents the phase boundary after addition of PBS to the water component. The black rhombs depict compositions measured by means of DLS. (b) Corresponding correlation functions obtained by DLS measurements at 25 °C.

When performing the enzyme-catalyzed ketone reduction, a PBS buffer solution is applied instead of pure water. The buffer causes, however, only minor changes (see Figure 2 - 3(a), red curve). There is some salting-out effect, especially on the oil-rich side, resulting in an increase in the miscibility gap. The presence of pronounced structuring in mixtures c – e remains unaffected. Mixture e, however, is in close proximity to the miscibility gap and very prone to phase separation. Mixture f is located in the biphasic area and not thermodynamically stable. The corresponding results of additional DLS measurements are given in the Supporting Information (see Chapter 2.5.2.2).

The third aqueous solvent system comprises binary W/IPA mixtures. As shown for mixture a in Figure 2 - 3, the IPA is distributed statistically in the water with no tendency to aggregate. Literature confirms that no signal is detectable by DLS measurements in the whole concentration range of W/IPA mixtures. Accordingly, there are no fluctuating structures with a diffusion coefficient small enough to be monitored by DLS.<sup>53</sup>

### 2.3.2 ADH-catalyzed ketone reduction

In the first attempt, the different solvents are examined for their suitability as reaction media for ADH-catalyzed reduction of the ketone *trans*-4-phenyl-3-buten-2-one (see Figure 2 - 4(a)). The water phase always contains PBS buffer. Initially, the reaction is performed in different mixtures across the phase diagram (see Figure 2 - 3(a)) in order to study the influence of the solvent structuring on the enzyme activity. The reaction outcome is monitored with MS and NMR measurements (see Chapter 2.5.3.1 – 2.5.3.2 in the Supporting Information), allowing identification and quantification of the reaction product.

Figure 2 - 4(b) depicts the results as a function of the water content. In the binary mixture IPA/BA (h), the enzyme is completely denatured and inactive. This is to be expected due to lack of hydration.<sup>22,23</sup> With increasing water content, the reaction yield remains between 70 % and 100 %, indicating an active enzyme. The highest yields of 98 – 100 % are obtained in slightly structured mixtures (b, g), while yields of 72 – 76 % are obtained in both unstructured (a) and highly structured mixtures (c, d). Accordingly, the structuring of the solvent has no impact on the reaction.

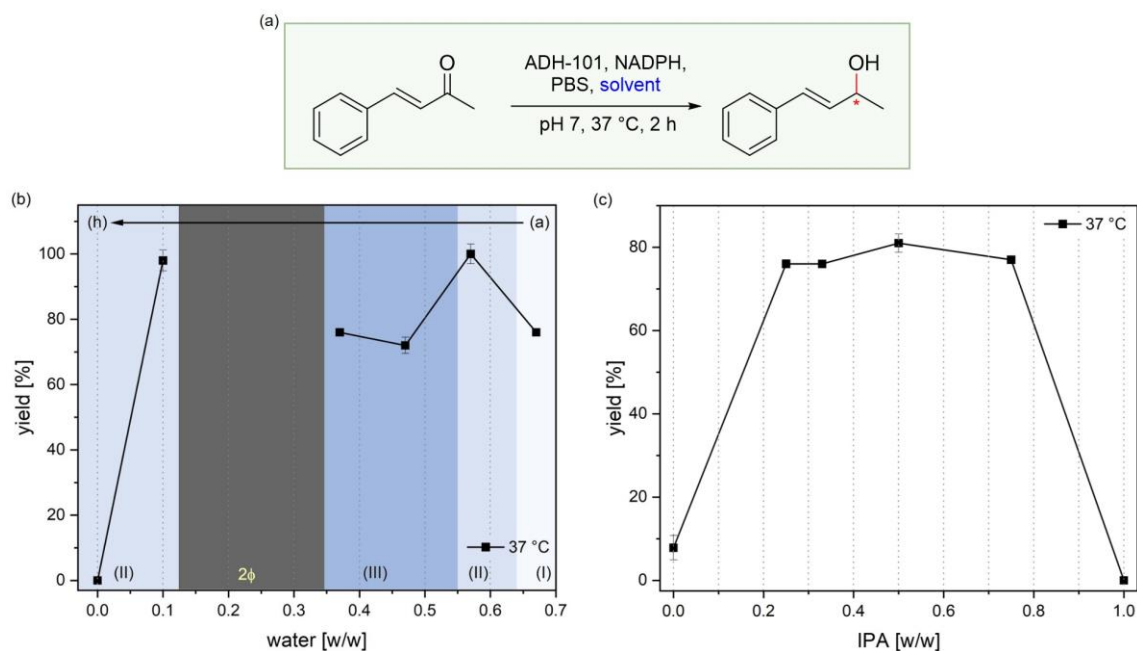


Figure 2 - 4: (a) ADH-catalyzed reduction of *trans*-4-phenyl-3-buten-2-one. The solvent is either a micellar solution of TPGS-750-M with IPA, a binary mixture of W/IPA, or a ternary mixture of W/IPA/BA. (b) Corresponding yield obtained by ADH-catalyzed reduction of the ketone in different mixtures of water, IPA, and BA. The compositions correlate with the mixtures a – h shown in Figure 2 - 3(a). The W/BA ratio varies, while the amount of IPA (33 % (w/w)) remains constant. The blue-shaded areas represent the extent of solvent structuring. Unstructured solvent mixtures are indicated as (I) and are less intense in color. (II) depicts slightly structured mixtures, and (III) represents mixtures with pronounced structuring. The black area identifies mixtures that are too prone to phase separation (2φ, e-f). (c) Yield of *trans*-4-phenyl-3-buten-2-ol obtained by ADH-catalyzed reduction of the ketone in different binary mixtures of water and IPA, as well as the pure solutions.

The yield of 76 % in the unstructured, binary mixture of W/IPA 67/33 (w/w) first appears conspicuous. The statistically distributed hydrotrope IPA is expected to solubilize the enzyme, rather resulting in its unfolding and denaturation.<sup>26,46</sup> For this reason, the enzyme activity is studied in different binary mixtures of water and IPA (see Figure 2 - 4(c)). Indeed, the best results are obtained in the binary mixtures regardless of their composition with yields of 76 – 81 %. The *pure* (buffered) water solution yields only 8 %, confirming the counterintuitive positive effect of IPA on the enzyme activity. Pure IPA, however, leads to the expected denaturation of the enzyme. Sufficient hydration of the enzyme is thus mandatory.

Since solvent structuring is one of the key parameters investigated in this work and high water content is favorable, the highly structured ternary mixture W/IPA/BA 47/33/20 (w/w/w) (mixture c in Figure 2 - 3) is compared with the unstructured binary mixture with an equal amount of IPA (W/IPA 67/33 (w/w) (mixture a)). The previous results prove good enzyme activity in both solutions. In the following, these solutions are defined as *SFME-c* (W/IPA/BA) and *BM-a* (W/IPA).

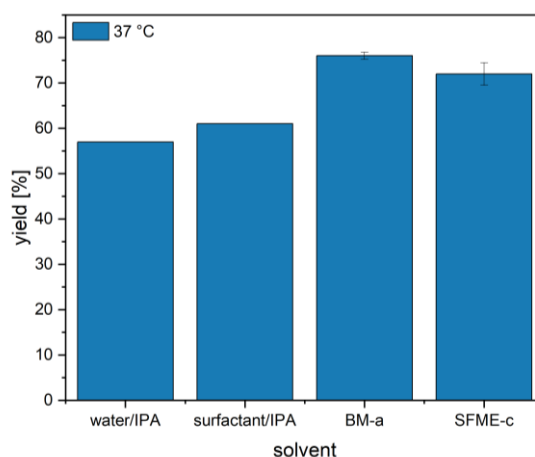


Figure 2 - 5: Yield of *trans*-4-phenyl-3-buten-2-ol obtained by ADH-catalyzed reduction of the ketone in different solvents. From left to right: W/IPA 91/9 (w/w), 2 % (w/w) aqueous surfactant solution with IPA 91/9 (w/w), BM-a (W/IPA 67/33 (w/w)), and SFME-c (W/IPA/BA 47/33/20 (w/w/w)). The solvents containing 9 % (w/w) IPA serve as reference and are single measurements.

Cortes-Clerget *et al.* performed the reduction in a phosphate buffer solution and aqueous TPGS-750-M solutions mixed with IPA.<sup>29</sup> These solvents serve as a reference and are indicated by W/IPA and surfactant/IPA, both in a ratio of 91/9 (w/w), whereby the surfactant solution consists of 2 % (w/w) TPGS-750-M in water. A 57 % yield is found in the W/IPA solution, 62 % in the surfactant/IPA system (see Figure 2 - 5). This is in good agreement with the reported conversion obtained by Cortes-Clerget, which is 57 % in W/IPA and 67 % in surfactant/IPA.<sup>29</sup> A slightly higher yield is obtained in the BM-a (76 %) and in the SFME-c (76 %), with the two solvents providing comparable results within the error (see Figure 2 - 5).

Performing the reduction in the *pure* micellar solution in the absence of IPA reduces the yield to 0.6 ( $\pm$  0.2) %, as it is the case in *pure* water solution (8 %). Accordingly, the behavior of the enzyme in the different solvents is considered more in detail. In the solvents containing IPA, the enzyme is only partially dissolved, resulting in turbid solutions (see Figure S.2 - 7 in the Supporting Information). In pure buffer solution as well as in pure surfactant solution, the solutions remain transparent, indicating complete solubilization of the enzyme. As mentioned in the introductory chapter, the solubilization of an enzyme can result in its unfolding and, thus, deactivation. The alcohol hence seems to act salting-out on the enzyme studied, which allows the enzyme to remain catalytically active. In addition, the IPA is also reported to be applied for the regeneration of NAD(P)H cofactors in ADH-catalyzed reduction reactions, in which ADH serves as the production and the regeneration enzyme.<sup>54</sup> Aono *et al.* reported a photochemical reduction system of NADPH and ADH, when hydrogenating 2-butanone.<sup>55</sup> A similar process could occur with the ADH-101 investigated in this work. The structuring of the SFME would not be affected by this since the amount of IPA required for such regeneration is less than 1 % (w/w) of the solvent. As reported in literature, the NADPH is added in catalytic amount as cofactor in our ADH-101-catalyzed reactions.<sup>29</sup> Apparently, the molecule has to be regenerated. The ADH-101 enzyme, thus, seems to include two functions: the activity of an ADH and the reduction of NADPH. Since it is a commercial enzyme, no more precise information can be provided at this point. It is only known that the enzyme is declared as wild type and expressed by *E. Coli*.

### 2.3.3 Heck cross-coupling

After optimizing the reaction media with regard to the enzyme activity, the solvents are applied to Heck cross-coupling reactions (see Figure 2 - 6) to identify the best solvent conditions for both reaction types. MS and NMR data used for product identification and quantification can again be found in the Supporting Information (see Chapter 2.5.4.1 – 2.5.4.2).

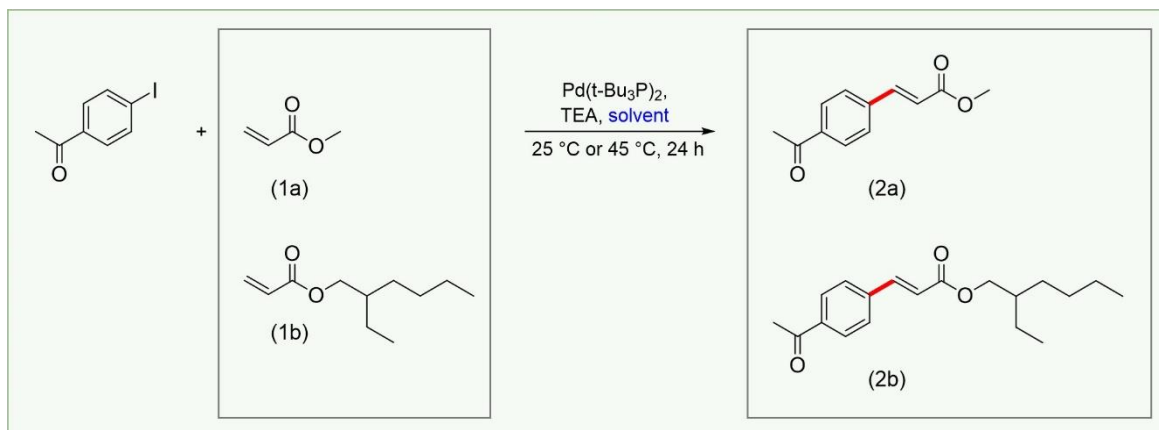


Figure 2 - 6: Heck cross-coupling of 4'-iodoacetophenone with MA (**1a**) or EHA (**1b**). The solvent is either a micellar solution of TPGS-750-M, a binary mixture of W/IPA, or a ternary mixture of W/IPA/BA.

First, the cross-coupling with methyl acrylate (MA, Figure 2 - 6, **1a**) is performed in different mixtures of water, IPA, and BA across the phase diagram (see Figure 2 - 7(a), red curve). In all mixtures, reaction yields between 75 – 100 % are obtained. As expected, the yield tends to increase with decreasing water content. A correlation with solvent structuring is not identifiable. It has to be noted that liquid-liquid phase separation occurs in mixture c – e upon the addition of TEA. Additional experiments reveal that besides the macroscopic structuring in the form of droplets, there is also still a mesoscopic structuring present in the larger volume phase. (see Figure S.2 - 17 in the Supporting Information). In comparison with the enzyme-catalyzed reaction (black curve), the deviations are higher for the Heck reaction. In general, this type of reaction is more susceptible during sample preparation. Proper degassing seems to be particularly crucial. Overall, the results reveal that both the enzyme-catalyzed and the Heck reaction perform well in the considered ternary SFME-c and in the BM-a.

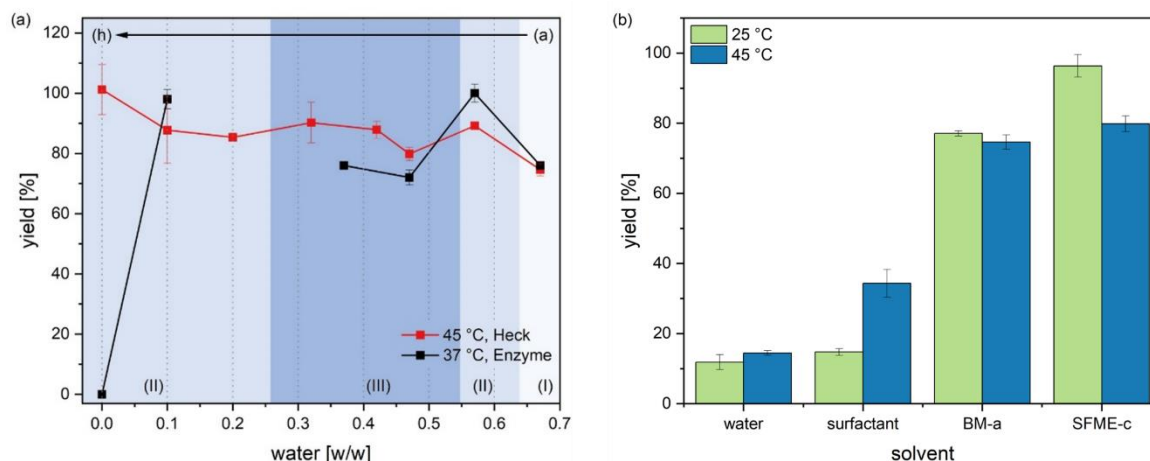


Figure 2 - 7: (a) Yield of **2a** obtained by Heck reaction (red), and yield of *trans*-4-phenyl-3-buten-2-ol obtained by ADH-catalyzed reduction (black) in different mixtures of water, IPA, and BA. The compositions correlate with the mixtures a – h shown in Figure 2 - 3(a). The W/BA ratio varies, while the amount of IPA (33 % (w/w)) remains constant. The blue-shaded areas represent the extent of solvent structuring. Unstructured solvent mixtures are indicated as (I) and are less intense in color. (II) depicts slightly structured mixtures, and (III) represents mixtures with pronounced structuring. (b) Yield of **2a** obtained by Heck cross-coupling of MA in different solvents. From left to right: water, 2 % (w/w) aqueous surfactant solution, BM-a (W/IPA 67/33 (w/w)) and SFME-c (W/IPA/BA 47/33/20 (w/w/w)).

The yields obtained in the BM-a (75 %) and the SFME-c (80 %) at 45 °C significantly exceed the yield in the reference solvents (see Figure 2 - 7(b), blue bars). The values are more than doubled compared to the surfactant system (34 %) and correspond to more than 5 times the yield achieved in pure water (14 %). It is conspicuous that the reaction solution in the SFME-c appears way more transparent than the other solvents (see Figure S.2 - 18 in the Supporting Information). The catalyst is finely dispersed, and the substrate appears to be dissolved. The better solubility of the reaction components may also explain the even better reaction outcome at milder temperatures of 25 °C (green bars). In contrast, elevated temperatures of 45 °C are required to improve the reaction outcome in water and the surfactant solution. Moreover, it is reported that tocopherol can form a complex with transition metals.<sup>56</sup> DLS measurements of the tocopherol-based TPGS-750-M surfactant together with the Pd-catalyst show indeed the formation of larger aggregates that increase in size with time (see Figure S.2 - 19 in the Supporting Information). This indicates the presence of interactions between the surfactant and the catalyst, which seems to reduce the catalytic activity during the Heck reaction. Higher temperatures may help to overcome these interactions. Overall, the highest yield of 96 % is achieved in the SFME-c under mild conditions of 25 °C. The reaction solvents are further studied using 2-ethylhexyl acrylate (EHA, **1b**) as substrate (see Figure S.2 - 20 in the Supporting Information). At 45 °C, yields between 92 – 100 % can be obtained in the surfactant system, the BM-a, and the SFME-c, with the SFME-c yielding the lowest result at 92 %. In turn, milder conditions of 25 °C lead to a decrease in the yield in the surfactant solution (59 %), while complete conversion can be achieved in the SFME-c.

### 2.3.4 One-pot cascade reaction

Finally, the two reaction types are combined and performed as a cascade reaction in one pot. The Heck cross-coupling of MA with 4'-iodoacetophenone is followed by an ADH-catalyzed reduction of the ketone (see Figure 2 - 8(a)).

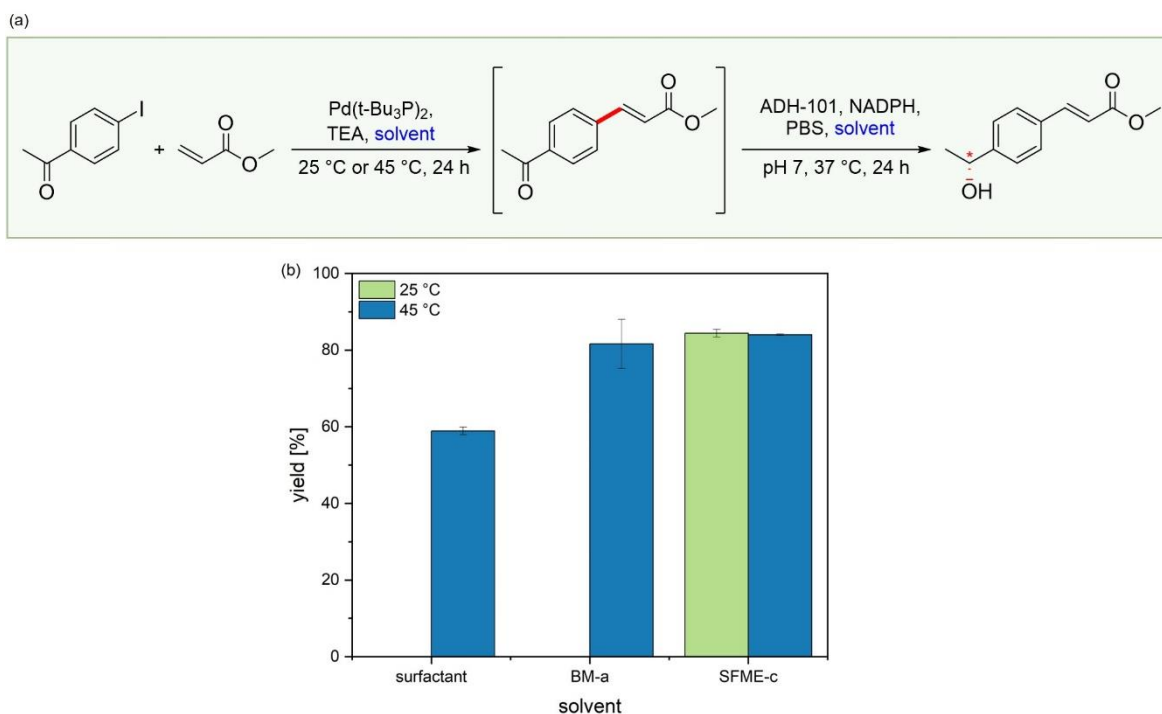


Figure 2 - 8: (a) Heck cross-coupling of 4'-iodoacetophenone with MA, followed by ADH-catalyzed reduction of the obtained ketone. The reaction is performed in one pot. (b) Yield of the one-pot cascade reaction in the different solvents. From left to right: 2 % (w/w) aqueous surfactant solution, BM-a (W/IPA 67/33 (w/w)), and SFME-c (W/IPA/BA 47/33/20 (w/w/w)).

As shown in Figure 2 - 8(b), the Heck reaction at 45 °C can be coupled successfully in the 3 solvents. A precise pH control in the coupling step is thereby crucial. In the surfactant system, a yield of 59 % is achieved, which is significantly higher than the yield obtained with the single Heck reaction without coupling at 34 %. Since both results can be monitored repeatedly, it is assumed that further converting the Heck reaction product results in a shift in the reaction equilibrium to the product side. In addition, the reaction time is extended by the coupling, albeit with a changed pH. Slightly higher yields of 78 % are reported by Cortes-Clerget.<sup>29</sup> Deviations may be explained by altered enzyme conditions. Enzymes from different batches can influence the reaction outcome, as shown in Figure S.2 - 8 in the Supporting Information. Under the same conditions, however, the BM-a and the SFME-c achieve even higher yields of 82 % (BM-a) and 84 % (SFME-c). Within the errors, both solvents yield comparable results. Based on the results obtained in the previous chapter, the first step of the cascade reaction is carried out at milder temperatures of 25 °C in the SFME-c. Even at the low temperatures, a high yield of 84 % can be maintained. The corresponding NMR and

MS data are shown in the Supporting Information (see Chapter 2.5.5.1 – 2.5.5.2). We also present information on the initial attempt for complete isolation and purification of the product of the cascade reaction in SFME-c (see Chapter 2.5.5 in the Supporting Information).

The results in Figure 2 - 8(b) demonstrate that solvent structuring is not essential for coupling a transition metal-catalyzed Heck reaction with an ADH-101-catalyzed reduction in one pot. When the enzyme stays in a partially undissolved, folded state, it also remains active in the presence of the catalyst. This is also shown in Figure S.2 - 9 in the Supporting Information. The ADH-catalyzed reduction of *trans*-4-phenyl-3-buten-one (compare Figure 2 - 4) is performed in presence of the Pd-catalyst. Despite the transition metal, there is no decrease in the yield, even in the unstructured BM-a. Besides, the coupled reaction product in the SFME-c is investigated by means of polarimetry, yielding a specific rotation  $[\alpha]_D^{20.8} = +23.6 (\pm 0.8)$ . This value is in good agreement with the literature value of  $[\alpha]_D^{20.0} = +23.3$ , obtained for the enantiopure methyl-(R,E)-3-(4-(1-hydroxyethyl)phenyl)acrylate.<sup>29</sup> The enzyme, thus, keeps both its activity and selectivity.

## 2.4 Conclusion and outlook

We presented a detailed study on the impact of solvents, in particular with regard to their structuring, on two types of reaction: transition metal-catalyzed Heck cross-couplings and enzyme-catalyzed ketone reductions. A micellar solution of TPGS-750-M in water serves as a reference and is compared to unstructured, binary mixtures of water (W) and isopropanol (IPA) as well as ternary mixtures of water, IPA, and benzyl alcohol (BA) with different extent of structuring.

The experiment reveals that in the case of the ADH enzyme investigated, no structuring is required to protect against the oil or the alcohol. In fact, the alcohol acts salting-out on the otherwise water-soluble enzyme, allowing it to retain its folding and, thus, its activity. Hence, the enzyme activity is maintained in the unstructured binary mixtures and the ternary mixtures, which possess pronounced structuring, resulting in a yield of about 70 – 80 %. The best yield of about 100 % is achieved in ternary mixtures of W/IPA/BA with minor structuring. The results obtained in our surfactant-free systems exceed the micellar reference system reported in the literature, which is also the case for the Heck reaction. In all mixtures of water, IPA, and BA, yields of 75 – 100 % are achieved for the cross-coupling. The binary mixture of W/IPA 67/33 (w/w) (BM-a) and the surfactant-free microemulsion of W/IPA/BA 47/33/20 (w/w/w) (SFME-c) allow for reducing the reaction temperature from 45 °C to 25 °C. While the reference system requires high temperatures, the milder conditions further improved the results in the BM-a and the SFME-c. The best yield at mild temperature is obtained in the SFME-c (96 %), which exhibits great solubilization of the reaction components.

Ultimately, the Heck cross-coupling is successfully coupled with the ADH-catalyzed reduction in one pot using the micellar solution, the BM-a, or the SFME-c as the reaction medium. Although the surfactant system enables the one-pot cascade reaction, the formation of micellar nanoreactors protecting the enzyme is not the crucial factor as previously assumed.<sup>29</sup> In fact, the solubility and the resulting stability of the reaction components are the key parameters. When the enzyme stays partially undissolved and folded, the transition metal catalyst has no negative impact on its activity. This is simply achieved by a binary mixture of water and IPA. Mixing the binary mixture with an oil results in mesoscopic structuring of the solvent and improved solubility of the hydrophobic reaction components while maintaining the enzyme active. Concurrently, a dynamic system is provided that does not intervene in the reactions as a consequence of too strong interactions.

Overall, structured solvent systems can improve reactions and, above all, make reactions in aqueous surrounding possible in the first place. However, it is not mandatory to build up complex and defined structures based on surfactants. Solvent structuring rather provides the opportunity to combine different molecules, which positively influence the solubility and stability of the reaction components, in a rather stable system.

In the next step, the surfactant-free reaction solutions should be applied to other substrates as well as to other transition metal-biocatalysis cascade reactions. It can thus be studied whether the reaction solvents can be used universally. The great solubilization power of the SFME seems to be the major advantage of this solvent type. For this reason, it would be highly recommended to investigate cascade reactions, including a photocatalysis step. Furthermore, photocatalytic reactions using organic dyes should be considered as a more environmentally benign approach compared to metal catalysis. Besides, the role of IPA and ADH-101 during cofactor regeneration is only considered briefly in this work. Further reactions with varying ratios of IPA and NADPH should be carried out. In addition, the oxidized NADP<sup>+</sup> should be used to initiate the reaction. This may give additional information to unravel the exact regeneration mechanism. Moreover, the first attempts for an upscaling should be taken into account. The surfactant-free aqueous solvents could prove very suitable for the industry. All compounds considered can be classified as sustainable and solvent recovery should be facilitated due to the volatile IPA and the possibility of inducing phase-separation in the SFME by, *e.g.*, changing the temperature. Generally, lowering the temperature during the Heck reaction and the low price of the applied chemicals also implicate economic advantages.

## 2.5 Supporting information

### 2.5.1 Methods

#### 2.5.1.1 ANS fluorescence measurements

An Infinite M Nano+ from Tecan Trading (Männedorf, Switzerland) was used to measure the fluorescence in a black Greiner 96 multiwell, half area,  $\mu$ Clear microtiter plate with a flat bottom. The aqueous solutions contained 8-anilino-1-naphthalenesulfonic acid (ANS) with a concentration of 20  $\mu$ M and a varying amount of TPGS-750-M. The samples were excited at 385 nm, and the emission was detected at 490 nm with a gain of 100 in *bottom reading* mode. ANS (> 95.0 %) was obtained from TCI (Eschborn, Germany).

#### 2.5.1.2 Malvern DLS measurements

Aqueous solutions of 2 % and 0.02 % (w/w) TPGS-750-M were measured in high precision cells of special optical glass (10 mm light path, from Hellma Analytics, Müllheim, Germany), using a Zetasizer Nano ZS from Malvern Panalytical (Malvern, UK). Each sample was filtered with a PTFE filter (0.2  $\mu$ m pore size) and measured 3 times. For determining the diameter of the aggregates, the refraction index, and the viscosity of water at 25 °C were applied.

#### 2.5.1.3 NMR measurements

$^1\text{H}$ -,  $^{13}\text{C}$ -, and HSQC-dept NMR measurements were performed in DMSO- $d_6$  on an AVANCE III HD 400 NMR from Bruker (Billerica, USA). Dichloromethane was added as an internal standard for quantitative analysis.

#### 2.5.1.4 Mass spectrometry

For the cascade reaction and the Heck reaction with MA, the molar mass of the reaction product was determined using an LC-Q-TOF 6540 UHD mass spectrometer (MS) from Agilent Technologies (Santa Clara, USA) equipped with a gas chromatography system (GC-MS). The atmospheric pressure chemical ionization (APCI) method was applied. For the enzyme-catalyzed reaction and the Heck reaction with EHA, the molar mass of the reaction product was identified by means of an AccuTOF GCX MS from Joel (Freising, Germany) coupled with a GC (GC-MS). As an ionization method, electron ionization (EI+) was used.

### 2.5.1.5 Product isolation with column chromatography

A column with a diameter of 1 cm was packed with silica gel 60. The mobile phase consisted of an n-hexane/EtOAc 70/30 (v/v) mixture. The fractions were analyzed using thin-layer chromatography (TLC) in the previously defined solvent and a UV lamp from neoLab (Heidelberg, Germany) with a wavelength of 254 nm. The solvents were removed by means of the rotary evaporator. In between, 2 – 3 mL chloroform was added three times to completely remove the solvent residues. n-Hexane ( $\geq 99\%$ ) was purchased from Sigma Aldrich (Darmstadt, Germany). Silica gel 60 (0.063 – 0.200 mm, for column chromatography) and the TLC silica gel 60 F<sub>254</sub> (aluminum sheets) were bought from Merck (Darmstadt, Germany). Chloroform (99.8 %) was obtained from Fisher Scientific (Schwerte, Germany).

## 2.5.2 Solvent characterization

### 2.5.2.1 Micellar solution

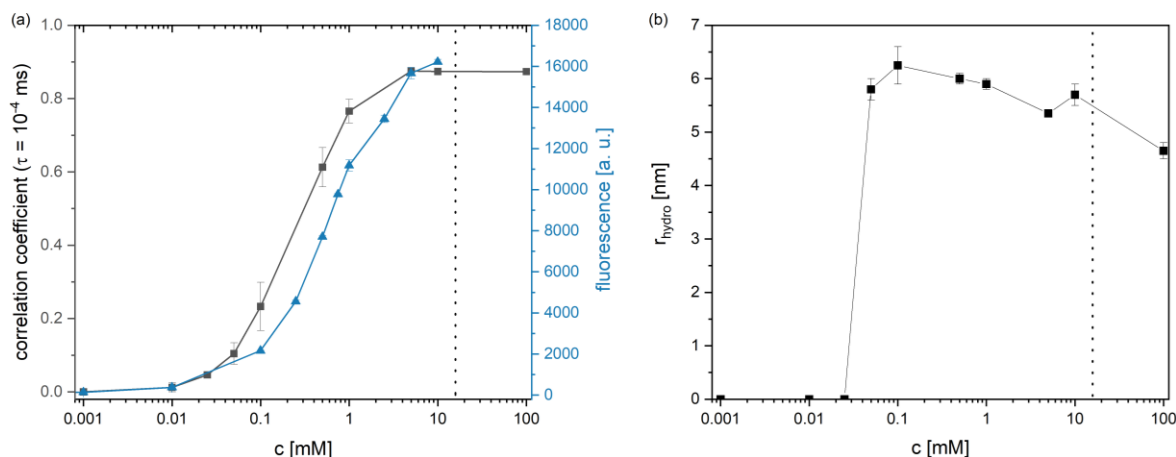
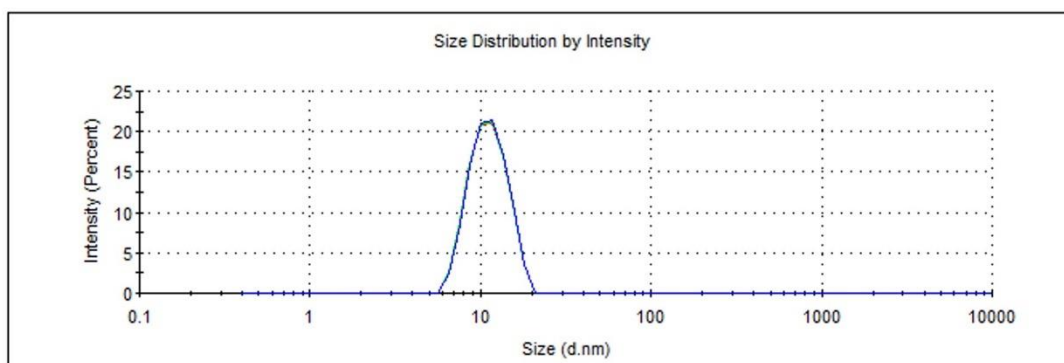


Figure S.2 - 1: (a) DLS and ANS fluorescence measurements of aqueous TPGS-750-M solutions as a function of the surfactant concentration. Since the fluorescence of ANS depends on the polarity of its environment, an increase in the signal can be correlated with the formation of micelles.<sup>57</sup> The same applies to the correlation coefficient at small lag times ( $10^{-4}$  ms), as the appearance of a signal arises from the incipient micelle formation.<sup>58</sup> The results obtained by DLS and fluorescence measurements are in good agreement, indicating micelle formation at concentrations higher than  $10 \mu\text{M}$ . (b) Hydrodynamic radius of the micelles as a function of surfactant concentration resulting from DLS measurements. The radius was determined using a cumulant fit of 1. order with the density and viscosity values for water at  $25 \text{ }^\circ\text{C}$ . The first radius can be determined at  $50 \mu\text{M}$ , which is considered to be the cmc of this surfactant. The values for the hydrodynamic radius are determined to be about 6 nm, whereby a decrease is detected at higher concentrations. The decrease can be attributed to the increased viscosity of the solution, which is not taken into account. The dotted line represents the reaction solution of 2 % (w/w) TPGS-750-M in water. The results clearly depict that micelles are present in this composition. Measurements of the interfacial tension for determining the cmc turned out to be inapplicable due to the slow diffusion of the large molecule.

It is important to note at this point that Andersson *et al.* detected significantly larger aggregates in an aqueous solution of 2 % (w/w) TPGS-750-M using a Malvern Zetasizer. Comparable aggregates with a diameter of 9 nm were detected as well, however, with a minor intensity of about 2 %. 98 % of the detected aggregates had a diameter of 60 nm, which is 5 times our value measured with DLS. The cryo-TEM measurement by Andersson and coworkers revealed that the detected aggregates are composed of smaller aggregates.<sup>40</sup> Thus, we assume that the radius of 6 nm (or the diameter of 12 nm) is actually the size of a single micelle. This would be in good agreement with the size of a single micelle reported by Andersson.<sup>40</sup> The larger aggregates could not be reproduced in our measurements, even when applying the same device (see Figure S.2 - 2). Hence, the larger aggregates appear to be hardly reproducible, possibly due to minor stability compared to the micelles, which can be easily reproduced in size.

**(a) 2 % (w/w) TPGS-750-M**

	Size (d.nm):	% Intensity:	St Dev (d.nm):
<b>Z-Average (d.nm):</b> 10,82	<b>Peak 1:</b> 11,36	100,0	2,760
<b>Pdl:</b> 0,023	<b>Peak 2:</b> 0,000	0,0	0,000
<b>Intercept:</b> 0,950	<b>Peak 3:</b> 0,000	0,0	0,000
<b>Result quality :</b> Good			

**(b) 0.02 % (w/w) TPGS-750-M**

	Size (d.nm):	% Intensity:	St Dev (d.nm):
<b>Z-Average (d.nm):</b> 11,96	<b>Peak 1:</b> 12,63	100,0	3,157
<b>Pdl:</b> 0,035	<b>Peak 2:</b> 0,000	0,0	0,000
<b>Intercept:</b> 0,835	<b>Peak 3:</b> 0,000	0,0	0,000
<b>Result quality :</b> Good			

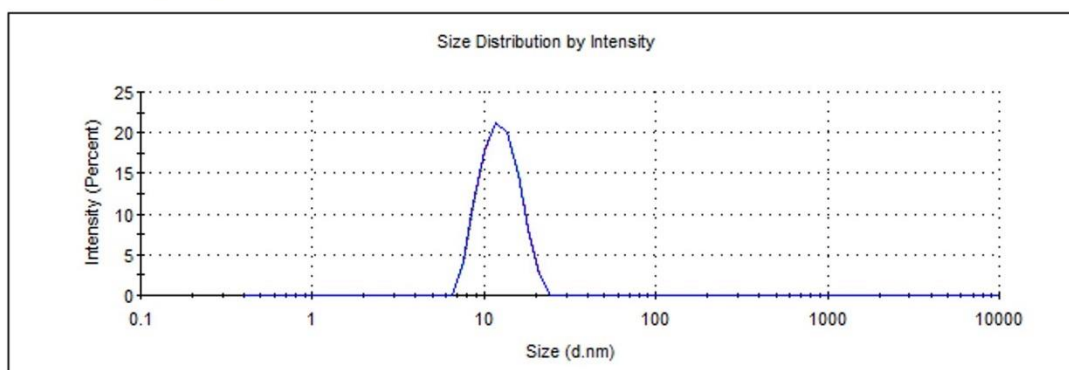


Figure S.2 - 2: Size distribution of 2 % (a) and 0.02 % (w/w) (b) TPGS-750-M in water obtained by Malvern DLS measurements. The determined diameters of 11.4 nm and 12.6 nm are in good agreement with the hydrodynamic radius of 6 nm shown in Figure S.2 - 1. Furthermore, the micellar solutions are very monodisperse with a polydispersity index (PDI) < 0.04.

## 2.5.2.2 Surfactant-free microemulsion

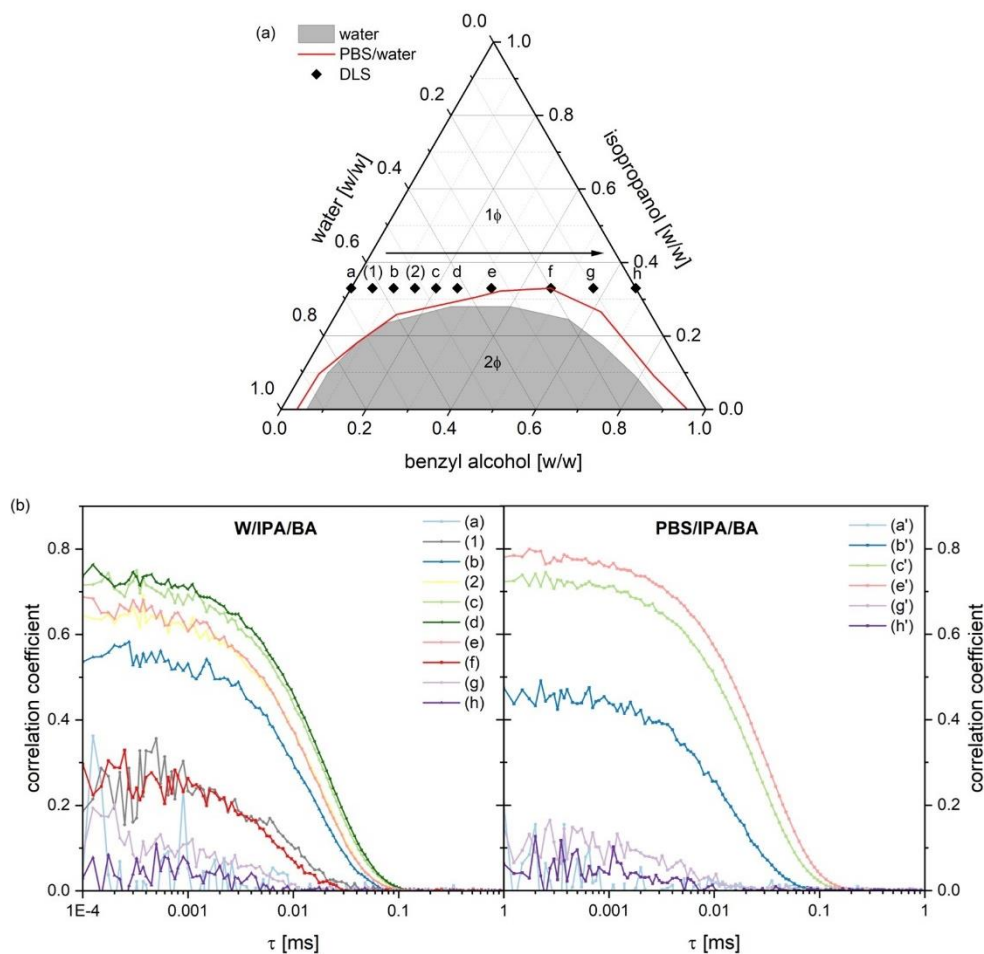


Figure S.2 - 3: Ternary phase diagram of water (W), isopropanol (IPA), and benzyl alcohol (BA) at 25 °C. The gray shaded area represents the miscibility gap ( $2\phi$ ), separated from the monophasic area ( $1\phi$ ). The red line represents the phase boundary for PBS buffer/IPA/BA. An increase in the miscibility gap at the oil-rich side is determined when replacing pure water by the buffer solution. The black rhombs depict compositions measured by means of DLS. (b) Corresponding correlation functions obtained by DLS measurements at 25 °C with either pure water (left) or buffer solution (right). The correlation function of sample e is increased with the buffer solution. This is attributed to its proximity to the phase boundary, resulting in a fairly temperature-sensitive mixture. Mixture f containing PBS is biphasic and, thus, not measured. Furthermore, it is noticeable that the point of inflection for PBS is shifted to higher lag times. This indicates a larger size of the aggregates. Overall, the reaction mixture c exhibit pronounced structuring with both pure water and PBS buffer solution.

## 2.5.3 Enzyme-catalyzed reaction

### 2.5.3.1 NMR measurements

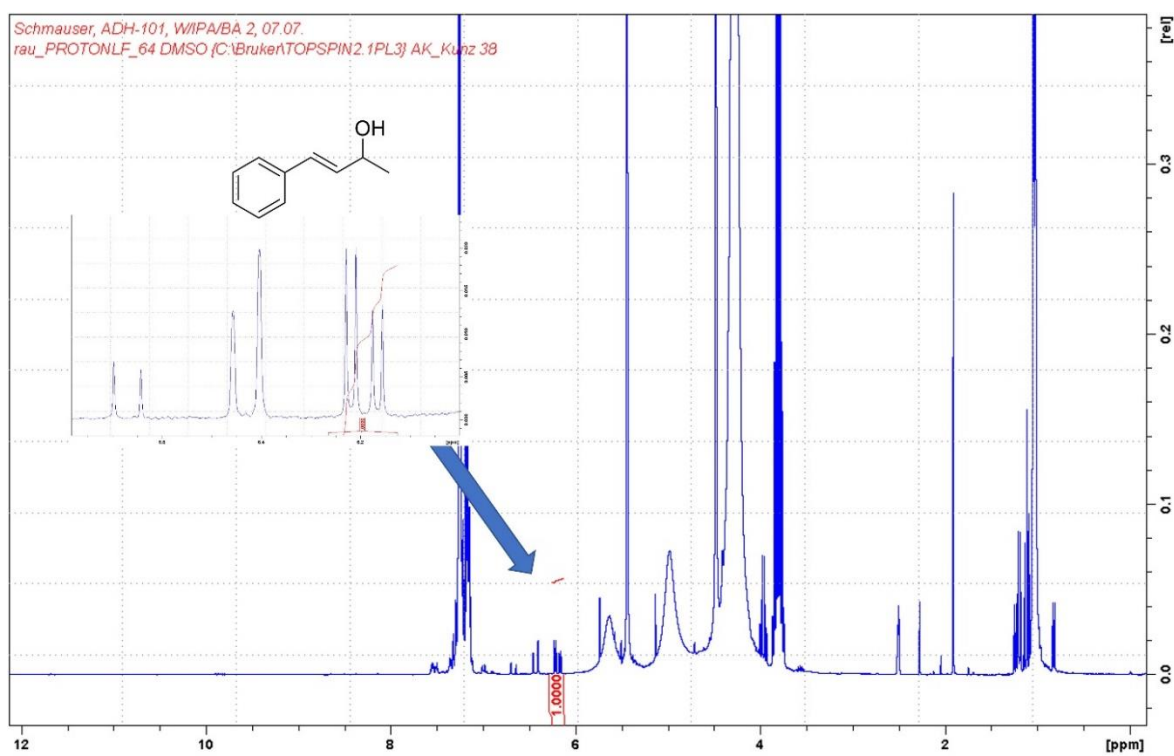


Figure S.2 - 4:  $^1\text{H-NMR}$  spectrum of the crude product of the enzyme-catalyzed reaction (2 h, 37 °C, SFME-c) in  $\text{DMSO-d}_6$ .

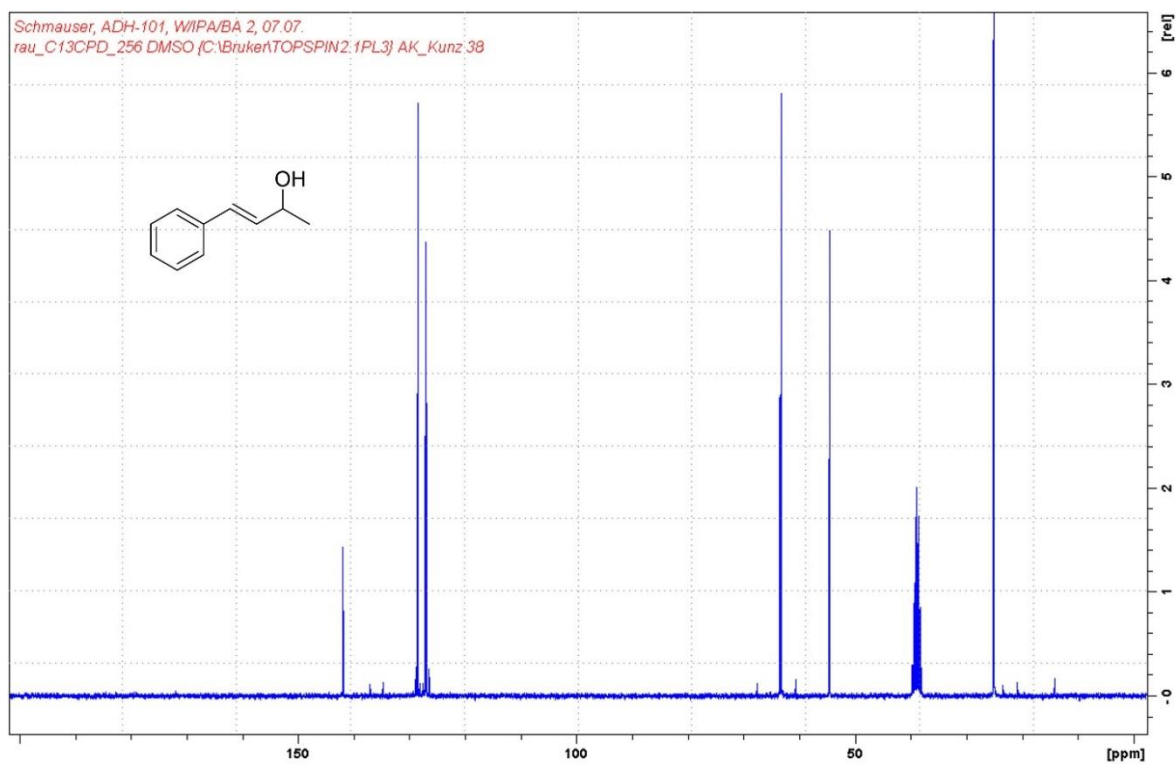


Figure S.2 - 5:  $^{13}\text{C}$ -NMR spectrum of the crude product of the enzyme-catalyzed reaction (2 h, 37 °C, SFME-c) in  $\text{DMSO-d}_6$ .

## 2.5.3.2 Mass spectrometry

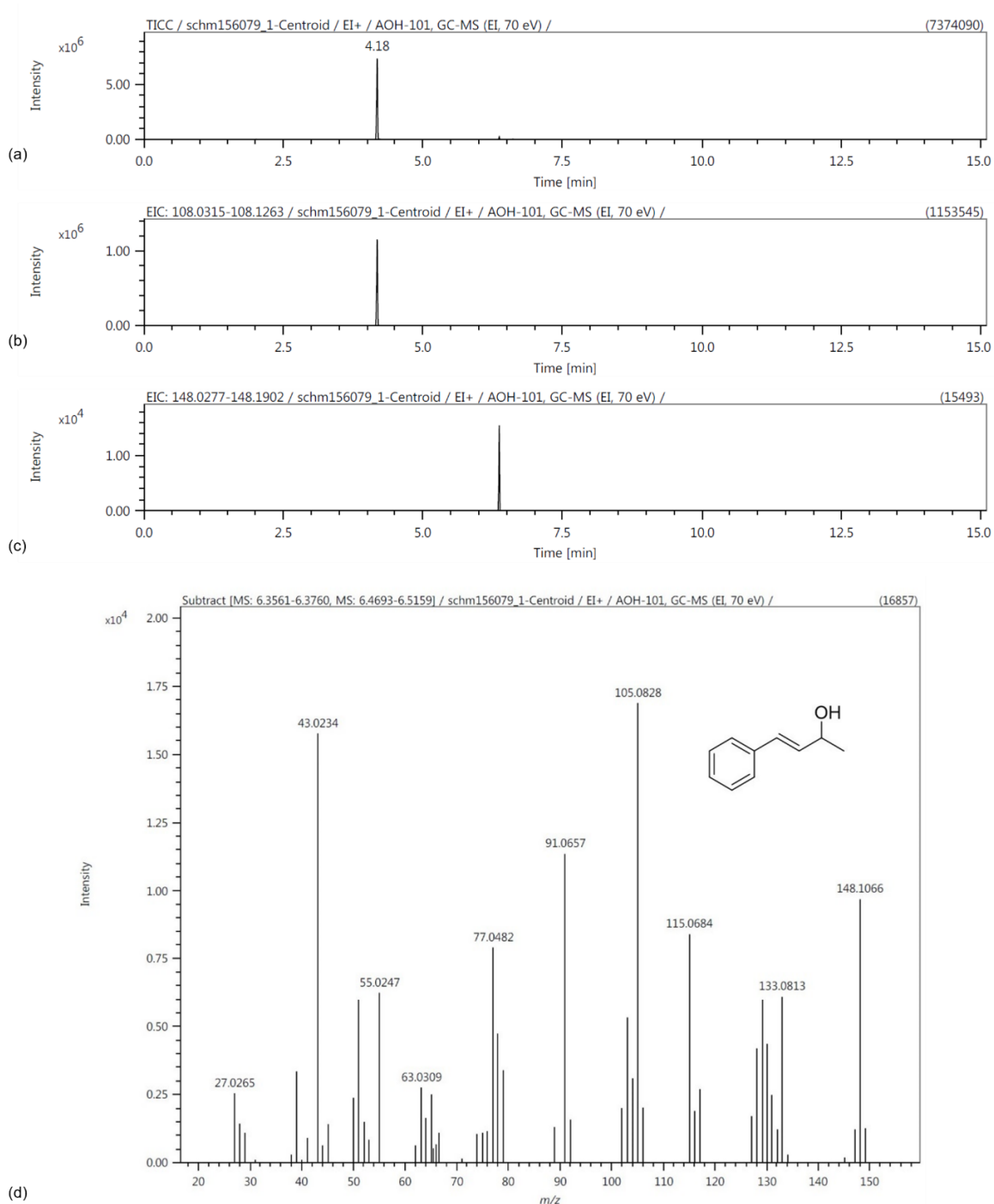


Figure S.2 - 6: MS results of the crude product of the enzyme-catalyzed reaction (2 h, 37 °C) in the SFME W/IPA/BA 57/33/10 (w/w/w). (a) Total ion current (TIC) chromatogram. (b) Extracted ion chromatogram (EIC) at a mass-to-charge ( $m/z$ ) of 108. (c,d) EIC at a  $m/z$  of 148 with the corresponding mass spectrum at 6.4 – 6.5 min. The measurements prove the presence of *trans*-4-phenyl-3-buten-2-ol with a molar mass of 148.2 g/mol. The peak at 4.2 min can be assigned to benzyl alcohol with a molar mass of 108.1 g/mol.

### 2.5.3.3 Visual observations

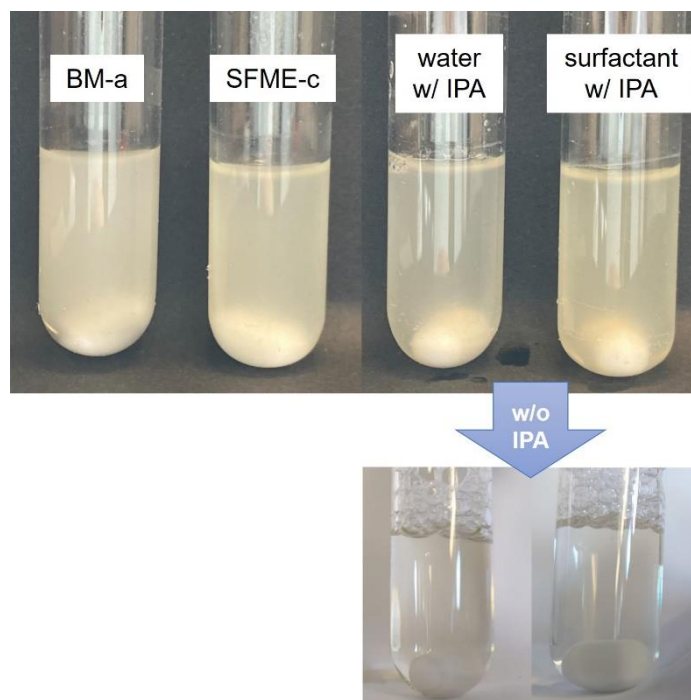


Figure S.2 - 7: Visual observation of the enzyme dissolved in different solvents after stirring. The same amount of enzyme was added to the solvents as used in the enzyme-catalyzed reactions. The solvents consisted of W/IPA 67/33 (w/w) (BM-a), W/IPA/BA 47/33/20 (w/w/w) (SFME-c), W/IPA 91/9 (w/w) (water w/ IPA), or surfactant solution/IPA 91/9 (w/w) (surfactant w/ IPA). The pictures below show the solutions without IPA. While the solutions are turbid in the presence of IPA, clear solutions are obtained in the absence of IPA.

## 2.5.3.4 Additional reactions

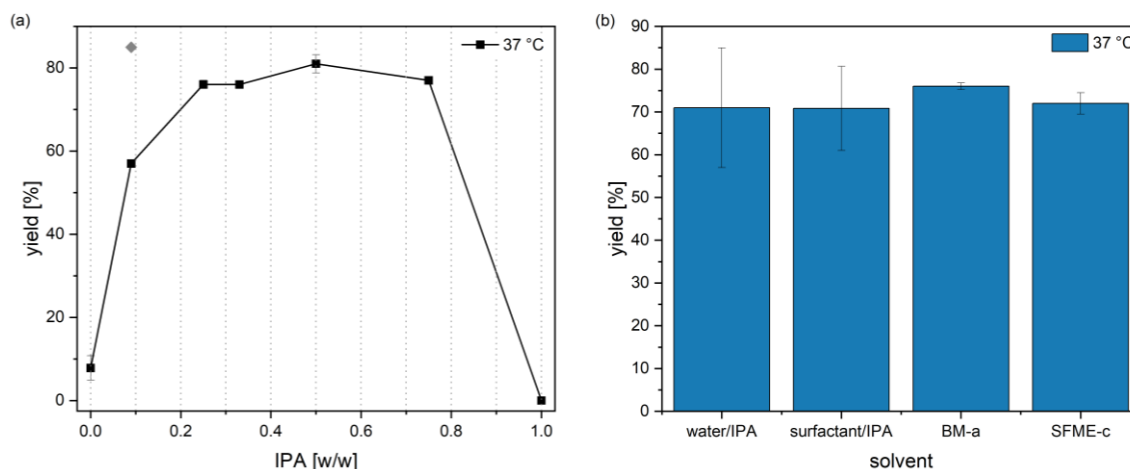


Figure S.2 - 8: Yield of trans-4-phenyl-3-buten-2-ol obtained by ADH-catalyzed reduction of the ketone. (a) The reaction with 9 % (w/w) IPA was only carried out once. The duplicate measurement (gray rhomb) was performed with another batch of enzyme, resulting in a significantly higher yield. (b) The duplicate reactions in water/IPA and surfactant/IPA were again carried out with enzymes from different batches. The lower yield is obtained with the first batch, the higher one with the second batch. This demonstrates the susceptibility of enzyme reactions to the smallest impurities, which can differ from batch to batch. Since the reactions shown in Figure S.2 - 9, performed with the second batch enzyme, depict the same trend among the solvents, the “outliers” can be explained by the batch change. Within the batch, the enzyme reactions only possess small deviations. For example, using the enzyme of the second batch, a yield of  $82.6 \pm 1.9$  % is obtained in the surfactant/IPA system.

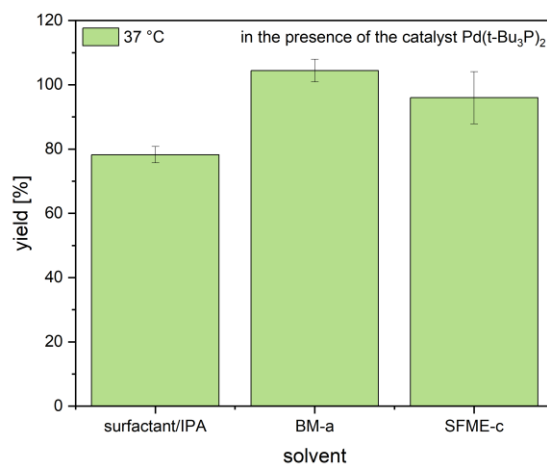


Figure S.2 - 9: Yield of trans-4-phenyl-3-buten-2-ol obtained by ADH-catalyzed reduction of the ketone in the presence of the catalyst used for the Heck reaction. The same amount of catalyst as applied in the Heck reaction is used to investigate the influence of the transition metal on the enzyme activity. The results reveal that the catalyst has no negative impact on the enzyme activity. On the contrary, even higher yields are obtained. The increase in the yield is, however, attributed to the change of the enzyme batch, which generally resulted in higher yields.

## 2.5.4 Heck reaction

### 2.5.4.1 NMR measurements

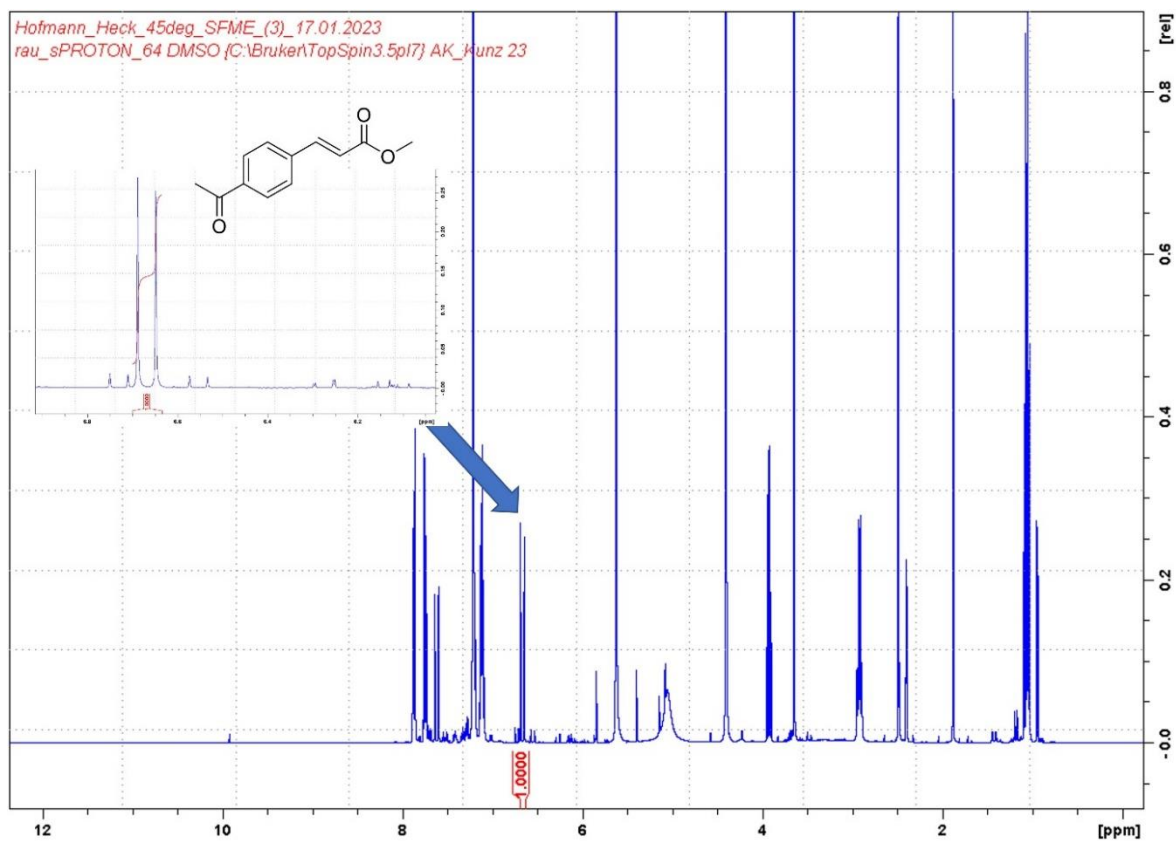


Figure S.2 - 10:  $^1\text{H-NMR}$  spectrum of the crude product of **2a** after the Heck cross-coupling (24 h, 45 °C, SFME-c) in DMSO- $d_6$ .

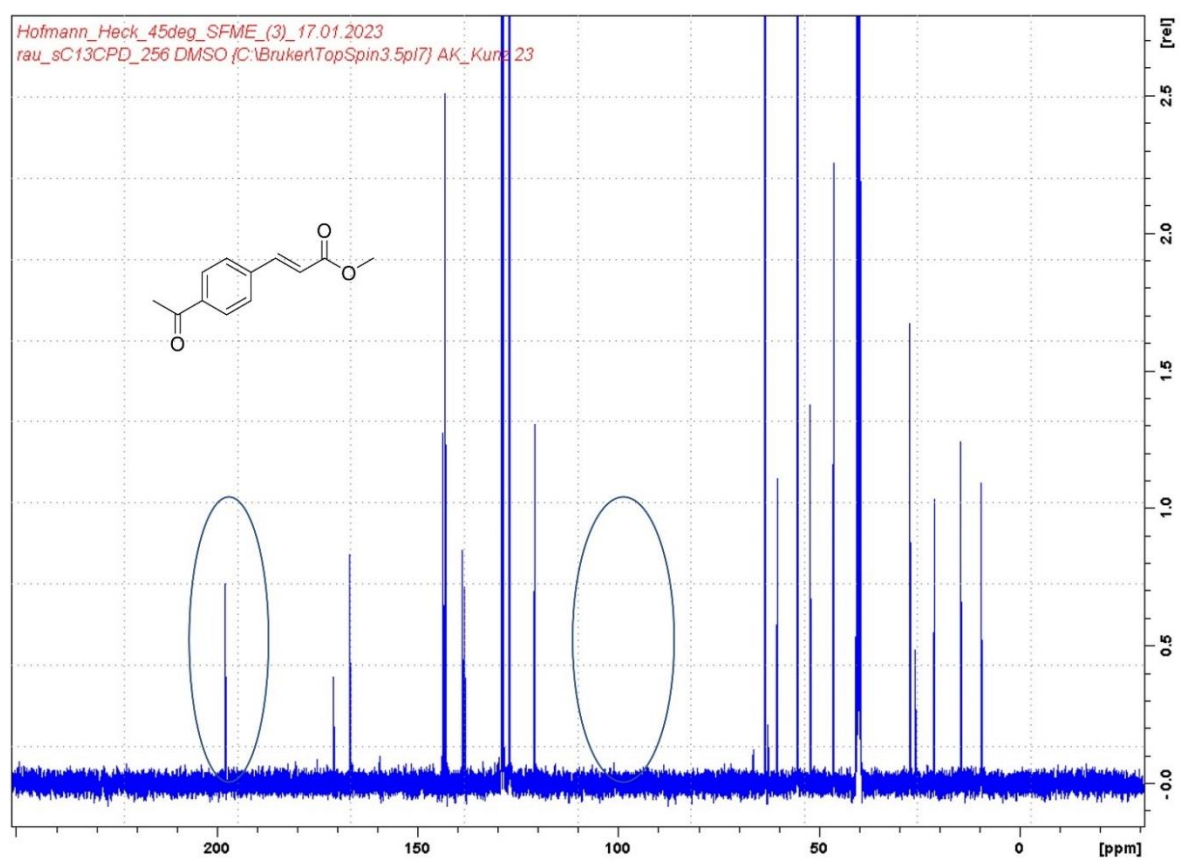


Figure S.2 - 11:  $^{13}\text{C}$ -NMR spectrum of the crude product of **2a** after the Heck cross-coupling (24 h, 45 °C, SFME-c) in  $\text{DMSO-d}_6$ .

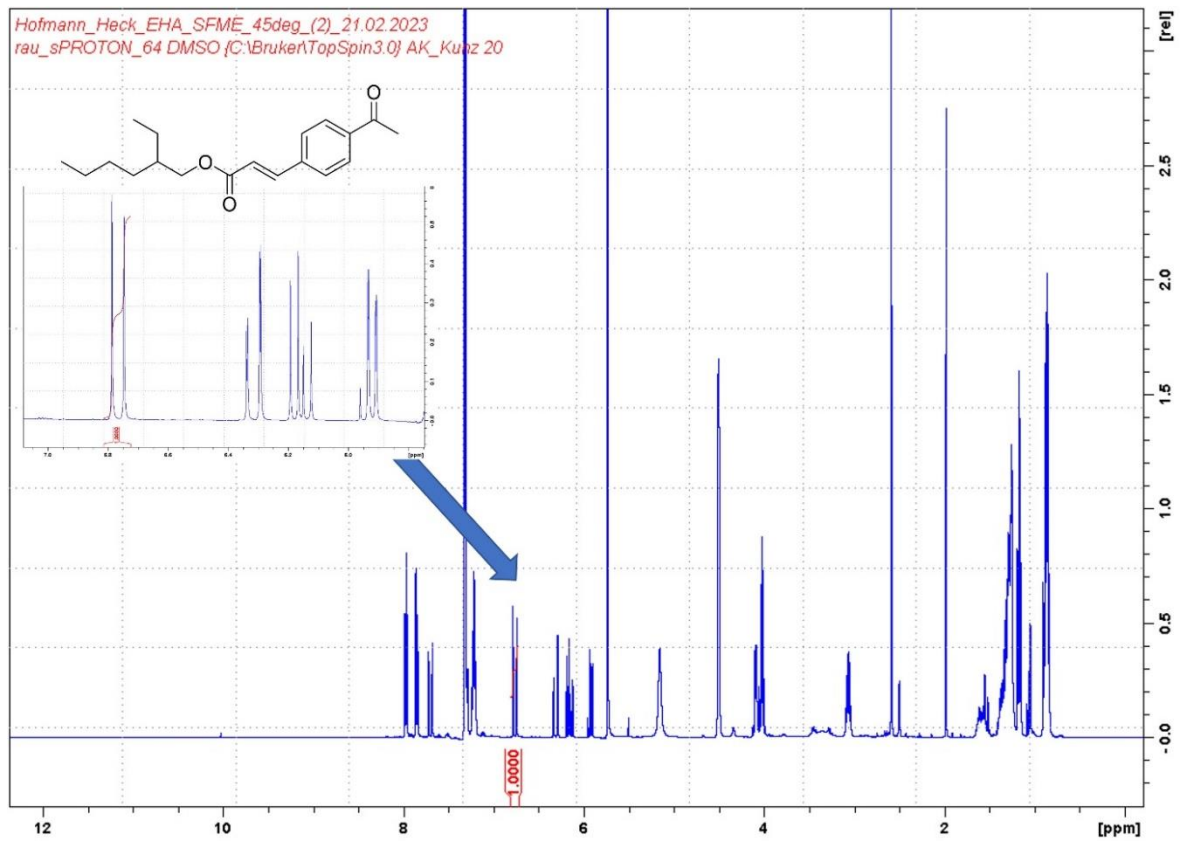


Figure S.2 - 12:  $^1\text{H-NMR}$  spectrum of the crude product of **2b** after the Heck cross-coupling (24 h, 45 °C, SFME-c) in  $\text{DMSO-d}_6$ .

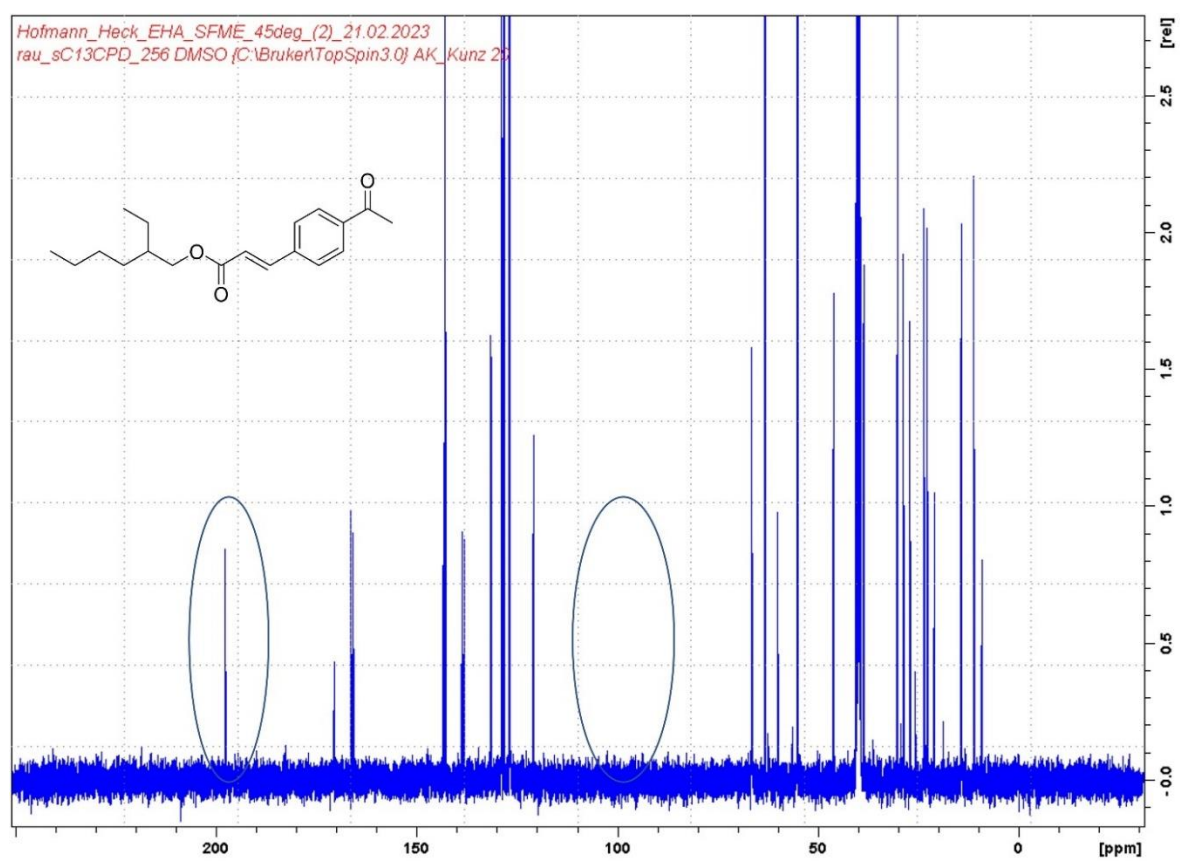


Figure S.2 - 13:  $^{13}\text{C}$ -NMR spectrum of the crude product of **2b** after the Heck cross-coupling (24 h, 45 °C, SFME-c) in  $\text{DMSO-d}_6$ .

## 2.5.4.2 Mass spectrometry

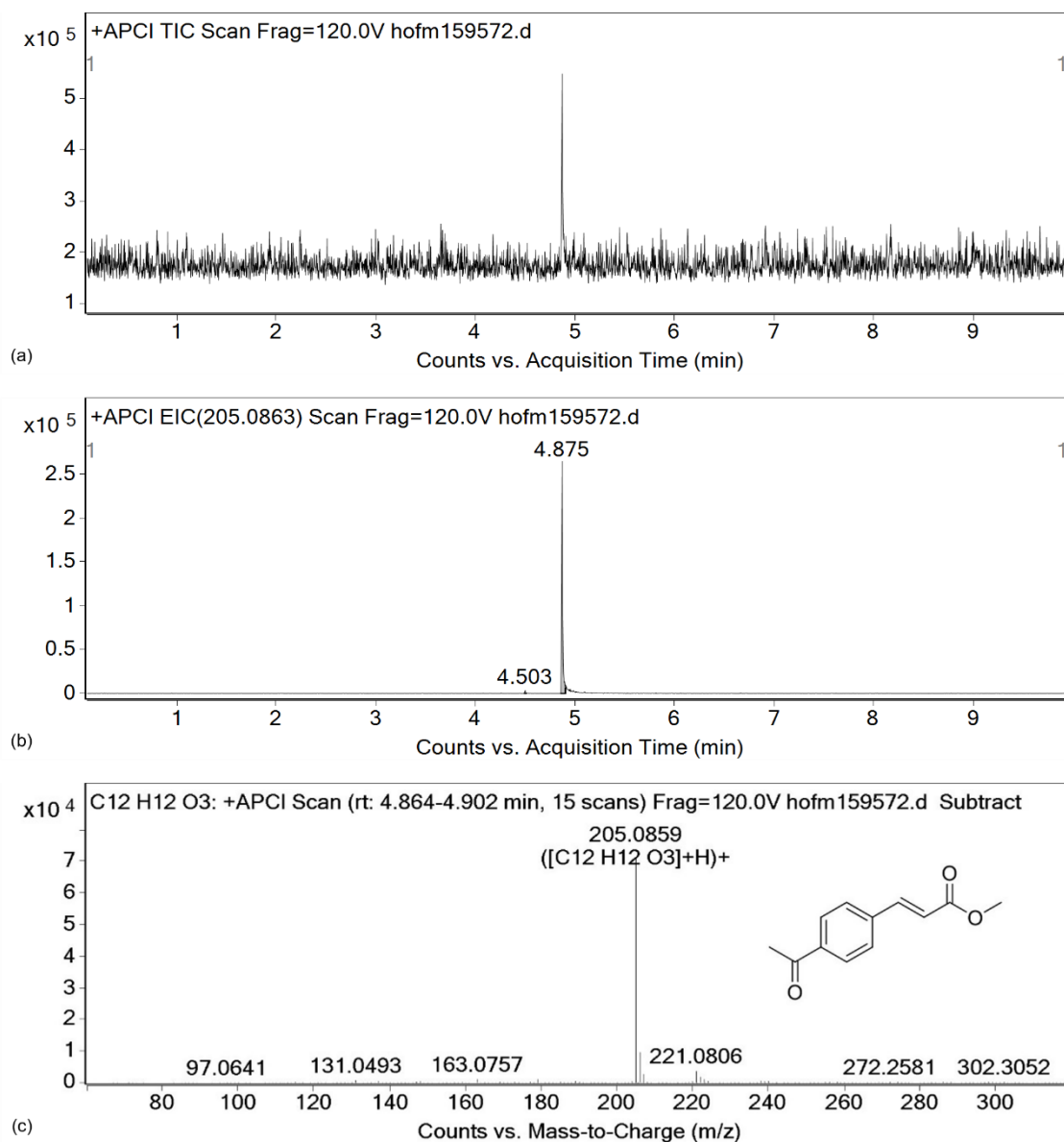


Figure S.2 - 14: MS results of the crude product of **2a** after the Heck cross-coupling (24 h, 45 °C) in the BM-a W/IPA 67/33 (w/w). (a) TIC chromatogram. (b,c) EIC at a  $m/z$  of 205.1 with the corresponding mass spectrum at 4.9 min. The measurements prove the presence of methyl-(E)-3-(4-acetylphenyl)-acrylate with a molar mass of 204.2 g/mol.

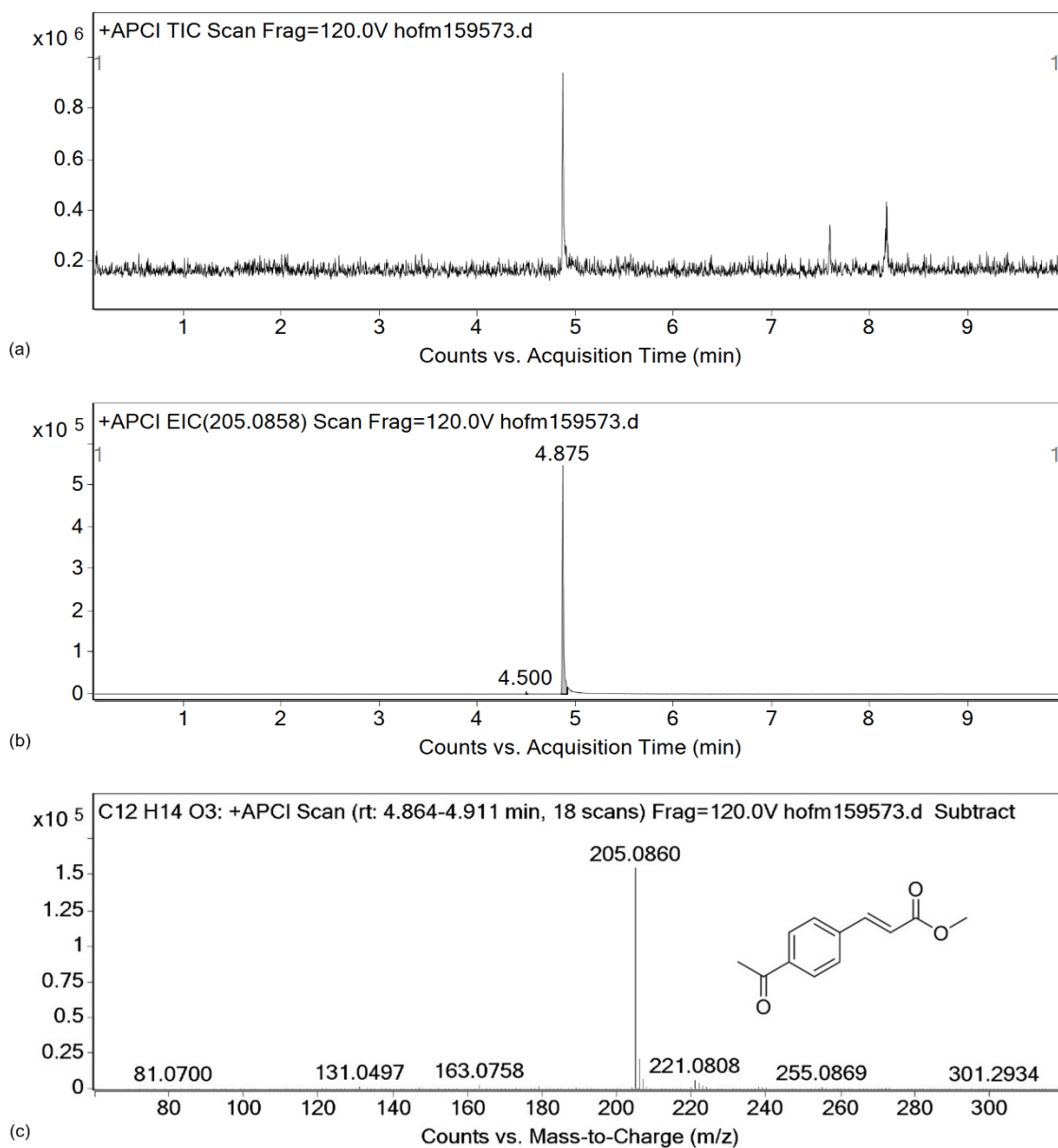
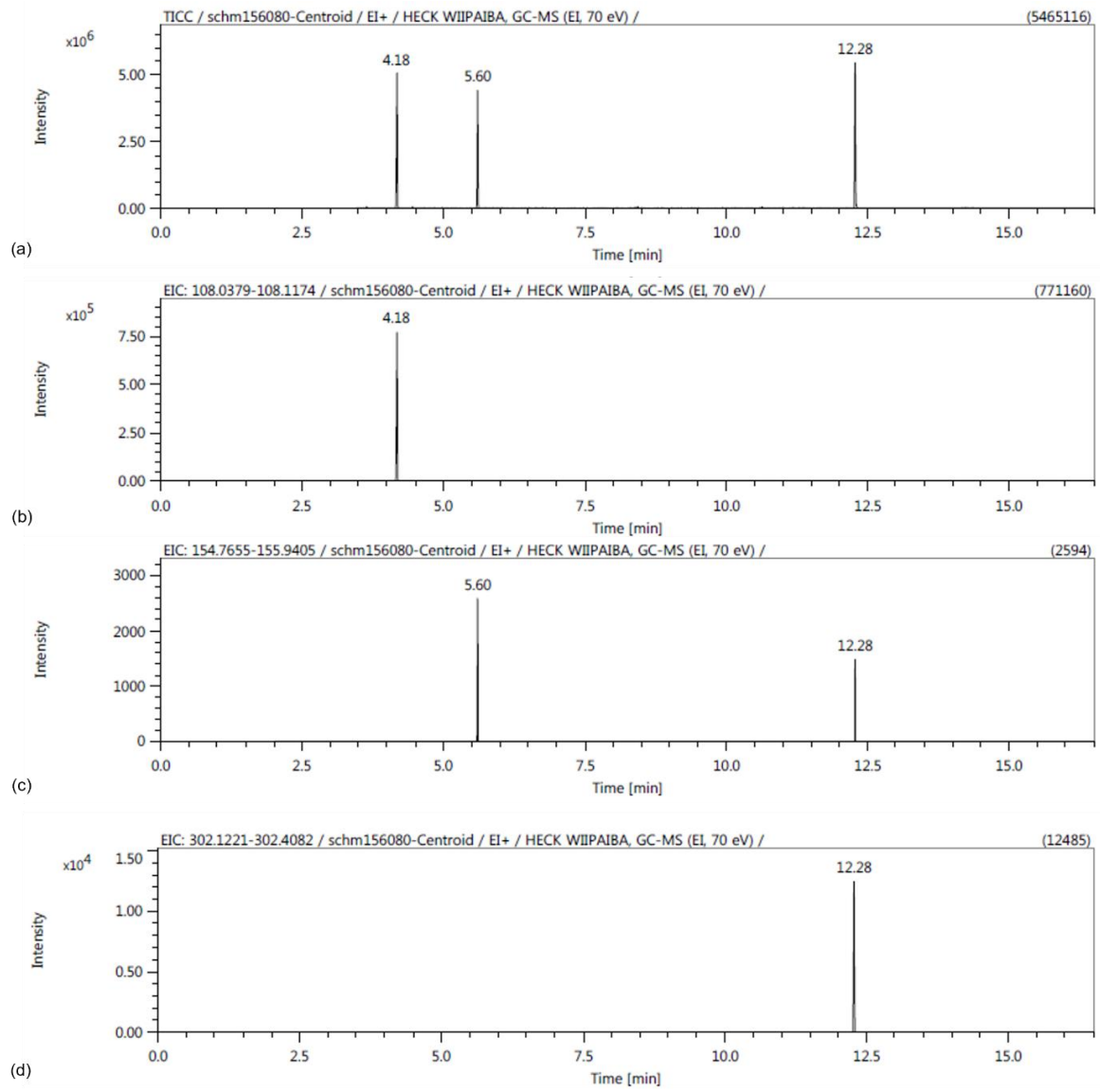


Figure S.2 - 15: MS results of the crude product of **2a** after the Heck cross-coupling (24 h, 45 °C) in the SFME-c W/IPA/BA 47/33/20 (w/w/w). (a) TIC chromatogram. (b,c) EIC at a m/z of 205.1 with the corresponding mass spectrum at 4.9 min. The measurements prove the presence of methyl-(E)-3-(4-acetylphenyl)-acrylate with a molar mass of 204.2 g/mol.



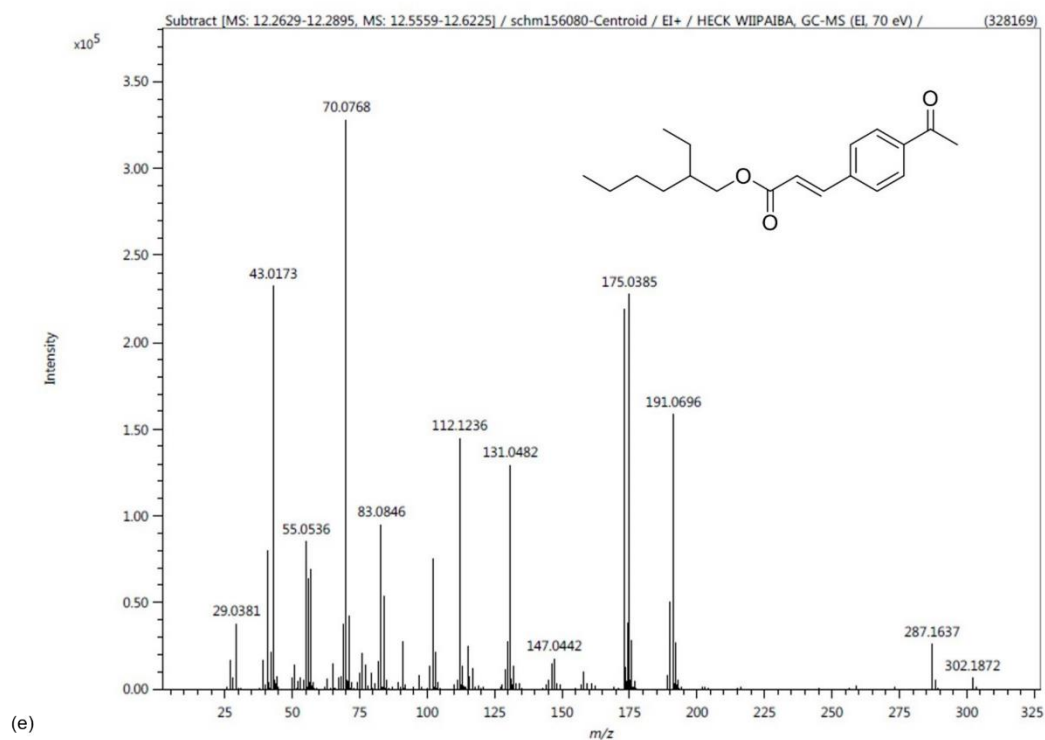


Figure S.2 - 16: MS results of the crude product of **2b** after the Heck cross-coupling (24 h, 45 °C) in the SFME-c W/IPA/BA 47/33/20 (w/w/w). (a) TIC chromatogram. (b,c) EIC at a m/z of 108 and 155 – 156. (d,e) EIC at a m/z of 302 with the corresponding mass spectrum at 12.3 min. The measurements prove the presence of **2b** with a molar mass of 302.4 g/mol. The peak at 4.2 min can be assigned to benzyl alcohol. The peak at 5.6 min corresponds to the fragment of 2-ethylhexyl acrylate.

## 2.5.4.3 Visual observations

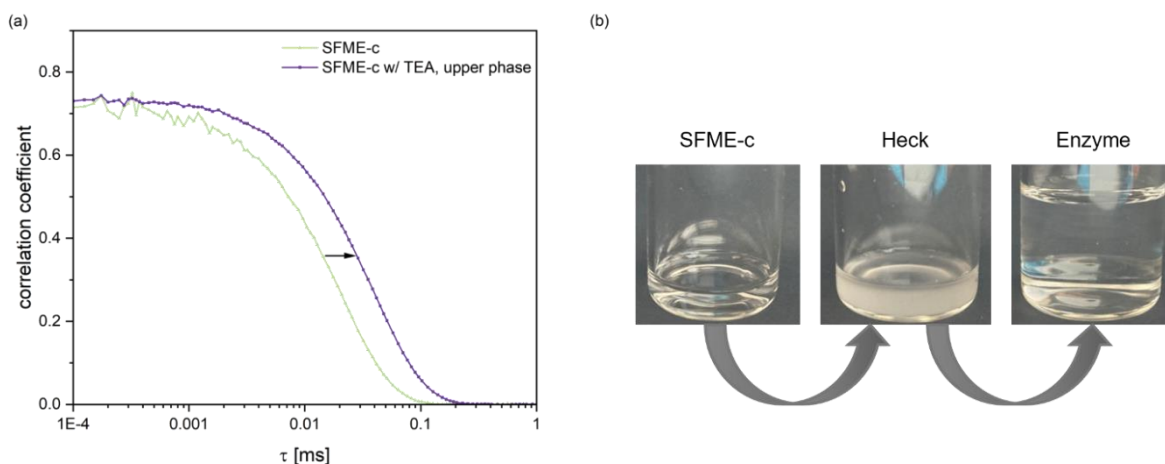


Figure S.2 - 17: (a) Correlation functions at 25 °C obtained by DLS measurements. The green curve results from the pure SFME-c (W/IPA/BA 47/33/20 (w/w/w)). In addition, 2.4 mL of SFME-c was mixed with 588  $\mu$ L TEA. The same ratio is used for the Heck reaction. The turbid mixture was centrifuged until phase separation and the upper, transparent phase ( $\sim 90\%$  (v/v)) was taken and measured by DLS (violet curve). Accordingly, despite liquid-liquid phase separation, there is still a pronounced structuring on a mesoscopic scale detected in the upper phase. The intercept is even shifted to higher lag times, indicating the presence of larger aggregates. (b) From left to right: Photographs of the pure SFME-c, the SFME-c mixed with TEA (as used for the Heck reactions) and the SFME-c/TEA mixture with additional amount of SFME-c (as used for the enzyme-catalyzed reaction).

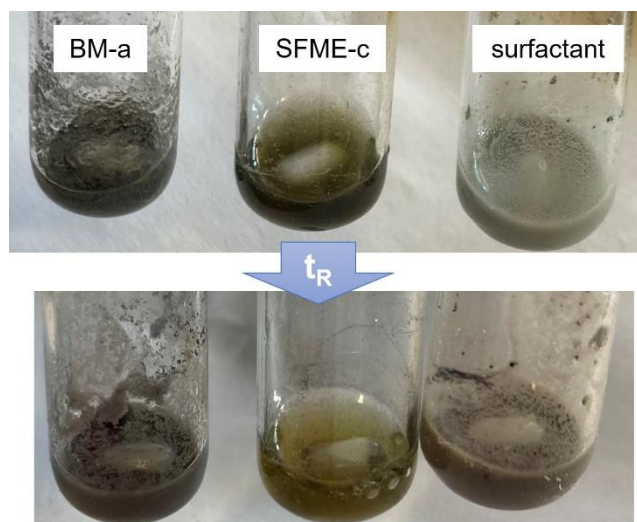


Figure S.2 - 18: Visual observations of the Heck reaction solutions before and after the reaction ( $t_R = 24$  h) at 45 °C. The best solubilization of the reaction components is achieved in the SFME-c (W/IPA/BA 47/33/20 (w/w/w)). The TEA leads to a phase separation of the ternary mixture, and the catalyst is finely dispersed. Overall, the solution appears rather transparent. In the BM-a W/IPA 67/33 (w/w) and the surfactant solution, a large part of the substrate remains undissolved, resulting in a very turbid dispersion.

## 2.5.4.4 DLS studies on TPGS-750-M in combination with the Pd-catalyst

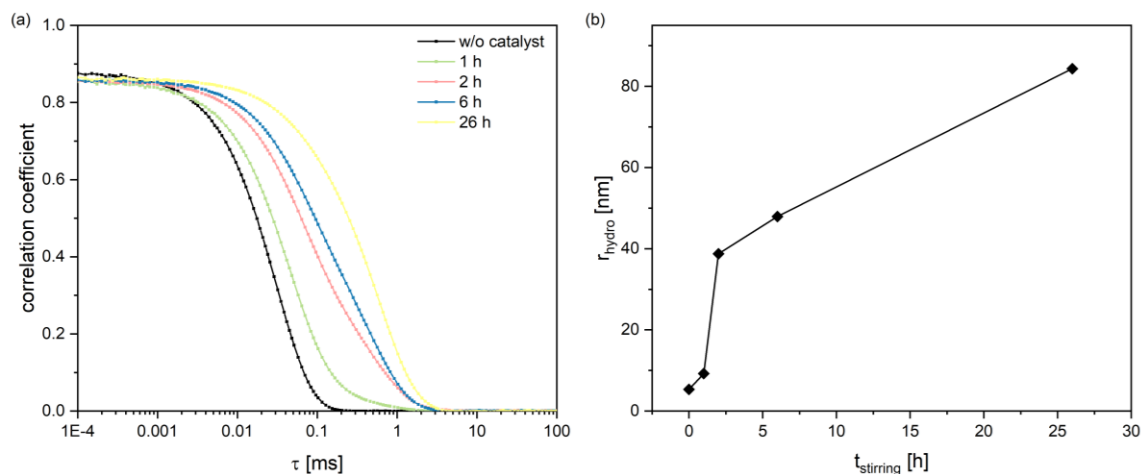


Figure S.2 - 19: (a) Correlation functions obtained by DLS measurements at 25 °C. The black curve represents the correlation function of an aqueous solution containing 2 % (w/w) of TPGS-750-M. The colored samples additionally contained the Pd(*t*-Bu<sub>3</sub>P)<sub>2</sub> catalyst in the same amount as used for the Heck reaction. The time given in the legend correlates with the time of stirring before starting the DLS measurement ( $t_{stirring}$ ). With the addition of the catalyst, the point of inflection is shifted to larger lag times  $\tau$ . Applying the refractive index and viscosity of water, hydrodynamic radii  $r_{hydro}$  are determined with a cumulant fit of 1. order (b). With increasing time, the dispersed aggregates increase in size. This leads to the conclusion that interactions between the surfactant and the catalyst are present, resulting in aggregates larger than single micelles.

## 2.5.4.5 Additional reactions

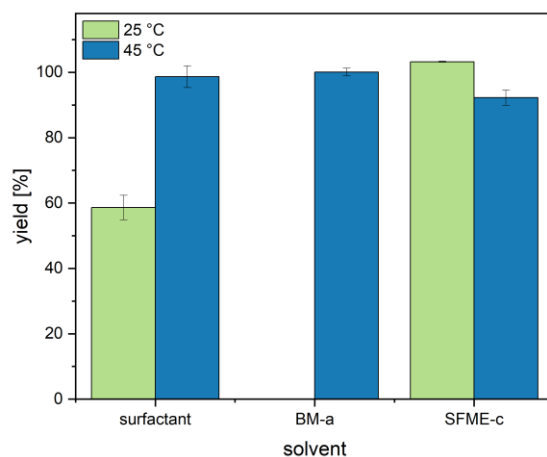


Figure S.2 - 20: Yield of **2b** obtained by Heck cross-coupling (24 h) in different solvents. From left to right: 2 % (w/w) aqueous surfactant solution, BM-a (W/IPA 67/33 (w/w)) and SFME-c (W/IPA/BA 47/33/20 (w/w/w)). Additionally, the Heck cross-coupling with EHA was performed with meglumine, or arginine as a base instead of TEA, in order to maintain a stable SFME-c without phase-separation. The change of the base, however, does not yield any product.

## 2.5.5 One-pot cascade reaction

It is important to note at this point that the reaction yield in this work is determined without complete purification and isolation of the reaction products. Initial attempts are made to completely isolate the reaction product of the cascade reaction in the SFME-c. With the current TLC method, there is incomplete separation of the product from the benzyl alcohol. Hence, in some fractions, both compounds are present (see Figure S.2 - 32). The product is collected such that there is only little benzyl alcohol impurity present, resulting in a decreased yield of 69 % (see Figure S.2 - 24). Changes in column length and eluent compositions should correct this problem. Nevertheless, NMR and MS measurements of pure product fractions are also provided in the following (see Figure S.2 - 21 - Figure S.2 - 23). The product can be described as a pale-yellow solid. Overall, the purification of the reaction product is not the basic idea of this work. Rather, the influence of the solvent on the reaction is paramount. For this purpose, all results are compared to the micellar reference system.

### 2.5.5.1 NMR measurements

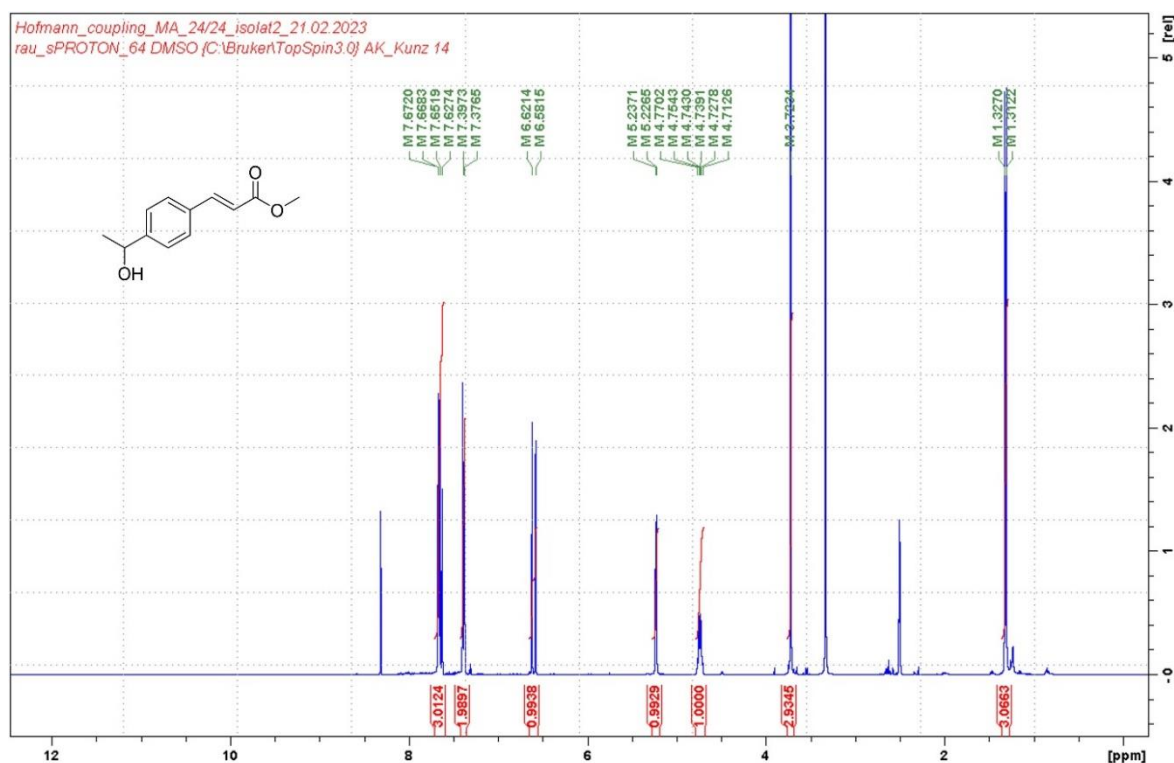


Figure S.2 - 21:  $^1\text{H}$ -NMR spectrum of the isolated product of the cascade reaction (24/24 h, 25/37 °C, SFME-c) in  $\text{DMSO-d}_6$ .

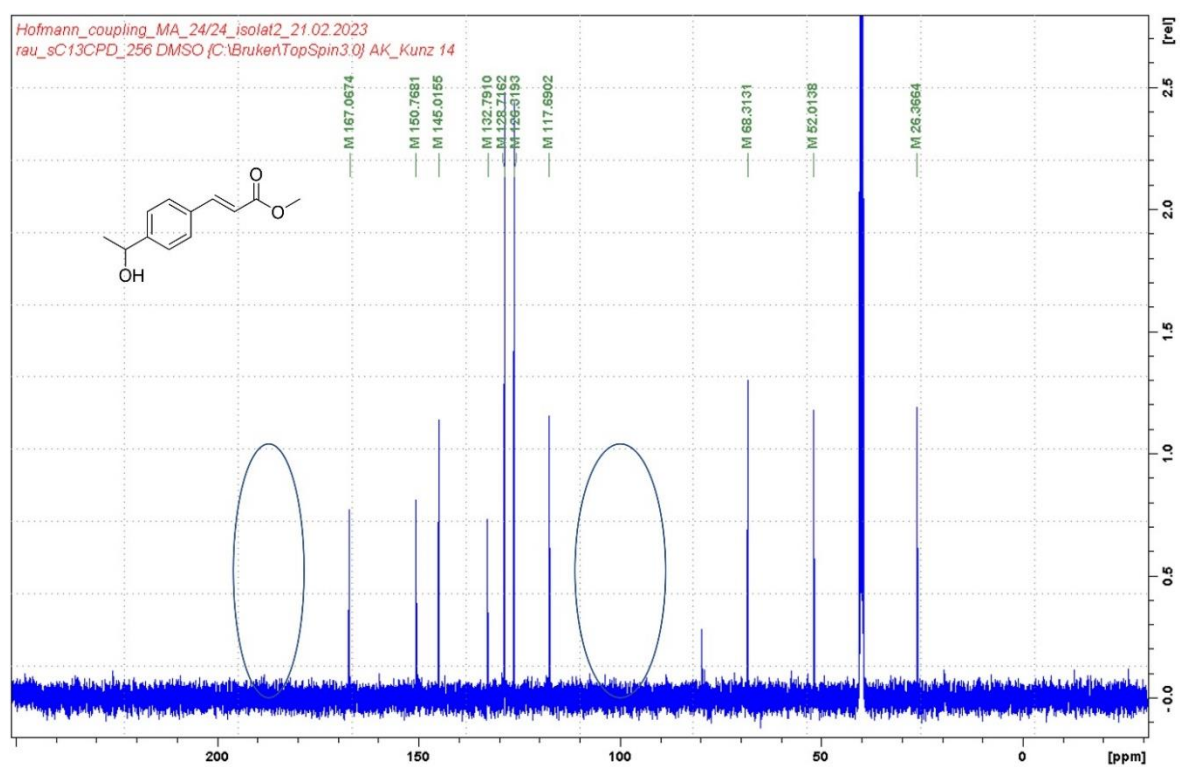


Figure S.2 - 22:  $^{13}\text{C}$ -NMR spectrum of the isolated product of the cascade reaction (24/24 h, 25/37 °C, SFME-c) in DMSO- $d_6$ .

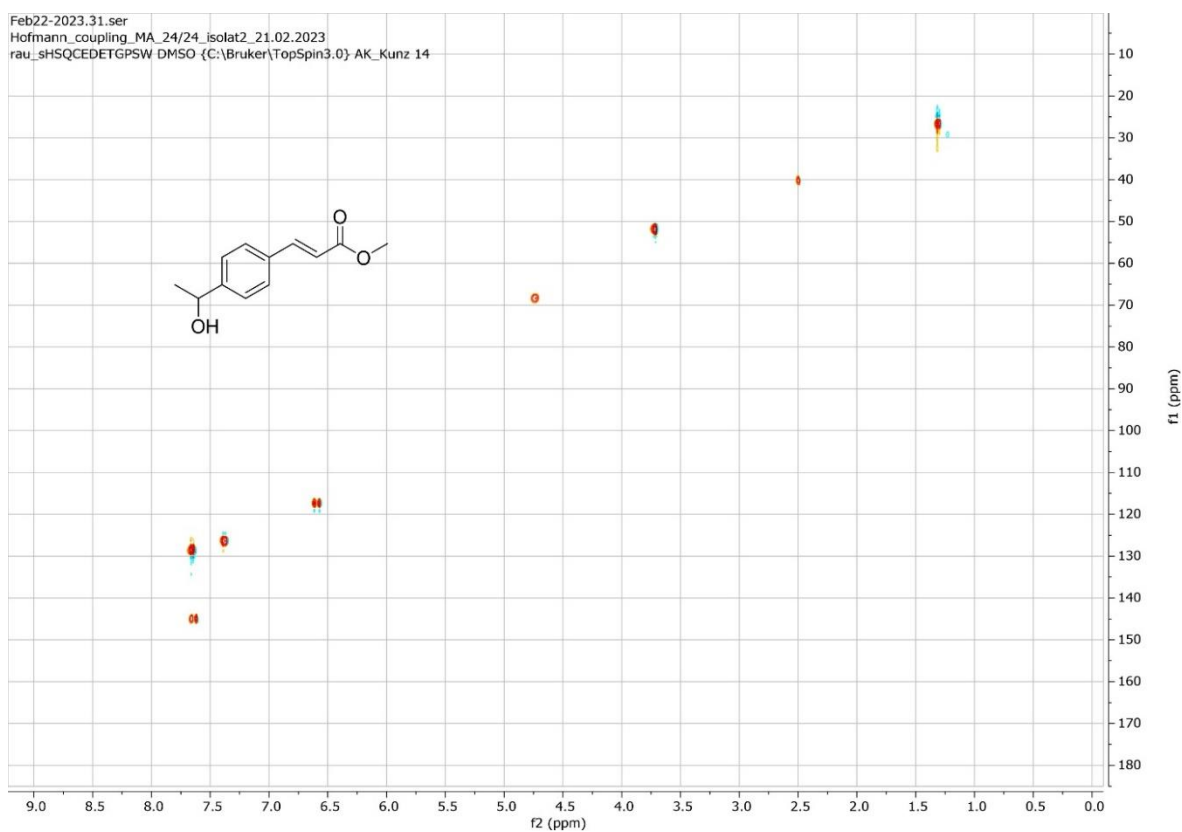


Figure S.2 - 23: HSQC-dept-NMR spectrum of the isolated product of the cascade reaction (24/24 h, 25/37 °C, SFME-c) in DMSO- $d_6$ .

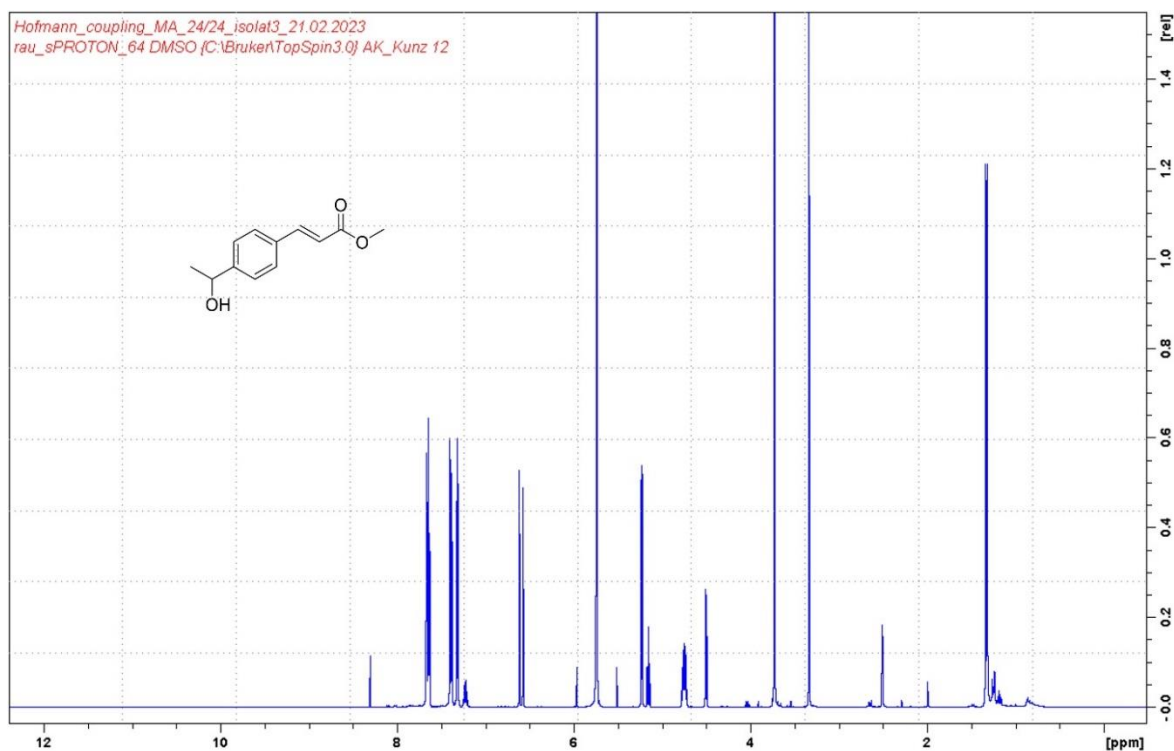
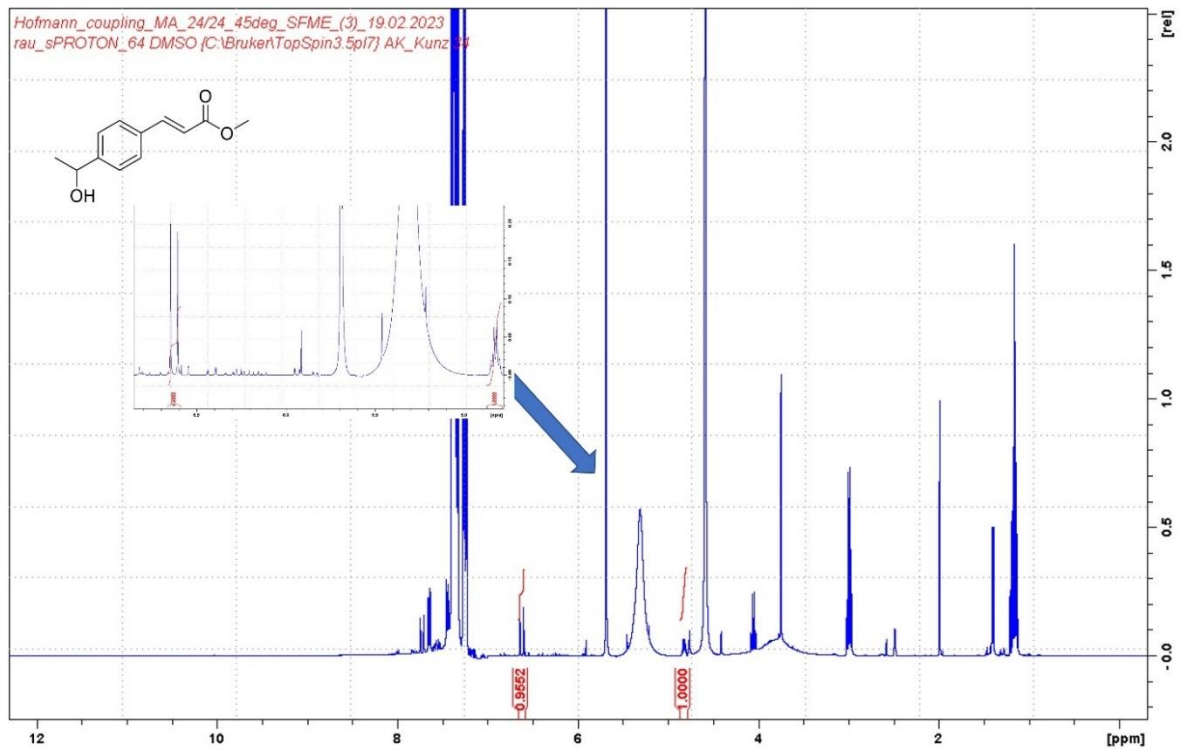


Figure S.2 - 24:  $^1\text{H-NMR}$  spectrum of the isolated product of the cascade reaction (24/24 h, 25/37 °C, SFME-c), contaminated with BA, in  $\text{DMSO-d}_6$ . As already mentioned, there is incomplete separation of the product from the benzyl alcohol with the current TLC method (see Figure S.2 - 32). Hence, in some fractions, both compounds are present. The product is collected such that there is only little benzyl alcohol impurity present, resulting in a decreased yield of 69 %.



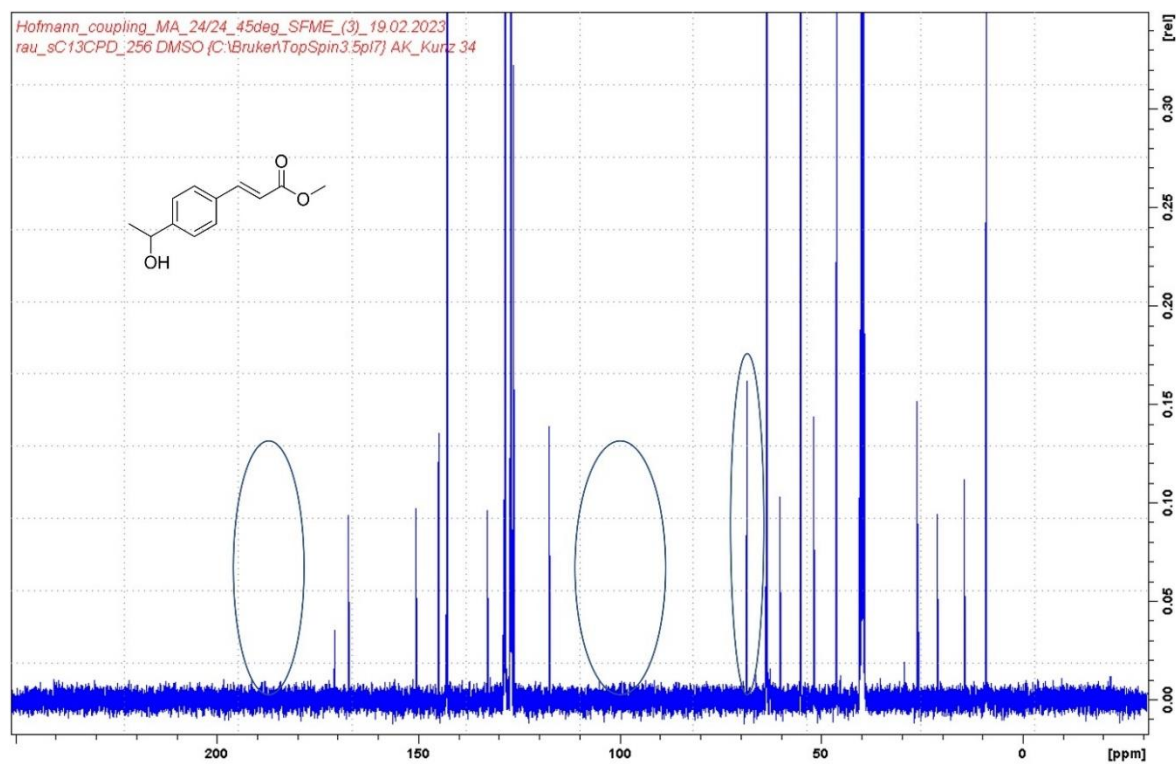
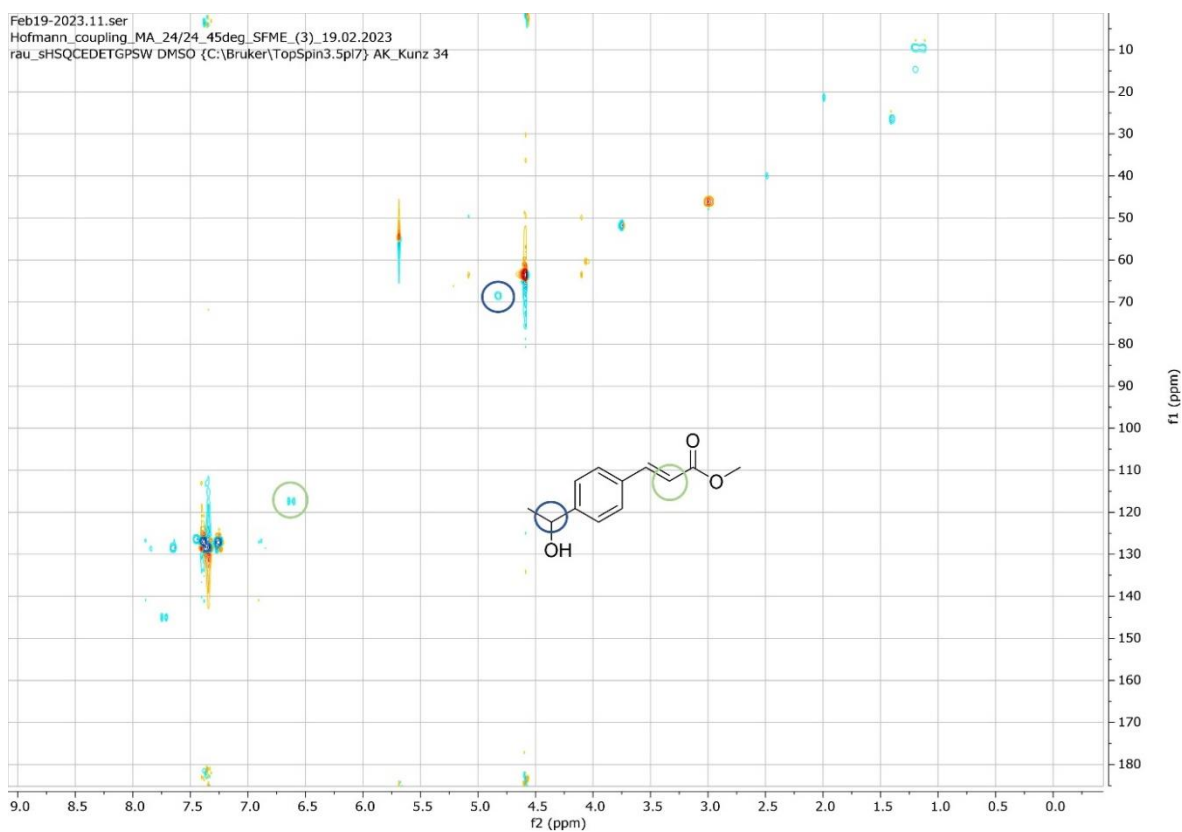


Figure S.2 - 26:  $^{13}\text{C}$ -NMR spectrum of the crude product of the cascade reaction (24/24 h, 45/37 °C, SFME-c) in  $\text{DMSO-d}_6$ .



## 2.5.5.2 Mass spectrometry

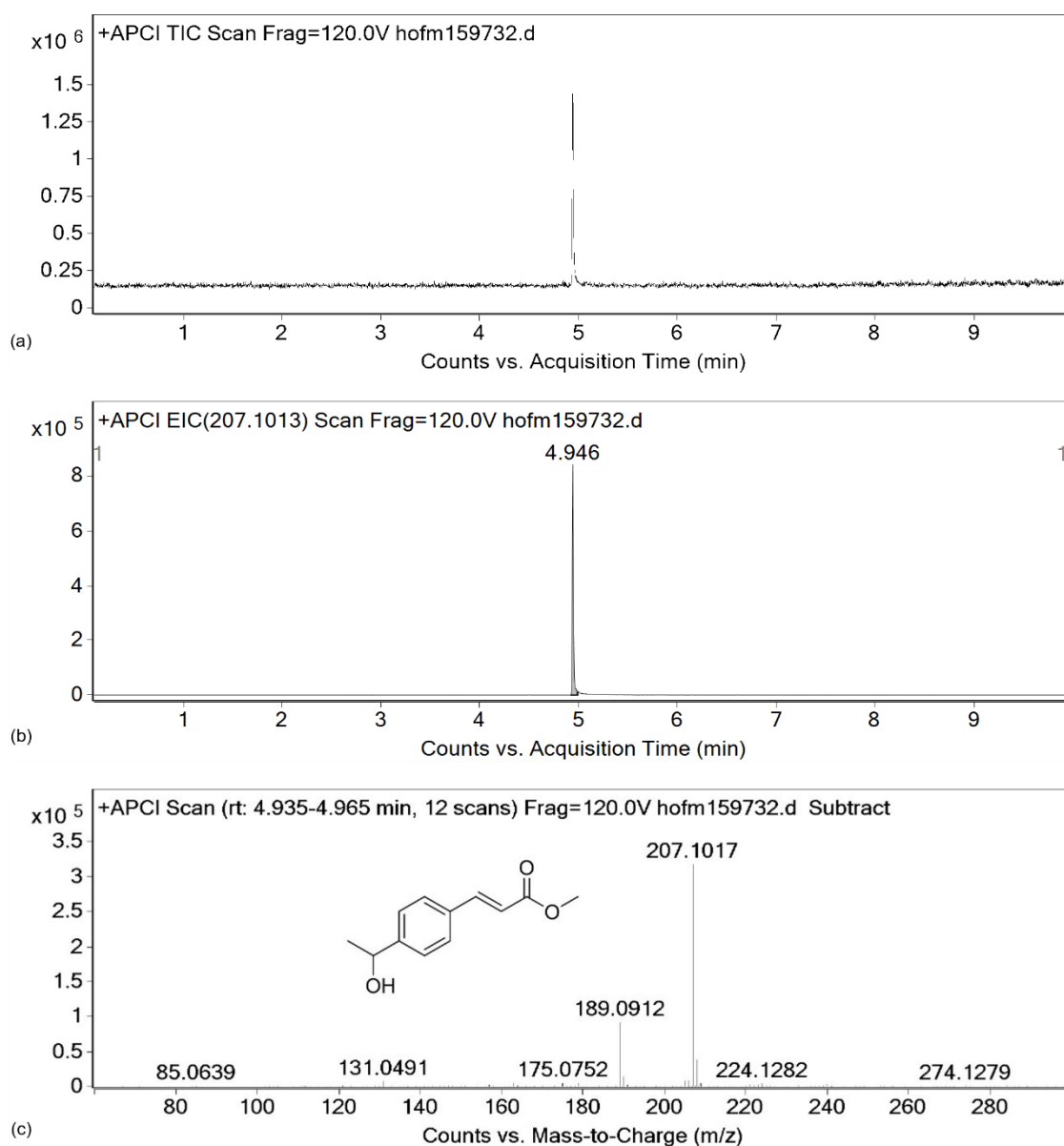


Figure S.2 - 28: MS results of the isolated product of the cascade reaction (24 h/24 h, 25 °C/37 °C) in the SFME-c W/IPA/BA 47/33/20 (w/w/w). (a) TIC chromatogram. (b,c) EIC at a m/z of 207.1 with the corresponding mass spectrum at 4.9 min. The measurements prove the presence of methyl-(R,E)-3-(4-(1-hydroxyethyl)phenyl)-acrylate with a molar mass of 206.2 g/mol. Moreover, there are no additional peaks discernible, reflecting successful isolation.

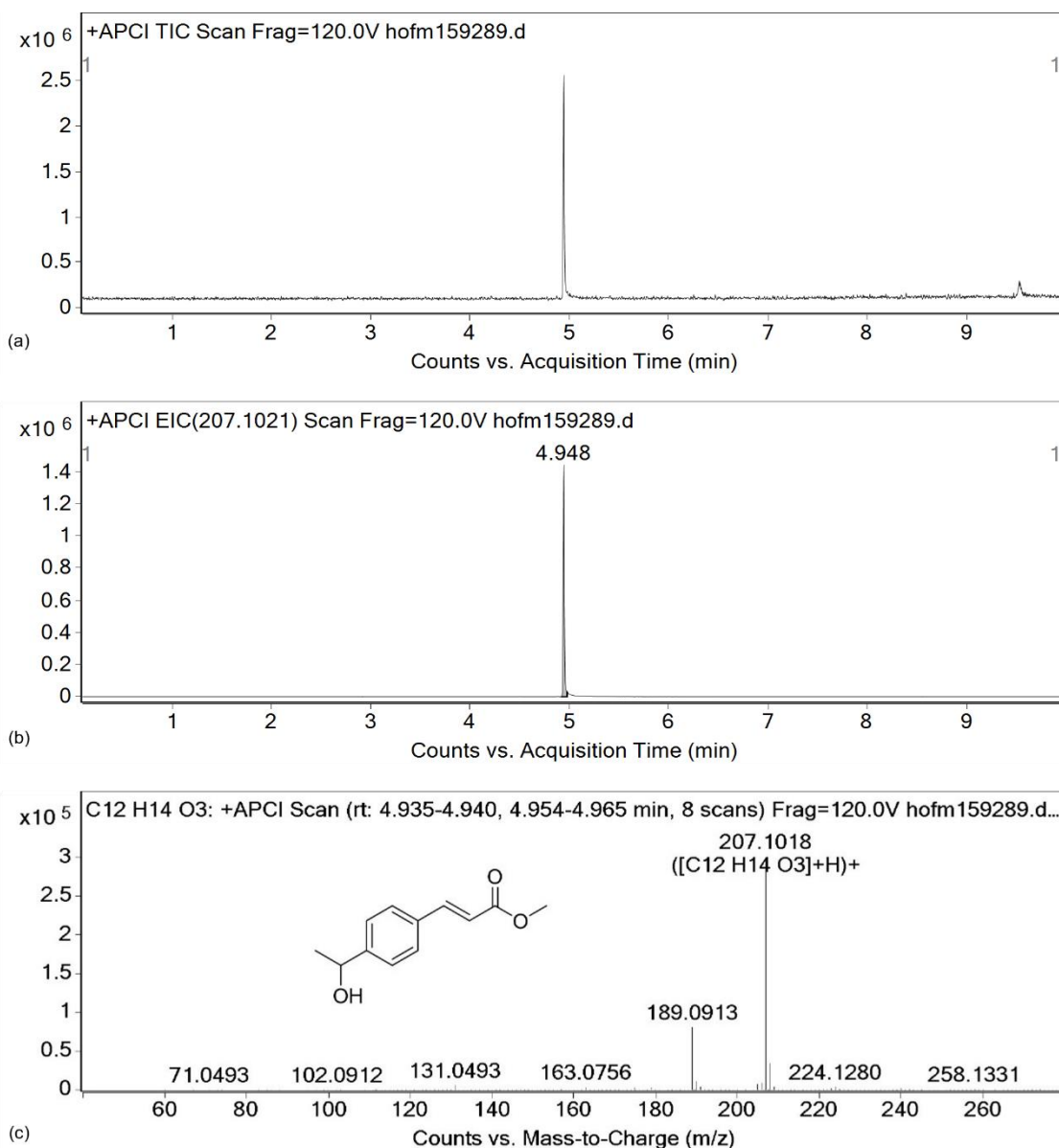


Figure S.2 - 29: MS results of the crude product of the cascade reaction (24 h/24 h, 45 °C/37 °C) in the surfactant solution. (a) TIC chromatogram. (b,c) EIC at a m/z of 207.1 with the corresponding mass spectrum at 4.9 min. The measurements prove the presence of methyl-(R,E)-3-(4-(1-hydroxyethyl)phenyl)-acrylate with a molar mass of 206.2 g/mol.

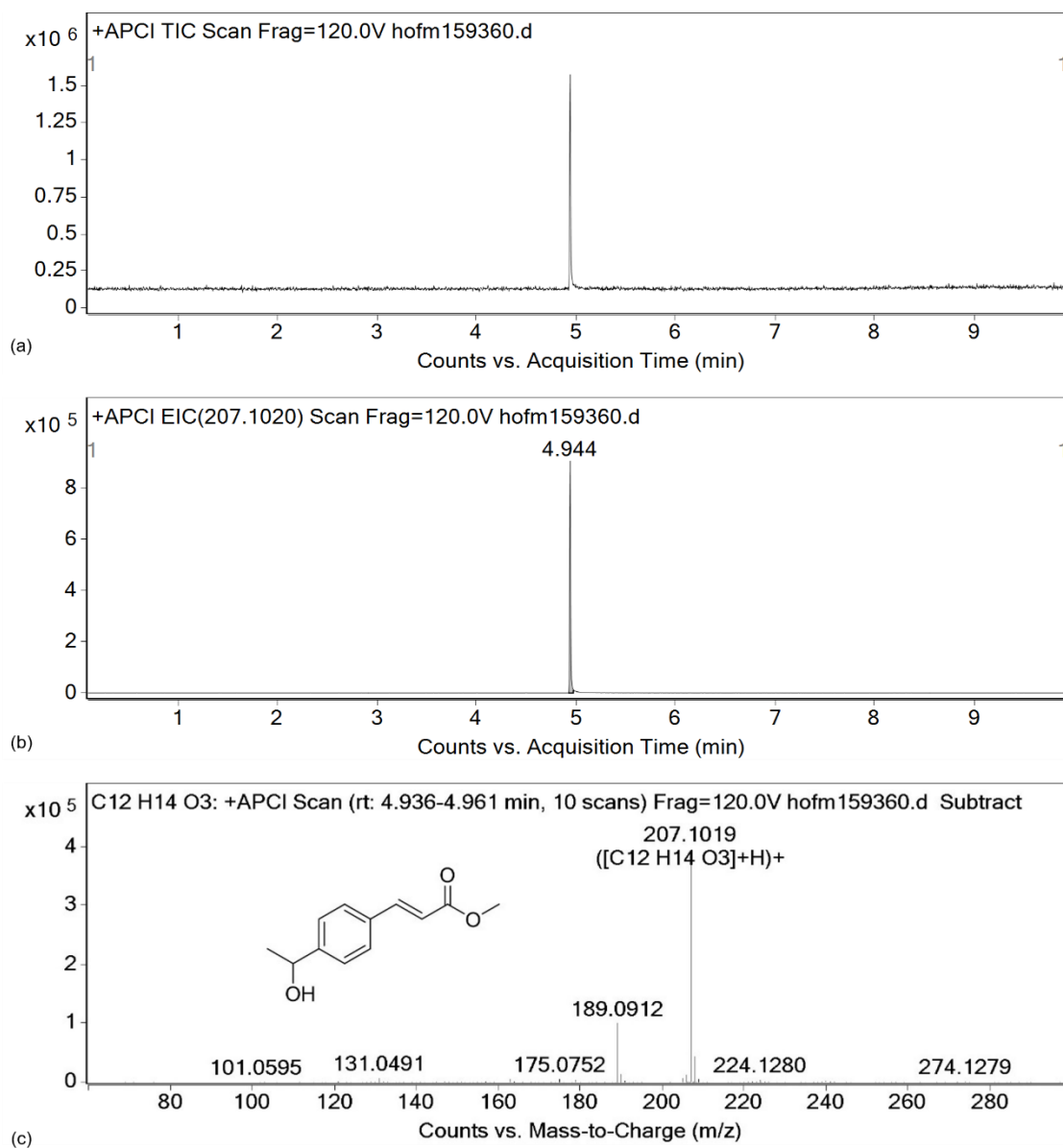


Figure S.2 - 30: MS results of the crude product of the cascade reaction (24 h/24 h, 45 °C/37 °C) in the BM-a W/IPA 67/33 (w/w). (a) TIC chromatogram. (b,c) EIC at a  $m/z$  of 207.1 with the corresponding mass spectrum at 4.9 min. The measurements prove the presence of methyl-(*R,E*)-3-(4-(1-hydroxyethyl)phenyl)-acrylate with a molar mass of 206.2 g/mol.

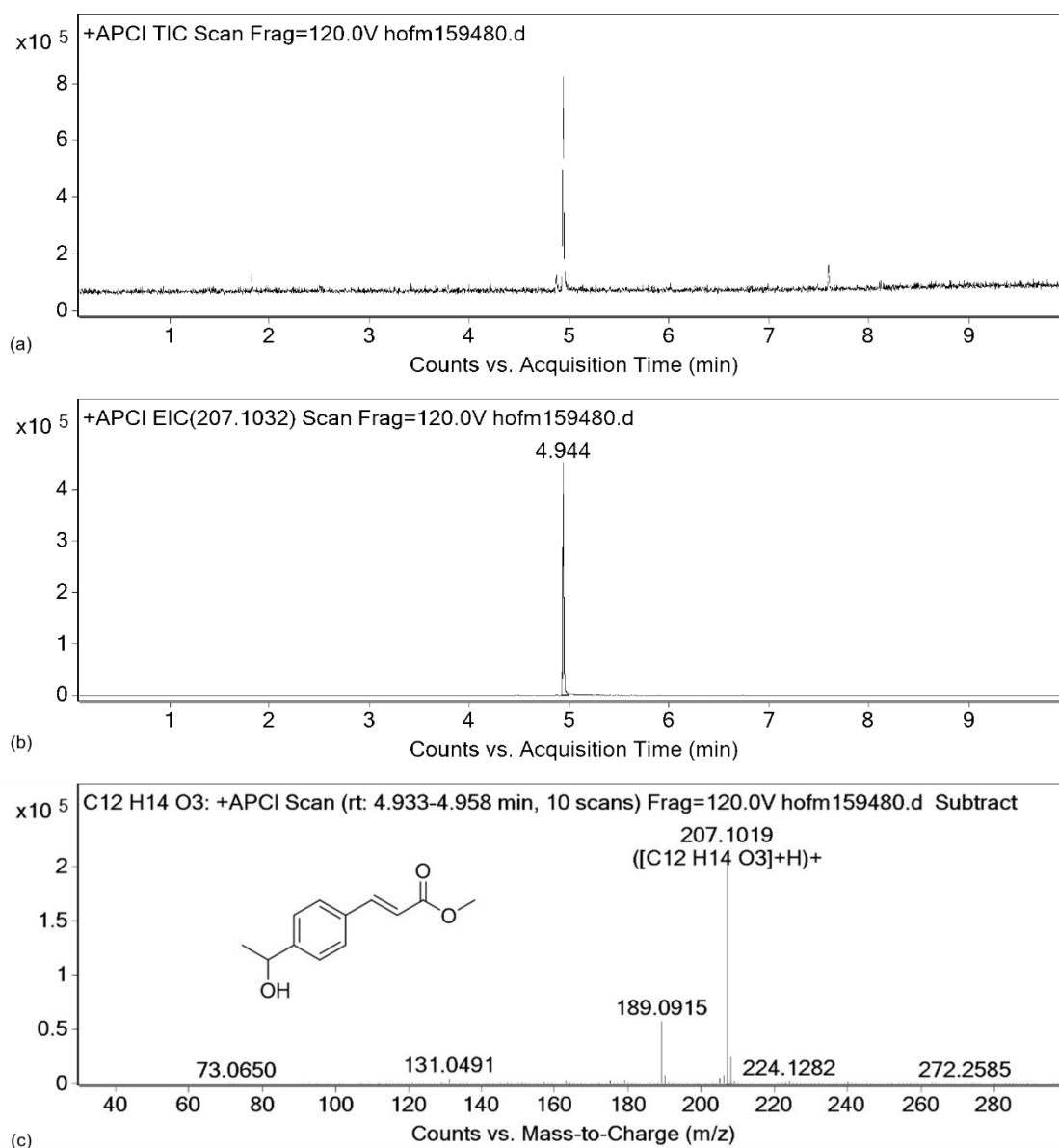


Figure S.2 - 31: MS results of the crude product of the cascade reaction (24 h/24 h, 45 °C/37 °C) in the SFME-c W/IPA/BA 47/33/20 (w/w/w). (a) TIC chromatogram. (b,c) EIC at a  $m/z$  of 207.1 with the corresponding mass spectrum at 4.9 min. The measurements prove the presence of methyl-(*R,E*)-3-(4-(1-hydroxyethyl)phenyl)-acrylate with a molar mass of 206.2 g/mol.

### 2.5.5.3 Thin-layer chromatography

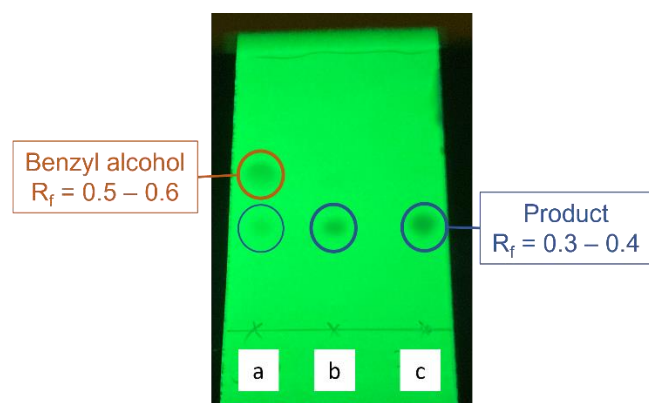


Figure S.2 - 32: TLC of some selected fractions during product isolation of a cascade reaction performed in the SFME-c W/IPA/BA 47/33/20 (w/w/w).

## 2.6 References

- (1) Hofmann, E.; Schmauser, L.; Neugebauer, J.; Touraud, D.; Gallou, F.; Kunz, W. Sustainable Cascade Reaction Combining Transition Metal-Biocatalysis and Hydrophobic Substrates in Surfactant-Free Aqueous Solutions. *Chem. Eng. J.* **2023**, *in minor revision*.
- (2) Shen, T.; Zhou, S.; Ruan, J.; Chen, X.; Liu, X.; Ge, X.; Qian, C. Recent Advances on Micellar Catalysis in Water. *Adv. Colloid Interface Sci.* **2021**, *287*, 102299. <https://doi.org/10.1016/j.cis.2020.102299>.
- (3) Dunn, P. J.; Wells, A. S.; Williams, M. T. *Green Chemistry in the Pharmaceutical Industry*, Wiley-VCH Verlag, 2010.
- (4) Grabner, B.; Schweiger, A. K.; Gavric, K.; Kourist, R.; Gruber-Woelfler, H. A Chemo-Enzymatic Tandem Reaction in a Mixture of Deep Eutectic Solvent and Water in Continuous Flow. *React. Chem. Eng.* **2020**, *5* (2), 263–269. <https://doi.org/10.1039/c9re00467j>.
- (5) Javaid, R.; Kawanami, H.; Chatterjee, M.; Ishizaka, T.; Suzuki, A.; Suzuki, T. M. Sonogashira C-C Coupling Reaction in Water Using Tubular Reactors with Catalytic Metal Inner Surface. *Chem. Eng. J.* **2011**, *167* (2–3), 431–435. <https://doi.org/10.1016/j.cej.2010.08.080>.
- (6) Tian, Y.; Hofmann, E.; Silva, W.; Pu, X.; Touraud, D.; Gschwind, R. M.; Kunz, W.; König, B. Enforced Electronic-Donor-Acceptor Complex Formation in Water for Photochemical Cross-Coupling. *Angew. Chemie Int. Ed.* **2023**, *62* (17). <https://doi.org/10.1002/anie.202218775>.
- (7) Hazra, S.; Gallou, F.; Handa, S. Water: An Underestimated Solvent for Amide Bond-Forming Reactions. *ACS Sustain. Chem. Eng.* **2022**, *10* (16), 5299–5306. <https://doi.org/10.1021/acssuschemeng.2c00520>.
- (8) Giedyk, M.; Narobe, R.; Weiß, S.; Touraud, D.; Kunz, W.; König, B. Photocatalytic Activation of Alkyl Chlorides by Assembly-Promoted Single Electron Transfer in Microheterogeneous Solutions. *Nat. Catal.* **2019**, *3* (1), 40–47. <https://doi.org/10.1038/s41929-019-0369-5>.
- (9) Zhang, Y.; Takale, B. S.; Gallou, F.; Reilly, J.; Lipshutz, B. H. Sustainable Ppm Level

- Palladium-Catalyzed Aminations in Nanoreactors under Mild, Aqueous Conditions. *Chem. Sci.* **2019**, *10* (45), 10556–10561. <https://doi.org/10.1039/c9sc03710a>.
- (10) Braga, F. C.; Rafique, J.; Gomes, R. da S.; de Lima, D. P.; Beatriz, A. In Water Morita-Baylis-Hillman Reactions of Acrylates Enabled by Aqueous Micellar Catalysis Using TPGS-750 M. *Sustain. Chem. Pharm.* **2023**, *31*, 100925. <https://doi.org/10.1016/j.scp.2022.100925>.
- (11) Lipshutz, B. H.; Ghorai, S.; Cortes-Clerget, M. The Hydrophobic Effect Applied to Organic Synthesis: Recent Synthetic Chemistry “in Water.” *Chem. - A Eur. J.* **2018**, *24* (26), 6672–6695. <https://doi.org/10.1002/chem.201705499>.
- (12) Liu, Y.; Liu, P.; Gao, S.; Wang, Z.; Luan, P.; González-Sabín, J.; Jiang, Y. Construction of Chemoenzymatic Cascade Reactions for Bridging Chemocatalysis and Biocatalysis: Principles, Strategies and Prospective. *Chem. Eng. J.* **2021**, *420* (2), 127659. <https://doi.org/10.1016/j.cej.2020.127659>.
- (13) Cavarzan, A.; Scarso, A.; Strukul, G. Efficient Nitrile Hydration Mediated by Rull Catalysts in Micellar Media. *Green Chem.* **2010**, *12* (5), 790–79. <https://doi.org/10.1039/b924244a>.
- (14) Ge, X.; Zhang, S.; Chen, X.; Liu, X.; Qian, C. A Designed Bi-Functional Sugar-Based Surfactant: Micellar Catalysis for C-X Coupling Reaction in Water. *Green Chem.* **2019**, *21* (10), 2771–2776. <https://doi.org/10.1039/c9gc00964g>.
- (15) La Sorella, G.; Strukul, G.; Scarso, A. Recent Advances in Catalysis in Micellar Media. *Green Chem.* **2015**, *17* (2), 644–683. <https://doi.org/10.1039/c4gc01368a>.
- (16) Rideout, D. C.; Breslow, R. Hydrophobic Acceleration of Diels-Alder Reactions. *J. Am. Chem. Soc.* **1980**, *102* (26), 7816–7817. <https://doi.org/10.1021/ja00546a048>.
- (17) Bunton, C. A.; Cerichelli, G.; Ihara, Y.; Sepulveda, L. Micellar Catalysis and Reactant Incorporation in Dephosphorylation and Nucleophilic Substitution. *J. Am. Chem. Soc.* **1979**, *101* (9), 2429–2435. <https://doi.org/10.1021/ja00503a032>.
- (18) Meziani, A.; Touraud, D.; Zradba, A.; Pulvin, S.; Pezron, I.; Clause, M.; Kunz, W. Comparison of Enzymatic Activity and Nanostructures in Water/Ethanol/Brij 35 and Water/1-Pentanol/Brij 35 Systems. *J. Phys. Chem. B* **1997**, *101* (18), 3620–3625. <https://doi.org/10.1021/jp963024u>.
- (19) Orlich, B.; Schomäcker, R. Enzyme Catalysis in Reverse Micelles. *Adv. Biochem. Eng. Biotechnol.* **2002**, *75*, 185–208. [https://doi.org/10.1007/3-540-44604-4\\_6](https://doi.org/10.1007/3-540-44604-4_6).
- (20) Martinek, K.; Levashov, A. V.; Klyachko, N. L.; Pantin, V. I.; Berezin, I. V. The

- Principles of Enzymes Stabilization. *Biochim. Biophys. Acta - Enzymol.* **1981**, 657 (1), 277–294. [https://doi.org/10.1016/0005-2744\(81\)90151-0](https://doi.org/10.1016/0005-2744(81)90151-0).
- (21) Silva, C.; Martins, M.; Jing, S.; Fu, J.; Cavaco-Paulo, A. Practical Insights on Enzyme Stabilization. *Crit. Rev. Biotechnol.* **2018**, 38 (3), 335–350. <https://doi.org/10.1080/07388551.2017.1355294>.
- (22) Zaks, A.; Klibanov, A. M. The Effect of Water on Enzyme Action in Organic Media. *J. Biol. Chem.* **1988**, 263 (17), 8017–8021. [https://doi.org/10.1016/S0021-9258\(18\)68435-2](https://doi.org/10.1016/S0021-9258(18)68435-2).
- (23) Karra-Chaabouni, M.; Pulvin, S.; Thomas, D.; Touraud, D.; Kunz, W. Role of Water Activity on the Synthesis of Geranyl Butyrate by a *Mucor Miehei* Esterase in a Solvent-Free System. *Biotechnol. Lett.* **2002**, 24 (23), 1951–1955. <https://doi.org/10.1023/A:1021173615101>.
- (24) Hastings, C. J.; Adams, N. P.; Bushi, J.; Kolb, S. J. One-Pot Chemoenzymatic Reactions in Water Enabled by Micellar Encapsulation. *Green Chem.* **2020**, 22 (18), 6187–6193. <https://doi.org/10.1039/d0gc01989e>.
- (25) Gröger, H.; Gallou, F.; Lipshutz, B. H. Where Chemocatalysis Meets Biocatalysis: In Water. *Chem. Rev.* **2022**. <https://doi.org/10.1021/acs.chemrev.2c00416>.
- (26) Leontidis, E. Chaotropic Salts Interacting with Soft Matter: Beyond the Lyotropic Series. *Curr. Opin. Colloid Interface Sci.* **2016**, 23, 100–109. <https://doi.org/10.1016/j.cocis.2016.06.017>.
- (27) Mehringer, J.; Do, T.-M.; Touraud, D.; Hohenschutz, M.; Khoshshima, A.; Horinek, D.; Kunz, W. Hofmeister versus Neuberger: Is ATP Really a Biological Hydrotrope? *Cell Reports Phys. Sci.* **2021**, 2 (2), 100343. <https://doi.org/10.1016/j.xcrp.2021.100343>.
- (28) Mehringer, J. Stability of Proteins in the Presence of Anionic Additives, University of Regensburg, 2021. <https://doi.org/10.5283/epub.51476>.
- (29) Cortes-Clerget, M.; Akporji, N.; Zhou, J.; Gao, F.; Guo, P.; Parmentier, M.; Gallou, F.; Berthon, J.; Lipshutz, B. H. Bridging the Gap between Transition Metal- and Bio-Catalysis via Aqueous Micellar Catalysis. *Nat. Commun.* **2019**, 10 (2169), 1–10. <https://doi.org/10.1038/s41467-019-09751-4>.
- (30) Cosgrove, S. C.; Thompson, M. P.; Ahmed, S. T.; Parmeggiani, F.; Turner, N. J. One-Pot Synthesis of Chiral N -Arylamines by Combining Biocatalytic Aminations with Buchwald-Hartwig N-Arylation. *Angew. Chem. Int. Ed.* **2020**, 59 (41), 18156–18160. <https://doi.org/10.1002/anie.202006246>.

- (31) Akporji, N.; Singhania, V.; Dussart-Gautheret, J.; Gallou, F.; Lipshutz, B. H. Nanomicelle-Enhanced, Asymmetric ERED-Catalyzed Reductions of Activated Olefins. Applications to 1-Pot Chemo- and Bio-Catalysis Sequences in Water. *Chem. Commun.* **2021**, 57 (89), 11847–11850. <https://doi.org/10.1039/D1CC04774D>.
- (32) Singhania, V.; Cortes-Clerget, M.; Dussart-Gautheret, J.; Akkachairin, B.; Yu, J.; Akporji, N.; Gallou, F.; Lipshutz, B. H. Lipase-Catalyzed Esterification in Water Enabled by Nanomicelles. Applications to 1-Pot Multi-Step Sequences. *Chem. Sci.* **2022**, 13 (5), 1440–1445. <https://doi.org/10.1039/D1SC05660C>.
- (33) Dussart-Gautheret, J.; Yu, J.; Ganesh, K.; Rajendra, G.; Gallou, F.; Lipshutz, B. H. Impact of Aqueous Micellar Media on Biocatalytic Transformations Involving Transaminase (ATA); Applications to Chemoenzymatic Catalysis. *Green Chem.* **2022**, 24 (16), 6172–6178. <https://doi.org/10.1039/D2GC02002E>.
- (34) Kincaid, J. R. A.; Wong, M. J.; Akporji, N.; Gallou, F.; Fialho, D. M.; Lipshutz, B. H. Introducing Savie: A Biodegradable Surfactant Enabling Chemo- and Biocatalysis and Related Reactions in Recyclable Water. *J. Am. Chem. Soc.* **2023**, 145 (7), 4266–4278. <https://doi.org/10.1021/jacs.2c13444>.
- (35) Zhou, J.; Guo, P.; Gai, Y.; Parmentier, M.; Gallou, F.; Kong, W.; Gao, F. Enzymatic Reaction Medium Containing Surfactant. WO2018134710, 2018.
- (36) Struwe, J.; Ackermann, L.; Gallou, F. Recent Progress in Copper-Free Sonogashira-Hagihara Cross-Couplings in Water. *Chem Catal.* **2023**, 3 (1), 100485. <https://doi.org/10.1016/j.checat.2022.12.002>.
- (37) Lipshutz, B. H.; Ghorai, S.; Abela, A. R.; Moser, R.; Nishikata, T.; Duplais, C.; Krasovskiy, A.; Gaston, R. D.; Gadwood, R. C. TPGS-750-M: A Second-Generation Amphiphile for Metal-Catalyzed Cross-Couplings in Water at Room Temperature. *J. Org. Chem.* **2011**, 76 (11), 4379–4391. <https://doi.org/10.1021/jo101974u>.
- (38) Lee, N. R.; Cortes-Clerget, M.; Wood, A. B.; Lippincott, D. J.; Pang, H.; Moghadam, F. A.; Gallou, F.; Lipshutz, B. H. Coolade. A Low-Foaming Surfactant for Organic Synthesis in Water. *ChemSusChem* **2019**, 12 (13), 3159–3165. <https://doi.org/10.1002/cssc.201900369>.
- (39) Moser, R.; Ghorai, S.; Lipshutz, B. H. Modified Routes to the “Designer” Surfactant PQS. *J. Org. Chem.* **2012**, 77 (7), 3143–3148. <https://doi.org/10.1021/jo202564b>.
- (40) Andersson, M. P.; Gallou, F.; Klumphu, P.; Takale, B. S.; Lipshutz, B. H. Structure of Nanoparticles Derived from Designer Surfactant TPGS-750-M in Water, As Used in

- Organic Synthesis. *Chem. - A Eur. J.* **2018**, *24* (26), 6778–6786.  
<https://doi.org/10.1002/chem.201705524>.
- (41) Xenakis, A.; Zoumpantioti, M.; Stamatis, H. Enzymatic Reactions in Structured Surfactant-Free Microemulsions. *Curr. Opin. Colloid Interface Sci.* **2016**, *22*, 41–45.  
<https://doi.org/10.1016/j.cocis.2016.02.009>.
- (42) Krickl, S. Investigation of Potential Applications of Surfactant-Free Microemulsions - Solubilisation, Separation and Extraction Processes and Reaction Media, University of Regensburg, 2018. <https://doi.org/10.5283/epub.38134>.
- (43) Krell, C.; Schreiber, R.; Hueber, L.; Sciascera, L.; Zheng, X.; Clarke, A.; Haenggi, R.; Parmentier, M.; Baguia, H.; Rodde, S.; Gallou, F. Strategies to Tackle the Waste Water from  $\alpha$ -Tocopherol-Derived Surfactant Chemistry. *Org. Process Res. Dev.* **2021**, *25* (4), 900–915. <https://doi.org/10.1021/acs.oprd.0c00547>.
- (44) Kunz, W.; Holmberg, K.; Zemb, T. Hydrotropes. *Curr. Opin. Colloid Interface Sci.* **2016**, *22*, 99–107. <https://doi.org/10.1016/j.cocis.2016.03.005>.
- (45) Schöttl, S.; Marcus, J.; Touraud, D.; Kunz, W.; Zemb, T.; Horinek, D. Emergence of Surfactant-Free Micelles from Ternary Solutions. *Chem. Sci.* **2014**, *5* (8), 2949–2954.  
<https://doi.org/10.1039/c4sc00153b>.
- (46) Krickl, S.; Touraud, D.; Bauduin, P.; Zinn, T.; Kunz, W. Enzyme Activity of Horseradish Peroxidase in Surfactant-Free Microemulsions. *J. Colloid Interface Sci.* **2018**, *516*, 466–475. <https://doi.org/10.1016/j.jcis.2018.01.077>.
- (47) Khmel'nitsky, Y. L.; Hilhorst, R.; Veeger, C. Detergentless Microemulsions as Media for Enzymatic Reactions: Cholesterol Oxidation Catalyzed by Cholesterol Oxidase. *Eur. J. Biochem.* **1988**, *176* (2), 265–271.  
<https://doi.org/10.1111/j.1432-1033.1988.tb14277.x>.
- (48) Younes, M.; Aquilina, G.; Castle, L.; Engel, K. H.; Fowler, P.; Fürst, P.; Gürtler, R.; Gundert-Remy, U.; Husøy, T.; Mennes, W.; Moldeus, P.; Oskarsson, A.; Shah, R.; Waalkens-Berendsen, I.; Wölflle, D.; Boon, P.; Crebelli, R.; Di Domenico, A.; Filipič, M.; Mortensen, A.; Van Loveren, H.; Woutersen, R.; Gergelova, P.; Giarola, A.; Lodi, F.; Frutos Fernandez, M. J. Re-Evaluation of Benzyl Alcohol (E 1519) as Food Additive. *EFSA J.* **2019**, *17* (10). <https://doi.org/10.2903/j.efsa.2019.5876>.
- (49) Corcoran, G. B.; Ray, S. D. Benzyl Alcohol. In *Encyclopedia of Toxicology: 3rd edn.*; Elsevier, 2014; Vol. 1, pp 429–432.  
<https://doi.org/10.1016/B978-0-12-386454-3.00251-7>.

- (50) Panjapakkul, W.; El-Halwagi, M. M. Techno-Economic Analysis of Alternative Pathways of Isopropanol Production. *ACS Sustain. Chem. Eng.* **2018**, *6* (8), 10260–10272. <https://doi.org/10.1021/acssuschemeng.8b01606>.
- (51) Dekker, M. L.; Clause, M.; Rosano, H. L.; Zradba, A. S. *Microemulsion Systems*, 24th edn.; Surfactant Science Ser., New York, PA, 1987.
- (52) Cortes-Clerget, M.; Akporji, N.; Zhou, J.; Gao, F.; Guo, P.; Parmentier, M.; Gallou, F.; Berthon, J.-Y.; Lipshutz, B. H. Bridging the Gap between Transition Metal- and Bio-Catalysis via Aqueous Micellar Catalysis. *Nat. Commun.* **2019**, *10* (2169), 1–10. <https://doi.org/10.1038/s41467-019-09751-4>.
- (53) Buchecker, T.; Krickl, S.; Winkler, R.; Grillo, I.; Bauduin, P.; Touraud, D.; Pfitzner, A.; Kunz, W. The Impact of the Structuring of Hydrotropes in Water on the Mesoscale Solubilisation of a Third Hydrophobic Component. *Phys. Chem. Chem. Phys.* **2017**, *19* (3), 1806–1816. <https://doi.org/10.1039/c6cp06696h>.
- (54) de Miranda, A. S.; Milagre, C. D. F.; Hollmann, F. Alcohol Dehydrogenases as Catalysts in Organic Synthesis. *Front. Catal.* **2022**, *2*, 1–32. <https://doi.org/10.3389/fctls.2022.900554>.
- (55) Aono, S.; Okura, I. Photochemical Reduction of NADP to NADPH and Hydrogenation of 2-Butanone Using 2,2'-Bipyridinium Salts as Electron Carriers. *Inorganica Chim. Acta* **1988**, *152* (1), 55–59. [https://doi.org/10.1016/S0020-1693\(00\)90732-1](https://doi.org/10.1016/S0020-1693(00)90732-1).
- (56) Barouh, N.; Bourlieu-Lacanal, C.; Figueroa-Espinoza, M. C.; Durand, E.; Villeneuve, P. Tocopherols as Antioxidants in Lipid-Based Systems: The Combination of Chemical and Physicochemical Interactions Determines Their Efficiency. *Compr. Rev. Food Sci. Food Saf.* **2022**, *21* (1), 642–688. <https://doi.org/10.1111/1541-4337.12867>.
- (57) Mast, R. C.; Haynes, L. V. The Use of the Fluorescent Probes Perylene and Magnesium 8-Anilinonaphthalene-1-Sulfonate to Determine the Critical Micelle Concentration of Surfactants in Aqueous Solution. *J. Colloid Interface Sci.* **1975**, *53* (1), 35–41. [https://doi.org/10.1016/0021-9797\(75\)90032-6](https://doi.org/10.1016/0021-9797(75)90032-6).
- (58) Topel, Ö.; Çakır, B. A.; Budama, L.; Hoda, N. Determination of Critical Micelle Concentration of Polybutadiene-Block-Poly(Ethyleneoxide) Diblock Copolymer by Fluorescence Spectroscopy and Dynamic Light Scattering. *J. Mol. Liq.* **2013**, *177*, 40–43. <https://doi.org/10.1016/j.molliq.2012.10.013>.

## Chapter 3 1,4-Addition of 3-bromophenylboronic acid to $\alpha,\beta$ -unsaturated cyclohexenone in surfactant-free aqueous solutions

### 3.0 Abstract

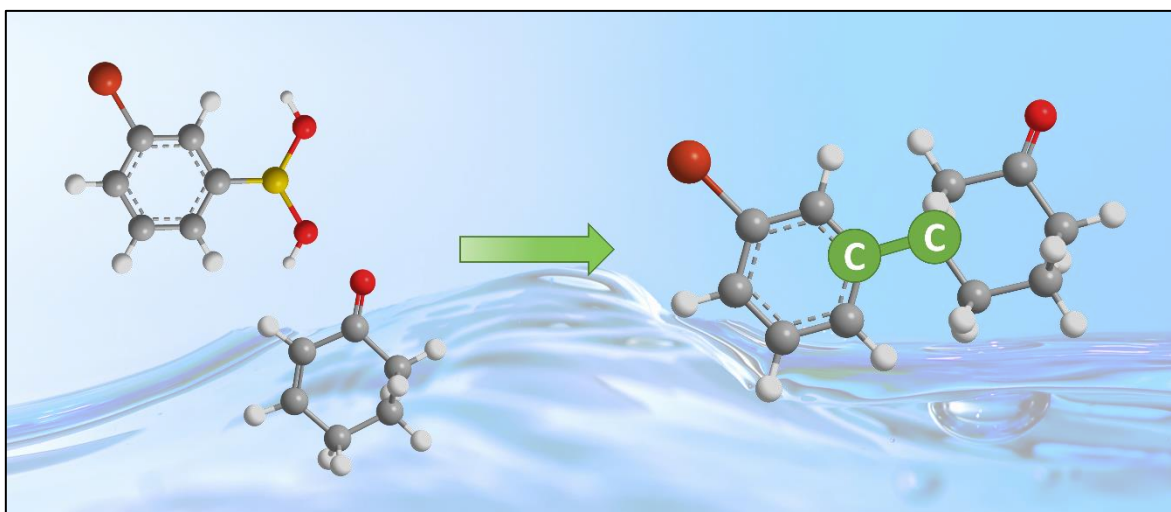


Figure 3 - 1: Schematic illustration of the 1,4-addition of 3-bromophenylboronic acid to cyclohexenone in an aqueous solvent.

Carbon-carbon bond-forming reactions display a crucial step in many syntheses performed in industry. In the case of the 1,4-addition of arylboronic acids to enones, excess amounts of the boronic acids are typically required. An aqueous micellar solution of the designer surfactant TPGS-750-M allows for reducing the substrate excess. The present work deals with the replacement of the complex micellar solvent by simpler aqueous solutions. In this context, the great solubilization power of surfactant-free microemulsions of water, short-chain alcohol, and oil appears to promote competitive side reactions. However, when a salt is applied as the hydrotrope, a stabilizing effect on the arylboronic acid is observed. Accordingly, an excellent yield is achieved in a surfactant-free microemulsion of water, the salt sodium 1-pentanesulfonate, and the oil tetrahydro linalool using the same stoichiometry as in the micellar system. The great advantage of the surfactant-free microemulsion as the reaction solvent is, thus, its opportunity to combine different molecules that can affect both the solubility and the stability of the reactants in a stable and sustainable solvent system. The structuring, however, does not appear to affect the reaction outcome.

### 3.1 Introduction

The Nobel Prize for palladium-catalyzed cross-couplings in the year 2010 best reflects the importance of carbon-carbon bond formation in organic syntheses.<sup>1,2</sup> The coupling reactions are crucial steps in industrial processes, including the pharmaceutical, agrochemical, and fine chemical industries.<sup>2-4</sup> A powerful reaction used for carbon-carbon bond formation represents the asymmetric 1,4-addition.<sup>5-7</sup> In this context, a common reaction applied in industry and often reported in the literature is the rhodium(Rh)-catalyzed addition of an arylboronic acid to an  $\alpha,\beta$ -unsaturated carbonyl compound (see Figure 3 - 2(1)).<sup>7-13</sup> Due to competitive protodeboronation (see Figure 3 - 1(2)), excess amounts of arylboronic acid are usually applied to ensure high yields.<sup>14-16</sup> The usage of an excess of up to 5 or 10 equivalents (equiv.) is reported.<sup>5,11-13,17-19</sup>

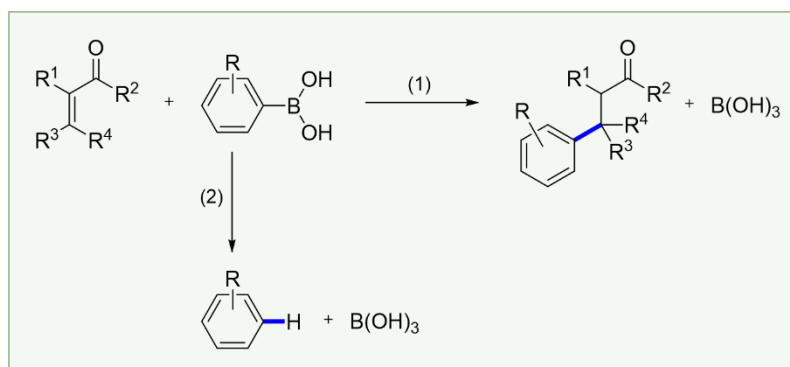


Figure 3 - 2: Reaction scheme of Rh-catalyzed reactions of an arylboronic acid. (1) 1,4-Addition of an arylboronic acid to an  $\alpha,\beta$ -unsaturated carbonyl compounds. (2) Protodeboronation reaction.

Linsenmeier *et al.* successfully transferred several cross-couplings between arylboronic acids and  $\alpha,\beta$ -unsaturated esters into a micellar solution of the designer surfactant TPGS-750-M (DL- $\alpha$ -tocopherol methoxypolyethylene glycol succinate, see Figure 3 - 3(a)). The reactions are carried out in the absence of any additional organic solvent using only 2 equiv. excess of the arylboronic acids.<sup>8</sup> Lipshutz *et al.* applied the designer surfactant PQS (polyethylene glycol ubiquinol sebacate) to perform 1,4-additions of arylboronic acids to enones in water. The surfactant is covalently bound to a BINAP (2,2'-bis(diphenylphosphino)-1,1'-binaphthyl) ligand, which is then attached to the Rh-catalyst (PQS-BINAP-Rh, see Figure 3 - 3(b)). Lipshutz and coworkers, thus, achieved high yields with only 1.2 equiv. of the arylboronic acids.<sup>20</sup> Both approaches perform reactions at room temperature.<sup>8,20</sup>

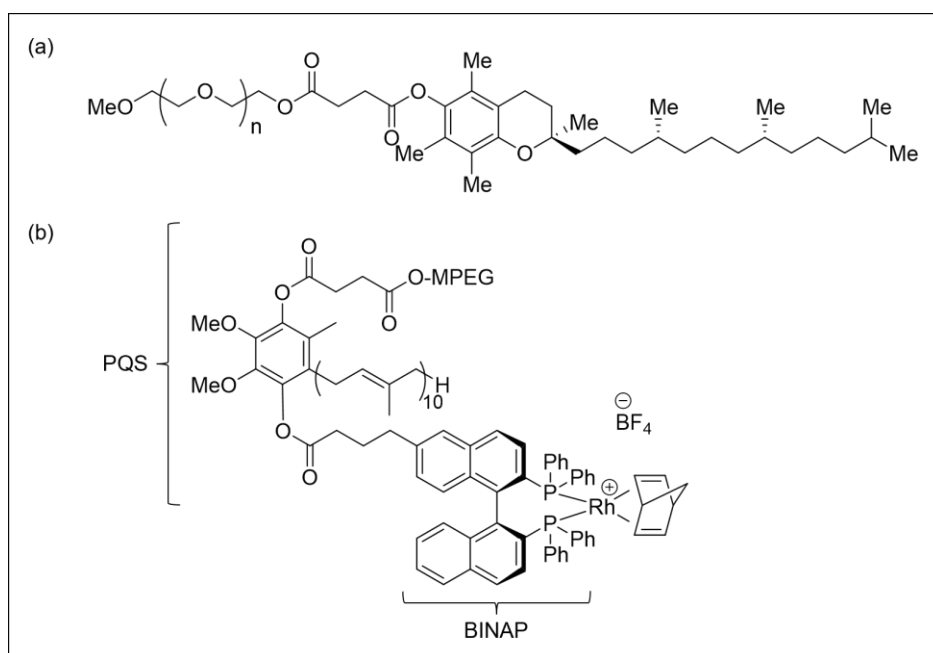


Figure 3 - 3: (a) Molecular structure of the designer surfactant TPGS-750-M. (b) Molecular structure of the designer surfactant PQS bound to the Rh-catalyst via a BINAP ligand. MPEG represents a polyethylene glycol monomethyl ether chain.

As previously explained in Chapter 2, the usage of surfactants can lead to difficulties with regard to recycling, biodegradability, and foam formation.<sup>21–23</sup> For this reason, the chapter deals with the replacement of the micellar reaction solvents by surfactant-free aqueous solutions. Different binary and ternary systems of water, hydrotrope, and oil are considered, including surfactant-free microemulsions. The focus is, thus, on the use of simple molecules. In particular, the difference between volatile alcohols and salts acting as hydrotropes is investigated. Furthermore, the impact of solvent structuring and reactant solubilization is discussed.

## 3.2 Material and methods

### 3.2.1 Chemicals

Hydroxy(cyclooctadiene)rhodium(I) dimer ( $[\text{Rh}(\text{OH})(1,5\text{-cod})]_2$ , assay 95 %), DL- $\alpha$ -tocopherol methoxypolyethylene glycol succinate (TPGS-750-M, CAS 1309573-60-1), cyclohexenone (purity  $\geq 95$  %), 2-methyl-2-pentanol (2M2P,  $\geq 99$  %), 3-bromophenylboronic acid ( $\geq 95$  %), deuterated dimethyl sulfoxide (DMSO- $d_6$ ,  $\geq 99.5$  atom% D), isoamyl alcohol (iAAIc,  $\geq 98$  %, FG), N-methyl-D-glucamine (meglumine,  $\geq 99$  %), tetrahydro linalool (THL,  $\geq 97$  %), sodium xylenesulfonate (SXS, impurities  $< 9.0$  % sodium sulfate), tetrapropylammonium bromide (TPA bromide,  $\geq 98$  %), sodium hydroxide (NaOH,  $\geq 98$  %), sodium carbonate ( $\text{Na}_2\text{CO}_3$ ,  $\geq 99.5$  %), and choline chloride ( $\geq 98$  %) were purchased from Sigma Aldrich (Darmstadt, Germany). Choline bromide ( $> 98$  %) and sodium 1-pentanesulfonate (SPentS,  $> 98$  %) were from TCI (Eschborn, Germany). Choline acetate (98 %) was bought from abcr (Karlsruhe, Germany). Ethanol (EtOH,  $> 99$  %), L-arginine (for biochemistry), L-histidine (for biochemistry), calcium hydroxide ( $\text{Ca}(\text{OH})_2$ , for analysis), and potassium carbonate ( $\text{K}_2\text{CO}_3$ , 99.5 – 100.5 %) were obtained from Merck (Darmstadt, Germany). Ethyl acetate (EtOAc,  $\geq 99.8$  %) was from Fisher Scientific (Schwerte, Germany). Dichloromethane ( $\geq 99.8$  %) was bought from Honeywell (Offenbach, Germany). t-Butanol (tBuOH,  $\geq 99$  %, for synthesis) was delivered by Carl Roth (Karlsruhe, Germany). All chemicals were used without further purification. Millipore water was used with a resistivity of 18 M $\Omega$  cm.

### 3.2.2 Methods

#### 3.2.2.1 Ternary phase diagram

Phase diagrams were recorded according to the method of Dekker *et al.*<sup>24</sup>, as described in Chapter 2.2.2.1.

#### 3.2.2.2 Dynamic light scattering

Dynamic light scattering (DLS) was performed as described in Chapter 1.2.2.5.

### 3.2.2.3 Critical point

To determine the critical point in a ternary phase diagram, 6 g of ternary mixtures within the miscibility gap close to the phase boundary were prepared and mixed vigorously with a Vortex. Afterward, the samples were centrifuged at 10'000 rpm (10'397 g) at  $25 \pm 0.1$  °C for 30 min (Sigma 1-18KS centrifuge, Osterode am Harz, Germany). The critical point was allocated in approximation to sample compositions yielding a 50:50 (v/v) ratio of the two phases after centrifugation.

### 3.2.2.4 General reaction procedure

A 5 mL snap cap vial was loaded with a magnetic stir bar, 418 mg 3-bromophenylboronic acid (2 equiv.), 288 mg  $K_2CO_3$  (2 equiv.), 24 mg  $[Rh(OH)(1,5-cod)]_2$  (0.05 equiv.), and 3 mL solvent. The reference solvent consisted of 2 % (w/w) TPGS-750-M in water. Besides, surfactant-free solvents were used, which are specified in the corresponding chapters. The mixtures were degassed with nitrogen for 90 s under stirring at 400 rpm. 101  $\mu$ L cyclohexenone (100 mg, 1 equiv.) was added to the solution, which was then again degassed for 90 s. The samples were sealed with parafilm and shaken briefly by hand or Vortex. Then, the reaction mixtures were stirred for 1 h at 750 rpm. In some samples, the  $K_2CO_3$  was replaced by 45 mg L-arginine (0.12 equiv.).

After 1 h, the mixtures were transferred in centrifuge tubes and centrifuged at 4'000 rpm (1790 g) for 180 s. Then, the reaction product was extracted 3 times with 3 mL EtOAc as described in Chapter 2.2.2.4. For some samples, for which phase separation occurred after centrifugation, the separated phases were examined individually in another series. For this reason, the upper and the lower phase were taken directly by means of a syringe prior to the addition of EtOAc. The brownish liquid was directly studied by NMR measurements. The upper phase was filtered using a PTFE filter (0.2  $\mu$ m pore size), reduced under vacuum (compare Chapter 2.2.2.4) and finally measured by NMR.

### 3.2.2.5 NMR measurements

NMR measurements were performed for product identification and quantification, as described in Chapter 2.5.1.3.

### 3.2.2.6 Mass spectrometry

The GC-MS method reported in Chapter 2.5.1.4 was applied for additional product identification.

### **3.2.2.7 pH measurements**

An Avantor pH glass electrode 211 from VMR (Darmstadt, Germany) was used to measure the pH of different bases dissolved in water and ternary mixtures at room temperature. The solutions were stirred at 800 rpm.

### 3.3 Results and discussion

#### 3.3.1 Alcohols as hydrotrope

In order to study the impact of different aqueous solvents on a 1,4-addition reaction, the cross-coupling between 3-bromophenylboronic acid and cyclohexenone is chosen as a model reaction (see Figure 3 - 4). The micellar solution consisting of 2 % (w/w) TPGS-750-M in water serves as the reference system. Under the conditions shown in Figure 3 - 4, a yield of  $100 \pm 7 \%$  is obtained using the reference system. The product is identified qualitatively and quantitatively by means of  $^1\text{H}$ -,  $^{13}\text{C}$ -, and HSQC-dept-NMR measurements (see Figure S.3 - 1 - Figure S.3 - 4 in the Supporting Information). Apparent yields slightly above 100 % can occur and correspond to the error in the analytical method (see Chapter 3.5).

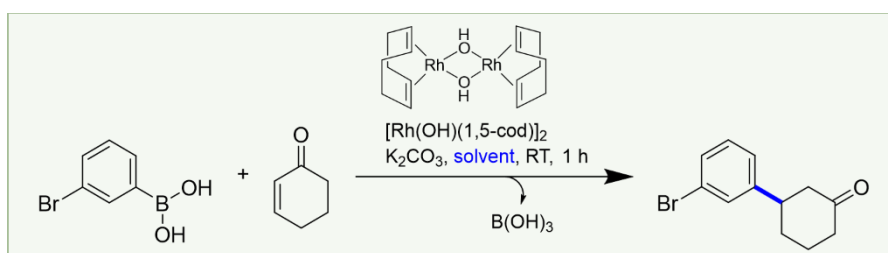


Figure 3 - 4: Rh-catalyzed 1,4-addition of 3-bromophenylboronic acid to cyclohexenone.

Ternary systems are investigated to locate the compositions where the most pronounced mesoscopic structuring occurs. For this purpose, dynamic light scattering (DLS) experiments are applied, assuming that a high correlation intercept at small lag times as well as large lag times of the correlation function indicate pronounced inhomogeneities.<sup>25</sup> In a first attempt, the most simple volatile alcohol ethanol (EtOH) is used as the hydrotrope in combination with water (W) and the oil tetrahydro linalool (THL) (see Figure 3 - 5). THL is a plant-based fragrance and chosen for its greenness and stability.<sup>26,27</sup> Due to the hydrophobic oil, a rather high amount of 45 % (w/w) EtOH is required to close the miscibility gap (see Figure 3 - 5(a)). The DLS experiment indicates slight structuring in mixture a (see Figure 3 - 5(b)). Mixture b, which is close to the critical point (asterisk), depicts the highest correlation intercept. Upon further addition of THL, the signal decreases until it disappears completely in mixture f. Accordingly, it can be expected that the molecules in mixtures e and f are statistically distributed without any tendency towards aggregation, while a more or less pronounced aggregation occurs in the other mixtures. Additional DLS measurements in the system W/EtOH/THL in comparison with the ternary system of W/EtOH/linalool are provided in the Supporting Information (see Figure S.3 - 5; Figure S.3 - 6).

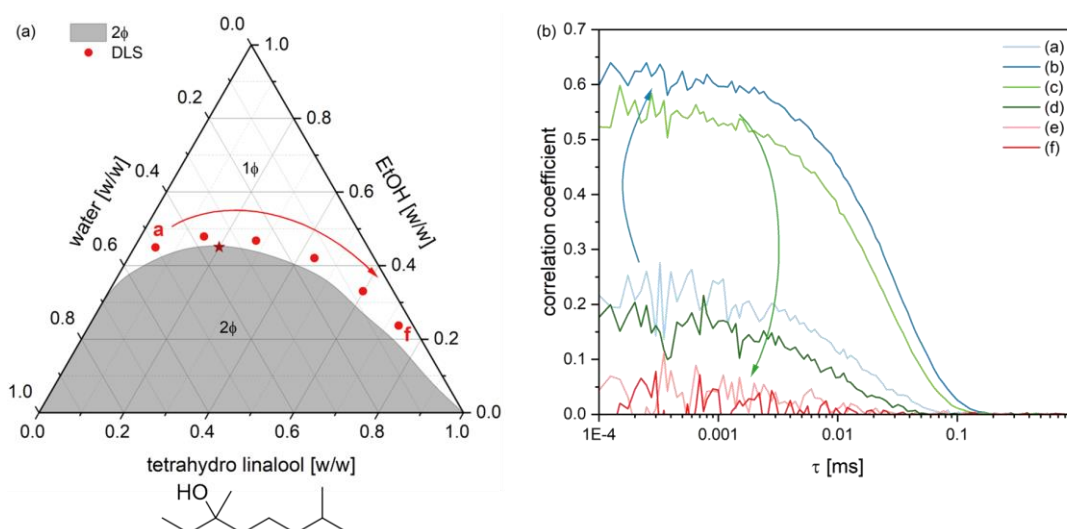


Figure 3 - 5: (a) Ternary phase diagram of water, EtOH, and THL at 25 °C. The gray shaded area represents the miscibility gap ( $2\Phi$ ), which is separated from the monophasic area ( $1\Phi$ ). The dots show the compositions measured by means of DLS. The red asterisk locates the critical point. (b) Corresponding correlation functions obtained by DLS measurements at 25 °C.

The reaction is carried out in the ternary mixture W/EtOH/THL in a ratio of 37/48/15 (w/w/w) (mixture b), which is referred to as surfactant-free microemulsion (SFME) based on the DLS experiments. However, no product can be detected in this mixture (see Figure S.3 - 7 in the Supporting Information). Regarding the proposed reaction mechanism (see Figure 3 - 6), it is supposed that the EtOH interacts with the catalyst in step (1). Thus, the catalyst would no longer be available to react with the arylboronic acid. In addition, interactions between bor(on)ic acids and alcohols are reported in the literature. Shibayama *et al.* observed interactions of boric acid with polyhydroxy alcohols but not with the monohydroxy alcohol isopropanol.<sup>28</sup> Peters reported interactions of bor(on)ic acids with the hydroxy groups of sugar molecules.<sup>29</sup> It is known that EtOH can form chains, which could allow the molecule to undergo similar interactions with boronic acids as polyhydroxy alcohols.<sup>31-33</sup>

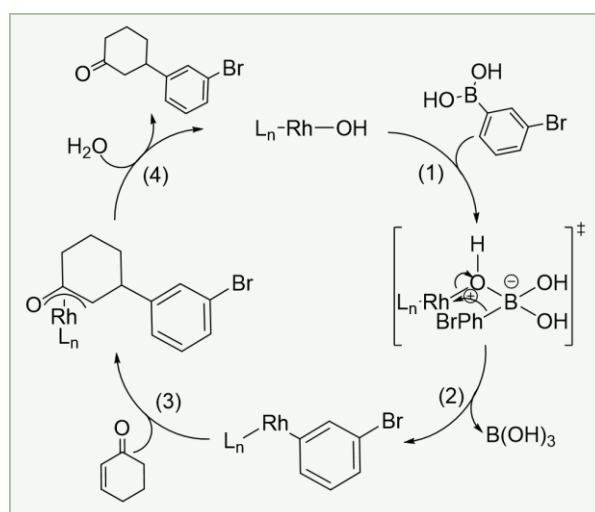


Figure 3 - 6: Proposed reaction mechanism for the Rh-catalyzed 1,4-addition of 3-bromophenylboronic acid to cyclohexenone, based on the cited literature.<sup>30</sup>

Furthermore, the large amounts of EtOH may also force interactions with both the catalyst and the arylboronic acid. Consequently, the hydrotrope is replaced by the tertiary alcohol t-butanol (tBuOH) (see Figure 3 - 7). The idea is to prevent interactions with the reactants by steric hinderance. As expected, the miscibility gap is even higher with up to 55 % (w/w) tBuOH. In general, a high miscibility gap may not necessarily pose a problem in later applications. A high proportion of a volatile component could even facilitate recycling afterward. The alcohol tBuOH is known to pre-aggregate in water (see Figure 3 - 7(c,d), mixture 1).<sup>25</sup> Accordingly, 3 % (w/w) of the oil is sufficient to induce mesoscopic inhomogeneities, resulting in a pronounced DLS signal (mixture a, 2). Mixture a (W/tBuOH/THL 51/46/3 (w/w/w)) and mixture 2 (W/tBuOH/THL 50/47/3 (w/w/w)) are referred to as SFMEs.

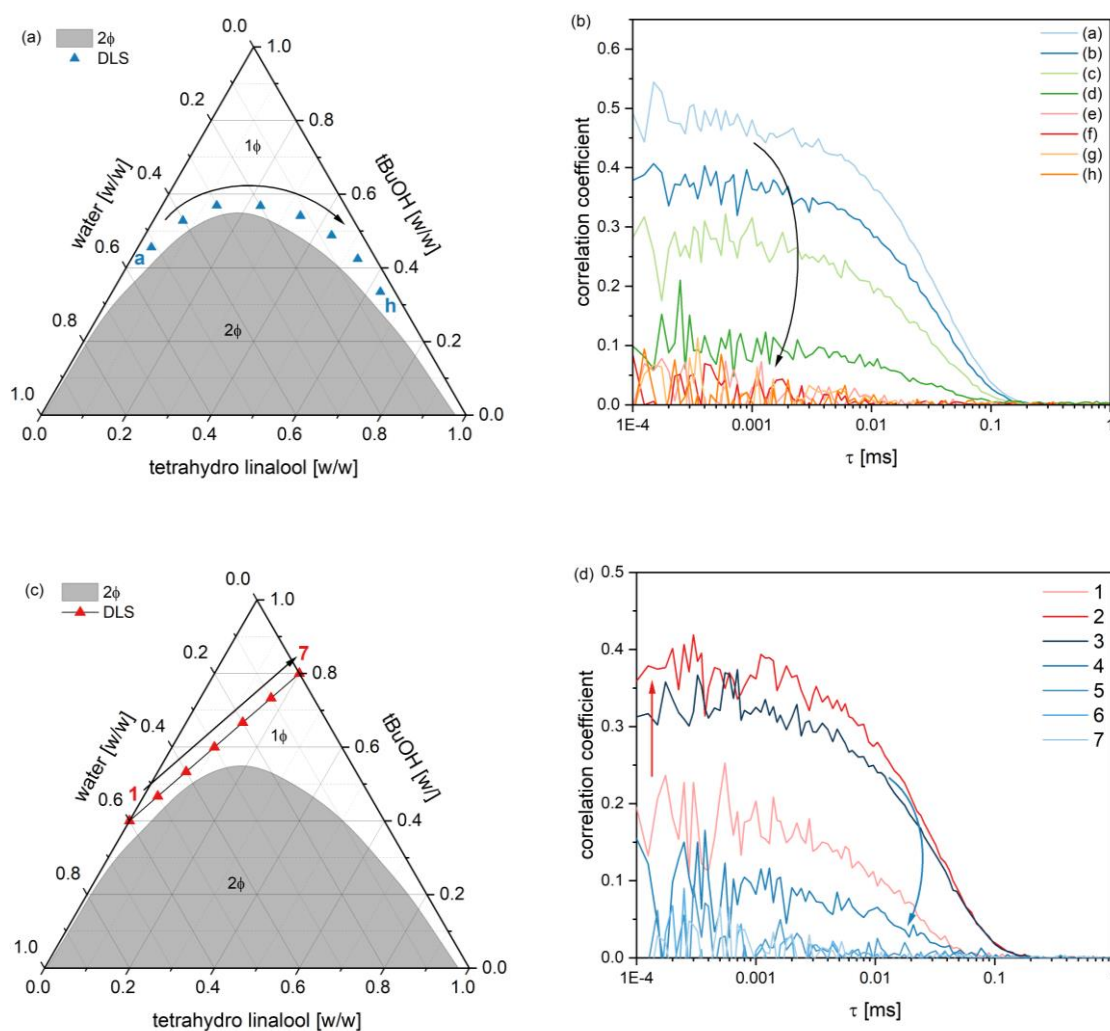


Figure 3 - 7: (a,c) Ternary phase diagram of water, tBuOH, and THL at 25 °C. The gray shaded area represents the miscibility gap (2 $\Phi$ ), which is separated from the monophasic area (1 $\Phi$ ). The triangles show the compositions measured by means of DLS. (b,d) Corresponding correlation functions obtained by DLS measurements at 25 °C.

The difference in their correlation intercepts may arise from the slight difference in composition. However, it is more likely that the difference results from deviations in the toluene

bath of the DLS device, which slightly evaporates over time. Generally, a series was always measured on the same day to ensure comparable results, at least within an experimental series. With a further increasing amount of THL, the correlation intercept decreases. The reaction is performed in the solution W/tBuOH/THL in a ratio of 40/54/6 (w/w/w) (mixture b, 3) to provide sufficient hydrophobic molecular surface. A yield of  $31 \pm 2 \%$  is detected (see Figure S.3 - 8 - Figure S.3 - 12 in the Supporting Information). Thus, the sterically hindered hydroxy group does not prevent interactions between the catalyst and the arylboronic acid, unlike EtOH. However, the yield is still far from that obtained in the micellar solution, in which complete conversion is observed.

The applied  $K_2CO_3$  leads to liquid-liquid phase separation. In order to study a possible effect of the solvent structuring, several basic compounds are studied with regard to their solubility and salting-out effect in the SFME (see Table S.3 - 1 in the Supporting Information). Among the bases studied, only tetrapropylammonium bromide can be dissolved in the amounts applied for the reaction without inducing phase separation of the solvent. Due to the toxicity of quaternary ammonium salts<sup>34,35</sup>, the amino acid L-arginine (see Figure 3 - 8(a)) is preferably used for reactions, which can only be dissolved to 1/8 of the molar amount of  $K_2CO_3$  originally applied. The pH of the reaction solvent is hence reduced from 12.3 to 11.4 when replacing  $K_2CO_3$  by L-arginine. The reaction yield in W/tBuOH/THL (40/54/6 (w/w/w)) is reduced from  $31 \pm 2 \%$  to  $11 \pm 1 \%$ . Despite the low yield, L-arginine is applied in the W/tBuOH/THL system to maintain a stable solution. Thus, the reaction is performed in the mixtures shown in Figure 3 - 7(c), which exhibit different extend of solvent structuring.

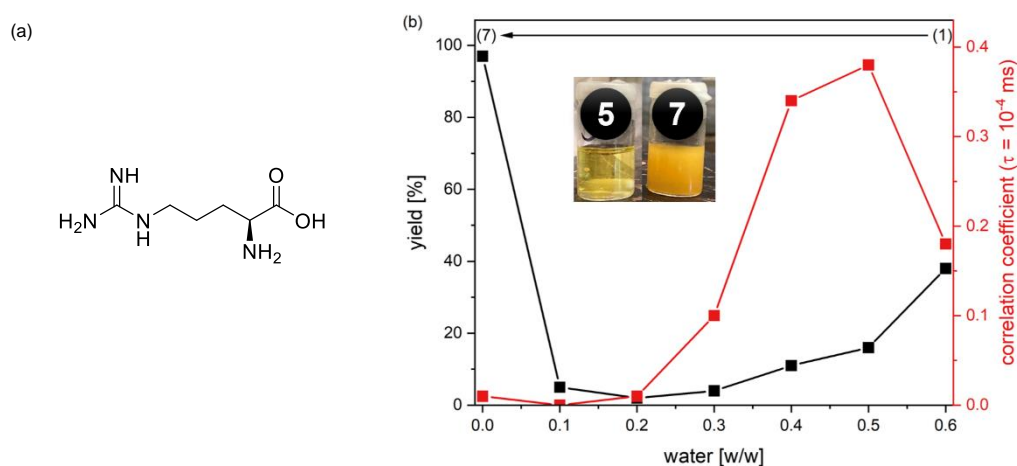


Figure 3 - 8: (a) Molecular structure of L-arginine. (b) Reaction yield of the 1,4-addition of 3-bromophenylboronic acid to cyclohexenone in the different mixtures of W/tBuOH/THL shown in Figure 3 - 7(c) using L-arginine instead of  $K_2CO_3$  as the base. The second y-axis represent the correlation intercept obtained from the DLS measurements shown in Figure 3 - 7(d) as an indicator for solvent structuring. The photographs are taken of samples 5 and 7 at the beginning of the reaction.

Figure 3 - 8(b) depicts the reaction yield obtained in these mixtures as a function of the water content. The best result is obtained with 97 % in the binary water-free mixture of

tBuOH and THL (80/20 (w/w)), although the molar amount of base is reduced. Water is required in step (4) of the reaction mechanism (see Figure 3 - 6). It is assumed that the binary mixture contains enough water *impurities* to enable this step. For this reason, the binary mixture, as well as the *pure* compounds, should be studied regarding their water content. The addition of 10 % (w/w) water to the binary mixture significantly decreased the reaction yield to 5 %. Then adding more water increases the yield again. It is conspicuous that mixtures 1 – 6 differ significantly in their macroscopic appearance from the “water-free” mixture 7 (see also Figure S.3 - 13 in the Supporting Information). In mixtures 1 – 6, the starting material dissolves completely with stirring, resulting in a yellow, transparent solution. In contrast, part of the starting material remains undissolved in the, thus, turbid and orange-colored mixture 7. Hence, the great solubilization power of the ternary mixtures has an unfavorable effect on the reaction. It can be assumed that the complete solubilization of the arylboronic acid enhances competitive protodeboronation reactions. Besides, there is no correlation between solvent structuring and the reaction outcome. Indeed, the arylboronic acid is also only partially dissolved in the micellar reference. Therefore, the high yield in the reference system appears not to be a consequence of the introduced interface rather than of the limited solubilization of the arylboronic acid, which prevents the substrate from undergoing competitive reactions before interacting with the catalyst.

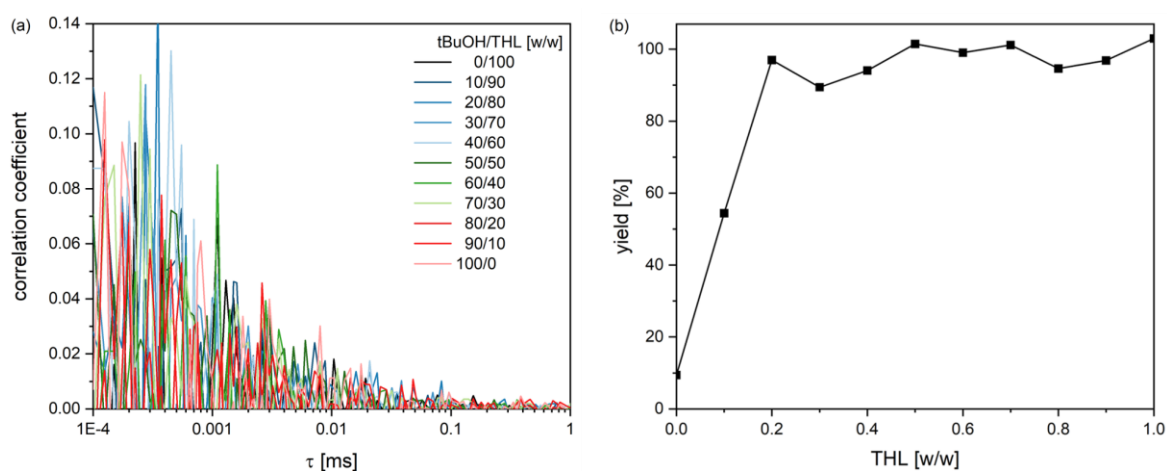


Figure 3 – 9: (a) Correlation functions of mixtures of tBuOH and THL obtained by DLS measurements at 25 °C. An overlay of all functions is shown as only noise is detected for all mixtures. In addition, the plots are provided in the Supplementary Information in a less dense representation (see Figure S.3 - 14). (b) Reaction yield obtained in mixtures of tBuOH and THL, using L-arginine as the base.

Based on the excellent yield in the binary mixture of tBuOH/THL (80/20 (w/w)), the reaction is carried out in the entire binary system with varying compositions (see Figure 3 – 9). As expected, the DLS experiments provide no signal other than noise. The molecules can thus be considered statistically distributed. In mixtures with a THL amount of 20 – 100 % (w/w), yields between 89 – 100 % are achieved. As pure tBuOH is approached, the yield drops to 9 %. At this point, a well-founded explanation cannot be given for this observation. A

possible explanation could be the water content. THL is delivered with a purity  $\geq 97\%$ , while tBuOH is declared with  $\geq 99\%$ . Accordingly, the water content may also be lower in tBuOH, which could limit the reaction mechanism in its last step (see Figure 3 - 6). Further experiments are necessary to confirm this. Moreover, the oil in the ternary mixtures (W/tBuOH/THL) is replaced by iso-amylalcohol (iAAlc) and 2-methyl-2-pentanol (2M2P). However, the change in the oil worsens the result (see Figure S.3 - 15 – Figure S.3 - 17).

### 3.3.2 Salts as hydrotrope

As shown above, the solubility and stability of the reactants are much more decisive parameters than solvent structuring. In order to still be able to carry out the reaction in surfactant-free aqueous solvents, the volatile hydrotropes are replaced by salt hydrotropes. Figure 3 – 10 depicts the phase diagram using sodium xylenesulfonate (SXS) or sodium 1-pentane-sulfonate (SPentS) as a hydrotrope.

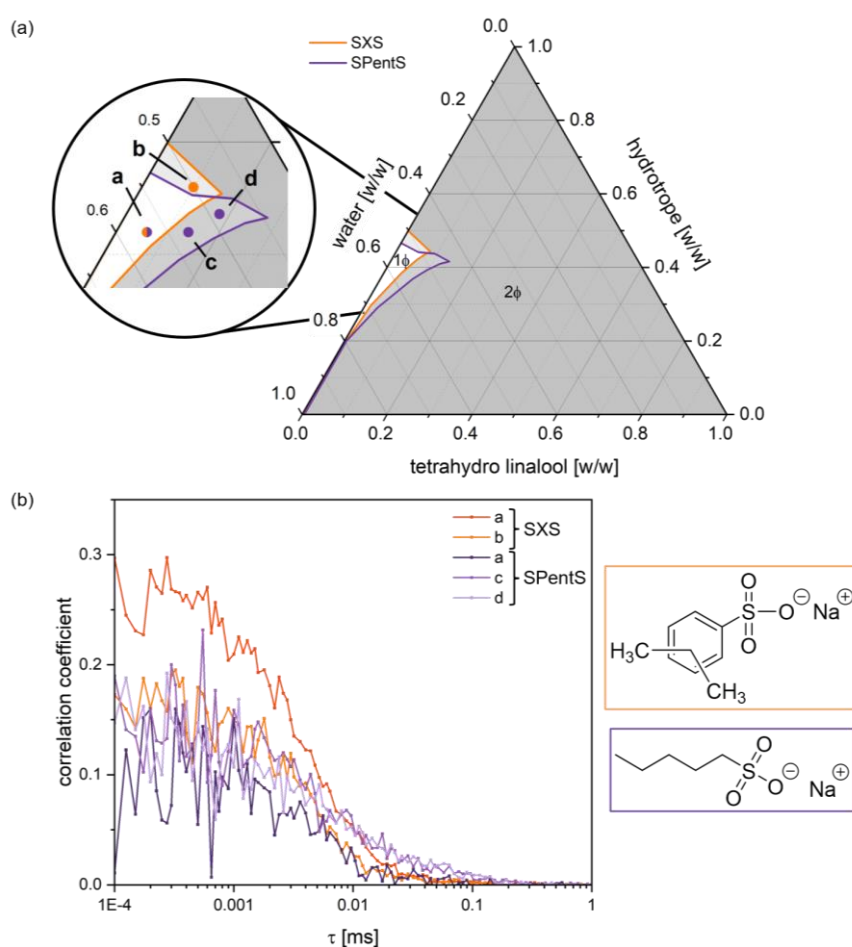


Figure 3 – 10: (a) Ternary phase diagram of water and THL with the hydrotrope SXS (orange) or SPentS (purple) at 25 °C. The gray shaded area represents the miscibility gap (2Φ), which is separated from the monophasic area (1Φ). The dots show the compositions measured by means of DLS. (b) Corresponding molecular structures and correlation functions obtained by DLS measurements at 25 °C. The compositions of the W/salt/THL mixtures are the following: a = 57/40/3, b = 50/45/5, c = 53/40/7, d = 49/42/9 (w/w/w).

The monophasic areas are rather limited in size. The DLS experiments in solutions within this area show correlation functions of minor intensity. It is therefore assumed that there is only a slight aggregation of the molecules. Nevertheless, the mixtures are referred to as SFME to distinguish them from solutions without distinct correlation function. SWAXS measurements need to prove the presence of mesoscopic structuring. The 3-bromophenylboronic acid is only partially dissolved in the SFMEs containing a salt hydrotrope. In the presence of cyclohexenone, both reactants become completely soluble. Hence, interactions between cyclohexenone and the arylboronic acid are expected to occur even in the absence of the catalyst. Moreover, the addition of  $K_2CO_3$  does not result in phase separation. It has to be noted that in order to achieve complete solubility, some samples need to be stirred vigorously using a Vortex. For this reason, the arylboronic acid is not always completely dissolved after 1 h of reaction, although the applied amount should be soluble. A summary of the solubility behavior of all reactants in the different surfactant-free solvents is provided in the Supporting Information (see Table S.3 - 3, Figure S.3 - 18). A yield of  $45 \pm 3 \%$  is obtained in W/SXS/THL (57/40/3 (w/w/w)) and  $100 \pm 7 \%$  in W/SPentS/THL (53/40/7 (w/w/w)) (see Figure S.3 - 19 - Figure S.3 - 22 in the Supporting Information). Both systems achieve better results than the SFMEs with the volatile alcohols. The SFME with SPentS even allows full conversion of the cyclohexenone, as is the case with the reference system, despite the complete (or at least better) solubilization of the arylboronic acid. Thus, the salts seem to have a stabilizing effect on the dissolved arylboronic acid. In that way, competitive protodeboronation is less favored, allowing the dissolved arylboronic acid to remain active for the 1,4-addition reaction. The sulfonate group of the salts likely interacts with the arylboronic acid via hydrogen bonding. The SXS, as an aromatic compound, can additionally interact via  $\pi$ -stacking. The interactions between SXS and 3-bromophenylboronic acid may, thus, be even too strong. Too much stabilization of the reactant would result in a decrease in its activity for the 1,4-addition, as well, and could explain the reduced yield with SXS compared to SPentS.

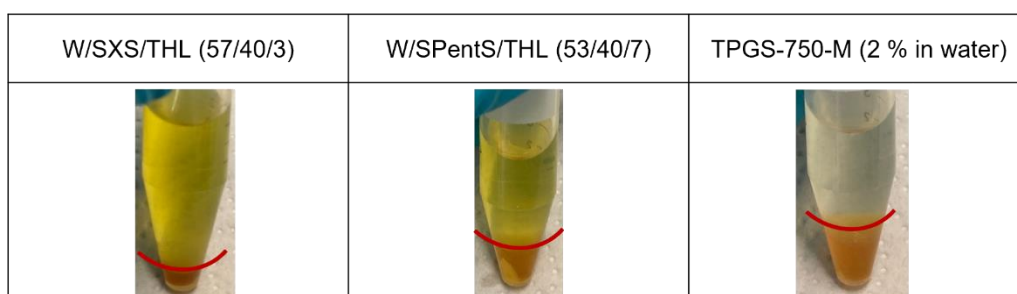


Figure 3– 11: Photographs of the centrifuged mixtures after the reaction. A second brownish liquid phase occurs that is rich in the product. All proportions are by mass (w/w).

Centrifugation of the mixtures after the reaction reveals the appearance of a second liquid phase using W/SXS/THL, W/SPentS/THL, and the surfactant solution as reaction solvent

(see brownish phase in Figure 3 – 11). NMR measurements prove an enrichment of the product in the new brownish phase (see Figure S.3 - 23 - Figure S.3 - 25 in the Supporting Information). In the case of W/SPentS/THL, even the entire product seems to be dissolved in the new phase. The solvent system, thus, extracts the product itself, which is of great advantage for later product isolation. In addition, the remaining solvent can be easily recycled for further reactions.

### 3.3.3 Hydrotrope mixtures

The small monophasic area in the ternary system of W/SPentS/THL prevents further studies on the influence of solvent structuring on the reaction. For this reason, pseudo-ternary systems with hydrotrope mixtures of tBuOH and SPentS are investigated (see Figure 3 - 12). Adding SPentS to tBuOH decreases the liquid-liquid miscibility gap. Due to the limited water solubility of SPentS, an increasing solid-liquid phase appears concurrently. Overall, the monophasic areas ( $1\Phi$ ) of the pseudo-ternary mixtures are significantly increased compared to that of W/SPentS/THL.

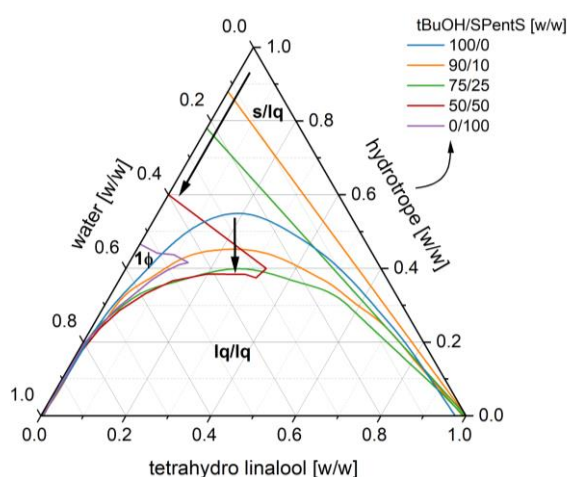


Figure 3 - 12: (Pseudo-)ternary phase diagram of water and THL with either tBuOH or SPentS or mixtures of both at 25 °C. The system includes 3 different areas: a monophasic area ( $1\Phi$ ) and biphasic areas with 2 liquid phases (lq/lq) or a solid and a liquid phase (s/lq) in equilibrium. The s/lq phase boundaries are extrapolated from the solubility limit of the hydrotrope mixtures in water and, therefore, only an approximation.

The hydrotrope mixture (HM) of tBuOH/SPentS in a ratio of 75/25 (w/w) is chosen for their great monophasic area and the rather small lq/lq miscibility gap. The DLS measurements indicate the presence of significant mesoscopic structuring, which should be most pronounced in W/HM/THL 14/35/51 (w/w/w) (see Figure 3 - 13, mixture h). Both the correlation intercept and the lag time of the correlation function are quite large. Accordingly, the mixture is referred to as SFME. The great correlation intercept of mixture d does not match the general trend. The mixture may be considered for SWAXS measurements and as a potentially interesting reaction solvent. Overall, the pseudo-ternary system allows one to perform the reaction in mixtures with different extent of structuring. In a first attempt, the reaction is

carried out in the mixture with most pronounced structuring (mixture h). Under these conditions, a yield of  $48 \pm 3 \%$  is achieved (see Figure S.3 - 27 in the Supporting Information). In addition, the same ratio is applied as in the mixture with pure SPentS as hydrotrope, but with the HM (W/HM/THL 53/40/7 (w/w/w)). During the reaction, the viscosity of the solution increases significantly, and the product is only detected in  $16 \pm 1 \%$  yield (see Figure S.3 - 28 in the Supporting Information). The decrease in the yield is attributed to the reduced amount of the stabilizing SPentS and, in the latter case, also to insufficient stirring. The yields obtained in all aqueous solvents studied are summarized in Table 3 - 1.

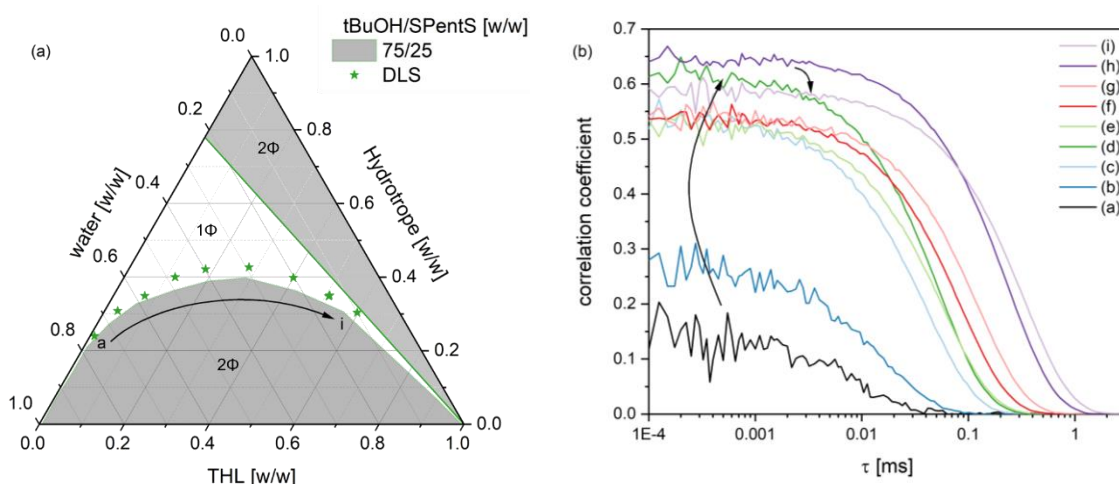


Figure 3 - 13: (a) Ternary phase diagram of water, and THL with a hydrotrope mixture of tBuOH/SPentS (75/25 (w/w)) at 25 °C. The gray area represents the biphasic areas ( $2\Phi$ ), which are separated from the monophasic area ( $1\Phi$ ). The stars show the compositions measured by means of DLS. (b) Corresponding correlation functions obtained by DLS measurements at 25 °C. DLS studies on the pseudo-ternary system with a hydrotrope mixture of tBuOH/SPentS 50/50 (w/w) can be found in the Supporting Information (see Figure S.3 - 26).

Table 3 - 1: The reaction yield obtained by 1,4-addition of 3-bromophenylboronic acid to cyclohexenone in different aqueous solvents. (\*The base  $K_2CO_3$  is replaced by arginine). SPentS\_tBuOH defines a mixture of SPentS/tBuOH with a ratio of 27/75 (w/w). All reactions are performed once. <sup>a</sup>The given error refers to the error determined for the method (for details see Figure S.3 - 1 in the Supporting Information).

solvent	(w/w/w)	yield <sup>a</sup> [%]
<b>TPGS-750-M</b>	reference	<b>100 ± 7</b>
W/EtOH/THL	37/48/15	0
W/tBuOH/iAAIc	60/36/4	0
W/tBuOH/2M2P	60/35/5	13 ± 1
W/tBuOH/THL*	40/54/6	11 ± 1
W/tBuOH/THL	40/54/6	31 ± 2
W/SXS/THL	57/40/3	45 ± 3
<b>W/SPentS/THL</b>	53/40/7	<b>100 ± 7</b>
W/SPentS_tBuOH/THL	53/40/7	16 ± 1
W/SPentS_tBuOH/THL	14/35/51	48 ± 1

### 3.4 Conclusion and outlook

A study of the 1,4-addition of 3-bromophenylboronic acid to cyclohexenone in different surfactant-free microemulsions (SFMEs) was reported. A yield of  $100 \pm 7\%$  is obtained in the micellar reference system of the surfactant TPGS-750-M. Starting in a surfactant-free system of water (W), ethanol (EtOH), and tetrahydro linalool (THL), disruptive interactions between the primary alcohol and the catalyst or the arylboronic acid appear to prevent a successful reaction. The sterically hindered alcohol t-butanol (tBuOH) enabled the reaction in  $31 \pm 2\%$  yield. The great solubilization power of the ternary mixtures seems to favor the competitive protodeboronation reaction, which limits the yield in this system. Furthermore, no correlation between the solvent structuring and the reaction outcome are observed.

Hence, the alcohol hydrotrope is replaced by the salts sodium xylenesulfonate (SXS) and sodium 1-pentanesulfonate (SPentS). In that way, the yield can be increased to  $45 \pm 3\%$  in a SFME of W/SXS/THL and to  $100 \pm 7\%$  in W/SPentS/THL. The excess of the arylboronic acid (2 equiv.) and the amount of the catalyst (5 mol%) can be kept low, despite complete solubilization of the arylboronic acid. The salts, therefore, appear to stabilize the dissolved substrate by hydrogen bonding interactions. Additional  $\pi$ -stacking between SXS and 3-bromophenylboronic acid may stabilize the substrate too much so that the substrate also might lose reactivity towards the 1,4-addition. The interactions between the salts and the substrate need to be verified experimentally, *e.g.*, by NMR measurements. In the SFMEs containing a salt hydrotrope as well as in the micellar reference system, a second liquid phase occurs during the reaction, which is rich in the product. These systems, therefore, facilitate product isolation and solvent recycling afterward.

Since the monophasic area in the ternary systems of W/salt/THL only comprises a limited range of compositions, the salt SPentS is mixed with tBuOH. The monophasic area in the pseudo-ternary phase diagram is thus increased significantly. Furthermore, very pronounced structuring is detected in the presence of the hydrotrope mixture (HM). The pseudo-ternary mixture with the HM allows a broader variation of the solvent composition due to a larger monophasic area. In the previously studied solutions containing the HM, the yield is limited to  $48 \pm 3\%$ . This is attributed to an insufficient amount of SPentS, which seems crucial for the stabilization of the arylboronic acid. Hence, different ratios of tBuOH/SPentS as well as different compositions of W/HM/THL should be considered. This should also provide further information on whether the solvent structuring can have an impact on the 1,4-addition. The previous results presented in this chapter exclude an

influence. Rather the solubilization and the stabilization of the reactants are the key parameters. This confirms the observations in Chapter 2. Accordingly, the micellar reference system does not enable the reaction in water at low substrate excess due to the introduced interface. In fact, the limited solubility of the arylboronic acid in this system allows for maintaining an active substrate. As we successfully stabilized the dissolved substrate, our systems may allow further reduction of the excess amount. This should be considered in the next studies. Besides, the binary system W/SPentS should be taken into account. Since the presence of an interface is not expected to be decisive, the addition of the stabilizing salt may be sufficient for a successful reaction process in water. Furthermore, the SFMEs W/salt/THL should be studied with regard to universal suitability. For this reason, other substrates should be cross-coupled via 1,4-addition.

### 3.5 Supporting information

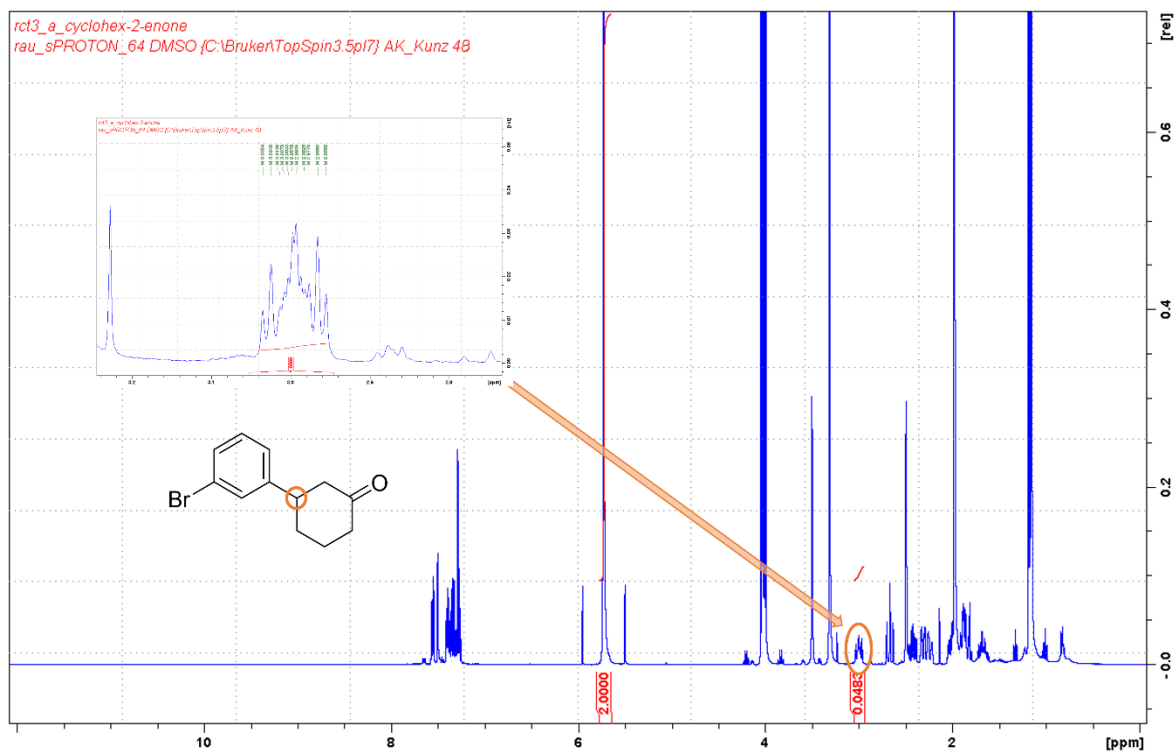


Figure S.3 - 1: <sup>1</sup>H-NMR spectrum of the crude product of the 1,4-addition in the surfactant solution (2 % (w/w) TPGS-750-M in water) dissolved in DMSO-d<sub>6</sub>.

It has to be noted at this point that in several reactions, the amount of the internal standard dichloromethane was determined by volume instead of weight. Further experiments revealed that this increases the experimental error. Therefore, the previous results only allow relative statements to be made. In the reference system, a yield of 107 % was detected. Complete conversion of the substrate was observed. Accordingly, the error of the method was determined to be 7 %. The method error is applied to measurements, that are not part of a series. In order to quantify the results more accurately, the experiments need to be repeated, and the internal standard must be weighted.

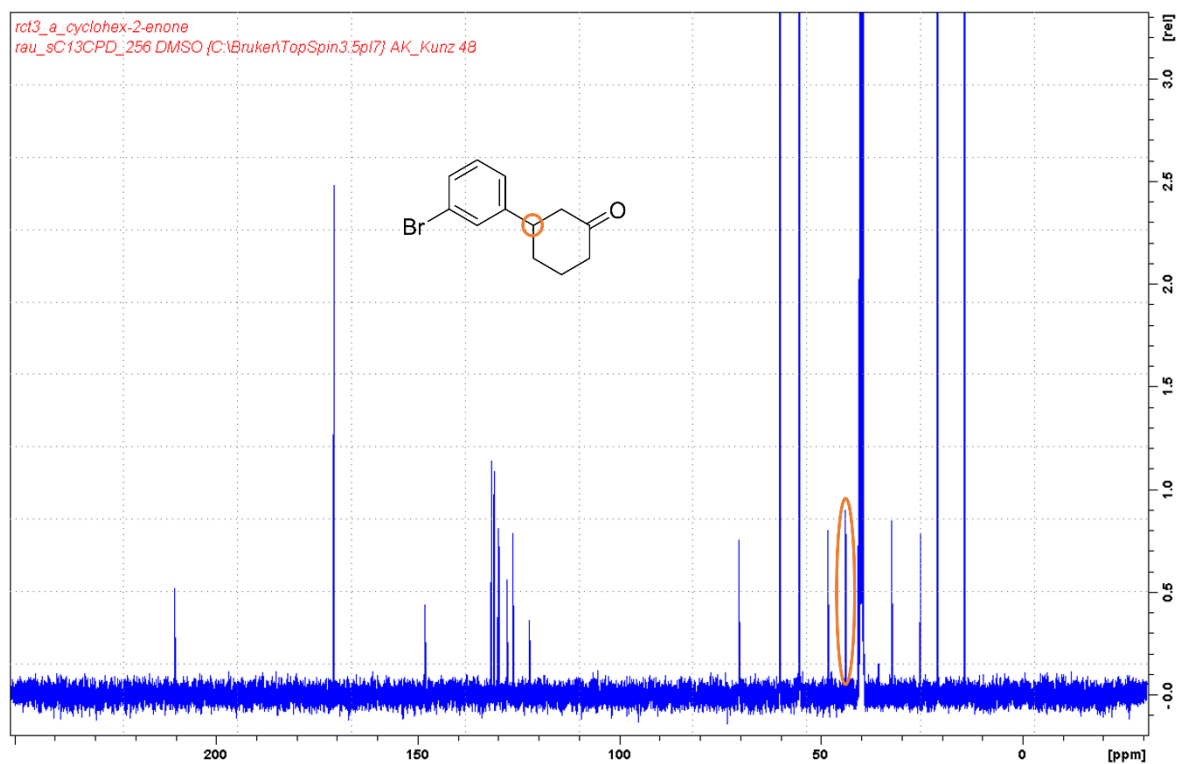


Figure S.3 - 2:  $^{13}\text{C}$ -NMR spectrum of the crude product of the 1,4-addition in the surfactant solution (2 % (w/w) TPGS-750-M in water) dissolved in  $\text{DMSO-d}_6$ .

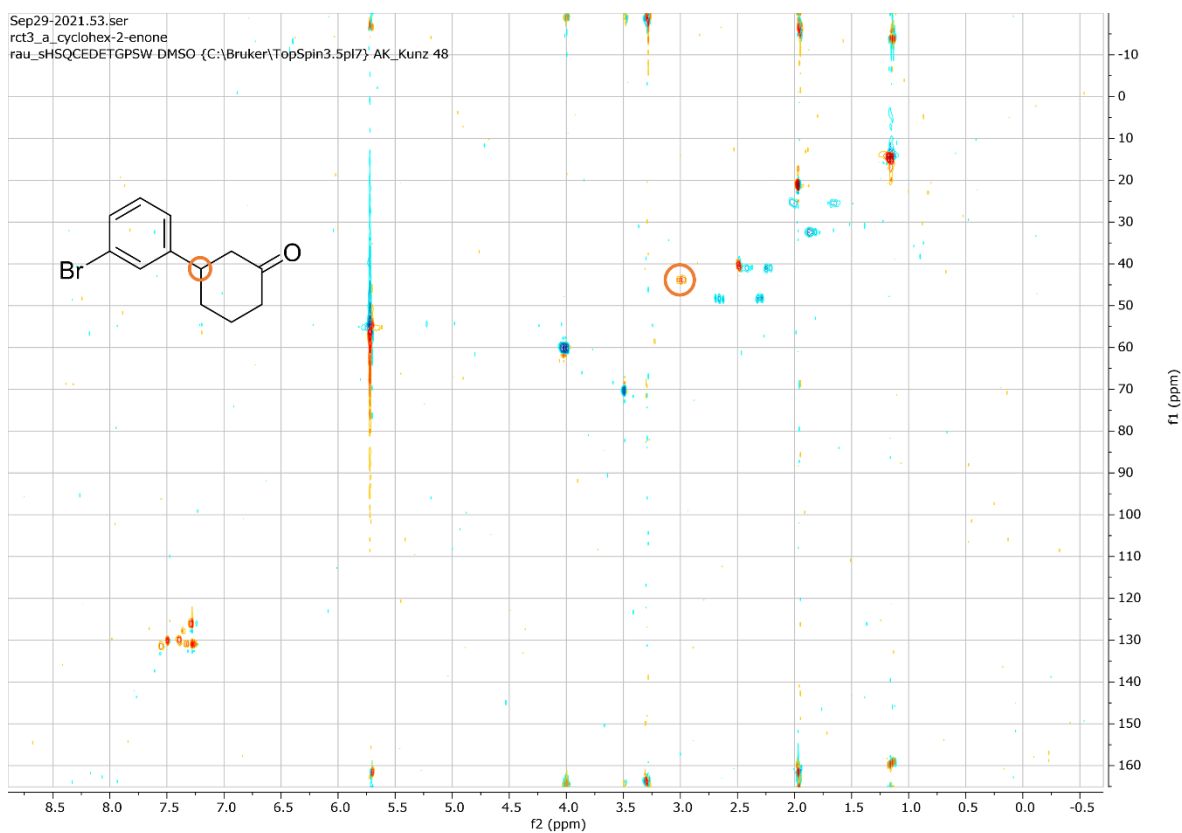


Figure S.3 - 3: HSQC-dept NMR spectrum of the crude product of the 1,4-addition in the surfactant solution dissolved in  $\text{DMSO-d}_6$ .

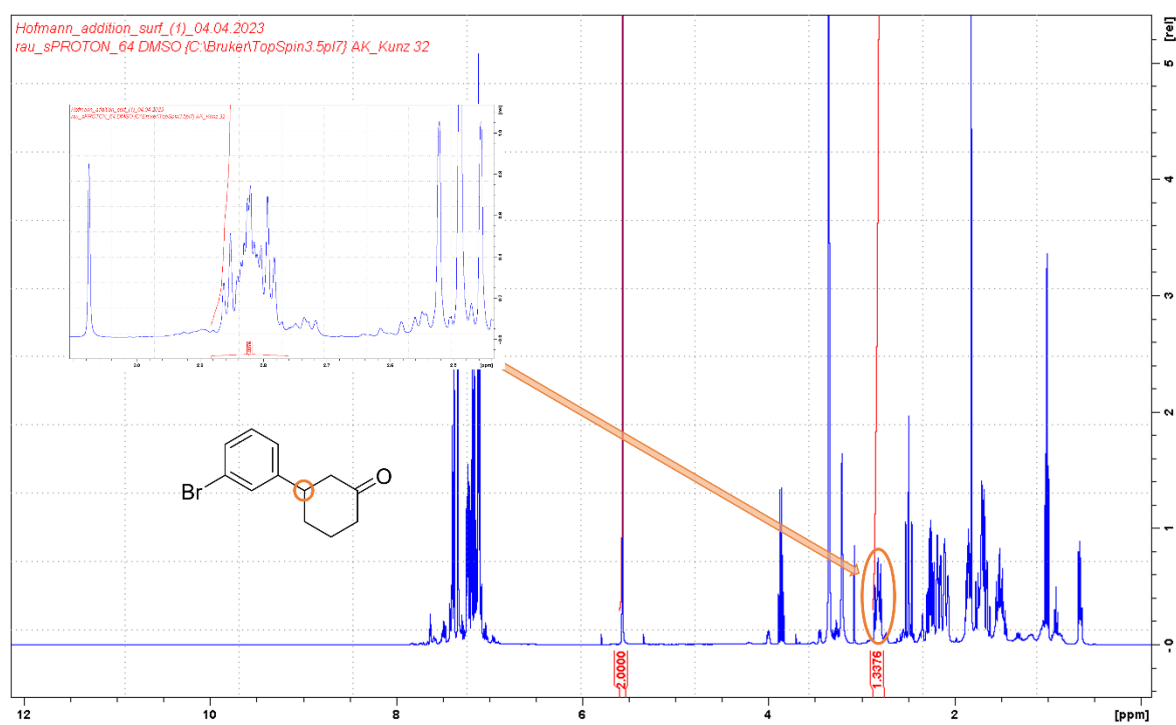


Figure S.3 - 4:  $^1\text{H}$ -NMR spectrum of the crude product of the 1,4-addition in the surfactant solution (2 % (w/w) TPGS-750-M in water) dissolved in DMSO- $d_6$ . The shown spectrum is used for product quantification.

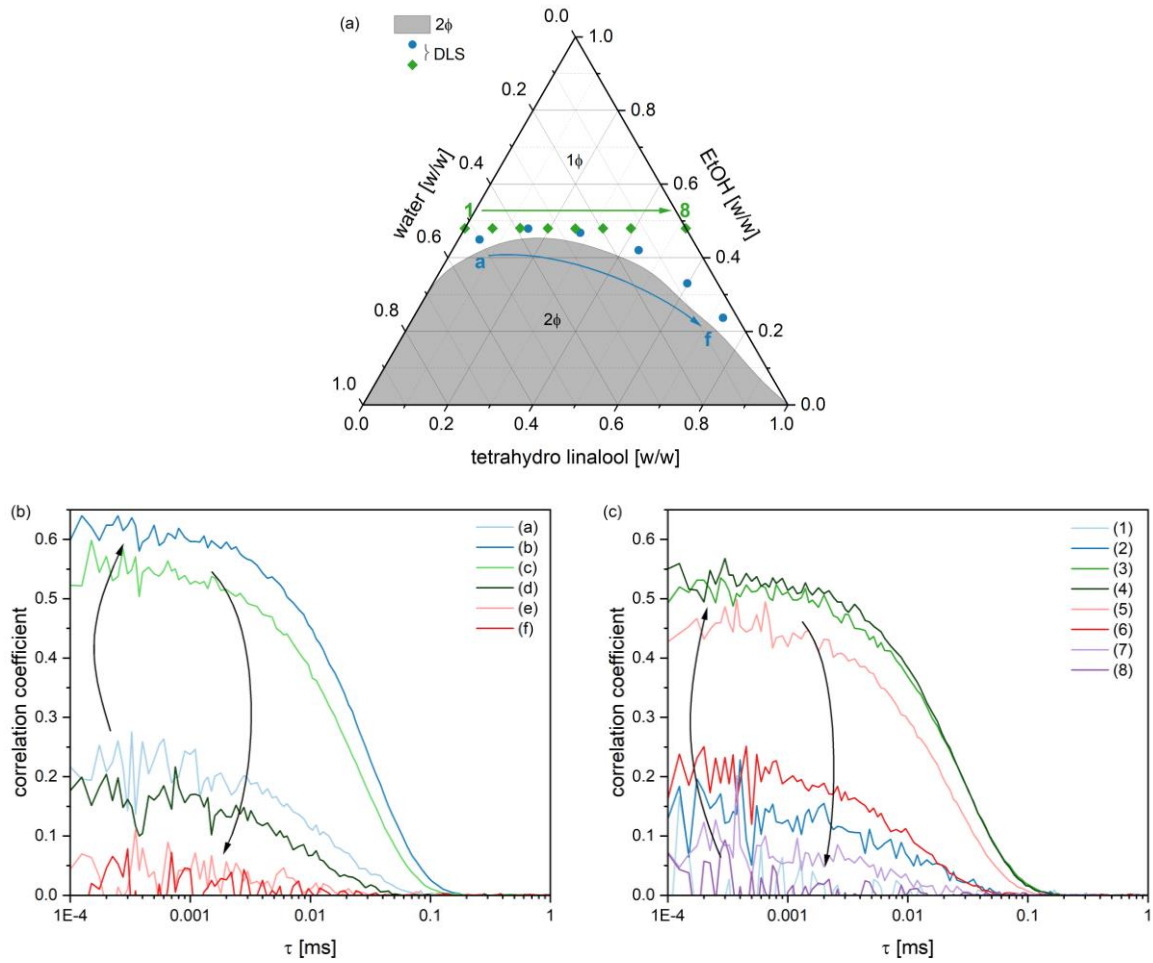


Figure S.3 - 5: (a) Ternary phase diagram of water, EtOH, and THL at 25 °C. The gray shaded area represents the miscibility gap ( $2\Phi$ ) which is separated from the monophasic area ( $1\Phi$ ). The dots and rhombs show the compositions measured by means of DLS. (b,c) Corresponding correlation functions obtained by DLS measurements at 25 °C.

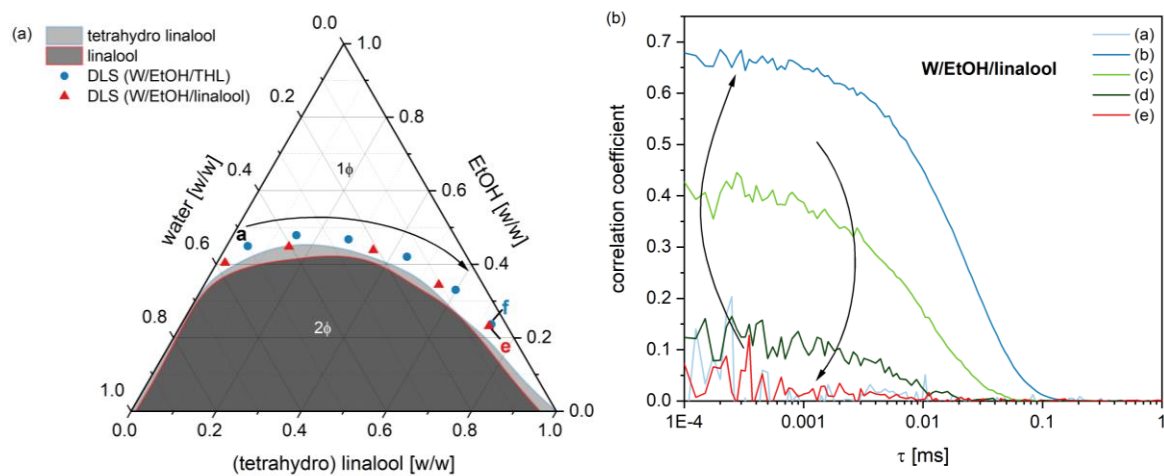


Figure S.3 - 6: (a) Ternary phase diagram of water, EtOH, and (tetrahydro) linalool at 25 °C. The gray shaded area represents the miscibility gap ( $2\Phi$ ) which is separated from the monophasic area ( $1\Phi$ ). The dots and rhombs show the compositions measured by means of DLS. (b) Corresponding correlation functions in W/EtOH/linalool mixtures obtained by DLS measurements at 25 °C.

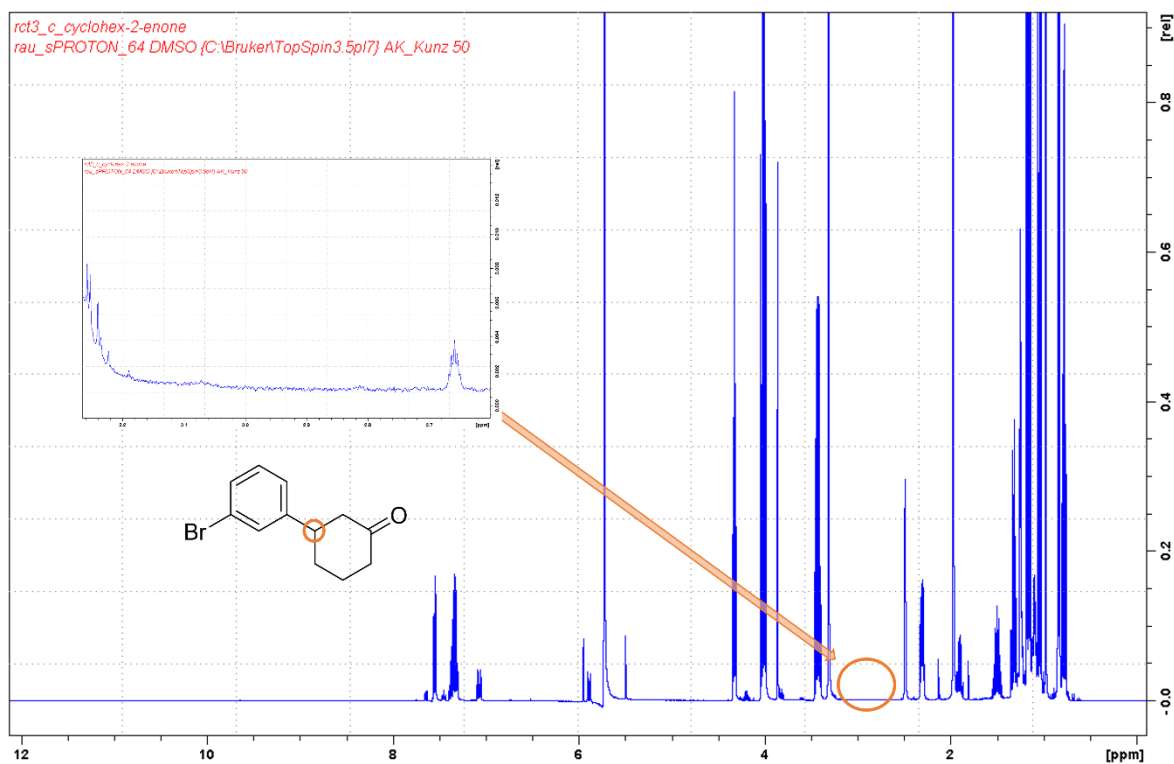


Figure S.3 - 7:  $^1\text{H-NMR}$  spectrum of the crude product of the 1,4-addition in the SFME W/EtOH/THL (37/48/15 (w/w/w)) dissolved in  $\text{DMSO-d}_6$ .

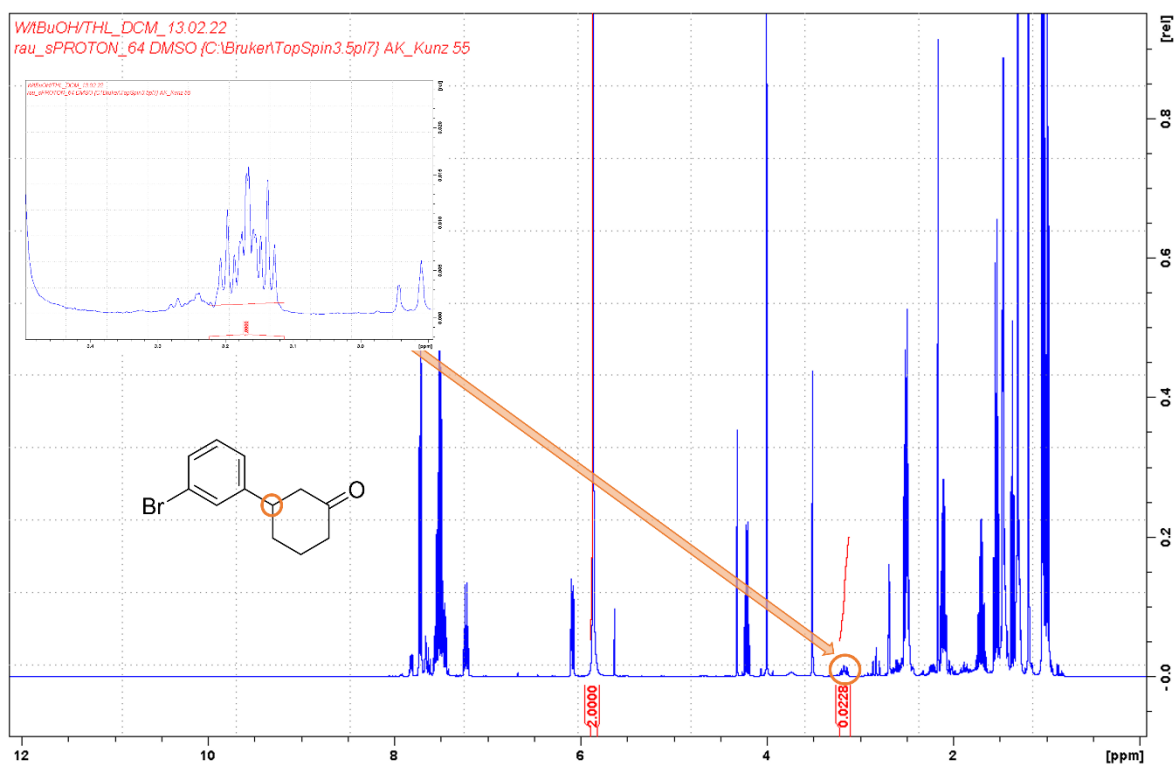
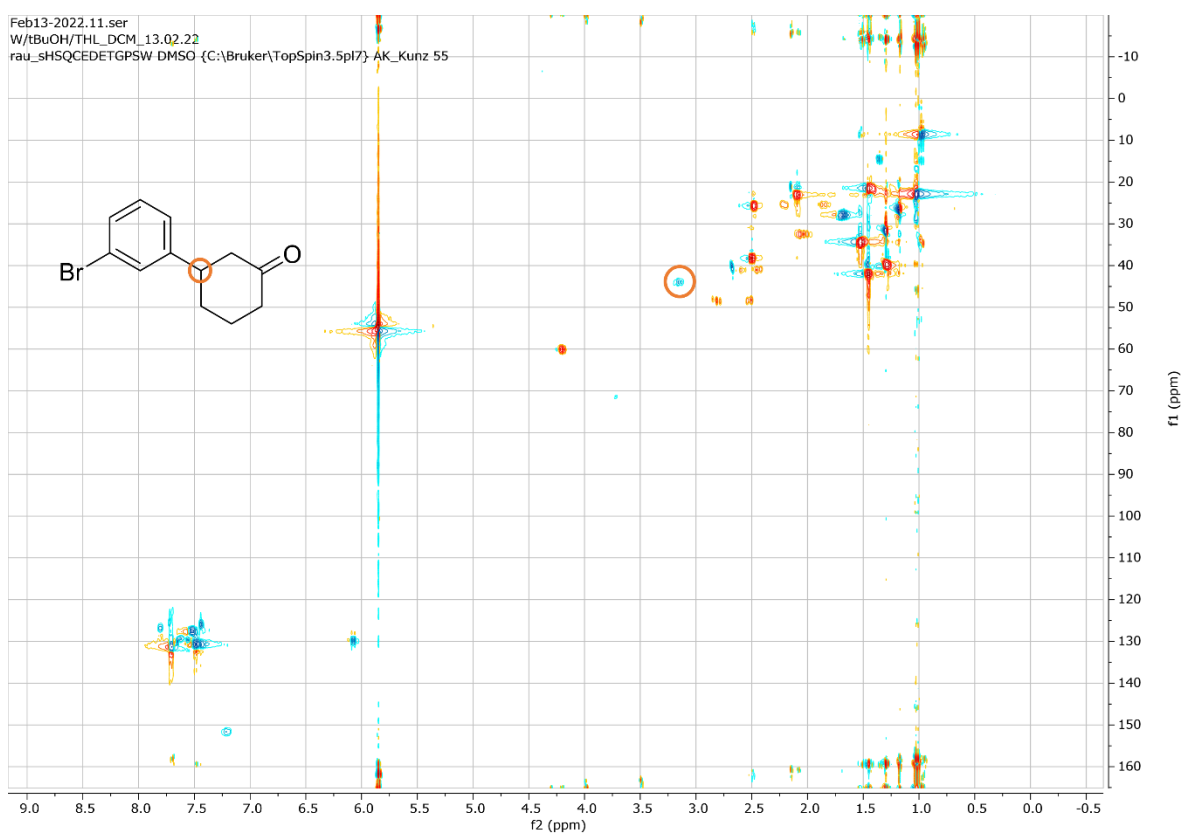
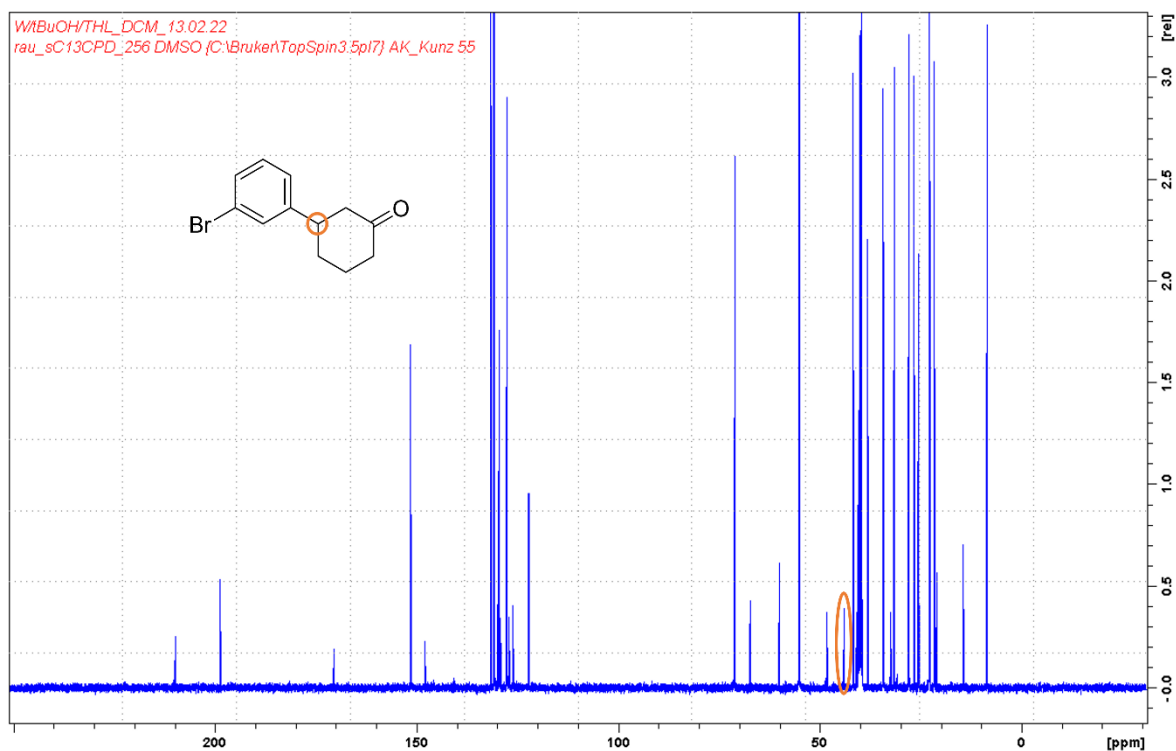


Figure S.3 - 8:  $^1\text{H-NMR}$  spectrum of the crude product of the 1,4-addition in the SFME W/tBuOH/THL (40/53/7 (w/w/w)) dissolved in  $\text{DMSO-d}_6$ .



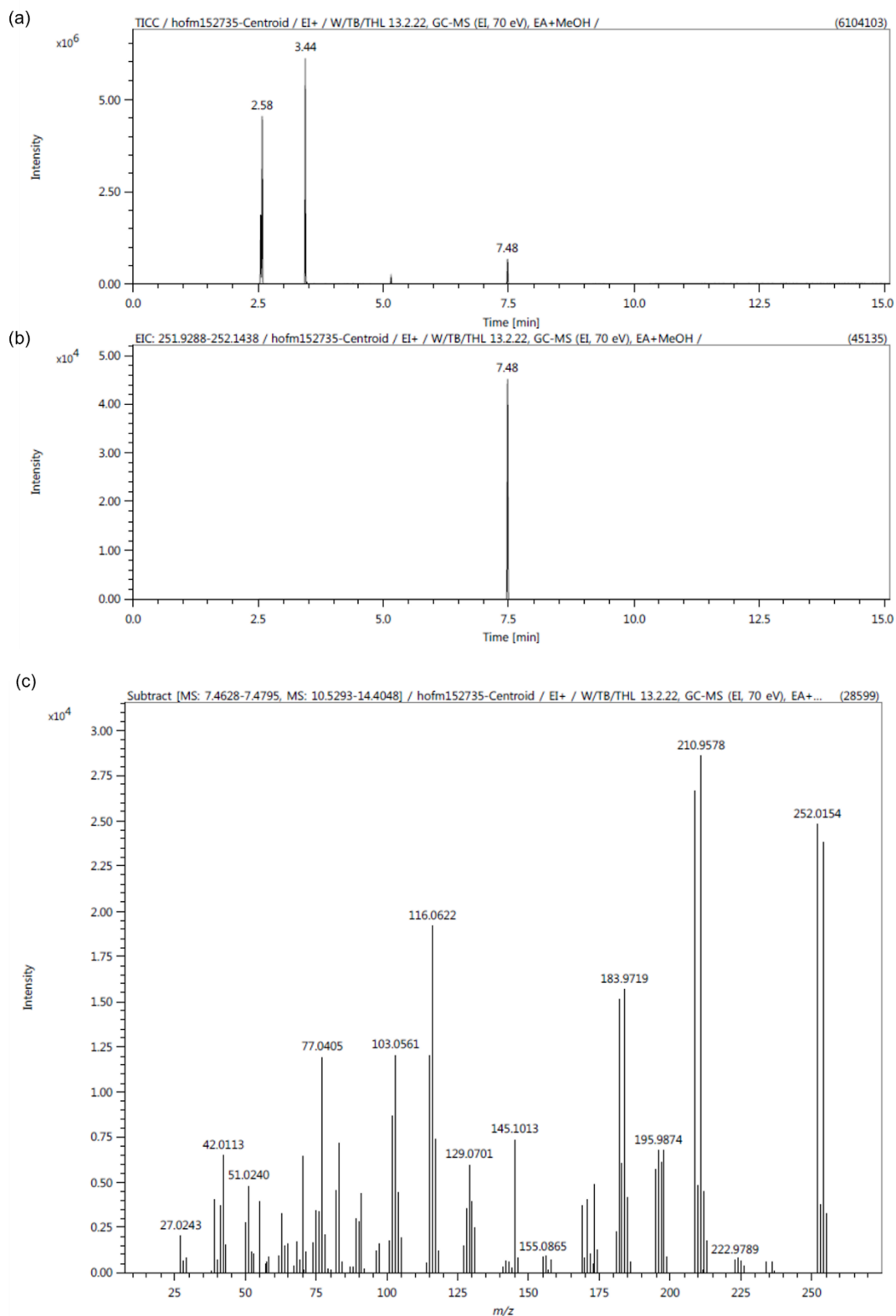


Figure S.3 - 11: MS results of the crude product of the 1,4-addition in the SFME W/tBuOH/THL (40/53/7 (w/w/w)). (a) Total ion current (TIC) chromatogram. (b,c) Extracted ion chromatogram (EIC) at a mass-to-charge ( $m/z$ ) of 252 with the corresponding mass spectrum at 7.5 min. The measurements prove the presence of 3-(3-bromophenyl) cyclohexanone with a molar mass of 253.1 g/mol.

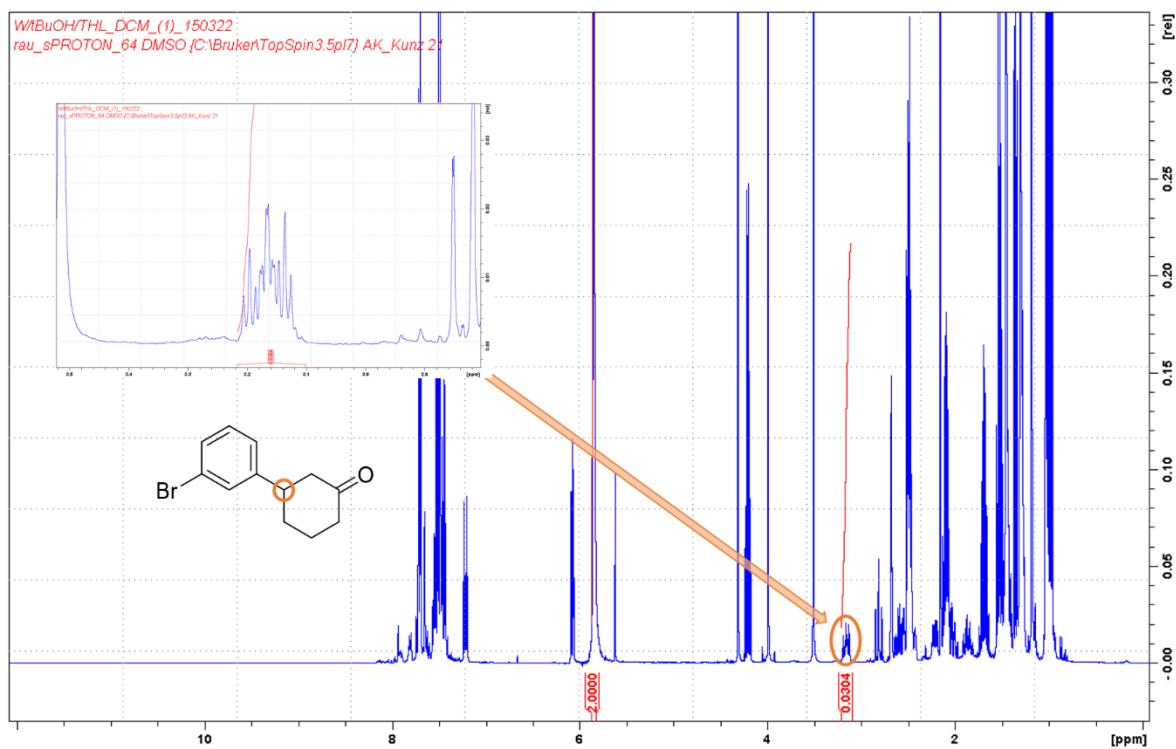


Figure S.3 - 12:  $^1\text{H-NMR}$  spectrum of the crude product of the 1,4-addition in the SFME W/tBuOH/THL (40/53/7 (w/w/w)) dissolved in DMSO- $d_6$ . The show spectrum is used for product quantification.

Table S.3 - 1: Different bases and their behavior in W/tBuOH/THL (40/54/6 (w/w/w)). In the standard reaction procedure, 0.7 M  $K_2CO_3$  are dissolved. Several basic compounds can be dissolved but induce liquid-liquid phase separation (2 $\Phi$ ) even at very reduced quantities. The best results (dissolved without phase separation, 1 $\Phi$ ) are obtained with choline bromide, tetrapropylammonium bromide, and arginine.

base	c [M]	
$K_2CO_3$	0.031	2 $\Phi$
$Ca(OH)_2$	0.019	insoluble
$Na_2CO_3$	0.017	2 $\Phi$
NaOH	0.081	2 $\Phi$
choline chloride	0.72	2 $\Phi$
choline acetate	0.89	2 $\Phi$
<b>choline bromide</b>	0.18	<b>1<math>\Phi</math></b>
	0.21	2 $\Phi$
<b>tetrapropylammonium (TPA) bromide</b>	0.83	<b>1<math>\Phi</math></b>
histidine	0.047	insoluble
<b>arginine</b>	0.087	<b>1<math>\Phi</math></b>
	0.13	2 $\Phi$

Table S.3 - 2: pH of different bases dissolved in different solvents at room temperature. The concentration is adjusted to ensure complete solubilization of the base in the absence of liquid-liquid phase separation of the solvent. <sup>(1)</sup> $K_2CO_3$  is added in the same amount as used in the reaction. This leads to phase separation in W/tBuOH/THL.

solvent	base	c [M]	pH
W/tBuOH/THL	-	-	7.0
	<b><math>K_2CO_3</math><sup>(1)</sup></b>	0.69	<b>12.3</b>
	<b>arginine</b>	0.086	<b>11.4</b>
	TPA bromide	0.71	8.5
	choline bromide	0.18	6.7
water	arginine	0.086	10.7
	TPA bromide	0.69	9.2
	choline bromide	0.18	6.3
W/SXS/THL	-	-	5.9
	<b><math>K_2CO_3</math></b>	0.69	<b>11.8</b>
W/SPentS/THL	-	-	5.9
	<b><math>K_2CO_3</math></b>	0.69	<b>11.9</b>

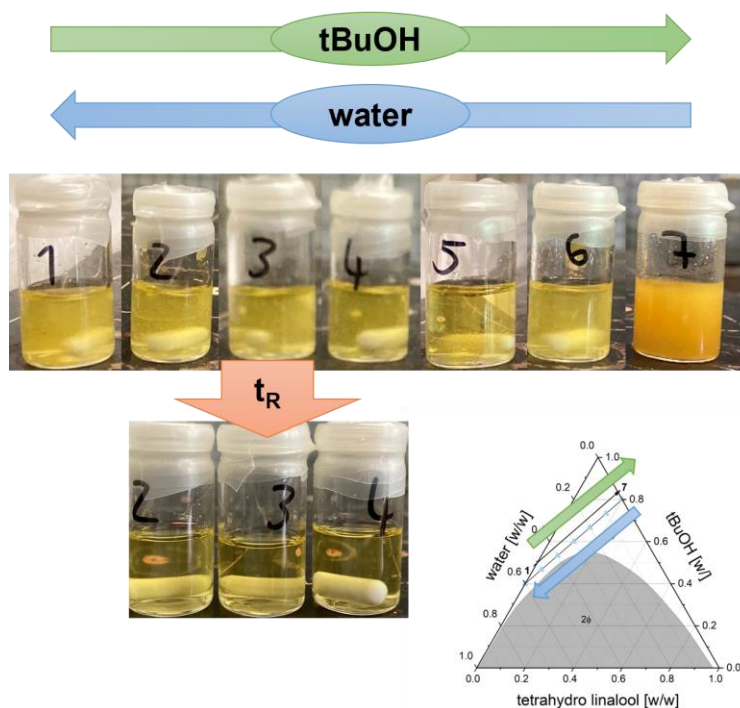


Figure S.3 - 13: Photographs of the reaction mixtures with different compositions of W/tBuOH/THL, using L-arginine as the base, at the beginning of the reaction and after 1 h stirring ( $t_R$ ). The different compositions are shown in the ternary phase diagram and in Figure 3 - 7(c). The samples containing water (1 – 6) show small amounts of undissolved reactants that dissolve with stirring. Then, the reactions are completely transparent and yellow in color. In the water-free sample (7), however, significant amounts of the starting material remain undissolved, and the sample appears orange and turbid.

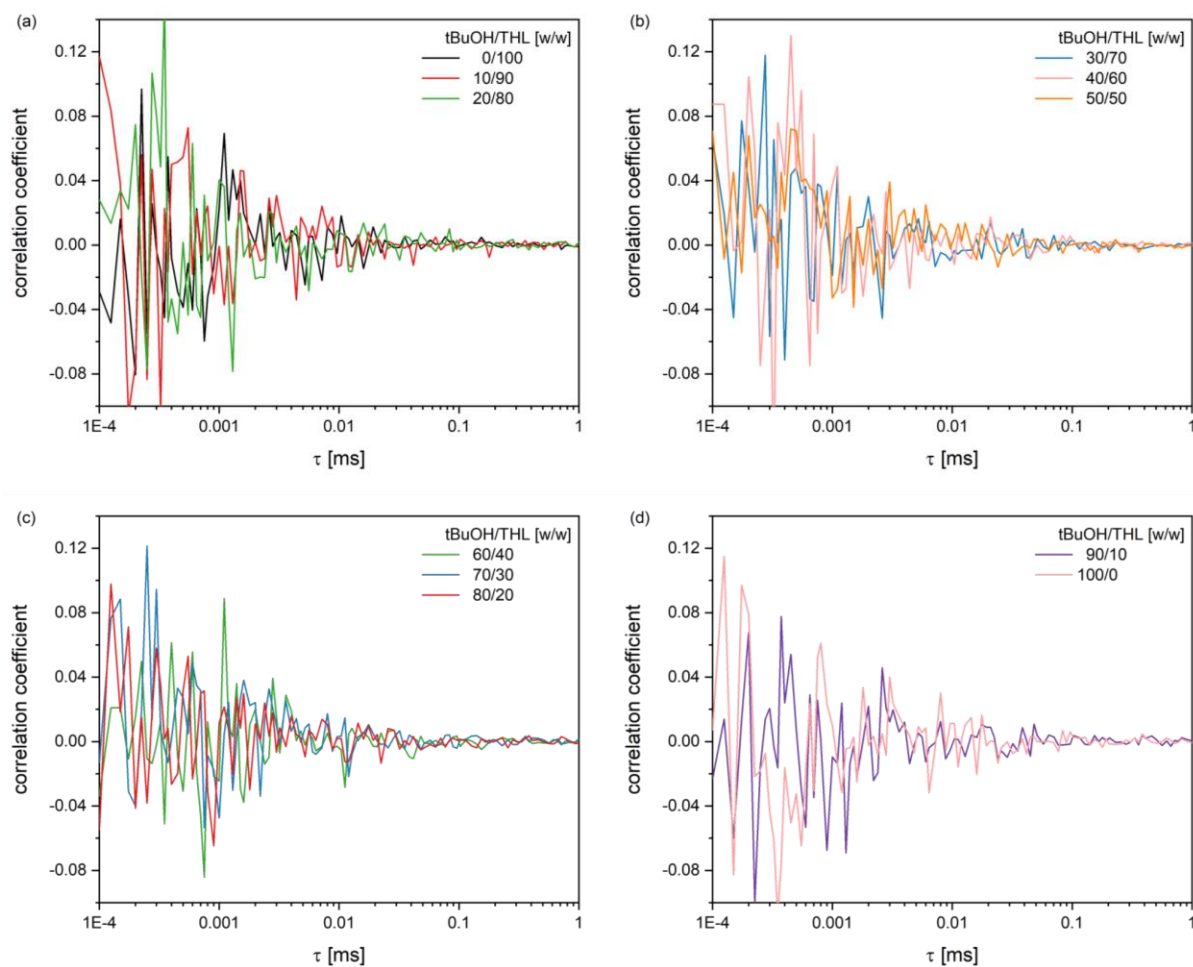


Figure S.3 - 14: Correlation functions of mixtures of tBuOH and THL obtained by DLS measurements at 25 °C.

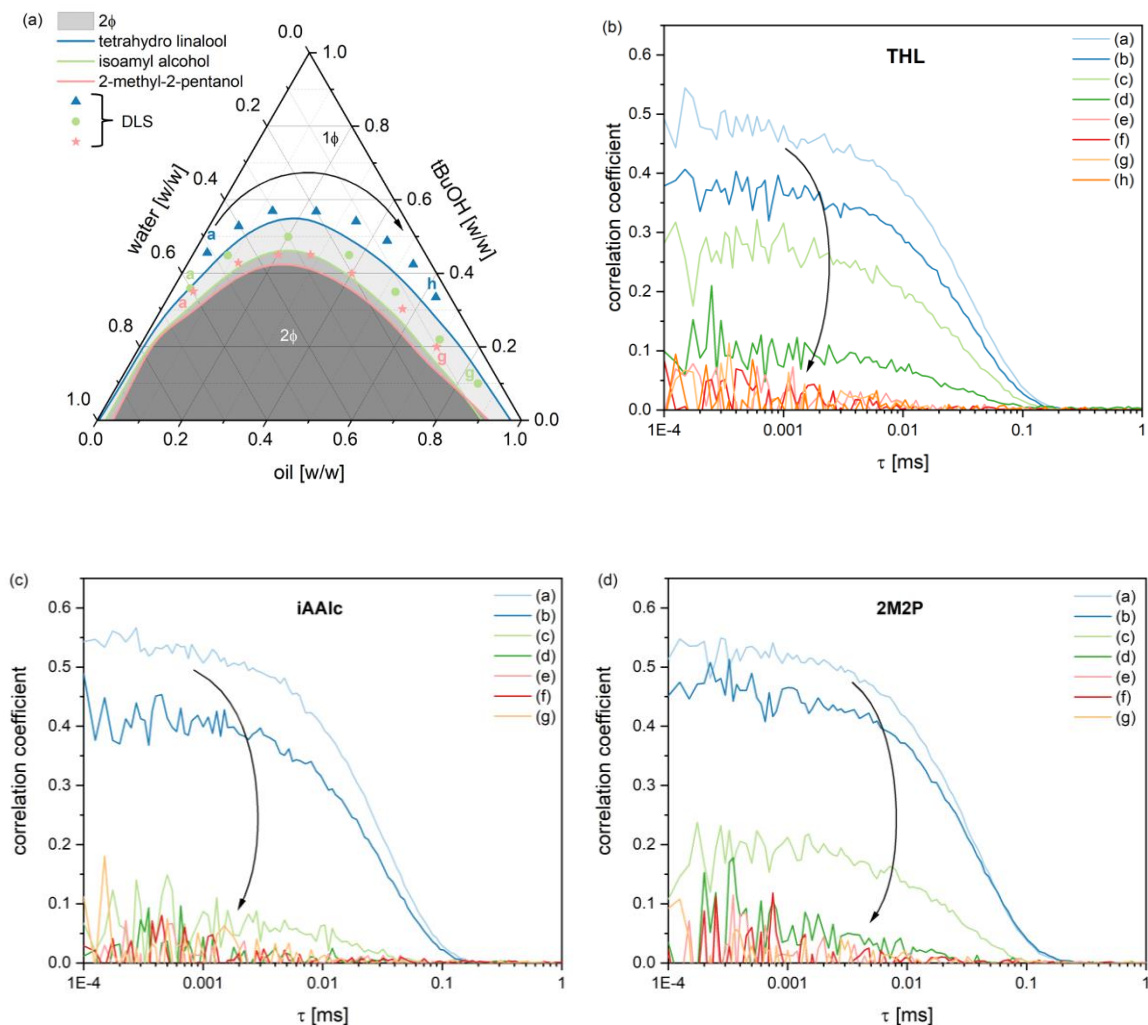


Figure S.3 - 15: (a) Ternary phase diagram of water, tBuOH, and different oils, including THL (blue curve), isoamyl alcohol (iAAlc, green curve), and 2-methyl-2-pentanol (2M2P, rose curve) at 25 °C. The gray area represents the miscibility gap (2 $\Phi$ ), which is separated from the monophasic area (1 $\Phi$ ). The colored symbols show the compositions measured by means of DLS. (b-d) Corresponding correlation functions obtained by DLS measurements at 25 °C. The more hydrophilic oils lower the miscibility gap and, hence, increase the solvent structuring. The changes in the DLS signals are, however, of minor intensity. The first reactions (see Figure S.3 - 16, Figure S.3 - 17) are performed under the standard conditions using  $K_2CO_3$ , which results in liquid-liquid phase separation. Accordingly, the effect of structuring cannot be taken into account. Overall, the results in the W/tBuOH/THL system reveal that the structuring seems to have no impact on the reaction. For this reason, the changes in the oil are not considered further.

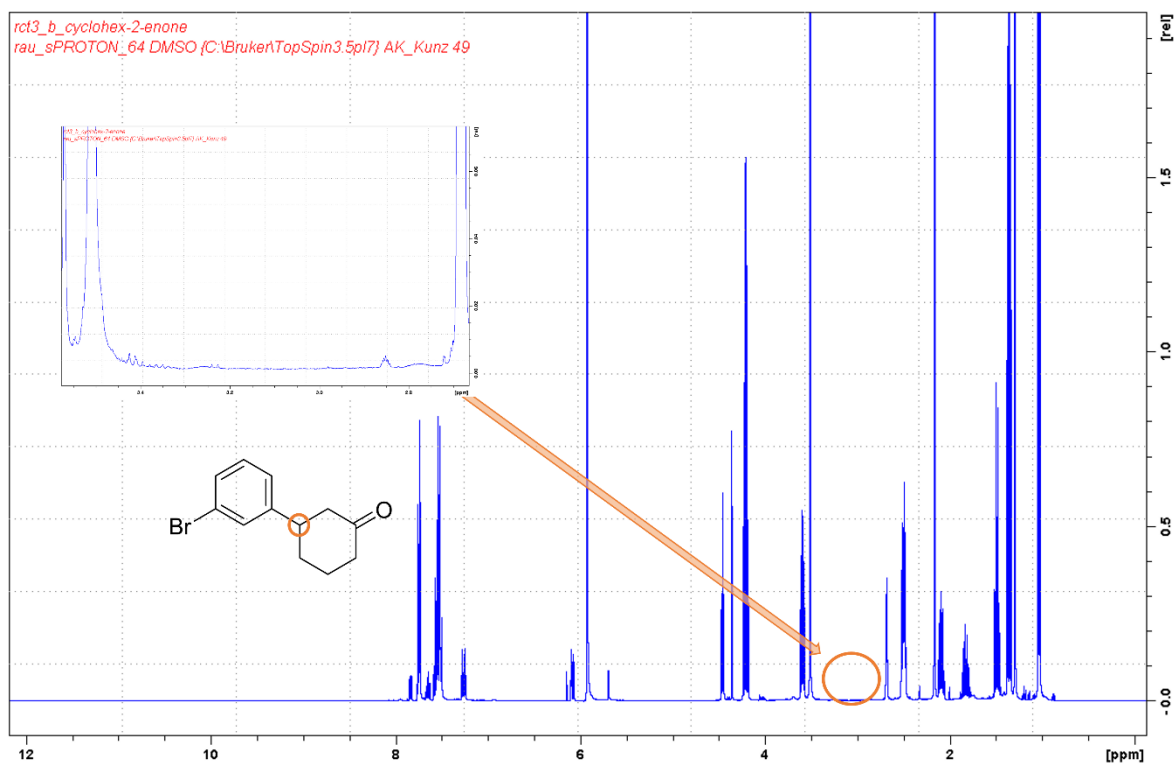


Figure S.3 - 16:  $^1\text{H-NMR}$  spectrum of the crude product of the 1,4-addition in the SFME W/tBuOH/iAlc (60/36/4 (w/w/w)) dissolved in DMSO- $d_6$ . No product can be detected.

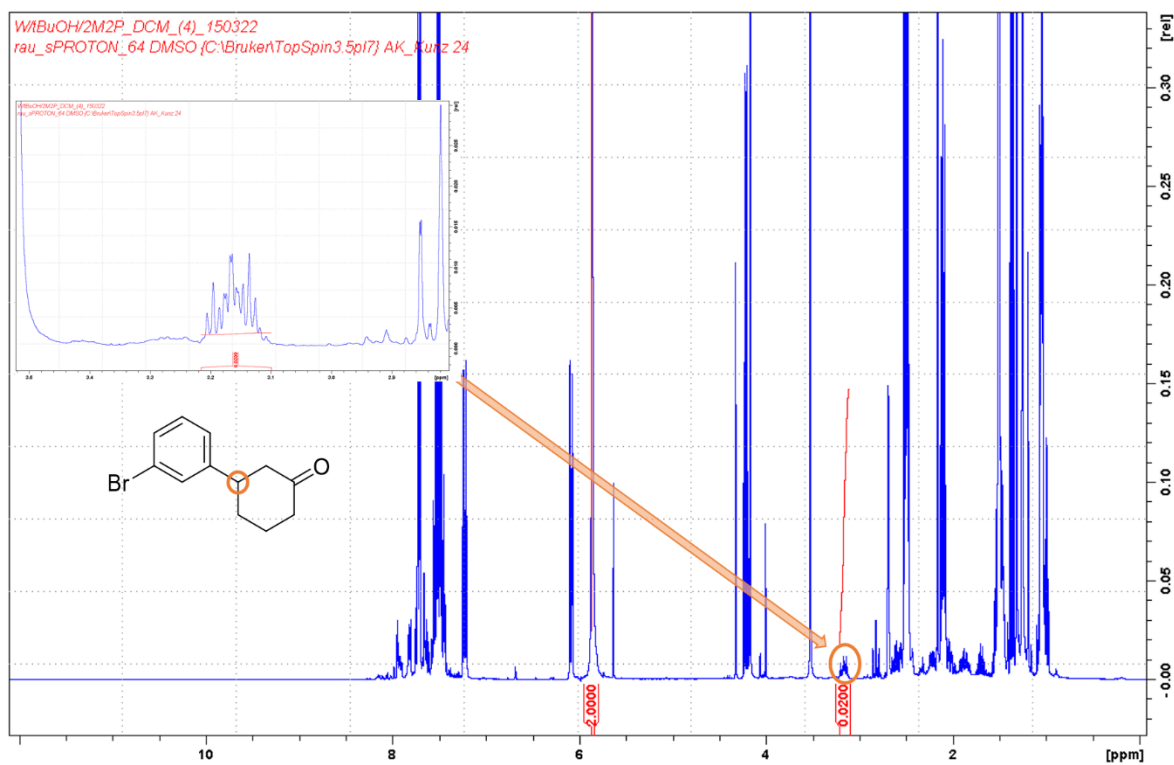


Figure S.3 - 17:  $^1\text{H-NMR}$  spectrum of the crude product of the 1,4-addition in the SFME W/tBuOH/2M2P (60/35/5 (w/w/w)) dissolved in DMSO- $d_6$ . A yield of  $13 \pm 1\%$  is detected.

Table S.3 - 3: Solubility behavior of different compounds in W/tBuOH/THL (40/54/6 (w/w/w)), W/tBuOH/2M2P (60/35/5 (w/w/w)), W/SXS/THL (57/40/3 (w/w/w)), and W/SPentS/THL (53/40/7 (w/w/w)). The same amounts are added as used for the reactions. Compounds can be dissolved in a homogeneous system (1 $\Phi$ ), dissolved resulting in liquid-liquid phase separation (2 $\Phi$ ), or partially undissolved (X). In order to achieve complete solubility, some samples need to be stirred vigorously using a Vortex. For this reason, the arylboronic acid is not always completely dissolved after 1 h of reaction, although the applied amount should be soluble.

compound(s)	W/tBuOH/THL	W/tBuOH/2M2P	W/SXS/THL	W/SPentS/THL
3-bromophenylboronic acid (A)	1 $\Phi$	X	X	X
cyclohexenone (B)	1 $\Phi$	1 $\Phi$	1 $\Phi$	1 $\Phi$
reactants (A) + (B)	1 $\Phi$	X	1 $\Phi$	1 $\Phi$
K <sub>2</sub> CO <sub>3</sub>	2 $\Phi$	2 $\Phi$	1 $\Phi$	1 $\Phi$
K <sub>2</sub> CO <sub>3</sub> + (A) + (B)	2 $\Phi$	2 $\Phi$	1 $\Phi$	1 $\Phi$

t <sub>R</sub> [min]	W/tBuOH/THL 40/54/6	W/tBuOH/2M2P 60/35/5	W/SXS/THL 57/40/3	W/SPentS/THL 53/40/7	TPGS-750-M 2 % in water
0					
30					
60					
after rct.					
after centr.					

Figure S.3 - 18: Photographs of reaction mixtures during the reaction (t<sub>R</sub>), after reaction (after rct.) and after centrifugation (after centr.). In the beginning, all surfactant-free solutions possess a yellow to orange color. The mixtures, which contain tBuOH, separate into two liquid phases upon the addition of K<sub>2</sub>CO<sub>3</sub>. The SFMEs, which contain salt hydrotropes, remain stable. There is a small amount of undissolved compound that is attributed to the catalyst. During the reaction, a second, brownish liquid phase occurs. The micellar reference system is initially a white suspension with a yellow, strongly aggregated solid sticking to the stirring bar. The yellow solid compound is the catalyst. During the reaction, the catalyst gets dispersed, and a second, brownish liquid phase occurs. All proportions are by mass (w/w). Liquid-liquid interfaces are indicated by a red line.

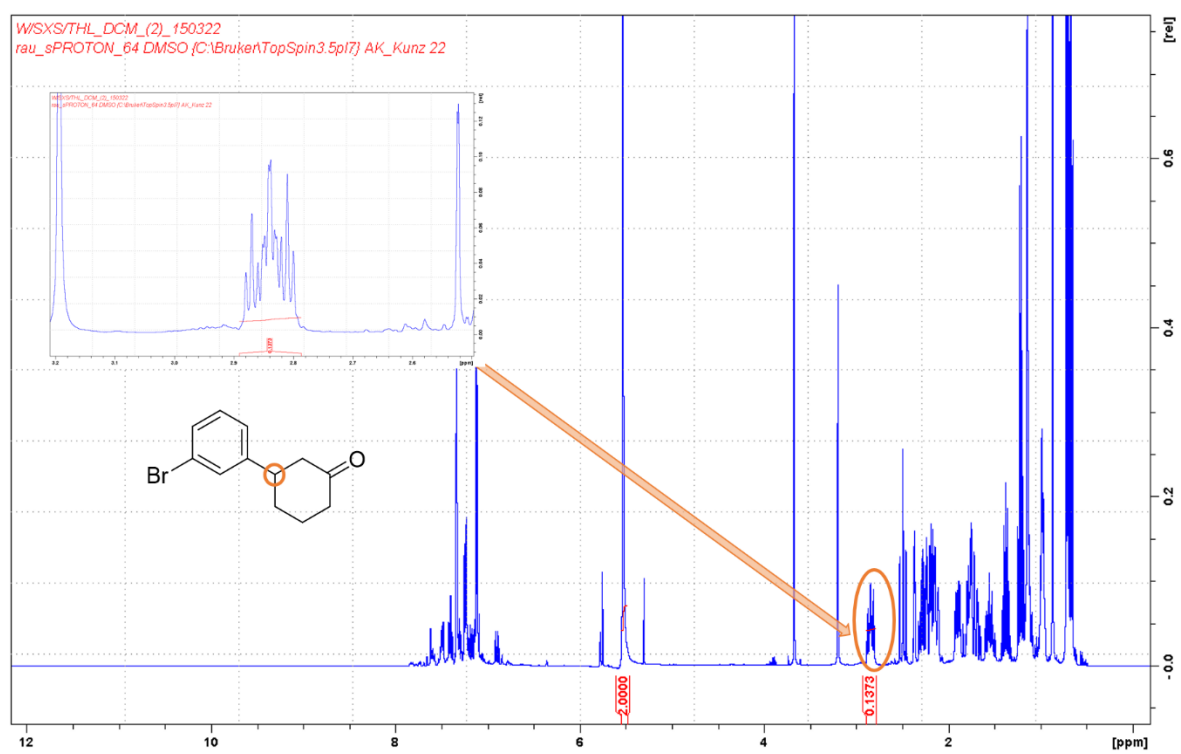


Figure S.3 - 19:  $^1\text{H-NMR}$  spectrum of the crude product of the 1,4-addition in the SFME W/SXS/THL (57/40/3 (w/w/w)) dissolved in  $\text{DMSO-d}_6$ . The show spectrum is used for product quantification.

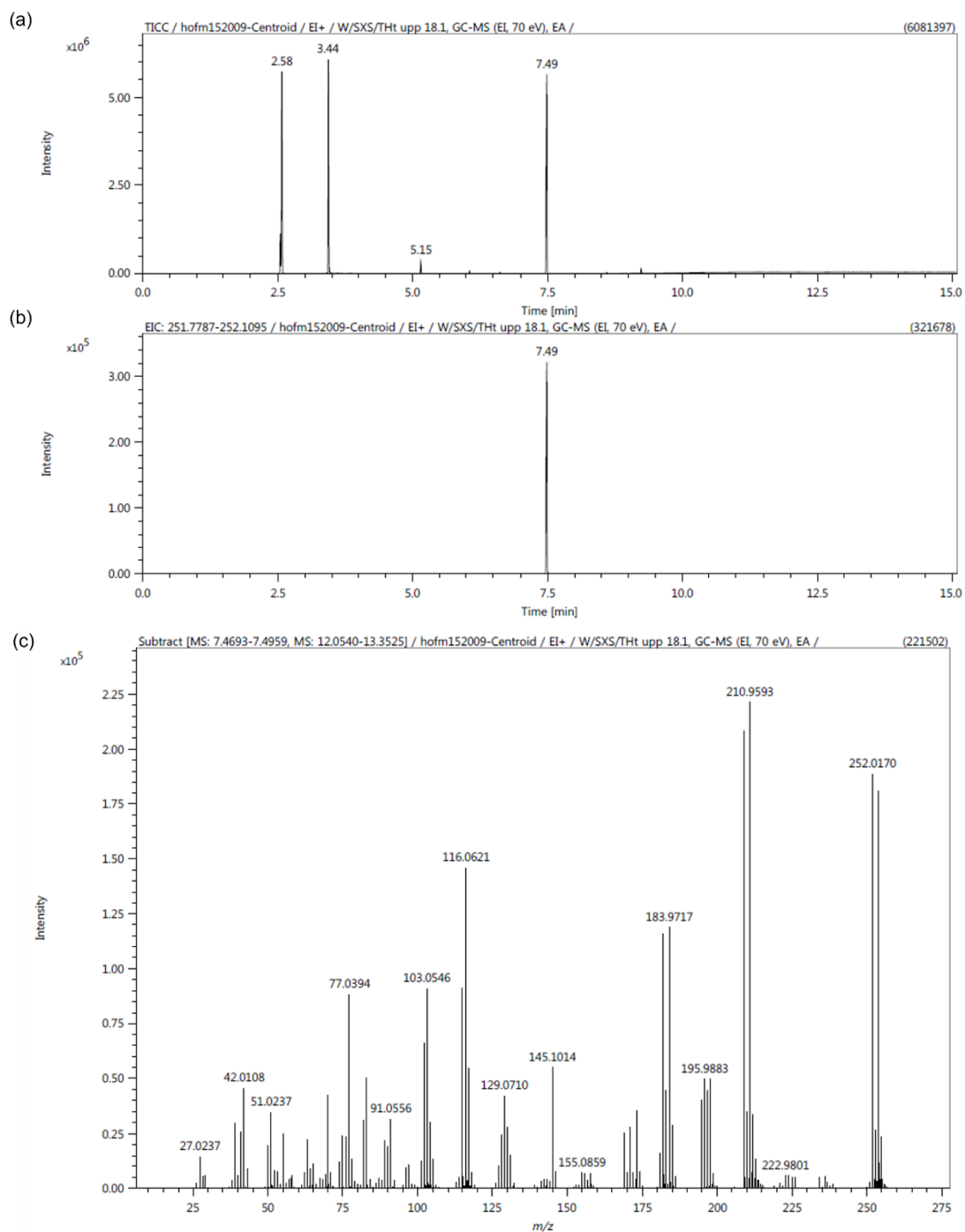


Figure S.3 - 20: MS results of the crude product of the 1,4-addition in the SFME W/SXS/THL (57/40/3 (w/w/w)). (a) TIC chromatogram. (b,c) EIC at a mass-to-charge ( $m/z$ ) of 252 with the corresponding mass spectrum at 7.5 min. The measurements prove the presence of 3-(3-bromophenyl) cyclohexanone with a molar mass of 253.1 g/mol.

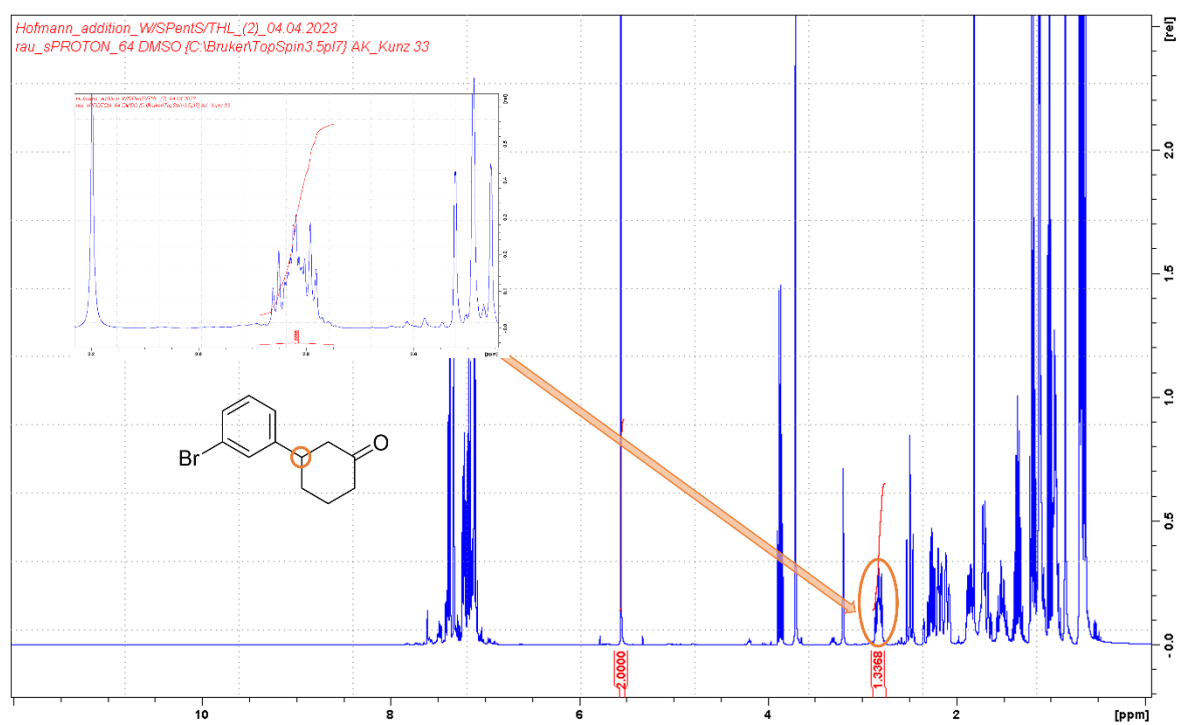


Figure S.3 - 21:  $^1\text{H-NMR}$  spectrum of the crude product of the 1,4-addition in the SFME W/SPentS/THL (53/40/7 (w/w/w)) dissolved in  $\text{DMSO-d}_6$ . The show spectrum is used for product quantification.

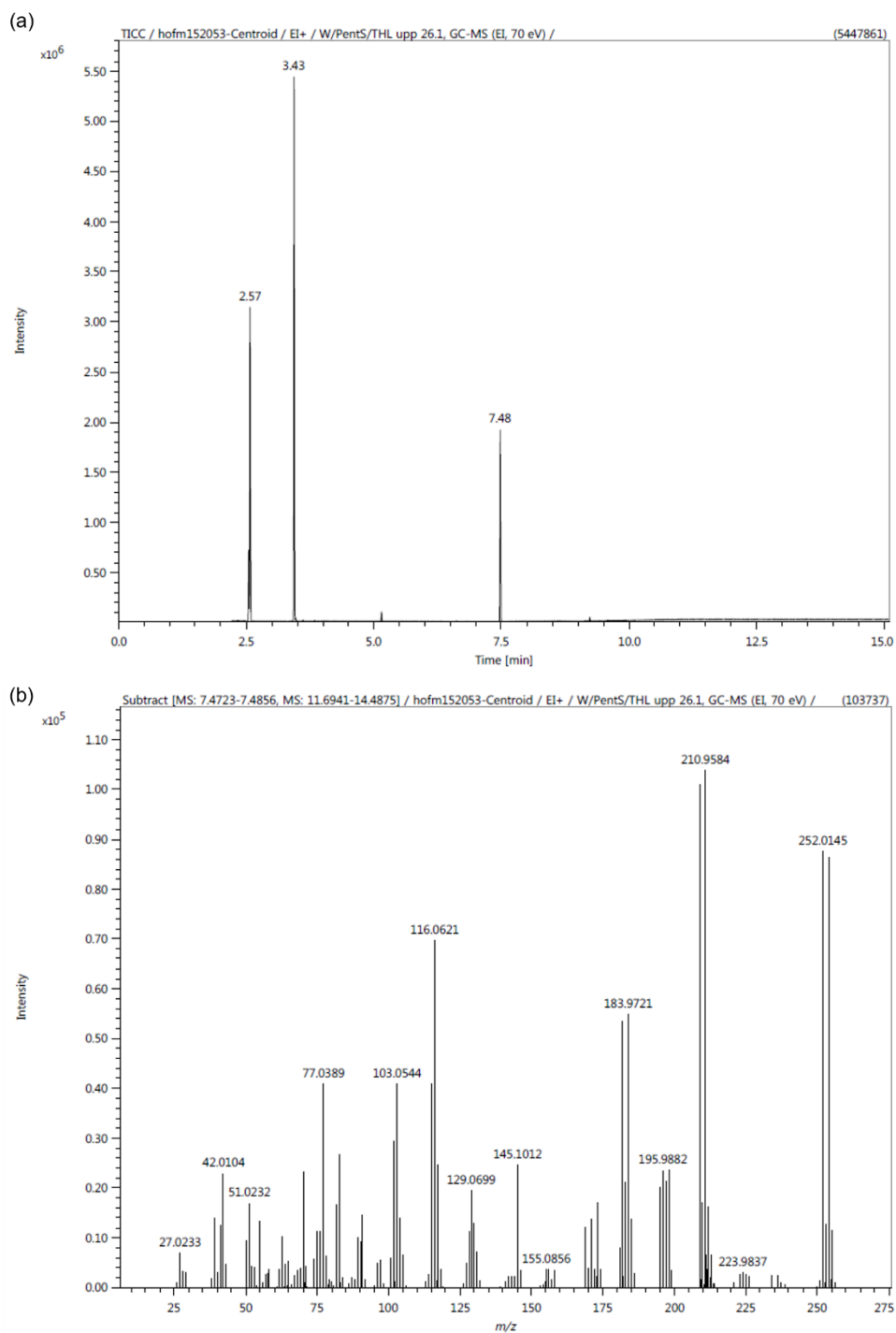


Figure S.3 - 22: MS results of the crude product of the 1,4-addition in the SFME W/SPentS/THL (53/40/7 (w/w/w)). (a) TIC chromatogram. (b) Mass spectrum at 7.5 min. The measurements prove the presence of 3-(3-bromophenyl) cyclohexanone with a molar mass of 253.1 g/mol.

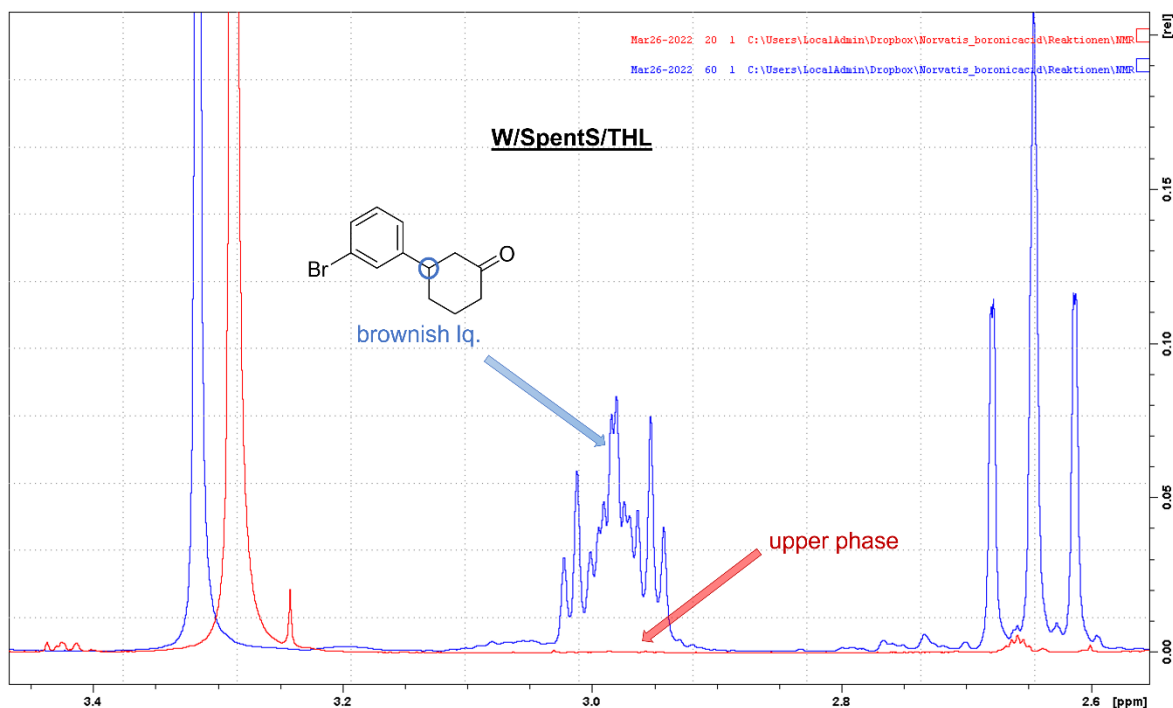


Figure S.3 - 23:  $^1\text{H-NMR}$  spectrum of the crude product of the 1,4-addition in the SFME W/SpentS/THL (53/40/7 (w/w/w)) dissolved in  $\text{DMSO-d}_6$ . The blue spectrum corresponds to the lower phase of the reaction mixture after centrifugation. The red spectrum shows the signals in the upper phase after evaporation of the solvents.

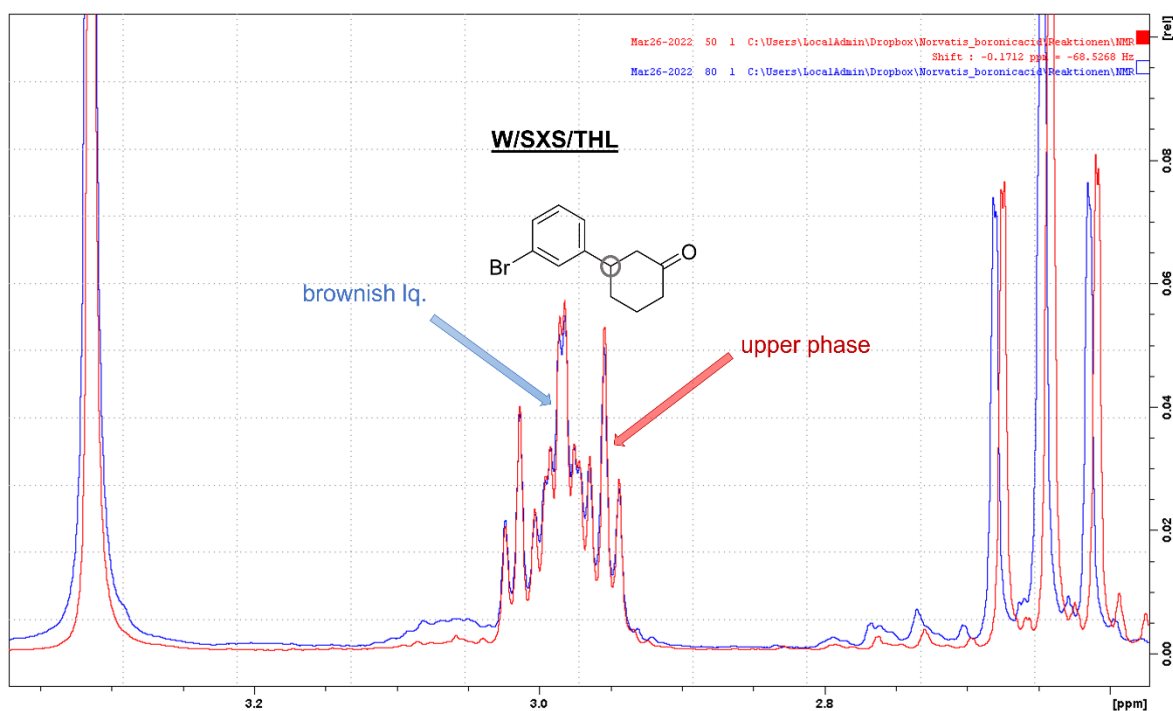


Figure S.3 - 24:  $^1\text{H-NMR}$  spectrum of the crude product of the 1,4-addition in the SFME W/SXS/THL (57/40/3 (w/w/w)) dissolved in  $\text{DMSO-d}_6$ . The blue spectrum corresponds to the lower phase of the reaction mixture after centrifugation. The red spectrum shows the signals in the upper/colorless phase after evaporation of the solvents. In some samples, the brownish phase floated and, thus, represented the upper phase.

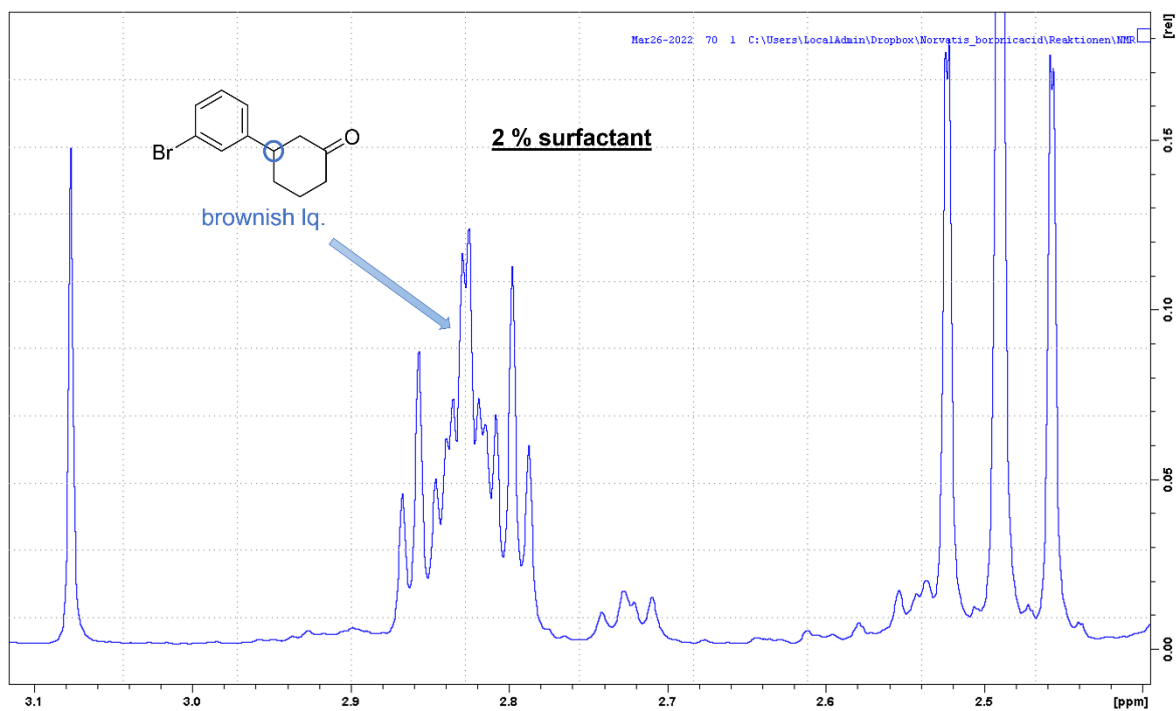


Figure S.3 - 25:  $^1\text{H-NMR}$  spectrum of the crude product of the 1,4-addition in the surfactant solution (2% (w/w) TPGS-750-M in water) dissolved in  $\text{DMSO-d}_6$ . The blue spectrum corresponds to the lower phase of the reaction mixture after centrifugation. The spectrum in the upper phase needs to be repeated.

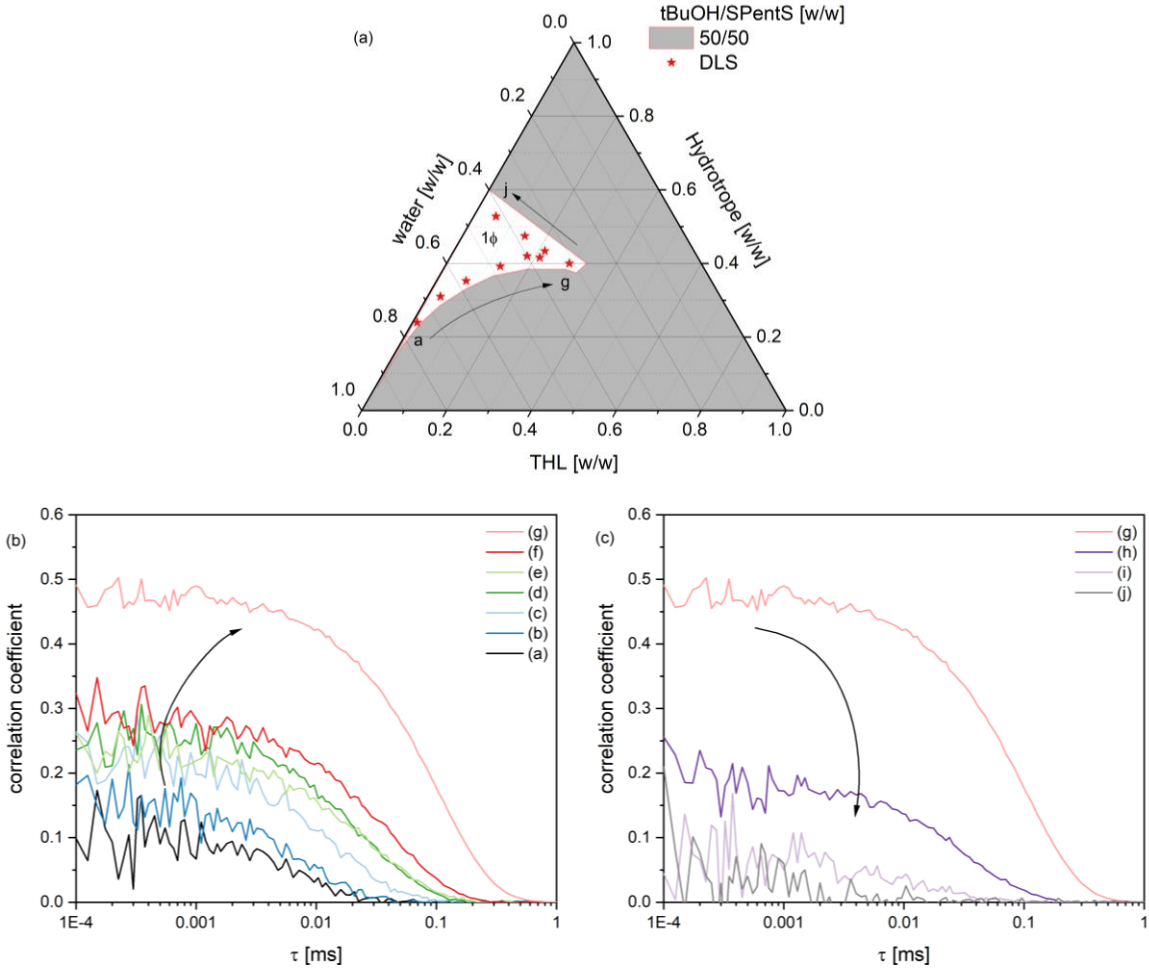
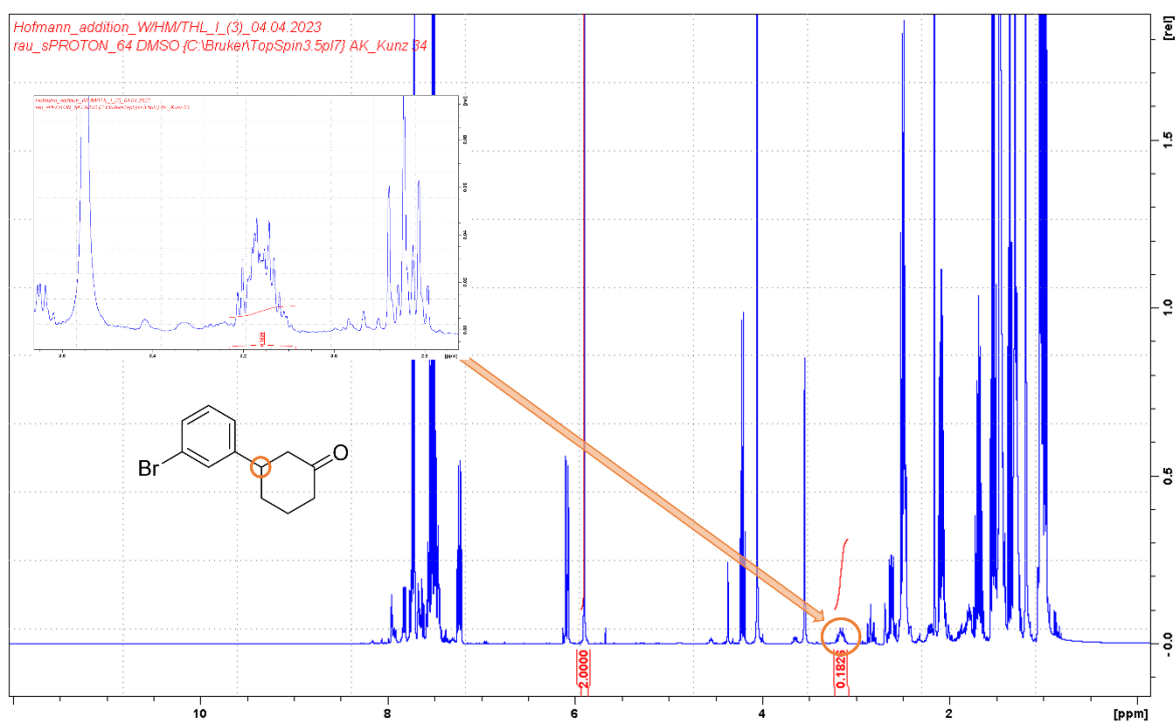
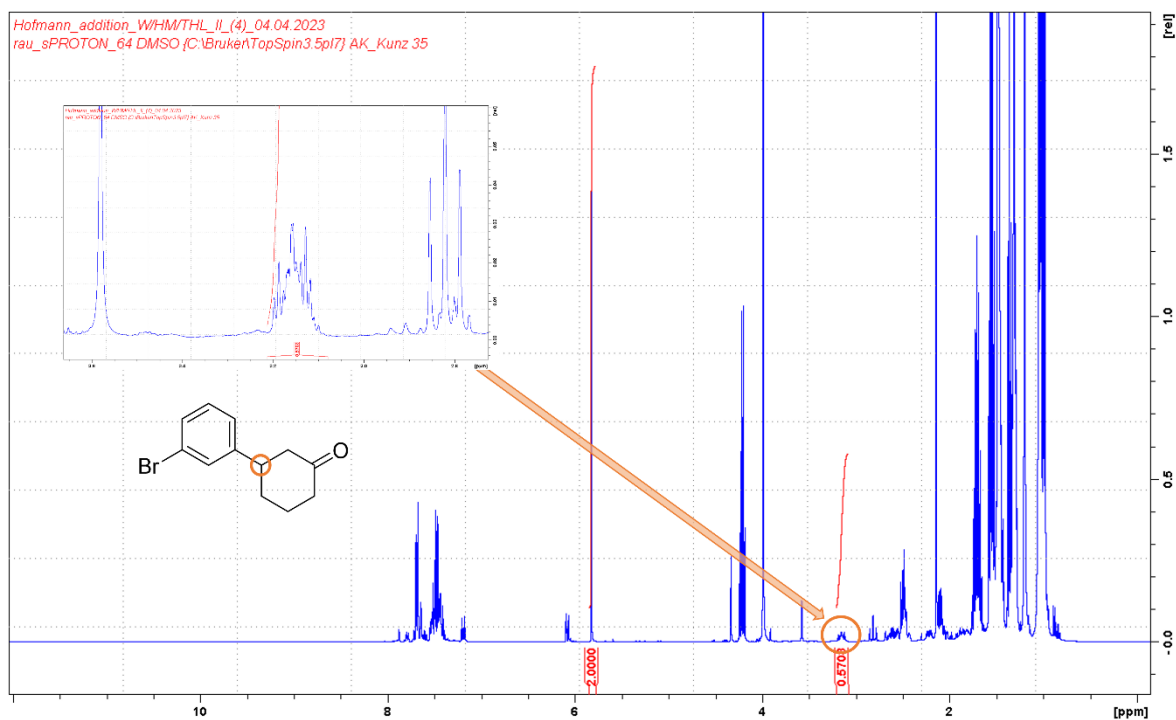


Figure S.3 - 26: (a) Ternary phase diagram of water and THL with a hydrotrope mixture of tBuOH/SPentS (50/50 (w/w)) at 25 °C. The gray shaded area represents the biphasic area (2Φ) which is separated from the monophasic area (1Φ). The stars show the compositions measured by means of DLS. (b,c) Corresponding correlation functions obtained by DLS measurements at 25 °C. The structuring is enhanced compared to the ternary systems with the individual hydrotropes.



### 3.6 References

- (1) Crawley, M. L.; Trost, B. M. *Applications of Transition Metal Catalysis in Drug Discovery and Development: An Industrial Perspective*; Wiley: Hoboken, New Jersey, USA, 2012. <https://doi.org/10.1002/9781118309872>.
- (2) Colacot, T. J. The 2010 Nobel Prize in Chemistry: Palladium-Catalysed Cross-Coupling. *Platin. Met. Rev.* **2011**, *55* (2), 84–90. <https://doi.org/10.1595/147106711X558301>.
- (3) Singh, B. K.; Kaval, N.; Tomar, S.; Eycken, E. Van Der; Parmar, V. S. Transition Metal-Catalyzed Carbon–Carbon Bond Formation Suzuki, Heck, and Sonogashira Reactions Using Microwave and Microtechnology. *Org. Process Res. Dev.* **2008**, *12* (3), 468–474. <https://doi.org/10.1021/op800047f>.
- (4) Prajapati, D.; Gohain, M. Recent Advances in the Application of Supercritical Fluids for Carbon—Carbon Bond Formation in Organic Synthesis. *Tetrahedron* **2004**, *60* (666), 815–833. <https://doi.org/10.1002/chin.200421232>.
- (5) Hayashi, T.; Yamasaki, K. Rhodium-Catalyzed Asymmetric 1,4-Addition and Its Related Asymmetric Reactions. *Chem. Rev.* **2003**, *103* (8), 2829–2844. <https://doi.org/10.1021/cr020022z>.
- (6) Rossiter, B. E.; Swingle, N. M. Asymmetric Conjugate Addition. *Chem. Rev.* **1992**, *92* (5), 771–806. <https://doi.org/10.1021/cr00013a002>.
- (7) Bartáček, J.; Svoboda, J.; Kocúrik, M.; Pochobradský, J.; Čegan, A.; Sedlák, M.; Váňa, J. Recent Advances in Palladium-Catalysed Asymmetric 1,4-Additions of Arylboronic Acids to Conjugated Enones and Chromones. *Beilstein J. Org. Chem.* **2021**, *17*, 1048–1085. <https://doi.org/10.3762/bjoc.17.84>.
- (8) Linsenmeier, A. M.; Braje, W. M. Efficient One-Pot Synthesis of Dihydroquinolinones in Water at Room Temperature. *Tetrahedron* **2015**, *71* (38), 6913–6919. <https://doi.org/10.1016/j.tet.2015.07.016>.
- (9) Itooka, R.; Iguchi, Y.; Miyaura, N. Rhodium-Catalyzed 1,4-Addition of Arylboronic Acids to  $\alpha,\beta$ -Unsaturated Carbonyl Compounds: Large Accelerating Effects of Bases and Ligands. *J. Org. Chem.* **2003**, *68* (15), 6000–6004. <https://doi.org/10.1021/jo0207067>.

- 
- (10) Amengual, R.; Michelet, V.; Genêt, J.-P. New Studies of Rh-Catalyzed Addition of Boronic Acids under Basic Conditions in Aqueous Medium. *Tetrahedron Lett.* **2002**, *43* (34), 5905–5908. [https://doi.org/10.1016/S0040-4039\(02\)01274-1](https://doi.org/10.1016/S0040-4039(02)01274-1).
- (11) Takaya, Y.; Ogasawara, M.; Hayashi, T. Asymmetric 1,4-Addition of Phenylboronic Acid to 2-Cyclohexenone Catalyzed by Rh(I)/Binap Complexes. *Chirality* **2000**, *12* (5–6), 469–471. [https://doi.org/10.1002/\(SICI\)1520-636X\(2000\)12:5/6<469::AID-CHIR29>3.0.CO;2-H](https://doi.org/10.1002/(SICI)1520-636X(2000)12:5/6<469::AID-CHIR29>3.0.CO;2-H).
- (12) Otomaru, Y.; Senda, T.; Hayashi, T. Preparation of an Amphiphilic Resin-Supported BINAP Ligand and Its Use for Rhodium-Catalyzed Asymmetric 1,4-Addition of Phenylboronic Acid in Water. *Org. Lett.* **2004**, *6* (19), 3357–3359. <https://doi.org/10.1021/ol048695m>.
- (13) Sakuma, S.; Sakai, M.; Itooka, R.; Miyaura, N. Asymmetric Conjugate 1,4-Addition of Arylboronic Acids to  $\alpha,\beta$ -Unsaturated Esters Catalyzed by Rhodium(I)/(S)-Binap. *J. Org. Chem.* **2000**, *65* (19), 5951–5955. <https://doi.org/10.1021/jo0002184>.
- (14) Sakai, M.; Hayashi, H.; Miyaura, N. Rhodium-Catalyzed Conjugate Addition of Aryl- or 1-Alkenylboronic Acids to Enones. *Organometallics* **1997**, *16* (20), 4229–4231. <https://doi.org/10.1021/om9705113>.
- (15) Navarre, L.; Darses, S.; Genet, J.-P. Tandem 1,4-Addition/Enantioselective Protonation Catalyzed by Rhodium Complexes: Efficient Access To  $\alpha$ -Amino Acids. *Angew. Chemie Int. Ed.* **2004**, *43* (6), 719–723. <https://doi.org/10.1002/anie.200352518>.
- (16) Brock, S.; Hose, D. R. J.; Moseley, J. D.; Parker, A. J.; Patel, I.; Williams, A. J. Development of an Enantioselective, Kilogram-Scale, Rhodium-Catalysed 1,4-Addition. *Org. Process Res. Dev.* **2008**, *12* (3), 496–502. <https://doi.org/10.1021/op700246g>.
- (17) Chen, G.; Tokunaga, N.; Hayashi, T. Rhodium-Catalyzed Asymmetric 1,4-Addition of Arylboronic Acids to Coumarins: Asymmetric Synthesis of (R)-Tolterodine. *Org. Lett.* **2005**, *7* (11), 2285–2288. <https://doi.org/10.1021/ol0507367>.
- (18) Yuan, W. C.; Cun, L. F.; Mi, A. Q.; Jiang, Y. Z.; Gong, L. Z. A Class of Readily Available Optically Pure 7,7'-Disubstituted BINAPs for Asymmetric Catalysis. *Tetrahedron* **2009**, *65* (21), 4130–4141. <https://doi.org/10.1016/j.tet.2009.03.066>.
- (19) Amengual, R.; Michelet, V.; Genêt, J.-P. A New and Practical Procedure for Asymmetric 1,4-Addition of Boronic Acids to  $\alpha,\beta$ -Unsaturated Ketones Catalyzed by

- Rh-(R)-Digm-BINAP System. *Synlett* **2002**, 2002 (11), 1791–1794.  
<https://doi.org/10.1055/s-2002-34861>.
- (20) Lipshutz, B. H.; Isley, N. A.; Moser, R.; Ghorai, S.; Leuser, H.; Taft, B. R. Rhodium-Catalyzed Asymmetric 1,4-Additions, in Water at Room Temperature, with In-Flask Catalyst Recycling. *Adv. Synth. Catal.* **2012**, 354 (17), 3175–3179.  
<https://doi.org/10.1002/adsc.201200160>.
- (21) Xenakis, A.; Zoupanioti, M.; Stamatis, H. Enzymatic Reactions in Structured Surfactant-Free Microemulsions. *Curr. Opin. Colloid Interface Sci.* **2016**, 22, 41–45.  
<https://doi.org/10.1016/j.cocis.2016.02.009>.
- (22) Krickl, S. Investigation of Potential Applications of Surfactant-Free Microemulsions - Solubilisation, Separation and Extraction Processes and Reaction Media, University of Regensburg, 2018. <https://doi.org/10.5283/epub.38134>.
- (23) Krell, C.; Schreiber, R.; Hueber, L.; Sciascera, L.; Zheng, X.; Clarke, A.; Haenggi, R.; Parmentier, M.; Baguia, H.; Rodde, S.; Gallou, F. Strategies to Tackle the Waste Water from  $\alpha$ -Tocopherol-Derived Surfactant Chemistry. *Org. Process Res. Dev.* **2021**, 25 (4), 900–915. <https://doi.org/10.1021/acs.oprd.0c00547>.
- (24) Dekker, M. L.; Clause, M.; Rosano, H. L.; Zradba, A. S. *Microemulsion Systems*, 24th edn.; Surfactant Science Ser., New York, PA, 1987.
- (25) Buchecker, T.; Krickl, S.; Winkler, R.; Grillo, I.; Bauduin, P.; Touraud, D.; Pfitzner, A.; Kunz, W. The Impact of the Structuring of Hydrotropes in Water on the Mesoscale Solubilisation of a Third Hydrophobic Component. *Phys. Chem. Chem. Phys.* **2017**, 19 (3), 1806–1816. <https://doi.org/10.1039/c6cp06696h>.
- (26) Vankar, P. S. Essential Oils and Fragrances from Natural Sources. *Resonance* **2004**, 9 (4), 30–41. <https://doi.org/10.1007/BF02834854>.
- (27) Cruz, S. M.; Mérida, M.; Pérez, F.; Santizo, A.; Cáceres, A.; Apel, M.; Henriquez, A. Chemical Composition of Essential Oil of *Litsea Guatemalensis* (Mexican Bay) from Different Provenances of Guatemala. *Acta Hort.* **2012**, 964 (964), 47–57.  
<https://doi.org/10.17660/ActaHortic.2012.964.5>.
- (28) Shibayama, M.; Sato, M.; Kimura, Y.; Fujiwara, H.; Nomura, S. <sup>11</sup>B n.m.r. Study on the Reaction of Poly(Vinyl Alcohol) with Boric Acid. *Polymer (Guildf)*. **1988**, 29 (2), 336–340. [https://doi.org/10.1016/0032-3861\(88\)90343-6](https://doi.org/10.1016/0032-3861(88)90343-6).
- (29) Peters, J. A. Interactions between Boric Acid Derivatives and Saccharides in Aqueous Media: Structures and Stabilities of Resulting Esters. *Coord. Chem. Rev.*

- 2014**, 268, 1–22. <https://doi.org/10.1016/j.ccr.2014.01.016>.
- (30) Cordova, A. *Catalytic Asymmetric Conjugate Reactions*; Wiley-VCH Verlag: Weinheim, Germany, 2010.
- (31) Jorgensen, W. L. Optimized Intermolecular Potential Functions for Liquid Alcohols. *J. Phys. Chem.* **1986**, 90 (7), 1276–1284. <https://doi.org/10.1021/j100398a015>.
- (32) Saiz, L.; Padró, J. A.; Guàrdia, E. Structure and Dynamics of Liquid Ethanol. *J. Phys. Chem. B* **1997**, 101 (1), 78–86. <https://doi.org/10.1021/jp961786j>.
- (33) Sato, T.; Buchner, R. Dielectric Relaxation Processes in Ethanol/Water Mixtures. *J. Phys. Chem. A* **2004**, 108 (23), 5007–5015. <https://doi.org/10.1021/jp035255o>.
- (34) Inng, H. R.; Wright, W. M. The Curariform Action of Quaternary Ammonium Salts. *Proc. R. Soc. B Biol. Sci.* **1931**, 109 (763), 337–353. <https://doi.org/10.1098/rspb.1931.0086>.
- (35) Cooper, J. C. Review of the Environmental Toxicity of Quaternary Ammonium Halides. *Ecotoxicol. Environ. Saf.* **1988**, 16 (1), 65–71. [https://doi.org/10.1016/0147-6513\(88\)90017-6](https://doi.org/10.1016/0147-6513(88)90017-6).



## Chapter 4 The role of meglumine in aqueous cross-coupling reactions: Anti-stacking agent and solubilizer for substrates and the photocatalyst 1,8:4,5-naphthalenetetracarboxdiimide

### 4.0 Abstract

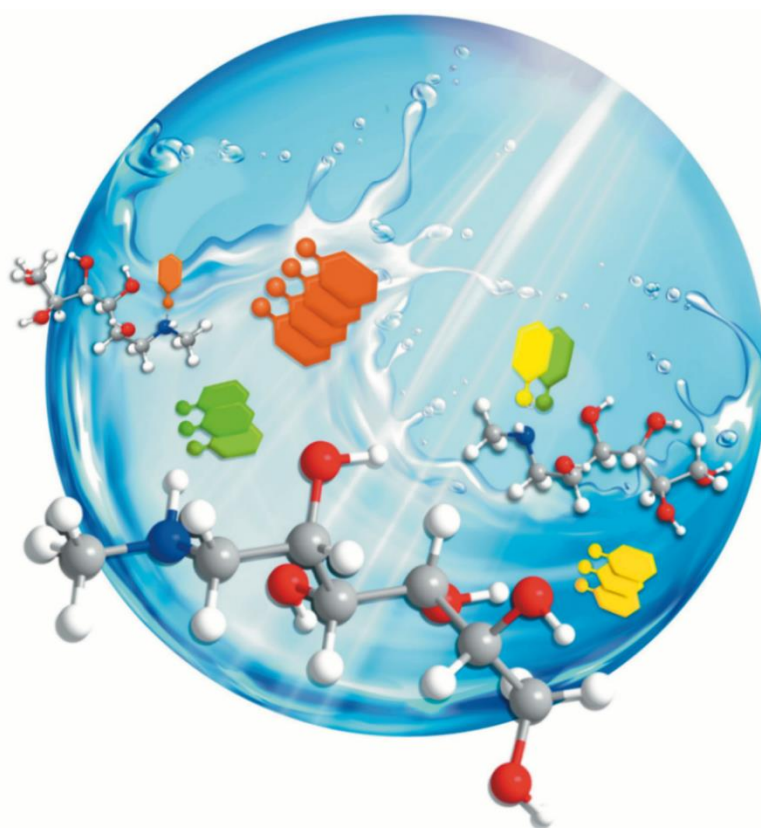


Figure 4 - 1: Schematic illustration of the role of meglumine in photochemical cross-coupling reactions in water via electron donor-acceptor complex formation. The illustration is published as a front cover in *Angewandte Chemie*, **2023**, 62 (17), in connection with the cited publication.<sup>1</sup>

The sugar-based meglumine (N-methyl-D-glucamine) is applied as a solubilizer for different aromatic compounds, which perform in cross-coupling reactions. First, meglumine allows solubilization of the poorly soluble photocatalyst 1,8:4,5-naphthalenetetracarboxdiimide in water. Different additives and solvent mixtures are compared to solubilize the catalyst, with meglumine being the most effective green additive when adjusting the pH. Electrochemical studies reveal a great redox potential of the photocatalyst. Hence, good to excellent yields are obtained for a few cross-coupling reactions in meglumine-based aqueous reaction solvents. The yield in more demanding reactions, however, is still deficient and needs to be

improved. Furthermore, meglumine is applied in C-C and C-S coupling reactions in water in the absence of an additional photocatalyst. In this context, the crucial role of the additive is either to increase the solubility of an already formed electron donor-acceptor (EDA) complex or to activate one substrate, which enables the formation of the reactive EDA complex in the first place. Accordingly, challenging cross-coupling reactions are presented with excellent yields.

The reactions shown in Chapter 4.3.1 were carried out by Dr. Ya-Ming Tian (University of Regensburg). Furthermore, Dr. Ya-Ming Tian performed and analyzed the reactions and absorbance measurements in Chapter 4.3.2 together with Xiang Pu (University of Regensburg, Germany). The NMR studies in Chapter 4.3.2 were performed and analyzed by Dr. Wagner Silva (University of Regensburg, Germany). The results shown in Chapter 4.3.2 are part of a publication in *Angewandte Chemie*<sup>1</sup> (Y.-M. Tian, E. Hofmann, W. Silva, X. Pu, D. Touraud, R. M. Gschwind, W. Kunz, B. König. Enforced Electronic-Donor-Acceptor Complex Formation in Water for Photochemical Cross-Coupling. *Angew. Chem.* **2023**). Besides, Regina Hoheisel (University of Regensburg, Germany) performed the UV/VIS absorption SEC measurements on my behalf.

## 4.1 Introduction

The amino sugar meglumine (N-methyl-D-glucamine, see Figure 4 - 2(a)) is widely used as a pharmaceutical excipient for improving the solubility and release rate of poorly water-soluble drugs.<sup>2-5</sup> The molecule is also of great interest for research due to its bio-degradability, physiological inertness, stability, and availability at low prices.<sup>6</sup> Hence, meglumine is also used for solubilizing plant materials in order to facilitate their exploitation and application.<sup>7,8</sup> In this work, meglumine acts as a potential solubilizer for different aromatic compounds, which are applied in different cross-coupling reactions. A brief background is provided on the molecules and applications discussed in the following.

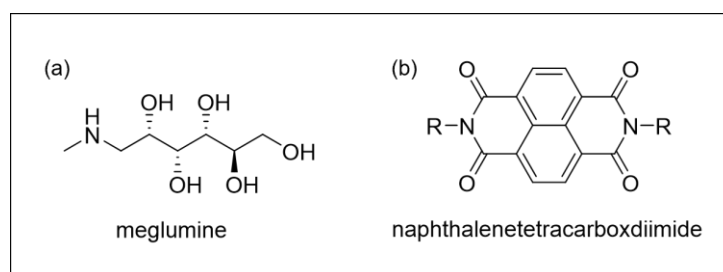


Figure 4 - 2: Molecular structure of meglumine (a) and naphthalenetetracarboxdiimide with substituents R (b).

In the first part, an organic photocatalyst will be considered. Organic dyes represent an interesting alternative to transition metal photocatalysts, as they are commonly less expensive and more environmentally friendly.<sup>9,10</sup> Ghosh *et al.* demonstrated a consecutive photoinduced electron transfer (*conPET*), which allows for overcoming the previously limited reduction power of typical visible light photoredox catalysts. The concept describes the usage of two photons in one catalytic cycle. After absorption of the first photon, the excited dye becomes a stronger oxidant (or reductant) and is converted into its radical anion. A reasonably stable and colored radical anion can absorb the second photon and is thus excited again. This provides sufficient energy for the conversion of less reactive chemical bonds (compare Figure 4 - 3).<sup>11</sup> Hence, rather stable aryl chlorides are successfully activated for carbon-carbon bond formation.<sup>11-13</sup> In this context, naphthalenetetracarboxdiimide derivatives (see Figure 4 - 2(b)) are considered as promising photoredox catalysts with strong redox potential. The poor solubility, however, limits their application. The solubility can be improved by the substitution of branched alkyl chains (R), but the synthesis of such derivatives is reported to be challenging.<sup>14</sup> Accordingly, their usage in photoredox chemistry is rather unexplored yet.<sup>9</sup> Ghosh reported the usage of a branched derivative in a photochemical conversion of aryl-bromides according to the *conPET* concept. In his work, an approximated excited state reduction potential of  $-2.9$  V is determined, which is sufficient

for the reduction of most organic substrates.<sup>13,14</sup> To the best of our knowledge, only derivatives branched and/or substituted at the core have been successfully applied as photoredox catalysts.<sup>9,14–16</sup>

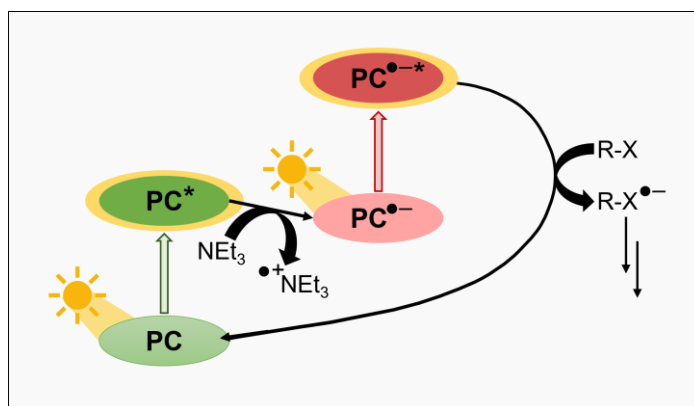


Figure 4 - 3: Schematic illustration of the conPET mechanism with the photocatalyst PC and the resulting activation of the substrate R-X, adapted from the cited literature.<sup>11</sup>

In the second part, electron donor-acceptor (EDA) complex formation is taken into account. An EDA complex describes the aggregation of an electron-donating molecule with low ionization potential and an electron-accepting compound with high electron affinity in the ground state.<sup>17</sup> EDA complexes typically exhibit new absorption bands at longer wavelengths which provide the possibility to activate the substrates by visible light irradiation without the presence of sensitizers or photoredox catalysts.<sup>18–21</sup> The association in EDA complexes is not as directional and robust as other interactions, e.g., hydrogen bonding, and the strength of electron-acceptor association is sensitive to various factors, such as solvent, temperature, and concentration.<sup>19–21</sup> In addition, the formation of EDA complexes and the selectivity of their subsequent transformations can be affected by their local environment, which has been used in asymmetric enzyme photocatalysis.<sup>21–24</sup> Moreover, it has been reported that the nature of the solvent not only plays a crucial role in the formation and stability of EDA complexes but also affects the electron transfer process. Thus, solvent effects have great potential to act as an external force influencing the photochemical properties of EDA complexes. Excitation of the EDA complex and the electron transfer process are accompanied by solvent reorientation, especially in polar solvents. In addition, the excited state species are more polarized than their ground state, resulting in stronger solvation in polar solvents which positively affects the relaxation dynamics of reactive intermediates.<sup>19,20</sup> Water, as the most polar medium among common solvents, is expected to affect the properties and transformations of EDA complexes. However, to the best of our knowledge, the synthetic use of EDA complexes in water has not been investigated in detail, likely due to the low solubility of most organic compounds in water and sensitivity to hydrolysis of functional groups or intermediates.

## 4.2 Material and methods

### 4.2.1 Chemicals

N-methyl-D-glucamine (meglumine, purity  $\geq 99\%$ ), triacetin (TriA, FCC, FG,  $\geq 99\%$ ), ethanolamine ( $\geq 99\%$ ), diethanolamine ( $\geq 98\%$ ), triethanolamine ( $\geq 99\%$ ), ferulic acid ( $\geq 99\%$ ), tetrahydro linalool (THL,  $\geq 97\%$ ), di(propylene glycol) n-propyl ether (DPnP,  $\geq 98.5\%$ ), deuterated dimethyl sulfoxide (DMSO-d<sub>6</sub>,  $\geq 99.5$  atom % D), and tetrabutylammonium tetrafluoroborate (NBu<sub>4</sub>BF<sub>4</sub>, 99%) were purchased from Sigma Aldrich (Darmstadt, Germany). 1,8:4,5-naphthalenetetracarboxdiimide (NDI,  $> 95.0\%$ ), D-(+)-glucosamine hydrochloride (glucosamine(HCl),  $> 98.0\%$ ), D-glucamine ( $> 97.0\%$ ), and N-ethyl-D-glucamine (eglumine,  $\geq 98.0\%$ ) were bought from TCI (Eschborn, Germany). Choline acetate (ChoAc, 98%) was bought from abcr (Karlsruhe, Germany). Acetonitrile (AcN, HPLC grade), ethanol (EtOH,  $> 99\%$ ), ferrocene (98%), and potassium bromide (KBr, for analysis) were obtained from Merck (Darmstadt, Germany). Sodium hydroxide solution (NaOH, 1 N) was from Carl Roth (Karlsruhe, Germany). Ethylamine (70% in water) was purchased from Fluka (Steinheim, Germany). Dimethyl sulfoxide (DMSO,  $> 99\%$ ) was delivered by Fisher Scientific (Schwerte, Germany). All chemicals were used without further purification. Millipore water (W) was used with a resistivity of 18 M $\Omega$  cm. The *Salix Cinerea* extract (fraction mainly composed of flavan-3-ol monomers) was gratefully received from Thomas Gruber (University of Regensburg, Germany).

### 4.2.2 Methods

#### 4.2.2.1 Solubility measurements of the photocatalyst NDI

3 mL of a solvent was supersaturated with an undefined amount of NDI (if not stated otherwise). The supersaturated mixtures were stirred at 40 °C for 1 h and subsequently at 25 °C for 1 h at 400 rpm. Then, the samples were filtered with a PTFE syringe filter (0.2  $\mu$ m pore size). UV/VIS absorbance was measured with an Infinite M Nano+ UV-VIS spectrometer (Tecan Trading, Männedorf, Switzerland) in semi-micro UV cuvettes with a length of 1 cm (Brand, Wertheim, Germany) at room temperature. Whenever the samples needed to be diluted, the measured absorbance was then extrapolated according to Lambert-Beer's law.<sup>25</sup> All samples were prepared in duplicates.

#### 4.2.2.2 Electrochemical measurements

**Cyclic voltammetry** The micropotentiostat and galvanostat CubePot (by M. Multerer and F. Wudy) were applied to monitor the cyclic voltammograms. The setup included a three-electrode system of platinum working and counter electrodes and an Ag/AgCl (3 M KCl) reference electrode. The Pt electrodes were carefully polished using aluminum oxide. Up to 10 cycles were carried out with a scan rate of 500 mV/s. Each solution was degassed prior to the measurements. 0.1 M of  $\text{NBu}_4\text{BF}_4$  in DMSO served as the supporting electrolyte solution. The cyclic voltammograms of the electrolyte solution were determined with and without 1 mM of NDI. In the last run, a spatula tip of ferrocene was added as an internal standard. The half-wave potential ( $E_{1/2}$ ) of the reversible reactions was then determined from the mean of the anodic ( $E_{p,a}$ ) and cathodic ( $E_{p,c}$ ) peak potentials according to Equation 4 – 1.<sup>26</sup>

$$E_{1/2} = \frac{E_{p,a} + E_{p,c}}{2} \quad \text{Eq. 4 - 1}$$

**Spectroelectrochemistry (SEC)** SEC measurements were carried out in an optically transparent thin-layer electrochemical cell (OTTLE, 0.2 mm path length). Pt minigrid electrodes (32 wires per cm) were applied as working and counter electrode. The (pseudo-)reference electrode was a Ag microwire. An Agilent 8453 spectrometer allowed for measuring the absorbance. Measurements were performed in a solution of 2.5 mM NDI in DMSO. A scan rate of 5 mV/S was applied.

#### 4.2.2.3 Determination of the lower critical solution temperature

An additive was dissolved in a binary mixture of water and DPnP in a ratio of 45/55 (w/w) and cooled down to 0 °C. The cooled samples were then slowly heated under constant stirring until turbidity was detected by visual observation.

#### 4.2.2.4 pH measurements

The pH electrode specified in Chapter 3.2.2.7 was used to measure the pH of the solvents under stirring at room temperature.

#### 4.2.2.5 Dynamic light scattering

Dynamic light scattering (DLS) experiments provided in Chapter 4.3.1 were performed as described in Chapter 1.2.2.5. The DLS measurements in Chapter 4.3.2 followed the same protocol, whereby sample preparation and measuring time were changed as follows: 0.02 M

of 4-methylbenzenethiol was added to pure water or water containing 0.05 M dissolved meglumine. The samples were shaken well and filtered into cylindrical scattering cells using a PTFE filter (0.2  $\mu\text{m}$  pore size). The measurements started immediately after filtration and ran for 7 h, during which the scattered light was detected every 2 min for 30 s. The hydrodynamic radius was determined with the second cumulant method using density and viscosity values for water at 25  $^{\circ}\text{C}$ .

#### **4.2.2.6 Ternary phase diagram**

Phase diagrams were recorded according to the method of Dekker *et al.*<sup>27</sup>, as described in Chapter 2.2.2.1.

#### **4.2.2.7 NMR measurements**

NMR measurements were performed for product identification and quantification, as reported in Chapter 2.5.1.3.

#### **4.2.2.8 Conductivity measurements**

Conductivity measurements were performed with a low-frequency WTW inoLab Cond 730 conductivity meter using the WTW TetraCon 325 electrode (Weilham, Germany). 20 mL of each sample containing 0.1 % (w/w) KBr was measured at a controlled temperature of  $25 \pm 0.1$   $^{\circ}\text{C}$ . While 0.05 M meglumine was completely dissolved, the samples containing 0.02 M 4-methylbenzenethiol were shaken well and filtered with a PTFE filter (0.2  $\mu\text{m}$  pore size) immediately before the measurements.

#### **4.2.2.9 Polarization microscope**

A solution of 0.05 M dissolved meglumine with 0.02 M 4-methylbenzenethiol or 0.03 M indole in water was shaken well and filtered with a PTFE filter (0.2  $\mu\text{m}$  pore size). Pictures were taken at specific time intervals to document the macroscopic behavior of the sample, in addition to images taken with a Leitz Orthoplan polarization microscope (Wetzlar, Germany) using 100-fold magnification, connected to a JVC (Yokohama, Japan) digital camera (TK-C1380).

## 4.3 Results and discussion

### 4.3.1 Solubilization and characterization of the photocatalyst 1,8:4,5-naphthalenetetracarboxdiimide

The first part focuses on the solubilization of the photocatalyst 1,8:4,5-naphthalenetetracarboxdiimide (NDI) using meglumine in comparison with other solvent (mixtures) and additives. Figure 4 - 4 summarizes the absorbance of NDI in different solvent mixtures. The molecular structures of the individual components are illustrated in Figure 4 - 5. The best solubility with maximum absorbance in the UV (blue bar) is achieved in the dipolar aprotic solvent dimethyl sulfoxide (DMSO), resulting in a deep yellow solution. DMSO is one of the most powerful organic solvents. Its great solubilizing power is mainly attributed to its high dielectric constant.<sup>28</sup> The second-best solvent is a ternary mixture of choline acetate (ChoAc), ethanol (EtOH), and triacetin (TriA). Mixtures of the food-grade components EtOH and TriA are applied, as their great solubilization power has already been proven in previous works (see Chapter 1). In fact, the mixture of EtOH and TriA dissolves higher amounts of NDI than the pure solvents themselves. The addition of ChoAc to the binary EtOH/TriA mixture increases the detected absorbance in the UV by a factor of almost 16.  $\pi$ -Cation interactions are considered as the major driving force. The comparison with other salts confirms this suggestion (Figure S.4 - 1 in the Supporting Information).

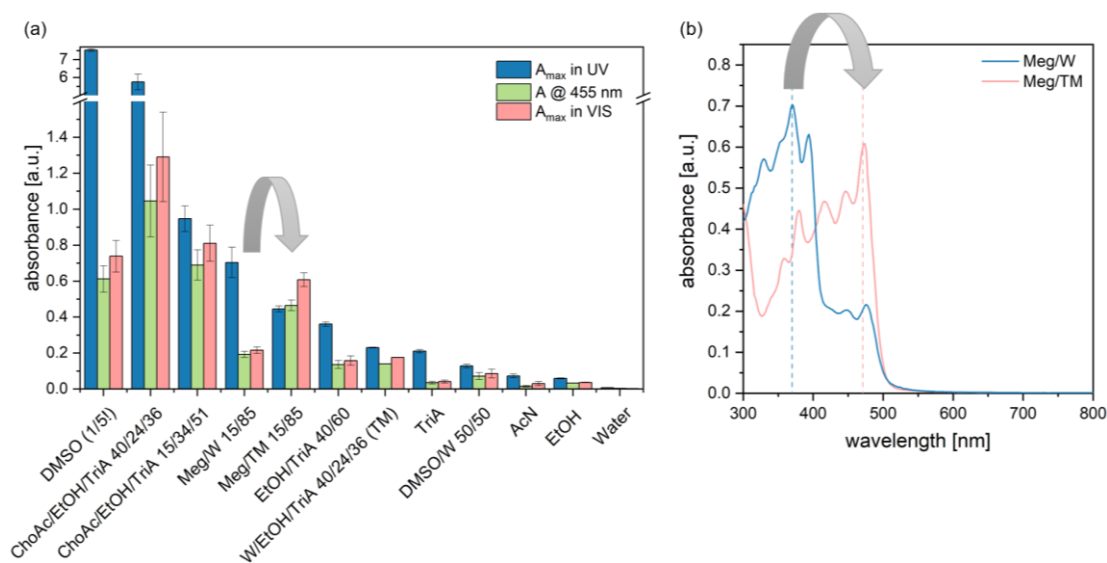


Figure 4 - 4: (a) Absorbance maxima of NDI saturated in various solvents and solvent mixtures. The absorbance maximum in the UV is compared to the maximum absorbance in the VIS, and at 455 nm. TM represents the ternary mixture W/EtOH/TriA (40/24/36). All ratios are given in weight (w/w). The absorbance in DMSO is divided by a factor of 5 in the figure for better representation. (b) Absorbance spectra of NDI saturated in meglumine (Meg)-containing solvents.

Since reactions are to be carried out in an aqueous medium at the end, the binary mixture of EtOH/TriA is mixed with water, reducing the absorbance of NDI further. The same is observed when mixing DMSO with water. The addition of meglumine allows for a remarkable improvement in NDI solubility in aqueous solutions. Meglumine is mixed with either water (Meg/W) or the ternary mixture of W/EtOH/TriA (Meg/TM). While the maximum absorbance in all other solvents is in the UV range, the maximum is shifted to the VIS in Meg/TM (see Figure 4 - 4(a,b), gray arrow). This offers a major advantage over the Meg/W system with the maximum in the UV since photocatalysis with visible light (sunlight in its simplest form) has greater environmental benefits than photochemical processes with high-energy UV radiation.<sup>29</sup> Besides, Figure 4 - 4(a) depicts the absorbance at 455 nm, which is currently the most commonly applied visible light wavelength along with 530 nm.<sup>30</sup> It is assumed that the poor solubility of the catalyst results from  $\pi$ - $\pi$ -stacking interactions. NMR measurements cannot confirm this assumption (see Figure S.4 - 2 in the Supporting Information). The experiments are, however, restricted by the low solubility of the catalyst. Nevertheless, aromatic additives are studied in order to intercalate and break the potential interactions between individual NDI molecules. For this purpose, an extract of the plant *Salix Cinerea*, the fraction of which mainly comprises flavan-3-ol monomers, and ferulic acid are applied. In both cases, however, no dissolved catalyst is detected (see Figure S.4 - 3 in the Supporting Information).

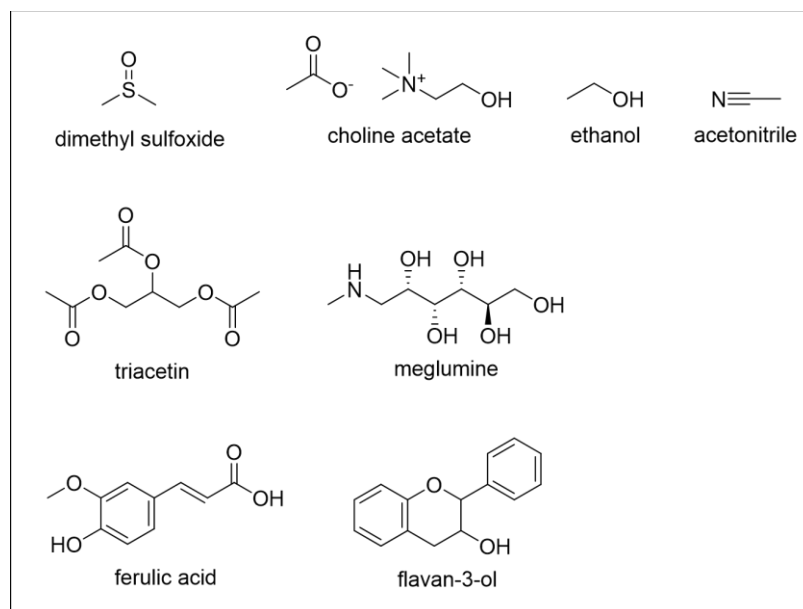


Figure 4 - 5: Molecular structure of solvents and additives applied for NDI solubilization.

Overall, none of the solvent systems achieve comparable results to DMSO. Calibration in this solvent provided an extinction coefficient  $\epsilon_{378\text{nm}} = 16.82 \pm 0.50 \text{ L mmol}^{-1} \text{ cm}^{-1}$  and a saturation concentration of 2 mM (see Figure 4 - 6). Due to the incomparably good solubility, electrochemical investigations are performed in this solvent.

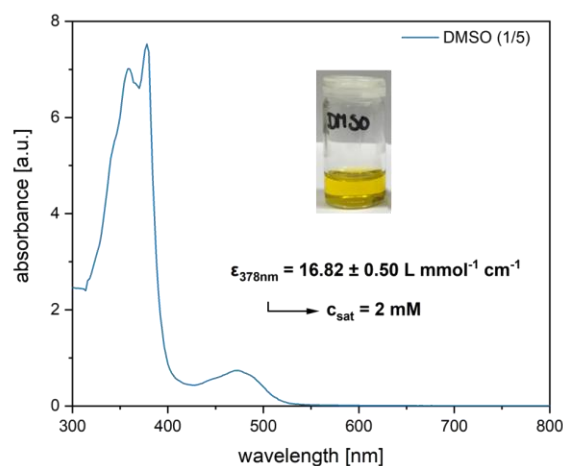


Figure 4 - 6: Absorbance of NDI in DMSO with a photograph of the corresponding sample, the determined extinction coefficient  $\epsilon$  at 378 nm, and the saturation concentration  $c_{\text{sat}}$ . The corresponding calibration curves are provided in the Supporting Information (see Figure S.4 - 4).

The cyclic voltammetry measurement reveals 2 reversible 1-electron charge transfer processes (see Figure 4 - 7(a,b)). The individual measurements of different cycles are provided in the Supporting Information (see Figure S.4 - 5). The determined anodic and cathodic peak potentials allow for calculating the half-wave potentials according to Equation 4 – 1 (see Chapter 4.2.2.2). Since measurements are carried out using Ag/AgCl reference electrode, the half-wave potential of ferrocene is measured as well. This allows converting the results to the SCE reference electrode. The resulting half-wave potentials are summarized in Table 4 - 1. The NDI can thus reach a ground state reduction potential of  $-1.0$  V (vs. SCE). In order to estimate the excited state reduction potential, UV/VIS absorption spectro-electrochemistry (SEC) is applied. In this context, the absorbance of the photocatalyst is measured as a function of the applied potential. The evolution of the absorbance spectra is shown in the Supporting Information (see Figure S.4 - 6).

Table 4 - 1: Experimentally determined half-wave potentials of unexcited NDI ( $E_{1/2}^{(i)}$ ) and excited NDI\* (approximated,  $E_{1/2}^{*(i)}$ ) as well as that of ferrocene against Ag/AgCl (3 M KCl) and SCE (saturated calomel electrode) reference electrodes. <sup>a</sup>The value is taken from the cited literature.<sup>31</sup>

E [V]	NDI		ferrocene	
	vs. Ag/AgCl	vs. SCE	vs. Ag/AgCl	vs. SCE
$E_{1/2}^{(1)}$	- 0.5	<b>- 0.6</b>	+ 0.5	+ 0.4 <sup>a</sup>
$E_{1/2}^{(2)}$	- 0.9	<b>- 1.0</b>	-	-
$E_{1/2}^{*(1)}$	-	<b>- 2.2</b>	-	-
$E_{1/2}^{*(2)}$	-	<b>- 3.0</b>	-	-

Figure 4 - 7(c) shows the spectra of the three NDI species: the neutral form (NDI, blue), the reduced radical anion (NDI<sup>•-</sup>, green), and the twice reduced anion (NDI<sup>2-</sup>, orange). It is assumed that the catalyst is directly reduced to the twice negatively charged species NDI<sup>2-</sup> during reactions. Considering the lowest energy state of excited NDI<sup>2-</sup> (\*, 612 nm), the electron experiences additional  $-2.0$  V. As a consequence, an approximated reduction potential of  $-3$  V (vs. SCE) is determined for the excited NDI<sup>2-</sup>\*. This is in agreement with the potential determined by Ghosh for a NDI derivative ( $-3$  V vs. SCE) and would be enough for activating, e.g., the alkyl chlorides ( $-2.8$  V vs. SCE) mentioned in the Introduction.<sup>12-14</sup>

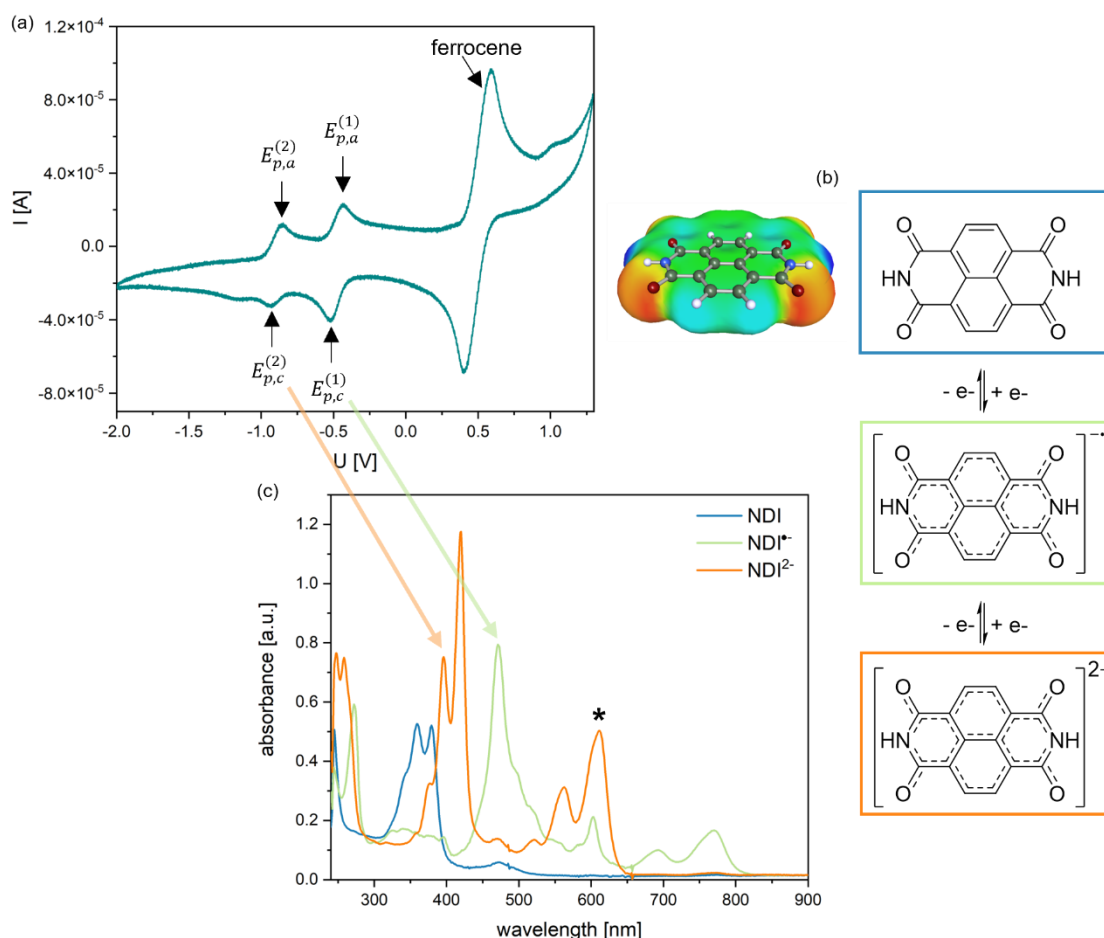


Figure 4 - 7: (a) Cyclic voltammogram of NDI and ferrocene in DMSO with the anodic  $E_{p,a}$  and cathodic peak potentials  $E_{p,c}$ . (b) Molecular structures of the different NDI species: the neutral form (blue), the reduced radical anion (green), and the twice reduced anion (orange). The colored molecular surface represents the COSMO-RS screening charge density  $\sigma$  of the lowest energy conformer. Highly positive  $\sigma$  are colored in red, highly negative  $\sigma$  in blue, and non-polar areas in green. (c) UV/VIS absorption SEC of the three NDI species shown in (b). The absorbance of the neutral form is detected at  $-0.05$  V, the absorbance of the radical anion at  $-0.45$  V, and the absorbance of the twice reduced form at  $-0.83$  V (vs. Ag).

After characterizing the electrochemical properties of the catalyst, the meglumine solvent systems are considered further as potential reaction solvents. The calibration of NDI in aqueous solutions containing meglumine proves to be difficult. In order to compare the different solvents, sample preparation includes supersaturation with NDI. For calibration measurements, defined amounts of the dissolved catalyst are required. However, even after

several hours of stirring and/or heating, not the smallest amount of catalyst dissolves. Due to the different shapes of the absorbance spectra, the extinction coefficient in DMSO cannot be simply transferred to another solvent. Other techniques starting from the supersaturated samples with unknown starting concentrations, such as NMR, HPLC, spiking, or simply back weighing after filtering, were limited by the overall poor solubility of NDI. For this reason, the effect of meglumine on the solubilization of the catalyst is first investigated in more detail with the aim of further improving the solubility.

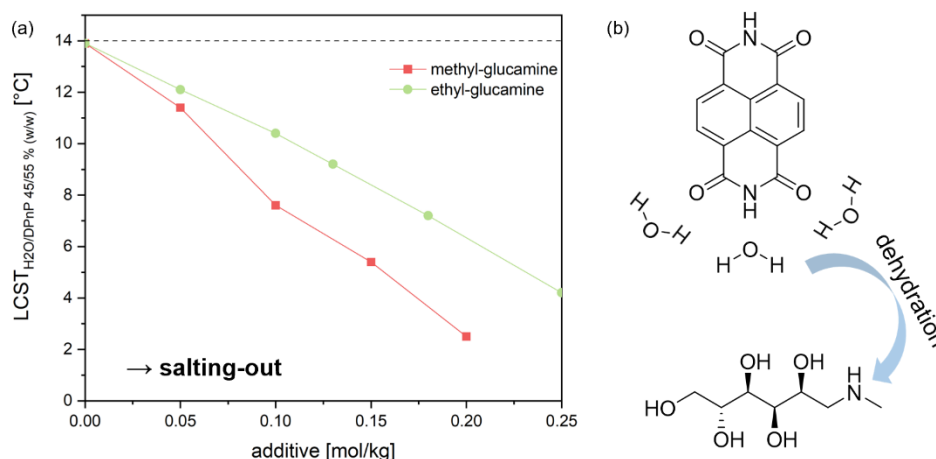


Figure 4 - 8: (a) Effect of meglumine (methyl-glucamine) and eglumine (ethyl-glucamine) on the LCST of a W/DPnP mixture as a function of the additive concentration. (b) Schematic illustration of the expected dehydration effect of meglumine on NDI.

In the first attempt, the salting-in/out behavior of meglumine and the derivative eglumine (ethyl-glucamine) is taken into account. Figure 4 - 8(a) shows the impact of meglumine and eglumine on the lower critical solution temperature (LCST) of a mixture of water and di(propylene glycol) n-propyl ether (DPnP). In the absence of any additive, the LCST is reached at 14 °C, which is also reported in the literature.<sup>32</sup> With the addition of an alkyl-glucamine additive, the LCST decreases. Accordingly, both additives act salting-out. This is to be expected since competition for water arises between the hydroxy group of DPnP and the hydroxy groups of the alkyl-glucamines. The same is observed for other sugar molecules, such as glucose and fructose.<sup>32</sup> The effect is more pronounced with meglumine than with eglumine. So, the first guess would be that meglumine dehydrates the catalyst and therefore decreases its solubility (see Figure 4 - 8(b)). The observed solubilization of NDI by meglumine thus seems to be the result of direct interaction between the catalyst and the additive. Several alkanolamines are considered to gain more insight into the decisive interactions (see Figure 4 - 9). Both the amount and type of functional groups and the steric hindrance are varied along the additives.

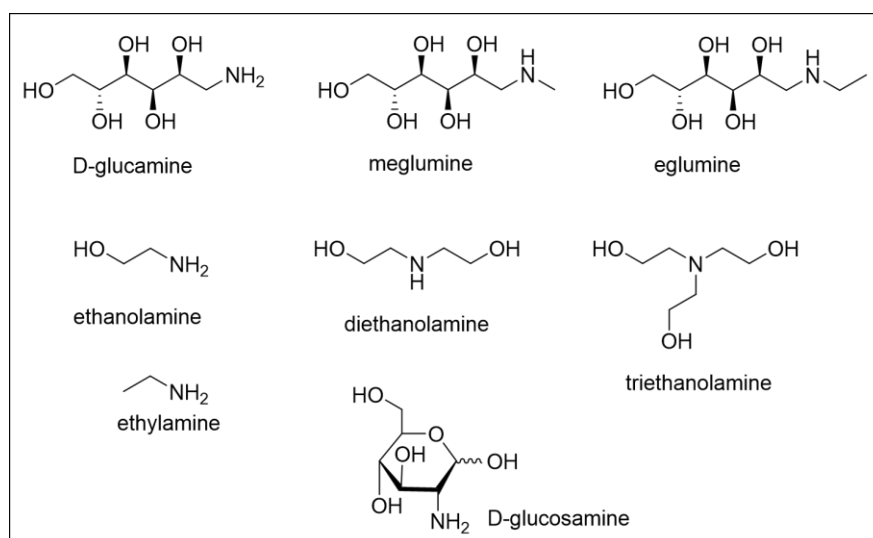


Figure 4 - 9: Molecular structure of the additives studied in water for the solubilization of NDI.

Figure 4 - 10(a) depicts the absorbance of NDI saturated in aqueous solutions containing different additives. The best NDI solubility is achieved using ethylamine (red curve). The absorbance in the UV (370 nm) is more than 2.7 times higher than in the other solutions. Then, considering the UV absorption, the effectiveness decreases as follows: meglumine > ethanolamine > eglumine > diethanolamine > glucamine. While all of these additive solutions result in a similar absorbance pattern with the greatest maximum in the UV, the highest absorbance in the triethanolamine solution is shifted to the VIS (cyan blue). Glucosamine(HCl) cannot dissolve the catalyst. It is conspicuous that the solubility correlates with the pH value determined by the basic additives. The best solution containing ethylamine also depicts the highest pH value at 12.2. The triethanolamine solution is the less basic solution. The ineffective glucosamine solution is acidic due to the bound HCl. The pH of the meglumine solution is with 11.3 the same as that of the eglumine solution. Despite the greater salting-out effect of meglumine, it is the better additive for solubilizing NDI. The ethyl group may thus result in a steric hindrance restricting interactions between the additive and the catalyst.

Based on the results, the influence of the pH is studied in more detail (see Figure 4 - 10(b)). The absorbance at 371 nm increases rapidly in sodium hydroxide (NaOH) solutions from a pH above 11 until the maximum is reached at 12.6. The absorbance of NDI saturated in a NaOH solution of pH 12.6 is more than 4 times higher than in the aqueous additive solutions. At higher pH, the NDI signal decreases rapidly, which may indicate instability of the molecule at pH values above 12.6. In the next step, the pH of the additive solutions is adjusted in order to investigate the impact of the additives independently of the pH values. A pH of 12.2 is chosen to avoid potential instabilities.

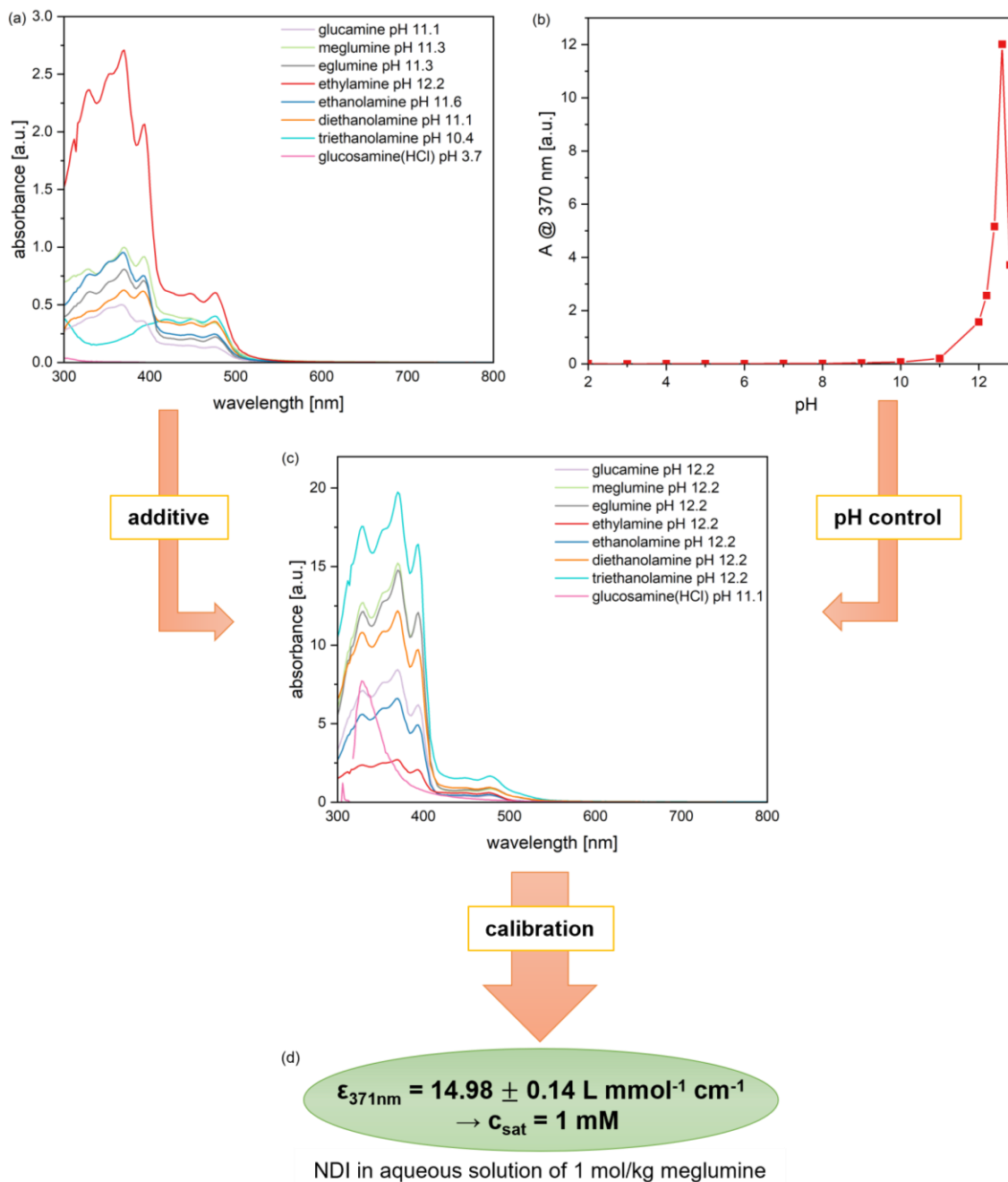


Figure 4 - 10: (a) Absorbance of NDI saturated in aqueous solutions containing 0.5 mol/kg of the additive given in the legend. The pH is measured in the additive solution in the absence of the catalyst. (b) Maximum absorbance of NDI saturated in NaOH solutions as a function of the pH value. (c) Absorbance of NDI saturated in aqueous solutions containing 0.5 mol/kg of the additive given in the legend. The pH of the solutions is adjusted to 12.2 (except for glucosamine, where the pH is 11.1). (d) Extinction coefficient of NDI at 371 nm and the calculated saturation concentration in an aqueous solution containing 1 mol/kg meglumine with an adjusted pH of 12.2. (a-c) During sample preparation, the solvents were supersaturated with 10 mM of the catalyst.

Figure 4 - 10(c) summarizes the absorbance of NDI saturated in the aqueous additive solutions with adjusted pH. Overall, a significantly higher NDI solubility is achieved by combining additive and pH control. Triethanolamine best solubilizes the catalyst, which absorbs the strongest in the UV (370 nm) in all additive solutions (except for glucosamine). The effectiveness changes to the following ordering: triethanolamine > meglumine/eglumine > diethanolamine > glucamine > ethanolamine > ethylamine. The number of hydroxy groups

seems to play a crucial role. Additives with more hydroxy groups tend to better solubilize the catalyst (triethanolamine > diethanolamine > ethanolamine > ethylamine). The spatial arrangement of the functional groups also seems to influence to which extent the additive can interact with NDI so that triethanolamine is more effective than meglumine, although the molecule possesses less hydroxy groups. The catalyst absorbance in the glucosamine solution differs from that in the other additive solutions. The pH is only adjusted to 11.1 due to the bound HCl, but the basic solution allows for detecting an absorbance. The ring conformation of the molecule may lead to a different environment of the catalyst, influencing its absorbance. Overall, the great improvement in NDI solubility allows for calibration. The focus remains on the aqueous meglumine solution due to the greenness of the molecule. The production of triethanolamine is based on the reaction between ethylene oxide and ammonia. Besides, the chemical often contains mono- and diethanolamine impurities, which form carcinogenic nitrosamine and can cause skin sensitization. In green and safe applications, triethanolamine is thus increasingly replaced.<sup>33,34</sup> In this work, the molecules were only utilized for a better understanding of the existing interactions. Finally, the determined extinction coefficient of NDI in an aqueous meglumine solution at pH 12.2 is determined to be  $\epsilon_{371\text{nm}} = 14.98 \pm 0.14 \text{ L mmol}^{-1} \text{ cm}^{-1}$ , resulting in a saturation concentration of 1 mM (see Figure 4 - 10(d)).

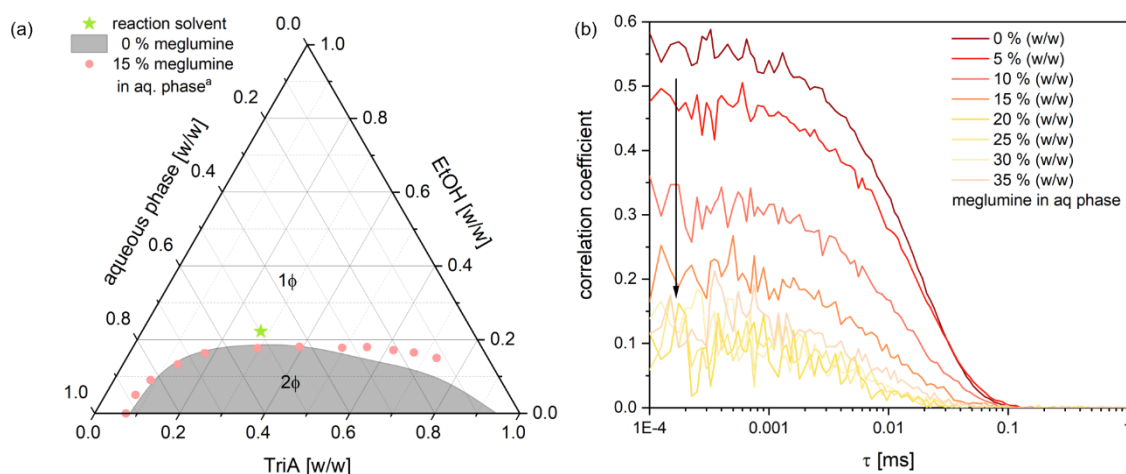


Figure 4 - 11: (a) Experimentally determined phase diagram of water, EtOH, and TriA at 25 °C. The gray shaded area represents the miscibility gap (2Φ), which is separated from the monophasic area (1Φ). The green star identifies the mixture applied as the reaction solvent. The rose dots represent the determined phase border in the presence of 15 % (w/w) meglumine in the aqueous phase. <sup>(a)</sup>Data gratefully received from Dr. Pierre Degot (former Ph.D. student at the University of Regensburg, Germany).<sup>8</sup> (b) Correlation function of the reaction mixture (green star in (a)) with an increasing amount of meglumine obtained by DLS measurements at 25 °C. The amount of meglumine refers to the water content.

For the photochemical reactions, solutions of meglumine dissolved in water are considered. In addition, meglumine is added to surfactant-free microemulsions (SFMEs). The hydrophobic pseudo-phase shall further improve the solubility of hydrophobic reactants during the reaction. Besides, information on the impact of a mesoscopic interface on photocatalysis

should be obtained. The initial results in W/EtOH/TriA reveal sufficient NDI absorbance and a shift of the maximum absorbance to wavelength in the VIS (compare Figure 4 - 4). For this reason, the system is investigated further. Figure 4 - 11(a) illustrates the localization of the composition chosen as the reaction mixture in the ternary phase diagram (green star). The mixture is selected due to high water content and a significant correlation function in the DLS, which indicates the presence of mesoscopic structuring (see Figure 4 - 11(b), brownish curve), Figure S.4 - 9). The mixture of W/EtOH/TriA with a ratio of 50/22/28 (w/w/w) is therefore referred to as an SFME. The addition of meglumine has no remarkable impact on the miscibility gap at the examined water-rich side of the phase diagram. However, the DLS signal decreases with an increasing amount of meglumine. The additive may also improve the solubility of TriA in water, reducing the tendency to aggregate with other TriA molecules. The effect, however, can only relate to TriA that is already dissolved in TriA-rich aggregates dispersed in water, since the overall miscibility gap does not decrease at this composition. Furthermore, TriA is known to be prone to hydrolysis (see Figure 4 - 12(a)).<sup>35,36</sup> The increasing amount of meglumine can catalyze the hydrolysis of TriA and thus reduce the amount of the hydrophobic compound in the system. The hydrolysis would result in an increasing amount of acetic acid.

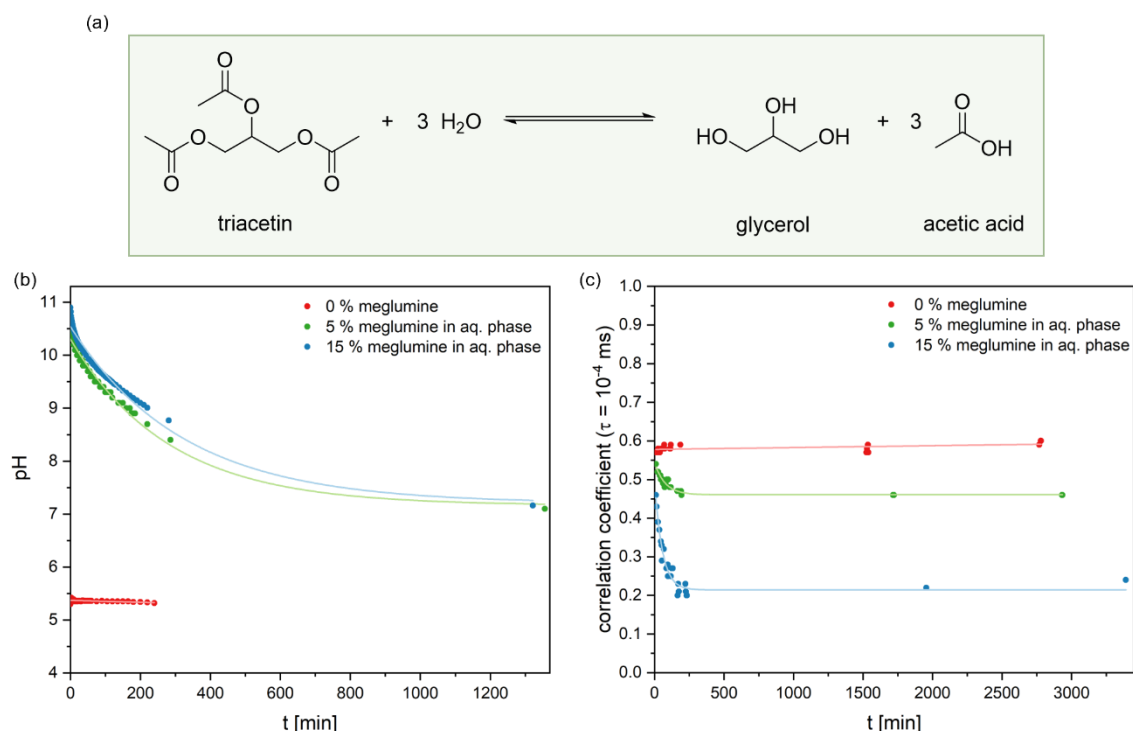


Figure 4 - 12: (a) Reaction mechanism of hydrolysis of triacetin (TriA). (b) pH of W/EtOH/TriA (50/22/28 (w/w/w)) containing different amounts of meglumine as a function of time with the corresponding exponential fit. (c) Correlation coefficient ( $\tau = 10^{-4}$  ms) of W/EtOH/TriA (50/22/28 (w/w/w)) obtained by DLS measurements as a function of time with the corresponding exponential fit. The W/EtOH/TriA mixture contains different amounts of meglumine, pre-dissolved in the aqueous (aq.) phase. The corresponding DLS measurements are provided in the Supporting Information (see Figure S.4 - 10). The time measurement started with the mixing of the (pseudo-)ternary mixture.

For this reason, both the pH and the DLS signal of the ternary mixture containing different amounts of meglumine are studied with respect to time (see Figure 4 - 12(b,c)). Immediately after mixing, the basic meglumine raises the pH of the SFME from 5.3 to 10.7 (5 % (w/w) in the aqueous phase) and 10.9 (15 % (w/w) in the aqueous phase). While the pH remains constant in the absence of meglumine, the pH of the solutions containing meglumine decreases immediately, indicating the formation of acetic acid. The same is observed for the correlation intercept. The presence of meglumine decreases the intercept already in the first measurement. The value continues to fall over time, whereby the decrease is most pronounced in the solution with the largest amount of meglumine. In the meglumine-free SFME, the correlation intercept remains more or less stable. The measurements thus confirm the catalytic effect of meglumine on the hydrolysis of triacetin.

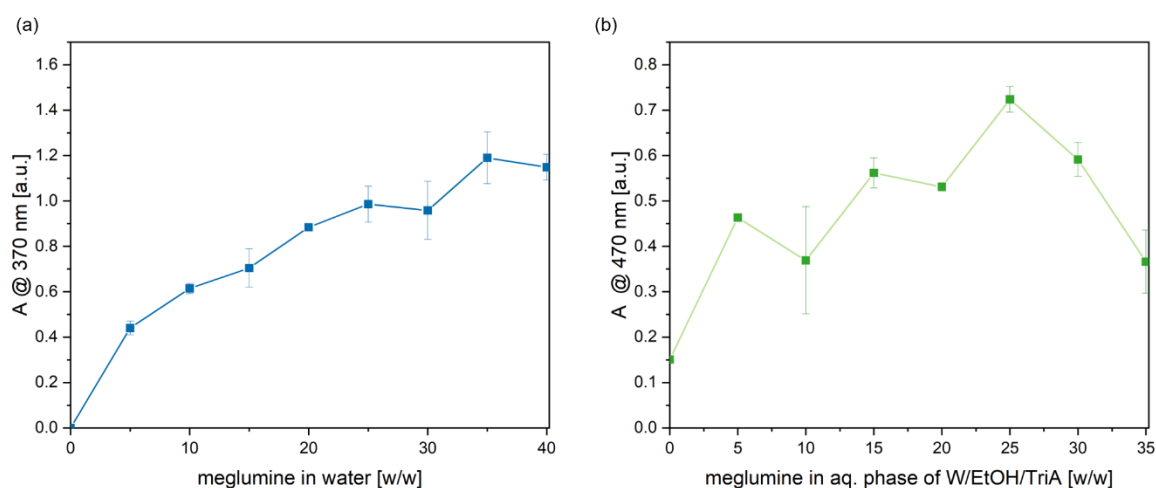
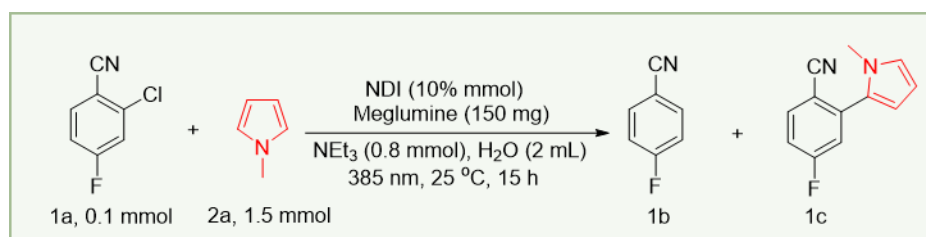


Figure 4 - 13: (a) Absorbance of NDI saturated in water containing an increasing amount of meglumine. (b) Absorbance of NDI saturated in the ternary reaction mixture of W/EtOH/TriA (50/22/28 (w/w/w)) containing an increasing amount of meglumine in the aqueous (aq.) phase.

Accordingly, the ternary mixtures with higher amounts of meglumine can no longer be referred to as an SFME. Nevertheless, the solubility of the catalyst is further considered since the absorption maximum in the VIS may be beneficial for photocatalysis. Figure 4 - 13 depicts the maximum absorbance of NDI saturated in meglumine/water solutions (a) and meglumine/W/EtOH/TriA solutions (b) as a function of the additive content. As expected, an increasing amount of dissolved meglumine in water results in an increase in the catalyst absorbance and, therefore, in its solubility. The absorbance in the ternary mixtures containing meglumine first tends to increase with an increasing amount of meglumine. With 30 % (w/w) meglumine in the aqueous phase (15 % (w/w) dissolved in the total mixture), the absorbance starts to decrease again. The hydrolysis of triacetin and the resulting decrease in the pH are assumed to be the origin of the decrease at high amounts of meglumine and for the overall discontinuous trend.

Table 4 - 2 summarizes the initial results of the photocatalytic C-C coupling reaction in aqueous meglumine solutions. Due to the initial calibration problems, the reactions are carried out in a turbid suspension with a defined amount of catalyst. The reaction shown in Table 4 - 2 is performed under optimized conditions, providing an excellent yield of 93 % (1c). The optimum wavelength is determined to be 385 nm, which is in agreement with the maximum absorbance of NDI in the UV when dissolved in meglumine/water. In the absence of light or NDI, no product or only 5 % are detected, which confirms that the reaction studied is a photocatalytic transformation. Performing the reaction without meglumine reduces the yield from 93 % to 60 %. The additive increases the solubility of the catalyst. As the solution is, however, supersaturated with the catalyst and the reaction runs for 15 h, the great impact of meglumine on the yield is not expected. For this reason, the influence of meglumine on cross-coupling reactions in water in the absence of photocatalysts will be considered in detail in the following Chapter 4.3.2. Removing both meglumine and NDI from the reaction solution yields only traces of the product.

Table 4 - 2: NDI-catalyzed C-C coupling reactions. The yields were determined by GC-MS analysis and are averages of two runs.  $NEt_3$  abbreviates the base triethylamine.



entry	deviations from the optimized conditions	yield of <b>1b</b> [%]	yield of <b>1c</b> [%]
1	none	3	<b>93</b>
2	no light	n.d.	n.d.
3	no NDI	n.d.	5
4	no meglumine	8	60
5	no NDI, no meglumine	n.d.	traces
6	455 nm, water, 2.5 mmol <b>2a</b>	22	75
7	455 nm, W/EtOH/TriA (50/22/28 (w/w/w)), 2.5 mmol <b>2a</b>	12	49

The reduced yield of 75 % in water at a higher wavelength (455 nm) is attributed to the absorbance spectrum. A summary of the optimization and control experiments can be found in the Supporting Information with the yields obtained for a variety of different substrates (see Table S.4 - 1 - Table S.4 - 3). Good to excellent yields are achieved in the initial experiments. However, excellent yields for really challenging reactions are still missing. Replacing water with the SFME W/EtOH/TriA further decreases the yield to only 49 %,

although the catalyst absorbance in the VIS is stronger in this solvent. Since the reaction requires the base triethylamine  $\text{NEt}_3$ , the present (and further produced) acetic acid is likely to interfere with the reaction. Indeed, all the organic reactions considered in this work are carried out under basic conditions. As a consequence, the TriA is replaced by the stable tetrahydro linalool (THL).

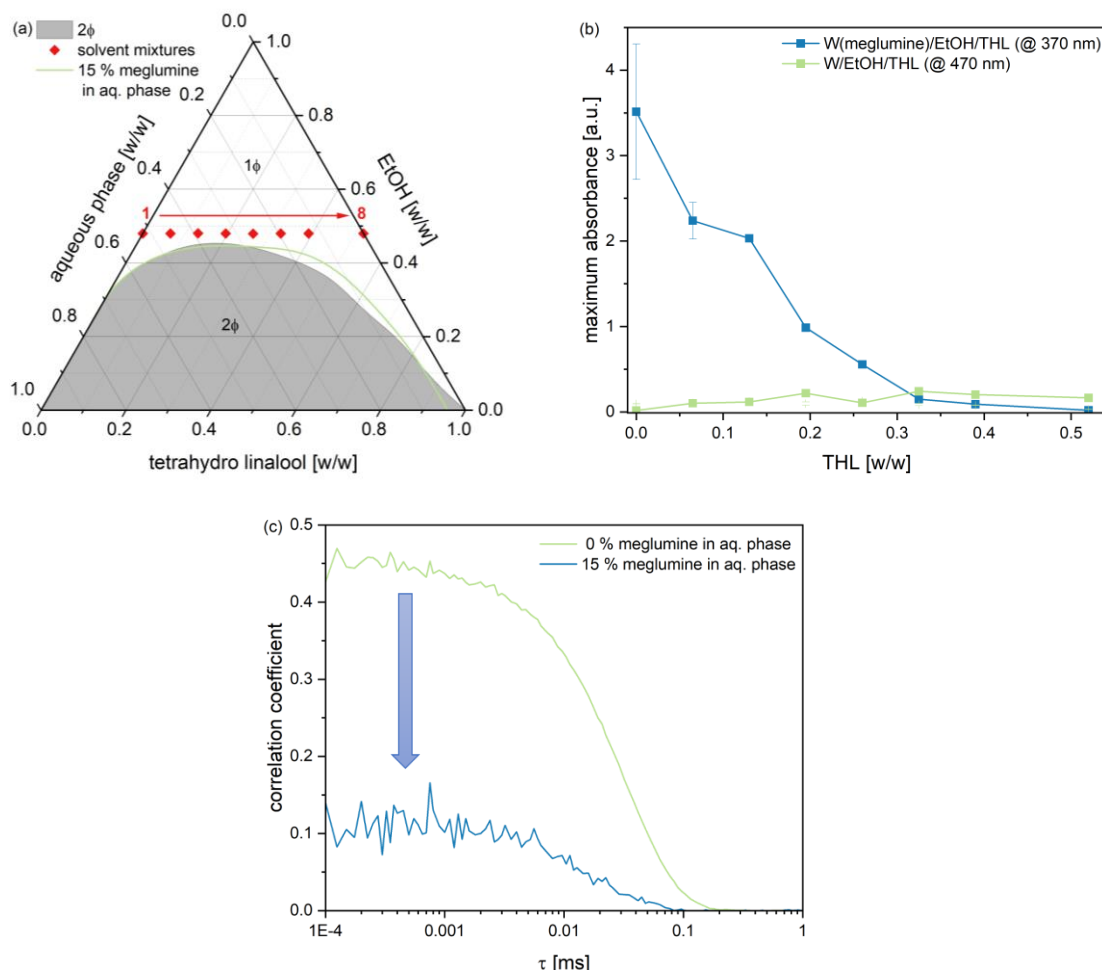


Figure 4 - 14: (a) Experimentally determined phase diagram of water, EtOH, and THL at 25 °C. The gray shaded area represents the miscibility gap ( $2\Phi$ ), which is separated from the monophasic area ( $1\Phi$ ). The red squares identify the compositions in which the solubility of the catalyst is studied. The green line shows the phase border when water contains 15 % (w/w) meglumine. (b) Maximum absorbance of the catalyst saturated in the solutions along the phase diagram (red squares in (a)). The aqueous (aq.) pseudo-phase contains either no meglumine or 0.5 mol/kg of meglumine with an adjusted pH of 12.2. During sample preparation, the solvents were supersaturated with 10 mM of the catalyst. (c) Correlation function of W/EtOH/THL 37/48/15 (w/w/w) with and without meglumine.

Figure 4 - 14(a) shows the ternary phase diagram of water, EtOH, and THL, which has already been discussed in the previous Chapter 3. The most pronounced structuring has been located between mixtures 3 and 4. The presence of meglumine (green curve) has again no distinct impact on the miscibility gap. Figure 4 - 14(b) compares the solubility of NDI in solutions along the phase diagram (red squares in Figure 4 - 14(a)) with and without meglumine in the aqueous phase. Based on the previous results, the additive is applied in combination with pH control (12.2). In the absence of meglumine, the absorbance of the

catalyst is of minor intensity (green curve). Moreover, no correlation with the extent of structuring is observed (compare Chapter 3.5 for the DLS experiments). The maximum absorbance is detected in the visible range. The corresponding absorbance spectra are provided in the Supporting Information (see Figure S.4 - 11). In solutions containing meglumine, the absorbance decreases with an increasing amount of THL, which correlates with a decrease in the water and thus meglumine content (blue curve). The solubility of the catalyst is, therefore, again a result of beneficial interactions of meglumine and NDI. Figure 4 - 14(c) represents the correlation function of the solution W/EtOH/THL 37/48/15 (w/w/w), which is selected as the reaction solvent due to high water content and a pronounced DLS signal. As observed in W/EtOH/TriA, meglumine decreases the detected correlation function. Hence, the previous decrease is not only a result of the hydrolysis of TriA. The meglumine seems to reduce the aggregation tendency of water and oil molecules without having a distinct impact on the miscibility gap.

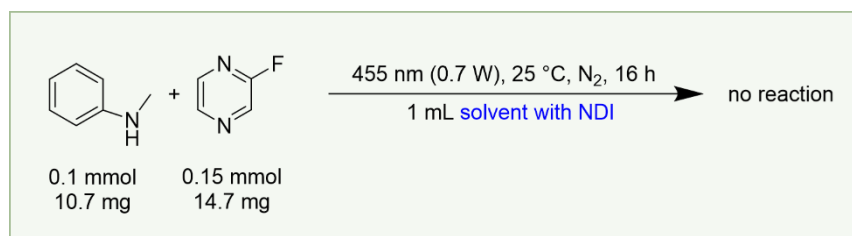


Figure 4 - 15: Reaction scope carried out in meglumine/water and meglumine/W/EtOH/THL solvent mixtures. 0.1 mM NDI is dissolved by supersaturation in meglumine/water mixtures (15/85 (w/w)) without and with pH control (12.2). In addition, the solvent mixture is mixed to (pseudo-)ternary mixture of W/EtOH/THL (37/48/15), whereby the water phase contains both meglumine and NDI.

In the next step, new reactions are performed in homogeneous, transparent solutions. For this purpose, NDI is dissolved in meglumine/water mixtures with and without pH adjustment. The mixtures are either used directly as reaction solvent or mixed with EtOH and THL to form a pseudo-ternary mixture W/EtOH/THL 37/48/15 (w/w/w). The reactions tested so far seem, however, too challenging for the beginning, so no product is detected. It is known that C-F bonds are very strong<sup>37</sup>, complicating its activation. Besides, triethylamine is omitted due to the presence of the base NaOH, which may not be able to reduce the catalyst. The collaboration on this topic with the group of Prof. König will continue, and the reactions are still ongoing. Nevertheless, these new insights into the photochemistry of 1,8:4,5-naphthalenetetracarboxydiimide and its solubilization by meglumine confirm the expected potential of the catalyst for green photocatalysis in water.

### 4.3.2 Enforcement of electronic-donor-acceptor formation

Due to the great impact of meglumine on the reaction, the role of meglumine is studied in several photochemical C-C and C-S coupling reactions in the absence of an additional photocatalyst. First, the C-C coupling between the electron acceptor 4-bromobenzonitrile (**a1**) and the electron donor indole (**b1**) is considered (see Figure 4 - 16(a)). In the presence of meglumine and irradiation with light (385 nm), the C2- and C7-arylated products (1:1, **c1**) are synthesized in 83 % yield. No product is detected without irradiation, and only 34 % is obtained in the absence of meglumine. Replacing the reaction solvent water by an organic solvent, such as DMSO or THF, yields either no product or only traces (< 1 %). Accordingly, both water and meglumine play a crucial role in this photochemical conversion. Additional control experiments are provided in the Supporting Information (see Table S.4 - 4). Moreover, this chapter focuses on single reactions to highlight the discovered mechanism. However, both the C-C and the C-S coupling reactions are successfully carried out with a great variety of substrates, which can be found in the corresponding publication.<sup>1</sup> The numbering corresponds to that in the publication and is, therefore, not always consecutive.

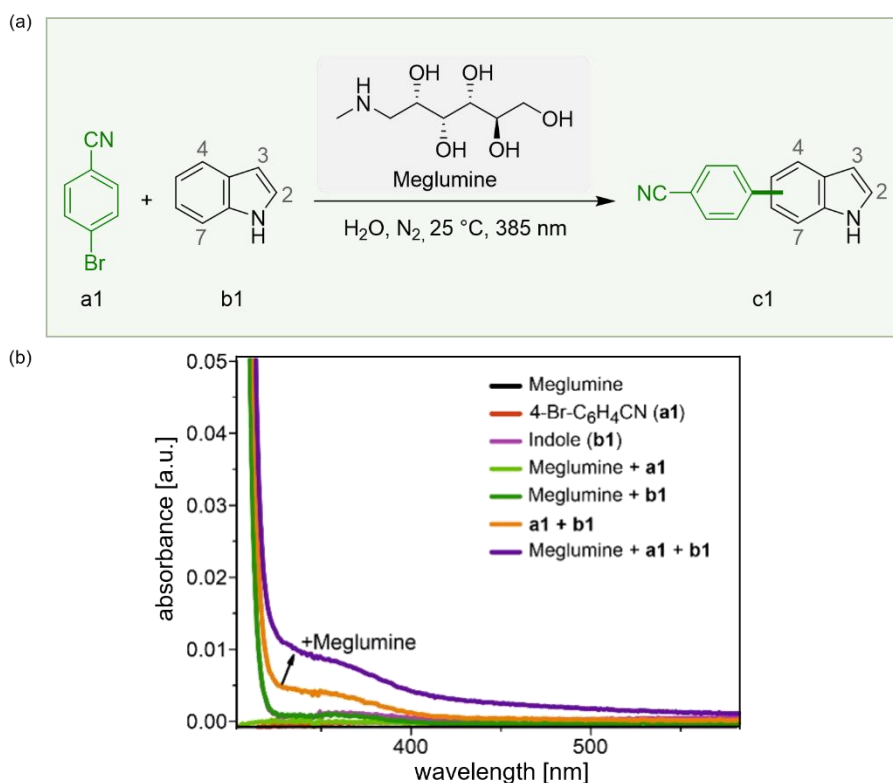


Figure 4 - 16: (a) Photochemical cross-coupling of 4-bromobenzonitrile (**a1**) with indole (**b1**) in the presence of meglumine. (b) UV/VIS absorbance measurements of different compounds in water.

UV/VIS absorbance measurements of different reagent combinations are recorded (see Figure 4 - 16(b)). Mixing the reactants **a1** and **b1** displays a new absorption band in the visible region (orange curve), which is assigned to an electron donor-acceptor (EDA) complex. The intensity of the absorption band is significantly higher with (purple curve) than

without meglumine. In contrast, there is no distinct absorption in the same range for mixtures of meglumine with only one of the substrates (green curves). NMR measurements confirm that meglumine does not form any tight complexes with **a1** or **b1** alone. Only aggregates composed of both **a1** and **b1**, interacting via  $\pi$ - $\pi$ -stacking, are able to interact with meglumine (see Figure S.4 - 13, Figure S.4 - 14; more detailed NMR studies can again be found in the associated publication<sup>1</sup>). As a consequence, meglumine is expected to improve the solubility of the EDA complex, which enhances the photochemical C-C coupling.

After exploration of the photochemical C-C cross-coupling in water, C-S coupling reactions are investigated. The reaction conditions are optimized using 4-chlorobenzonitrile and benzenethiol as model substrates. In the presence of meglumine and irradiation with light (385 nm), a yield of 91 % is obtained. In the absence of meglumine or light, no product is detected. Meglumine is thus indispensable for this photochemical transformation.

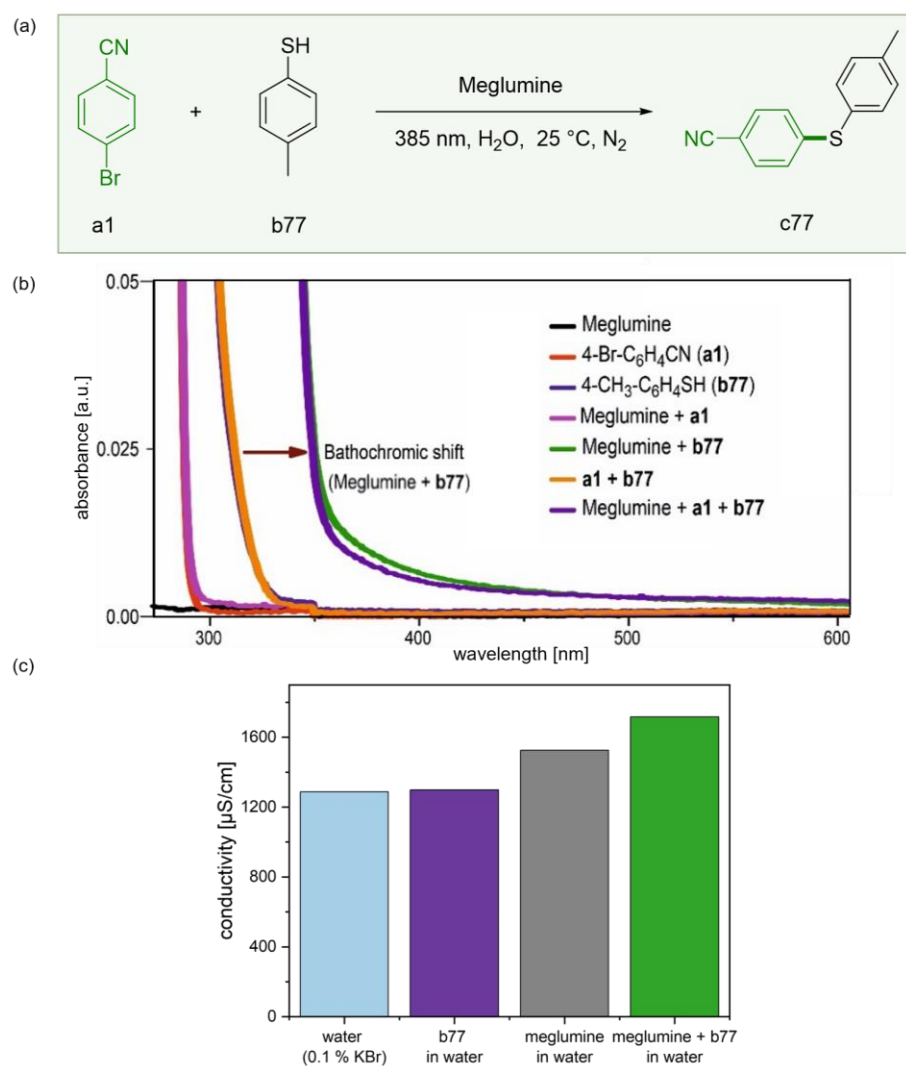


Figure 4 - 17: (a) Photochemical cross-coupling of 4-bromobenzonitrile (**a1**) with 4-methylbenzenethiol (**b77**) in the presence of meglumine. (b) UV/VIS absorbance measurements of different compounds in water. (c) Conductivity measurements of aqueous solutions at 25 °C. All solutions contain 0.1 % (w/w) KBr to ensure a sufficient amount of charge carrier. Besides, the solutions contain meglumine, **b77**, and both or none of the additives.

Replacing water by DMF decreased the yield to 30 %. Therefore, the solvent water has again a pivotal role. The control experiments are once more summarized in the Supporting Information (see Table S.4 - 5). The reaction mechanism of the C-S coupling reactions is studied with the substrates **a1** and 4-methylbenzenethiol (**b77**) (see Figure 4 - 17(a)). The coupled product is obtained in 84 % yield. In contrast to the C-C coupling, no changes in the UV/VIS absorption are observed when mixing the two substrates in water (see Figure 4 - 17(b)). However, the addition of meglumine to **b77** in water results in a bathochromic shift, indicating an interaction between the two molecules. Conductivity measurements confirm this observation (see Figure 4 - 17(c)). In the absence of meglumine, 4-methylbenzenethiol does not lead to a significant change in conductivity. As a basic compound, meglumine itself increases conductivity. However, the highest conductivity is measured when both meglumine and **b77** are present. Accordingly, an acid-base reaction, deprotonating **b77**, takes place, which leads to a higher amount of charge carrier and, thus, a higher conductivity.

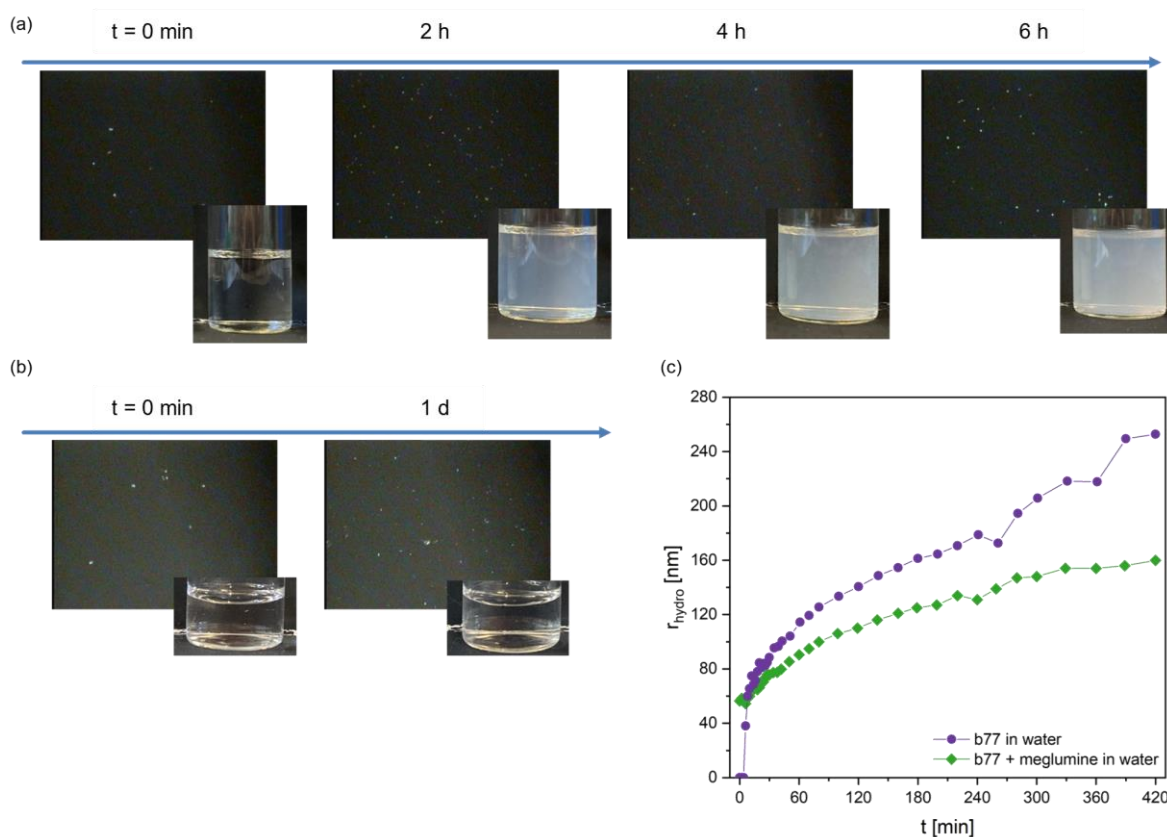


Figure 4 - 18: (a) Visual observations of **b77** in an aqueous solution of meglumine after filtration ( $t = 0$  min). (b) Visual observations of **b1** in an aqueous solution of meglumine. (a,b) The samples are filtered ( $t = 0$  min) and studied using a polarizing microscope with 100-fold magnification and a camera over time. (c) Hydrodynamic radii as a function of time in aqueous solutions containing **b77** with (green curve) and without (purple curve) meglumine determined by DLS measurements at 25 °C.

The visual observations also differ for the C-C and C-S coupling reactions (see Figure 4 - 18(a,b)). While the mixture of **b1** and meglumine stays transparent and clear for at least 1 d (b), the mixture of **b77** and meglumine becomes turbid with time (a). In both mixtures, tiny crystals are present immediately after filtration caused by rapid precipitation of the substrate. The solutions thus appear to be supersaturated with the substrate after filtration. Due to the distinct turbidity of the mixture of **b77** and meglumine with time, the substrate of the C-S coupling reaction is studied by light scattering (see Figure 4 - 18(c)). DLS measurements show the presence of aggregation of **b77** in water with and without meglumine. In the absence of meglumine, no aggregates are initially detected, and a signal is detected after several minutes, representing fast-growing aggregates which are expected to originate from the crystal growth of the substrate itself. In the presence of meglumine, aggregates of almost 60 nm are detected at the beginning of the measurement (immediately after filtration). Over time, the presence of meglumine significantly reduces the rate of aggregation. After 7 h, these aggregates have a size of 253 nm without meglumine, while the aggregates in the meglumine-containing solution are only 160 nm in size at the end of the measurements. As a consequence, it is assumed that meglumine acts as an anti-stacking agent for **b77**. The interactions between meglumine and the aromatic compound seem to reduce the  $\pi$ - $\pi$ -stacking interactions between individual **b77** molecules and, therefore, slow down its crystal growth and, finally, its precipitation. In that way, the substrate stays longer in solution and remains active for the C-S coupling.

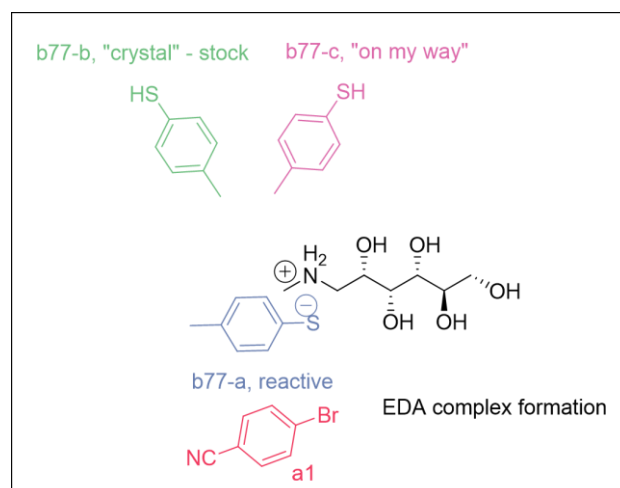


Figure 4 - 19: Schematic illustration of the 3 different types of **b77** and their interaction with **a1** and meglumine.

NMR measurements reveal the presence of 3 different types of 4-methylbenzenethiol (**b77-a**, **b77-b**, **b77-c**). The ratio is determined to be 100 : 52 : 11 : 0.4 (meglumine : **b77-a** : **b77-b** : **b77-c**). The most abundant species **b77-a** is in closest contact with meglumine and considered as the *reactive* species. **b77-b** diffuses much slower than the other substrate species and is determined to be in contact with meglumine and **b77-a**. This species is assigned

to stock substrate. The third species **b77-c** has the lowest concentration and only interacts with **b77-a**. It is designated as free, en route between the other domains (see Figure 4 - 19 and Figure S.4 - 15 - Figure S.4 - 17 in the Supporting Information). Overall, the meglumine activates the thiol-substrate by deprotonation and keeps it in solution. The activated **b77** can thus form an EDA complex with **a1**, which can be converted photochemically. In contrast, the meglumine only interacts with the already formed EDA complex in the case of the C-C coupling, enhancing its solubility. The different mechanisms are illustrated in Figure 4 - 20.

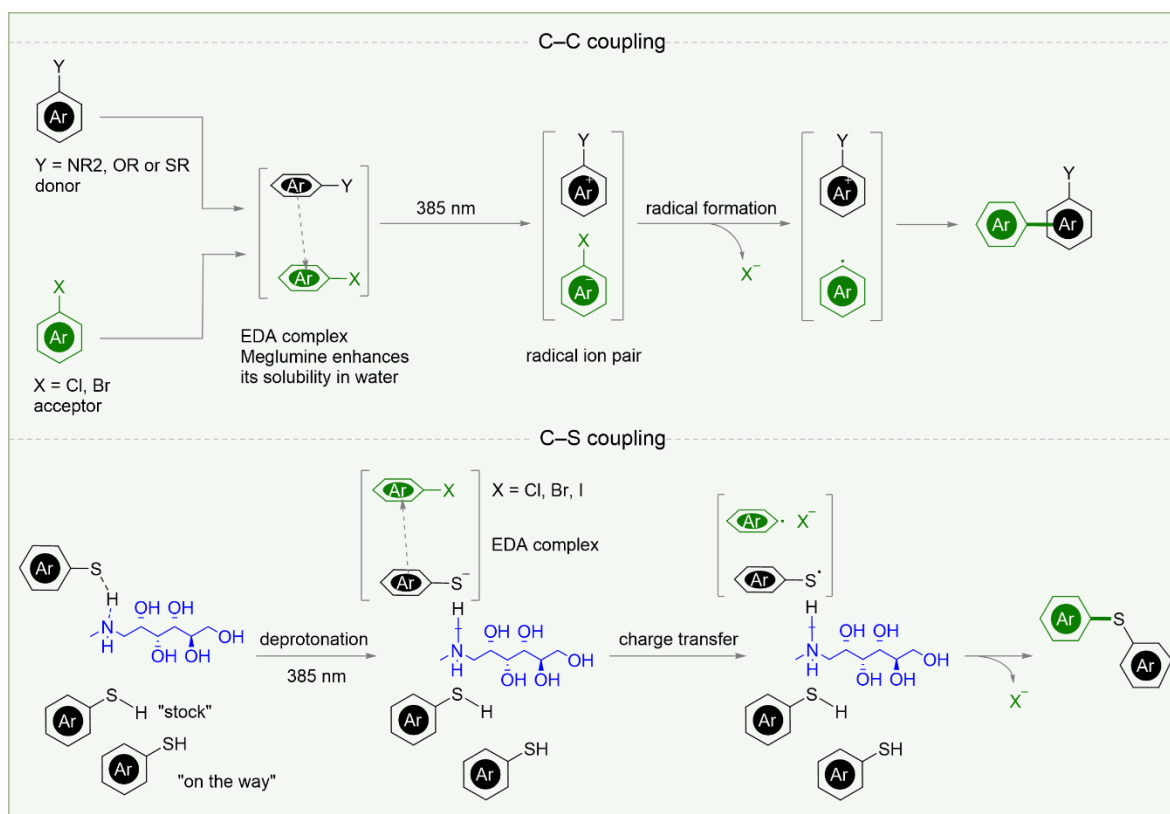


Figure 4 - 20: Proposed reaction mechanisms for C-C and C-S coupling reactions.

## 4.4 Conclusion and outlook

In this chapter, the impact of meglumine on the solubilization of aromatic compounds is investigated in several cases. In particular, the effect on cross-coupling reactions is considered in this context. In the first part, the focus is on the poorly soluble photocatalyst 1,8:4,5-naphthalenetetracarboxdiimide. The best solubility of the catalyst is achieved in DMSO with a concentration of 2 mM. Electrochemical measurements reveal a promising excited state reduction potential of  $-3.0$  V (vs. SCE). Although meglumine possesses salting-out properties, the additive enables the solubilization of the catalyst in aqueous solutions. Several alkanolamines are compared with respect to their solubilization power. The best result is obtained using an aqueous triethanolamine solution with an adjusted pH of 12.2, followed by an aqueous meglumine solution at the same pH. A pH higher than 11 in combination with an additive with a sufficient number of hydroxy groups, thus, solubilize the catalyst best. Besides, the arrangement of the hydroxy groups also influences the interactions with the catalyst, which demonstrates the better result with triethanolamine. A concentration of 1 mM of the catalyst can be dissolved in the meglumine solutions (pH 12.2). The exact reason for the great solubilizing effect of meglumine on the catalyst has not yet been clarified. Accordingly, in-depth NMR studies should be performed in order to gain deeper information. For this purpose, the currently used NDI should be replaced by a branched and thus better soluble derivative. Otherwise, the dissolved concentrations may still be too low, in particular in the absence of NaOH. Overall, an aqueous reaction solvent with a green additive and an organic photocatalyst is generated. Photocatalytic C-C coupling reactions are presented with good to excellent yields. An excellent yield for a challenging reaction type, however, is still lacking. Furthermore, the aqueous solvent is mixed with ethanol and triacetin, which shifts the maximum absorbance from the UV to the VIS. Due to an instability of triacetin under basic conditions, the reaction outcome deteriorates. For this reason, the oil is replaced by the stable tetrahydro linalool. Initial reactions carried out have been too challenging and therefore have not yielded any product. Accordingly, a variety of reaction types still have to be tested. Based on the great redox potential, a good performance of the catalyst is also expected for demanding reaction types. As a consequence, it seems worthwhile to further optimize the reaction conditions. In this context, the impact of the base sodium hydroxide, applied for pH adjustment, has to be taken into account. If the conditions are too basic, promoting competing side reactions, lower catalyst concentrations of 0.4 mM in the absence of NaOH should be preferred. In addition, the initial reactions in the meglumine/water system reveal a significant impact of meglumine on the reaction. In the absence

of meglumine, the reaction yield is decreased by 35 %. This can either be attributed solely to the solubilizing effect of meglumine, or meglumine also has an influence on the cross-coupling reaction.

For this reason, the impact of meglumine on photochemical C-C and C-S coupling reactions in the absence of an additional photocatalyst is investigated in water at room temperature. A great variety of substrates as well as measuring techniques, including in-depth NMR analysis, DLS experiments, conductivity measurements, and optical methods, are applied. This allows unraveling 2 different modes of operation of meglumine during the reactions. In the case of C-C coupling, electron donor-acceptor (EDA) complexes formed between the aromatic substrates via  $\pi$ - $\pi$ -stacking. The EDA complex interacts with meglumine, which improves its solubility and, therefore, enhances the photochemical transformation. In the case of C-S coupling, the meglumine already interacts with one of the substrates. The benzenethiol (derivative) is deprotonated and thus activated by an acid-base reaction with meglumine. In addition, the interaction of the aromatic compound with meglumine has a kind of anti-stacking effect since  $\pi$ - $\pi$ -interactions are hindered. This slows the precipitation of the substrate and therefore keeps to substrate in solution for the reaction. The activated substrate then forms an EDA complex, which enables the final transformation.

The present chapter confirms the solubilizing effect of meglumine on aromatic compounds and reveals the great potential of the additive for application in organic cross-coupling reactions. Moreover, the results demonstrate that organic reactions can also be transferred to water without creating a hydrophobic pseudo-phase, but with the aid of simple green additives, such as meglumine.

## 4.5 Supporting information

### 4.5.1 Solubilization and characterization of the photocatalyst 1,8:4,5-naphthalenetetracarboxdiimide

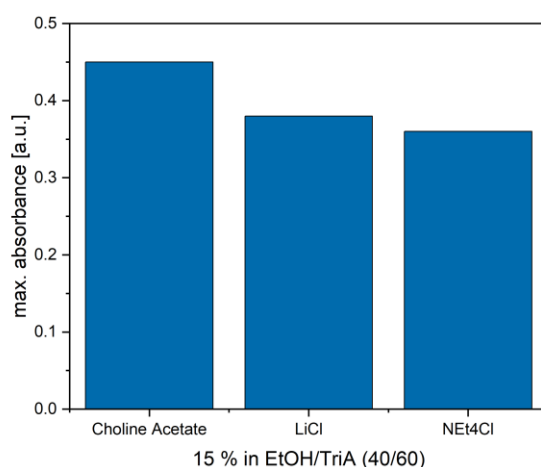


Figure S.4 - 1: Maximum absorbance of NDI saturated in EtOH/TriA mixtures containing different salts. The difference in absorbance of NDI in ChoAc/EtOH/TriA compared to Figure 4 - 4 is due to a change in the measuring protocol. Absorbance was measured in a black Greiner 96 multiwell, half area,  $\mu$ Clear microtiter plate with a flat bottom instead of cuvettes. Moreover, the solvents were only saturated at room temperature. Nevertheless, the comparison within the salt group allows conclusions to be drawn. Although the best result is obtained with ChoAc, the other salts LiCl and NEt<sub>4</sub>Cl enable good NDI absorbance as well. The absorbance in the solvent system EtOH/TriA (40/60) in the absence of the salt cannot be provided for the changed measuring conditions. However, the addition of 15 % ChoAc to EtOH/TriA increased the absorbance by a factor of about 2.6 (under the conditions in Figure 4 - 4). Accordingly, an absorbance of about 0.17 is expected in EtOH/TriA in the absence of any salt under the present conditions. All proportions are provided by weight (w/w).

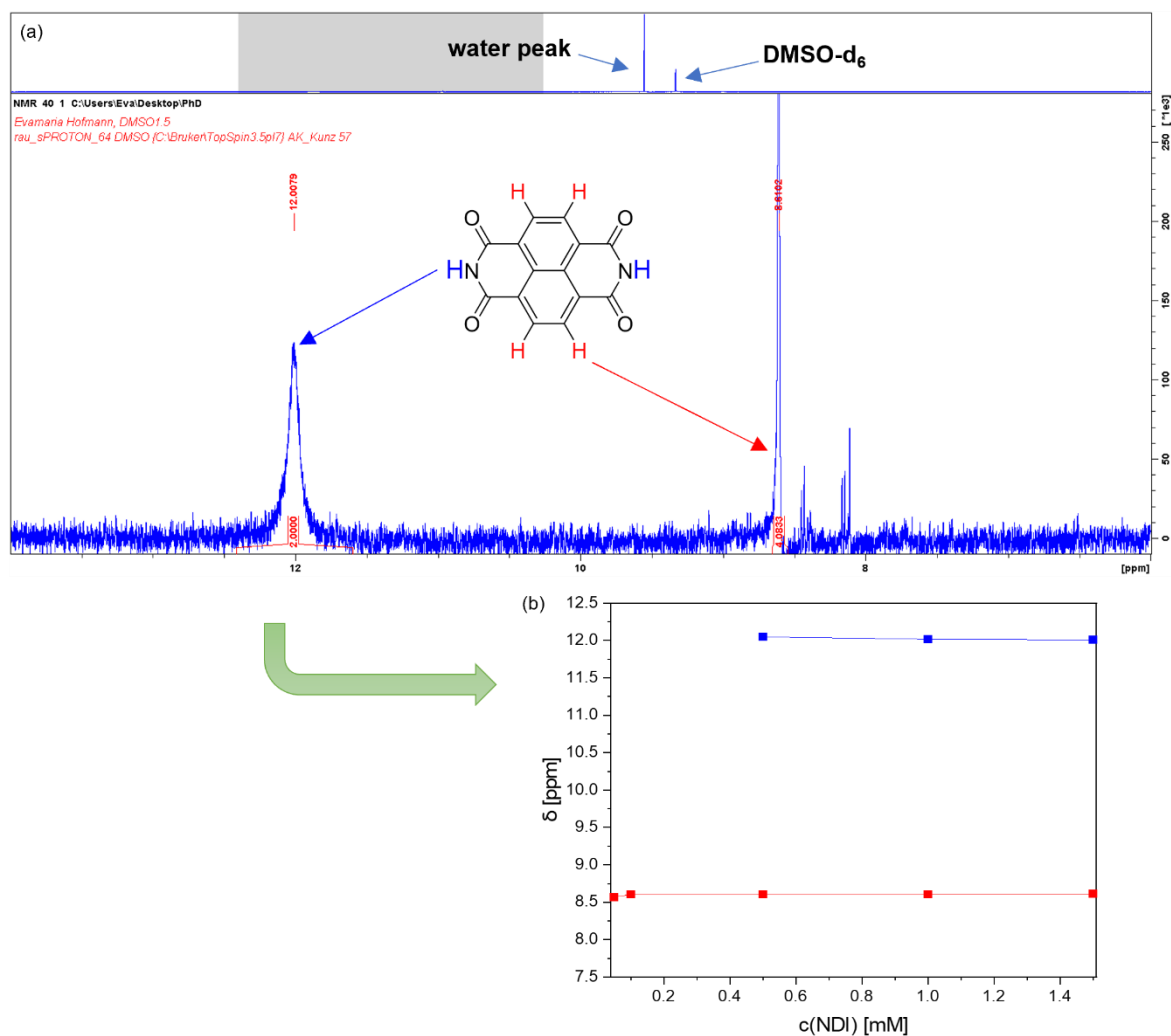


Figure S.4 - 2: (a)  $^1\text{H}$ -NMR spectrum of NDI dissolved in  $\text{DMSO-d}_6$  with the assigned protons of NDI. (b) The chemical shift  $\delta$  of the assigned protons as a function of the catalyst concentration.  $\pi$ -Stacking should result in a decrease in the chemical shift.<sup>38</sup> The stacking cannot be confirmed by the experiments. The dissolved concentrations may be too low, or stacking may be too strong so that the interactions occur already at very low concentrations.

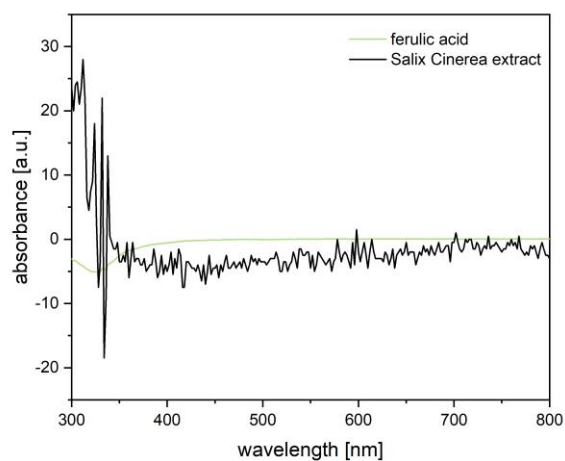


Figure S.4 - 3: Absorbance spectra of aqueous solutions of 0.1 mol/kg ferulic acid in water at pH 12.2 or 1 % (w/w) of an extract of the plant *Salix Cinerea* in water/EtOH 52/48 (w/w) after supersaturation with 10 mM of NDI. The solvent conditions were adapted to provide complete solubility of the additives. With regard to the absorbance spectra, it is assumed that no catalyst is dissolved. In both cases, the measurement of a clear baseline was problematic. However, the solubilization of the catalyst should nevertheless result in more distinct peaks, at least at higher wavelengths.

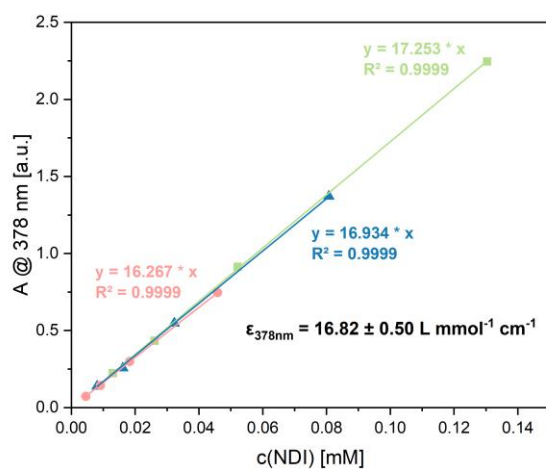


Figure S.4 - 4: Calibration curves of NDI in DMSO. The determined extinction coefficient is the average of 3 measurements.

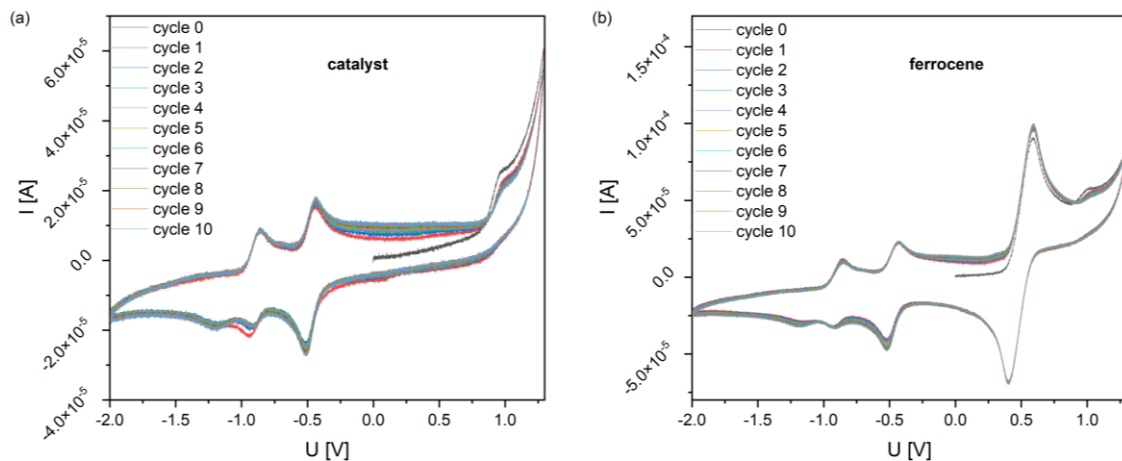


Figure S.4 - 5: Cyclic voltammograms measured in 10 cycles of the catalyst (a) and with ferrocene (b) in DMSO (in the absence of meglumine).

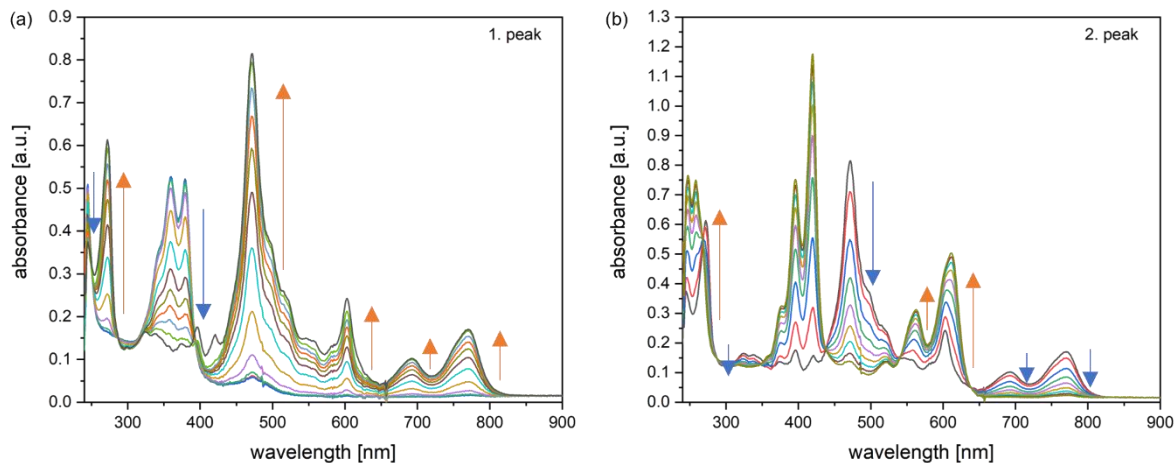


Figure S.4 - 6: UV/VIS absorption SEC of NDI in DMSO (in the absence of meglumine) in the range of  $-0.05$  V to  $-0.53$  V (a) and in the range of  $-0.53$  V to  $-0.85$  V (vs. Ag) (b).

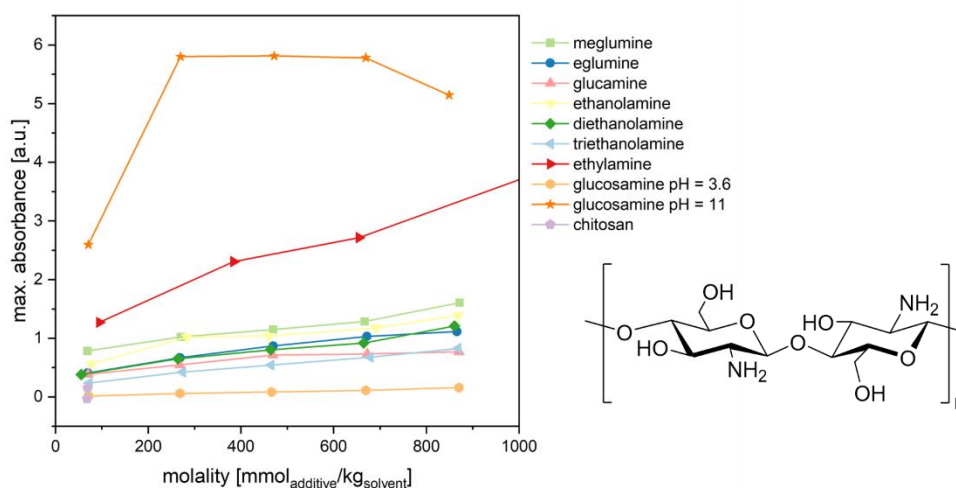


Figure S.4 - 7: Maximum absorbance of NDI saturated with 10 mM in aqueous solutions containing different additives as a function of the additive molality (without pH control). The NDI absorbance increases with an increasing amount of additive. The glucosamine solution with an adjusted pH of 11, however, behaves again differently. First, a sharp increase is detected. Then the absorbance stagnates before decreasing again. At the moment, no well-founded explanation can be provided. Further experiments may be necessary, but it has to be noted that the measurements are only performed once. Accordingly, the glucosamine measurements may just be an outlier. Furthermore, initial experiments are performed using chitosan. The molecular structure is shown in the figure. The molality is based on the molar mass of a single monomer. In that way, comparison of the results of chitosan and glucosamine mainly differ in the distance of the functional groups present and not in their total number. However, due to impurities, the chitosan solution is strongly acidic with a pH of 3. For this reason, no NDI is dissolved. The addition of a base results in the precipitation of a black compound. In the next attempt, this compound should be filtered. The chitosan is not expected to precipitate at higher pH, nor should the polymer be colored. Filtering should remove the impurities and allow better investigation of the compound. The chitosan was gratefully received from Maximilian Rothammer (Ph.D. student at the Institute for Biogenic Polymer, TUM Campus Straubing, Germany).

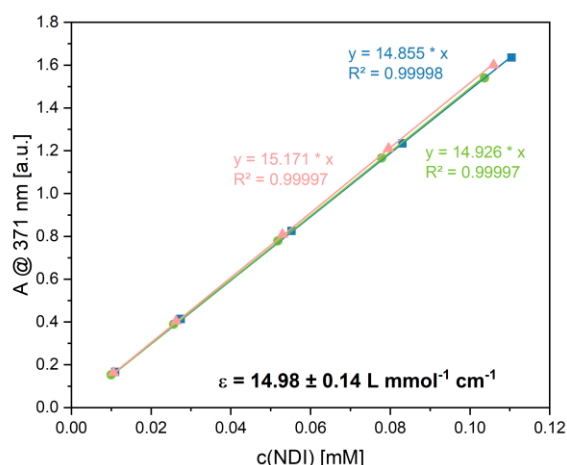


Figure S.4 - 8: Calibration curves of NDI in an aqueous solution containing 1 mol/kg meglumine with an adjusted pH of 12.2. The determined extinction coefficient is the average of 3 measurements.

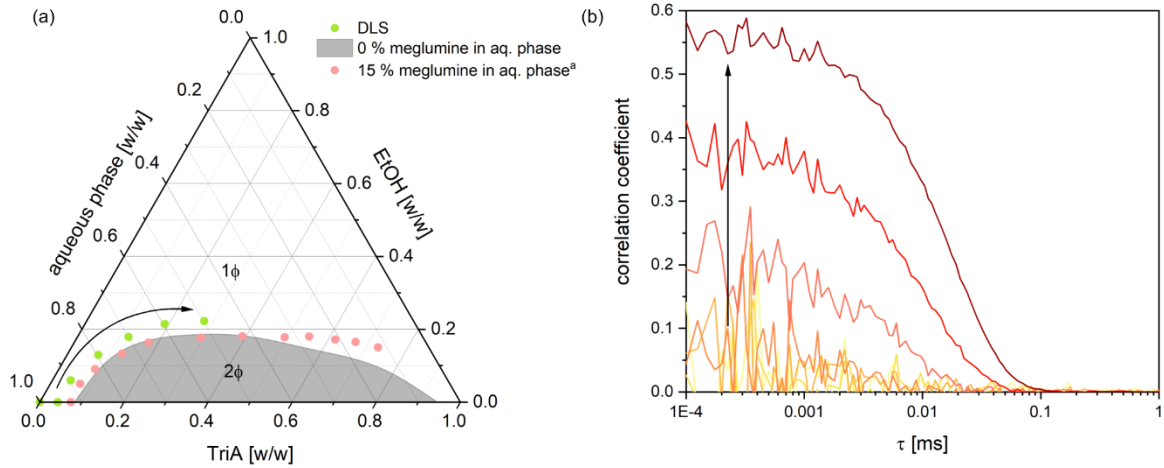


Figure S.4 - 9: (a) Experimentally determined phase diagram of water, EtOH, and TriA at 25 °C. The gray shaded area represents the miscibility gap ( $2\Phi$ ), which is separated from the monophasic area ( $1\Phi$ ). The rose dots identify the mixtures measured by means of DLS. The green dots represent the determined phase border in the presence of 15 % (w/w) meglumine in the aqueous phase. <sup>(a)</sup>Data gratefully received from Dr. Pierre Degot (former Ph.D. student at the University of Regensburg, Germany).<sup>8</sup> (b) Corresponding correlation functions obtained by DLS measurements at 25 °C. With an increasing amount in TriA, the correlation intercept increases, indicating an increasing aggregation on a mesoscopic scale.

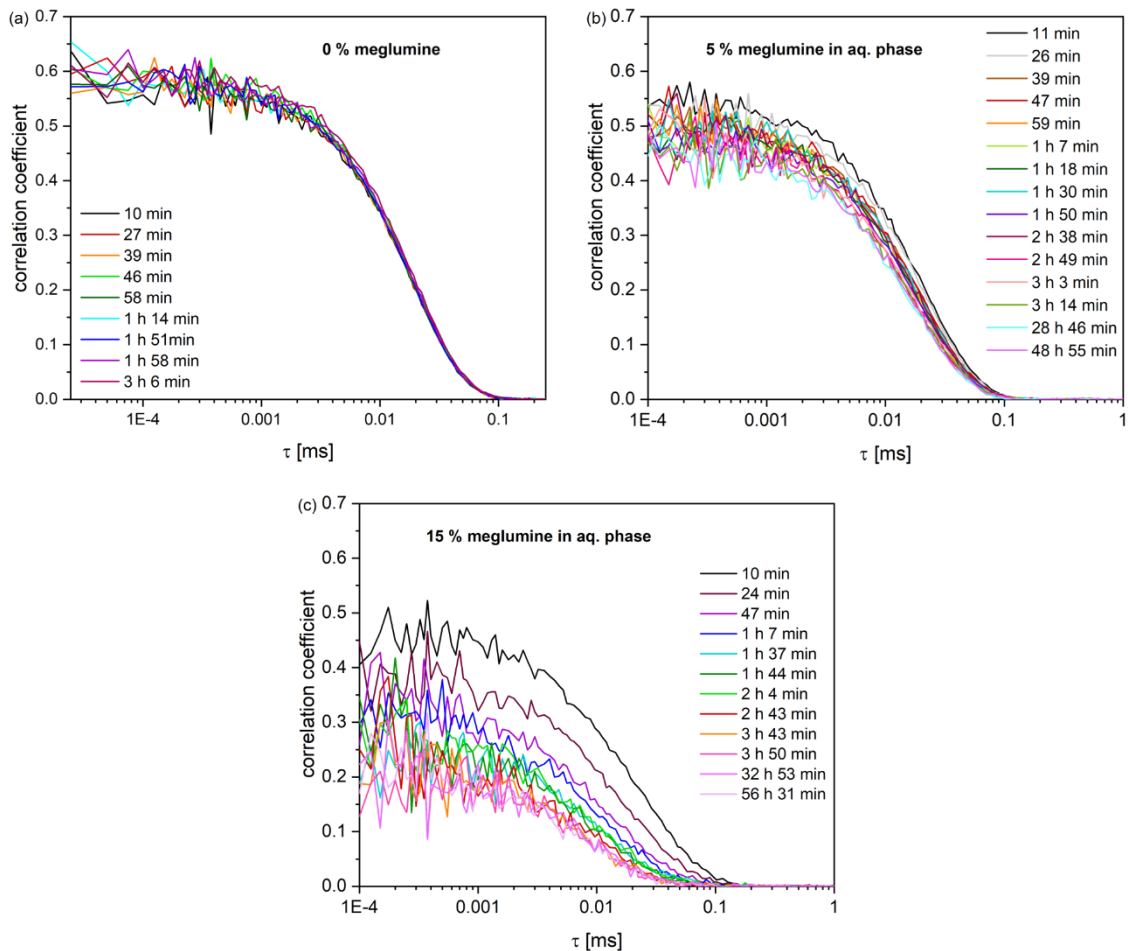


Figure S.4 - 10: Correlation functions of W/EtOH/TriA (50/22/28 (w/w/w)) obtained by DLS measurements at 25 °C as a function of time. The time measurement started with the mixing of the (pseudo-)ternary solution. The ternary mixture contained 0 % (a), 5 % (b), or 15 % (w/w) meglumine (c) with respect to the water component.

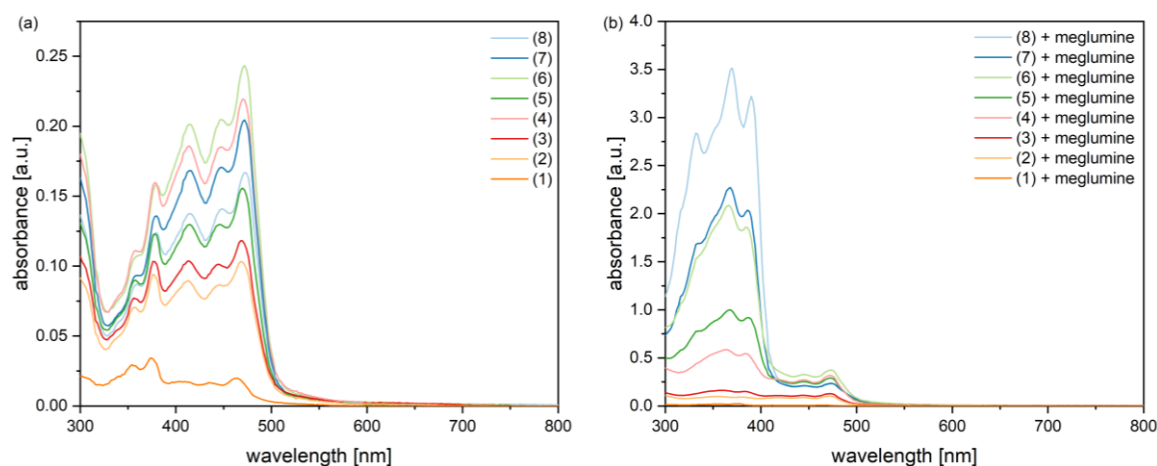


Figure S.4 - 11: Absorbance of NDI saturated with 10 mM in different mixtures of W/EtOH/THL (for the compositions, see Figure 4 - 14) with (b) and without 0.5 mol/kg meglumine in water (a). When meglumine is added, the pH is adjusted to 12.2.

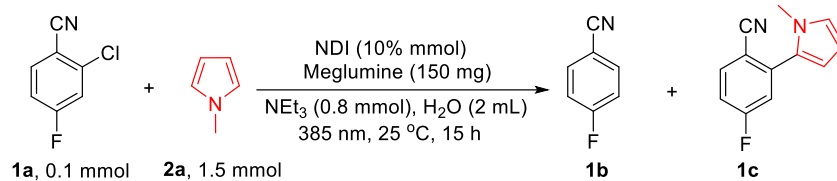
### General reaction procedure for NDI-catalyzed reactions

Unless specified otherwise, a mixture of 0.1 mmol arylhalobenzene (such as **1a**), 1.5 mmol aryl heterocyclic compound (such as **2a**), 10 % mmol NDI, 150 mg meglumine and 0.8 mmol  $\text{NEt}_3$  was added to an oven-dried 5 mL snap vial equipped with a magnetic stirring bar. The capped vial was evacuated and back filled with  $\text{N}_2$  for 3 times, and 2 mL solvent (such as  $\text{H}_2\text{O}$ ) was added to the vial by syringe. The solution was then bubbled with  $\text{N}_2$  for 5 min. Then, the cap was sealed with parafilm. The reaction mixture was stirred and irradiated with a 385 nm (2.4 W) LED (for the screening of the light sources, 400 nm and 455 nm LEDs were used) at 25 °C for 15 h, then diluted with ethyl acetate (2 mL) and filtered through a plug of celite ( $\varnothing$  3 mm x 8 mm). After addition of *n*-dodecane (0.2 mmol) as an internal standard for calibration, the product yield was determined by GC-MS.

Table S.4 - 1: Optimization experiments of NDI-catalyzed cross-coupling reactions. <sup>a</sup>The yields were determined by GC-MS analysis and are averages of two runs. The photograph illustrates the reaction solutions in the absence of the starting materials **1a** and **2a**.

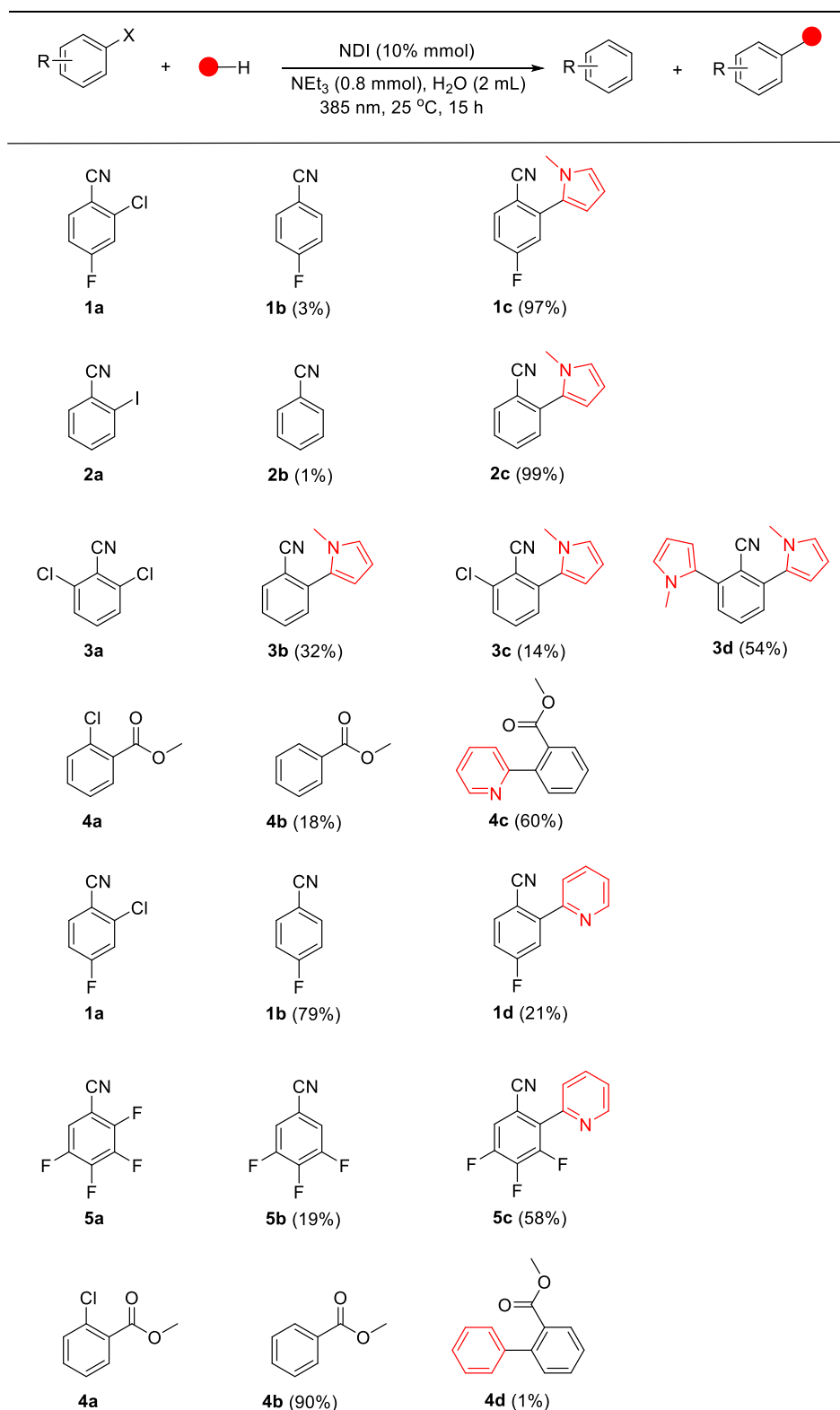
entry	<b>2a</b>	meglumine	NEt <sub>3</sub>	light (nm)	yield of <b>1b</b> (%)	yield of <b>1c</b> (%)
1	2.5 mmol	150 mg	0.8 mmol	455	22	75
2	2.5 mmol	150 mg	0.8 mmol	400	10	88
3	2.5 mmol	150 mg	0.8 mmol	385	7	93
4	2.5 mmol	100 mg	0.8 mmol	385	9	90
5	2.5 mmol	200 mg	0.8 mmol	385	7	93
6	2.5 mmol	300 mg	0.8 mmol	385	7	93
7	2.0 mmol	150 mg	0.8 mmol	385	5	95
8	1.5 mmol	150 mg	0.8 mmol	385	<b>3</b>	<b>97</b>
9	1.0 mmol	150 mg	0.8 mmol	385	12	88
10	0.5 mmol	150 mg	0.8 mmol	385	35	65
11	1.5 mmol	150 mg	0.4 mmol	385	8	92
12	1.5 mmol	150 mg	0.2 mmol	385	12	80

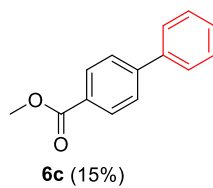
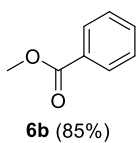
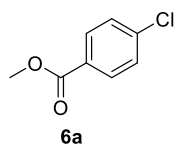
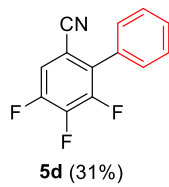
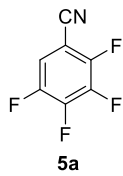
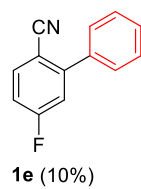
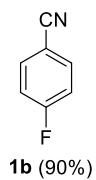
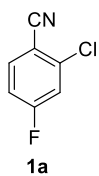
Table S.4 - 2: Control reactions of NDI-catalyzed cross-coupling reactions. <sup>a</sup>The yields were determined by GC-MS analysis and are averages of two runs.



entry	deviations from optimized conditions	yield of <b>1b</b> (%)	yield of <b>1c</b> (%)
1	None	3	97
2	No light	n.d.	n.d.
3	No NDI	n.d.	5
4	No meglumine	8	60
5	No NDI, No meglumine	n.d.	trace

Table S.4 - 3: Variation of the substrates in the NDI-catalyzed cross-coupling reactions. <sup>a</sup>The yields were determined by GC-MS analysis and are averages of two runs.





## 4.5.2 Enforcement of electronic-donor-acceptor formation

All reagents were purchased from Alfa-Aesar, TCI, Sigma-Aldrich, ABCR, Acros, or Fluorochem and were checked for purity by GC-MS and/or  $^1\text{H-NMR}$  spectroscopy and used as received. Unless noted otherwise, all manipulations were performed using standard Schlenk manifold technique. Extra-dry anhydrous *N,N*-dimethylformamide, and dimethyl sulfoxide were purchased from Acros.

### 4.5.2.1 General reaction procedure

#### 4.5.2.1.1 Procedures for the optimization of the reaction conditions (C–C coupling)

Unless specified otherwise, a mixture of 4-bromobenzonitrile, indole, and an additive (meglumine) was added to an oven-dried 5 mL snap vial equipped with a magnetic stirring bar. The capped vial was evacuated and back filled with  $\text{N}_2$  for 3 times, and 2 mL solvent ( $\text{H}_2\text{O}$  or other organic solvents) was added to the vial by syringe. The solution was then bubbled with  $\text{N}_2$  for 5 min. Then, the cap was sealed with parafilm. The reaction mixture was stirred and irradiated with a 385 nm (2.4 W or 700 mW) LED (for the screening of the light sources, 365 nm, 385 nm, 400 nm, 455 nm, and 528 nm LEDs were used) at 25 °C (for the control experiments, reactions were also conducted under 60 °C and 90 °C) for 15 h (according to different conditions, the reaction time has been adjusted, see details in the optimization tables), then diluted with 2 mL ethyl acetate and filtered through a plug of celite ( $\varnothing$  3 mm x 8 mm). After the addition of *n*-dodecane (0.2 mmol) as an internal standard for calibration, the product yield was determined by GC-MS.

#### 4.5.2.1.2 Procedures for the isolation of the final products (monoarylation C–C coupling)

Unless specified otherwise, a mixture of **a**–(hetero)aryl halides (0.5 mmol), **b**–electron donor substrate (0.75 mmol) and meglumine (1.25 mmol) was added to an oven-dried 10 mL snap vial equipped with a magnetic stirring bar. The capped vial was evacuated and back filled with  $\text{N}_2$  for 3 times, and  $\text{H}_2\text{O}$  (6 mL) was added to the vial by syringe. The solution was then bubbled with  $\text{N}_2$  for 5 min. Then, the cap was sealed with parafilm. The reaction mixture was stirred and irradiated with a 385 nm LED (2.4 W) at 25 °C for 15 h (reaction time and temperature were adjusted according to different substrates). Saturated brine (5 mL) was then added to the reaction system and extracted with ethyl acetate (10 mL x 3). The combined organic phase was then washed with  $\text{H}_2\text{O}$  (10 mL), dried over sodium sulfate, and concentrated under vacuum. The residue was purified by silica gel flash chromatography to give the desired product.

**4.5.2.1.3 Procedures for the optimization of the reaction conditions (C–S coupling)**

Unless specified otherwise, a mixture of 4-chlorobenzonitrile, benzenethiol, and an additive (meglumine) was added to an oven-dried 5 mL snap vial equipped with a magnetic stirring bar. The capped vial was evacuated and back filled with N<sub>2</sub> (for the control experiments, reaction under air was also conducted) for 3 times, and 2 mL solvent (H<sub>2</sub>O or other organic solvents) was added to the vial by syringe. The solution was then bubbled with N<sub>2</sub> for 5 min. Then, the cap was sealed with parafilm. The reaction mixture was stirred and irradiated with a 385 nm (2.4 W or 700 mW) LED (for the screening of the light sources, 365 nm, 385 nm, 400 nm, and 528 nm LEDs were used) at 25 °C (for the control experiments, reactions were also conducted under 60 °C) for 15 h, then diluted with 2 mL ethyl acetate and filtered through a plug of celite (Ø 3 mm × 8 mm). After the addition of *n*-dodecane (0.2 mmol) as an internal standard for calibration, the product yield was determined by GC-MS.

**4.5.2.1.4 Procedures for the isolation of the final products (C–S coupling)**

Unless specified otherwise, a mixture of (hetero)aryl halides (0.5 mmol), benzenethiols (0.75 mmol) and meglumine (1.25 mmol) was added to an oven-dried 10 mL snap vial equipped with a magnetic stirring bar. The capped vial was evacuated and back filled with N<sub>2</sub> for 3 times, and H<sub>2</sub>O (6 mL) was added to the vial by syringe. The solution was then bubbled with N<sub>2</sub> for 5 min. Then, the cap was sealed with parafilm. The reaction mixture was stirred and irradiated with a 385 nm LED (700 mW) at 25 °C for 15 h (reaction time and temperature were adjusted according to different substrates). Saturated brine (5 mL) was then added to the reaction system and extracted with ethyl acetate (10 mL × 3). The combined organic phase was then washed with H<sub>2</sub>O (10 mL), dried over sodium sulfate, and concentrated under vacuum. The residue was purified by silica gel flash chromatography to give the desired product.

All photochemical reactions for the substrate scopes were performed with OSRAM Oslon SSL 80 royal LEDs ( $\lambda = 385 \text{ nm} \pm 15 \text{ nm}$ , 700 mW or 2.4 W). The samples were irradiated with an LED through the bottom side and cooled from the side using custom-made aluminum water-cooling blocks connected to a thermostat. The reaction mixture and the LED cooling block were temperature-controlled. Gram-scale reactions were performed in a glass tube photochemical reactor setup irradiated from the outside. UV-Vis and fluorescence measurements were performed with a Varian Cary 100 UV/Vis spectrophotometer and FluoroMax 4 spectrofluorometer, respectively.

Table S.4 - 4: Control experiments for the reaction of 4-bromobenzonitrile with indole. Standard reaction conditions: **a1** (0.1 mmol), **b1** (0.15 mmol), and meglumine (0.25 mmol) in 2 mL H<sub>2</sub>O under 385 nm LED (2.4 W) light irradiation at 25 °C under N<sub>2</sub> atmosphere for 15 h. n.d., product was not detected. <sup>a</sup>Yields were determined by GC-MS analysis with *n*-dodecane as an internal standard and are the average of 2 runs. <sup>b</sup>Reaction time: 12 h.

Entry	Deviations from Optimized Conditions	Yields <sup>a</sup>		
		c1	(C2:C7)	c50
1	None	83 %	(1:1)	n.d.
2	No meglumine	34 %	(1:1)	n.d.
3	No light, 25 °C	n.d.		n.d.
4	No light, 60 °C	n.d.		n.d.
5	No light, 90 °C	n.d.		n.d.
6 <sup>b</sup>	60 °C instead of 25 °C	82 %	(1:1)	5%
7	2 °C instead of 25 °C	27 %	(1.3:1)	n.d.
8	0.7 W LED	73 %	(1:1)	n.d.
9	<b>a1</b> (0.4 mmol), <b>b1</b> (0.1 mmol) meglumine (0.4 mmol), 80 °C	15 %	(1:1)	72%

Table S.4 - 5: Control experiments for the reaction of 4-chlorobenzonitrile with benzenethiol. Standard reaction conditions: **a59** (0.1 mmol), **b59** (0.15 mmol), and meglumine (0.25 mmol) in 2 mL H<sub>2</sub>O under 385 nm LED (0.7 W) light irradiation at 25 °C under N<sub>2</sub> atmosphere for 15 h. n.d., product was not detected. <sup>a</sup>Yields were determined by GC-MS analysis with *n*-dodecane as an internal standard and are the average of 2 runs.

Entry	Deviations from Optimized Conditions	Yields <sup>a</sup>	
		c59	d1
1	None	91 %	9 %
2	No light, 25 °C	n.d.	n.d.
3	No light, 60 °C	n.d.	n.d.
4	No meglumine	n.d.	n.d.
5	2.4 W LED instead of 0.7 W LED	80 %	20 %
6	DMF instead of H <sub>2</sub> O	30 %	62 %
7	air instead of N <sub>2</sub>	74 %	13 %

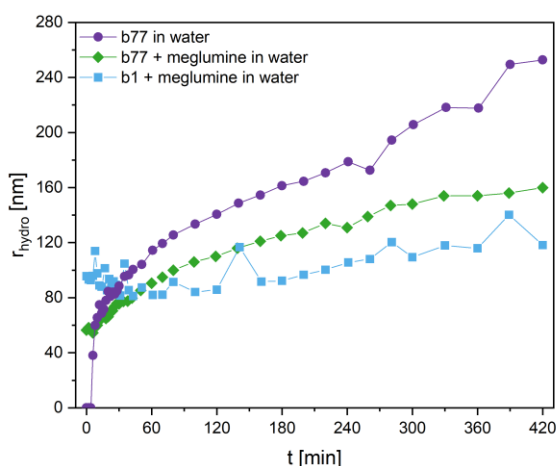


Figure S.4 - 12: Hydrodynamic radii as a function of time in aqueous solutions containing 0.02 M **b77** or 0.03 M **b1** with/without 0.05 M meglumine. Considering **b1**, aggregation is observed as well after filtration from the DLS measurements and crystals are visible immediately after filtration (Figure 4 - 18). There is no interaction between **b1** and meglumine from the NMR studies, so the aggregation arises from the crystal growth of the substrate itself. Compared to the solution of **b77** and meglumine, the size of the aggregates is already larger at the beginning of the measurements and increases more slowly, which may result from general lower solubility of **b1** in water than **b77** in water.

## 4.5.2.2 NMR measurements

NMR experiments were performed using a Bruker Avance III 600 MHz operating at 600.03 MHz for protons, equipped with a 5-mm high-resolution TBIF probe and with pulsed gradient units, capable of producing magnetic field pulsed gradients in the z-direction of  $0.54 \text{ Tm}^{-1}$ . The temperature was certified by internal NMR calibration samples from Bruker®. In all measurements, the samples were equilibrated for 10 min before acquisition.

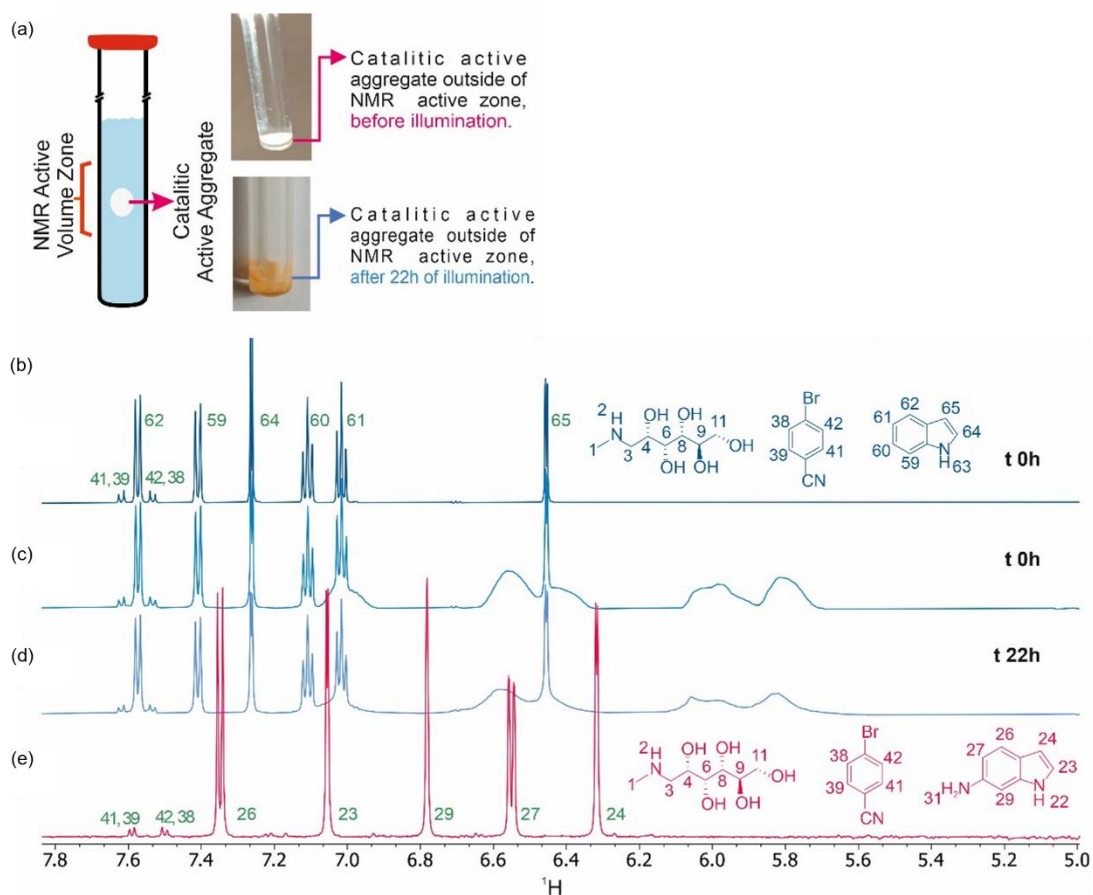


Figure S.4 - 13: (a) Schematic diagram of the NMR active volume zone (left) and comparison pictures of the mixture of 0.05 M 4-bromobenzonitrile (**a1**) + 0.07 M indole (**b1**) + 0.125 M meglumine in  $\text{D}_2\text{O}$  before (top right) and after illumination (bottom right) out of the NMR detection zone. (b)  $^1\text{H-NMR}$  spectrum of mixture of 0.05 M 4-bromobenzonitrile (**a1**) + 0.07 M indole (**b1**) + 0.125 M meglumine in  $\text{D}_2\text{O}$  with the aggregate capsule out of the NMR detection zone. (c) With the aggregate capsule inside of NMR detection zone before illumination. (d) With the aggregate capsule inside of the NMR detection zone after 22 h of illumination. (e) In contrast, the  $^1\text{H-NMR}$  spectrum of 0.05 M 4-bromobenzonitrile (**a1**) + 0.075 M 6-aminoindole (**b13**) + 0.1 M meglumine in  $\text{D}_2\text{O}$  does not show aggregation.

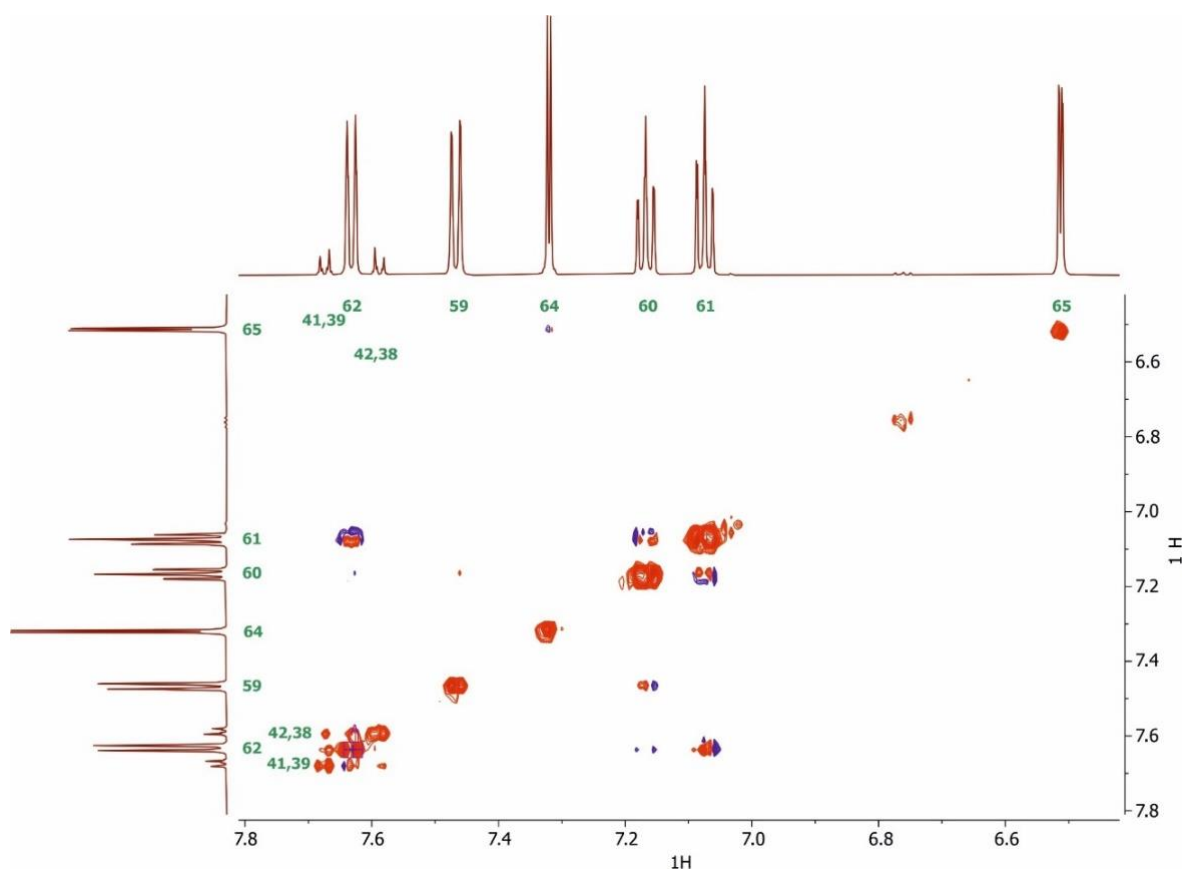


Figure S.4 - 14: NOESY, 600 MHz with cryoprobe. Prepared sample: 0.07 M indole + 0.05 M 4-bromobenzonitrile + 2  $\mu$ M dioxane in  $D_2O$ , 298 K. NS 64, TD F1 512, TD F2 4048, mixing time 0.4 s and relaxation delay 3.0 s. The 2D NOESY spectrum allows identification of intermolecular contact between proton 62 of indole with both aromatic protons of 4-bromobenzonitrile, with the most intense NOE corresponding to the correlation between protons 62-41, 39, suggesting the formation of aggregate in the absence of meglumine.

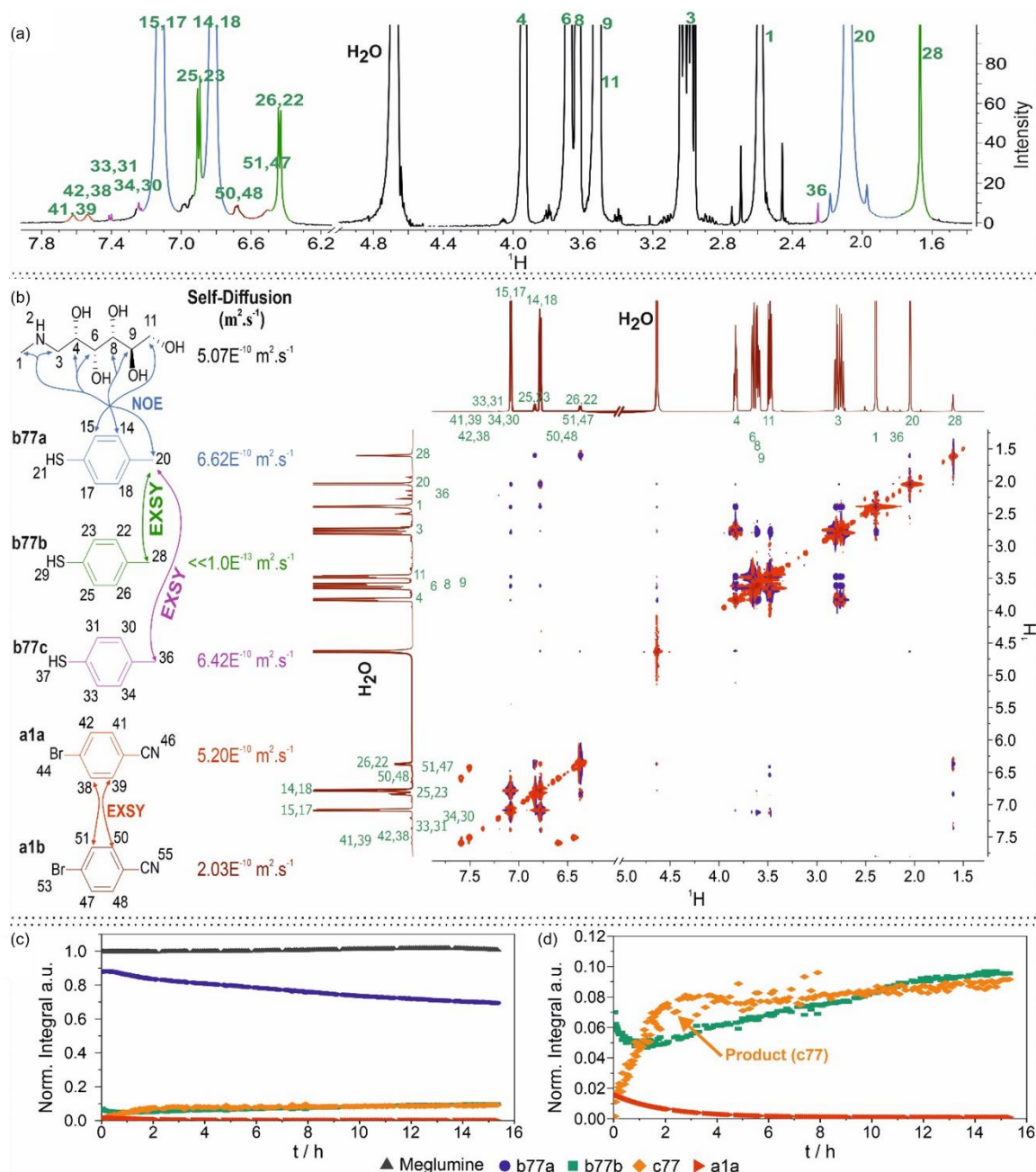


Figure S.4 - 15: Measurements to investigate the mechanism of C-S coupling reaction. (a)  $^1\text{H-NMR}$  spectrum of **a1** (0.05 mmol) and **b77** (0.075 mmol) in the presence of meglumine (0.125 mmol) in  $\text{D}_2\text{O}$  (1 mL). (b) NMR spectra of **a1** (0.05 mmol) and **b77** (0.075 mmol) in the presence of meglumine (0.125 mmol) in  $\text{D}_2\text{O}$  (1 mL) show several sets of signals for both **a1** and **b77**, their NOE, exchange interactions and self-diffusion coefficients show unspecific interactions, micro crystals and three compartments (for details see the literature<sup>1</sup>). (c) In-situ NMR reaction profile of the reaction of **a1** (0.05 mmol) and **b77** (0.075 mmol) in the presence of meglumine (0.125 mmol) in  $\text{D}_2\text{O}$  (1 mL) without stirring and under illumination (365 nm). (d) Expanded region to show the development of **b77-b** versus the product **c77**. The minimum of **b77-b** in combination with an initially stable concentration of **b77-a** suggest a "stock function" of **b77-b**.

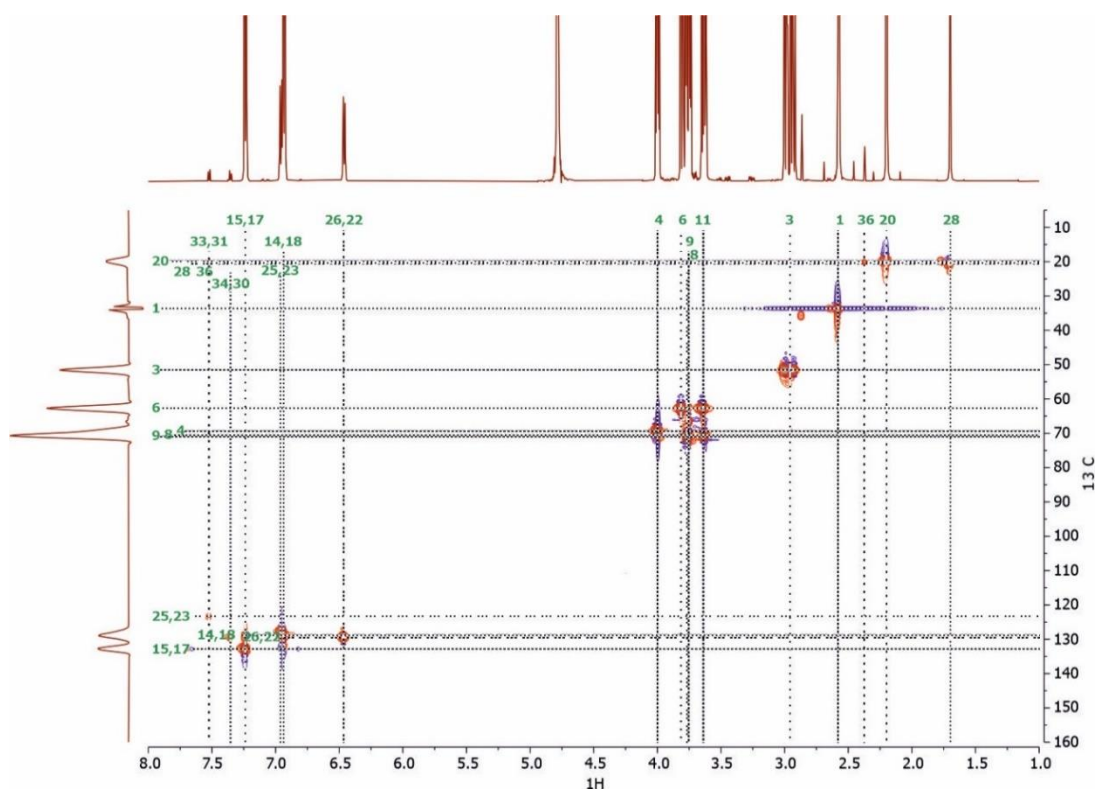


Figure S.4 - 16:  $^1\text{H}$ - $^{13}\text{C}$  HSQC, 600 MHz. Prepared sample: 0.05 M 4-methylbenzenethiol + 0.05 M meglumine + 2  $\mu\text{M}$  dioxane in  $\text{D}_2\text{O}$ , 298K, NS 32, TD F1 256, TD F2 2024 and relaxation delay 2.0 s. Together with the proton spectrum of the prepared sample containing an equimolar proportion of 4-methylbenzenethiol and meglumine, 3 sets of  $\text{CH}_3$  and 3 pairs of aromatic protons, corresponding to 3 different domains of 4-methylbenzenethiol in this system can be identified. The quantification through the proton spectrum, using meglumine as a reference, provides the following proportion: 100 : 52 : 11 : 0.4 (meglumine : **b77-a** : **b77-b** : **b77-c**).

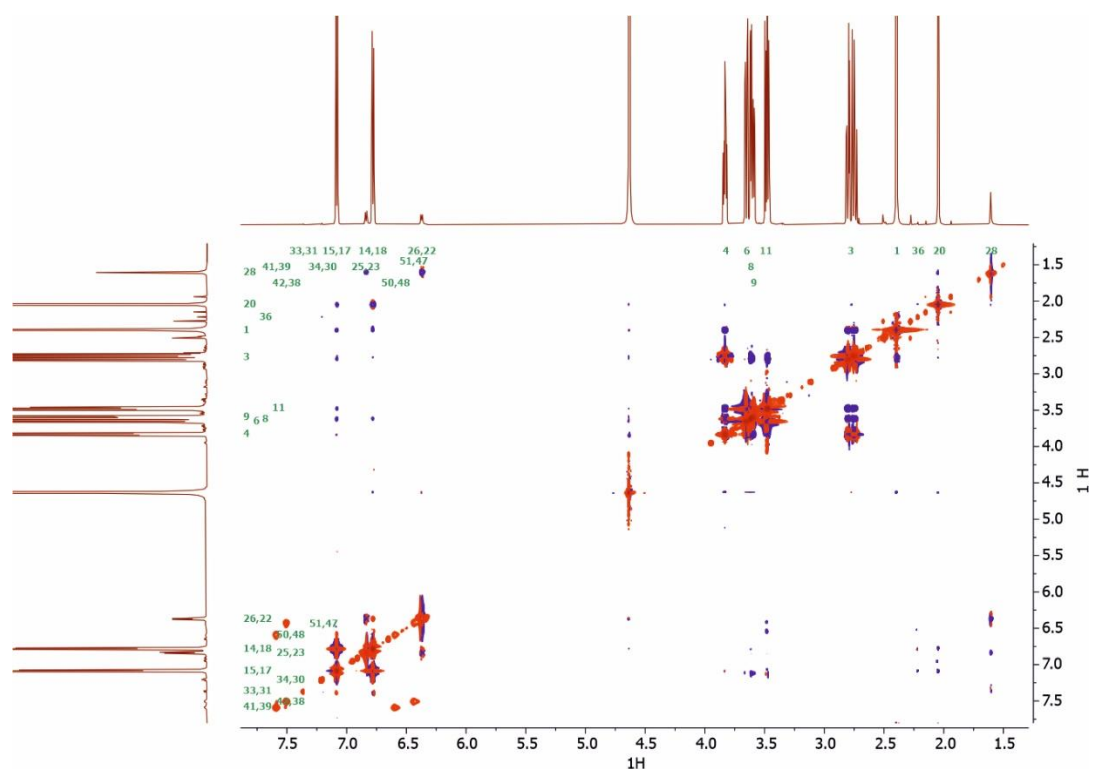


Figure S.4 - 17: NOESY, 600 MHz. Prepared sample: 0.05 M 4-bromobenzonitrile + 0.075 M 4-methylbenzenethiol + 0.125 M meglumine + 2  $\mu$ M dioxane in  $D_2O$ , 298K. NS 32, TD F1 512, TD F2 4096, mixing time 0.6 s and relaxation delay 3.0 s. From the NOESY spectra we can see that the methyl groups of the **b77-b** and **b77-c** are in contact with the methyl of **b77-a**. **b77-a** is in close contact with meglumine, with all aromatic protons and the methyl group showing cross peaks with meglumine protons, indicating a rather unspecific orientation in relation to meglumine. No intermolecular contact with 4-bromobenzonitrile was attributed, and 4-bromobenzonitrile was not able to determine by NOESY due to low solubility.

## 4.6 References

- (1) Tian, Y.; Hofmann, E.; Silva, W.; Pu, X.; Touraud, D.; Gschwind, R. M.; Kunz, W.; König, B. Enforced Electronic-Donor-Acceptor Complex Formation in Water for Photochemical Cross-Coupling. *Angew. Chemie Int. Ed.* **2023**, *62* (17).  
<https://doi.org/10.1002/anie.202218775>.
- (2) Aloisio, C.; de Oliveira, A. G.; Longhi, M. Solubility and Release Modulation Effect of Sulfamerazine Ternary Complexes with Cyclodextrins and Meglumine. *J. Pharm. Biomed. Anal.* **2014**, *100*, 64–73. <https://doi.org/10.1016/j.jpba.2014.07.008>.
- (3) Aloisio, C.; G. de Oliveira, A.; Longhi, M. Cyclodextrin and Meglumine-Based Microemulsions as a Poorly Water-Soluble Drug Delivery System. *J. Pharm. Sci.* **2016**, *105* (9), 2703–2711. <https://doi.org/10.1016/j.xphs.2015.11.045>.
- (4) Aloisio, C.; Antimisiaris, S. G.; Longhi, M. R. Liposomes Containing Cyclodextrins or Meglumine to Solubilize and Improve the Bioavailability of Poorly Soluble Drugs. *J. Mol. Liq.* **2017**, *229*, 106–113. <https://doi.org/10.1016/j.molliq.2016.12.035>.
- (5) Gupta, P.; Bansal, A. K. Ternary Amorphous Composites of Celecoxib, Poly(Vinyl Pyrrolidone) and Meglumine with Enhanced Solubility. *Pharmazie* **2005**, *60* (11), 830–836.
- (6) Chen, H.-S.; Guo, R.-Y. Meglumine: An Efficient, Biodegradable, and Recyclable Green Catalyst for One-Pot Synthesis of Functionalized Dihydropyridines. *Monatshette für Chemie - Chem. Mon.* **2015**, *146* (8), 1355–1362.  
<https://doi.org/10.1007/s00706-015-1416-9>.
- (7) Fusina, A.; Degot, P.; Touraud, D.; Kunz, W.; Nardello-Rataj, V. Enhancement of Water Solubilization of Quercetin by Meglumine and Application of the Solubilization Concept to a Similar System. *J. Mol. Liq.* **2022**, *368*, 120756.  
<https://doi.org/10.1016/j.molliq.2022.120756>.
- (8) Degot, P.; Funkner, D.; Huber, V.; Köglmaier, M.; Touraud, D.; Kunz, W. Extraction of Curcumin from Curcuma Longa Using Meglumine and Pyroglutamic Acid, Respectively, as Solubilizer and Hydrotrope. *J. Mol. Liq.* **2021**, *334*, 116478.  
<https://doi.org/10.1016/j.molliq.2021.116478>.
- (9) Reiß, B.; Wagenknecht, H.-A. Naphthalene Diimides with Improved Solubility for Visible Light Photoredox Catalysis. *Beilstein J. Org. Chem.* **2019**, *15*, 2043–2051.

- <https://doi.org/10.3762/bjoc.15.201>.
- (10) Li, R.; Chen, X.; Wei, S.; Sun, K.; Fan, L.; Liu, Y.; Qu, L.; Zhao, Y.; Yu, B. A Visible-Light-Promoted Metal-Free Strategy towards Arylphosphonates: Organic-Dye-Catalyzed Phosphorylation of Arylhydrazines with Trialkylphosphites. *Adv. Synth. Catal.* **2018**, *360* (24), 4807–4813. <https://doi.org/10.1002/adsc.201801122>.
- (11) Ghosh, I.; Ghosh, T.; Bardagi, J. I.; König, B. Reduction of Aryl Halides by Consecutive Visible Light-Induced Electron Transfer Processes. *Science*. **2014**, *346* (6210), 725–728. <https://doi.org/10.1126/science.1258232>.
- (12) Giedyk, M.; Narobe, R.; Weiß, S.; Touraud, D.; Kunz, W.; König, B. Photocatalytic Activation of Alkyl Chlorides by Assembly-Promoted Single Electron Transfer in Microheterogeneous Solutions. *Nat. Catal.* **2019**, *3* (1), 40–47. <https://doi.org/10.1038/s41929-019-0369-5>.
- (13) Lambert, F. L.; Ingall, G. B. Voltammetry of Organic Halogen Compounds. IV. The Reduction of Organic Chlorides at the Vitreous (Glassy) Carbon Electrode. *Tetrahedron Lett.* **1974**, *15* (36), 3231–3234. [https://doi.org/10.1016/S0040-4039\(01\)91870-2](https://doi.org/10.1016/S0040-4039(01)91870-2).
- (14) Ghosh, T. Visible Light-Induced Reductive Photoredox Catalysis in Organic Synthesis, University of Regensburg, 2016.
- (15) Liu, Z.; Li, X.; Chen, J.; Li, C.; Luo, F.; Cheng, F.-X.; Liu, J.-J. Merging of the Photocatalyst Decatungstate and Naphthalene Diimide in a Hybrid Structure for the Oxidative Coupling of Amines. *Dalt. Trans.* **2022**, *51* (21), 8472–8479. <https://doi.org/10.1039/D2DT01003H>.
- (16) Wang, S.-H.; Khurshid, F.; Chen, P.-Z.; Lai, Y.-R.; Cai, C.-W.; Chung, P.-W.; Hayashi, M.; Jeng, R.-J.; Rwei, S.-P.; Wang, L. Solution-Processable Naphthalene Diimide-Based Conjugated Polymers as Organocatalysts for Photocatalytic CO<sub>2</sub> Reaction with Extremely Stable Catalytic Activity for Over 330 Hours. *Chem. Mater.* **2022**, *34* (11), 4955–4963. <https://doi.org/10.1021/acs.chemmater.2c00168>.
- (17) Foster, R. Electron Donor-Acceptor Complexes. *J. Phys. Chem.* **1980**, *84* (17), 2135–2141. <https://doi.org/10.1021/j100454a006>.
- (18) Rosokha, S. V.; Kochi, J. K. Fresh Look at Electron-Transfer Mechanisms via the Donor/Acceptor Bindings in the Critical Encounter Complex. *Acc. Chem. Res.* **2008**, *41* (5), 641–653. <https://doi.org/10.1021/ar700256a>.
- (19) Mori, T.; Inoue, Y. Charge-Transfer Excitation: Unconventional yet Practical Means

- for Controlling Stereoselectivity in Asymmetric Photoreactions. *Chem. Soc. Rev.* **2013**, *42* (20), 8122. <https://doi.org/10.1039/c3cs60117j>.
- (20) Lima, C. G. S.; de M. Lima, T.; Duarte, M.; Jurberg, I. D.; Paixão, M. W. Organic Synthesis Enabled by Light-Irradiation of EDA Complexes: Theoretical Background and Synthetic Applications. *ACS Catal.* **2016**, *6* (3), 1389–1407. <https://doi.org/10.1021/acscatal.5b02386>.
- (21) Crisenza, G. E. M.; Mazzarella, D.; Melchiorre, P. Synthetic Methods Driven by the Photoactivity of Electron Donor–Acceptor Complexes. *J. Am. Chem. Soc.* **2020**, *142* (12), 5461–5476. <https://doi.org/10.1021/jacs.0c01416>.
- (22) Prier, C. K.; Arnold, F. H. Chemomimetic Biocatalysis: Exploiting the Synthetic Potential of Cofactor-Dependent Enzymes To Create New Catalysts. *J. Am. Chem. Soc.* **2015**, *137* (44), 13992–14006. <https://doi.org/10.1021/jacs.5b09348>.
- (23) Emmanuel, M. A.; Greenberg, N. R.; Oblinsky, D. G.; Hyster, T. K. Accessing Non-Natural Reactivity by Irradiating Nicotinamide-Dependent Enzymes with Light. *Nature* **2016**, *540* (7633), 414–417. <https://doi.org/10.1038/nature20569>.
- (24) Biegasiewicz, K. F.; Cooper, S. J.; Gao, X.; Oblinsky, D. G.; Kim, J. H.; Garfinkle, S. E.; Joyce, L. A.; Sandoval, B. A.; Scholes, G. D.; Hyster, T. K. Photoexcitation of Flavoenzymes Enables a Stereoselective Radical Cyclization. *Science* (80-. ). **2019**, *364* (6446), 1166–1169. <https://doi.org/10.1126/science.aaw1143>.
- (25) Swinehart, D. F. The Beer-Lambert Law. *J. Chem. Educ.* **1962**, *39* (7), 333–335. <https://doi.org/10.1021/ed039p333>.
- (26) Kissinger, P. T.; Heineman, W. R. Cyclic Voltammetry. *J. Chem. Educ.* **1983**, *60* (9), 702. <https://doi.org/10.1021/ed060p702>.
- (27) Dekker, M. L.; Clause, M.; Rosano, H. L.; Zradba, A. S. *Microemulsion Systems*, 24th edn.; Surfactant Science Ser., New York, PA, 1987.
- (28) Balakin, K. V.; Ivanenkov, Y. A.; Skorenko, A. V.; Nikolsky, Y. V.; Savchuk, N. P.; Ivashchenko, A. A. In Silico Estimation of DMSO Solubility of Organic Compounds for Bioscreening. *J. Biomol. Screen.* **2004**, *9* (1), 22–31. <https://doi.org/10.1177/1087057103260006>.
- (29) Yoon, T. P.; Ischay, M. A.; Du, J. Visible Light Photocatalysis as a Greener Approach to Photochemical Synthesis. *Nat. Chem.* **2010**, *2* (7), 527–532. <https://doi.org/10.1038/nchem.687>.
- (30) Speckmeier, E.; Zeitler, K. 3 Practical Aspects of Photocatalysis. In *Photocatalysis in*

*Organic Synthesis*; König, B., Ed.; Georg Thieme Verlag: Stuttgart, 2019.

<https://doi.org/10.1055/sos-SD-229-00059>.

- (31) Pavlishchuk, V. V.; Addison, A. W. Conversion Constants for Redox Potentials Measured versus Different Reference Electrodes in Acetonitrile Solutions at 25°C. *Inorganica Chim. Acta* **2000**, *298* (1), 97–102. [https://doi.org/10.1016/S0020-1693\(99\)00407-7](https://doi.org/10.1016/S0020-1693(99)00407-7).
- (32) Grundl, G.; Müller, M.; Touraud, D.; Kunz, W. Salting-out and Salting-in Effects of Organic Compounds and Applications of the Salting-out Effect of Pentasodium Phytate in Different Extraction Processes. *J. Mol. Liq.* **2017**, *236*, 368–375. <https://doi.org/10.1016/j.molliq.2017.03.091>.
- (33) Yushchenko, D. Y.; Zhizhina, E. G.; Pai, Z. P. Methods for the Synthesis of Triethanolamine. *Catal. Ind.* **2019**, *11* (2), 113–118. <https://doi.org/10.1134/S2070050419020120>.
- (34) Jessop, P. G.; Ahmadpour, F.; Buczynski, M. A.; Burns, T. J.; Green II, N. B.; Korwin, R.; Long, D.; Massad, S. K.; Manley, J. B.; Omidbakhsh, N.; Pearl, R.; Pereira, S.; Predale, R. A.; Sliva, P. G.; VanderBilt, H.; Weller, S.; Wolf, M. H. Opportunities for Greener Alternatives in Chemical Formulations. *Green Chem.* **2015**, *17* (5), 2664–2678. <https://doi.org/10.1039/C4GC02261K>.
- (35) Yamasaki, E. THE SUCCESSIVE STAGES OF THE HYDROLYSIS OF TRIACETIN. *J. Am. Chem. Soc.* **1920**, *42* (7), 1455–1468. <https://doi.org/10.1021/ja01452a020>.
- (36) Limpanuparb, T.; Punyain, K.; Tantirungrotechai, Y. A DFT Investigation of Methanolysis and Hydrolysis of Triacetin. *J. Mol. Struct. THEOCHEM* **2010**, *955* (1–3), 23–32. <https://doi.org/10.1016/j.theochem.2010.05.022>.
- (37) Zhou, L. Recent Advances in C-F Bond Cleavage Enabled by Visible Light Photoredox Catalysis. *Molecules* **2021**, *26* (22), 7051. <https://doi.org/10.3390/molecules26227051>.
- (38) Davies, D. B.; Djimant, L. N.; Veselkov, A. N. <sup>1</sup>H NMR Investigation of Self-Association of Aromatic Drug Molecules in Aqueous Solution. Structural and Thermodynamical Analysis. *J. Chem. Soc. Faraday Trans.* **1996**, *92* (3), 383. <https://doi.org/10.1039/ft9969200383>.



## Chapter 5 Overcoming the unproductive singlet-born radical reaction in the flavin-catalyzed photooxidation of 4-methoxybenzyl alcohol by solvent structuring

### 5.0 Abstract

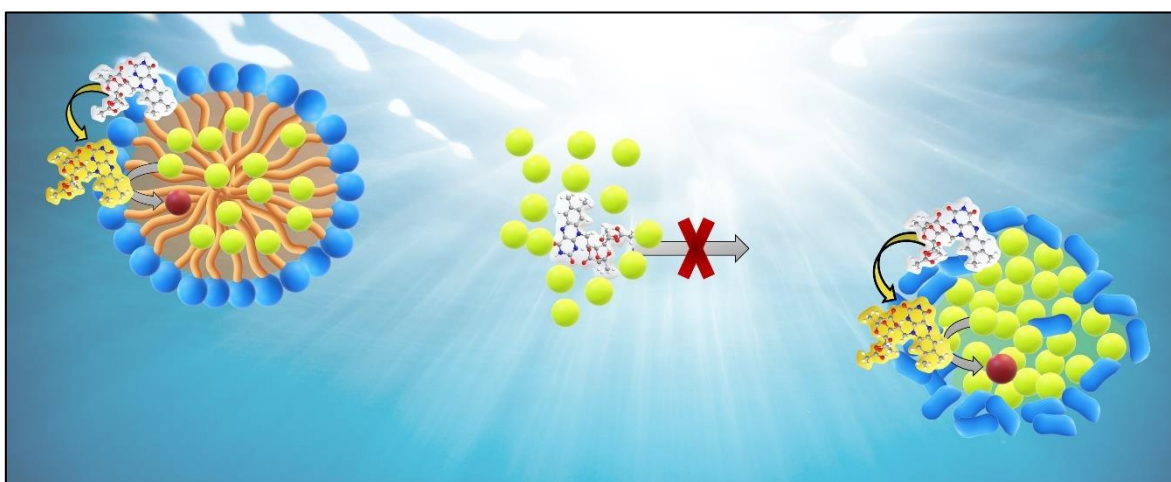


Figure 5 - 1: Schematic illustration of the photocatalytic oxidation of 4-methoxybenzyl alcohol at high substrate concentrations enabled by solvent structuring.

The usage of organic dyes, such as riboflavin and derivatives, represents an environmentally friendly alternative to metal-based photocatalysis. For successful oxidation of 4-methoxybenzyl alcohol, the tetraacetyl riboflavin (TARF) photocatalyst needs to achieve the excited triplet state. At high substrate concentrations, the excited singlet TARF increasingly returns to the ground state via routes other than the oxidation product, resulting in a decrease in the product quantum yield. In order to overcome this problem, solvent structuring is introduced by either a micellar solution of  $C_8EO_5$  or surfactant-free microemulsions consisting of water, the short-chain alcohol ethanol or t-butanol, and the hydrophobic reaction substrate. The structured solvents elongate the lifetime of the excited TARF and increase the overall product quantum yield compared to the reference system of water and acetonitrile. Several solvent systems are characterized in terms of structuring, oxygen solubility, viscosity, and their impact on the lifetime of the excited catalyst as well as on the product quantum yield.

The chapter was created in cooperation with Dr. Roger Jan Kutta (University of Regensburg, Germany). In this context, the PQY measurements were carried out together with Dr. Kutta, and the corresponding analysis was performed by Dr. Kutta. The transient absorption measurements were mainly carried out by Dr. Kutta. The evaluation of the experimental results by Dr. Kutta is still pending.

## 5.1 Introduction

In photoredox catalysis, organic dyes represent an environmentally friendly alternative for the widely used Ru- and Ir-complexes. In particular, the vitamin B<sub>2</sub> called *riboflavin* (RF, see Figure 5 - 2(a)) is a green and widespread approach in this context. RF and its derivative tetraacetyl riboflavin (TARF, see Figure 5 - 2(b)) strongly absorb blue light up to 500 nm, allowing visible light to be used as an abundant source of energy.<sup>1-4</sup> The acetylation makes TARF more stable against intramolecular photoreduction.<sup>5</sup> It has to be noted, however, that the synthesis of TARF comprises solvents such as perchloric acid, which no longer allows declaring the molecule itself to be green.<sup>5,6</sup> Despite that, photocatalytic processes, including TARF instead of metal-based catalysts, are still considered environmentally benign.<sup>1</sup> In general, flavins possess 3 redox states, as the oxidized form can either be reduced by a single electron or fully reduced by two electrons. In addition, each redox state exhibits 3 protonation levels depending on the pH.<sup>7</sup>

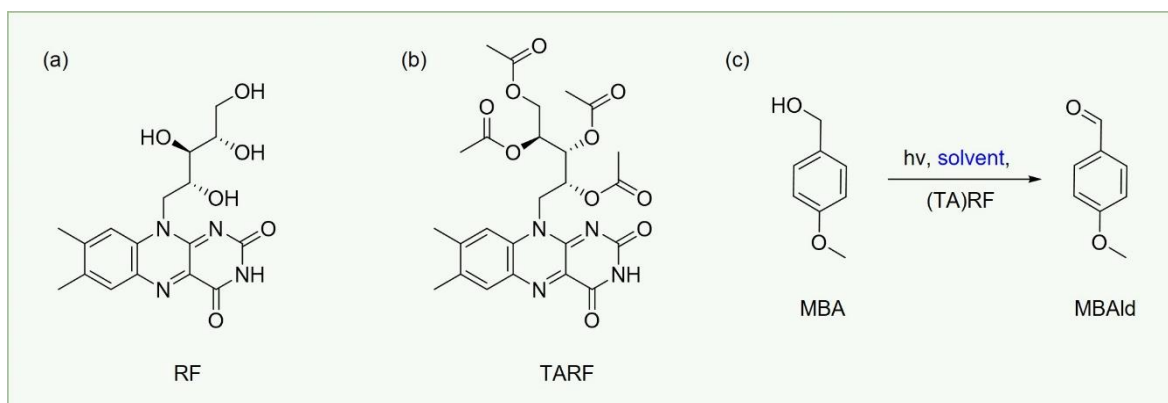


Figure 5 - 2: Molecular structure of riboflavin (RF) (a) and tetraacetyl riboflavin (TARF) (b). (c) Photocatalytic oxidation of 4-methoxybenzyl alcohol (MBA) to the corresponding aldehyde (MBAld) in the presence of (TA)RF.

The photooxidation of 4-methoxybenzyl alcohol (MBA) catalyzed by flavin and derivatives is reported in the literature (see Figure 5 - 2(c)).<sup>4,8-10</sup> Initially, close contact between substrate and flavins was considered to improve photooxidation efficiency and selectivity because of the distance-dependent electron transfer. But Megerle *et al.* revealed that this assumption is not universal.<sup>4,11</sup>

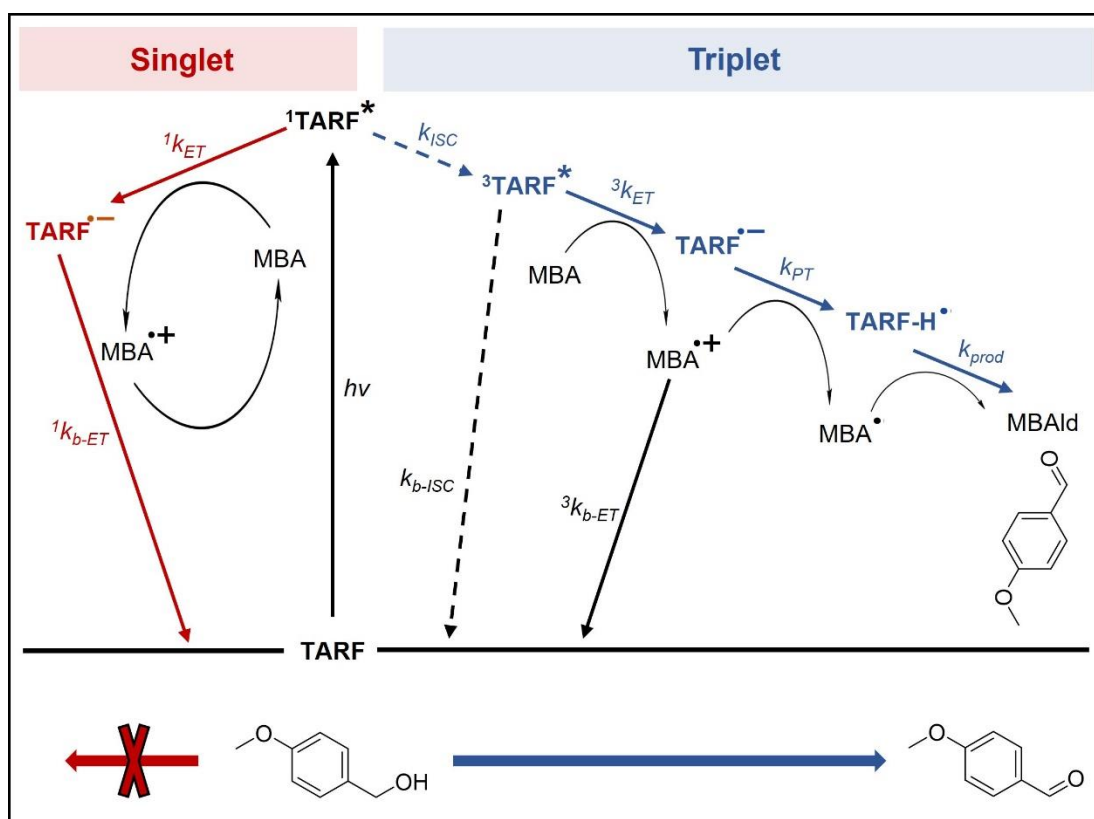


Figure 5 - 3: Simplified representation of the photooxidation of MBA and the role of TARF. <sup>1</sup> and <sup>3</sup> identify the <sup>1</sup>singlet and the <sup>3</sup>triplet excited state of TARF. The following steps are illustrated: (back) electron transfer ((b)-ET), (back) intersystem crossing ((b)-ISC), proton transfer (PT), and product conversion (prod). The scheme is drawn according to the cited literature with modifications in its presentation. Detailed explanations are provided in the text and the literature.<sup>4</sup>

Figure 5 - 3 depicts the photoinduced dynamics between the photoexcited catalyst TARF\* and the substrate MBA. The first contact leads to an electron transfer (ET) from MBA to the excited singlet state <sup>1</sup>TARF\*, resulting in a radical anion TARF•<sup>-</sup> and the radical cation MBA•<sup>+</sup>. In pure MBA, thus, in the absence of any additional solvent, only the back ET (b-ET) from MBA•<sup>+</sup> to TARF•<sup>-</sup> is detected. Hence, practically no oxidation product is monitored in pure MBA. Photoexcitation of TARF just results in a fast cycle of ET (4 ps) and b-ET (50 ps) (see Figure 5 - 3, Singlet). Since the competing quenching rate by MBA is more than 3 orders of magnitudes faster than intersystem crossing (ISC), the excited triplet state of <sup>3</sup>TARF\* does not contribute to the process.<sup>4,12,13</sup> In order to create a distance between TARF and MBA, Megerle *et al.* applied an inert solvent, namely acetonitrile (AcN) and water. This creates an additional diffusion-controlled step. The MBA first needs to approach to close proximity by random walk, allowing ISC to <sup>3</sup>TARF\* to occur in the meantime. As a consequence, proton transfer (PT) and further ET enable the formation of the oxidation product 4-methoxybenzyl aldehyde (MBAlD) (see Figure 5 - 3, Triplet). As already described in Chapter 0, molecule diffusion is linked to the viscosity of the surrounding solvent according to the Stokes-Einstein equation (see Equation 5 – 1)<sup>14,15</sup>

$$D = \frac{k_B T}{6\pi\eta r_{hydro}} \quad \text{Eq. 5 - 1}$$

with diffusion coefficient  $D$ , the Boltzmann constant  $k_B$ , temperature  $T$ , solvent viscosity  $\eta$ , and hydrodynamic radius  $r_{hydro}$ .

An increasing substrate concentration again decreases the distance between the substrate and the catalyst. When the distance becomes too small, the diffusion of the MBA competes with the ISC. Accordingly, the MBA again quenches the excited singlet TARF, which can be monitored as a shortened fluorescence lifetime. At high substrate concentrations of several 100 mM, preassociated TARF-MBA-aggregates are present underlying the unproductive recombination cycle of ET and b-ET. For this reason, the product quantum yield (PQY), which defines the fraction of absorbed photons yielding the desired product, depends on the substrate concentration and depicts a bell-shaped curve (see Figure 5 - 4(a)).<sup>11,16,17</sup> As shown in Figure 5 - 4(b), the absorbance in the region of 300 nm is dominated by the product MBAId. This allows the determination of the PQY by means of absorbance measurements.<sup>4</sup> Another important parameter influencing the reaction is the amount of dissolved oxygen. Oxygen allows the regeneration of the photocatalyst and is thus essential. However, dissolved oxygen is also known to quench excited triplet states. As a consequence, excessive amounts of dissolved oxygen can also have a negative effect on the reaction.<sup>5,18</sup>

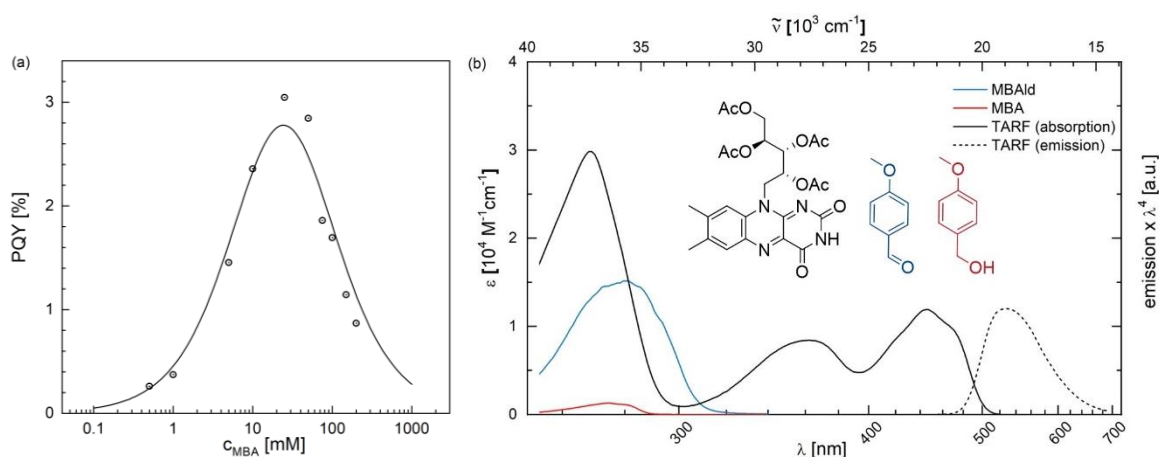


Figure 5 - 4: (a) PQY of MBAId as a function of the substrate concentration  $c_{MBA}$  in W/AcN 50/50 (v/v). (b) Absorbance spectra of MBA, MBAId, and TARF, as well as the emission spectrum of TARF in W/AcN 50/50 (v/v). Both figures are taken from the cited literature, slightly modified in their presentation, and reprinted with permission.<sup>4</sup>

The present work deals with the impact of the reaction media on the photooxidation of MBA catalyzed by TARF. In particular, solvent structuring induced by micelles or surfactant-free microemulsions (SFMEs) is investigated. The solvent structuring is applied to create distance between substrate and catalyst at high substrate concentrations. Besides, viscosity and oxygen solubility in the solvents are taken into account. Both the micellar solution and the SFME increase the lifetime of the excited TARF and the overall PQY.

## 5.2 Material and methods

### 5.2.1 Chemicals

4-Methoxybenzyl alcohol (MBA, purity  $\geq 98\%$ ) and riboflavin (RF<sup>1</sup>,  $\geq 98\%$ ) were purchased from Sigma Aldrich (Darmstadt, Germany). Riboflavin (RF<sup>2</sup>,  $\geq 97\%$ ) and t-butanol (tBuOH, 99%) were obtained from Roth (Karlsruhe, Germany). Ethanol (EtOH,  $\geq 99.9\%$ ), acetonitrile (AcN, HPLC grade), and 1-octanol ( $\geq 99.0\%$ ) were from Merck (Darmstadt, Germany). The surfactant Akypo CO 50 (C<sub>8</sub>EO<sub>5</sub>, 1% (w/w) water) was bought from Kao Chemicals (Emmerich am Rhein, Germany). Tetraacetyl riboflavin (TARF) was synthesized by co-workers of Prof. König (University of Regensburg, Germany), as described by Larson *et al.*<sup>5</sup> Millipore water (W) was used with a resistivity of 18 M $\Omega$  cm.

### 5.2.2 Methods

#### 5.2.2.1 Ternary phase diagram

Ternary phase diagrams were recorded as reported in Chapter 2.2.2.1.

#### 5.2.2.2 Critical point

To determine the critical point in the ternary phase diagram of water, EtOH, and MBA, the method described in Chapter 3.2.2.3 was applied.

#### 5.2.2.3 Dynamic light scattering

Dynamic light scattering (DLS) measurements were performed as described in Chapter 1.2.2.5.

#### 5.2.2.4 Viscosity measurements

The viscosity was determined using the rolling-ball viscometer AMVn from Anton-Paar (Graz, Austria). Each solvent was measured 10 times at an angle of 30° and 10 times at an angle of 70°. Finally, the density of the solvents, determined using the device defined in Chapter 1.5.1, was taken into account to calculate the viscosity. All measurements were performed at  $25 \pm 0.1$  °C.

### 5.2.2.5 Oxygen solubility

The amount of dissolved oxygen in the different solvents was determined as described in Chapter 1.2.2.4.

### 5.2.2.6 UV/VIS spectroscopy

The saturated samples were first oversaturated and stirred at room temperature for 3 h and then filtered with a PTFE syringe filter (0.2  $\mu\text{m}$  pore size) before measuring the absorbance by means of the spectrometer described in Chapter 4.2.2.1. The same UV cuvettes with a length of 1 cm were used.

### 5.2.2.7 Partition coefficient

First, the absorbance of 1 mg of photocatalyst dissolved in 20 mL water was measured (see Chapter 5.2.2.6). 5 mL of the solution was mixed with 5 mL of 1-octanol and stirred for 14 h at 650 rpm at room temperature. After a further 2 h rest time for phase separation, the absorbance was measured in the aqueous phase. The amount of dissolved catalyst in the oil phase was determined from the difference in the aqueous phase before and after mixing with 1-octanol.

### 5.2.2.8 Product quantum yield

The relative product quantum yield (PQY) in the presence of molecular oxygen was determined by recording absorption spectra of a particular system after stepwise temporally and geometrically defined illumination (pulse width  $\Delta t = 1$  s,  $\lambda_{\text{exc}} = 450$  nm; LED Thorlabs) in 10 x 2 mm quartz cell filled with 120  $\mu\text{L}$  sample. The absorption was monitored along the 10 mm path via a referenced single beam spectrometer (Cary 60, Agilent). These sequences of spectra showing the product build-up upon illumination were decomposed into the contributing species spectra and corresponding concentration-time profiles. The initial slope of the product build-up over illumination time is proportional to the product quantum yield. For comparison within all measurements, the illumination times were corrected by the corresponding overlap integrals between the normalized spectrum of the excitation source and the absorption spectrum of TARF, that was excited. The absolute quantum yield was calculated from recording also the product formation of the known photo-oxidation of 4-methoxybenzyl alcohol to the corresponding aldehyde by TARF in W/AcN 50/50 (v/v).<sup>4</sup>

### 5.2.2.9 Fluorescence decay time

A self-constructed time-correlated single photon counting (TCSPC) setup<sup>19</sup> was applied to record emission decay data at single detection wavelength. A quartz cuvette with four optical windows of the dimension 2 mm x 10 mm was used. The sample was excited along the

2 mm pathlength, and the emission was recorded orthogonally to this. The optical density of the sample was set to about 0.1 at the excitation wavelength over 2 mm pathlength.

#### **5.2.2.10 Transient absorption measurements from femto- to microseconds**

Detailed information on the measurements of transient absorption from femto- to microseconds can be found in the cited literature.<sup>4,20,21</sup> More precise information on the experimental setup cannot be provided at this time. Measurements were performed in all solvent systems with varying amount of MBA.

## 5.3 Results and discussion

### 5.3.1. Partition coefficient of riboflavin and derivative

The catalyst riboflavin (RF) and its derivative tetraacetyl riboflavin (TARF) are studied regarding their partition between water and an oil phase. This should give an indication of the location of the catalyst within the microemulsion systems. The solvent structuring is introduced to increase the distance between the catalyst and the substrate. Collective compartmentalization would achieve exactly the opposite effect. Table 5 - 1 summarizes the partition coefficient values, while the absorbance spectra are shown in the Supporting Information (see Figure S.5 - 1). RF exhibits an average  $\log P$  value of  $-1.25$ . The choice of the supplier does not particularly affect the result. The molecule is, thus, hydrophilic and expected to be located in the water pseudo-phase, separated from the hydrophobic substrate 4-methoxybenzyl alcohol (MBA). In the absence of solvent structuring, distinct interactions between RF and the substrate are present. As a consequence, RF enhances the solubility of MBA in water and vice versa (see Figure S.5 - 2). The acetylation increases the  $\log P$  value to 0.48 for TARF. Despite the slight hydrophobic character, the catalyst is expected to tend to go to the interface with a  $\log P$  value close to 0. This should still allow sufficient separation of the substrate while still maintaining sufficient contact possibility for the final photooxidation. Accordingly, both catalysts are considered in the following. However, the focus is on the more stable TARF.

Table 5 - 1: Experimentally determined partition coefficient  $P$  of RF and TARF. RF is compared from the suppliers Sigma Aldrich (RF<sup>1</sup>) and Roth (RF<sup>2</sup>).

molecule	$\log P$	
RF <sup>1</sup>	- 1.30	} hydrophilic
RF <sup>2</sup>	- 1.20	
TARF	0.48	slightly hydrophobic

### 5.3.2. Surfactant-free solvent structuring

First, solvent structuring is introduced in the absence of any surfactant by forming surfactant-free microemulsions (SFMEs). For this purpose, ternary mixtures of water (W), the hydrophobic MBA, and a short-chain alcohol are considered. In a first attempt, ethanol (EtOH) is applied as the hydrotrope (see Figure 5 - 5(a)). Only 19 % (w/w) EtOH is required to close the miscibility gap between water and the substrate. The colored dots represent the compositions of the reaction mixtures in W/EtOH 75/25 (w/w) with an increasing amount of MBA. The W/EtOH ratio is chosen so that MBA can be dissolved up to 1.5 M in a thermodynamically stable system. Concurrently, the mixtures are not located too far from the miscibility gap in order to still pass the region in which mesoscopic structuring is present. Figure 5 - 5(b) depicts the correlation functions of the reaction mixtures obtained by dynamic light scattering (DLS). It is again assumed that a higher correlation intercept and larger lag times of the correlation functions correlate with more pronounced structuring.<sup>22</sup>

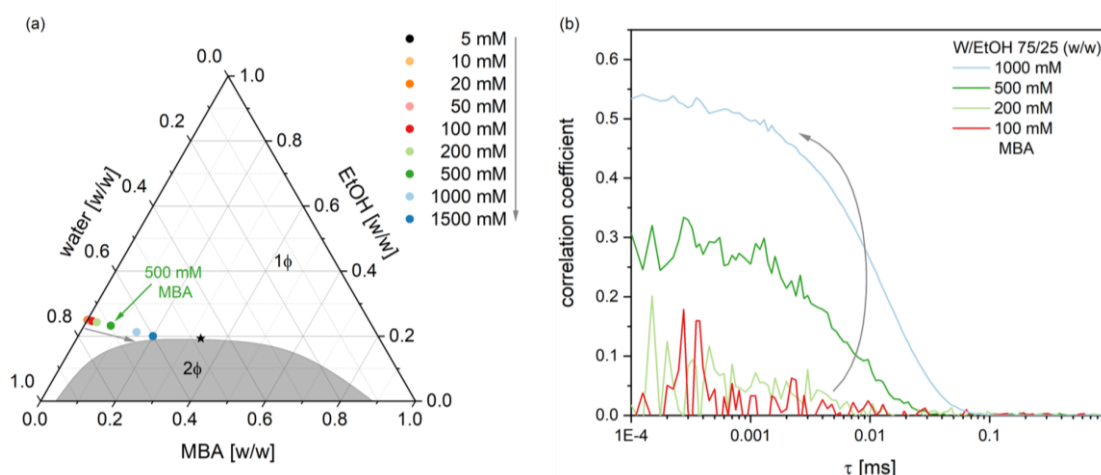


Figure 5 - 5: (a) Experimentally determined phase diagram of water, EtOH, and MBA at 25 °C. The biphasic area ( $2\Phi$ ) is represented by the gray shaded area, separated from the monophasic region ( $1\Phi$ ). The dots show the compositions applied during reactions with an increasing amount of MBA. The critical point is represented by the black star. (b) Correlation functions of the reaction mixtures obtained by DLS measurements at 25 °C.

In mixtures containing up to 100 mM MBA, no signal induced by solvent structuring can be detected. Correlation functions start to appear at 200 mM and increase with an increasing amount of MBA. A distinct signal is detected in mixtures with 1 M MBA. For this solution, it is therefore assumed that aggregates rich in MBA are dispersed in a water-rich pseudo-phase. For this reason, the mixture is designated as SFME. Further DLS measurements are performed in mixtures with a constant amount of 22 % (w/w) EtOH and varying W/MBA ratio (see Figure S.5 - 3 in the Supporting Information). The most pronounced correlation coefficient is measured in a mixture of W/EtOH/MBA 43/22/35 (w/w/w) close to the critical point (black star). A schematic illustration of the determination of the critical point is provided in Figure S.5 - 4 in the Supporting Information.

In the case of the hydrotrope EtOH, solvent structuring is only present at MBA concentrations  $> 100$  mM. However, as shown in the introductory chapter, MBA concentrations of 20 – 200 mM are of particular interest since the product quantum yield (PQY) in the reference system starts to decrease in this range. For this purpose, the hydrotrope is exchanged by t-butanol (tBuOH), which is known to pre-structure in water.<sup>22</sup> Figure 5 - 6 depicts the results obtained using tBuOH as the hydrotrope. In comparison with EtOH, a larger amount of 28 % (w/w) tBuOH is necessary to close the miscibility gap (see Figure 5 - 6(a)). Buchecker *et al.* reported the most pronounced DLS signal for W/tBuOH ratios of 60/40 and 70/30 (w/w).<sup>22</sup> For this reason, the ratios mentioned, as well as 65/35 (w/w), are considered in the ternary phase diagram with MBA (see Figure 5 - 6(b-d)). The DLS measurements confirm pre-structuring for all 3 ratios. The correlation functions increase again with an increasing amount of the substrate.

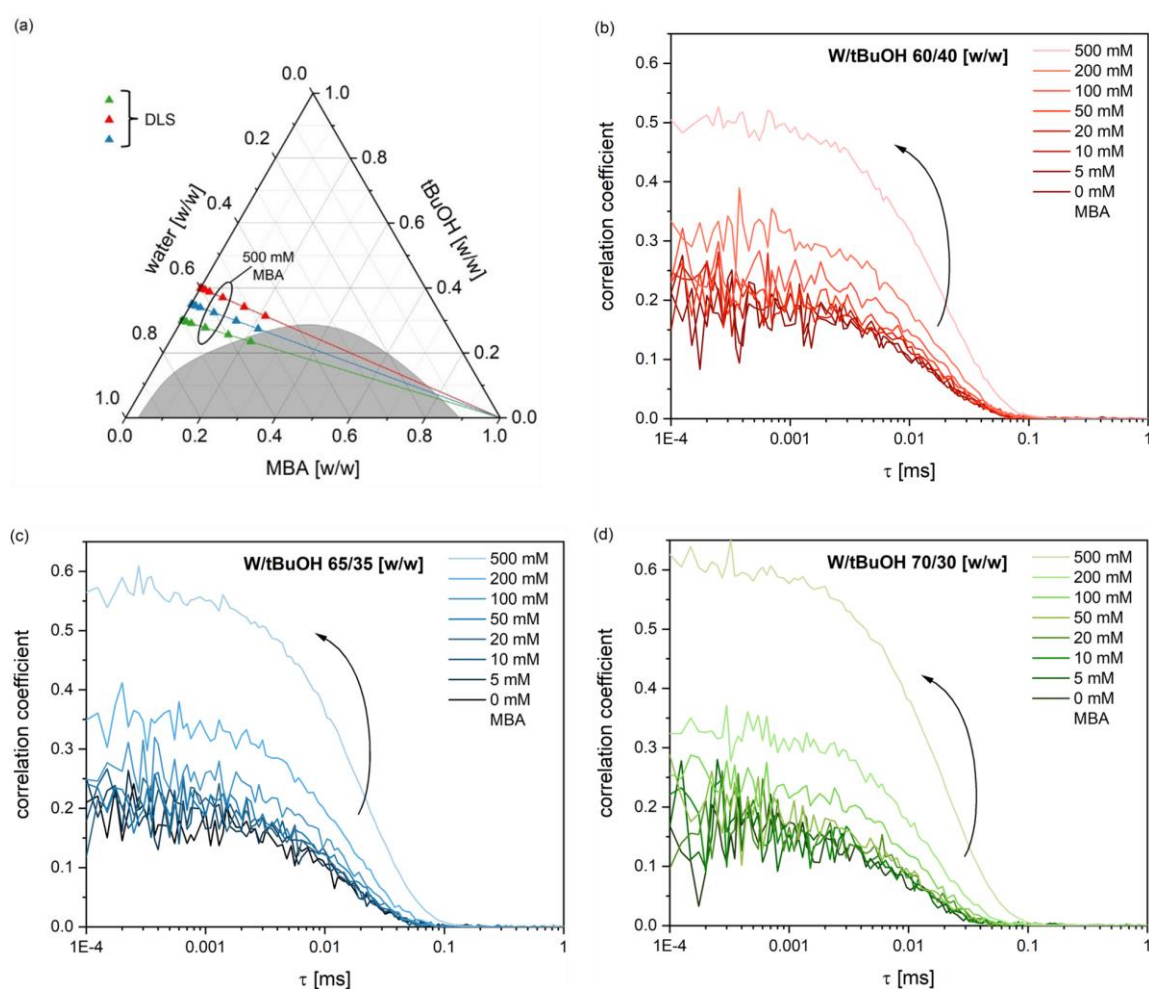


Figure 5 - 6: (a) Experimentally determined phase diagram of water, tBuOH, and MBA at 25 °C. The biphasic area ( $2\Phi$ ) is represented by the gray shaded area, separated from the monophasic region ( $1\Phi$ ). The triangles show the compositions applied during reactions and DLS measurements with an increasing amount of MBA. (b-d) Correlation functions of the reaction mixtures obtained by DLS measurements at 25 °C with varying ratios of W/tBuOH.

The highest correlation intercept is detected with W/tBuOH 70/30 (w/w) (green). Accordingly, the most pronounced structuring is expected with this ratio. However, pre-structuring is the lowest. In addition, phase separation already occurs at 1.5 M MBA, which is not the case for the other ratios studied. Since the ratio 65/35 (w/w) (blue) exhibits sufficient pre-structuring in the absence of MBA and reaches a more pronounced signal than 60/40 (w/w) (red) at high MBA concentration, the ratio is selected as a reaction solvent. For the concentrations studied, the structuring in the ternary system W/tBuOH/MBA is significantly more pronounced than in the W/EtOH/MBA reaction mixtures.

The reference system consists of a mixture of water and acetonitrile (AcN) in a ratio 50/50 (v/v). AcN is added to water to overcome the limited water solubility of MBA. DLS experiments are carried out to study a possible solvent structuring in the ternary reaction mixtures of W/AcN/MBA (see Figure 5 – 7). Different W/AcN ratios are considered. In the absence of the hydrophobic substrate, no signal is detected. Thus, no pre-structuring is expected to be present. By adding 500 mM MBA to the binary mixtures, correlation functions are measured, which are most pronounced for W/AcN 60/40 (v/v), followed by a ratio of 50/50 (v/v). Overall, the signal is of minor intensity. The signal of W/AcN 60/40 (v/v) is comparable to the result obtained with W/EtOH 75/35 (w/w). In mixtures with W/AcN ratios of 80/20 and 100/0 (v/v), 500 mM MBA is no longer soluble.

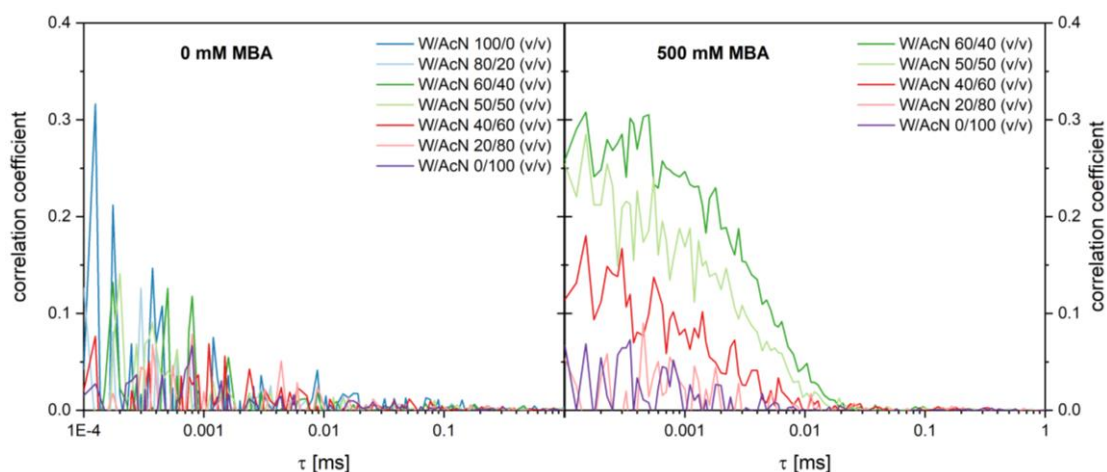


Figure 5 – 7: Correlation functions of the reference mixtures consisting of water and AcN. Different ratios of W/AcN are studied in the absence of MBA (left) and at 500 mM MBA (right).

### 5.3.3. Surfactant-based solvent structuring

The second approach to introducing structuring considers micellar systems. The idea is to incorporate the catalyst into the micellar interface in order to decelerate but not prevent contact with the substrate. The MBA is expected to be dissolved in the hydrophobic micellar core forming a surfactant-based microemulsion (SBME). The non-ionic surfactant pentaoethylene glycol monoethyl ether ( $C_8EO_5$ ) is chosen based upon the studies of Mitchell *et al.*, who reported the absence of liquid crystal formation for  $C_8EO_4$ .<sup>23</sup> Indeed, the chosen surfactant  $C_8EO_5$  is already liquid in its *pure* state (1 % (w/w)  $H_2O$ ). A surfactant concentration of 1.5 M is used to obtain a molar ratio of 1/1 to the substrate at its highest concentration studied. As expected, aggregates are already present in the absence of MBA, which is confirmed by DLS measurements (see Figure 5 - 8(a)). The minor correlation intercept is attributed to the lack of contrast at this high concentration. Moreover, absorbance measurements exclude interference with the absorbance of the produced aldehyde at about 300 nm (see Figure 5 - 8(b)).

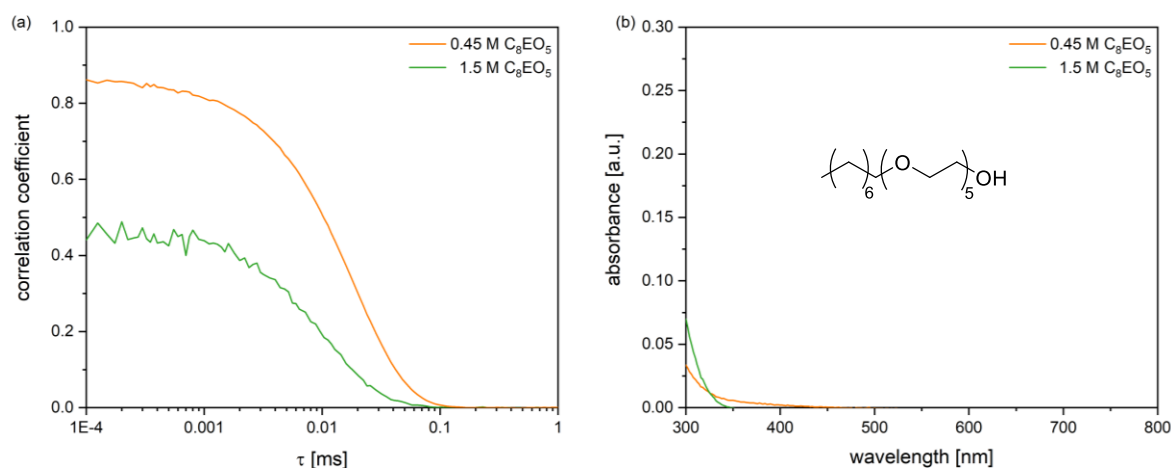


Figure 5 - 8: (a) Correlation functions of 0.45 M and 1.5 M  $C_8EO_5$  in water obtained by DLS measurements at 25 °C. (b) Absorbance spectra of the same solutions in a cuvette with a path length of 1 cm.

Although the formation of liquid crystals does not occur, the micellar solution of 1.5 M  $C_8EO_5$  is rather viscous, which will influence the diffusion of the dissolved molecules according to the Stokes-Einstein equation (see Equation 5 – 1). For this reason, the viscosities of the solvents are summarized in Table 5 - 2. The viscosity increases as follows:  $W/AcN < W/EtOH < W/tBuOH < C_8EO_5$ . While the viscosity is still comparable in the first three systems, the viscosity is about 10 times higher in the micellar solution of 1.5 M  $C_8EO_5$ . As a consequence, the diffusion of MBA is decreased significantly in this solvent.

In order to allow comparable diffusion of MBA, the micellar solution is diluted to the viscosity of W/tBuOH. Hence, C<sub>8</sub>EO<sub>5</sub> is also applied with a concentration of 0.45 M. Upon dilution, the correlation intercept increases (see Figure 5 - 8). This supports the assumption that the minor intercept in the case of 1.5 M is just the result of a contrast issue. As mentioned in the introduction, the photocatalytic activity of TARF is also affected by the amount of dissolved oxygen. Among the solvents studied, W/AcN dissolves oxygen best, followed by W/tBuOH and W/EtOH (see Table 5 - 2). The oxygen content is lowest in the micellar solution. With increasing surfactant concentration, the amount of dissolved oxygen decreases further.

*Table 5 - 2: Experimentally determined viscosity and oxygen solubility in different solvents. The diffusion coefficient is given relative to the diffusion coefficient in the reference (W/AcN) and is calculated by the ratio of the viscosities according to the Stokes-Einstein equation (see Equation 5 – 1).*

solvent	viscosity	rel. diffusion	O <sub>2</sub> solubility
	[mPas]	coefficient	[%]
W/AcN 50/50 [v/v]	0.810	1	63.2
W/EtOH 75/25 [w/w]	1.993	0.407	31.5
W/tBuOH 65/35 [w/w]	3.461	0.234	43.3
0.45 M C <sub>8</sub> EO <sub>5</sub>	3.513	0.231	25.7
1.5 M C <sub>8</sub> EO <sub>5</sub>	33.044	0.025	24.3

#### 5.3.4. Fluorescence decay of (TA)RF in different solvents

The fluorescence decay of TARF is monitored as a function of the concentration of the substrate, a possible quencher. An unfavored quenching of the excited state of the catalyst is reflected by a decrease in the fluorescence lifetime. Figure S.5 - 6 in the Supporting Information depicts the decay curves after exciting the photocatalyst in different solvents. This allows the determination of the fluorescence lifetime of the singlet excited state (see Figure 5 - 9). In the absence of the substrate, the excited TARF possesses the longest lifetime  $\tau_0$  of 5.8 ns in the micellar solution with 1.5 M C<sub>8</sub>EO<sub>5</sub> (see Figure 5 - 9(a), zoom, black curve). The solvent has the greatest viscosity and the lowest solubility of oxygen among the solvents studied here. Hence, the solvent limits both the concentration and the diffusion of the dissolved oxygen, which may also explain the long lifetime. Measurements need to be performed on a degassed sample to verify this.

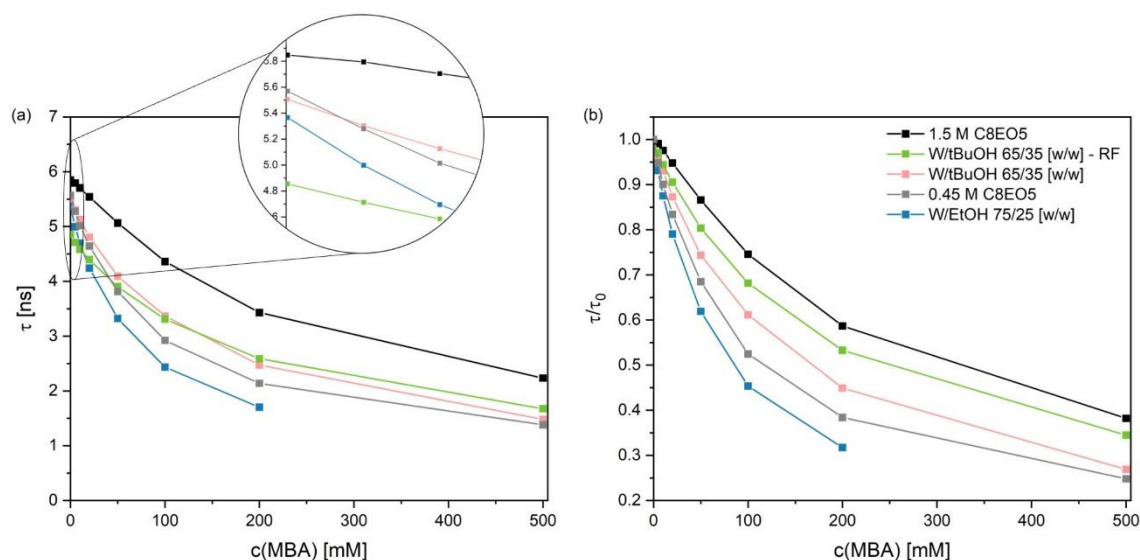


Figure 5 - 9: (a) Excited singlet state lifetime of (TA)RF  $\tau$  obtained by TCSPC in the different reaction solvents. (b)  $\tau$  normalized to the lifetime in the pure solvent ( $\tau_0$ ).

The second longest lifetime is obtained in the diluted micellar solution (5.6 ns, gray), closely followed by the W/tBuOH system (5.5 ns, rose). Finally, the lifetime of excited TARF is the shortest in W/EtOH (5.4 ns, blue), which exhibits the lowest viscosity and the second-greatest oxygen solubility. The solvent viscosity and the correlated oxygen diffusion seems to be the more decisive factor. However, the measured values are all quite close in a range of 5.4 – 5.8 ns. In the W/tBuOH system, the lifetime of TARF is compared to the lifetime of RF. In the pure solvent, the lifetime of RF is only 89 % (4.9 ns, green) of the lifetime of TARF.

As expected, an increasing amount of the substrate MBA leads to a decrease in the lifetime of the singlet excited state of the photocatalyst. This confirms the quenching effect of MBA. Figure 5 - 9(b) presents the lifetime as a function of MBA normalized to the lifetime in the pure solvent ( $\tau_0$ ). Accordingly, only the quenching effect of MBA is considered. Again, the best result is obtained with 1.5 M C<sub>8</sub>EO<sub>5</sub>, leading to the slowest decrease in  $\tau$ .

The micelles, hence, seem to have a shielding effect against the potential quenchers oxygen and MBA. Besides, the high viscosity and the correlated slow diffusion of MBA may also explain the result. The most rapid decrease and, thus, the strongest quenching effect is observed in W/EtOH. The fluorescence in the presence of 500 mM MBA is even too fast to detect. W/EtOH is the less structured solvent system, at least until 500 mM MBA. This could already indicate a successful shielding in the other solvents.

Although  $\tau_0$  of the catalyst is slightly larger in the 0.45 M surfactant solution than in W/tBuOH, the decrease with increasing substrate concentration is more pronounced in the micellar solution. Both solvents have a comparable viscosity. In addition, the amount of dissolved oxygen is 1.7 times higher in W/tBuOH, which would actually lead to expecting the opposite. Accordingly, better shielding of the excited photocatalyst in the surfactant-free

microemulsion may explain this observation. At 500 mM MBA, the curves converge again. Comparing TARF to RF in W/tBuOH, RF experiences better stabilization. The more hydrophilic RF is expected to be located in the water-pseudo phase. This may explain the better shielding effect on its excited singlet state. Overall, all solvents studied are expected to improve the lifetime of TARF compared to the reference system W/AcN. The data of the reference system are, however, currently not accessible.

### 5.3.5. Product quantum yield of 4-methoxybenzyl aldehyde

Figure 5 - 10 depicts the PQY of 4-methoxybenzyl aldehyde (MBAId) as a function of the substrate concentration. For comparison, 2 concentrations are measured in the reference system W/AcN (green). As shown in the inserted reference from the literature, the maximum in the PQY lies in between, at 20 mM MBA. It is apparent that all solvent systems yielded better results than the reference. The overall PQY is greater, and the shape of the peaks is broader.

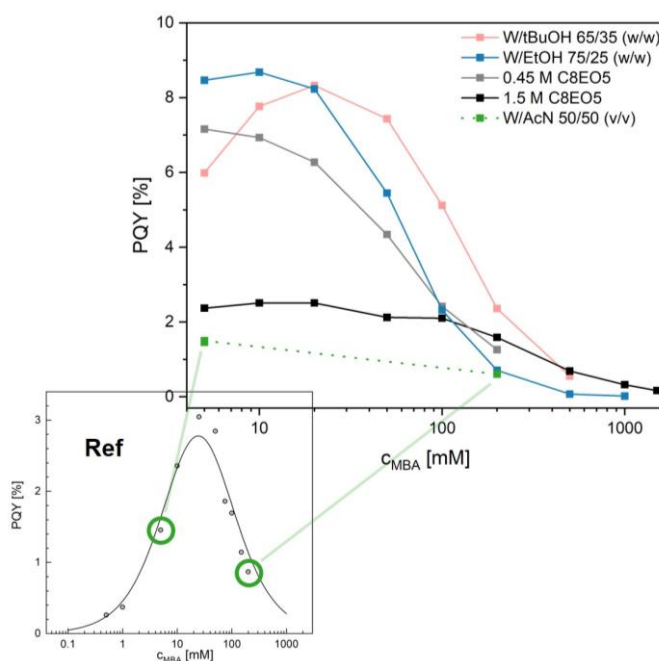


Figure 5 - 10: PQY of MBAId in the different reaction solvents as a function of the concentration of MBA. The inserted reference in W/AcN 50/50 (v/v) (Ref) is taken from the literature and reprinted with permission.<sup>4</sup>

The greatest maximum in the PQY of 8.7 % is obtained in W/EtOH (blue) at 10 mM MBA. Concurrently, the PQY decreases the fastest in this solvent system. This is in good agreement with the results observed in the previous chapter. The quenching effect of MBA on the singlet state of TARF is the highest in W/EtOH, leading to this fast decay in the PQY at increasing substrate concentrations. In the diluted micellar solution (gray), the maximum in the PQY is shifted to even smaller MBA concentrations ( $\leq 5$  mM), but the decay is slower than in W/EtOH. Thus, both W/EtOH and 0.45 M C<sub>8</sub>EO<sub>5</sub> provide higher PQY than the

reference solvent, but the decay starts at smaller substrate concentrations. Higher concentrations may increasingly push the substrate to the interface and thus closer to the catalyst, which could explain the earlier decay. The fact that the solubility limit is already reached in the diluted micellar solution with 500 mM MBA could support this assumption.

The concentrated micellar solution (black) yields only slightly higher PQY than the reference, although stabilization of the excited TARF is best in this solvent. The successful shielding of the photocatalyst may be the reason for the slow decay of the PQY in 1.5 M  $C_8EO_5$ . As the viscosity, however, is rather high, the diffusion of the substrate may be too restricted. If the MBA approaches the catalyst too slowly, the excited TARF may return to the ground state by non-productive b-ISC. Moreover, the oxygen solubility may be too low to ensure sufficient catalyst regeneration.

In the W/tBuOH system, a maximum in the PQY of 8.3 % is reached at 20 mM MBA. The surfactant-free microemulsion system is thus able to maintain the high quantum yield for the longest among all structured solvents. Based on the present experiments, it cannot be determined whether the solvent structuring and its resulting shielding of the catalyst from potential quenchers is the main reason for this result. The viscosity seems not to be the crucial parameter as it matches that of the diluted micellar solution, which yields worse results. However, the higher amount of dissolved oxygen may play an important role due to the regeneration of the photocatalyst. Furthermore, due to lacking stability of RF, the PQY cannot be compared at this point. As a consequence, no statement can be made as to whether the shielding of RF in the aqueous pseudo-phase prevents the final contact with the substrate. But as SFMEs are known to be highly dynamic,<sup>24</sup> this is not expected. More stable but still hydrophilic derivatives of RF should be considered.

In order to study the pre-aggregation of substrate and catalyst at high MBA concentrations, transient absorption measurements from femto- to microseconds were performed. The analysis of these results is, however, still pending. This kind of measurement allows for detecting spectra and kinetics of the excited singlet and triplet species as well as the radical intermediates.<sup>4</sup> The knowledge about the presence of TARF-MBA aggregates at certain MBA concentrations should provide a better understanding of whether the solvent structuring successfully shields the catalyst and prevents TARF-MBA aggregation, or whether the PQY is improved due to optimization of molecule diffusion and oxygen solubility.

## 5.4 Conclusion and outlook

In the present work, the impact of solvent structuring on the photocatalytic oxidation of 4-methoxybenzyl alcohol (MBA) by means of the photocatalyst tetraacetyl riboflavin TARF is investigated. For this purpose, micellar solutions of the surfactant  $C_8EO_5$  are applied in different concentrations. In addition, surfactant-free solvents of water (W) and a short-chain alcohol are considered. The addition of MBA to the water-alcohol mixtures induces structuring, designated as surfactant-free microemulsions (SFMEs). In the case of water and ethanol (EtOH), pronounced structuring only appears above 500 mM, while the mixture of water and t-butanol (tBuOH) is already pre-structured in the absence of MBA. The slightly hydrophobic TARF is expected to be located at the interface. The hydrophilic riboflavin should be dissolved in the water pseudo-phase. However, due to stability reasons, the focus is on TARF.

The lifetime of the excited singlet state of TARF is studied as a function of the substrate concentration. The lifetime decreases with increasing MBA concentrations. Compared to the reference system, which consists of water and acetonitrile, all structured solvents are expected to elongate the lifetime. The concentrated micellar solution shielded the catalyst the best against the quenching effect of MBA. Besides the presence of micelles, the solvent possesses a high viscosity and low oxygen solubility. Accordingly, the micelles may shield the excited TARF from quenching by MBA or oxygen. But the viscosity also restricts the diffusion of the quenchers, which could also be the decisive factor. The W/EtOH system shows the slightest improvement, which is attributed to the lacking structuring at low MBA concentrations. The viscosity of the diluted micellar solution matches that of the W/tBuOH mixture. Accordingly, the better shielding in the SFMEs of W/tBuOH/MBA seems to arise from the kind of structuring. Comparing TARF with RF reveals that the more hydrophilic RF, located in the water pseudo-phase, is even better stabilized in W/tBuOH.

Finally, all structured solvents improve the overall PQY compared to the reference system. The concentrated micellar solution only slightly improved the absolute PQY, which may be explained by the low substrate diffusion. However, the good shielding leads to a comparatively slow decrease with increasing MBA. The best absolute PQY is obtained in W/EtOH, which also shows the fastest decay due to insufficient shielding. The diluted micellar solution, as well as the surfactant-free W/tBuOH system, also yield high PQY. In the case of W/tBuOH, the maximum in the PQY appears at the highest MBA concentration (20 mM) among all structured solvents.

Accordingly, the SFME W/tBuOH/MBA seems to efficiently shield the TARF and still allows the reaction to occur, as the substrate diffusion is not too restricted in the low viscous solvent. Even better results are expected with RF due to the elongated lifetime of the excited singlet state compared to TARF. For this reason, more stable, hydrophilic RF derivatives should be considered, such as sugar derivatives. An even better shielding in the aqueous-pseudo phase may allow reactions at even higher MBA concentrations. This is not possible in the diluted, low viscous micellar solution, as the solubility limit of MBA is already exceeded at 1 M substrate. Furthermore, the impact of the dissolved amount of oxygen should be investigated in more detail. The optimum concentration has to be identified that allows the best catalyst regeneration without quenching its excited state before substrate conversion. In order to gain a final understanding of the impact of structuring on the TARF-MBA pre-aggregation, an evaluation of the transient absorbance measurements is indispensable. In addition, molecular dynamic simulations could provide more precise information about the location of the catalyst in the structured solvents on a molecular level. At this point, all conclusions are rather speculative. It remains to be seen whether the solvent structuring really has an impact or whether, as in the previous projects, other parameters influence the reaction predominantly.

## 5.5 Supporting information

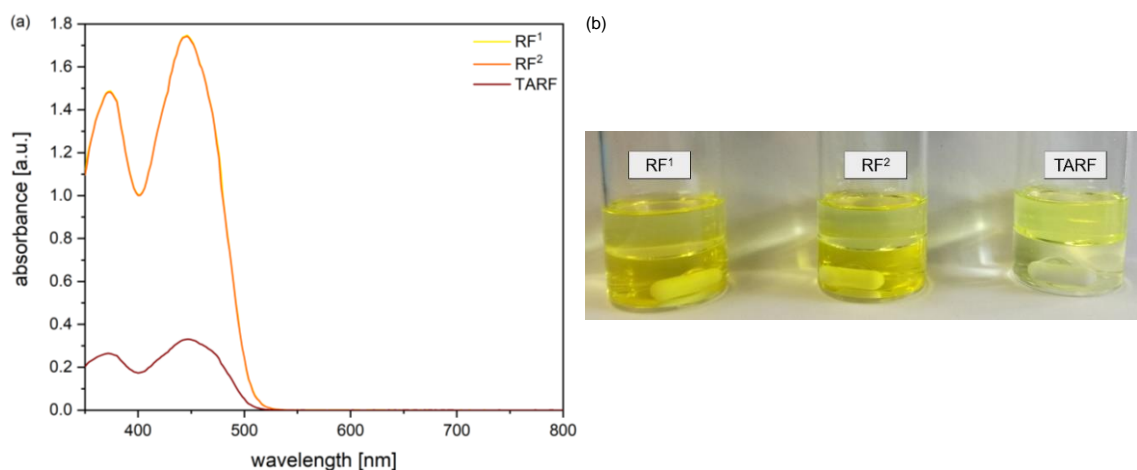


Figure S.5 - 1: (a) Absorbance spectra of RF and TARF in the water phase for determination of the  $\log P$  value. RF is compared from the suppliers Sigma Aldrich (RF<sup>1</sup>) and Roth (RF<sup>2</sup>). (b) Corresponding photographs of the distribution of RF and TARF between the water and the octanol phase.

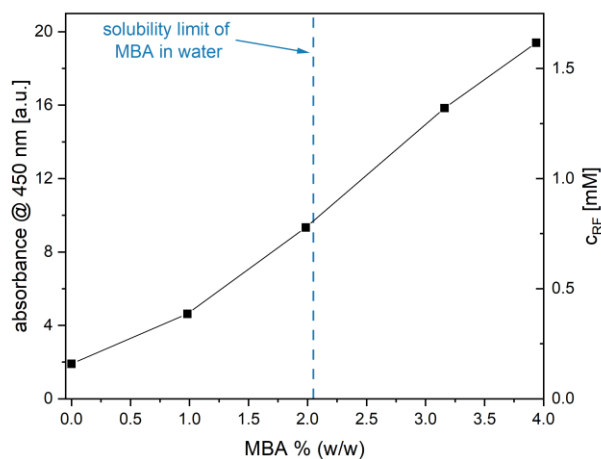


Figure S.5 - 2: Absorbance and dissolved concentration of RF in water as a function of the amount of MBA in water. For calculating the concentration of dissolved RF from the experimentally determined absorbance, the extinction coefficient  $\epsilon_{RF, 450 \text{ nm}} = 12'500 \text{ L}/(\text{mol cm})$  and Lambert-Beer's law are applied.<sup>25,26</sup>

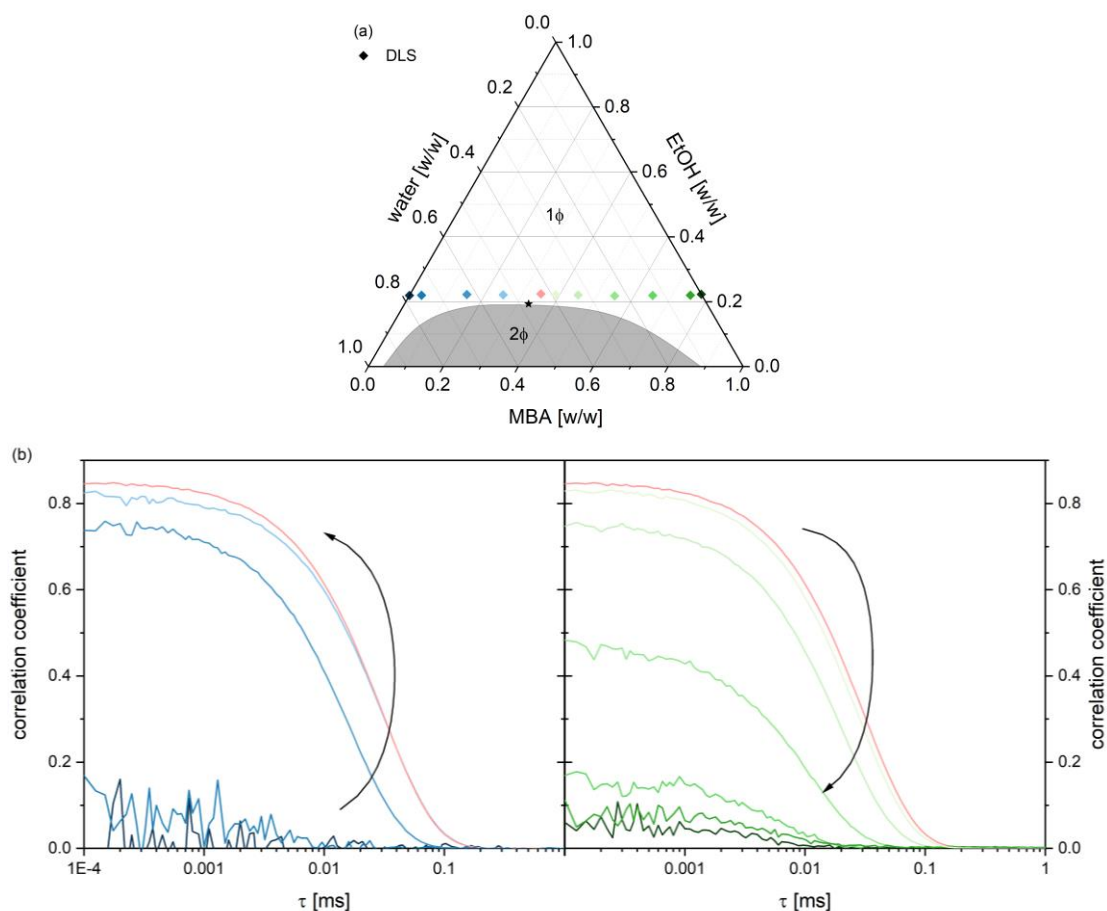


Figure S.5 - 3: (a) Experimentally determined phase diagram of water, EtOH, and MBA at 25 °C. The biphasic area ( $2\Phi$ ) is represented by the gray shaded area, separated from the monophasic region ( $1\Phi$ ). The rhombs depict compositions measured by means of DLS. The critical point is marked with a black star. (b) Corresponding correlation functions obtained by DLS measurements at 25 °C.

Dynamic light scattering experiments are performed in mixtures with a constant amount of 22 % (w/w) EtOH and varying W/MBA ratio (see Figure S.5 - 3(a, colored rhombs) and (b)). No signal is detected in the binary W/EtOH mixture (dark blue), although it is known that cluster formation is present.<sup>22,27,28</sup> However, this kind of aggregation occurs at a smaller molecular scale than considered in this work, and the fluctuations exhibit too high diffusion coefficients.<sup>22</sup> With an increasing amount of MBA, the signal increases significantly, indicating pronounced structuring (blue). The most pronounced correlation coefficient is measured in a mixture of W/EtOH/MBA 43/22/35 (w/w/w) (rose) close to the critical point (black star). With the further addition of MBA, the correlation function decreases again (green). In the binary mixture EtOH/MBA, a weak signal is detected. It is thus assumed that only loose aggregates or even no aggregates at all are present.

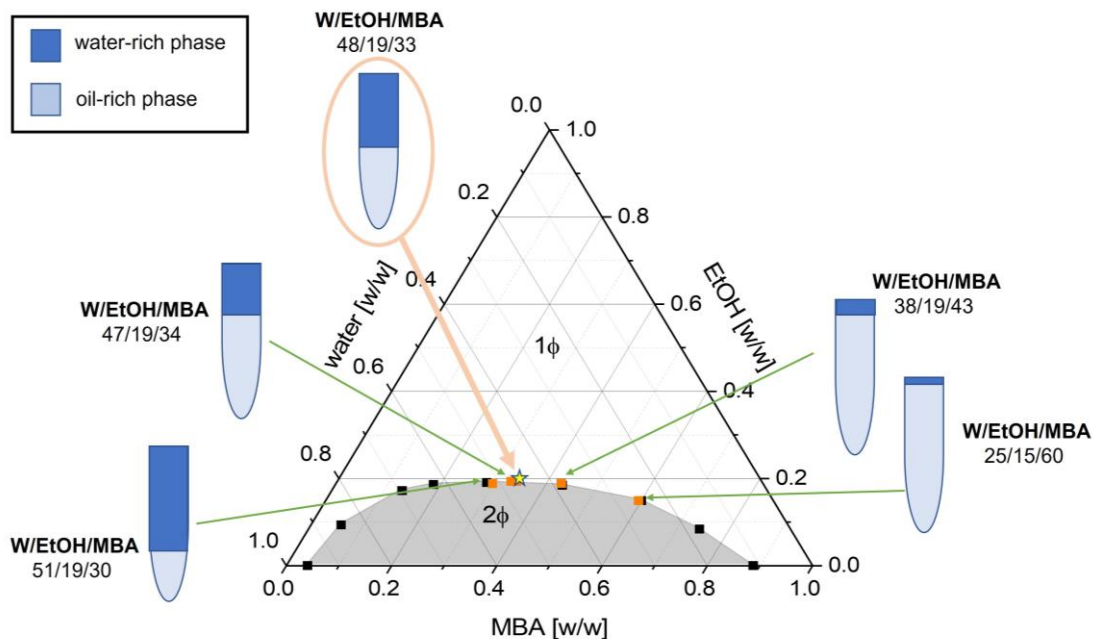


Figure S.5 - 4: Schematic representation of the determination of the critical point in a ternary system.

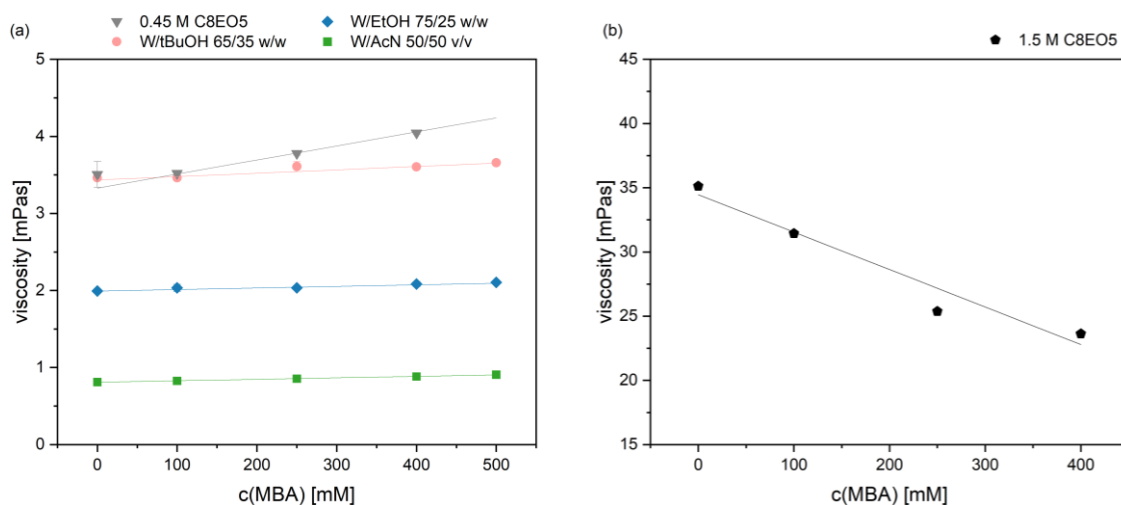


Figure S.5 - 5: (a,b) Experimentally determined viscosity of the different reaction solvents as a function of the MBA concentration. The solvents in (a) depict a linear increase of the viscosity with an increasing MBA concentration. The increase is comparable for W/EtOH, W/tBuOH, and W/AcN. The diluted micellar solution shows a stronger increase, which may be attributed to the swelling of the micelles due to the incorporated MBA. The viscosity of the concentrated micellar solution (b) decreases with increasing substrate concentration. It is assumed that the MBA is increasingly incorporated in the micellar interface, which makes the interface more and more flexible, leading to a decrease in viscosity. The viscosity of the concentrated micellar solution containing MBA was measured 10 times at an angle of  $90^\circ$ .

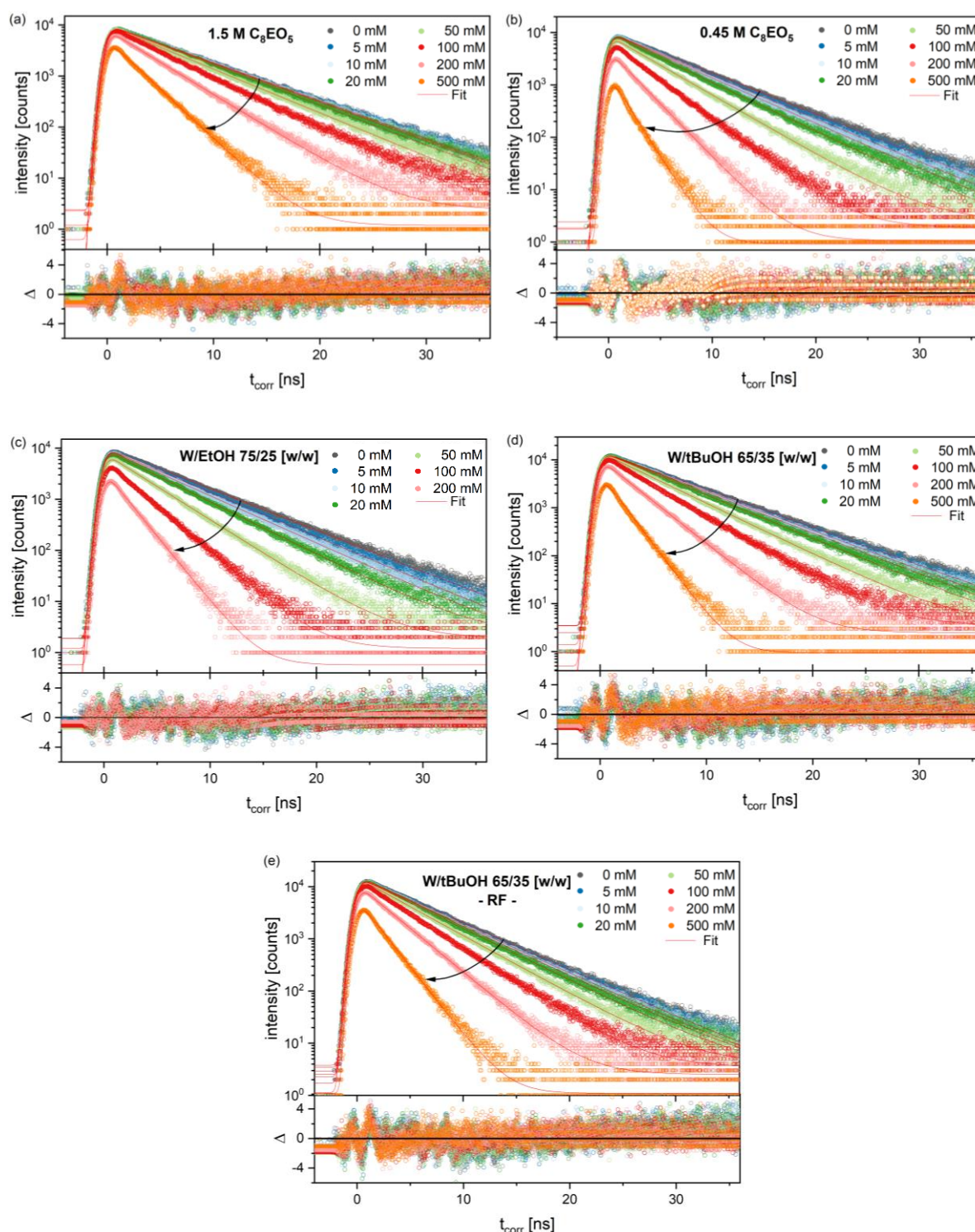


Figure S.5 - 6: Fluorescence decay of the photocatalyst TARF in the different reaction solvents obtained by TCSPC. The decay is monitored for increasing MBA concentrations (blue to orange). In the case of W/tBuOH, the decay is also detected for RF. The measurements are performed up to 500 mM MBA, except for W/EtOH. In this case, the decay at 500 mM is too fast to detect. The same is observed for 1 M MBA in W/tBuOH. With 0.45 M surfactant, the substrate is no longer soluble at 1 M.

## 5.6 References

- (1) Srivastava, V.; Singh, P. K.; Srivastava, A.; Singh, P. P. Synthetic Applications of Flavin Photocatalysis: A Review. *RSC Adv.* **2021**, *11* (23), 14251–14259. <https://doi.org/10.1039/d1ra00925g>.
- (2) Gualandi, A.; Rodeghiero, G.; Della Rocca, E.; Bertoni, F.; Marchini, M.; Perciaccante, R.; Jansen, T. P.; Ceroni, P.; Cozzi, P. G. Application of Coumarin Dyes for Organic Photoredox Catalysis. *Chem. Commun.* **2018**, *54* (72), 10044–10047. <https://doi.org/10.1039/C8CC04048F>.
- (3) Majek, M.; Jacobi von Wangelin, A. Metal-Free Carbonylations by Photoredox Catalysis. *Angew. Chemie Int. Ed.* **2015**, *54* (7), 2270–2274. <https://doi.org/10.1002/anie.201408516>.
- (4) Megerle, U.; Wenninger, M.; Kutta, R.-J.; Lechner, R.; König, B.; Dick, B.; Riedle, E. Unraveling the Flavin-Catalyzed Photooxidation of Benzylic Alcohol with Transient Absorption Spectroscopy from Sub-Pico- to Microseconds. *Phys. Chem. Chem. Phys.* **2011**, *13* (19), 8869. <https://doi.org/10.1039/c1cp20190e>.
- (5) Larson, R. A.; Stackhouse, P. L.; Crowley, T. O. Riboflavin Tetraacetate: A Potentially Useful Photosensitizing Agent for the Treatment of Contaminated Waters. *Environ. Sci. Technol.* **1992**, *26* (9), 1792–1798. <https://doi.org/10.1021/es00033a013>.
- (6) Anastas, P. T.; Warner, J. C. *Green Chemistry: Theory and Practice*, Reprint edn.; Oxford University Press, 2000.
- (7) König, B.; Kümmel, S.; Svobodová, E.; Cibulka, R. Flavin Photocatalysis. *Phys. Sci. Rev.* **2018**, *3* (8), 20170168. <https://doi.org/10.1515/psr-2017-0168>.
- (8) Svoboda, J.; Schmaderer, H.; König, B. Thiourea-Enhanced Flavin Photooxidation of Benzyl Alcohol. *Chem. - A Eur. J.* **2008**, *14* (6), 1854–1865. <https://doi.org/10.1002/chem.200701319>.
- (9) Daďová, J.; Kümmel, S.; Feldmeier, C.; Cibulková, J.; Pažout, R.; Maixner, J.; Gschwind, R. M.; König, B.; Cibulka, R. Aggregation Effects in Visible-Light Flavin Photocatalysts: Synthesis, Structure, and Catalytic Activity of 10-Arylflavins. *Chem. - A Eur. J.* **2013**, *19* (3), 1066–1075. <https://doi.org/10.1002/chem.201202488>.
- (10) Cibulka, R.; Vasold, R.; König, B. Catalytic Photooxidation of 4-Methoxybenzyl

- Alcohol with a Flavin-Zinc(II)-Cyclen Complex. *Chem. - A Eur. J.* **2004**, *10* (24), 6223–6231. <https://doi.org/10.1002/chem.200400232>.
- (11) Megerle, U.; Lechner, R.; König, B.; Riedle, E. Laboratory Apparatus for the Accurate, Facile and Rapid Determination of Visible Light Photoreaction Quantum Yields. *Photochem. Photobiol. Sci.* **2010**, *9* (10), 1400–1406. <https://doi.org/10.1039/c0pp00195c>.
- (12) Salzmann, S.; Marian, C. M. The Photophysics of Alloxazine: A Quantum Chemical Investigation in Vacuum and Solution. *Photochem. Photobiol. Sci.* **2009**, *8* (12), 1655–1666. <https://doi.org/10.1039/b9pp00022d>.
- (13) Penzkofer, A.; Stierl, M.; Mathes, T.; Hegemann, P. Absorption and Emission Spectroscopic Characterization of Photo-Dynamics of Photoactivated Adenylyl Cyclase Mutant BPAC-Y7F of *Beggiatoa* Sp. *J. Photochem. Photobiol. B Biol.* **2014**, *140*, 182–193. <https://doi.org/10.1016/j.jphotobiol.2014.06.017>.
- (14) Einstein, A. Über Die von Der Molekularkinetischen Theorie Der Wärme Geforderte Bewegung von in Ruhenden Flüssigkeiten Suspendierten Teilchen. *Ann. Phys.* **1905**, *17*, 549–560. <https://doi.org/10.1002/andp.19053220806>.
- (15) Misono, T. Dynamic Light Scattering (DLS). In *Measurement Techniques and Practices of Colloid and Interface Phenomena*; Springer: Singapore, 2019. [https://doi.org/10.1007/978-981-13-5931-6\\_10](https://doi.org/10.1007/978-981-13-5931-6_10).
- (16) Warneck, P.; Wurzinger, C. Product Quantum Yields for the 305-Nm Photodecomposition of Nitrate in Aqueous Solution. *J. Phys. Chem.* **1988**, *92* (22), 6278–6283. <https://doi.org/10.1021/j100333a022>.
- (17) Braslavsky, S. E. Glossary of Terms Used in Photochemistry, 3rd Edition (IUPAC Recommendations 2006). *Pure Appl. Chem.* **2007**, *79* (3), 293–465. <https://doi.org/10.1351/pac200779030293>.
- (18) Mühldorf, B.; Wolf, R. C-H Photooxygenation of Alkyl Benzenes Catalyzed by Riboflavin Tetraacetate and a Non-Heme Iron Catalyst. *Angew. Chemie - Int. Ed.* **2016**, *55* (1), 427–430. <https://doi.org/10.1002/anie.201507170>.
- (19) Kutta, R. J. Blitzlichtphotolyse - Untersuchung Zu LOV-Domänen Und Photochromen Systemen, University of Regensburg, 2012.
- (20) Kutta, R. J.; Langenbacher, T.; Kensy, U.; Dick, B. Setup and Performance of a Streak Camera Apparatus for Transient Absorption Measurements in the Ns to Ms Range. *Appl. Phys. B Lasers Opt.* **2013**, *111* (2), 203–216.

<https://doi.org/10.1007/s00340-012-5320-2>.

- (21) Megerle, U.; Pugliesi, I.; Schriever, C.; Sailer, C. F.; Riedle, E. Sub-50 Fs Broadband Absorption Spectroscopy with Tunable Excitation: Putting the Analysis of Ultrafast Molecular Dynamics on Solid Ground. *Appl. Phys. B Lasers Opt.* **2009**, *96* (2–3), 215–231. <https://doi.org/10.1007/s00340-009-3610-0>.
- (22) Buchecker, T.; Krickl, S.; Winkler, R.; Grillo, I.; Bauduin, P.; Touraud, D.; Pfitzner, A.; Kunz, W. The Impact of the Structuring of Hydrotropes in Water on the Mesoscale Solubilisation of a Third Hydrophobic Component. *Phys. Chem. Chem. Phys.* **2017**, *19* (3), 1806–1816. <https://doi.org/10.1039/c6cp06696h>.
- (23) Mitchell, D. J.; Tiddy, G. J. T.; Waring, L.; Bostock, T.; McDonald, M. P. Phase Behaviour of Polyoxyethylene Surfactants with Water. Mesophase Structures and Partial Miscibility (Cloud Points). *J. Chem. Soc. Faraday Trans. 1 Phys. Chem. Condens. Phases* **1983**, *79* (4), 975. <https://doi.org/10.1039/f19837900975>.
- (24) Zemb, T. N.; Klossek, M.; Lopian, T.; Marcus, J.; Schöettl, S.; Horinek, D.; Prevost, S. F.; Touraud, D.; Diat, O.; Marčelja, S.; Kunz, W. How to Explain Microemulsions Formed by Solvent Mixtures without Conventional Surfactants. *Proc. Natl. Acad. Sci.* **2016**, *113* (16), 4260–4265. <https://doi.org/10.1073/pnas.1515708113>.
- (25) Kemter, K. Untersuchungen Zur Riboflavin Synthase Und Flavokinase Aus Verschiedenen Organismen, Technical University of Munich, 2002.
- (26) Swinehart, D. F. The Beer-Lambert Law. *J. Chem. Educ.* **1962**, *39* (7), 333–335. <https://doi.org/10.1021/ed039p333>.
- (27) Dixit, S.; Crain, J.; Poon, W. C. K.; Finney, J. L.; Soper, A. K. Molecular Segregation Observed in a Concentrated Alcohol–Water Solution. *Nature* **2002**, *416* (6883), 829–832. <https://doi.org/10.1038/416829a>.
- (28) Gereben, O.; Pusztai, L. Investigation of the Structure of Ethanol–Water Mixtures by Molecular Dynamics Simulation I: Analyses Concerning the Hydrogen-Bonded Pairs. *J. Phys. Chem. B* **2015**, *119* (7), 3070–3084. <https://doi.org/10.1021/jp510490y>.



## Chapter 6 In-depth study of binary ethanol-triacetin mixtures in relation with their excellent solubilization power

### 6.0 Abstract

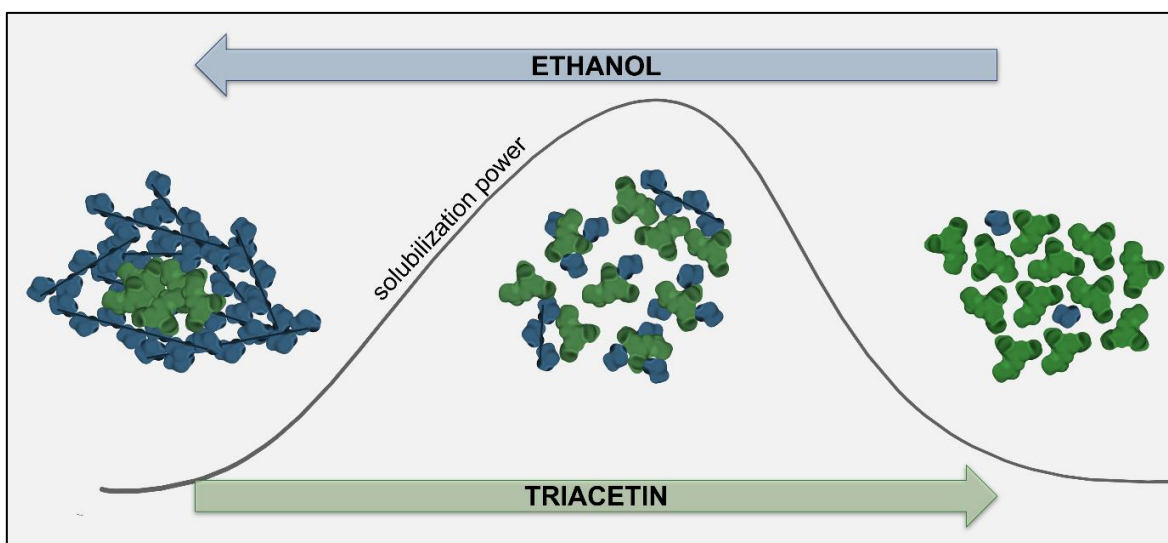


Figure 6 - 1: Schematic illustration of the molecular distribution in binary mixtures of ethanol and triacetin and the resulting solubilization power of the mixtures.

A significant synergistic effect is observed when solubilizing curcumin or tetrahydrocurcumin in binary mixtures of ethanol and triacetin. The present work deals with a detailed investigation of the solvent system by means of COSMO-RS-based calculations, dynamic light scattering, small-and-wide-angle X-ray scattering, and dielectric relaxation spectroscopy. Theoretical calculations lead to the conclusion that the enhanced solubility is not primarily the result of an interaction optimum between individual surface charge densities. Scattering experiments also exclude the formation of mesoscopic structures as the main reason. However, dielectric relaxation spectra suggest that in the concentration range of  $0.3 \leq x(\text{triacetin}) \leq 0.6$ , ethanol molecules are released from their living polymer ethanol network and can interact with triacetin on a molecular level. The mesoscopic aggregation, thus, decreases. The concentration range of the ethanol-triacetin complexes has a significant overlap with the range of maximum solubility of (tetrahydro)curcumin. Nevertheless, despite detailed investigations, the exact origin of the solubilization power remains speculative.

This chapter is submitted to *Physical Chemistry Chemical Physics* (Hofmann, E.; Saridis, A.; Touraud, D.; Buchner, R.; Kunz, W. *PCCP*. **2023**, submitted).<sup>1</sup> Small-and-wide-angle X-ray scattering was performed on my behalf by Dr. Olivier Diat at the Institute of Separation Chemistry Marcoule (France). The solubility of tetrahydrocurcumin was studied by Anna Saridis (University of Regensburg, Germany).

## 6.1 Introduction

Solubility represents one of the most important and basic properties in chemistry and industry. However, especially natural compounds, like curcumin, often possess poor solubility. This does not only affect their final applications but already their exploitation by, e.g., liquid-liquid extraction, where the solubility of the compound is crucial.<sup>2–10</sup> Degot *et al.*<sup>11</sup> reported a simple food-grade solvent system of ethanol (EtOH) and triacetin (TriA) for the extraction of curcumin, a widely used natural, hydrophobic dye. Binary mixtures of EtOH and TriA can dissolve significant amounts of curcumin. A large synergistic solubilization is observed in mixtures with a molar fraction of TriA of 0.24 – 0.46.<sup>7,11</sup>

To enhance the solubility of practically water-insoluble compounds, such as curcumin in water, solvent structuring can be introduced. A compartmentalization of the solvent into pseudo-phases on a mesoscopic scale can be achieved by the formation of micelles in aqueous surfactant solutions. Also binary mixtures of water and a hydrotrope can exhibit pre-structuring that influences the solubilization power of the solvent.<sup>12–14</sup> The presence of mesoscale inhomogeneities in macroscopically transparent solutions is commonly investigated by scattering experiments, including dynamic light scattering (DLS) and small-(and-wide)-angle X-ray scattering (S(W)AXS).<sup>14–20</sup> Both techniques were applied in this study to investigate mesoscale structuring in binary TriA/EtOH mixtures.

A theoretical approach allowing the investigation of unstructured liquid systems is given by the COSMO-RS model, which combines quantum chemical calculations with fast statistical thermodynamics.<sup>21,22</sup> In the initial step, *COnductor-like Screening MOdel* (COSMO) calculations determine the screening charge density  $\sigma$  of a molecule placed in a virtual conductor. The COSMO surface is then divided into smaller segments. Molecular interactions are thus displayed by local pairwise interacting surface segments with specific  $\sigma$  values. This allows extending the COSMO model to *Real Solvents* (COSMO-RS). By calculating the (pseudo-)chemical potential  $\mu_S^{(i)}$  of a compound  $i$  according to Equation 6 - 1, several

macroscopic thermodynamic properties become accessible, such as vapor pressure, solubilities, and partition coefficients.<sup>21–28</sup>

$$\mu_S^{(i)} = \mu_{C,S}^{(i)} + \int p^{(i)}(\sigma) \cdot \mu_S(\sigma) d\sigma \quad \text{Eq. 6 - 1}$$

The distribution of the screening charge density on the molecular surface is described by the probability distribution function  $p^{(i)}(\sigma)$ , the so-called  $\sigma$ -profile. The  $\sigma$ -potential  $\mu_S$  describes the affinity of the system S to a surface of polarity  $\sigma$ . Finally, the size and shape differences of the molecules in the system are included by the combinatorial term  $\mu_{C,S}^{(i)}$ .<sup>21,23–25</sup>

Dielectric relaxation spectroscopy (DRS), which measures the interaction of a sample with a low-amplitude electric field in the Mega- to Gigahertz range, probes the cooperative dynamics of the sample on the microscopic to mesoscopic level. In DRS, the response of the sample is conveniently expressed in terms of the complex permittivity  $\hat{\epsilon}(\nu)$ .<sup>29,30</sup>

$$\hat{\epsilon}(\nu) = \epsilon'(\nu) - i\epsilon''(\nu) \quad \text{Eq. 6 - 2}$$

with the relative permittivity  $\epsilon'(\nu)$  and the dielectric loss  $\epsilon''(\nu)$ . The relative permittivity indicates in how far the sample polarization can follow an external field of frequency  $\nu$ . At  $\nu$  close to 0, all polarization mechanisms of the sample contribute, yielding the dielectric constant  $\epsilon$  (static permittivity,  $\lim_{\nu \rightarrow 0} \epsilon'(\nu)$ ). With increasing  $\nu$ , this is less and less the case due to various processes governed by intermolecular interactions, such as dipole rotation. Accordingly,  $\epsilon'(\nu)$  drops until the high-frequency permittivity  $\epsilon_\infty$  ( $= \lim_{\nu \rightarrow \infty} \epsilon'(\nu)$ ), determined by intramolecular polarizability, is reached in the Terahertz range. In this dispersion region from  $\epsilon$  to  $\epsilon_\infty$  the sample absorbs electromagnetic radiation, expressed by  $\epsilon''(\nu)$ . The dynamics in dipolar solvents are mainly caused by more-or-less diffusive reorientation of permanent molecular dipoles.<sup>29–31</sup> In hydrogen bond-forming solvents, such as water or alcohols, cooperative relaxation processes occur that are commonly described by the “wait-and-switch-type” model,<sup>32–34</sup> akin to the dynamics of living polymers.<sup>35</sup> In these systems the slowest (lowest frequency) contribution to  $\hat{\epsilon}(\nu)$  monitors the cooperative rearrangement of the intermolecular H-bond system.

## 6.2 Material and methods

### 6.2.1 Chemicals

Dichloromethane (DCM, purity  $\geq 99.8\%$ ) was purchased from Fisher Scientific (Reinach, Switzerland). Ethanol (EtOH,  $> 99\%$ ) was delivered by Merck (Darmstadt, Germany). Triacetin (TriA, 99 %, FCC, FG) was from Sigma Aldrich (Darmstadt, Germany). Synthetic curcumin I ( $> 97\%$ ) was purchased from TCI (Eschborn, Germany). 1-Butanol (1BuOH, ultrapure, spectrophotometric grade, 99.0+ %) was from Alfa Aesar (Karlsruhe, Germany). Tetrahydrocurcumin (THC, 98 %) was purchased from Carbolution (St. Ingbert, Germany). All chemicals were used without further purification.

### 6.2.2 Methods

#### 6.2.2.1 Solubility experiments

Mixtures of EtOH and TriA were supersaturated with THC and stirred for 1 h at room temperature while being shielded from the light. Then, the samples were filtered using PTFE syringe filters (0.45  $\mu\text{m}$  pore size) and diluted with technical-grade EtOH. The absorbance of the diluted samples was measured in 1 cm quartz glass cuvettes by means of a Lambda 18 UV/VIS spectrometer from PerkinElmer (Rodgau, Germany). The procedure was repeated 3 times for all EtOH/TriA ratios.

#### 6.2.2.2 Theoretical calculations

The BIOVIA *COSMOthermX* software<sup>36</sup> (version 19.0.4 by Dassault Systèmes, 2019), based on the COSMO-RS model<sup>21,24,37</sup>, was applied to predict the chemical potential of (tetrahydro)curcumin in binary mixtures of EtOH and TriA. The chemical potential is computed iteratively on FINE<sup>37</sup> level using a TZVPD<sup>38</sup> basis set. Curcumin was taken from the *COSMObase TZVPD-FINE 19.0* database. The conformational analysis of THC was performed by means of the *COSMOconfX* software<sup>39</sup> (version 4.3 by Dassault Systèmes, 2018) and the *TURBOMOLE* program<sup>40</sup> (version TmoleX 3.4 by Dassault Systèmes, 2007-2013). Geometry optimizations were carried out using DFT/COSMO calculations on the TZVPD-FINE level.

Density functional theory (DFT) calculations were carried out using the B3LYP hybrid functional by means of the Gaussian ® 09W program<sup>41</sup> (version 7.0, 1995-09, Gaussian). The 6-31++G(d,p) basis set was applied and the molecular properties were determined in EtOH or in a continuum with a dielectric constant of 6.8. The results are summarized in the Supporting Information (see Figure S.6 - 1, Table S.6 - 1).

### 6.2.2.3 Dynamic light scattering

Dynamic light scattering (DLS) experiments were performed as described in Chapter 1.2.2.5.

### 6.2.2.4 Small-and-wide-angle X-ray scattering

Small-and-wide-angle X-ray scattering (SWAXS) measurements were carried out on a bench-built XENOCs using a Mo radiation X-ray source ( $\lambda = 0.0071$  nm). A large online scanner detector (diameter: 345 mm, from MAR Research) was used to record the scattered beam. A large  $q$ -range ( $0.2 - 40$  nm<sup>-1</sup>) was covered with an off-center detection. The collimation was applied using a 12:∞ multilayer Xenocs mirror (for Mo radiation) connected to 2 sets of scatter-less FORVIS slits providing a  $0.8 \times 0.8$  nm X-ray beam at the sample position. Pre-analysis of the data was performed with a FIT2D software. The scattered intensities are detected versus the magnitude of the scattering vector  $q = [(4\pi)/\lambda \sin(\vartheta/2)]$  with the wavelength of the incident radiation  $\lambda$  and the scattering angle  $\vartheta$ . The solutions were filled in 2 mm quartz capillaries. Usual corrections for background (empty cell and detector noise) subtractions and intensity normalization using high-density polyethylene film as a standard were applied. The experimental resolution was  $\Delta q/q = 0.05$ . The scattering vector calibration standard was silver behenate in a sealed capillary. All measurements were carried out at room temperature.

### 6.2.2.5 Auxiliary measurements

The densities of the binary mixtures EtOH/TriA were measured with the vibrating-tube densimeter DMA 5000 A from Anton Paar (Austria) at  $25 \pm 0.01$  °C. The rolling-ball viscometer AMVn from Anton Paar (Austria) was applied to determine the dynamic viscosities of the solutions at  $25 \pm 0.01$  °C. The densities and viscosities are given in the Supporting Information (see Figure S.6 - 2).

### 6.2.2.6 Dielectric relaxation spectroscopy

Dielectric spectra were recorded using a frequency-domain reflectometer equipped with an Agilent E8364B vector network analyzer (VNA) and two open-ended coaxial dielectric probes (Agilent 85070E-20 ( $0.05 \leq \nu \leq 20$  GHz) and 85070E-50 ( $5 - 50$  GHz)).<sup>42</sup> The dielectric probes are mounted into cells thermostatted at  $25 \pm 0.01$  °C by means of a Huber

CG-505 thermostat. Air, purified mercury, and EtOH were used for the primary three-point calibration of the VNA. A secondary calibration was performed to improve the accuracy of the spectra using DCM, 1BuOH, and EtOH for Padé approximation.

For the formal description of  $\hat{\varepsilon}(\nu)$ , dielectric spectra are generally decomposed into sums of  $n$  individual relaxation processes,  $j$  (counted in order of increasing peak frequency), by fitting  $\varepsilon'(\nu)$  and  $\varepsilon''(\nu)$  simultaneously to mathematical models of the type<sup>28,29</sup>

$$\hat{\varepsilon}(\nu) = \sum_{j=1}^n S_j F_j(\nu) + \varepsilon_{\infty} \quad \text{Eq. 6 - 3}$$

with amplitudes  $S_j$  and band-shape models

$$F_j(\nu) = \left( \left( 1 + (i2\pi\nu\tau_j)^{1-\alpha_j} \right)^{\beta_j} \right)^{-1} \quad \text{Eq. 6 - 4}$$

In Equation 6 – 4,  $\tau_j$  is the relaxation time,  $0 \leq \alpha_j < 1$  and  $0 < \beta_j \leq 1$  are shape parameters of mode  $j$ . The static permittivity becomes accessible as  $\varepsilon = \varepsilon_{\infty} + \sum S_j$ . The equations used in this work are the Debye function (D with  $\alpha_j = 0$  and  $\beta_j = 1$ ) and the Cole-Cole function (CC,  $\beta_j = 1$ ).

For relaxation processes arising from the reorientation of permanent molecular dipoles, including those connected to the cooperative dynamics of the H-bond system, their amplitude,  $S_j$ , is connected to concentration,  $c_j$ , and effective dipole moment,  $\mu_{\text{eff},j}$ , of the causing dipole via<sup>29</sup>

$$\frac{\varepsilon + A_j(1-\varepsilon)}{\varepsilon} S_j = \frac{N_A c_j}{3\varepsilon_0 k_B T} \mu_{\text{eff},j}^2 \quad \text{Eq. 6 - 5}$$

Here  $N_A$  is the Avogadro constant,  $\varepsilon_0$  the permittivity of free space,  $k_B$  the Boltzmann constant,  $T$  the Kelvin temperature, and  $A_j$  ( $= 1/3$  for spherical particles) a shape-dependent cavity field factor.

## 6.3 Results and discussion

### 6.3.1 Synergistic effect of solubilization and local interactions in ethanol/triacetin mixtures

Degot *et al.* first described the significant solubility of curcumin in binary mixtures of ethanol (EtOH) and triacetin (TriA) and the observed correlation with the predicted chemical potential (see Figure 6 - 2(a,b)).<sup>11</sup> In general, the chemical potential corresponds to the affinity of the solute for a solvent. Accordingly, the predicted chemical potential can be applied to compare the solubility of the solute in different solvents.<sup>26</sup> The calculations predict maximum solubility of curcumin in a EtOH/TriA mixture with TriA mole fraction  $x(\text{TriA}) = 0.47$ . This is in good agreement with the experimentally determined range of maximum solubility,  $(0.24 \leq x(\text{TriA}) \leq 0.46)$ .<sup>11</sup>

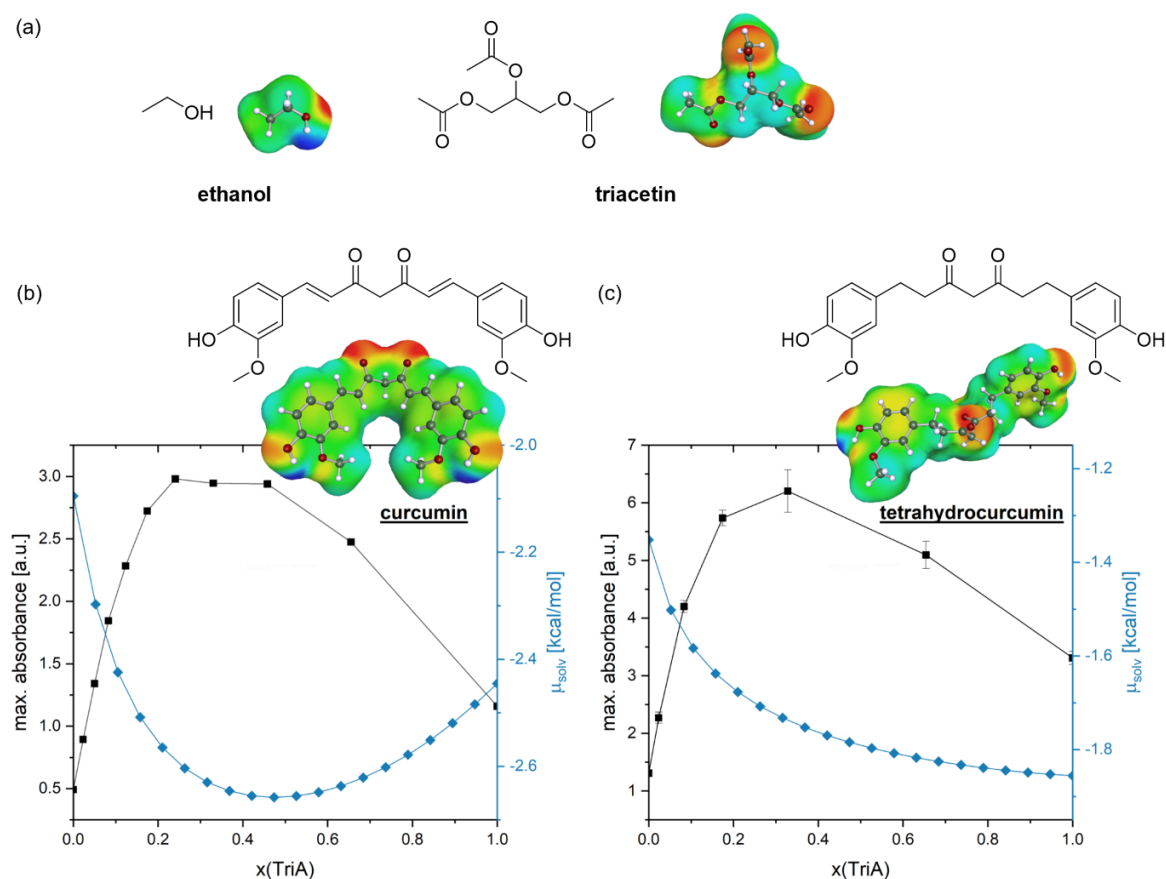


Figure 6 - 2: (a) Molecular structure and the corresponding molecular surface of EtOH and TriA. The colored molecular surface represents the screening charge density  $\sigma$  of the conformer with the lowest energy. Highly positive  $\sigma$  are colored in red, highly negative  $\sigma$  in blue, and non-polar areas in green. (b,c) Maximum absorbance (black curve) of curcumin (b, data taken from Degot *et al.*<sup>11</sup>) and tetrahydrocurcumin (THL) (c) in binary EtOH/TriA mixtures as a function of the amount of TriA. The supersaturated mixtures are diluted 1000-fold. The blue curves depict the predicted chemical potential of curcumin and THL, respectively.

The pronounced synergistic effect in the solubilization of curcumin was therefore explained by an optimum interplay of interacting surface segment densities, which form the basis for the calculation of the chemical potential.<sup>11</sup> More detailed interpretation of the prediction and the  $\sigma$ -profiles of the components is provided in the Supplementary Information (see Figure S.6 - 3).

The same solvent system is applied to solubilize tetrahydrocurcumin (THC) (see Figure 6 - 2(c)). As is the case for curcumin, the solubility of THC in pure TriA is better than in pure EtOH. Furthermore, a pronounced synergistic effect is observed, resulting in maximum solubility in EtOH/TriA with  $x(\text{TriA}) = 0.33$ . The COSMO-RS-based calculations predict better solubility in TriA compared to EtOH. A minor synergy in the mixtures is predicted as well. However, the largest affinity is predicted for pure TriA instead of the binary EtOH/TriA mixture. Thus, COSMO-RS prediction and experimental observation disagree significantly. We may therefore assume that for THC local interactions between individual surface segments with their specific screening charge density are not the main reason for the great solubilization power of EtOH/TriA mixtures.

### 6.3.2 Mesoscopic structuring of the binary mixtures

As mentioned in the introductory chapter, mesoscopic aggregation within a solvent can affect its solubilizing properties. Hence, dynamic light scattering (DLS) and small-angle X-Ray scattering (SWAXS) experiments are performed (see Figure 6 - 3). In DLS, a high correlation intercept for small lag times and larger lag times of the correlation functions are assumed to correlate with pronounced structuring. Moreover, mesoscopic inhomogeneities are indicated by low  $q$ -scattering in SWAXS experiments.<sup>14</sup> Figure 6 - 3(a) summarizes both the low  $q$ -scattering from SWAXS measurements (blue curve and (b)) and the correlation intercept at small lag times from DLS (black curve and (c)). Starting from a negligible signal in pure EtOH, the signals increase with an increasing amount of TriA. Both signals reach their maximum in a EtOH/TriA mixture with a molar ratio of 83/17, indicating the most pronounced structuring.

Further addition of TriA leads to a decrease in the signals down to that of the unstructured pure TriA. Solutions with  $0.12 \leq x(\text{TriA}) \leq 0.24$  are considered to depict mesoscopic structuring as their DLS and SWAXS signals exceed the value of 0.1. However, most pronounced structuring and maximum THC solubility (yellow-shaded area) do not coincide. Instead, the latter is shifted to the concentration range of decreasing scattering signals. Accordingly, the presence of mesoscopic inhomogeneities cannot really explain the solubilization maximum.

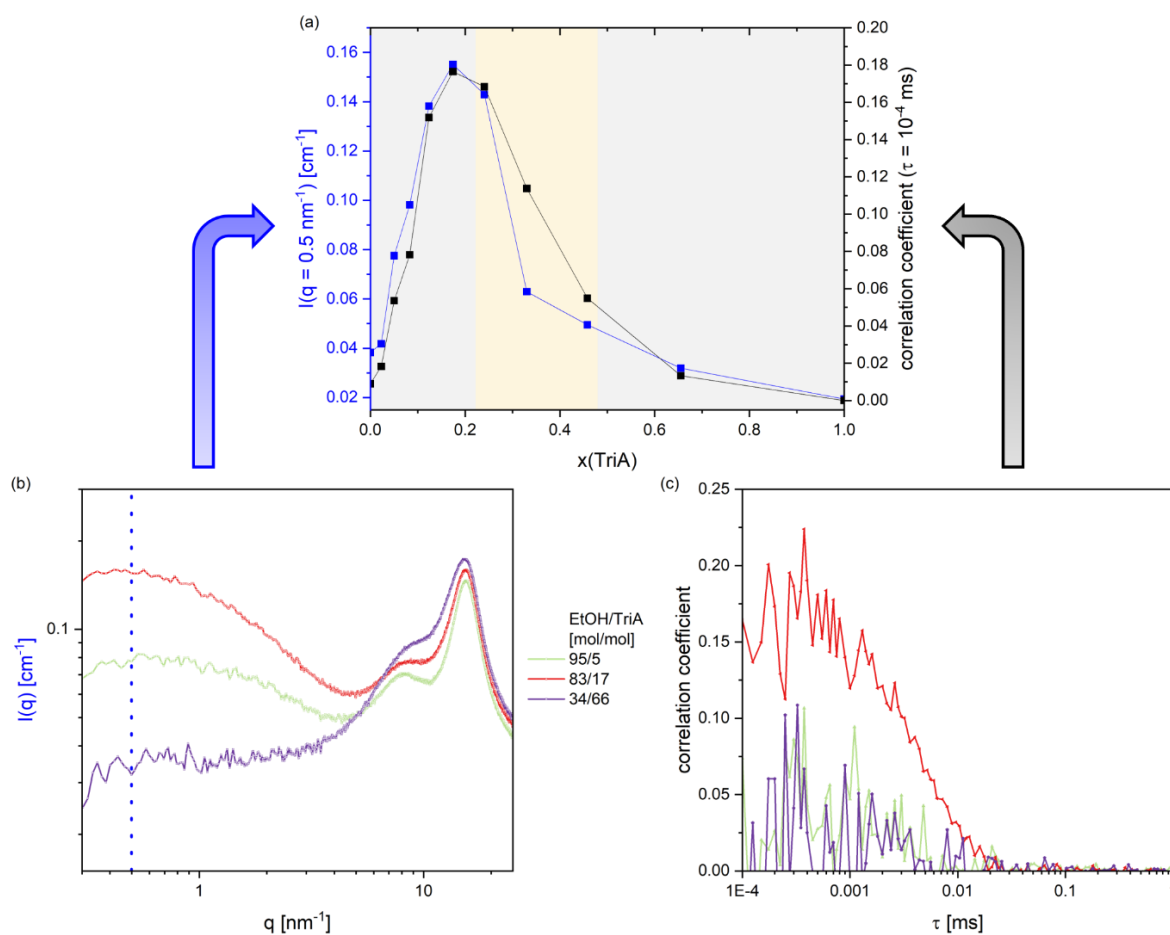


Figure 6 - 3: (a) Intensity value ( $q = 0.5 \text{ nm}^{-1}$ ) determined by SWAXS measurements (blue curve), and the correlation coefficient ( $\tau = 10^{-4}$  ms) obtained by DLS measurements (black) with respect to the amount of TriA. The yellow-shaded area marks the compositions in which the greatest solubility of (tetrahydro)curcumin is observed. (c) Selected SWAXS spectra. (d) Selected correlation functions obtained by DLS. The spectra of all measurements are given in the Supplementary Information (see Figure S.6 - 4, Figure S.6 - 5).

### 6.3.3 Dielectric relaxation in the binary mixtures

Figure 6 - 4 summarizes the dielectric spectra of mixtures of EtOH and TriA. The dielectric constant  $\varepsilon$  ( $= \lim_{\nu \rightarrow 0} \varepsilon'(\nu)$ ) decreases from 24.3 in pure EtOH ( $x_1 = 0$ , black curve) to 6.8 in pure TriA ( $x_1 = 1$ , purple curve). The values are in good agreement with values reported in the literature of 24.2 for EtOH (25 °C)<sup>43</sup> and 7.3 for TriA (20 °C)<sup>44</sup>. The frequency of maximum dielectric loss first increases with increasing TriA content but beyond a molar TriA fraction of 0.6 the maximum shifts again to smaller  $\nu$ .

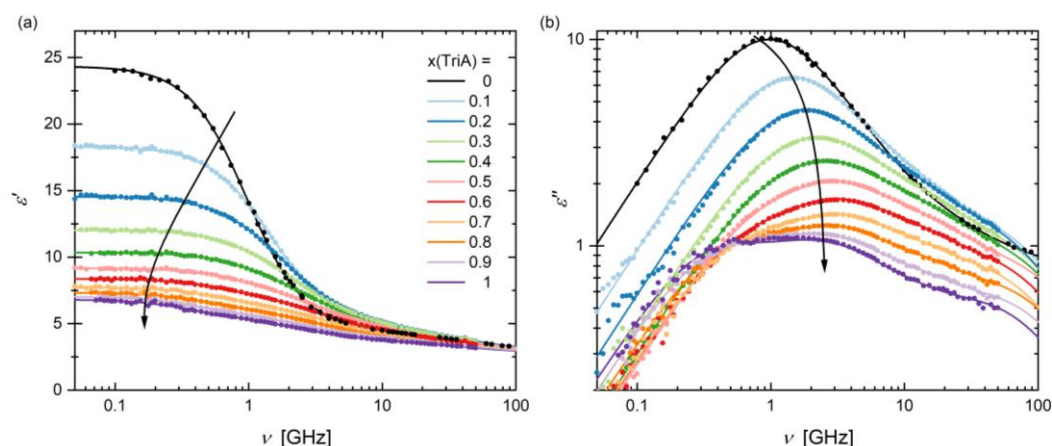


Figure 6 - 4: Relative permittivity  $\epsilon'(\nu)$  (a) and dielectric loss  $\epsilon''(\nu)$  (b) in mixtures of EtOH and TriA at 25 °C. The legend depicts the molar fraction of TriA. The experimental data are represented by the symbols, the fits by the line. Pure EtOH ( $x(\text{TriA}) = 0$ ) is fitted using the D+D+D model. Pure TriA ( $x(\text{TriA}) = 1$ ) is fitted with a D+CC+D+D model. The binary mixtures are fitted by means of a D+D+D+D model.

Figure 6 - 5(a) shows the dielectric loss of EtOH up to 100 GHz.<sup>45</sup> Similar to methanol, up to this frequency, this spectrum is best described by the superposition of three Debye (D) relaxations.<sup>34,46,47</sup> The Debye modes represent cooperative H-bond network relaxation ( $\sim 1$  GHz), reorientation of individual EtOH dipoles ( $\sim 20$  GHz), and fast H-bond switching ( $\sim 70$  GHz). Additionally, two intermolecular vibrations associated with H-bond bending and H-bond stretching can be detected in the Terahertz range.<sup>45,47</sup> The latter are weak and outside the frequency range of  $0.05 \leq \nu \leq 50$  GHz covered in the present work. Accordingly, they will be neglected in the following discussion, although some influence on the reported mixture values of  $S_4$ ,  $\tau_4$ , and  $\epsilon_\infty$  (Table S.6 - 2) cannot be excluded.

The spectrum of neat triacetin (Figure 6 - 5(b)) is even more complex, as already four modes are required for its formal description in the covered frequency range. The largest contributions are a Debye mode at  $\sim 0.35$  GHz ( $j = 1$ ;  $D_1$  in Figure 6 - 5(b)) and a weakly broadened ( $\alpha_2 = 0.059$ ) Cole-Cole relaxation at  $\sim 2.5$  GHz ( $j = 2$ ;  $CC_2$ ), followed by further Debye relaxations at  $\sim 15$  GHz ( $j = 3$ ;  $D_3$ ) and  $\sim 50$  GHz ( $j = 4$ ;  $D_4$ ). This is clearly a reflection of the high intramolecular flexibility of TriA with its three strongly polar ( $\sim 1.8$  D group dipole moment<sup>48</sup>) acetate ester residues. Unfortunately, except for the  $\sim 0.35$  GHz contribution, these peak frequencies are close to ethanol modes. Accordingly, relaxations  $j = 2, 3$ , and  $4$  of the superposition of four Debye modes, which yields the best description of all mixture spectra (Table S.6 - 2, Figure 6 - 5(c,d)), are composites with unresolved contributions from both EtOH and TriA. This is corroborated by the smooth transition of the corresponding amplitudes ( $S_2, S_3, S_4$ ; Figure S.6 - 6) and relaxation times ( $\tau_2, \tau_3, \tau_4$ ; Figure S.6 - 7) with increasing  $x(\text{TriA})$  from the EtOH values to those of neat TriA. Note that in contrast to neat TriA but similar to EtOH, the relaxation at  $\sim 2$  GHz is not broadened for the mixtures, *i.e.*,  $\alpha_2 = 0$ , suggesting that H-bond dynamics governs the underlying molecular motions even at

$x(\text{TriA}) = 0.9$ .<sup>35</sup> The initial decrease and subsequent leveling of the corresponding relaxation time,  $\tau_2$  (Figure S.6 - 7(a)), despite the monotonically rising mixture viscosity (Figure S.6 - 2), points into the same direction.<sup>29</sup>

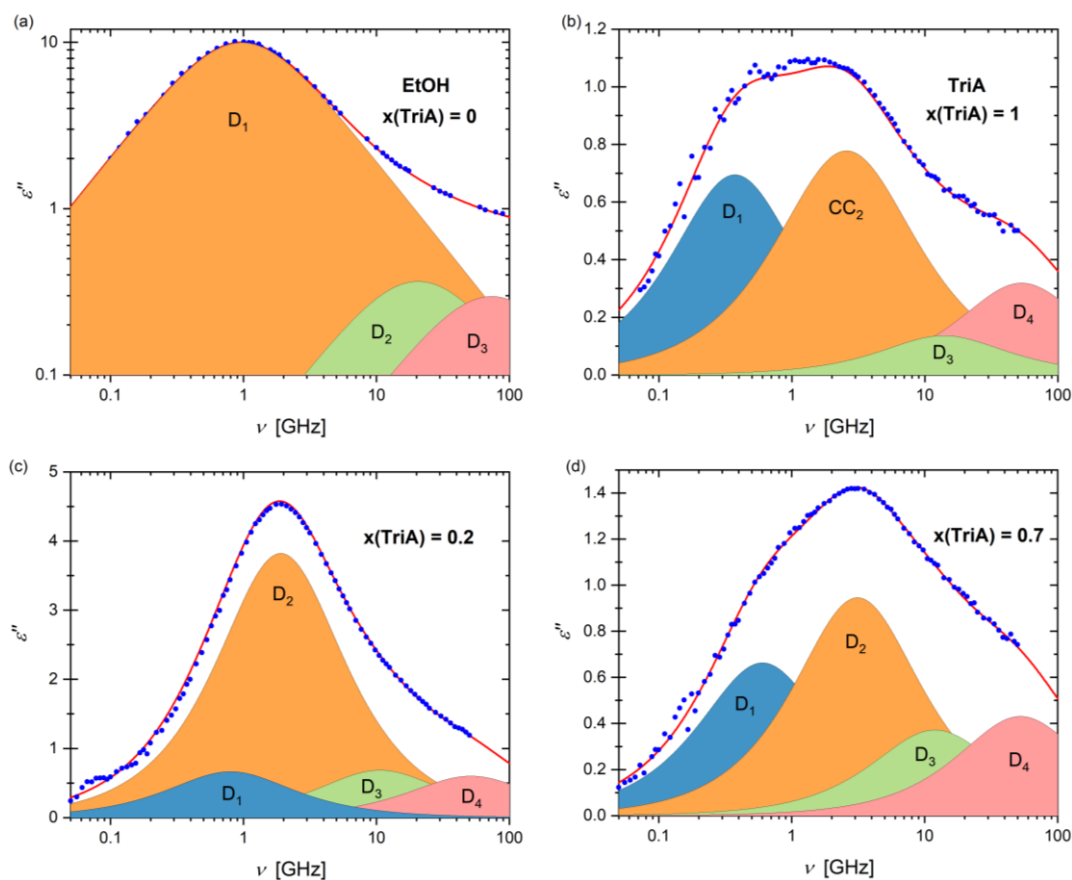


Figure 6 - 5: Dielectric loss  $\varepsilon''(\nu)$  in mixtures of EtOH and TriA with varying molar fractions  $x$  of TriA. The symbols represent the experimental data, the line shows the fit. The contributions of the individual relaxation modes are represented by the colored-shaded areas, including Debye (D) and Cole-Cole (CC) functions.

Starting from the value of neat EtOH ( $\sim 19.9$ ), the amplitude of the  $\sim 2$  GHz mode ( $D_2$ ) strongly drops with increasing TriA content, reaching  $S_2 = 2.31$  at  $x(\text{TriA}) = 0.6$  (Figure 6 - 6(a)). However,  $S_2$  does not vanish for neat triacetin, as would be expected if only EtOH were contributing, but levels at  $S_2 = 1.71$ . Thus, a quantitative evaluation of  $S_2$  with Equation 6 – 5 based on the analytical alcohol concentration is only reasonable for  $x(\text{TriA}) < 0.6$ . Even then, the effective dipole moments,  $\mu_{\text{eff},2}$  (orange symbols in Figure 6 - 6(b)), obtained by assuming a spherical cavity field ( $A_2 = 1/3$ ), should be taken with a grain of salt. Nevertheless, it is interesting to see that  $\mu_{\text{eff},2}$  decreases linearly from 3.6 D for neat EtOH to  $\sim 2.7$  D at  $x(\text{TriA}) = 0.3$  but then stays roughly constant. These experimental values are significantly larger than the effective dipole moment of a single EtOH molecule (2.2 D) obtained with Gaussian. Such enhanced experimental dipole moments are typical for monohydroxy alcohols and indicate mutual alignment of molecular dipoles in H-bonded chains.<sup>49</sup> Therefore, we speculate that the observed linear decrease of

$\mu_{\text{eff},2}$  reflects the breakup of alcohol chains by the three strong H-bond acceptor groups of triacetin. Until  $x(\text{TriA}) \approx 0.3$ , apparently all EtOH molecules are bound by TriA. It is interesting to note here that the limits for optimum (tetrahydro)curcumin solubilization roughly coincide with solvent compositions of (nominal) saturation of all three TriA acceptor sites by EtOH (EtOH:TriA = 3:1;  $x(\text{TriA}) = 0.25$ ) and of just enough EtOH to form at least one H-bond to TriA ( $x(\text{TriA}) = 0.5$ ).

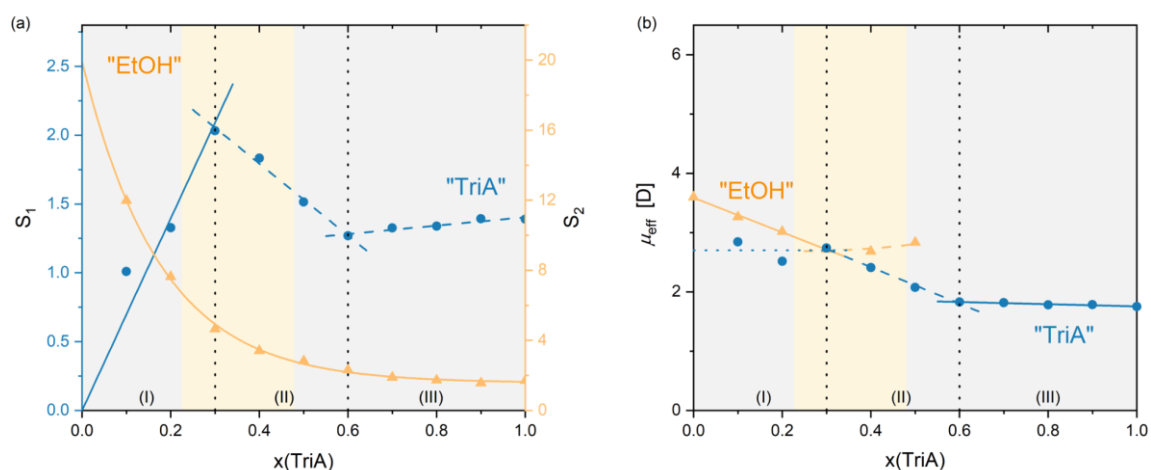


Figure 6 - 6: (a) The amplitudes  $S_1$  and  $S_2$  as a function of the amount of TriA. (b) Effective dipole moment calculated with the Cavell equation (see Equation 6 – 5) for the amplitudes  $S_1$  ("TriA") and  $S_2$  ("EtOH"), assuming a spherical cavity field factor  $A_1$  of  $1/3$ . The yellow-shaded area marks the compositions in which the greatest solubility of (tetrahydro)curcumin is observed. The dotted lines separate the 3 areas distinguished in the interpretation.

In contrast to the smooth variation of  $S_2$ , the concentration dependence of the TriA-dominated amplitude  $S_1$  is peculiar (Figure 6 - 6(a)). After the expected initial increase of this amplitude with rising TriA concentration, a sharp breakpoint is observed at  $x(\text{TriA}) \approx 0.3$ , from where  $S_1$  markedly decreases before rising again at  $x(\text{TriA}) \geq 0.6$ , albeit with a much smaller slope. Note that the breakpoint at  $x(\text{TriA}) \approx 0.3$  and the subsequent drop of  $S_1$  are in the range of maximum (tetrahydro)curcumin solubility. The blue curve in Figure 6 - 6(b) shows corresponding effective dipole moments,  $\mu_{\text{eff},1}$ , obtained from  $S_1$  and the molar concentration of TriA with Equation 6 – 5, assuming a spherical cavity field ( $A_1 = 1/3$ ) for TriA. The initial linear increase of  $S_1$  translates into a constant value of  $\mu_{\text{eff},1} \approx 2.7$  D for  $x(\text{TriA}) \leq 0.3$ , followed by a linear decrease in the range  $0.3 \leq x(\text{TriA}) \leq 0.6$ , and again a constant value of  $\sim 1.8$  D up to neat TriA.

Two points are worth noting here. First: for  $x(\text{TriA}) \geq 0.6$ , the associated relaxation time,  $\tau_1$ , is proportional to viscosity (Figure S.6 - 7(b)). This Stokes-Einstein-Debye behavior indicates diffusive reorientation of individual molecules.<sup>29</sup> The derived effective volume of rotation of  $\sim 23 \text{ \AA}^3$  is  $\sim 9\%$  of the molecular volume of  $263 \text{ \AA}^3$  obtained with Gaussian for the minimum energy conformation of TriA and thus in the expected range for molecular

reorientation close to slip hydrodynamic boundary conditions.<sup>29</sup> However, the effective dipole moment ( $\sim 1.8$  D) is much smaller than the value of 5.5 D predicted by Gaussian for this molecule but comparable to the group dipole moment ( $\sim 1.8$  D<sup>48</sup>) of an acetate ester moiety. This possibly means that at least for  $x(\text{TriA}) \geq 0.6$ , mode  $D_1$  monitors the rotation of individual ester groups and not the overall reorientation of TriA molecules.

Second: the concentration range of decreasing  $\mu_{\text{eff},1}$  coincides with that of constant  $\mu_{\text{eff},2}$  and thus matches solvent compositions where the EtOH:TriA ratio drops from (nominal) saturation of all three TriA acceptor sites (EtOH:TriA = 3:1;  $x(\text{TriA}) = 0.25$ ) to just enough EtOH to form at least one H-bond to TriA ( $x(\text{TriA}) = 0.5$ ). As already discussed above, these mixture compositions roughly coincide with the region of maximum (tetrahydro)curcumin solubility. However, the reason why  $\mu_{\text{eff},1}$  increases when  $x(\text{TriA})$  drops from 0.6 to 0.3 and then stays constant at  $\sim 2.7$  D remains unclear. Probably, this is connected to the pronounced peak of mesoscopic structuring observed in scattering experiments at  $x(\text{TriA}) \approx 0.2$  (Figure 6 - 3), but without further molecular-level information from detailed computer simulations, any further discussion is speculative.

## 6.4 Conclusion and outlook

We reported a detailed investigation of the binary solvent system ethanol/triacetin (EtOH/TriA) by means of COSMO-RS-based calculations, dynamic light scattering, small- and wide-angle X-ray scattering, and dielectric relaxation spectroscopy (DRS). The results are correlated with the range of high (tetrahydro)curcumin solubility, showing a maximum in mixtures of EtOH/TriA with TriA mole fractions of 0.24 – 0.46.

The calculated chemical potential allows predicting the solubility of curcumin in the EtOH/TriA system, as reported by Degot *et al.*<sup>11</sup> The predictions are based on the interaction of local interacting surface densities. However, predictions fail in the case of tetrahydrocurcumin, for which the most pronounced solubility is predicted in TriA instead of the binary mixture. As a consequence, the significant solubility of the solutes investigated cannot be explained solely by an optimum in interacting molecular surfaces of a specific charge density. The scattering methods cannot provide the explanation either. Although mesoscopic inhomogeneities are detected ( $0.12 \leq x(\text{TriA}) \leq 0.24$ ), the structuring already decreases when solubilization becomes highest.

The dielectric relaxation measurements are analyzed particularly with respect to amplitude and relaxation time of the TriA-associated mode  $D_1$  and the EtOH-dominated relaxation  $D_2$ . The concentration dependence of the derived effective dipole moments,  $\mu_{\text{eff},1}$  and, with restrictions,  $\mu_{\text{eff},2}$ , reveals the presence of three different areas within the EtOH/TriA system. The TriA-poor area ( $x(\text{TriA}) < 0.3$ ) is dominated by EtOH chains. Scattering experiments indicate the presence of pronounced mesoscopic structures in this range. The TriA-rich area ( $x(\text{TriA}) > 0.6$ ) describes statistically distributed TriA molecules. The range comprising the solubility maximum of (tetrahydro)curcumin starts in the first area, but mainly correlates with the second area ( $0.3 \leq x(\text{TriA}) \leq 0.6$ ). In binary mixtures of the second area, EtOH chains are apparently broken, and alcohol molecules act as H-bond donors to TriA. In this range of maximum solubility, the molar ratio of EtOH:TriA drops from  $\sim 3:1$ , *i.e.*, all acceptor sites of TriA are nominally involved, to  $\sim 1:1$ . H-bonding between individual EtOH and TriA molecules is also relevant for  $x(\text{TriA}) > 0.6$ , but here the number of H-bond donors is not sufficient to bind to TriA molecules.

Despite the detailed investigation of the solvent system, the origin of its excellent solubilization power remains unclear. The demolition of the living polymer ethanol network by the triacetin may be essential to allow interactions between the solvent and the

(tetrahydro)curcumin solutes to occur. The EtOH-TriA complexes themselves may also be responsible, allowing optimum interactions with the solutes. However, these considerations remain speculative at this point. Theoretical modeling of the interactions between the different species presented (EtOH chains, EtOH-TriA complexes, free molecules) and the solutes may allow further insights into the solubilization process. The experimental investigation of different alcohols as well as hydrophobic solvents with varying functional groups (*e.g.*, without ester groups) should also further deepen the understanding. The complexity of understanding the mechanism of solubility (of potential substrates and catalysts) underscores the overall complexity of optimizing reaction processes.

## 6.5 Supporting information

### 6.5.1 Gaussian calculations

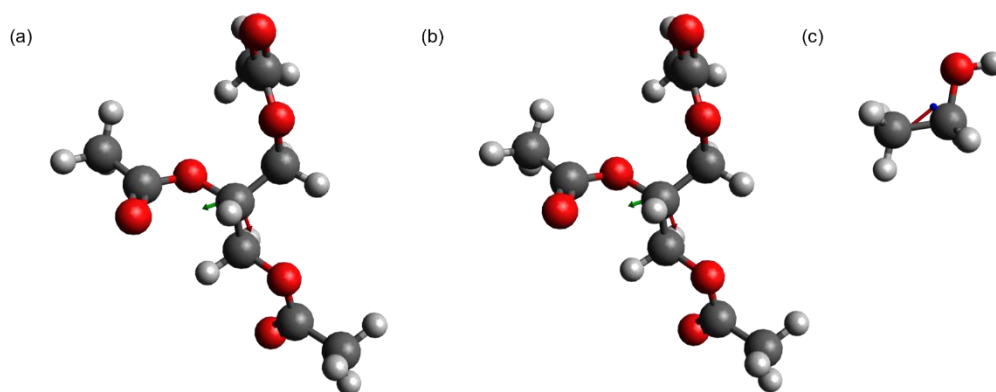


Figure S.6 - 1: Optimized geometry of TriA in EtOH (a), TriA in a continuum with a dielectric constant of 6.8 (b), and EtOH in EtOH (c) using Gaussian software. The Avogadro software<sup>50</sup> (Version 1.1.1) is used for visualization of the molecules.

Table S.6 - 1: Theoretically determined dipole moment  $\mu$  of TriA and EtOH in different solvents, whereby the solvent "TriA" is represented by a continuum with a dielectric constant of 6.8. Calculations were performed by means of the Gaussian program.

molecule	TriA		EtOH
solvent	EtOH	"TriA"	EtOH
$\mu$ [D]	5.3	5.5	2.2

## 6.5.2 Density and viscosity measurements

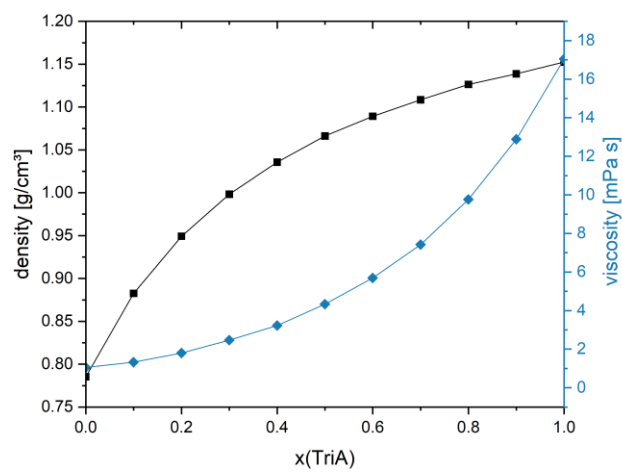


Figure S.6 - 2: Experimentally determined densities and viscosities of binary EtOH/TriA mixtures at 25 °C as a function of the amount of TriA.

## 6.5.3 COSMOtherm calculations

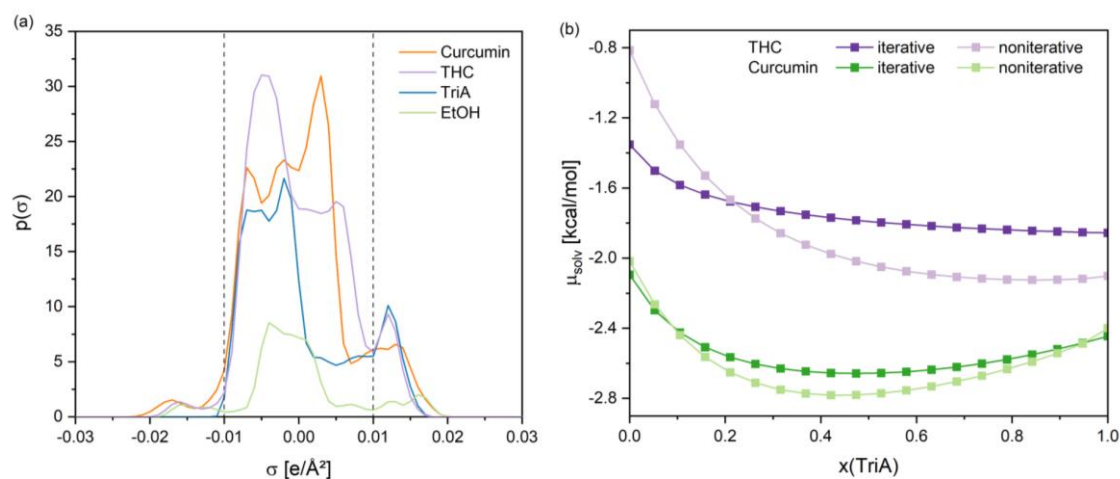


Figure S.6 - 3: (a) Predicted  $\sigma$ -profiles of curcumin (orange curve), THC (purple curve), TriA (blue curve), and EtOH (green curve). The contributions of the individual conformers are weighted by their weight factor given in the corresponding pure compounds. (b) Comparison of iteratively and non-iteratively predicted chemical potential of the solutes THC and curcumin in mixtures of EtOH/TriA as a function of the amount of TriA.

Degot *et al.* revealed a correlation between the predicted chemical potential at infinite dilution (non-iterative calculations) and the experimentally determined solubilities.<sup>11</sup> In the published work<sup>11</sup>, the  $\sigma$ -profiles were taken into account to interpret the results (see Figure S.6 - 3(a)). TriA (blue curve) has a rather non-polar surface ( $\sigma$  around 0 e/Å<sup>2</sup>) with some highly polar surface segments with hydrogen bond acceptor abilities ( $\sigma > 0.01$  e/Å<sup>2</sup>, oxygen atoms). Due to the lack of potential hydrogen bond donor segments with sufficient negative  $\sigma$ , an electrostatic misfit is present in pure TriA. By the addition of EtOH (green curve), which possesses both potential hydrogen bond donor ( $\sigma < 0.01$  e/Å<sup>2</sup>) and acceptor segments ( $\sigma > 0.01$  e/Å<sup>2</sup>), the misfit can be reduced. Curcumin (orange curve) has mainly non-polar surface segments. In addition, the molecule also exhibits hydrogen bond donor and acceptor abilities. In mixtures of EtOH and TriA, the curcumin can thus interact via Van-der-Waals interactions, especially with the non-polar TriA, and can form hydrogen bonds with both solvent molecules. The EtOH was expected to reduce the overall electrostatic misfit of the solution due to lacking hydrogen bond donor segments on both molecular surfaces, curcumin and TriA. Accordingly, it was assumed that the synergistic solubilization arises due to an optimum interplay of Van-der-Waals, electrostatic, and hydrogen bonding interactions. In addition, the small molecule size of EtOH may allow faster penetration between the curcumin molecules.<sup>11</sup> Since predictions fail in the case of tetrahydrocurcumin, we tried to optimize the predictions by using iterative calculations. However, no improvement was observed (see Figure S.6 - 3(b)). Furthermore, it is noticeable that the  $\sigma$ -profile

of THC (Figure S.6 - 3(a), purple curve) is very similar to that of TriA. This could explain the predicted minimum in the chemical potential of THC in pure TriA.

## 6.5.4 Scattering experiments

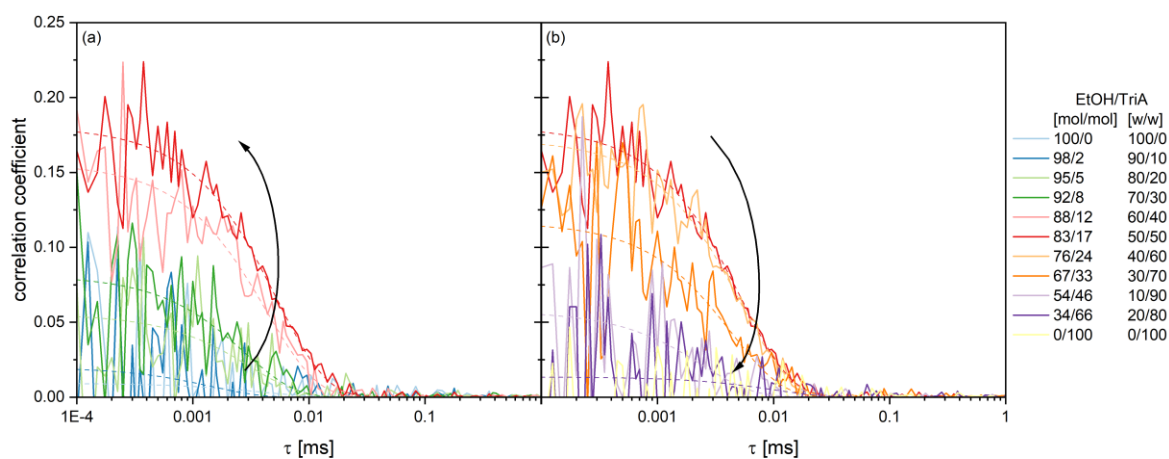


Figure S.6 - 4: Correlation functions of binary EtOH/TriA mixtures obtained by DLS measurements at 25 °C with their exponential fits (dashed line).

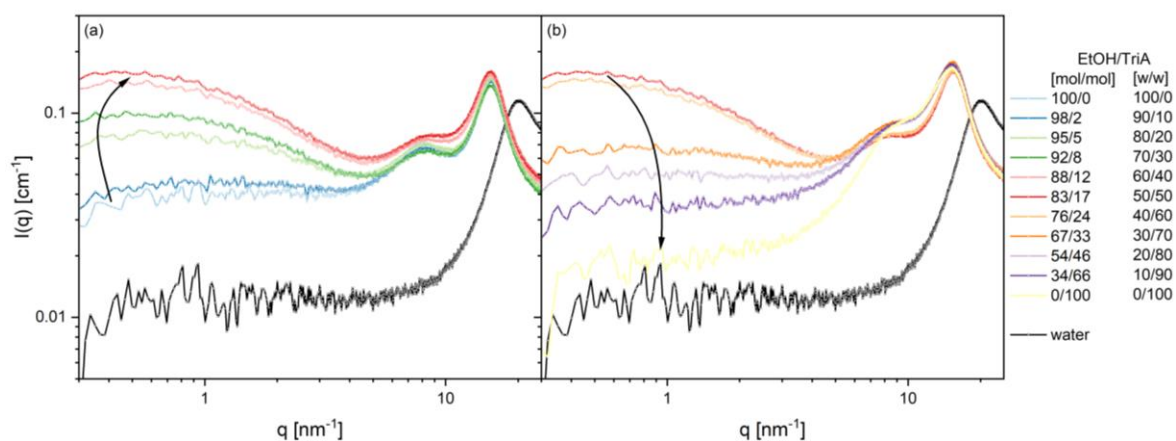


Figure S.6 - 5: Experimentally determined SWAXS spectra of binary mixtures EtOH/TriA.

## 6.5.5 DRS measurements

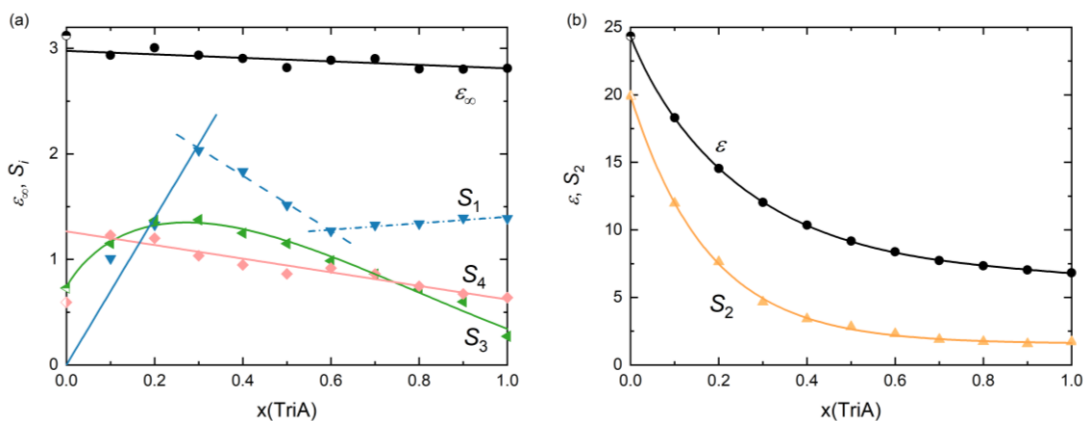


Figure S.6 - 6: The amplitudes  $S_i$ , the infinite-frequency limit  $\epsilon_\infty$ , and the dielectric constant  $\epsilon$  in mixtures of EtOH and TriA as a function of the TriA fraction  $x(\text{TriA})$ .

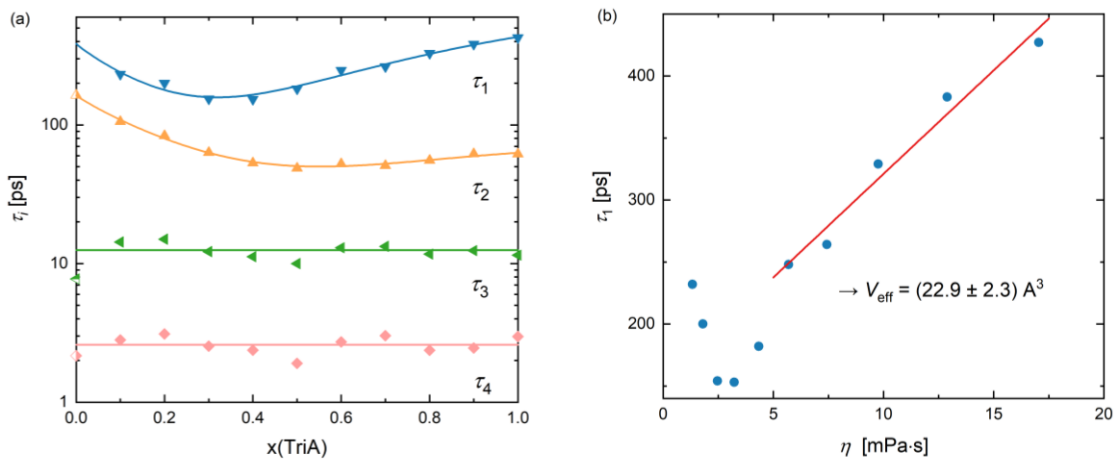


Figure S.6 - 7: (a) Relaxation times,  $\tau_i$  ( $i=1-4$ ), of TriA/EtOH mixtures at 25 °C. (b) Stokes-Einstein-Debye plot (relaxation time  $\tau_1$  as a function of viscosity,  $\eta$ ) for the TriA associated mode  $D_1$ .

Table S.6 - 2: Dielectric constant  $\epsilon$ , infinite-frequency permittivity  $\epsilon_\infty$ , relaxation amplitudes  $S_i$ , and relaxation times  $\tau_i$  [ps] of the sum of four Debye equations fitted to the DR spectra of binary EtOH/TriA mixtures with varying TriA fraction  $x(\text{TriA})$  at 25 °C.

$x(\text{TriA})$	$\epsilon$	$\epsilon_\infty$	$S_1$	$\tau_1$	$S_2$	$\tau_2$	$S_3$	$\tau_3$	$S_4$	$\tau_4$
0.1	18.303	2.936	1.009	232	11.978	106	1.151	14.3	1.229	2.81
0.2	14.542	3.006	1.327	200	7.639	83.5	1.37	15.0	1.200	3.11
0.3	12.031	2.936	2.033	154	4.652	63.2	1.376	12.2	1.034	2.54
0.4	10.346	2.904	1.833	153	3.412	53.2	1.249	11.2	0.947	2.37
0.5	9.167	2.818	1.515	182	2.822	48.8	1.150	10.0	0.862	1.91
0.6	8.370	2.887	1.269	248	2.310	52.5	0.987	13.0	0.917	2.72
0.7	7.724	2.903	1.326	264	1.891	50.9	0.861	13.3	0.861	3.02
0.8	7.335	2.804	1.338	329	1.729	55.6	0.717	11.7	0.746	2.37
0.9	7.031	2.803	1.392	383	1.564	61.9	0.599	12.4	0.673	2.46
1	6.816	2.81	1.389	427	1.707	61.8	0.272	11.5	0.637	2.98

## 6.6 References

- (1) Hofmann, E.; Saridis, A.; Touraud, D.; Buchner, R.; Kunz, W. In-Depth Study of Binary Ethanol-Triacetin Mixtures in Relation with Their Excellent Solubilization Power. *Phys. Chem. Chem. Phys.* **2023**, *submitted*.
- (2) Letcher, T. M. *Developments and Applications in Solubility*; The Royal Society of Chemistry: Cambridge, UK, 2007.
- (3) Coltescu, A.-R.; Butnariu, M.; Sarac, I. The Importance of Solubility for New Drug Molecules. *Biomed. Pharmacol. J.* **2020**, *13* (02), 577–583.  
<https://doi.org/10.13005/bpj/1920>.
- (4) Coimbra, M.; Isacchi, B.; van Bloois, L.; Torano, J. S.; Ket, A.; Wu, X.; Broere, F.; Metselaar, J. M.; Rijcken, C. J. F.; Storm, G.; Bilia, R.; Schiffelers, R. M. Improving Solubility and Chemical Stability of Natural Compounds for Medicinal Use by Incorporation into Liposomes. *Int. J. Pharm.* **2011**, *416* (2), 433–442.  
<https://doi.org/10.1016/j.ijpharm.2011.01.056>.
- (5) Alshamrani, M.; Khan, M. K.; Khan, B. A.; Salawi, A.; Almoshari, Y. Technologies for Solubility, Dissolution and Permeation Enhancement of Natural Compounds. *Pharmaceuticals* **2022**, *15* (6), 653. <https://doi.org/10.3390/ph15060653>.
- (6) Teiten, M.-H.; Eifes, S.; Dicato, M.; Diederich, M. Curcumin—The Paradigm of a Multi-Target Natural Compound with Applications in Cancer Prevention and Treatment. *Toxins (Basel)*. **2010**, *2* (1), 128–162.  
<https://doi.org/10.3390/toxins2010128>.
- (7) Omosa, L. K.; Midiwo, J. O.; Kuete, V. *Curcuma Longa*; Elsevier, 2017.  
<https://doi.org/10.1016/B978-0-12-809286-6.00019-4>.
- (8) Pratsinis, H.; Kletsas, D. Special Issue “Anti-Aging Properties of Natural Compounds.” *Cosmetics* **2019**, *6* (4), 67. <https://doi.org/10.3390/cosmetics6040067>.
- (9) Zhang, Q.-W.; Lin, L.-G.; Ye, W.-C. Techniques for Extraction and Isolation of Natural Products: A Comprehensive Review. *Chin. Med.* **2018**, *13* (1), 20.  
<https://doi.org/10.1186/s13020-018-0177-x>.
- (10) Paul, R.; Solans, C.; Erra, P. Study of a Natural Dye Solubilisation in o/w Microemulsions and Its Dyeing Behaviour. *Colloids Surfaces A Physicochem. Eng.*

- Asp.* **2005**, 253 (1–3), 175–181. <https://doi.org/10.1016/j.colsurfa.2004.11.003>.
- (11) Degot, P.; Huber, V.; Hofmann, E.; Hahn, M.; Touraud, D.; Kunz, W. Solubilization and Extraction of Curcumin from *Curcuma Longa* Using Green, Sustainable, and Food-Approved Surfactant-Free Microemulsions. *Food Chem.* **2021**, 336, 127660. <https://doi.org/10.1016/j.foodchem.2020.127660>.
- (12) Rani, S.; Mishra, S.; Sharma, M.; Nandy, A.; Mozumdar, S. Solubility and Stability Enhancement of Curcumin in Soluplus® Polymeric Micelles: A Spectroscopic Study. *J. Dispers. Sci. Technol.* **2020**, 41 (4), 523–536. <https://doi.org/10.1080/01932691.2019.1592687>.
- (13) Iwunze, M. O. Binding and Distribution Characteristics of Curcumin Solubilized in CTAB Micelle. *J. Mol. Liq.* **2004**, 111 (1–3), 161–165. <https://doi.org/10.1016/j.molliq.2003.12.013>.
- (14) Buchecker, T.; Krickl, S.; Winkler, R.; Grillo, I.; Bauduin, P.; Touraud, D.; Pfitzner, A.; Kunz, W. The Impact of the Structuring of Hydrotropes in Water on the Mesoscale Solubilisation of a Third Hydrophobic Component. *Phys. Chem. Chem. Phys.* **2017**, 19 (3), 1806–1816. <https://doi.org/10.1039/c6cp06696h>.
- (15) Krickl, S.; Buchecker, T.; Meyer, A. U.; Grillo, I.; Touraud, D.; Bauduin, P.; König, B.; Pfitzner, A.; Kunz, W. A Systematic Study of the Influence of Mesoscale Structuring on the Kinetics of a Chemical Reaction. *Phys. Chem. Chem. Phys.* **2017**, 19 (35), 23773–23780. <https://doi.org/10.1039/c7cp02134h>.
- (16) Minatti, E.; Viville, P.; Borsali, R.; Schappacher, M.; Deffieux, A.; Lazzaroni, R. Micellar Morphological Changes Promoted by Cyclization of PS- b -PI Copolymer: DLS and AFM Experiments. *Macromolecules* **2003**, 36 (11), 4125–4133. <https://doi.org/10.1021/ma020927e>.
- (17) Lee, A. S.; Gast, A. P.; Bütün, V.; Armes, S. P. Characterizing the Structure of PH Dependent Polyelectrolyte Block Copolymer Micelles. *Macromolecules* **1999**, 32 (13), 4302–4310. <https://doi.org/10.1021/ma981865o>.
- (18) Manet, S.; Lecchi, A.; Impéror-Clerc, M.; Zholobenko, V.; Durand, D.; Oliveira, C. L. P.; Pedersen, J. S.; Grillo, I.; Meneau, F.; Rochas, C. Structure of Micelles of a Nonionic Block Copolymer Determined by SANS and SAXS. *J. Phys. Chem. B* **2011**, 115 (39), 11318–11329. <https://doi.org/10.1021/jp200212g>.
- (19) Klossek, M. L.; Touraud, D.; Zemb, T.; Kunz, W. Structure and Solubility in Surfactant-Free Microemulsions. *ChemPhysChem* **2012**, 13 (18), 4116–4119.

- <https://doi.org/10.1002/cphc.201200667>.
- (20) Marcus, J.; Touraud, D.; Prévost, S.; Diat, O.; Zemb, T.; Kunz, W. Influence of Additives on the Structure of Surfactant-Free Microemulsions. *Phys. Chem. Chem. Phys.* **2015**, *17* (48), 32528–32538. <https://doi.org/10.1039/C5CP06364G>.
- (21) Klamt, A. Conductor-like Screening Model for Real Solvents: A New Approach to the Quantitative Calculation of Solvation Phenomena. *J. Phys. Chem.* **1995**, *99* (7), 2224–2235. <https://doi.org/10.1021/j100007a062>.
- (22) Klamt, A. *COSMO-RS From Quantum Chemistry to Fluid Phase Thermodynamics and Drug Design*, Elsevier, 2005.
- (23) Klamt, A. The COSMO and COSMO-RS Solvation Models. *WIRCAH* **2017**, *8* (1), 1–11. <https://doi.org/10.1002/wcms.1338>.
- (24) Eckert, F.; Klamt, A. Fast Solvent Screening via Quantum Chemistry: COSMO-RS Approach. *AIChE J.* **2002**, *48* (2), 369–385. <https://doi.org/10.1002/aic.690480220>.
- (25) Klamt, A.; Eckert, F.; Arlt, W. COSMO-RS: An Alternative to Simulation for Calculating Thermodynamic Properties of Liquid Mixtures. *Annu. Rev. Chem. Biomol. Eng.* **2010**, *1*, 101–122. <https://doi.org/10.1146/annurev-chembioeng-073009-100903>.
- (26) Benazzouz, A.; Moity, L.; Pierlot, C.; Molinier, V.; Aubry, J. M. Hansen Approach versus COSMO-RS for Predicting the Solubility of an Organic UV Filter in Cosmetic Solvents. *Colloids Surf. A* **2014**, *458*, 101–109. <https://doi.org/10.1016/j.colsurfa.2014.03.065>.
- (27) Dupeux, T.; Gaudin, T.; Marteau-Roussy, C.; Aubry, J.-M.; Nardello-Rataj, V. COSMO-RS as an Effective Tool for Predicting the Physicochemical Properties of Fragrance Raw Materials. *Flavour Fragr. J.* **2022**, *37* (2), 106–120. <https://doi.org/10.1002/ffj.3690>.
- (28) Klamt, A.; Krooshof, G. J. P.; Taylor, R. COSMOSPACE: Alternative to Conventional Activity-Coefficient Models. *AIChE J.* **2002**, *48* (10), 2332–2349. <https://doi.org/10.1002/aic.690481023>.
- (29) Buchner, R.; Hefter, G. Interactions and Dynamics in Electrolyte Solutions by Dielectric Spectroscopy. *Phys. Chem. Chem. Phys.* **2009**, *11* (40), 8984. <https://doi.org/10.1039/b906555p>.
- (30) Kremer, F.; Schönhals, A. *Broadband Dielectric Spectroscopy*, 2003.

- (31) Böttcher, C. F. J.; Bordewijk, P. *Theory of Electric Polarization*, vol. 2.; Elsevier: Amsterdam, Netherlands, 1978.
- (32) Petong, P.; Pottel, R.; Kaatze, U. Dielectric Relaxation of H-Bonded Liquids. Mixtures of Ethanol and n -Hexanol at Different Compositions and Temperatures. *J. Phys. Chem. A* **1999**, *103* (31), 6114–6121. <https://doi.org/10.1021/jp991046l>.
- (33) Petong, P.; Pottel, R.; Kaatze, U. Water–Ethanol Mixtures at Different Compositions and Temperatures. A Dielectric Relaxation Study. *J. Phys. Chem. A* **2000**, *104* (32), 7420–7428. <https://doi.org/10.1021/jp001393r>.
- (34) Sato, T.; Buchner, R. Dielectric Relaxation Processes in Ethanol/Water Mixtures. *J. Phys. Chem. A* **2004**, *108* (23), 5007–5015. <https://doi.org/10.1021/jp035255o>.
- (35) Patil, S.; Sun, R.; Cheng, S.; Cheng, S. Molecular Mechanism of the Debye Relaxation in Monohydroxy Alcohols Revealed from Rheo-Dielectric Spectroscopy. *Phys. Rev. Lett.* **2023**, *130* (9), 098201. <https://doi.org/10.1103/PhysRevLett.130.098201>.
- (36) BIOVIA COSMOthermX, Release 19. COSMOlogic GmbH & Co. KG, a Dassault Systèmes company 2019.
- (37) Klamt, A.; Volker, J.; Bürger, T.; Lohrenz, J. C. W. Refinement and Parametrization of COSMO-RS. *J. Phys. Chem. A* **1998**, *102* (26), 5074–5085. <https://doi.org/10.1021/jp980017s>.
- (38) Becke, A. D. Density-Functional Exchange-Energy Approximation with Correct Asymptotic Behavior. *Phys. Rev. A* **1988**, *38* (6), 3098–3100. <https://doi.org/10.1103/PhysRevA.38.3098>.
- (39) BIOVIA COSMOconfX 4.3. COSMOlogic GmbH & Co. KG, a Dassault Systèmes company 2018.
- (40) TURBOMOLE TmoleX 4.3. COSMOlogic GmbH & Co. KG, a Dassault Systèmes company.
- (41) Gaussian 09W Version 7.0. Gaussian 1995.
- (42) Sonnleitner, T.; Turton, D. A.; Waselikowski, S.; Hunger, J.; Stoppa, A.; Walther, M.; Wynne, K.; Buchner, R. Dynamics of RTILs: A Comparative Dielectric and OKE Study. *J. Mol. Liq.* **2014**, *192*, 19–25. <https://doi.org/10.1016/j.molliq.2013.09.019>.
- (43) Heyding, R. D.; Winkler, C. A. Solvent Effect on Iodide Exchange. *Can. J. Chem.* **1951**, *29* (9), 790–803. <https://doi.org/10.1139/v51-091>.

- 
- (44) Gouw, I. R. T. H.; Vlugter, I. R. J. G. Physical Properties of Triglycerides IV. Dielectric Constant. *Fette, Seifen, Anstrichm.* **1967**, *69* (4), 223–226. <https://doi.org/10.1002/lipi.19670690401>.
- (45) Buchner, R. *Unpublished Data*.
- (46) Fukasawa, T.; Sato, T.; Watanabe, J.; Hama, Y.; Kunz, W.; Buchner, R. Relation between Dielectric and Low-Frequency Raman Spectra of Hydrogen-Bond Liquids. *Phys. Rev. Lett.* **2005**, *95* (19), 197802. <https://doi.org/10.1103/PhysRevLett.95.197802>.
- (47) Yomogida, Y.; Sato, Y.; Nozaki, R.; Mishina, T.; Nakahara, J. Dielectric Study of Normal Alcohols with THz Time-Domain Spectroscopy. *J. Mol. Liq.* **2010**, *154* (1), 31–35. <https://doi.org/10.1016/j.molliq.2010.03.007>.
- (48) Exner, O. *Dipole Moments in Organic Chemistry*; Thieme: Stuttgart, 1975.
- (49) Vasiltsova, T.; Heintz, A.; Nadolny, H.; Weingärtner, H. Application of a New Statistical Mechanical Model for Calculating Kirkwood Factors in Self Associating Liquid Systems to Alkanol + CCl<sub>4</sub> Mixtures. *Phys. Chem. Chem. Phys.* **2009**, *11* (14), 2408–2419. <https://doi.org/10.1039/b818532h>.
- (50) Hanwell, M. D.; Curtis, D. E.; Lonie, D. C.; Vandermeersch, T.; Zurek, E.; Hutchison, G. R. Avogadro: An Advanced Semantic Chemical Editor, Visualization, and Analysis Platform. *J. Cheminform.* **2012**, *4* (1), 17. <https://doi.org/10.1186/1758-2946-4-17>.



## Chapter 7 The application of the theoretical COSMO-RS model for predicting ternary phase diagrams

### 7.0 Abstract

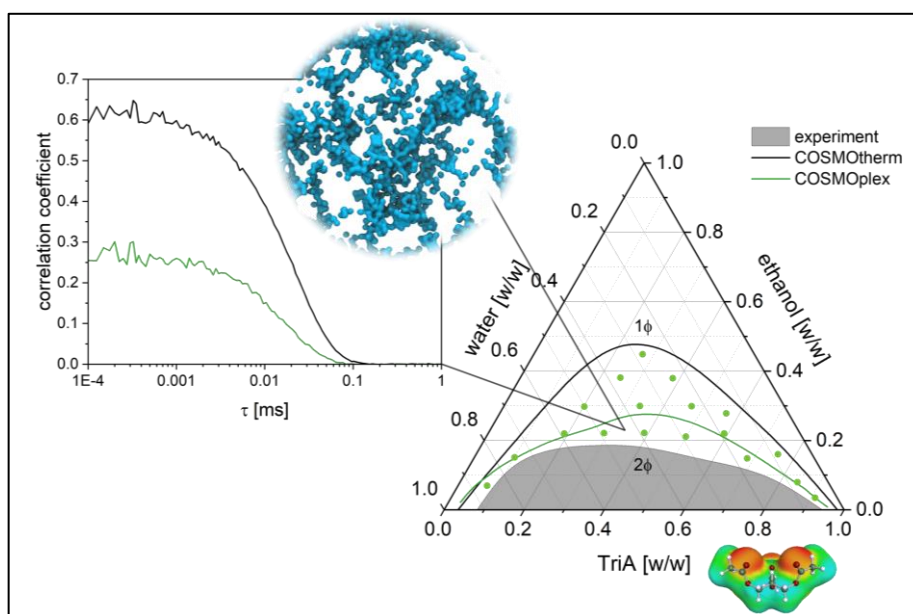


Figure 7 - 1: Graphical abstract illustrating a ternary phase diagram with some selected investigations on its structuring behavior. The MD simulation is taken from the cited literature, reprinted with permission of ACS, and illustrates the mesoscopic aggregation of water in a surfactant-free microemulsion.<sup>1</sup>

Theoretical predictions are becoming more and more crucial in both research and industry. Predictions allow for reducing the number of time- and material-consuming experiments and, thus, reduce unnecessary contact with harmful chemicals. Besides, it can be a valuable tool for deepening the understanding of experimental results. COSMOtherm represents one of these tools. The software is based on the COSMO-RS model and is well-established for predicting physicochemical properties such as solubilities. We applied the program for calculating ternary phase diagrams, including tie lines and the localization of the critical point. In this context, ternary systems consisting of water, different short-chain alcohols, and methyl methacrylate are investigated theoretically and experimentally. The COSMOtherm predictions are in good agreement with our experimental results and thus suitable for fast screening of critical points. We also point out the limitation of the program regarding complex, structured ternary systems and suggest alternative calculations based upon the extended program version COSMOplex. In this way, we can significantly improve the predictions of the phase diagram of water, ethanol, and triacetin. Our results depict the impact of structuring on the calculations and strategies to distinguish between structured and unstructured systems by theoretic screening experiments.

The experimental investigation of the ternary phase diagrams of water, alcohol, and methyl methacrylate was performed by Jonas Blahnik<sup>2</sup> at the University of Regensburg (Germany). Small-and-wide-angle X-ray scattering was performed on my behalf by Dr. Philipp Schmid at the Institute of Separation Chemistry Marcoule (France).

## 7.1 Introduction

In the previous chapters of this thesis, the focus is on replacing harmful chemicals and reducing energy consumption in the sense of Green Chemistry. The first principle of Green Chemistry, however, considers prevention.<sup>3</sup> Any material without realized value is considered to be waste that should be prevented.<sup>3,4</sup> Accordingly, trial-error chemistry should not be the method of choice. Theoretical predictions represent a reasonable tool for avoiding time- and material-consuming experiments.<sup>5-7</sup> By reducing the number of experiments conducted, the exposure of workers to chemicals and associated risks is reduced in the same way. In addition, predictions can help identifying hazards of new chemicals even before collecting physicochemical properties experimentally.<sup>4,8</sup> Besides the important saving of time and costs, predictions hence can also have a positive impact on human health and the environment. For collected experimental results, calculations can provide insights for better interpretation.<sup>5</sup> Consequently, computational predictions have received increasing attention in research and industry over the past few decades.<sup>5-10</sup>

A theoretical model used in academic research and industry represents the *COnductor-like Screening MOdel for Real Solvents*, COSMO-RS for short.<sup>11,12</sup> The basic principle of this model is explained in Chapter 6.1. The COSMOtherm software, which is based on the COSMO-RS model, can be applied for predicting solubilities and phase diagrams, among other things.<sup>12,13</sup> In order to predict liquid-liquid equilibria (LLE), the thermodynamic prerequisite of equal chemical potentials of all species  $i$  in the two phases (I and II) has to be fulfilled (see Equation 7 – 1). The chemical potential of compound  $i$  can be determined according to Equation 7 – 2 using the pseudo-chemical potential  $\mu_S^{(i)}$  (see Equation 6 – 1), the molar fraction  $x_i$ , the universal gas constant  $R$ , and the temperature  $T$ . By calculating the LLE of a ternary system, the miscibility gap of partially miscible liquids can be predicted.<sup>13,14</sup>

$$\mu_i^I = \mu_i^{II} \quad \text{Eq. 7 - 1}$$

$$\mu_i = \mu_S^{(i)} + RT \ln(x_i) \quad \text{Eq. 7 - 2}$$

The phase separation within the miscibility gap is an example of phase transitions that exhibit critical points. Such systems depict thermodynamic anomalies in, e.g., density and composition close to the critical point. Thermodynamic fluctuations in the composition result in an “early” closing of the miscibility gap.<sup>13,15–17</sup> The COSMO-RS model assumes that liquid mixtures have an isotropic distribution of the molecules within a phase (mean-field assumption).<sup>13,18</sup> This discrepancy leads to a systematic overestimation of a miscibility gap (see Figure 7 - 2, dashed line). The model thus neglects the thermodynamic fluctuations. However, COSMOtherm can correct the overestimation by introducing an additional renormalization step (see Figure 7 - 2, dotted line). Detailed information on the calculations can be found in the cited literature.<sup>11,13–19</sup>

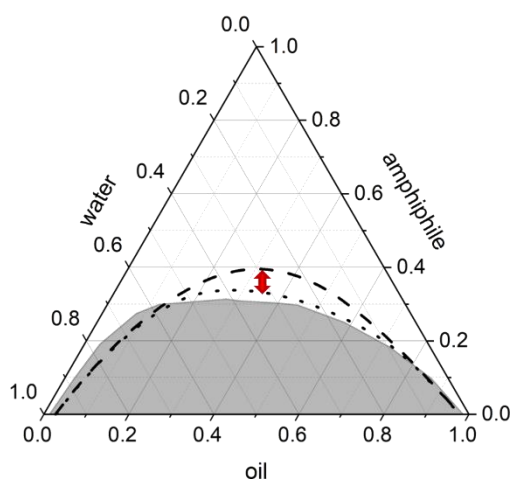


Figure 7 - 2: Schematic illustration of a ternary phase diagram consisting of water, an amphiphile, and an oil. The gray shaded area depicts an experimentally determined miscibility gap. The dashed line is predicted by COSMO-RS LLE calculations. The dotted line is predicted by COSMOtherm, including a renormalization step.

Based upon mean-field approximation, the COSMO-RS model itself is limited to homogeneous systems.<sup>13</sup> However, as shown in the previous chapters of this work, inhomogeneous, structured systems like surfactant-free (SFMEs) and surfactant-based microemulsions (SBMEs) are of great importance and find several applications in research and industry.<sup>20–24</sup> In order to overcome the inability of the COSMO-RS model to treat self-organizing, inhomogeneous systems, the extended COSMOplex version was introduced. For COSMOplex calculations, a simulation box with a specific volume is cut into different layers along the z-axis. The box can exhibit different geometries, and the layers can differ significantly from each other (see Figure 7 - 3). But since every layer is a homogeneous layer in itself, it can be treated using COSMO-RS theory. Iterative calculations on a given starting distribution of the molecules in the different layers are performed until defined convergence criteria are fulfilled. The starting distribution of the molecules has to be provided. Its choice, however, affects only the number of steps required for the system to converge and not the

overall result. The iteration steps are based on calculating the chemical potentials of all compounds, taking into account the relevant conformations, positions, and orientations. The resulting molecule distribution determines the volume population of each layer. For the next iteration step, a pressure function is considered, which is the response to overpopulation in the layers.<sup>25,26</sup> Providing detailed information on the calculation is beyond the scope and given in the cited literature.<sup>25,26</sup> The COSMOplex tool was successfully applied to surfactant-based systems for predicting critical micelle concentrations (cmc) of non-ionic surfactants and the description of a Winsor III<sup>27,28</sup> phase.<sup>25</sup> In addition, the method is able to generate membranes as a skin model.<sup>29</sup> Hahn *et al.* first predicted the structuring in SFMEs using COSMOplex. They set up a layered simulation box with periodic boundary conditions in which molecules are distributed equally. By studying the path lengths and the relative amplitude heights of the resulting fluctuations, a prediction of mesoscopic inhomogeneities in the systems studied becomes possible.<sup>26</sup>

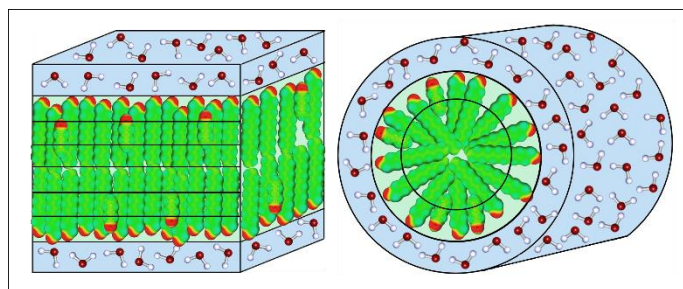


Figure 7 - 3: Schematic illustration of a layered simulation setup of COSMOplex (based on Klamt *et al.*<sup>25</sup>).

## 7.2 Material and methods

### 7.2.1 Chemicals

Methyl methacrylate (MMA, purity 99 %, stabilized with  $\leq 30$  ppm 4-methoxyphenol), ethanol (EtOH, 99.8 %), n-propanol (NPA, 99.5 %), CombiTitrant 5, methanol (anhydrous for analysis, max. 0.003 % H<sub>2</sub>O), and dimethyl sulfoxide-d<sub>6</sub> (DMSO-d<sub>6</sub>, 99.5 atom % D) were obtained from Merck (Darmstadt, Germany). t-Butanol (tBuOH, 99 %) was purchased from Carl Roth (Karlsruhe, Germany). Isopropanol (IPA, 99.8 %) was bought from Fisher Scientific (Schwerte, Germany). Triacetin (TriA, 99 %, FCC, FG) was delivered from Sigma Aldrich (Darmstadt, Germany). All chemicals were used without further purification. Millipore water (W) was used with a resistivity of 18 M $\Omega$  cm.

### 7.2.2 Methods

#### 7.2.2.1 Ternary phase diagrams

Phase diagrams were recorded according to the method of Dekker *et al.*<sup>30</sup>, as described in Chapter 2.2.2.1.

#### 7.2.2.2 Critical point determination

To determine the critical point of the phase diagrams, ternary mixtures in the biphasic region close to the phase border were prepared. The samples were shaken by hand and centrifuged in 15 mL, volume-scaled centrifuge tubes at 11'182 rpm (13'000 g) for 90 min at 25 °C  $\pm$  1 °C to achieve complete phase separation (Sigma 1-18KS centrifuge, Osterode am Harz, Germany). The critical point was allocated in approximation to sample compositions yielding a 50:50 (v/v) ratio of the two phases after centrifugation. In the case of the ternary system water, ethanol, and triacetin (W/EtOH/TriA), the biphasic samples were treated with a Vortex and centrifuged at 10'000 rpm (10'397 g) for 30 min at 25 °C  $\pm$  1 °C. The stability of the phase separation was checked the next day.

#### 7.2.2.3 Tie line determination

Tie lines were determined by centrifuging ternary mixtures in the biphasic region. For this purpose, samples of 10 g were shaken by hand and centrifuged in 15 mL centrifuge tubes for 20 min at 11'182 rpm (13'000 g, T = 25 °C  $\pm$  1 °C) using a Sigma 3-18KS centrifuge (Osterode am Harz, Germany). The upper, oil-rich phase was diluted in DMSO-d<sub>6</sub> and

analyzed by  $^1\text{H-NMR}$  using an Avance III HD 400 NMR-spectrometer (400 MHz, Bruker, Billerica, USA). The MMA-to-alcohol ratio was calculated by comparing the derived integrals, and the right-hand end of the tie-lines was calculated by extrapolating the MMA-alcohol ratio to the phase border. The water content of the lower, water-rich phase was determined by a mean of 5 volumetric Karl Fischer titrations using a KF Titrino plus by Metrohm (Herisau, Switzerland). The left-hand end of the tie lines was calculated by extrapolating the water content to the phase border. In the case of W/EtOH/TriA, the biphasic samples were again treated with a Vortex and centrifuged at 14'000 rpm (20'379 g) for 10 min at  $25\text{ }^\circ\text{C} \pm 1\text{ }^\circ\text{C}$ . After phase separation, the water content in both phases was determined by volumetric Karl Fischer titration. The intercept with the miscibility gap provided the amount of the remaining compounds EtOH and TriA.

#### **7.2.2.4 Scattering experiments**

Small-and-wide-angle X-ray scattering (SWAXS) measurements were performed as described in Chapter 6.2.2.4. In addition, dynamic light scattering (DLS) measurements were carried out as described in Chapter 1.2.2.5.

#### **7.2.2.5 COSMOtherm predicted ternary phase diagrams**

The BIOVIA COSMOthermX software<sup>31</sup> (version 19.0.4 by Dassault Systèmes), which is based on COSMO-RS theory<sup>11,32,33</sup>, was applied to compute liquid-liquid phase equilibria (LLE) of several mixtures within the ternary phase diagram. Calculations were performed on FINE<sup>32</sup> level using a TZVPD<sup>34</sup> basis set. If not stated otherwise, the renormalization step was used.

#### **7.2.2.6 COSMOplex predicted ternary phase diagrams**

The BIOVIA COSMOplex software<sup>35</sup> (version 19.07.24 by Dassault Systèmes) was used for predicting the ternary phase diagrams consisting of water, ethanol, and ethyl acetate (W/EtOH/EtOAc) or W/EtOH/TriA. The COSMOplex model<sup>25</sup> is applied, which is an extension of the COSMO-RS model. Calculations were performed using a TZVP<sup>34</sup> basis set. In all calculations, the directional version of COSMOplex (dirplex) and a specified damping (step-forward ratio: 0.01; increase/decrease factor: 1.0) was used. The self-consistent electrostatic potential (epot) was switched on.

In the case of W/EtOH/TriA, a layered simulation box of 20 nm with 10 layers per nm was applied. COSMOplex calculations were performed on a lamellar microemulsion system (polar bulk phase (b) – self-organizing-system (s.o.s.) – non-polar bulk (b)) at  $25\text{ }^\circ\text{C}$  by providing different system starting compositions. The composition of the bulk phases was initially estimated by automatic, polarity-based, and refining LLE calculations. Strict convergence

criteria were held (rmsd(cluster probabilities): 0.01; rmsd(potential profiles): 0.0001 kcal/mol; rmsd(pressure profile): 0.10 bar).

In the case of W/EtOH/EtOAc, a layered simulation box of 21 nm (10 layers per nm) was used with a lamellar b - s.o.s. - b (20 nm - 1 nm - 20 nm) system. The starting composition of the system was provided as well as the initial composition of the bulk phases extracted from previous COSMOtherm LLE calculations. In the beginning, the s.o.s. system is assumed to consist only of the hydrotrope. Furthermore, the polarity-based distribution is selected. The default conversion criteria were held.

## 7.3 Results and discussion

### 7.3.1 Prediction of critical points and tie lines in ternary systems

Ternary mixtures of water, short-chain alcohols, and methyl methacrylate (MMA) are studied regarding their suitability as reaction medium for free radical polymerization. The alcohols used are t-butanol (tBuOH), n-propanol (NPA), isopropanol (IPA), and ethanol (EtOH). MMA represents both the oil phase of the ternary system and the monomer of the reaction (see Figure 7 - 4).

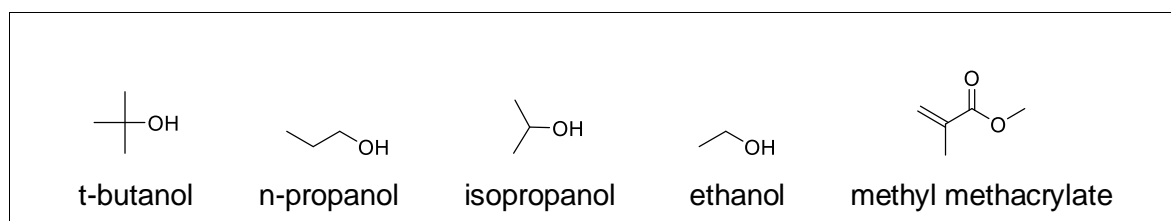


Figure 7 - 4: Molecular structure of t-butanol (tBuOH), n-propanol (NPA), isopropanol (IPA), ethanol (EtOH), and methyl methacrylate (MMA).

The experimentally determined phase diagrams are shown in Figure 7 - 5 (orange curve). The variation of the alcohol, acting as the hydrotrope, leads to a reduction of the miscibility gap in the following order: tBuOH > NPA > IPA > EtOH. The same is true for the critical point (CP) of the system (orange rhomb). The CP is shifted to higher MMA contents following the same ordering. In this way, the tie lines change from right-tilted to left-tilted when replacing tBuOH with EtOH. Blahník *et al.* proved that the position of the critical point is crucial for the outcome of the radical polymerization of MMA. The reaction was performed in monophasic ternary mixtures in close proximity to the miscibility gap. Depending on whether the reaction medium is located right or left of the critical point influences the morphology of the resulting polymer.<sup>2</sup>

Recognizing the importance of the localization of the critical point for polymerization reactions, COSMO-RS-based LLE predictions are studied regarding their applicability (see Figure 7 - 5, black curve). The height of the miscibility is well predicted for the alcohols NPA, IPA, and EtOH. In the case of tBuOH, the miscibility gap is slightly underestimated but still within an acceptable range. As explained in the introduction, the miscibility gap tends to be overestimated in calculations due to thermodynamic fluctuations, which need to be corrected by a renormalization step. By switching off the renormalization, an excellent fit with the experimental results can be obtained (see Figure S.7 - 1 in the Supporting Information). However, since t-butanol pre-structures in water<sup>36</sup>, too poor fluctuations are not considered

to be the origin of the deviation. We assume that the deviation results from the bulky shape of the hydrotrope, which influences COSMO-RS theory in the form of the combinatorial term, and thus in the calculation of interactions<sup>32</sup>, as the available surface may be approximated incorrectly.

The predicted localization of the critical point (gray shaded area) is in good agreement with the experiment for tBuOH and NPA. The cases of IPA and EtOH show deviations. In the case of EtOH, experimental determinations were challenging, and the CP is still located at the border of the predicted area. In the case of IPA, the CP is close to the center of the phase diagram, so that minor errors in predictions lead to an immediate change in the tilt of the tie lines.

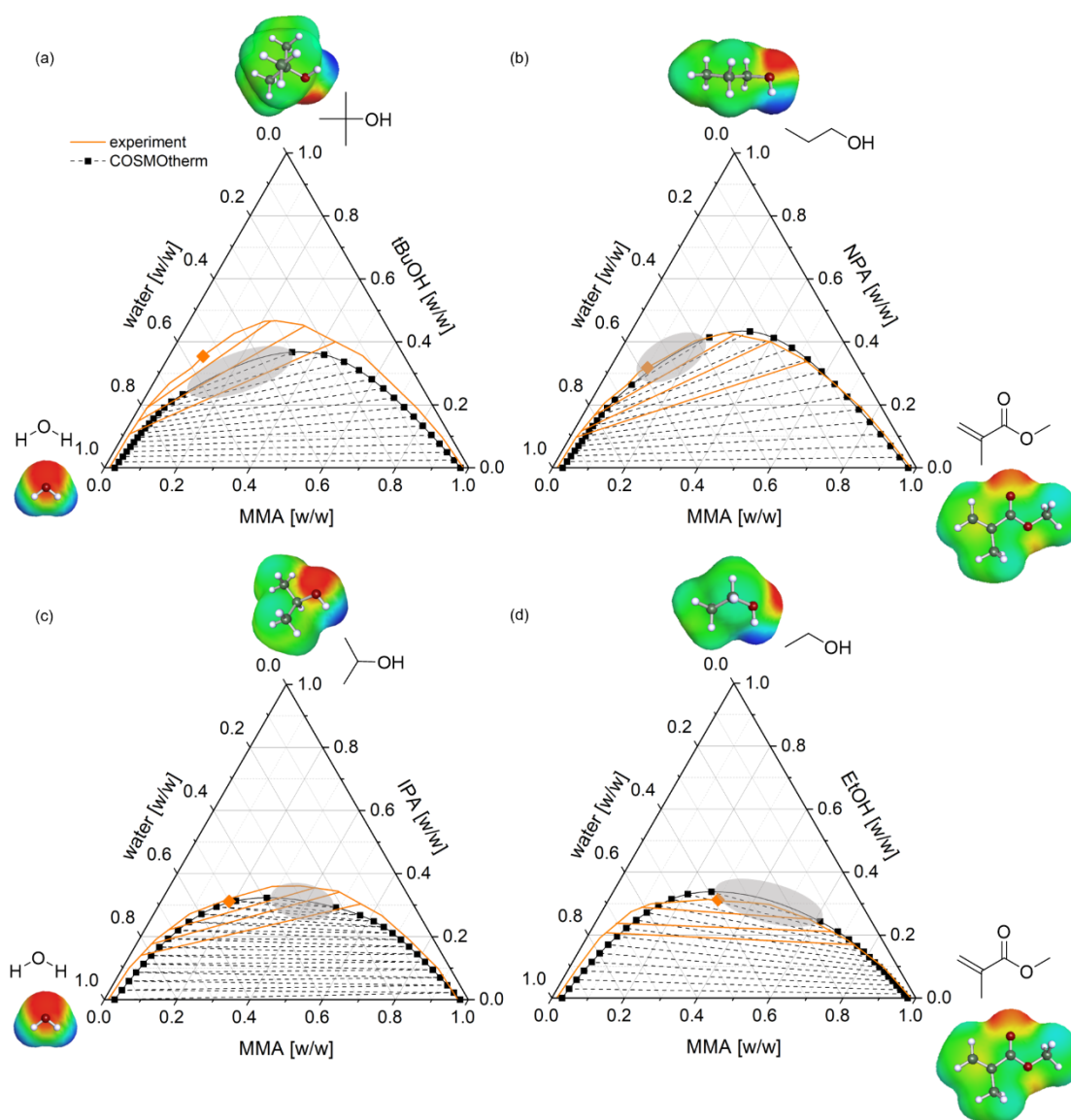


Figure 7 - 5: Ternary phase diagrams of water, short-chain alcohol, and MMA with the corresponding tie lines at 25 °C. The phase diagrams are determined experimentally (orange) or theoretically by COSMOtherm predictions (black, renormalized). The orange rhomb depicts the experimentally determined critical point (CP) of the phase diagram, while the predicted area of the CP is indicated by gray shading. The molecules are represented by the  $\sigma$ -surfaces of their CO conformers (lowest energy conformers).

Overall, the ordering of the size of the miscibility gap, as well as the localization of the CP with respect to the amount of MMA, follows the same ordering as the experiment: tBuOH > NPA > IPA > EtOH. For the initial setup of the experiment, the exact position of the CP is of less importance than knowing whether the CP is on the water- or oil-rich side of the phase diagram. Even in the case of the bulky t-butanol, the predicted CP fits quite well. Consequently, the COSMOtherm software is a qualified tool for predicting the position of the CP in a ternary phase diagram and, thus, the tilt of the tie lines. Even if slight deviations are possible, it allows quick screening of different hydrotropes to find an optimum starting system. COSMO-RS was already applied successfully for predicting ternary phase diagrams with their corresponding tie lines. However, the focus lies on ternary systems containing ionic liquids or deep eutectic solvents, which exhibit a negligible monophasic region due to the poor solubility of the components in each other.<sup>37,38</sup> Here, we applied the prediction method on systems exhibiting a large monophasic area. To our knowledge, the program has not yet been evaluated systematically for its applicability for CP screening in such systems. Though, the change in the tilt of the tie lines can influence not only polymerization but also product purification after organic syntheses or extraction by phase separation. Inducing phase separation is a common method for pre-concentrating the solute in the oil- or water-rich phase before applying other separation methods.<sup>39-41</sup>

### 7.3.2 Predictions of complex ternary phase diagrams with structured areas

In the following, the oil component is substituted by the food-grade component triacetin (TriA, see Figure 7 - 6). The ternary system consisting of water, EtOH, and TriA finds application in extraction and as a reaction solvent, as shown in Chapter 1. The experimentally determined ternary phase diagram exhibits a small miscibility gap with a CP at the oil-rich side near the center (see Figure 7 - 7(a)). COSMOtherm predictions again allow precise prediction of the tie lines and, thus, of the localization of the CP. The miscibility gap, however, is strongly overestimated, although renormalization is taken into account. While the miscibility gap is closed with less than 20 % (w/w) EtOH in the experiments, the predictions require almost 50 % (w/w). As explained in the introductory chapter, COSMOtherm is limited to homogeneous liquids.

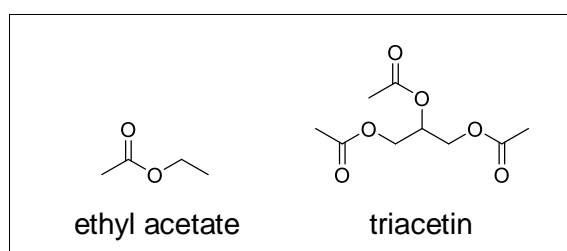


Figure 7 - 6: Molecular structure of ethyl acetate (EtOAc) and triacetin (TriA).

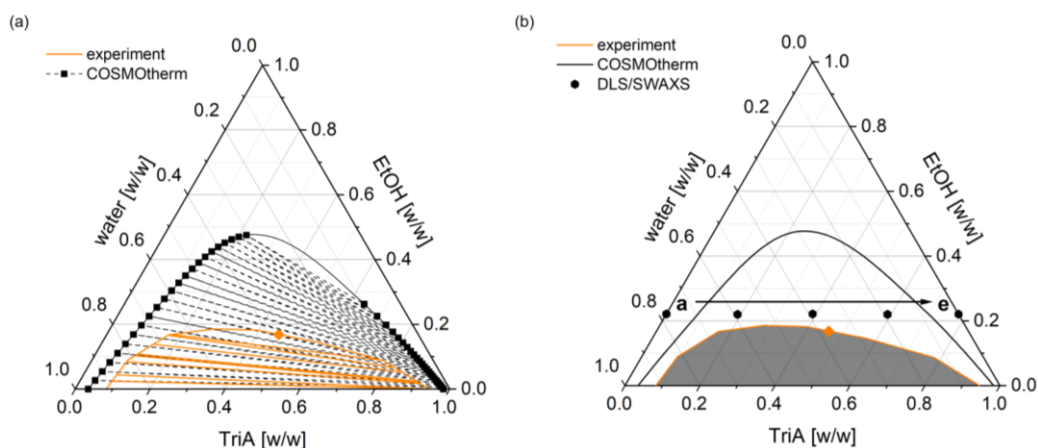


Figure 7 - 7: (a, b) Ternary phase diagram of water, EtOH, and TriA at 25 °C determined experimentally (orange) or theoretically by COSMOtherm calculations (black, renormalized). The critical point is presented by an orange rhomb. The black dots in (b) shows the compositions measured by DLS and SWAXS (see Figure 7 - 9).

For this purpose, the system is investigated regarding the presence of mesoscopic structuring. Inhomogeneity may explain the misprediction. First, samples with varying water/oil ratio and constant amount of EtOH are considered (see Figure 7 - 7(b)). DLS measurements are analyzed with regard to the correlation coefficient. A high correlation coefficient at small lag times  $\tau$  is expected to correlate with pronounced structuring.<sup>36</sup> In addition, SWAXS measurements are examined for the scattering intensity at low  $q$  values, indicating the presence of mesoscopic structuring.<sup>42,43</sup> Figure 7 - 9 shows the results obtained by scattering experiments. Starting from the binary mixture W/EtOH (mixture a), the low  $q$ -scattering and the correlation coefficient increases with an increasing amount of TriA. The maximum is reached at W/EtOH/TriA 39/22/39 (w/w/w) (mixture c), close to the CP. Further addition of TriA results in a decrease in both values. Hence, the experiments reveal pronounced mesoscopic structuring in mixture c, assuming the presence of both water- and TriA-rich aggregation in the solution.

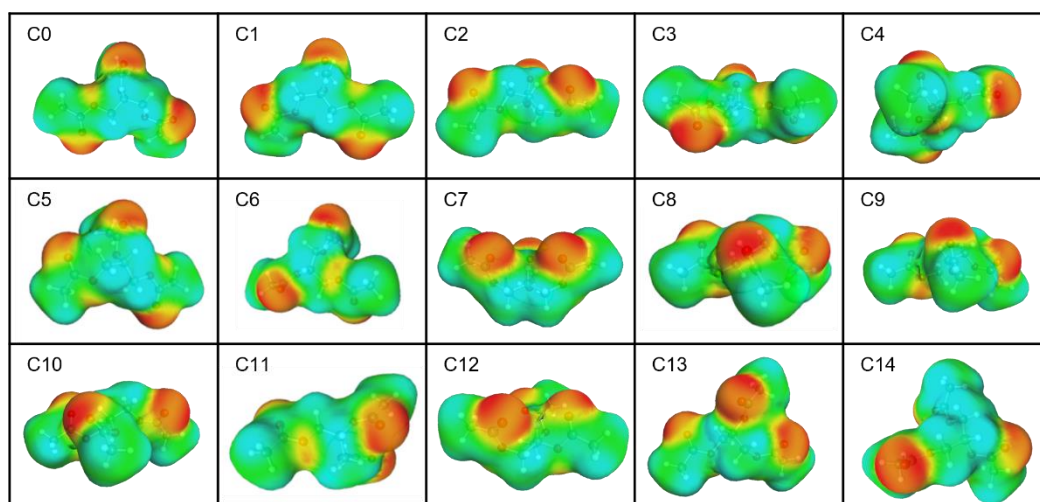


Figure 7 - 8:  $\sigma$ -surfaces of the individual triacetin conformers. Highly positive screening charge densities  $\sigma$  are colored in red, highly negative  $\sigma$  in blue, and non-polar areas in green.

The presence of distinct inhomogeneity, especially in the center of the phase diagram, may explain the overestimation in the prediction, which is also most pronounced in the center. Furthermore, the molecular structure of TriA is significantly more complex than that of MMA. The bulkiness will again affect the combinatorial term. Additionally, some of the conformers may also possess an amphiphilic character. The orientation of the three acetyl groups in the conformers C7 and C12 leads to the formation of a hydrophilic part of the molecule, separated from the hydrophobic glycerol backbone (see Figure 7 - 8). This could support the stabilizing effect of the amphiphilic hydrotrope on mesoscopic structuring and explain why structuring is more pronounced on the TriA-rich side.

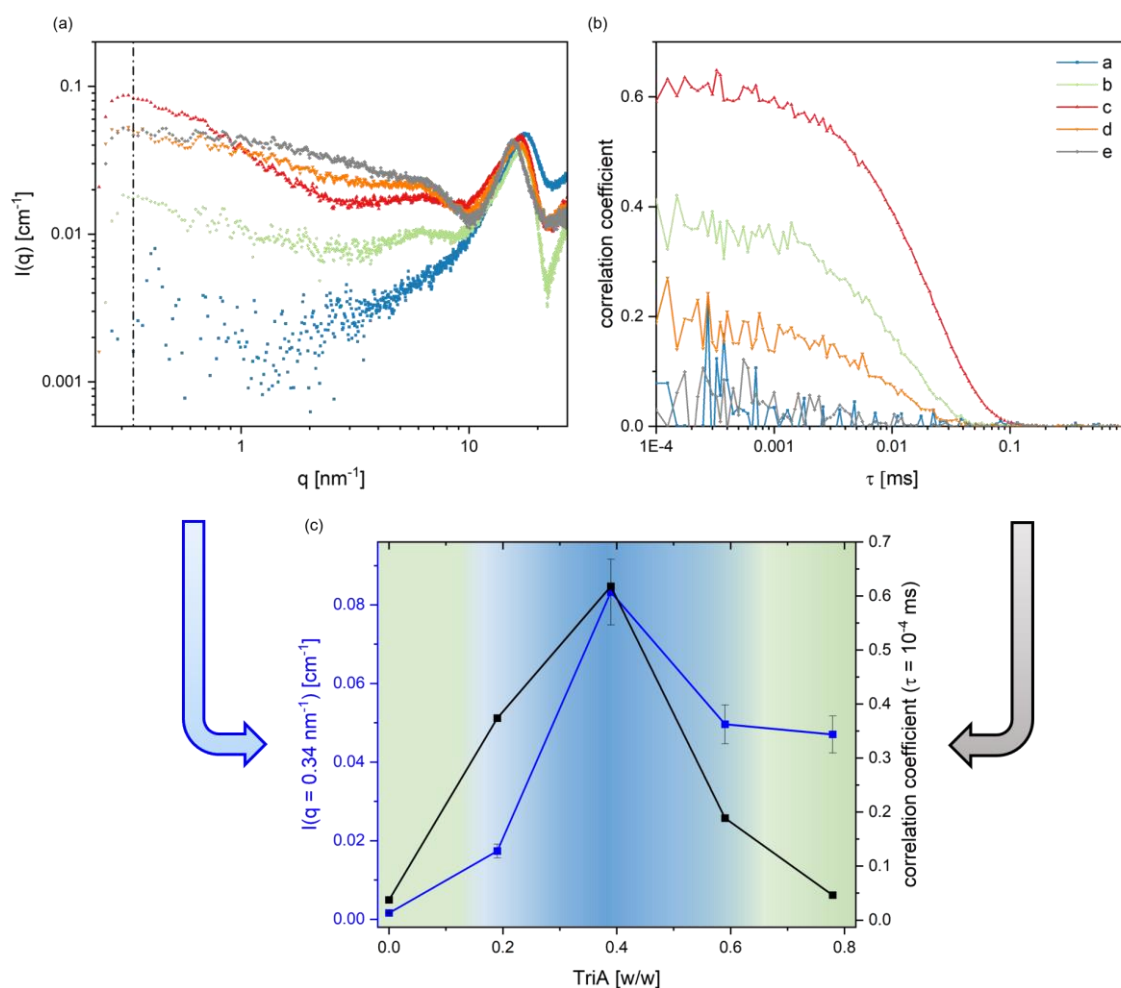


Figure 7 - 9: SWAXS (a) and DLS (b) measurements of W/EtOH/TriA mixtures. The compositions are shown in Figure 7 - 7. (c) Intensity value ( $q = 0.34 \text{ nm}^{-1}$ ) determined by SWAXS measurements and the correlation coefficient ( $\tau = 10^{-4} \text{ ms}$ ) obtained by DLS measurements with respect to the amount of TriA. The blue-shaded area marks the compositions in which mesoscopic structuring is most pronounced. (The exact DLS fits are provided in the Supporting Information, see Figure S.7 - 2).

In order to overcome the problem of inhomogeneity during calculations, COSMOplex calculations are performed. As a reference, the calculations are also applied to the ternary system water, ethanol, and ethyl acetate (W/EtOH/EtOAc) (see Figure 7 - 6). The system has a similar size of miscibility gap and depicts no structuring as known from previous studies (see Figure 7 - 10(d), Figure 7 - 11).<sup>44</sup> The simulation box is cut into the three phases

bulk – self-organizing-system (s.o.s.) – bulk. In the case of TriA, only the starting compositions of the mixtures are provided, and calculations are run until the system converges. The mixtures separate into a water- and a TriA-rich phase (bulk phases) and a s.o.s. phase in between (see Figure 7 - 10(a)). The size of the three phases is not predetermined. But the size of the entire simulation box is predetermined on the basis that a sufficient number of molecules are inside.

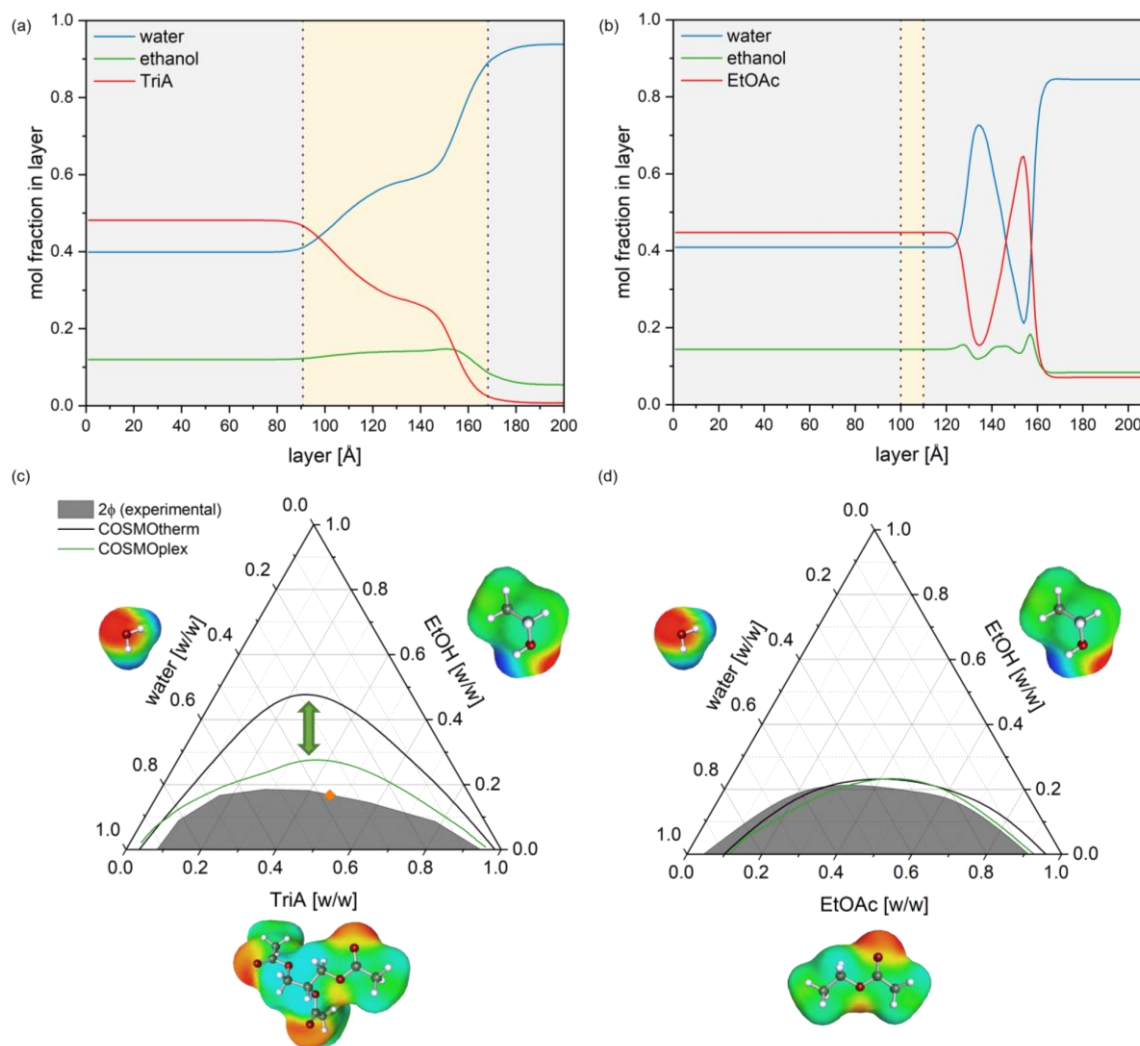


Figure 7 - 10: COSMOplex simulation box of W/EtOH/TriA 21/7/72 (w/w/w) (a) and W/EtOH/EtOAc 26/14/60 (w/w/w) (b). The mol fraction of the individual conformers in the converged system is given with respect to the box layer. The bulk phases are indicated in gray, and the s.o.s. phase in yellow. In the TriA system, the size of the phases is determined during calculations. In the EtOAc system, the size of the phases has to be provided. (c, d) Phase diagrams predicted by COSMOtherm (black, renormalized) and COSMOplex (green) in comparison with the experiment (gray shaded). The orange rhomb points the CP. The molecules are presented by the  $\sigma$ -surfaces of their C0 conformers.

The compositions on both ends of the simulation box are identified as the endpoints of a tie line. The s.o.s. phase is provided to allow the reorganization of the molecules between the bulk phases. In the case of EtOAc, the oil is not recognized as the nonpolar component. For this purpose, the size of the three phases and their individual starting compositions have to be predetermined. It has to be noted at this point that the reorganization of the

compositions in the EtOAc system takes place in the layers after the s.o.s. phase (see also Figure S.7 - 5). A larger size of the s.o.s. phase thus should be considered. The determination of the miscibility gap is, however, not affected by this, as stable end compositions are nevertheless reached at the box ends. For both systems, starting compositions with increasing hydrotrope content are considered. Figure 7 - 10(c) and (d) summarize the phase diagrams determined experimentally and theoretically. The miscibility gap of W/EtOH/EtOAc is predicted very accurately with both COSMOtherm and COSMOplex. Accordingly, in the absence of mesoscopic structuring, COSMO-RS is a powerful tool for predicting the phase diagram. In the more complex case of W/EtOH/TriA, the COSMOplex calculations improve the predictions tremendously. The highest point of the miscibility gap is shifted from COSMOtherm via COSMOplex to the experiment as follows: 48 % > 28 % > 18 % (w/w). But it has to be noted that the more precise results using COSMOplex come with longer computing time. Especially in the TriA system, since stricter convergence criteria are chosen, as done by Hahn *et al.* when applying COSMOplex to SFMEs.<sup>26</sup> Calculations carried out by COSMOtherm are significantly faster for both systems. Running the calculations for the mixture W/EtOH/TriA 23/12/65 (w/w/w) with 8 CPUs results in a calculation time of 1 h using COSMOtherm and 34 h using COSMOplex. Altogether, the predicted phase diagram of W/EtOH/TriA is considerably improved, even though there is still no perfect fit. The optimization, therefore, confirms that inhomogeneity seems to be the reason for the misprediction. Accordingly, the entire system is studied experimentally regarding mesoscopic structuring in the area of the predictions. Figure 7 - 11 depicts the results obtained in the W/EtOH/EtOAc system.

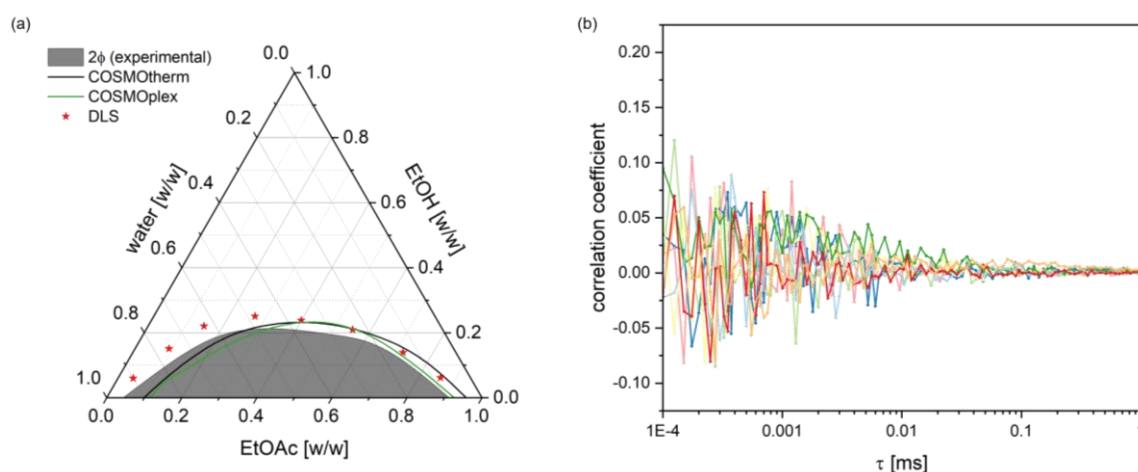


Figure 7 - 11: (a) Phase diagram of W/EtOH/EtOAc at 25 °C, determined experimentally (gray shaded) or theoretically by COSMOtherm (black, renormalized) and COSMOplex (green). The asterisks identify the compositions of the mixtures measured by means of DLS. (b) Corresponding correlation functions obtained by DLS measurements. The distinct sample assignment can be found in the Supporting Information, Figure S.7 - 3.

As expected, there are no distinct correlation functions present (b), indicating that solutions in the monophasic area are homogeneous and free of mesoscopic aggregation. In the W/EtOH/TriA system, correlation functions of different intensities are detected (see Figure 7 - 12). In the following, we distinguish 3 different groups. (i) Mixtures with a correlation coefficient  $0 < c. c. < 0.05$  are considered to be homogeneous (red curves, b). These mixtures exhibit either no correlation function at all or data that cannot be properly fitted with an exponential function ( $R^2 < 0.5$ ) since scattered light cannot be properly distinguished from the noise. Even taking into account the exponential fits, the c. c. is always below 0.05 and, thus, negligible. (ii) The second class includes correlation functions of low intensity ( $0.05 \leq c. c. < 0.1$ ) that can be fitted in an appropriate manner ( $R^2 \geq 0.5$ ). These mixtures induce light scattering by molecule aggregation (blue curves, c). The aggregation is, however, expected to be of minor intensity. (iii) Samples with a distinct correlation function ( $c. c. > 0.1$ ,  $R^2 > 0.9$ ) are considered to exhibit pronounced structuring (green curves, d). It is conspicuous that the COSMOtherm predicted miscibility gap encloses the mixtures, which exhibit a certain inhomogeneity. The samples containing higher EtOH content are clearly identified as homogeneous.

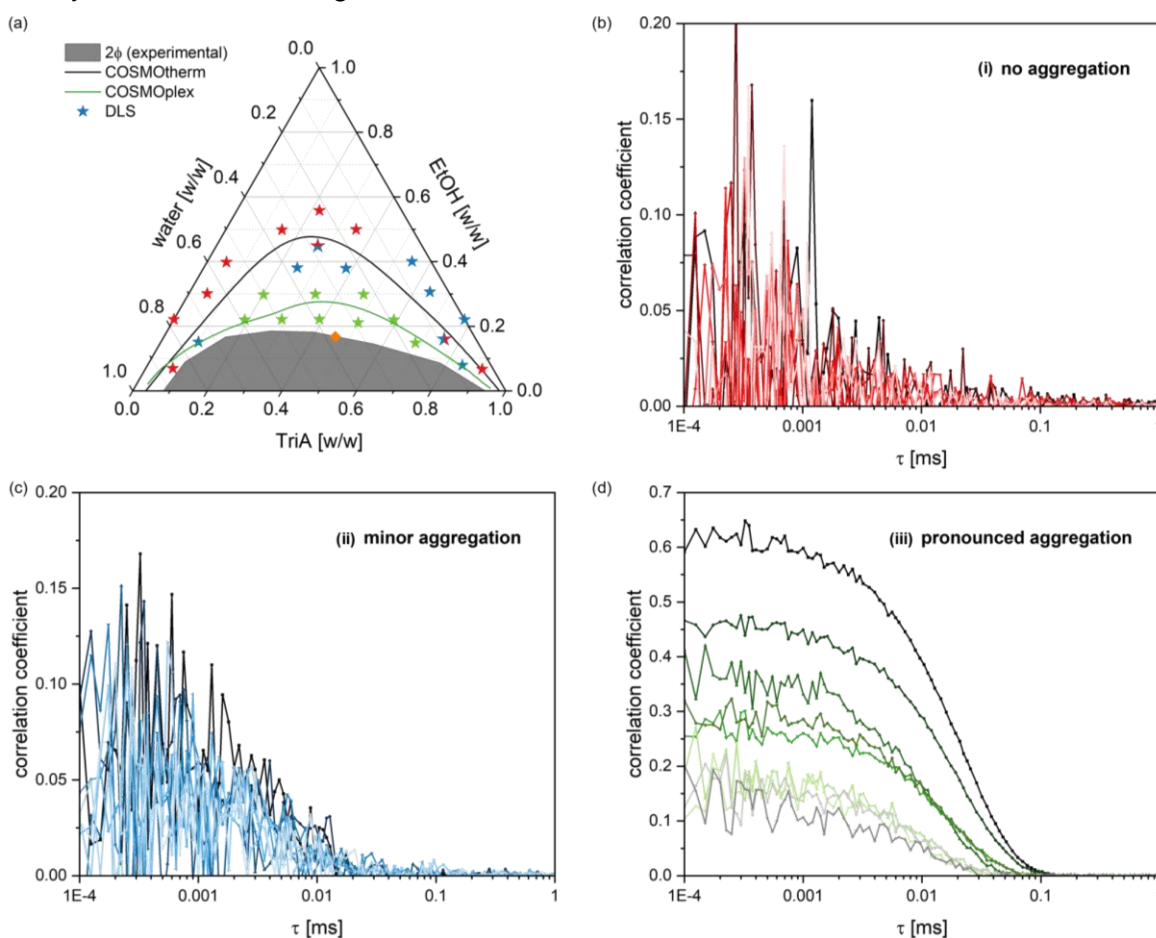


Figure 7 - 12: (a) Phase diagram of W/EtOH/TriA at 25 °C, determined experimentally (gray shaded) or theoretically by COSMOtherm (black, renormalized) and COSMOplex (green). The asterisks identify the compositions of the mixtures measured by means of DLS. (b, c, d) Corresponding correlation functions obtained by DLS measurements with a correlation coefficient  $\approx 0$  (red, b),  $< 0.1$  (blue, c), or  $> 0.1$  (green, d). The distinct sample assignment can be found in the Supporting Information, Figure S.7 - 4.

Two mixtures located at the predicted phase-transition boundary are marked with a two-colored asterisk. These mixtures are border cases with a correlation coefficient of  $0 < c. c. < 0.05$  and an  $R^2 > 0.5$  or vice versa. Furthermore, there are outliers in the oil-rich region that exhibit minor aggregation (blue stars) but are located outside the COSMOtherm predicted miscibility gap. This may be a symmetry problem, but we cannot provide a coherent explanation at this moment. Experimentally, it confirms the localization of the structured area at the oil-rich side as detected by SWAXS measurements (see Figure 7 - 9). Overall, the general trend between predictions and experiments agrees well. The results are again a clear indication that the error in the predictions results from inhomogeneities. Apparently, the deviations in the prediction do not necessarily present a drawback of the method. In the previous chapters of this thesis, the localization of structured solutions has posed a crucial and laborious step in the preliminary considerations for the choice of reaction solvent. The deviations from COSMOtherm predictions to the experiment but also to COSMOplex predictions may allow rapid identification of structured ternary systems. Of course, this assumption still has to be verified by further tests on other phase diagrams, but the initial results are very promising.

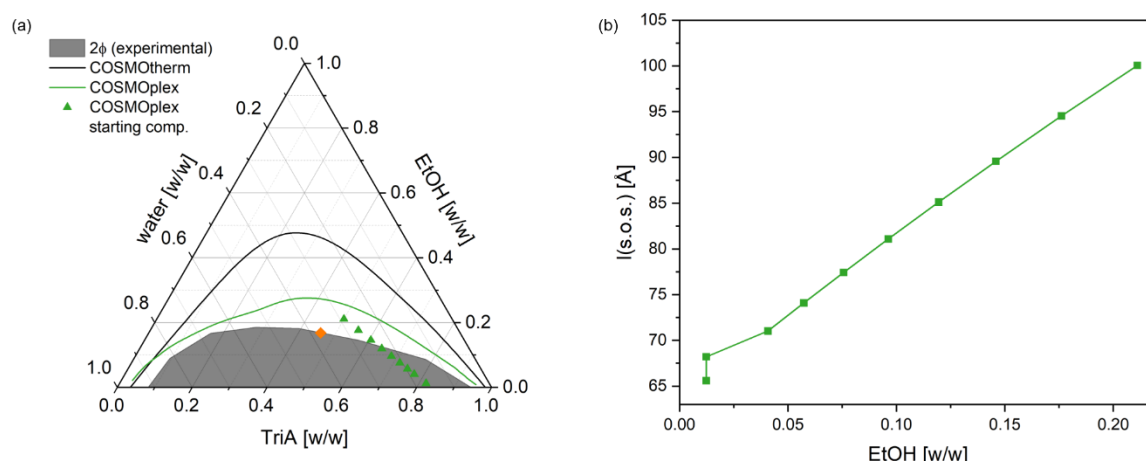


Figure 7 - 13: (a) Ternary phase diagram of W/EtOH/TriA at 25 °C, determined experimentally (gray shaded) or theoretically by COSMOtherm (black, renormalized) and COSMOplex (green). The green triangles represent the starting compositions of the COSMOplex calculations. The critical point is marked by the orange rhomb. (b) The length of the s.o.s. phase after COSMOplex calculations as a function of the EtOH content of the starting compositions.

Considering the distribution of the molecules in W/EtOH/TriA within the simulation box of COSMOplex after the system converged, another observation might prove helpful (see Figure S.7 - 5). The size of the three phases is not specified at the beginning and is, thus, determined during the calculations. With an increasing amount of EtOH and approximating the area with the most pronounced structuring (see Figure 7 - 13(a)), the size of the s.o.s. phase increases as well (b). In a mixture with 21 % (w/w) ethanol, the s.o.s. phase fills half of the simulation box (100 Å). Hence, the length of the s.o.s. phase should be considered further since it may be another indicator for the presence of structuring in a ternary system.

There may be a threshold value for the s.o.s. length, at which mesoscopic structured solutions are present. For this purpose, other ternary systems have to be investigated. The W/EtOH/EtOAc system cannot be taken into account since the length of the individual phases has to be predetermined.

Figure 7 - 14 depicts the experimentally determined tie lines in the W/EtOH/TriA system. The colored dots represent the starting composition of the mixtures that is used to determine the endpoints of the tie lines. It is conspicuous that the hydrotrope content of the tie lines is below the content in the initial mixture. A tie line crossing the initial composition would be expected. But the hydrotrope concentration also possesses a maximum in the s.o.s. phases according to the COSMOplex calculations (see Figure S.7 - 5). It seems reasonable that there is an accumulation of the amphiphilic hydrotrope at the interface of the two bulk phases. This could indeed be observed in the experimental results of the W/alcohol/MMA systems as well (see Figure S.7 - 6). That suggests that mixtures in the biphasic area do not only separate into the 2 macroscopic phases but that there is a third “phase” representing a transition area. A mixture within the miscibility gap would, therefore, not simply separate along the tie line but slightly below at a smaller amount of hydrotrope.

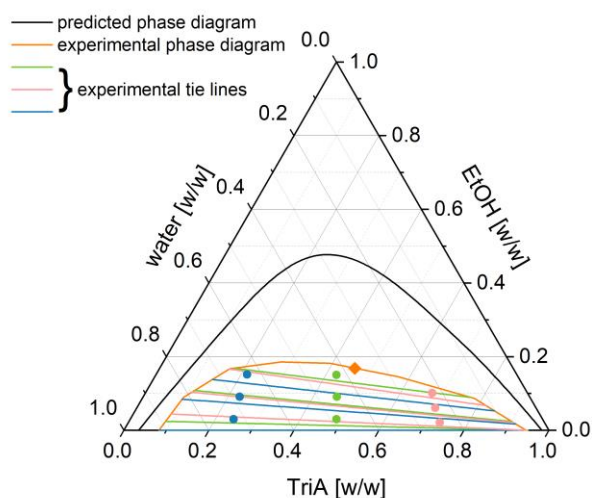


Figure 7 - 14: Ternary phase diagram of W/EtOH/TriA at 25 °C, determined experimentally (orange) and theoretically by COSMOtherm (black, renormalized). The colored lines represent the experimentally determined tie lines with their experimental starting compositions (dots). The orange rhomb indicates the CP.

## 7.4 Conclusion and outlook

COSMO-RS-based predictions of liquid-liquid equilibria are compared with experimentally determined ternary phase diagrams. First, we compared the size of the miscibility gap, the localization of the critical point, and the tie lines of systems consisting of water, different short-chain alcohols, and methyl methacrylate. The size of the miscibility gap decreases, and the critical point is shifted to higher amounts of methyl methacrylate when varying the hydrotrope in the following order: t-butanol > n-propanol > isopropanol > ethanol. Calculations on COSMOtherm allow predicting the correct ordering of the alcohols. The quantitative size of the predicted miscibility gap is in rather good agreement with the experiments as well. However, the miscibility gap of water/t-butanol/methyl methacrylate is slightly underestimated, which is attributed to the bulky size of the hydrotrope. Overall, COSMOtherm proves to be a valuable tool that allows the screening of ternary systems for the localization of the critical point and, in most cases, the tilt of their tie lines. This can support the research in radical polymerization, but also in extraction and organic chemistry, where tie lines play a crucial role in the separation of extracted or synthesized compounds.<sup>2,39-41</sup>

In the next step, we focused on a more complex oil compound. In this context, the system water, ethanol, and triacetin is investigated experimentally and theoretically. COSMOtherm predictions greatly overestimate the size of the miscibility gap. The ternary system is extensively studied regarding mesoscopic structuring by dynamic light scattering and small-and-wide-angle X-ray scattering. The deviation of the predictions from the experiment can indeed be explained by mesoscopic inhomogeneities in the monophasic solutions, which cannot be predicted by COSMOtherm. Since COSMOtherm deviations from the experiment enclose the area where structuring occurs, it may be a suitable way to localize structured areas by comparing the predictions with experimentally determined miscibility gaps. In order to improve the predictions, we replaced COSMOtherm, which is unable to treat inhomogeneous solutions, by COSMOplex, which is based on a layered simulation box allowing inhomogeneities. We can significantly improve the predictions with a three-phase (bulk – self-organizing-system (s.o.s.) – bulk) setup of the simulation box. In addition, the predicted length of the s.o.s. phase by COSMOplex calculations increased remarkably when approaching the structured area near the critical point. This may represent another helpful parameter for localizing structured areas. All applications of mesoscopic structured liquids could benefit from a rapid prediction of mesoscopic structured compositions in ternary systems. COSMOtherm especially impresses with its short computing time. Both COSMOtherm and COSMOplex calculations are also applied to a reference system of water,

ethanol, and ethyl acetate, which exhibit no structuring in the monophasic area. Indeed, both programs are able to predict the phase diagram in good agreement with the experiment. It has to be noted at this point that Blahnik *et al.* also observed correlation functions in DLS experiments for their systems, indicating some aggregation, which is not reflected in the COSMOtherm calculations. However, supplementary X-ray scattering data are lacking.<sup>2</sup> For this reason, the data are not considered further at this moment, but it has to be kept in mind that the calculation setup still has to be applied to other ternary systems to prove its applicability. Differences in the type of aggregation are also conceivable.

Furthermore, experiments and predictions depict an accumulation of the hydrotrope at the interface of the two bulk phases that form after phase separation in a mixture in the biphasic area. This is observable for systems with methyl methacrylate and triacetin. We assume that there might be rather an interphase between the two bulk phases. Therefore, mixtures in the miscibility gap do not separate along a tie line but slightly below at smaller hydrotrope concentrations.

Altogether, the initial calculations show auspicious results regarding the prediction of critical points, tie lines, and the area of structuring in ternary systems. However, it is indispensable to apply the calculations on further ternary systems to verify their predictive power. Especially systems with bulky oil compounds should be considered. In this way, one can exclude that COSMOtherm deviations do not result from structuring but from a misinterpretation of the single molecules. In addition, one could verify whether the critical point can still be located, at least relatively, when the molecular shape becomes more complex. Since COSMOplex improves the predictions for water, ethanol, and triacetin but still deviates from the experiment, the parameters of the simulation box may be optimized further. The size of the simulation box, as well as the convergence criteria, should be varied in a first attempt.

There are still several questions to be answered before making a definitive statement about the predictive power of COSMO-RS-based programs with regard to ternary systems. However, as demonstrated in the previous chapters of this work, the combination of mesoscopic structured liquids with complex organic reactions is a great challenge. Thus, it seems worthwhile to focus on developing an appropriate prediction strategy to support solvent optimization. Handling, computing time, and initial results encourage staying with the COSMO-RS model.

## 7.5 Supporting information

### 7.5.1 Ternary phase diagram W/tBuOH/MMA

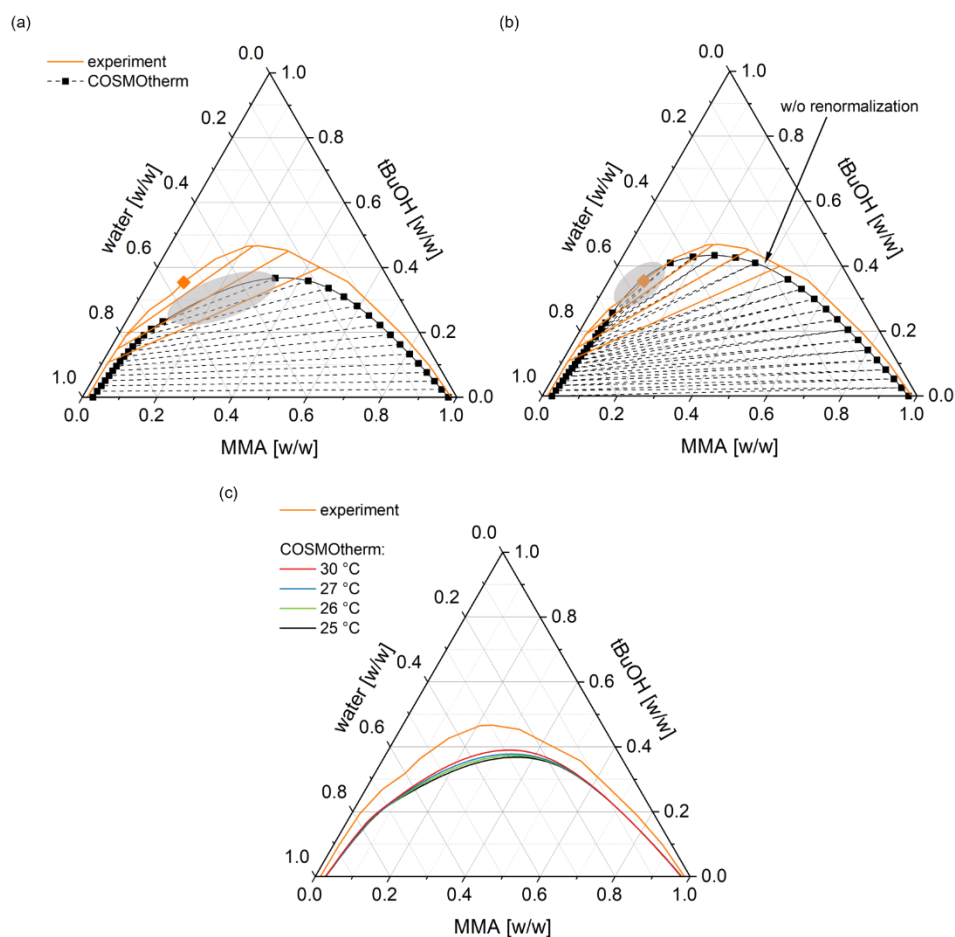


Figure S.7 - 1: Ternary phase diagrams of water, tBuOH, and MMA with the corresponding tie lines at 25 °C. The phase diagrams are determined experimentally (orange) or theoretically by COSMOtherm predictions (black). The orange rhomb depicts the experimentally determined critical point (CP) of the phase diagram, while the predicted area of the CP is indicated by gray shading. Predictions are shown with (a, c) and without (b) renormalization. The influence of temperature fluctuations during experiments can be excluded. Predictions depict a negligible influence (c).

### 7.5.2 Fitted DLS spectra of W/EtOH/TriA (constant amount of EtOH)

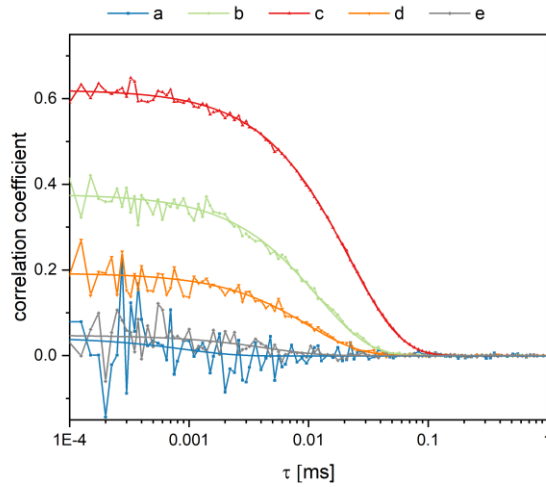


Figure S.7 - 2: DLS measurements discussed in Figure 7 - 9 with their exponential fits.

### 7.5.3 DLS spectra of W/EtOH/TriA and W/EtOH/EtOAc in the ternary phase diagram

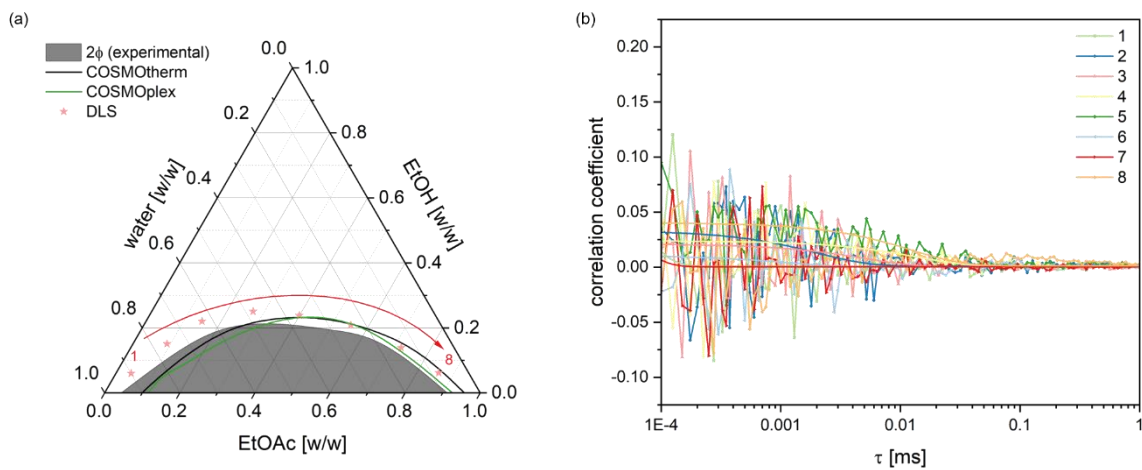


Figure S.7 - 3: (a) Phase diagram of W/EtOH/EtOAc at 25 °C, determined experimentally (gray shaded) or theoretically by COSMOtherm (black, renormalized) and COSMOplex (green). The asterisks identify the compositions of the mixtures measured by means of DLS. (b) Corresponding correlation functions obtained by DLS measurements with their exponential fit.

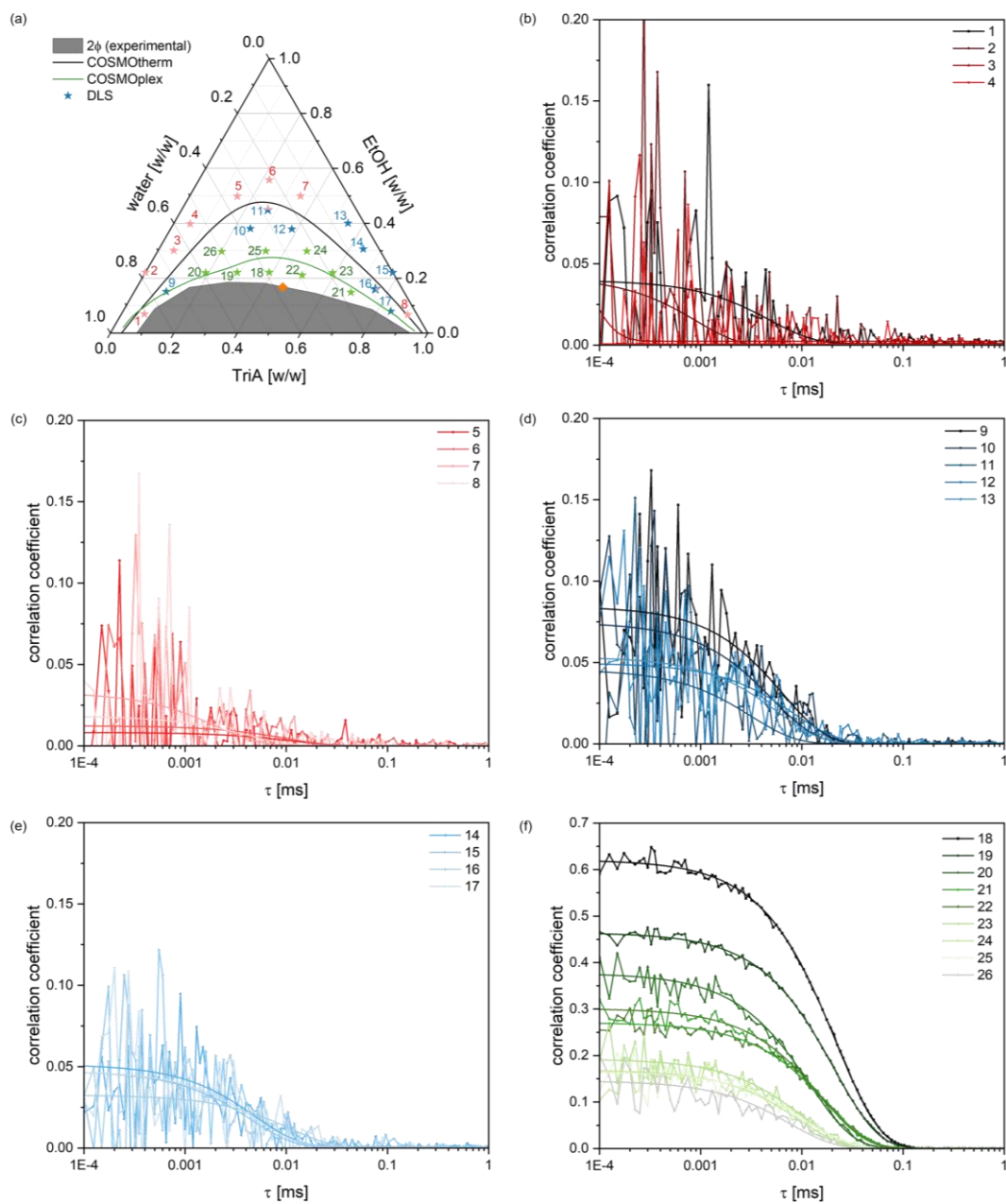
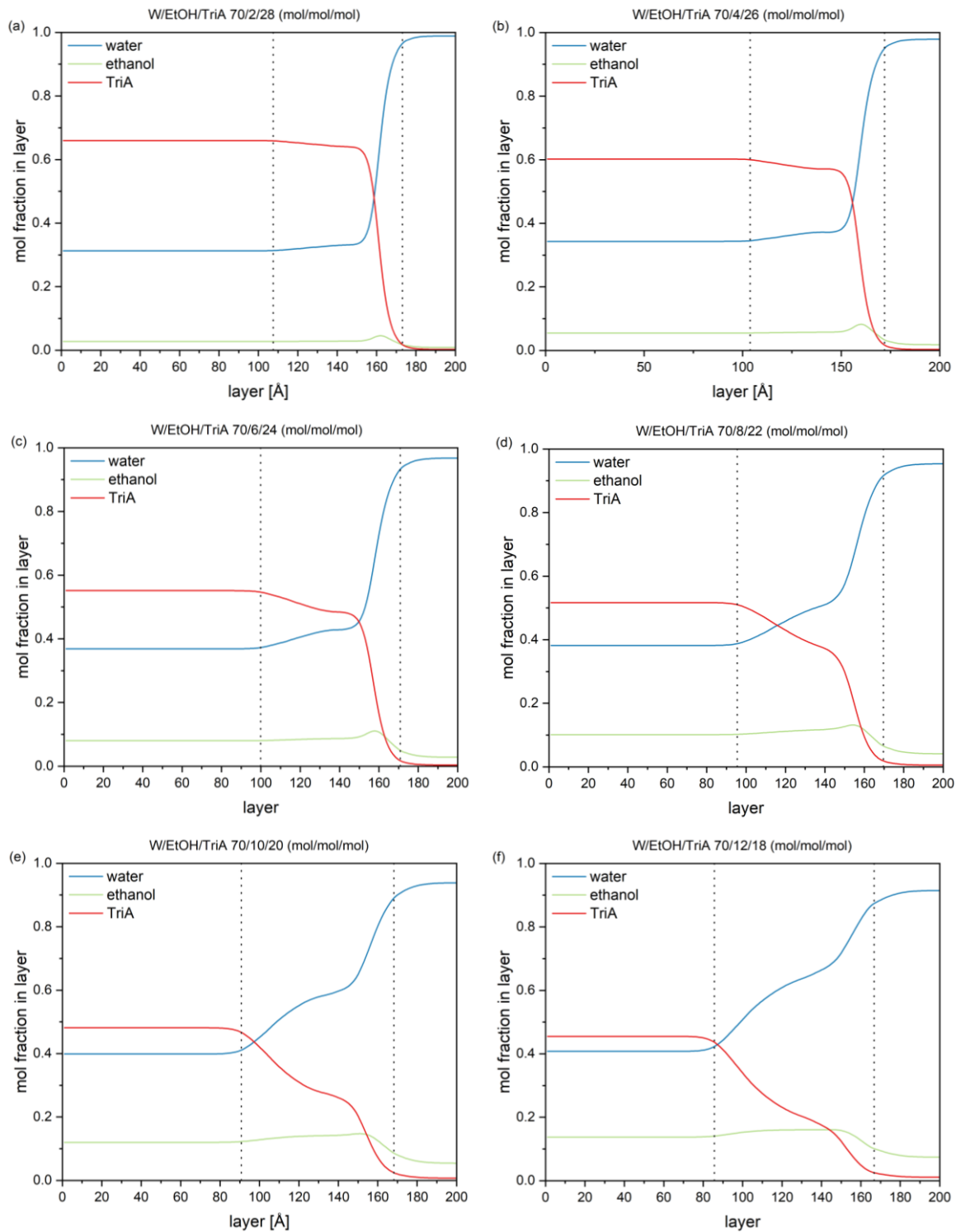
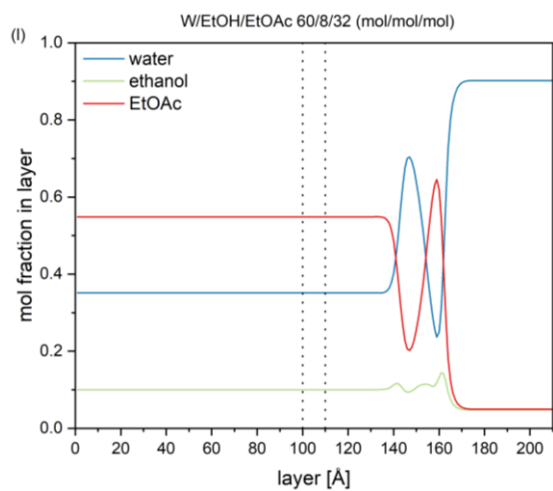
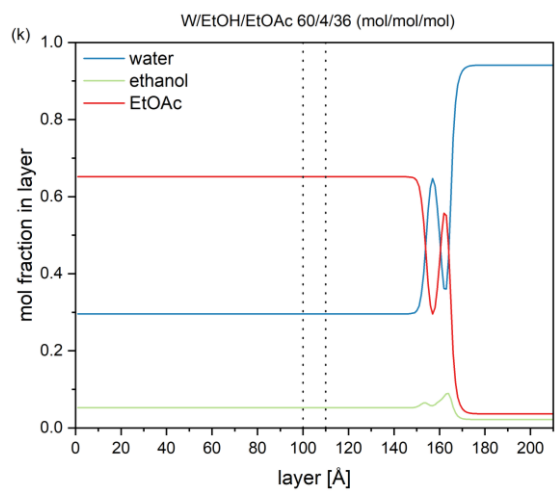
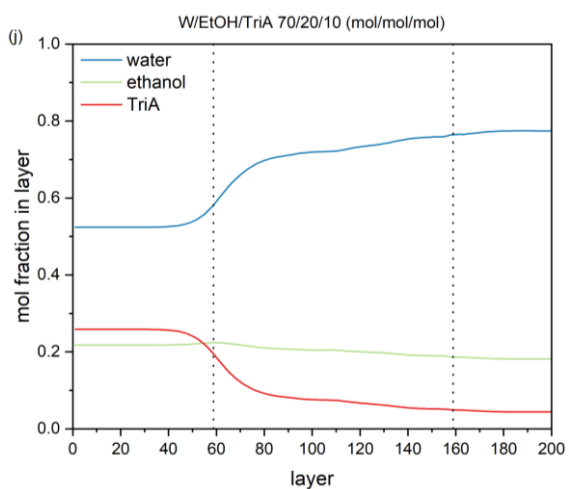
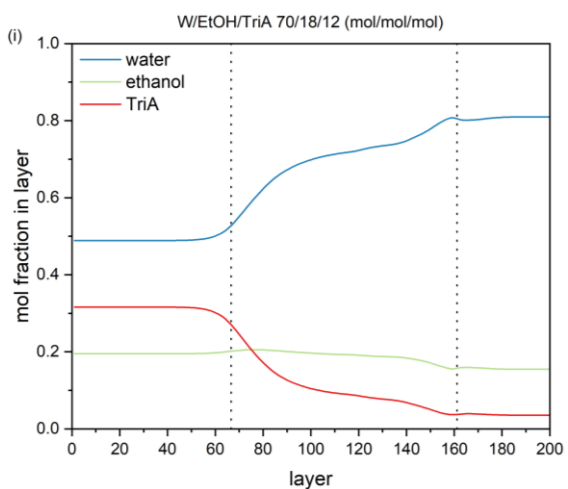
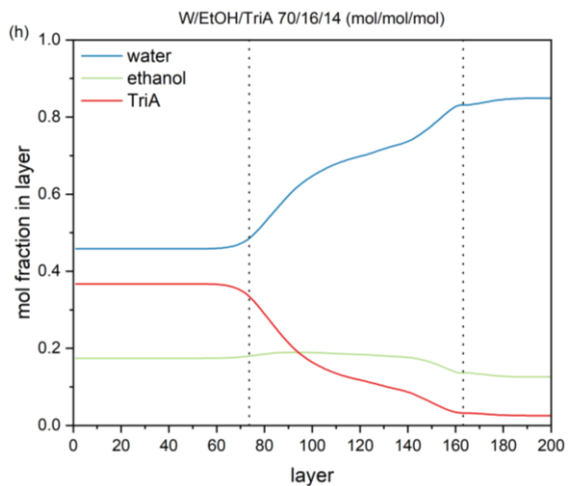
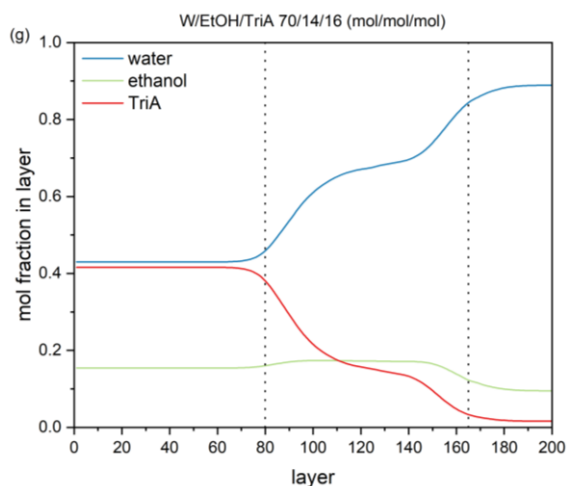


Figure S.7 - 4: (a) Phase diagram of W/EtOH/TriA at 25 °C, determined experimentally (gray shaded) or theoretically by COSMOtherm (black, renormalized) and COSMOplex (green). The asterisks identify the compositions of the mixtures measured by means of DLS. (b) Corresponding correlation functions obtained by DLS measurements with their experimental fits.

### 7.5.4 COSMOplex simulation boxes of the converged systems





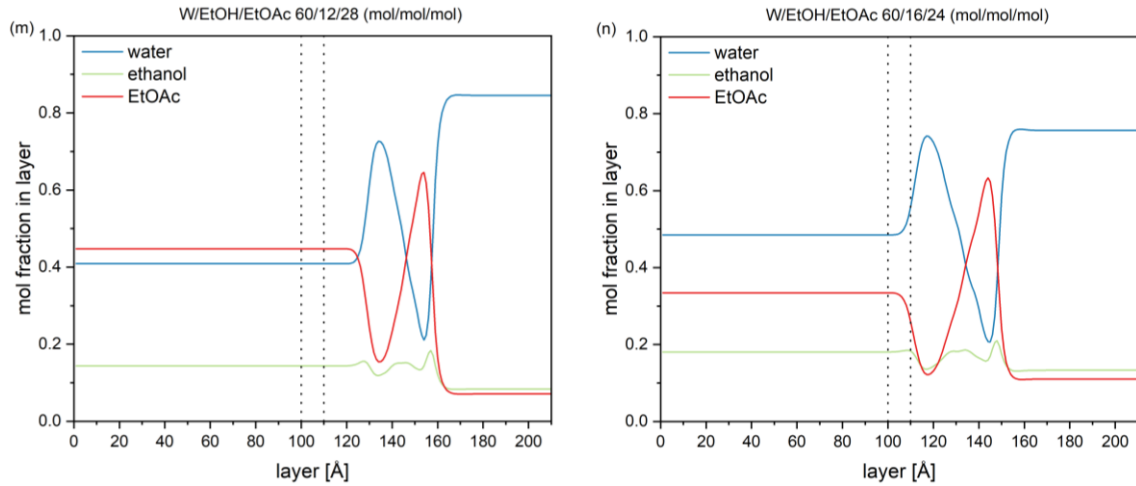


Figure S.7 - 5: COSMOplex simulation boxes of W/EtOH/TriA (a - j) and W/EtOH/EtOAc (k - n). The box is separated into the three phases bulk – s.o.s. – bulk. The mol fraction of the individual conformers in the converged system is given with respect to the box layer.

### 7.5.5 Experimental tie lines of W/alcohol/MMA systems

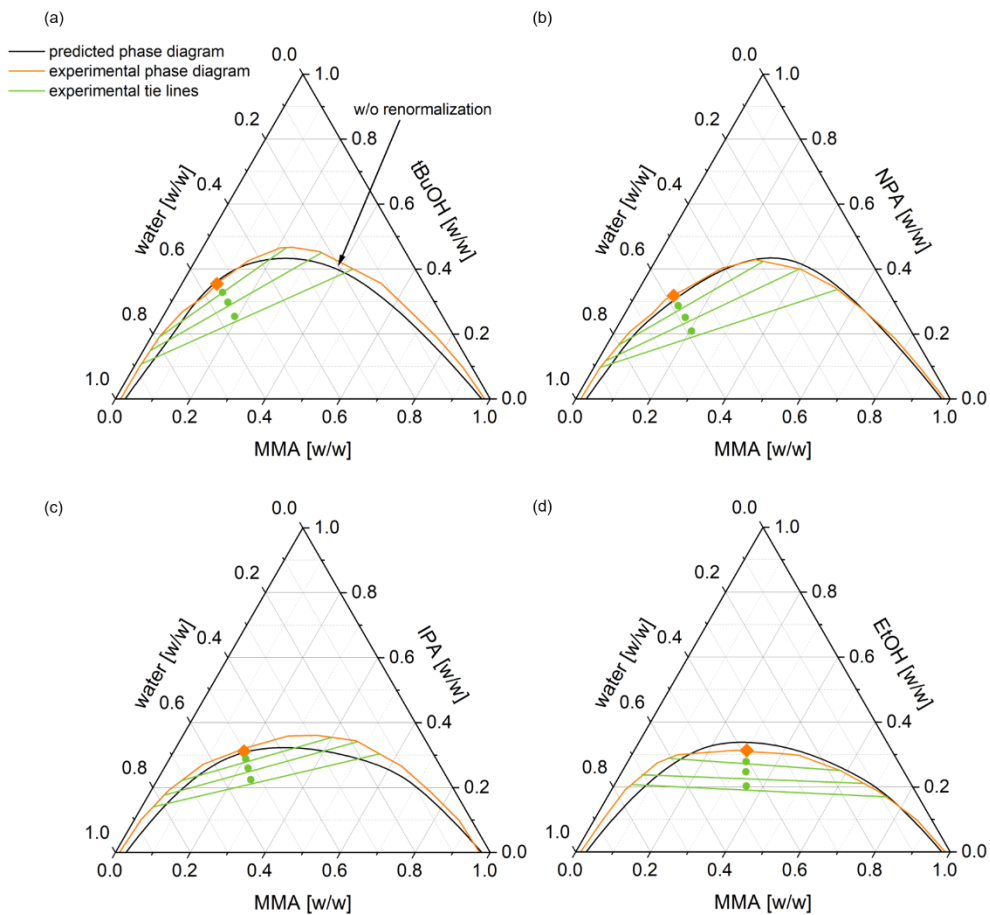


Figure S.7 - 6: Ternary phase diagram of W/alcohol/MMA at 25 °C, determined experimentally (orange) and theoretically by COSMOtherm (black). The green lines represent the experimentally determined tie lines with their experimental starting compositions (dots). The orange rhomb indicates the CP.

## 7.6 References

- (1) Lopian, T.; Schöttl, S.; Prévost, S.; Pellet-Rostaing, S.; Horinek, D.; Kunz, W.; Zemb, T. Morphologies Observed in Ultraflexible Microemulsions with and without the Presence of a Strong Acid. *ACS Cent. Sci.* **2016**, *2* (7), 467–475. <https://doi.org/10.1021/acscentsci.6b00116>.
- (2) Blahnik, J.; Krickl, S.; Schmid, K.; Müller, E.; Lupton, J.; Kunz, W. Microemulsion and Microsuspension Polymerization of Methyl Methacrylate in Surfactant-Free Microemulsions (SFME). *J. Colloid Interface Sci.* **2023**, *submitted*.
- (3) Anastas, P. T.; Warner, J. C. *Green Chemistry: Theory and Practice*, Reprint edn.; Oxford University Press, 2000.
- (4) Anastas, P.; Eghbali, N. Green Chemistry: Principles and Practice. *Chem. Soc. Rev.* **2010**, *39* (1), 301–312. <https://doi.org/10.1039/b918763b>.
- (5) Hautier, G.; Jain, A.; Ong, S. P. From the Computer to the Laboratory: Materials Discovery and Design Using First-Principles Calculations. *J. Mater. Sci.* **2012**, *47* (21), 7317–7340. <https://doi.org/10.1007/s10853-012-6424-0>.
- (6) Weger, D.; Pierre, A.; Perrot, A.; Kränkel, T.; Lowke, D.; Gehlen, C. Penetration of Cement Pastes into Particle-Beds: A Comparison of Penetration Models. *Materials (Basel)*. **2021**, *14* (2), 389. <https://doi.org/10.3390/ma14020389>.
- (7) Díaz-Somoano, M.; Unterberger, S.; Hein, K. R. G. Prediction of Trace Element Volatility during Co-Combustion Processes. *Fuel* **2006**, *85* (7–8), 1087–1093. <https://doi.org/10.1016/j.fuel.2005.10.013>.
- (8) Nieto-Draghi, C.; Fayet, G.; Creton, B.; Rozanska, X.; Rotureau, P.; De Hemptinne, J. C.; Ungerer, P.; Rousseau, B.; Adamo, C. A General Guidebook for the Theoretical Prediction of Physicochemical Properties of Chemicals for Regulatory Purposes. *Chem. Rev.* **2015**, *115* (24), 13093–13164. <https://doi.org/10.1021/acs.chemrev.5b00215>.
- (9) Engkvist, O.; Norrby, P. O.; Selmi, N.; Lam, Y. hong; Peng, Z.; Sherer, E. C.; Amberg, W.; Erhard, T.; Smyth, L. A. Computational Prediction of Chemical Reactions: Current Status and Outlook. *Drug Discov. Today* **2018**, *23* (6), 1203–1218. <https://doi.org/10.1016/j.drudis.2018.02.014>.
- (10) Xue, Y.; Liu, Z.; Gao, X.; Jin, C.; Wen, L.; Yao, X.; Ren, J. GPS-SNO: Computational

- Prediction of Protein S-Nitrosylation Sites with a Modified GPS Algorithm. *PLoS One* **2010**, 5 (6), e11290. <https://doi.org/10.1371/journal.pone.0011290>.
- (11) Klamt, A. Conductor-like Screening Model for Real Solvents: A New Approach to the Quantitative Calculation of Solvation Phenomena. *J. Phys. Chem.* **1995**, 99 (7), 2224–2235. <https://doi.org/10.1021/j100007a062>.
- (12) Klamt, A.; Eckert, F.; Arlt, W. COSMO-RS: An Alternative to Simulation for Calculating Thermodynamic Properties of Liquid Mixtures. *Annu. Rev. Chem. Biomol. Eng.* **2010**, 1, 101–122. <https://doi.org/10.1146/annurev-chembioeng-073009-100903>.
- (13) Eckert, F. COSMOtherm Reference Manual Release 19. COSMOlogic GmbH & Co. KG, a Dassault Systèmes company 2019.
- (14) Diedenhofen, M.; Klamt, A. COSMO-RS as a Tool for Property Prediction of IL Mixtures-A Review. *Fluid Phase Equilib.* **2010**, 294 (1–2), 31–38. <https://doi.org/10.1016/j.fluid.2010.02.002>.
- (15) Klein, M. J.; Tisza, L. Theory of Critical Fluctuations. *Phys. Rev.* **1949**, 76 (12), 1861–1868. <https://doi.org/10.1103/PhysRev.76.1861>.
- (16) Greer, S. C.; Moldover, M. R. Thermodynamic Anomalies at Critical Points of Fluids. *Annu. Rev. Phys. Chem.* **1981**, 32 (1), 233–265. <https://doi.org/10.1146/annurev.pc.32.100181.001313>.
- (17) Sengers, J. V.; Sengers, J. M. H. L. Thermodynamic Behavior of Fluids Near the Critical Point. *Annu. Rev. Phys. Chem.* **1986**, 37 (1), 189–222. <https://doi.org/10.1146/annurev.pc.37.100186.001201>.
- (18) De Pablo, J. J.; Prausnitz, J. M. Liquid-Liquid Equilibria for Binary and Ternary Systems Including the Critical Region. Transformation to Non-Classical Coordinates. *Fluid Phase Equilib.* **1989**, 50 (1–2), 101–131. [https://doi.org/10.1016/0378-3812\(89\)80285-7](https://doi.org/10.1016/0378-3812(89)80285-7).
- (19) Goldstein, R. E.; Walker, J. S. Theory of Multiple Phase Separations in Binary Mixtures: Phase Diagrams, Thermodynamic Properties, and Comparisons with Experiments. *J. Chem. Phys.* **1983**, 78 (3), 1492–1512. <https://doi.org/10.1063/1.444839>.
- (20) Chen, S.-H.; Rajagopalan, R. *Micellar Solutions and Microemulsions*; Springer-Verlag: New York, 1990. <https://doi.org/10.1007/978-1-4613-8938-5>.
- (21) Orlich, B.; Schomäcker, R. Enzyme Catalysis in Reverse Micelles. *Adv. Biochem.*

- Eng. Biotechnol.* **2002**, *75*, 185–208. [https://doi.org/10.1007/3-540-44604-4\\_6](https://doi.org/10.1007/3-540-44604-4_6).
- (22) Khmel'nitsky, Y. L.; Hilhorst, R.; Veeger, C. Detergentless Microemulsions as Media for Enzymatic Reactions: Cholesterol Oxidation Catalyzed by Cholesterol Oxidase. *Eur. J. Biochem.* **1988**, *176* (2), 265–271. <https://doi.org/10.1111/j.1432-1033.1988.tb14277.x>.
- (23) Han, Y.; Liu, S.; Du, Y.; Li, D.; Pan, N.; Chai, J.; Li, D. A New Application of Surfactant-Free Microemulsion: Solubilization and Transport of Drugs and Its Transdermal Release Properties. *J. Taiwan Inst. Chem. Eng.* **2022**, *138*, 104473. <https://doi.org/10.1016/j.jtice.2022.104473>.
- (24) Lipshutz, B. H.; Ghorai, S.; Cortes-Clerget, M. The Hydrophobic Effect Applied to Organic Synthesis: Recent Synthetic Chemistry “in Water.” *Chem. - A Eur. J.* **2018**, *24* (26), 6672–6695. <https://doi.org/10.1002/chem.201705499>.
- (25) Klamt, A.; Schwöbel, J.; Huniar, U.; Koch, L.; Terzi, S.; Gaudin, T. COSMOplex: Self-Consistent Simulation of Self-Organizing Inhomogeneous Systems Based on COSMO-RS. *Phys. Chem. Chem. Phys.* **2019**, *21* (18), 9225–9238. <https://doi.org/10.1039/c9cp01169b>.
- (26) Hahn, M.; Krickl, S.; Buchecker, T.; Jošt, G.; Touraud, D.; Bauduin, P.; Pfitzner, A.; Klamt, A.; Kunz, W. Ab Initio Prediction of Structuring/Mesoscale Inhomogeneities in Surfactant-Free Microemulsions and Hydrogen-Bonding-Free Microemulsions. *Phys. Chem. Chem. Phys.* **2019**, *21* (15), 8054–8066. <https://doi.org/10.1039/c8cp07544a>.
- (27) Pizzino, A.; Molinier, V.; Catté, M.; Salager, J. L.; Aubry, J. M. Bidimensional Analysis of the Phase Behavior of a Well-Defined Surfactant (C10E4)/Oil (n -Octane)/Water-Temperature System. *J. Phys. Chem. B* **2009**, *113* (50), 16142–16150. <https://doi.org/10.1021/jp907261u>.
- (28) Winsor, P. A. Hydrotropy, Solubilisation and Related Emulsification Processes. *Trans. Faraday Soc.* **1948**, *44*, 376–398. <https://doi.org/10.1039/tf9484400376>.
- (29) Schwöbel, J. A. H.; Klamt, A. Mechanistic Skin Penetration Model by the COSMOperm Method: Routes of Permeation, Vehicle Effects and Skin Variations in the Healthy and Compromised Skin. *Comput. Toxicol.* **2019**, *11*, 50–64. <https://doi.org/10.1016/j.comtox.2019.02.004>.
- (30) Dekker, M. L.; Clause, M.; Rosano, H. L.; Zradba, A. S. *Microemulsion Systems*, 24th edn.; Surfactant Science Ser., New York, PA, 1987.

- 
- (31) BIOVIA COSMOthermX, Release 19. COSMOlogic GmbH & Co. KG, a Dassault Systèmes company 2019.
- (32) Klamt, A.; Volker, J.; Bürger, T.; Lohrenz, J. C. W. Refinement and Parametrization of COSMO-RS. *J. Phys. Chem. A* **1998**, *102* (26), 5074–5085. <https://doi.org/10.1021/jp980017s>.
- (33) Eckert, F.; Klamt, A. Fast Solvent Screening via Quantum Chemistry: COSMO-RS Approach. *AIChE J.* **2002**, *48* (2), 369–385. <https://doi.org/10.1002/aic.690480220>.
- (34) Becke, A. D. Density-Functional Exchange-Energy Approximation with Correct Asymptotic Behavior. *Phys. Rev. A* **1988**, *38* (6), 3098–3100. <https://doi.org/10.1103/PhysRevA.38.3098>.
- (35) BIOVIA COSMOplex, Release 19. COSMOlogic GmbH & Co. KG, a Dassault Systèmes company 2019.
- (36) Buchecker, T.; Krickl, S.; Winkler, R.; Grillo, I.; Bauduin, P.; Touraud, D.; Pfitzner, A.; Kunz, W. The Impact of the Structuring of Hydrotropes in Water on the Mesoscale Solubilisation of a Third Hydrophobic Component. *Phys. Chem. Chem. Phys.* **2017**, *19* (3), 1806–1816. <https://doi.org/10.1039/c6cp06696h>.
- (37) Gouveia, A. S. L.; Oliveira, F. S.; Kurnia, K. A.; Marrucho, I. M. Deep Eutectic Solvents as Azeotrope Breakers: Liquid-Liquid Extraction and COSMO-RS Prediction. *ACS Sustain. Chem. Eng.* **2016**, *4* (10), 5640–5650. <https://doi.org/10.1021/acssuschemeng.6b01542>.
- (38) Ferreira, A. R.; Freire, M. G.; Ribeiro, J. C.; Lopes, F. M.; Crespo, J. G.; Coutinho, J. A. P. Overview of the Liquid-Liquid Equilibria of Ternary Systems Composed of Ionic Liquid and Aromatic and Aliphatic Hydrocarbons, and Their Modeling by COSMO-RS. *Ind. Eng. Chem. Res.* **2012**, *51* (8), 3483–3507. <https://doi.org/10.1021/ie2025322>.
- (39) Schwarze, M.; Pogrzeba, T.; Volovych, I.; Schomäcker, R. Microemulsion Systems for Catalytic Reactions and Processes. *Catal. Sci. Technol.* **2015**, *5* (1), 24–33. <https://doi.org/10.1039/c4cy01121j>.
- (40) Hinze, W. L.; Pramauro, E.; Poole, C. F. A Critical Review of Surfactant-Mediated Phase Separations (Cloud-Point Extractions): Theory and Applications. *Crit. Rev. Anal. Chem.* **1993**, *24* (2), 133–177. <https://doi.org/10.1080/10408349308048821>.
- (41) Krickl, S. Investigation of Potential Applications of Surfactant-Free Microemulsions – Solubilisation, Separation and Extraction Processes and Reaction Media, University

- of Regensburg, 2018.
- (42) Zemb, T. N.; Klossek, M.; Lopian, T.; Marcus, J.; Schöetl, S.; Horinek, D.; Prevost, S. F.; Touraud, D.; Diat, O.; Marčelja, S.; Kunz, W. How to Explain Microemulsions Formed by Solvent Mixtures without Conventional Surfactants. *Proc. Natl. Acad. Sci. U. S. A.* **2016**, *113* (16), 4260–4265. <https://doi.org/10.1073/pnas.1515708113>.
- (43) Diat, O.; Klossek, M. L.; Touraud, D.; Deme, B.; Grillo, I.; Kunz, W.; Zemb, T. Octanol-Rich and Water-Rich Domains in Dynamic Equilibrium in the Pre-Ouzo Region of Ternary Systems Containing a Hydrotrope. *J. Appl. Crystallogr.* **2013**, *46* (6), 1665–1669. <https://doi.org/10.1107/S002188981302606X>.
- (44) Huber, V. Formulation and Extraction of Natural Dyes with Surfactant-Free Microemulsions, University of Regensburg, 2019.

---

## Chapter 8 Epilogue

### Conclusion and outlook

In the present work, the applicability of surfactant-free microemulsions (SFMEs) is studied on different types of reactions, namely photocatalytic, enzymatic, and organic cross-coupling reactions. The effect of solvent structuring on the reactivity is considered, as is the solvent effect on solubilization.

In the first chapter (**Natural-like vanilla extract from curcuminoids**), systems established for the natural extraction of curcuminoids are investigated for the photochemical conversion of curcuminoids to vanillin and the related flavors vanillic acid and p-hydroxybenzaldehyde. The mesoscopic structured SFME of water, ethanol, and triacetin appears to be disadvantageous for the reaction compared to the less structured binary mixture of ethanol and triacetin. This is attributed to a lower dissolved oxygen concentration but also to a possible hindrance in the propagation of the reaction from the radical and charged intermediates to the more hydrophobic unreacted substrate by the pseudo-phases. However, despite the adverse impact on the reaction itself, the SFME enables significantly higher substrate concentrations when coupling the photochemical conversion directly to the extraction. Accordingly, the SFME provides comparable or even better results than the less structured binary solvent, depending on the reaction time. To the best of our knowledge, this is the first time that a nature-based production method of not only vanillin but also vanillic acid and p-hydroxybenzaldehyde has been presented. Hence, it is suggested to transfer the reaction to a continuous flow reactor in the next step to develop a scalable method. Overall, the method presented may possess great potential for industrial application.

In Chapters 2 (**One-pot cascade reaction**) and 3 (**1,4-Addition in surfactant-free aqueous solutions**), organic cross-coupling reactions are presented that are catalyzed by transition metal catalysts. The reference system is given by a micellar solution of the designer surfactant TPGS-750-M (DL- $\alpha$ -tocopherol methoxypolyethylene glycol succinate). To our knowledge, this is the first time that organic cross-coupling reactions have been successfully transferred to SFMEs. In the case of the 1,4-addition of cyclohexenone to an arylboronic acid, SFMEs are compared containing alcohol or salt hydrotropes. All SFMEs achieved an improved solubilization of the substrates compared to the micellar system. While the alcohol systems reduce the yield, the SFME of water, sodium 1-pentanesulfonate, and tetrahydro linalool provides the same excellent yield as the micellar system. The

decisive parameter for a successful reaction is the stabilization of the arylboronic acid to avoid side reactions. Accordingly, stabilizing interactions between the salt and the substrate are expected, which has to be investigated further. A correlation with the mesoscopic interface, however, is not observed. The same applies to the studied Heck reaction. Heck reactions are successfully carried out in an SFME of water, isopropanol, and benzyl alcohol, as well as in an unstructured binary mixture of isopropanol and water. While the reaction requires elevated temperatures in the micellar solution, the reaction in the surfactant-free solutions is further improved at room temperature. The reactivity is thus enhanced in the absence of the designer surfactant. Moreover, the SFME depicts again significantly better solubilization of the reactants than the micellar solution. Further, the Heck reaction is successfully coupled with a biocatalytic step in both surfactant-free solutions, yielding even better results than in the micellar system. The isopropanol exhibits an essential salting-out effect on the alcohol dehydrogenase enzyme used (ADH-101), which tolerates large amounts of the alcohol. The partially undissolved enzyme remains active, and consequently, nanoreactors introduced by solvent structuring are not required, as previously assumed. The crucial parameters are rather the solubility and stability of the reaction components, whereby a better solubility is not necessarily favorable due to possible resulting instabilities.

Chapter 4 (**The role of meglumine in aqueous cross-coupling**) deals with the impact of the additive meglumine on the solubilization of aromatic compounds and on organic cross-coupling reactions. First, the solubility of the organic photocatalyst 1,8:4,5-naphthalenetetracarboxdiimide is taken into account. The metal-free compound is a promising photocatalyst owing to the great (approximated) excited state reduction potential at  $-3$  V. In this work, the catalyst is dissolved in water with the aid of several alkanolamines, among which meglumine turned out to be the most suitable green additive. Accordingly, good to excellent yields are achieved in a few cross-coupling reactions. However, the reaction conditions need to be optimized further so that the catalyst can also be applied for more challenging reactions. In the second approach, meglumine is applied in photochemical C-C and C-S coupling reactions in the absence of a photocatalyst. In that way, excellent yields can be achieved for demanding reactions in water. Two different mechanisms are revealed: In C-C coupling reactions, meglumine only interacts with an already formed electron donor-acceptor (EDA) complex between the substrates, increases its solubility, and, therefore, enhances the reaction. In C-S coupling reactions, meglumine interacts with the thiol. The additive enhances the solubility of the thiol substrate and activates the substrate via a deprotonation reaction. The activated thiol forms an EDA complex with the second substrate, which finally undergoes a photochemical transformation. Overall, the chapter demonstrates that challenging organic reactions can also be transferred to water in the absence

---

of solvent structuring by applying an appropriate additive, as is the green meglumine. The additive can improve the solubility and reactivity of aromatic compounds.

The 5<sup>th</sup> chapter (**Flavin-catalyzed photooxidation**) presents the idea of optimizing the properties of a photocatalyst by solvent structuring. For this reason, the oxidation of 4-methoxybenzyl alcohol catalyzed by tetraacetyl riboflavin (TARF) is considered. At high substrate concentrations, the substrate increasingly quenches the catalyst in its excited singlet state. For a productive transformation, however, the catalyst has to reach its excited triplet state. Hence, solvent structuring is introduced by micellar solutions of the surfactant C<sub>8</sub>EO<sub>5</sub> or by SFMEs of water, a short-chain alcohol, and the substrate in order to shield the catalyst from the substrate. The experiments confirm an elongation of the lifetime of the excited singlet TARF as well as an improvement of the product quantum yield. At this stage, the improvement cannot be directly linked to the solvent structuring as other parameters such as oxygen solubility and solvent viscosity influences the reaction as well. As a consequence, further analysis in the form of transient absorbance measurements is required.

At the end, more fundamental questions are discussed apart from reactions. In Chapter 6 (**In-depth study of ethanol-triacetin mixtures**), the great synergistic effect observed in binary mixtures when solubilizing (tetrahydro)curcumin is studied. The synergy can neither be explained by an optimum of interacting surface charge densities (studied by COSMO-RS calculations) nor by mesoscopic aggregation (studied by scattering experiments). Dielectric relaxation spectroscopy measurements reveal a concentration range, in which ethanol molecules are no longer bound in chains and thus interact with triacetin. This concentration range exhibits a significant overlap with the range of maximum solubility of (tetrahydro)curcumin. Either the demolition of the living polymer ethanol network by the triacetin or the ethanol-triacetin complexes themselves are assumed to increase the solubility of (tetrahydro)curcumin at these compositions. Although different mechanistic studies are performed, some assumptions remain speculative. For this reason, theoretical modeling of the interactions between the different ethanol/triacetin species and the solutes should be considered. The complexity of just one aspect, like solubilization, demonstrates the overall complexity of reactions, which are influenced by the interplay of multiple parameters.

Finally, Chapter 7 (**COSMO-RS predictions of ternary phase diagrams**) deals with the predictions of critical points and tie lines as well as mesoscopic structured compositions within ternary systems. All predictions are based on the COSMO-RS model (conductor-like solvent model for real solvents). Critical points and tie lines are calculated in ternary systems of water, a short-chain alcohol, and methyl methacrylate, which can be applied as a reaction solvent for polymerization reactions. Overall, the calculations agree well with the experiment despite minor deviations. In particular, the relative location of the critical point

is well predicted. This allows fast screening of different systems in order to find the best hydrotrope for a specific application. Furthermore, the ternary phase diagram of water, ethanol, and triacetin is predicted using COSMOtherm (unable to deal with solvent inhomogeneities) and using COSMOplex (can treat inhomogeneities). While COSMOtherm strongly overestimates the miscibility gap, calculations are improved by applying COSMOplex. Further improvements are necessary. However, it is already noticeable that the deviation from COSMOtherm to COSMOplex and to the experimental phase diagram encloses compositions, in which mesoscopic inhomogeneities are detected. Accordingly, the combination of both prediction tools or the combination of COSMOtherm and the experiment allows predicting the area of mesoscopic structuring within a ternary system. Furthermore, systems that possess no structuring can be identified since COSMOtherm and the experiments are in good agreement, as shown for water, ethanol, and ethyl acetate. The presented method has to be applied to several different systems to test its universal applicability. The first results, however, seem promising. Theoretical calculations can avoid time- and material-consuming experiments. As shown in the other chapters, a great experimental effort is required to optimize the reaction solvent conditions. Predictions providing an initial idea of the system and its structuring are therefore desirable.

---

The presented results allow for answering some of the questions stated at the beginning of this work. **Can micellar reaction solutions, in particular solutions with complex designer surfactants, be replaced by simple and green SFMEs?** It is unequivocally proven that complex micellar solutions can be replaced by simple and green SFMEs. The designer surfactant TPGS-750-M is successfully replaced in both chemo- and biocatalysis (Chapters 2, 3). Furthermore, SFMEs can be a suitable solvent for photochemistry (Chapters 1, 5).

**Which reaction types require an interface? And what are the decisive parameters for organic reactions performed in water?** None of the presented reactions carried out in designer surfactant solutions require an interface, making the usage of a surfactant unessential. It has been previously assumed that the nanoreactors built up by surfactants are required for protecting enzymes against denaturation and for solubilization, stabilization, and compartmentation of organic components in water. The crucial parameters in the studied reactions are indeed the solubilization and stabilization of the reaction components. However, no need for an interface for this purpose can be revealed in the present studies. Stabilization can be achieved by partial salting out or stabilizing interactions with another molecule in the absence of a separating interface. Despite the lack of compartmentation, the reactivity can be kept high in unstructured aqueous solutions. Consequently, the same excess amounts of substrate can be applied as in the micellar solutions. The good reactivity in the aqueous media is also attributed to enhanced solubility. However, as shown in Chapter 4, this can also be achieved by the addition of simple additives. Reactions are reported in the literature, in which a defined interface is expected to be indispensable. However, until now, it is difficult to answer which types of organic reactions really require an interface to be performed in water. This work greatly showcased that micellar solutions can improve or enable reactions in water for reasons other than the interface. Even in the case of enzymes, there is probably no universal rule that structuring is required when there are potentially denaturing compounds present. It is assumed that for a large number of reactions carried out in micellar solutions, the interface or encapsulation of components is not the crucial point. From the results of this work, it can be deduced that a more detailed investigation is generally required before stating the decisive role of an interface in reactions.

**Do SFMEs possess some unique advantages over micellar solvents with regard to organic reactions in water?** The greatest advantage of the SFMEs compared to the micellar solution and also to binary solutions is the great solubilization power of the systems. In the organic reactions studied in this work, the solubility of the compounds is expected to be limited by both stacking interactions and hydrophobicity. The designer surfactant may not be able to break the stacking as effectively as the small hydrotropes can, which could

explain the minor solubilization power of the micellar system. Although this assumption has to be investigated further. In general, the better solubility can also increase the reactivity. However, better solubility does not always correlate with a better reaction outcome (as shown for the enzyme and the arylboronic acid in Chapters 2, 3). The instabilities of some reactants and catalysts can, however, be addressed by the addition of stabilizing additives. The variability of SFMEs allows their constituents to be adjusted accordingly. The difference in the dynamic of the structuring may also present an advantage of the SFME over micellar solutions. In Chapter 1, the structuring appears to hinder the photochemical reaction but concurrently increases the extractability of the starting material. The less dynamic micellar solution may hinder the reaction even more since compartmentation is reinforced. Further experiments are required to confirm this assumption, but this type of reaction could present a possible application field, in which SFMEs bring a general benefit. The extraction power of the SFME can trump that of the binary mixture, and the more dynamic structuring and, thus, the less defined interface could trump the micellar system. This could be essential in photochemical reactions that run preferentially in the absence of an interface but whose reaction components are poorly soluble.

**Which interesting industrial applications for SFMEs result from this in the synthetic chemistry?** At several points in this work, it has been noted that hydrotropes are commonly less foaming and have a less pronounced tendency to go to the interface. Furthermore, the constituents of the SFMEs have been selected considering their *greenness*. These characteristics already put SFMEs in an attractive light for application in industry. Their suitability as a reaction solvent for cross-coupling reactions that can be found in several syntheses in industry, already proves the applicability of SFMEs for industrial-relevant reactions.

With regard to the previously discussed solubilization power of this solvent type, industrial-relevant photocatalytic reactions should be considered in the next step. Although even the SFMEs did not always achieve complete solubility during the reaction, the solutions studied in this work have been way more transparent than the micellar reaction mixtures shown in literature. Since light penetration is essential in photocatalysis, turbid suspensions need to be avoided. Although SFME deteriorated the photochemical transformation in Chapter 1, the greater solubility can have a much more crucial, positive impact. In this context, the coupling with, e.g., a biocatalytic step would be very beneficial for later industrial application. Every coupled step reduces the effort of a process by the intermediate steps required for the replacement of the solvent. However, it is suggested to work on already established reaction systems, including established catalysts. It has been shown that solubilizing and optimizing a “new” catalyst for reactions can be laborious and time-consuming. Together

with the solvent optimization for different reaction types, in a rather novel coupling field, there is a risk of going down a rabbit hole.

Besides photocatalysis, another interesting approach would be the expansion of chemo-bio-catalysis on larger cascade reactions. In this context, research should not be limited to Heck and 1,4-addition reactions. Other (transition) metal-catalyzed reactions, such as Sonogashira cross-coupling and alkyne hydration, may be considered in combination with an enzyme-catalyzed reaction step. In the last step, it is suggested to use the already applied ADH-101 because of its great tolerance towards alcohols. Moreover, initial results suggest that the enzyme can regenerate its own cofactor NADPH, which eliminates the need for a second enzyme.

Last but not least, the universal applicability of the previously developed SFME systems should be investigated. Although the adaptability of an SFME is a great advantage in order to overcome specific problems during reactions, a reaction solvent applicable to different reaction types would present a great tool for the industry. In particular, with respect to the effort required for the development of new SFMEs suitable for reactions, a broader applicability is desirable. The micellar solution of TPGS-750-M, *e.g.*, is successfully applied in different reaction types, as shown in this work and in the literature. Accordingly, different substrates and different reactions should be investigated in the already presented systems. A promising solvent may also be considered for initial upscaling tests.

## List of publications

- (1) **Hofmann, E.**; Degot, P.; Touraud, D.; König, B.; Kunz, W. Novel Green Production of Natural-like Vanilla Extract from Curcuminoids. *Food Chem.* **2023**, *417*, 135944. <https://doi.org/10.1016/j.foodchem.2023.135944>.
- (2) **Hofmann, E.**; Schmauser, L.; Neugebauer, J.; Touraud, D.; Gallou, F.; Kunz, W. Sustainable Cascade Reaction Combining Transition Metal-Biocatalysis and Hydrophobic Substrates in Surfactant-Free Aqueous Solutions. *Chem. Eng. J.* **2023**, *in minor revision*.
- (3) **Hofmann, E.**; Saridis, A.; Touraud, D.; Buchner, R.; Kunz, W. In-Depth Study of Binary Ethanol-Triacetin Mixtures in Relation with Their Excellent Solubilization Power. *Phys. Chem. Chem. Phys.* **2023**, *submitted*.
- (4) Tian, Y.; **Hofmann, E.**; Silva, W.; Pu, X.; Touraud, D.; Gschwind, R. M.; Kunz, W.; König, B. Enforced Electronic-Donor-Acceptor Complex Formation in Water for Photochemical Cross-Coupling. *Angew. Chemie Int. Ed.* **2023**, *62* (17). <https://doi.org/10.1002/anie.202218775>.
- (5) Mehringer, J.; **Hofmann, E.**; Touraud, D.; Koltzenburg, S.; Kellermeier, M.; Kunz, W. Salting-in and Salting-out Effects of Short Amphiphilic Molecules: A Balance between Specific Ion Effects and Hydrophobicity. *Phys. Chem. Chem. Phys.* **2021**, *23* (2), 1381–1391. <https://doi.org/10.1039/d0cp05491g>.
- (6) Delforce, L.; **Hofmann, E.**; Nardello-Rataj, V.; Aubry, J.-M. TiO<sub>2</sub> Nanoparticle Dispersions in Water and Nonaqueous Solvents Studied by Gravitational Sedimentation Analysis: Complementarity of Hansen Parameters and DLVO Interpretations. *Colloids Surfaces A Physicochem. Eng. Asp.* **2021**, *628*, 127333. <https://doi.org/10.1016/j.colsurfa.2021.127333>.
- (7) Degot, P.; Huber, V.; **Hofmann, E.**; Hahn, M.; Touraud, D.; Kunz, W. Solubilization and Extraction of Curcumin from Curcuma Longa Using Green, Sustainable, and Food-Approved Surfactant-Free Microemulsions. *Food Chem.* **2021**, *336*, 127660. <https://doi.org/10.1016/j.foodchem.2020.127660>.

## Declaration in lieu of oath

- (1) I hereby declare that I have completed this dissertation without the impermissible help of third parties and without using any resources other than those indicated; the data and concepts taken directly or indirectly from other sources are identified with citations to the literature.
- (2) The people listed at the beginning of a chapter supported my work in the manner described, free of charge.
- (3) No further persons were involved in the creation of the present dissertation. In particular, I have not made use of the paid assistance of a doctoral consultant or other persons for this purpose. No one has received monetary benefits either directly or indirectly for work that is associated with the content of the dissertation submitted.
- (4) The dissertation has not previously been submitted to another examination authority in the same or a similar form, neither in Germany nor abroad.

Regensburg, 24.05.2023

---

Evamaria Hofmann

## Eidesstattliche Erklärung

- (1) Ich erkläre hiermit an Eides statt, dass ich die vorliegende Arbeit ohne unzulässige Hilfe Dritter und ohne Benutzung anderer als der angegebenen Hilfsmittel angefertigt habe; die aus anderen Quellen direkt oder indirekt übernommenen Daten und Konzepte sind unter Angabe des Literaturzitats gekennzeichnet.
- (2) Die zu Beginn eines Kapitels aufgeführten Personen haben meine Arbeit in der beschriebenen Weise unentgeltlich unterstützt.
- (3) Weitere Personen waren an der inhaltlich-materiellen Herstellung der vorliegenden Arbeit nicht beteiligt. Insbesondere habe ich hierfür nicht die entgeltliche Hilfe eines Promotionsberaters oder anderer Personen in Anspruch genommen. Niemand hat von mir weder unmittelbar noch mittelbar geldwerte Leistungen für Arbeiten erhalten, die im Zusammenhang mit dem Inhalt der vorgelegten Dissertation stehen.
- (4) Die Arbeit wurde bisher weder im In- noch im Ausland in gleicher oder ähnlicher Form einer anderen Prüfungsbehörde vorgelegt.

Regensburg, 24.05.2023

---

Evamaria Hofmann